New Theoretical Concepts for Understanding Organic Reactions

NATO ASI Series

Advanced Science Institutes Series

A Series presenting the results of activities sponsored by the NATO Science Committee, which aims at the dissemination of advanced scientific and technological knowledge, with a view to strengthening links between scientific communities.

The Series is published by an international board of publishers in conjunction with the NATO Scientific Affairs Division.

A Life Sciences **B Physics**	Plenum Publishing Corporation London and New York
C Mathematical and Physical Sciences **D Behavioural and Social Sciences** **E Applied Sciences**	Kluwer Academic Publishers Dordrecht, Boston and London
F Computer and Systems Sciences **G Ecological Sciences** **H Cell Biology**	Springer-Verlag Berlin, Heidelberg, New York, London, Paris and Tokyo

Series C: Mathematical and Physical Sciences - Vol. 267

New Theoretical Concepts for Understanding Organic Reactions

edited by

J. Bertrán
Department of Chemistry,
Universitat Autònoma de Barcelona,
Spain

and

I. G. Csizmadia
Department of Chemistry,
University of Toronto,
Canada

Kluwer Academic Publishers

Dordrecht / Boston / London

Published in cooperation with NATO Scientific Affairs Division

Proceedings of the NATO Advanced Study Institute on
New Theoretical Concepts for Understanding Organic Reactions
Sant Feliu de Guíxols, Spain
19 June – 2 July 1988

Library of Congress Cataloging in Publication Data

NATO Advanced Study Institute on New Theoretical Concepts for Understanding Organic Reactions (1988 : San Feliu de Guixols, Spain)
New theoretical concepts for understanding organic reactions / edited by J. Bertrán and I.G. Csizmadia.
p. cm. -- (NATO ASI series. Series C, Mathematical and physical sciences ; vol. 267)
"Proceedings of the NATO Advanced Study Institute on New Theoretical Concepts for Understanding Organic Reactions, Sant Feliu de Guíxols, Spain, 19 June-2 July, 1988."
Includes index.
1. Chemistry, Physical and theoretical--Congresses. 2. Chemistry, Organic--Congresses. I. Bertrán, J. (Juan), 1931- .
II. Csizmadia, I. G. III. Title. IV. Series: NATO ASI series. Series C, Mathematical and physical sciences ; no. 267.
QD476.N38 1988
547.1--dc19 89-2824

ISBN-13: 978-94-010-7539-8 e-ISBN-13: 978-94-009-2313-3
DOI: 10.1007/978-94-009-2313-3

Published by Kluwer Academic Publishers,
P.O. Box 17, 3300 AA Dordrecht, The Netherlands.

Kluwer Academic Publishers incorporates the publishing programmes of
D. Reidel, Martinus Nijhoff, Dr W. Junk and MTP Press.

Sold and distributed in the U.S.A. and Canada
by Kluwer Academic Publishers,
101 Philip Drive, Norwell, MA 02061, U.S.A.

In all other countries, sold and distributed
by Kluwer Academic Publishers Group,
P.O. Box 322, 3300 AH Dordrecht, The Netherlands.

printed on acid free paper

All Rights Reserved
© 1989 by Kluwer Academic Publishers
Softcover reprint of the hardcover 1st edition 1989

No part of the material protected by this copyright notice may be reproduced or utilized in any form or by any means, electronic or mechanical, including photocopying, recording or by any information storage and retrieval system, without written permission from the copyright owner.

TABLE OF CONTENTS

Foreword vii
Organizing Comittees ix
List of Lecturers and Tutors xi
List of Participants xv

I.G. Csizmadia
Multidimensional theoretical stereochemistry and conformational potential energy surface topology 1

H. Bernhard Schlegel
Some practical suggestions for optimizing geometries and locating transition states 33

Paul G. Mezey
Reaction topology and quantum chemical molecular design on potential energy surfaces 55

Paul G. Mezey
Topology of molecular shape and chirality 77

M.A. Robb and F. Bernardi
Adiabatic and diabatic surfaces in the treatment of chemical reactivity. I. Theory 101

F. Bernardi, M. Olivucci and M.A. Robb
Adiabatic and diabatic surfaces in the treatment of chemical reactivity. II. An illustrative application to the Diels Alder reaction 147

Sason S. Shaik
A qualitative valence bond model for organic reactions 165

Jean Louis Rivail
Solvent effects on potential energy surfaces and chemical kinetics 219

Juan Bertran
Modifications of potential energy surfaces by solvation and catalysis 231

F.A. Gianturco
Computational tests of potential energy surfaces from dynamical properties 257

Susan C. Tucker and Donald G. Truhlar
Dynamical formulation of transition state theory: variational transition states and semiclassical tunneling 291

William H. Miller
Theoretical models for reaction dynamics in polyatomic molecular systems 347

A. Bottoni, M. Duran, J.M. Lluch and M.R. Peterson
Practical applications of new theoretical concepts in organic chemistry 373

Subject Index 387

FOREWORD

People who attended the NATO Advanced Study Institute (ASI) entitled NEW THEORETICAL CONCEPTS FOR UNDERSTANDING ORGANIC REACTIONS held at Sant Feliu de Guíxols on the Costa Brava of Spain had a unique experience. They have seen the evolution of the field from qualitative arguments through the generation of Potential Energy Surfaces (PES) to the use of PES in molecular dynamics. The excellent lectures that were dedicated to the various aspects of Potential Energy Surfaces clearly revealed a colossal amount of material that represents our current understanding of the overall problem. It is our hope that the present volume will recreate the excitement in the readers that we all experienced during the meeting in Spain.

One can say, without too much exaggeration, that chemistry has become and exercise on potential energy surfaces (PES). Structural (position of the energy minima), spectroscopic (vicinity around the minima), and reactivity (reaction path along the surface) properties may be determined from the analysis of PES. New theoretical tools, together with recent developments in computer technology and programming, have allowed to obtain a better knowledge of these surfaces, and to extract further chemical information from them, so new horizons have been added to Theoretical Organic Chemistry.

This book collects contributions that review the latest advances of theoretical concepts for the study of organic reactions in terms of mathematical, computational and interpretative methods. In particular, it collects topics such as interpretation of PES, computation of stationary points, diabatic and adiabatic PES, reaction topology, solvent effect and catalysis, reactivity patterns, validity of transition state theory, molecular dynamics and reaction path models.

Needless to say, the success of any International Meeting depends on a number of people, and the present ASI is no exception. This meeting highly succeeded owing to the hard work of the members of the International and Local Organizing Commitees, to the bright interventions of Lecturers and Tutors, and to the huge enthousiasm exhibited by all Participants. We must thus thank very much all those people. Last but not least, we must thank especially NATO for its sponsorship and for providing the financial support required to complete successfully this Advanced Study Institute.

J. Bertrán
I. G. Csizmadia

November 10, 1988

INTERNATIONAL ORGANIZING COMMITTEE

Prof. Juan BERTRAN	Departament de Química Facultat de Ciències Universitat Autònoma de Barcelona 08193 Bellaterra (Barcelona) SPAIN
Prof. Paul G. MEZEY	Department of Chemistry University of Saskatchewan Saskatoon, Saskatchewan CANADA S7B 0W0
Prof. Michael A ROBB	Department of Chemistry King's College London Strand London WC2R 2LS England
Prof. Antonio OLIVA	Departament de Química Facultat de Ciències Universitat Autònoma de Barcelona 08193 Bellaterra (Barcelona) SPAIN

LOCAL ORGANIZING COMMITTEE

Prof. Juan BERTRAN
Prof. Antonio OLIVA
Dr. José Mª LLUCH
Dr. Miquel DURAN
Dr. Agustí LLEDOS
Ms. Angels GONZALEZ-LAFONT
Ms. Mariona SODUPE
Mr. Miquel SOLA
Ms. Joana MARTINEZ, Secretary

LIST OF LECTURERS

Prof. Fernando BERNARDI	Dipartamento di Chimica Universita di Bologna Via Selmi, 2 40126 BOLOGNA ITALY
Prof. Juan BERTRAN	Departament de Química Facultat de Ciències Universitat Autònoma de Barcelona 08193 Bellaterra (Barcelona) SPAIN
Prof. Imre G. CSIZMADIA	Department of Chemistry University of Toronto 80, St. George Street Toronto, Ontario CANADA M5S 1A1
Prof. Franco A. GIANTURCO	Dipartimento di Chimica Universita di Roma "La Sapienza" Città Universitaria 008185 Roma ITALY
Prof. Paul G. MEZEY	Department of Chemistry University of Saskatchewan Saskatoon, Saskatchewan CANADA S7N 0W0
Prof. William H. MILLER	Department of Chemistry University of California Berkeley, California 94720 USA
Prof. Jean-Louis RIVAIL	Laboratoire de Chimie Théorique Université de Nancy I B.P. 239 54506 Vandoeuvre-Les-Nancy Cedex FRANCE

Prof. Michael A. ROBB

Department of Chemistry
King's College London
Strand
London WC2R 2LS
ENGLAND

Prof. SASON S. SHAIK

Department of Chemistry
Ben-Gurion University
of the Negev
P.O.B. 653
Beer-Sheva 84105
ISRAEL

Prof. H. Bernhard SCHLEGEL

Department of Chemistry
Wayne State University
Detroit, Michigan 48202
USA

Prof. Paul v.R. SCHLEYER

Institüt für Organische
Chemie
Universität Erlangen
-Nürnberg
Henkestrasse, 42
8520 Erlangen
FED. REP. GERMANY

Prof. Donald G. TRUHLAR

Department of Chemistry
University of Minnesota
207, Pleasant Street S.E.
Minneapolis,
Minnesota 55455
USA

LIST OF TUTORS

Dr. Andrea BOTTONI

Dipartimento di Chimica
Universitá di Bologna
Via Selmi, 2
40126 Bologna
ITALY

Dr. Miquel DURAN

Departament de Química
Facultat de Ciències
Universitat Autònoma de Barcelona
08193 Bellaterra (Barcelona)
SPAIN

Dr. José Mª LLUCH

Departament de Química
Facultat de Ciències
Universitat Autònoma de Barcelona
08193 Bellaterra (Barcelona)
SPAIN

Dr. Mike R. PETERSON

Department of Chemistry
University of Toronto
Toronto, Ontario M5S 1A1
CANADA

ADVANCED STUDY

LIST OF PARTICIPANTS

Mr. Carlo ADAMO	Dipartimento de Chimica Universitá di Napoli Via Mezzocanone, 4 80134 Napoli ITALY
Mr. Manuel ALCAMI	Departamento de Química (C-XIV) Universidad Autónoma de Madrid Cantoblanco 28049 MADRID SPAIN
Dr. Pietro AMODEO	Dipartimento de Chimica Universitá di Napoli Via Mezzocanone, 4 80134 Napoli ITALY
Dr. Juan ANDRES	Departament de Química Física Universitat de València Dr. Moliner, 50 46100 Burjassot (València) SPAIN
Dr. Janos G. ANGYAN	Chinoin Research Centre P.O. BOX 110 H-1325 Budapest HUNGARY
Mr. Luis ARNAUT	Departamento de Química Universidade de Coimbra 3045 Coimbra PORTUGAL
Dr. Gustavo ARTECA	Department of Chemistry University of Saskatchewan Saskatoon, Saskatchewan CANADA S7N 0W0
Dr. Carmen BARRIENTOS	Departamento de Química Física Facultad de Ciencias Universidad de Valladolid 47005 Valladolid SPAIN

Dr. Jean-Claude BARTHELAT	Université Paul Sabatier 118, route de Narbonne 31062 Toulouse Cedex FRANCE
Ms. Laura BONATI	Dipartimento di Chimica Fisica Universitá di Milano Via Golgi, 19 20133 Milano ITALY
Ms. Michelle CARNELL	Lehrstuhl für Theoretische Chemie Universität Bonn Wegelerstrasse 12 D-5300 Bonn F.R. GERMANY
Dr. Allen CLABO	Institüt für Organische Chemie Universität Erlangen-Nürnberg Henkestrasse 42 D-8520 Erlangen F.R. GERMANY
Ms. M. N. D. S. CORDEIRO	Faculdade de Ciências Universidade do Porto Praça Gomes Teixeira 4000 Porto PORTUGAL
Ms. Betty COUSSENS	Department of Chemistry University of Leuven Celestijnenlaan 200F 3030 Heverlee BELGIUM
Mr. Gary FOX	Department of Chemistry Wayne State University Detroit, Michigan 48202 USA
Dr. Franca FRATERNALI	Dipartimento di Chimica Universitá di Napoli Via Mezzocanone 4 80134 Napoli ITALY

Dr. J. Luis GARCIA de PAZ	Departamento de Química (C-XIV) Universidad Autónoma de Madrid Cantoblanco 28049 Madrid SPAIN
Dr. Carlo GATTI	Dipartimento di Chimica Fisica Centro del C.N.R. Via Golgi, 19 20133 Milano ITALY
Dr. José A.N.F. GOMES	Faculdade de Ciências Universidade do Porto Praça Gomes Teixeira 4000 Porto PORTUGAL
Dr. Alfonso HERNANDEZ-LAGUNA	Instituto de Estructura de la Materia Serrano, 119 28006 MADRID SPAIN
Dr. Miriam KARNI	Technion Israel Institute of Technology Haifa 32000 ISRAEL
Dr. Alessandro LAMI	Istituto di Chimica Quantica Via Risorgimento 35 56100 Pisa ITALY
Dr. Antonio LARGO-CABRERIZO	Departamento de Química Física Facultad de Ciencias Universidad de Valladolid 47005 Valladolid SPAIN
Dr. Adriana LISINI	Dipartimento di Scienze Chimiche Universitá di Trieste Piazzale Europa, 1 34127 Trieste ITALY

Dr. Rafael LOPEZ-FERNANDEZ	Departamento de Química (C-XIV)) Universidad Autónoma de Madrid Cantoblanco 28049 Madrid SPAIN
Mr. John F. MARCOCCIA	Department of Chemistry University of Toronto Toronto, Ontario CANADA M5S 1A1
Ms. Maria-Isabel MENENDEZ	Departamento de Química Física Universidad de Oviedo 33007 OVIEDO SPAIN
Ms. Camilla MINICHINO	Istituto di Chimica Universitá della Basilicata Via Nazario Sauro, 85 85100 Potenza ITALY
Mr. Victor M.S. MORAIS	Av. Inf. D. Henrique 450 4400 Vila Nova de Gaia PORTUGAL
Dr. Giorgio MORO	Dipartimento di Chimica Fisica Universitá di Milano Via Golgi, 19 20133 Milano ITALY
Mr. Ricardo A. MOSQUERA	Departamento de Química Física Facultad de Química Av. de las Ciencias 15706 Santiago de Compostela SPAIN
Ms. Fabrizia NEGRI	Dipartimento di Chimica Universitá di Bologna Via Selmi, 2 40126 Bologna ITALY

Dr. Mint-Tho NGUYEN	Department of Organic Chemistry University of Groningen Nijenborgh 16 9747 AG Groningen THE NETHERLANDS
Dr. Cemil ÖGRETIR	Department of Chemistry Faculty of Arts and Sciences Anadolu University 26470 Eskisehir TURKEY
Mr. Massimo OLIVUCCI	Dipartimento di Chimica Universitá di Bologna Via Selmi, 2 40126 Bologna ITALY
Dr. Fulvia ORSINI	Dipartimento di Chimica Organica C.N.R. Via Venezian, 21 20133 Milano ITALY
Mr. Alberto A.C.C. PAIS	Departamento de Química Universidade de Coimbra 3049 Coimbra PORTUGAL
Mr. Juan-Luis PASCUAL-AHUIR	Departamento de Química Física Universitat de València Dr. Moliner, 50 46100 Burjassot (València) SPAIN
Dr. Demetrio PITEA	Dipartimento di Chimica Fisica Universitá di Milano Via Golgi, 19 20133 Milano ITALY
Dr. José-Joaquín QUIRANTE	Departamento de Química Física Universidad de Málaga Campus de Teatinos 29071 Málaga SPAIN

Dr. Sachchida N. RAI	Theoretische Chemie Bergische Universität Gauss Str. 20 5600 Wuppertal F.R. GERMANY
Mr. Willi REUTER	Lehrstühl für Theoretische Chemie Universität Bonn Wegelerstrasse 12 D-5300 Bonn F.R. GERMANY
Dr. Isabel ROZAS	Instituto de Química Médica Juan de la Cierva, 3 28006 Madrid SPAIN
Ms. Beverly A. RUF	Department of Chemistry University of California Berkeley, California 94720 USA
Dr. Enrique SÁNCHEZ-MARCOS	Departamento de Química Física Universidad de Sevilla Tramontana, s/n 41012 Sevilla SPAIN
Mr. Ramón SAYÓS	Departament de Química Física Universitat de Barcelona Av. Diagonal, 647 08028 Barcelona SPAIN
Dr. Guido SELLO	Dipartimento di Chimica Organica Università di Milano Via Venezian 21 20133 Milano ITALY
Dr. Thomas SCHÖNHERR	Institut für Theoretische Chemie Universitätsstr. 1 D-4000 Düsseldorf F.R. GERMANY

Mr. Hanoch SENDEROWITZ	School of Chemistry Tel-viv University Ramat-Aviv 69978 Tel-Aviv ISRAEL
Ms. Suzi TUCKER	Department of Chemistry University of Minnesota 207 Pleasant Street S.E. Minneapolis, Minnesota 55455 USA
Dr. Jesús M. UGALDE	Kimika Fakultatea Euskal Herriko Unibertsitatea Posta Kutxa 1072 20080 Donostia SPAIN
Dr. Petros VALTAZANOS	National Hellenic Research Foundation 48, Vas. Constantinou Athens 11635 GREECE
Ms. Corinne VAUGHAN	King's College Strand London WC2R 2LS ENGLAND
Mr. Saulo VAZQUEZ	Departamento de Química Física Universidad de Santiago Av. de las Ciencias s/n 15706 Santiago de Compostela SPAIN
Mr. Malte von ARNIM	Lehrstuhl für Theoretische Chemie Universität Bonn Wegelerstrasse 12 D-5300 Bonn F.R. GERMANY
Mr. Peng WANG	Department of Chemistry University of California Berkeley, California 94720 USA
Dr. Ian WILLIAMS	School of Chemistry University of Bristol Bristol BS8 ITS ENGLAND

MULTIDIMENSIONAL THEORETICAL STEREOCHEMISTRY AND CONFORMATIONAL POTENTIAL ENERGY SURFACE TOPOLOGY

I.G. Csizmadia
Department of Chemistry
University of Toronto
Toronto, Ontario
Canada MSS 1A1

ABSTRACT. Since a conformational process involves the rearrangement of the atomic nuclei coupled with the redistribution of electron density, conformational potential energy surfaces are offered as prototypes for reactive potential energy surfaces.

After some brief historic interaction it is demonstrated that in an "ideal" case one dimensional conformational analysis can be extended to a multidimensional stereochemistry in terms of conformational potential energy surface topology.

In a "non-ideal" case, where excessive attractive or repulsive interactions occur upon substitution, critical points are either "created" or "annihilated" with respect to an "ideal system" and therefore the conformational potential energy surface topology is modified.

Introduction

Many times, a mathematical object has been proved to be invaluable in advancing our chemical understanding, even if that mathematical object represented an over-simplification of reality. Take for example the Atomic Orbitals (AO). They are, by every definition, mathematical objects. They are the numerical solutions for the atomic Hartree-Fock equations. This means that they are the result of a mathematical simplification where a one-electron problem (Hartree-Fock equation) is solved instead of a many-electron problem (Schrodinger equation). The atomic orbitals, or single-centered one-electron functions, are nevertheless bona fide, genuine mathematical objects. We may use, from time to time, these mathematical objects to construct multi-centered one-electron functions or molecular orbitals (MO), by linear combinations, or we may construct from these atomic orbitals

J. Bertrán and I. G. Csizmadia (eds.),
New Theoretical Concepts for Understanding Organic Reactions, 1–31.
© 1989 by Kluwer Academic Publishers.

valence bond (VB) structures in the form of Slater determinants. Nevertheless, in all these activities we treat these atomic orbitals (AO) as mathematical objects. However, beyond these practical utilities, atomic orbitals serve, additional, conceptual purposes.

Chemists have gotten a lot of mileage out of the concept of atomic orbitals during the past several decades. The concept of orbital overlap in determining bond strength, orbital ionization potentials in identifying various excited states of ions and orbital symmetries in formulating selection rules for electronic excitations are only a few of the most prominent examples. Similarly, molecular orbitals are used in assigning molecular electronic transitions as well as molecular ionization states, not to mention the orbital symmetry rules of Woodward and Hoffmann. All in all, orbitals have been more than just mathematical objects in the past several decades. They in fact, became the conceptual tools of chemists in advancing our understanding in numerous areas of chemistry.

Similarly, we may consider potential energy surfaces as mathematical objects. Potential energy surfaces are the artifacts of the Born-Oppenheimer approximation. When one solves the combined electronic and nuclear Schrodinger equation one obtains only energy levels. However, in the fixed nuclear approximation the potential energy surface, as function of nuclear motion, emerges. So, for all practical purposes the potential energy surface is a mathematical object that is the result of a mathematical simplification of the overall problem. Yet, in the conceptual sense a potential energy surface is more than a mathematical object.

In fact, we might say, without too much exaggeration, that chemistry became an exercise on potential energy surfaces. When, for example, a synthetic organic chemist isolates a certain new compound he proves that a minimum exists for the molecular composition of that molecule he isolated. When the X-ray crystallographic determines its molecular structure it identifies the position of the minimum on that potential energy surface by the molecular geometry. When a vibrational spectroscopist analyses the ir spectrum of a certain new compound, he determines the steepness of the potential energy surface around its minimum. If the molecule exists in another isomeric form then we know that the surface must have another minimum. When the thermodynamicist determines the equilibrium constant for the isomerization as the function of temperature then he can make a statement about the relative stabilities of the two isomers. When the physical organic chemist is studying the isomerization reaction of that certain new compound, he is making an exercise on that potential energy surface. Through his kinetic measurements he may determine the height of the barrier that exists between the initial minimum and the minimum associated with the product. In his mechanistic statement he may refer to the path that inter-connects these two minima and passes through one or more transition states (saddle points) of the potential energy surface. All of these are events on a particular electronic ground potential energy surface. Spectroscopists, however, studying the electronic uv-vis spectra of that certain new organic compound, are really investigating the transition from its electronic ground potential energy surface to

some low lying electronic excited state potential energy surfaces. Finally, photo-chemists are studying reaction paths involving at least two (the ground and excited) potential energy surfaces of that system. All in all, most chemical phenomena is best understood in terms of potential energy surfaces. It is not surprising therefore that Conformational Analysis is no exception.

Conformational Potential Energy surfaces however, have importance beyond their immediate utility in Organic Chemistry. On the one hand they represent stepping stones towards conformational problems of biomedical interest such as protein foldings. On the other hand they represent prototypes for reactive potential energy surfaces. In any chemical reaction the nuclei undergo geometrical rearrangement which is coupled with the rearrangement of the electron distribution. This is also true for conformational changes and that is the reason why they might be treated as prototypes for reactive changes. The difference lies in the degree of electronic rearrangement. In a conformational process the redistribution of electron density is relatively small and, apart from a relatively few cases, no electron pairs are impaired. This is not true in general for a reactive process.

Of course there are boundary cases for both of these classes. An exception is, from the conformational change, the cis-trans isomerization of ethylene which does involve the impairing of the Π-electron pair. In contrast to this the proton transfer reaction as well as many other simple reactive processes conserve the electron pairing scheme. Consequently, we might say that conformational potential energy surfaces do represent prototypes of reactive potential energy surfaces as their differences lie mostly in the degree of redistribution of electron density.

Brief historical background

Ever since 1964 my research group has been concerned with problems of theoretical organic chemistry that could be described in terms of potential energy hypersurfaces, or their cross sections: potential energy surfaces and potential energy curves. One of our earliest pieces of work was associated with the pyramidal inversion of $:CH_3^-$.

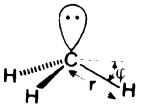

We have found that the potential energy curve $E = E(\varphi)$ that takes energy as a function of deviation from coplanarity (φ) does not describe well enough the chemical reality. A potential energy surface $E = E(\varphi, r)$ in which both out-of-plane bend (φ) and C-H bond stretch (r) are involved is far more descriptive than a rigid cross-section, $E = E(\varphi)$, of this surface. This potential energy surface, $E=E(\varphi, r)$,

clearly indicated that the C-H bond length is considerably shorter in the planar conformation than it is in the pyramidal form. In other words the reaction coordinate is not a straight line as illustrated in Figure 1.

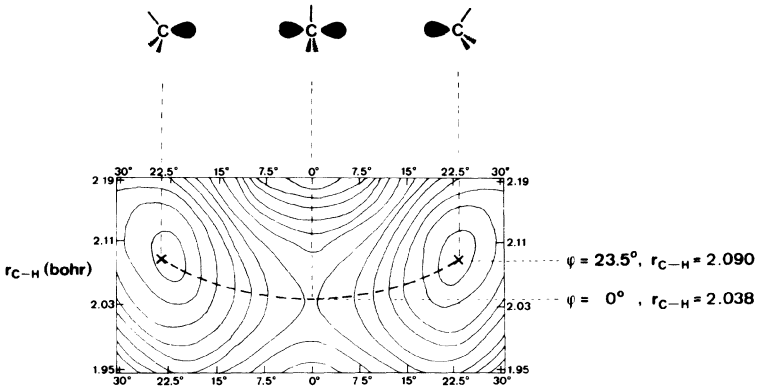

Figure 1. Inversion-stretching potential energy surface, E = (φ, r), for $:CH_3^-$

Our preliminary results were first presented (1, 2) in 1967 but the final details were not published (3) until 1969. Later on, substituted methyl anions, $H_2C\text{-}X^-$ were investigated, generating rotation-inversion surfaces. In the case of the methoxide anion tautomer: $H_2C\text{-}OH^-$ (4) the pyramidal inversion coordinate at carbon was augmented with rotation (torsion) about the C-O bond (θ) and the situation was analogous in the case of $H_2C\text{-}NO_2^-$ (5), generating potential energy surfaces of the type: E = E(φ, θ). Also, the inversion of NH_3 (being iso-electronic and iso-protic to $:CH_3^-$) was investigated (6) and a rotation-inversion potential energy surface, E = E(γ, θ), of its substituted derivative (7) has been studied in some details:

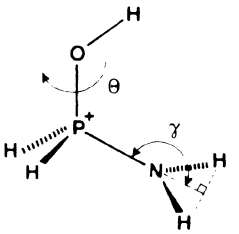

Beyond potential energy surfaces, we initiated the study of potential energy hyper-surfaces over a decade ago. Our preliminary results were presented (8) in 1976, and the final work was published (9) in 1978. The subject of this research was the determination of the complete torsional hypersurface of n-butane for the first time.

By today, "Theoretical Stereochemistry" (10) and "Theoretical Conformational Analysis" (11) have grown to a huge enterprise which is impossible to review in anything less than a whole book. What is hoped to be achieved in the next few pages is to demonstrate how potential energy surfaces can be analysed for the determination of crucial

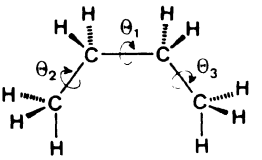

conformations (stationary or critical points of the surface) and how stereochemical rules might emerge from the topology of conformational potential energy surfaces. The work reported here is at the ab initio SCF level of quantum chemistry.

Molecular Geometry Optimization

It is perhaps of some value to look at the properties of the various critical points associated with a given potential energy surface before we touch on the optimization methods that may be applied for the determination of molecular conformations. Let us take the one-dimensional case, where energy (E) is a function of a single variable, a torsional angle, (θ) such a potential curve has two types of critical points: minima and maxima. In a quadradic representation the minima and maxima have the same explicit form but in the former case the force constant (k) is positive and in the latter case the force constant is negative. The quadratic functions as well as the characteristics of the first and second derivatives are shown in Figure 2. The number of negative second derivatives is normally referred to as the index (λ) of the critical point and, as can be seen in Figure 2, $\lambda = 0$ for a minimum and $\lambda = 1$ for a maximum. For a two dimensional case, whose energy (E) is a function of two torsional variables, θ_1 and θ_2),

$$E = E(\theta_1, \theta_2),$$

there are three types of critical points: minima ($\lambda = 0$), saddle points ($\lambda = 1$) and maxima ($\lambda = 2$) as depicted in Figure 3.

For a potential energy hypersurface of three independent variables:

$$E = E(\theta_1, \theta_2 \cdot \theta_3)$$

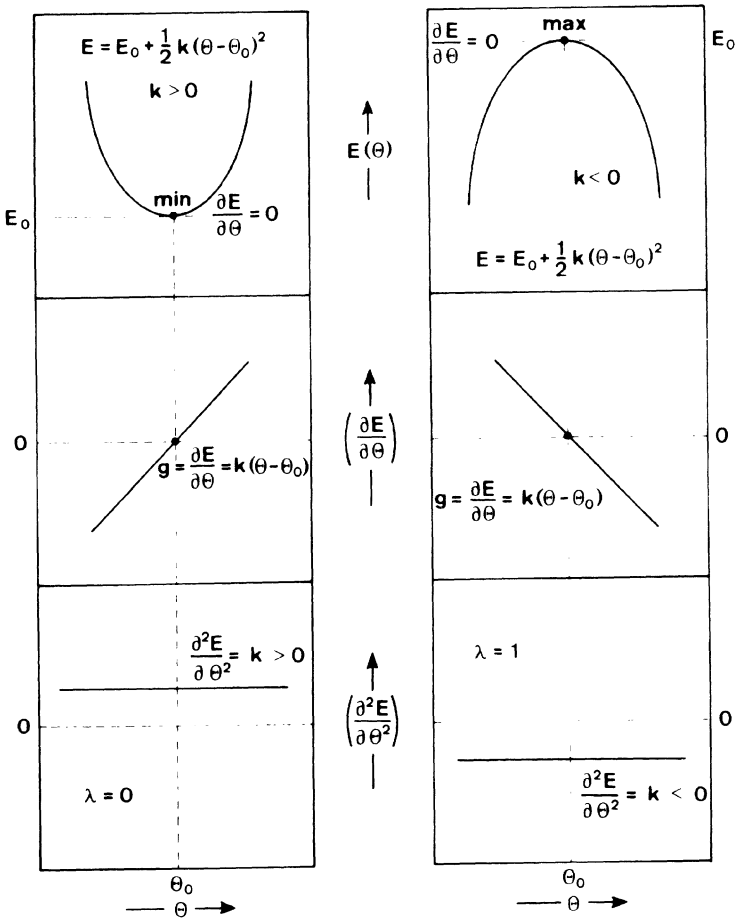

Figure 2. Characteristics of minima and maxima of a potential energy curve. Note that g is the gradient, k is the force constant of the potential energy function and λ is the index of the critical point in question.

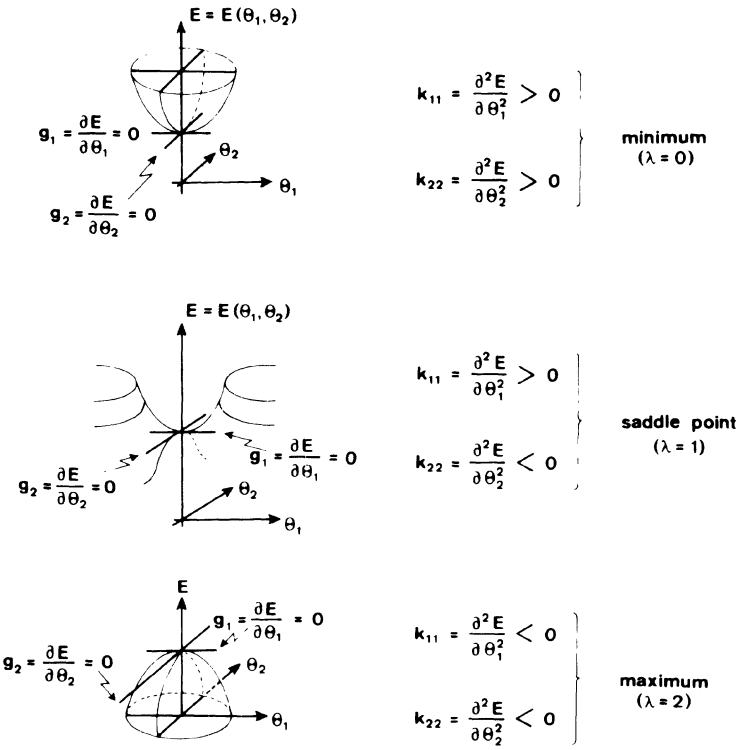

Figure 3. Three types of critical points of a potential energy surface and their characteristics in terms of second partial derivatives. The index (λ) of a critical point is the number of negative second derivatives.

there are four types of critical points: minima (λ= 0), 1st order or normal saddle points (λ = 1), 2nd order or supper saddle points (λ= 2) and maxima (λ = 3). The situation is summarized in Table 1.

As can be generalized from Figures 2 and 3, at a minimum of a potential energy surface of any dimension the gradient vector length (F) is zero by definition:

$$F = \sum_{i=1}^{\substack{\text{all}\\\text{modes}}} \left(\frac{\partial E}{\partial \theta_i}\right)^2 = \sum_{i=1}^{\substack{\text{all}\\\text{modes}}} g_i^2 = 0$$

At a point somewhat away from the minimum, the sum of the squares of the gradients (F) is greater than zero:

$$F = \sum_{i=1}^{\substack{\text{all}\\\text{modes}}} \left(\frac{\partial E}{\partial \theta_i}\right)^2 = \sum_{i=1}^{\substack{\text{all}\\\text{modes}}} g_i^2 = 0$$

and the minimization of F will yield the location of a critical point (minimum, saddle point, etc.). This equation forms the basis of a gradient geometry optimization algorithm since the gradients of the energy can be computed analytically at the SCF level (12).

This method is called the "Sum of Squares" of the Gradients" method (13), and although it can be used for the location of minima (reactants, products and reactive intermediates) its real value is in the search for the location of saddle points (transition states).

The second derivatives of E with respect to θ that in fact corresponds to the force constants (k) may be estimated numerically as follows:

$$k_i = \frac{\partial^2 E}{\partial \theta_i^2} = \frac{\partial F}{\partial \theta_i} \approx \frac{\Delta F}{\Delta \theta_i}$$

The second partial derivatives of the energy are important for the characterization of the critical points into minima, saddle points and maxima. The number of negative second partial derivatives, called the index (λ) of the critical point, has been summarized in Table I for cases up to three independent variables. The second formalism (the variable metric method) is really suited for the location of energy minima (14). This more general method involves the use of a quadratic fit about the critical point under investigation and an iterative search for the location of the critical point in that vicinity. The iterative process is illustrated schematically in Figure 4.

Both of these methods are known, collectively, as "Direct Gradient Optimization Methods". The word "direct" implies that we do not have the SCF potential energy at our disposal, but we do know that it exists and we carry out optimization directly on this SCF surface computing the energy and their gradients point by point one after the other. Of course we must have an initial guess where the critical points are located. Unless we have pretty good chemical intuition we do not know where they are located and in fact we do not have the faintest idea how many critical points to search for!

Table I. Index, Number and type of Critical points Associated with Potential Energy Surfaces of Different Dimensions.

Index of critical point \ Type of pot. energy function	n = 1 Curve $E = E(\theta)$	n = 2 Surface $E = E(\theta_1,\theta_2)$	n = 3 Hypersurface $E = E(\theta_1,\theta_2,\theta_3)$
$\lambda = 0$	min	min	min
$\lambda = 1$	max	saddle	saddle
$\lambda = 2$	-	max	super-saddle
$\lambda = 3$	-	-	max

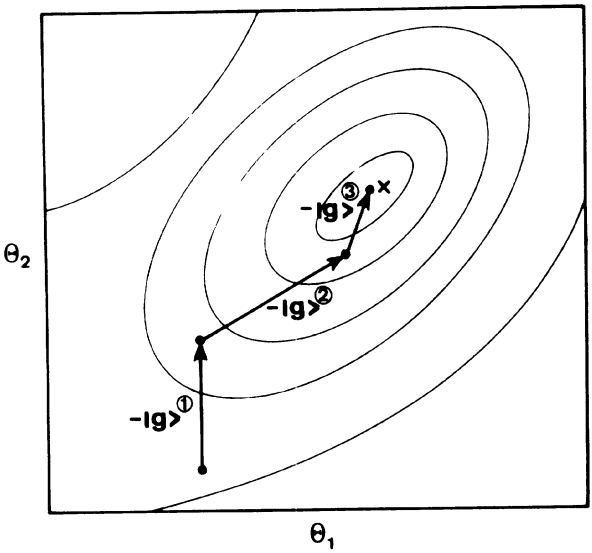

Figure 4. A schematic illustration for gradient geometry optimization on a potential energy surface of the type: $E = E(\theta_1, \theta_2)$.

In other words, direct molecular geometry optimization is not much more than a nearly blind search for critical points on an exact, but unknown, potential energy surface guided, or sometimes misguided, by chemical intuition.

For conformational analysis our chemical intuition is quite reliable, however, conceptually it does not go beyond the one-dimensional or single rotational (ie. torsional) case. On the other hand, nature very often demands from us two or three dimensional conformational analyses.

It is clear therefore that in the course of investigations of conformational potential energy surfaces and hypersurfaces, prior knowledge concerning the numbers of the various types of critical (stationary) points would be extremely useful. In particular, the number of critical points with order (index) zero, which correspond to minima or stable species, and first order saddle points, which may correspond to transition states, are of great interest to chemists. For this reason it is of some proactical value to fit, to a set of computed SCF points, an analytic function of the type:

Curve $n = 1;\ E = E_o + \sum_{i=1}^{N} c_i f_i(\theta)$

Surface $n = 2;\ E = E_o + \sum_{i=1}^{N} c_i f_{1i}(\theta_1).f_{2i}(\theta_2)$

Hyper-surface $n = 3;\ E = E_o + \sum_{i=1}^{N} c_i f_{1i}(\theta_1).f_{2i}(\theta_2).f_{3i}(\theta_3)$

The component functions, $f_i(\theta)$, usually incorporate trigonometric $\sin k\ (\theta - \theta_o)$; $\cos k(\theta - \theta_o)$ and sometimes Gaussian functions: $\exp k\ (\theta - \theta)^2$. The coefficients, c_i, are to be determined by a least square fitting method.

The location of the critical points can be determined by solving the gradient equation which in turn is readily available by analytic differentiation of the above least square fit. The gradient equation for curves (n = 1) is simply

$$\frac{dE}{d\theta} = \sum_i C_i \frac{df_i(\theta)}{d\theta} = 0$$

and analogous equations may be derived for higher dimensions (ie n > 1). The details of surface fitting has been discussed earlier (15). Determining the location of the critical points in this fashion we now have a pretty good initial guess for direct gradient optimization for the structures of significant conformations.

Topological properties of conformational potential energy surfaces

Conformational changes have one very interesting property: the independent variables $\{\theta_j\}$ are periodic, that is, after 360° rotation

by Figure 5 for the case of ethane: $H_3C\text{-}CH_3$, taking θ as the torsion about the C-C bond.

This implies that the topological object for a single variable θ is a circle or a 1-torus (Cf. Figure 6).

Using the height as the dependent variable we may find that the number of minima is one ($\beta_o = 1$) and the number of maxima is also one ($\beta_1 = 1$).

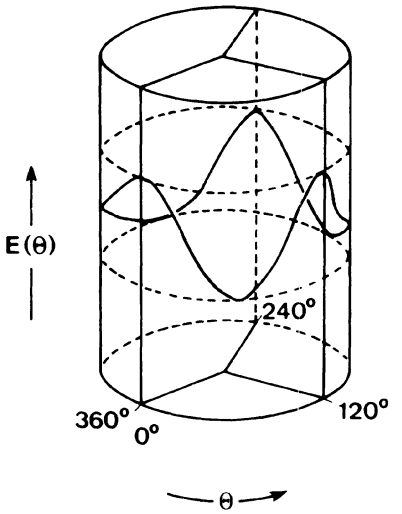

Figure 5. Cylindrical representation of the potential energy curve associated with torsion about the C-C bond in ethane.

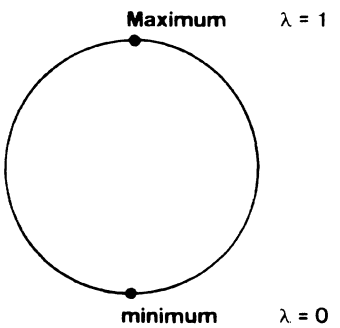

Figure 6. The topology of a circle (a 1-torus).

In the case of a surface, where energy is a function of two periodic coordinates, the surface is mapped onto a 2-torus. This

doughnut shaped object is obtained by the following procedure (see Figure 7). The planar unit cell is rolled into a horizontal cylinder,

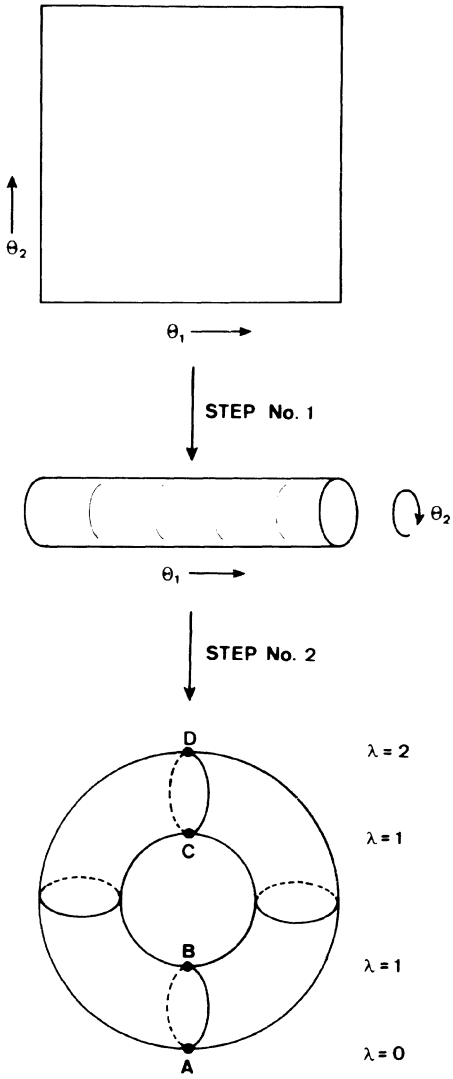

Figure 7. Procedure for mapping the planar surface unit cell onto a 2-torus. For the torus, the θ_1 coordinate may be taken as the direction A-D-A (or equivalently B-C-B) while θ_2 is defined by the orthogonal motion A-B-A or (C-D-C).

to join the top to the bottom. Next, the cylinder is stretched and bent around into a torus such that the two open ends are joined. On the 2-torus we find one minimum (A), thus $\beta_o = 1$, two saddle points (B and C), thus $\beta_1 = 2$, and one maximum (D) therefore $\beta_2 = 1$.

It is not too difficult to predict that 3-torus (a 4 dimensional object) has four types of critical points (c.f. Table 1) in the following numbers: minima: $\beta_o = 1$, normal saddle points: $\beta_1 = 3$, super saddle points: $\beta_2 = 3$ and maxima: $\beta_3 = 1$. In the language of algebraic topology these β_λ values are called Betti numbers which for the $n \leq 4$ cases are summarized in Table II.

Table II. Betti numbers for conformational potential energy surfaces up to four independent variables.

n	β_λ								
1				1		1			
2			1		2		1		
3		1		3		3		1	
4	1		4		6		4		1

Clearly the Betti numbers, for these periodic variables that lead to n-tori, are the binomial coefficients:

$$\beta_\lambda = \binom{n}{\lambda} = \frac{n!}{\lambda!(n-\lambda)!}$$

As it is clear from Table 2 an alternating sum rule is applicable to the Betti numbers:

$$\beta_0 - \beta_1 + \beta_2 - \ldots = \sum_{\lambda=0}^{n} (-1)^\lambda \beta_\lambda = 0$$

Although the Betti numbers represent the number of critical points on the n-tori the number of critical points on conformational potential energy surfaces may be different from the Betti numbers. However, there are two theorems in algebraic topology (16, 17) that are very useful (18). One of them relates the number of critical points of a conformational potential energy hypersurface (N_λ) and the Betti numbers (β_λ) in the following way:

$$N_\lambda \geq \beta_\lambda$$

The other theorem shows that the alternating sum rule that was developed for β_λ also holds for N_λ:

$$N_0 - N_1 + N_2 - \ldots = \sum_{\lambda=0}^{n} (-1)^\lambda N_\lambda$$

However, there is no statement in algebraic topology that would connect N_λ and β_λ in such ways as:

$$N_\lambda = f(\beta_\lambda)$$

or

$$N_\lambda = \kappa . \beta_\lambda$$

Any such relationship must have its root in chemistry and not in mathematics.

THEORETICAL STEREOCHEMISTRY

Molecular structures, including selected conformations, are widely referred to in the literature (19). However, even today focus is given to only one-dimensional conformational analysis (20). Now then, let us consider ethane, propane and n-butane, classic examples for single, double and triple rotors respectively, as rotation about their C-C bonds lead to potential energy curve $E = E(\theta)$, potential energy surface $E = E(\theta_1, \theta_2,)$, and potential energy hypersurface $E = E(\theta_1, \theta_2, \theta_3)$, respectively.

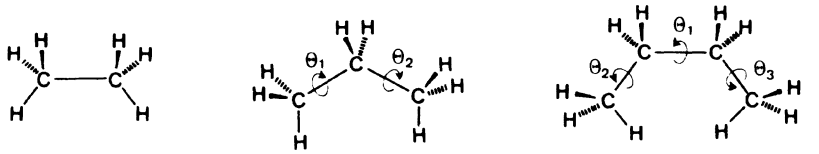

For the case of the ethane the classical potential energy curve is shown schematically in Figure 8, together with its topological pattern that is nothing more than a straight line indicating the whereabouts of of minima ($\lambda = 0$) and maxima ($\lambda = 1$). For the full cycle of 360 rotation there are 3 minima and 3 maxima (note that at the ends each maximum is counted as a half), corresponding for the three fold periodicity of the $-CH_3$ group .

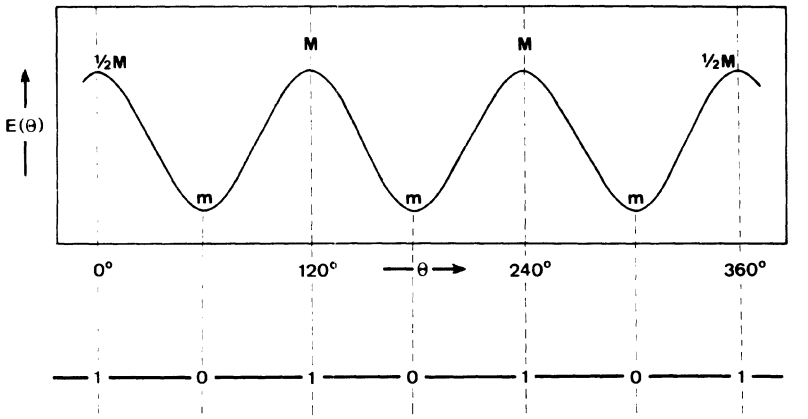

Figure 8. Potential energy curve, $E = E(\Theta)$, of ethane above and its topological representation below. On the potential energy curve m is minimum; and M is maximum; on the topological representation 0 stands for minimum (ie. $\lambda = 0$) and 1 stands maximum (ie. $\lambda = 1$).

We find therefore the following relationship between the number of critical points (N_λ) for ethane ($n = 1$) and the corresponding Betti numbers (β_λ):

λ	0	1
β_λ	1	1
N_λ	3	3

$$N_\lambda = 3\beta_\lambda$$

Thus the actual potential energy surface $E = E(\Theta_1, \Theta_2)$, for propane is depicted, for its full cycle (360°x360°) of rotation, in Figure 9 while a 120°x120° segment is shown in Figure 10 in the form of a topological diagram.

One should note again that critical points at the edges count as 1/2 and critical points at the corners count 1/4. Thus we have in this segment (Figure 10) a total of 1 minimum, 4x1/2 = 2 saddle points and 4x1/4 = 1 maximum. These numbers 1,2,1 correspond to the Betti numbers (β_λ) of the $n = 2$ case.

As far as the number of critical points (N_λ) are concerned we must realize that there are 9 such units of (120°x120°) segment in the full cycle of rotation (360°x360°) so we obtain the following relationship:

λ	0	1	2
β_λ	1	2	1
N_λ	9	18	9

$$N_\lambda = 9\beta_\lambda$$

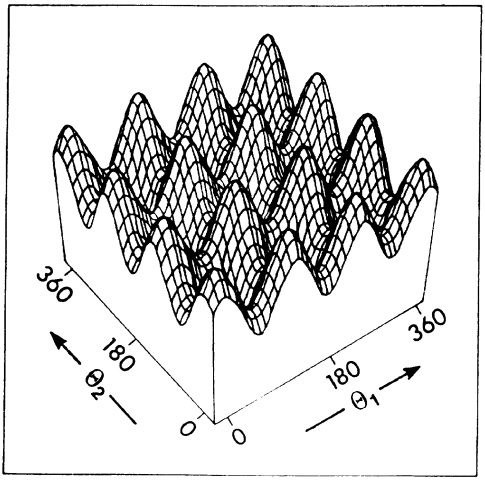

Figure 9. A pseudo three dimensional representation of the conformational potential energy surface: $E = E(\Theta_1, \Theta_2)$ of propane showing the full cycle of rotation (360°x360°).

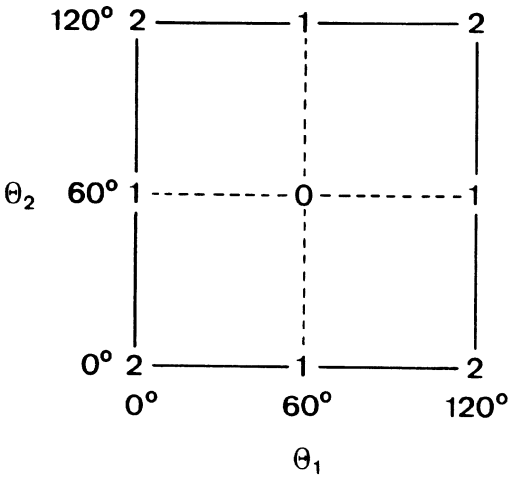

Figure 10. A topological diagram of the propane potential energy surface showing a 120°x120° segment only. 0 is a minimum (ie. $\lambda = 0$), 1 is a saddle point (ie. $\lambda = 1$) and 2 is a maximum (ie. $\lambda = 2$).

Thus for hypersurfaces, defined by three coordinates, $E = (\theta_1, \theta_2, \theta_3)$, critical points lying on faces, edges and corners count ½, ¼ and 1/8 each, respectively. This case will be illustrated by the conformational analysis of n-butane. Of course the potential energy hypersurface (a 4 dimensional object) cannot be drawn so we may only illustrate it through cross-sections.

One dimensional cross-sections, i.e. $E = E(\theta_1)$ and $E = E(\theta_2)$ of the overall potential hypersurface: $E = E(\theta_1, \theta_2, \theta_3)$ are shown in Figures 11 and 12, respectively while two dimensional cross section of the type $E = E(\theta_1, \theta_2)$ and $E = E(\theta_2, \theta_3)$ are shown in Figures 13 and 14, respectively.

From chemical intuition we may arrive at 12 critical points, 2 minima, 4 first order (or regular) saddle points, 4 second order (or super) saddle points and 2 maxima. These structures are given by Figures 15 and 16. These structures are also in agreement with classical stereochemical considerations, namely no-eclipsing yields minima, one-eclipsing yields first order (or regular) saddle points, two-eclipsings yields second order (or super) saddle points while three-eclipsings yield maxima. Fortunately, the potential energy hypersurface of n-butane is simple enough to establish this 1:1 correspondence between the structures of critical points and that of classical molecular conformations as the structures of half of the critical points are determined by symmetry alone. The geometries of these critical points as well as their relative energy values have been published elsewhere (9, 15).

The topological features of the n-butane conformational potential energy hypersurface is shown in Figure 17. Although there are only 2 unique minima, 4 unique first order saddle points, 4 unique second order saddle points and 2 unique maxima, according to Figures 15 and 16, some of these, however, occur more than once. Thus, in a unit cell, after counting the critical points correctly we have 3 minima, 9 first order saddle points, 9 super saddle points and 3 maxima. For the full rotation along all three variables: 360°x360° there are 9 unit cells so we obtain the following relationship for n = 3:

λ	0	1	2	3
β_λ	1	3	3	1
N_λ	27	81	81	27

$$N_\lambda = 27\beta_\lambda$$

Thus we may conclude for the case of saturated hydrocarbons the following relationship between β_λ and N_λ (21)

$$N_\lambda = \beta_\lambda = m^n\binom{n}{\lambda} = 3^n\binom{n}{\lambda}$$

where m happens to be equal to 3. This equation is analogous to Mezey's upper and lower bound relationship (22).

On this basis, it is not too difficult to predict the topology of the n-pentane hypersurface:

$$E = E(\Theta_1, \Theta_2, \Theta_3, \Theta_4).$$

For the full cycle of rotation (360°x360°x360°x360°) the following numbers are expected since $\kappa = m^n = 3^n = 3^4 = 81$

λ	0	1	2	3	4
β_λ	1	4	6	4	1
N_λ	81	324	486	324	81
Type of critical point	minima	1st order saddle points	2nd order saddle points	3rd order saddle points	maxima

$$N_\lambda = 81\beta_\lambda$$

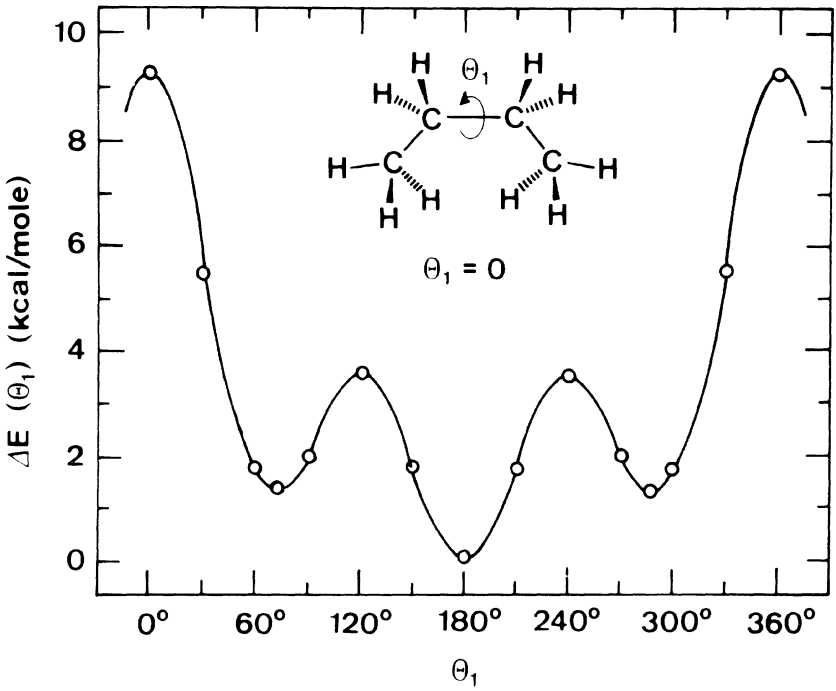

Figure 11. Potential energy for central C-C bond rotation in n-butane ($\Theta_2 = \Theta_3 = 60°$).

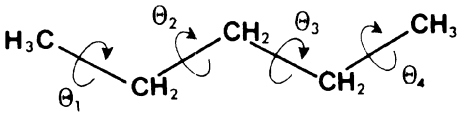

There are two points to note, one of them is associated with the actual λ values of critical points of surfaces as they related to the λ values of the component potential energy curves. Take for example a CH_3 rotation; its topology is shown by the line of Figure 18. Now, let us construct a potential energy surface that is associated with two independent CH_3 rotations (Figure 19). We may note from this figure that the index (λ) of the critical points of the surface relate through a simple additivity rule to the critical points of CH_3 rotation potential curves:

$$\lambda(\theta_1, \theta_2) = \lambda(\theta_1) + \lambda(\theta_2)$$

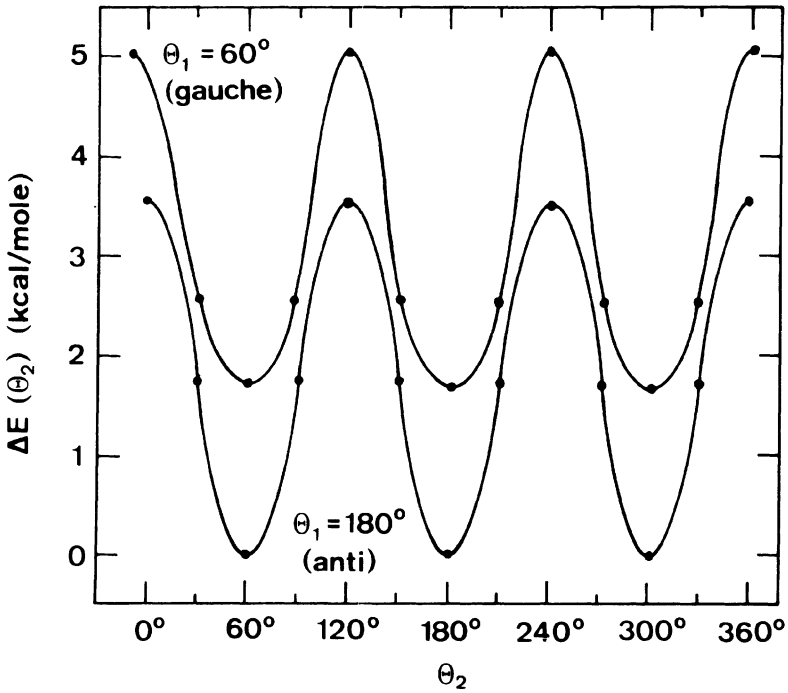

Figure 12. Potential energy curves for methyl group torsion in n-butane (θ_3 = 60°).

Three independent CH_3 rotations yield a potential energy hypersurface as may be the case for iso-butane: $(CH_3)_3CH$ (cf. Figure 20).

Note that iso-butane has a higher symmetry therefore only a 120°x120°x120° segment is illustrated. However, the potential energy hypersurface of iso-butane and that of n-butane are topologically equivalent. Again the indices of the potential energy curves are additive:

$$\lambda(\theta_1, \theta_2, \theta_3) = \lambda(\theta_1) + \lambda(\theta_2) + \lambda(\theta_3)$$

The second point to note is that a minimum is always surrounded with 1st order saddle points (transition states) for both the cases of surfaces and hypersurfaces (Figure 21A). In contrast to this is a 1st order saddle point (transition state) with $\lambda = 1$ is always surrounded by two lower level critical points ie. minima ($\lambda = 0$) and the rest of the neighbouring critical points are of one higher level, $\lambda = 1$, (ie. maximum for a surface and 2nd order or supper saddle point for a hypersurface) as shown in Figure 21B.

Considering heteroatom containing saturated systems we find that some of them follow the above rule (23). Both ethanol and ethylamine behave the same way as propane. They all have 9:18:9 critical points. Clearly this indicates that the 3^n factor originates from the number of

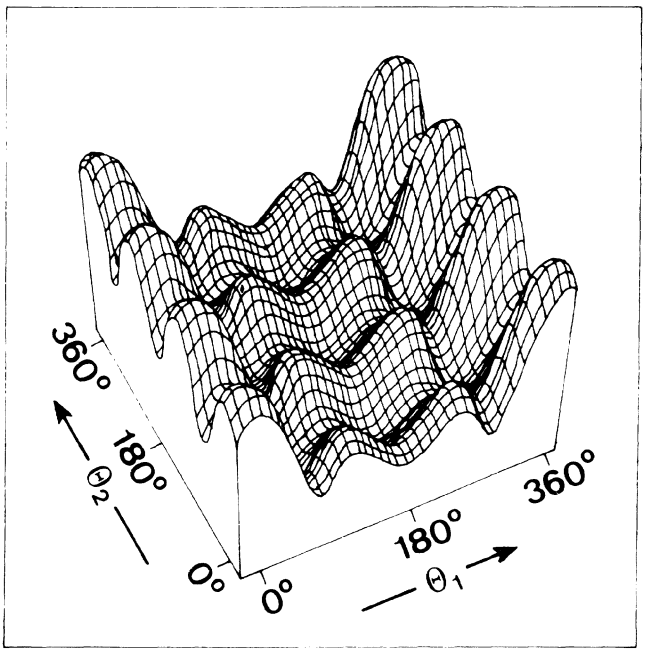

Figure 13. Cross-section $E(\theta_1, \theta_2)$ of the n-butane hyper-surface ($\theta_3 = 60°$).

bond eclipsings one makes along a full rotation and that number is 3, even for ethanol as the OH proton must eclipse with 3 other bonds (two C-H and one C-C).

However, the situation is different for systems containing two adjacent hetero atoms such as we found in methylated hydroxylamines.

In this case instead of $\kappa = m^2 = 3^2 = 9$ we have the following relationship:

$$\kappa = m_1 . m_2 = 2.3 = 6$$

The $m_1 = 2$ is clearly the result of double eclipsing when rotation is taking place about the N-O bonds, while the methyl rotation has characteristically $m_2 = 3$.

	N_0	N_1	N_2
CH_3-O-NH_2	6	12	6
HO-NH-CH_3	6	12	6

On the basis of this we may generalize the rule for hypersurfaces

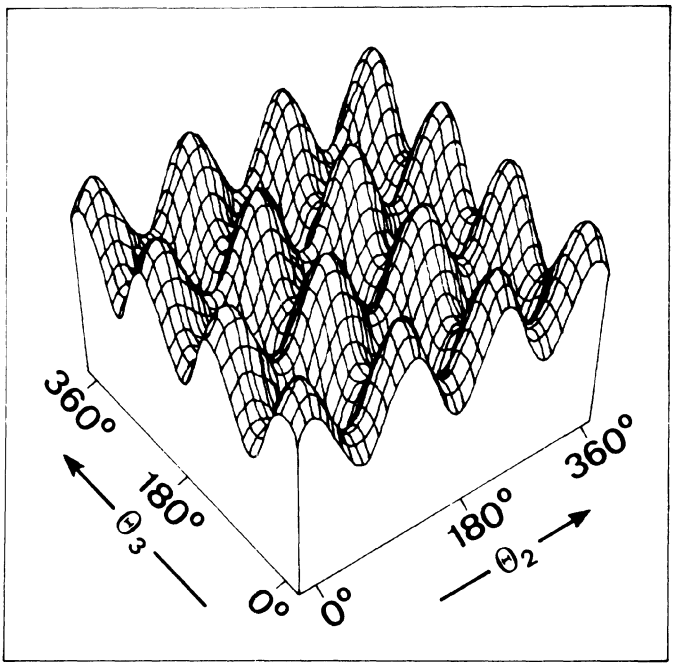

Figure 14. Cross-section $E(\Theta_2, \Theta_3)$ of the n-butane hypersurface ($\Theta_1 = 180°$).

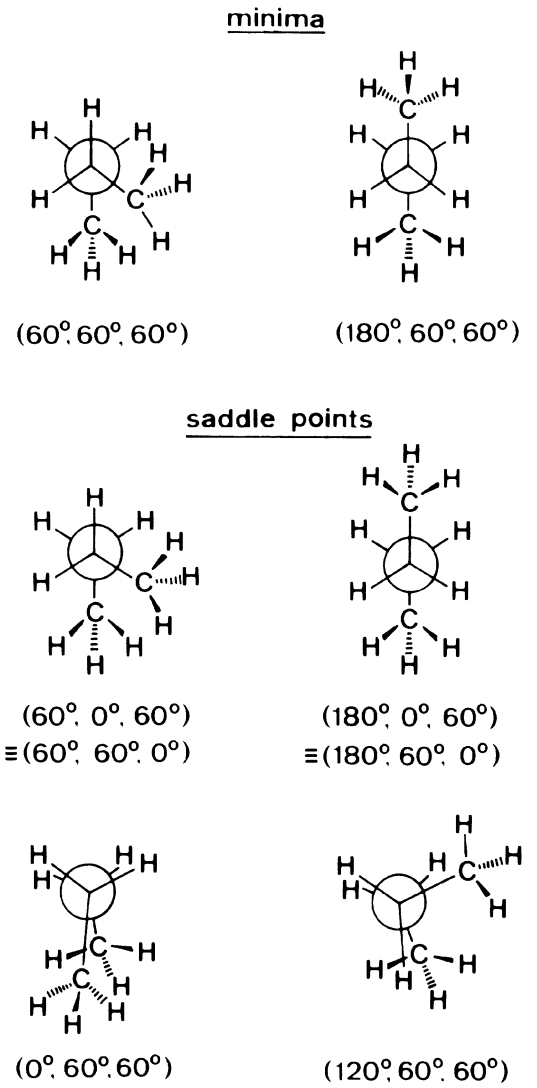

Figure 15. Intuitive structures for the minima and first order saddle points of the n-butane hypersurface.

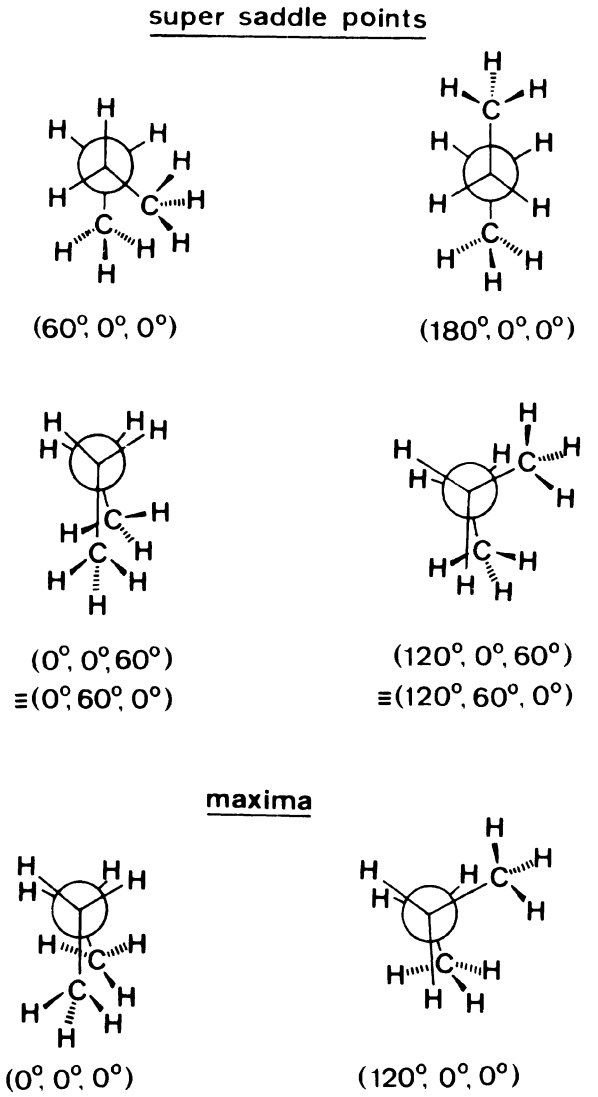

Figure 16. Intuitive structures for the second order saddle points and maxima of the n-butane hypersurface.

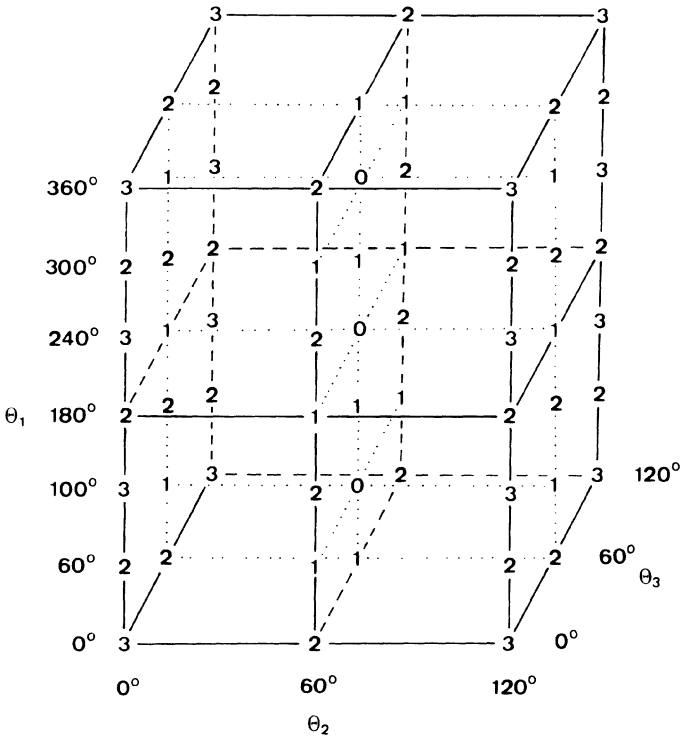

Figure 17. Unit cell for the n-butane coordinate space, showing the location and types of critical points: (0) minima, (1) first order saddle points, (2) second order saddle points, (3) maxima.

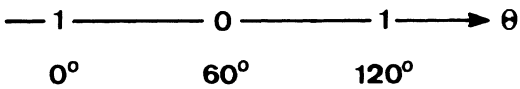

Figure 18. Topological representation of the potential energy curve for the rotation of a single CH_3 group.

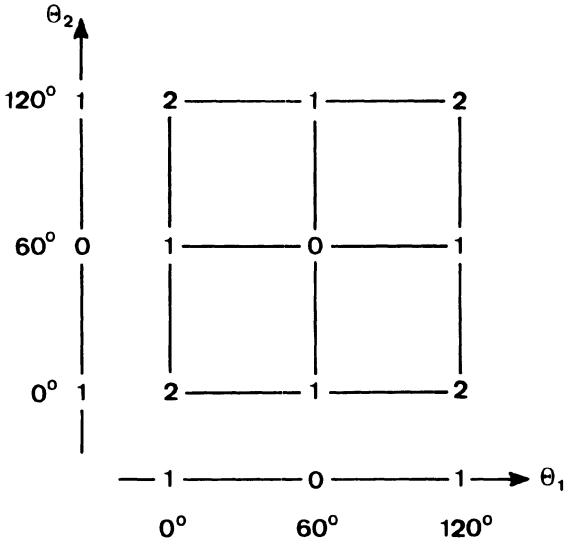

Figure 19. Topological representation of the potential energy surface for the rotation of two CH_3 groups.

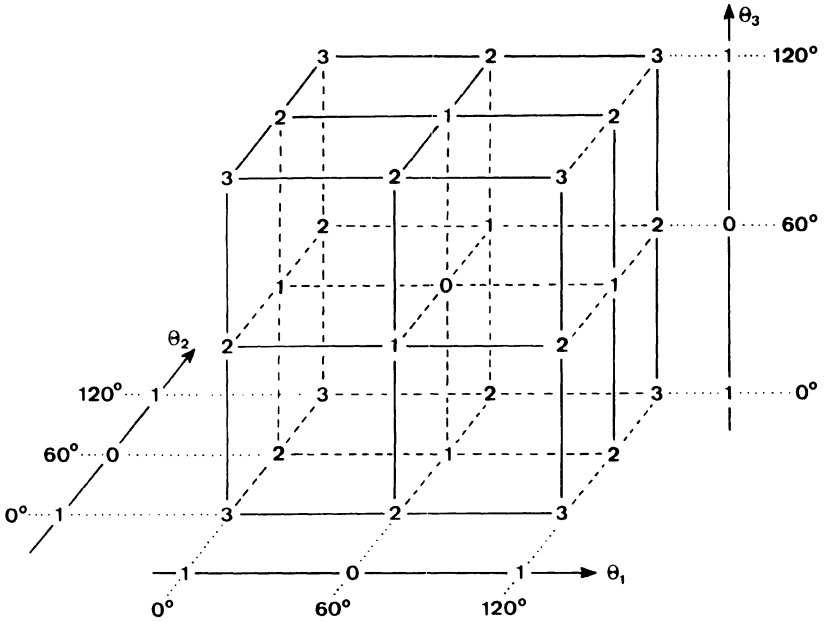

Figure 20. Topological representation of the potential energy hypersurface for the rotation of three CH_3 groups.

such as those associated with <u>dimethyl peroxides</u> and <u>dimethyl hydroxilamines</u>. Note that $m_1 = 2$ while the methyl rotations (m_2 and m_3) have three fold periodicity. Consequently,

$$\kappa = m_1 . m_2 . m_3 = 2.3.3 = 18$$

and that is expected to result in the following number of critical points for the above three potential energy hypersurfaces.

	N_0	N_1	N_2	N_3
$m_1 = 2$ CH_3-O-O-CH_3	18	54	54	18
$m_1 = 2$ CH_3-NH-O-CH_3	18	54	54	18
$m_1 = 2$ CH_3 CH_3 N-OH	18	54	54	18

In conclusion we should illustrate, with one particular system, how exceptions may occur. Consider z-3-thio-2-propenal with two torsional angles: φ and ω leading to a potential energy surface of the type: $E = E(\varphi, \omega)$.

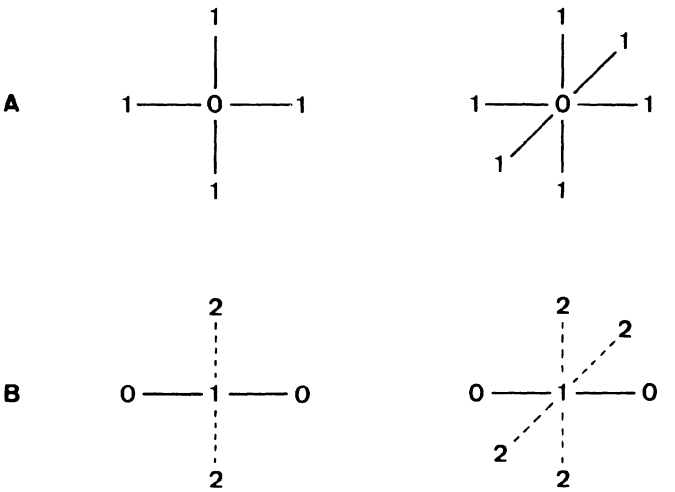

Figure 21. A. The topological environment of a 0-th order critical point (minimum).
B. The topological environment of a 1st order critical point (saddle point or transition state).
The solid lines represent reaction paths.

The topology of the potential energy curves is shown in Figure 22.

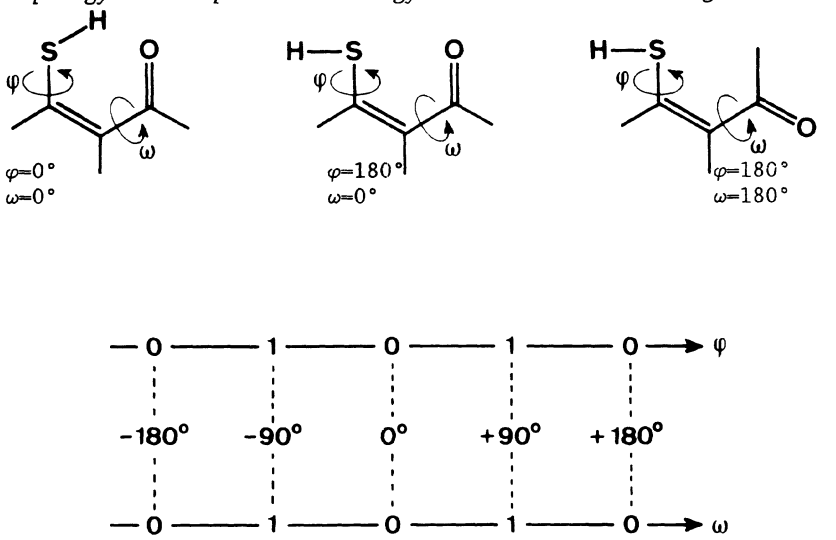

Figure 22. Topology of potential energy curves associated with torsion about the C-SH bond (φ) and about the C-CHO bond (ω) in z-thio-2-propenal.

From the additivity rule of the critical point indices

$$\lambda(\varphi.\ \omega) = \lambda(\varphi) + \lambda(\omega)$$

we may predict the topology of the conformational energy surface, $E = E(\varphi, \omega)$, which is shown in Figure 23.

Now then let us replace the mercapto hydrogen by a F atom (24). The (0,0) conformation, which is at the centre of the above topological map, becomes an antiaromatic system with 8 Π-electrons:

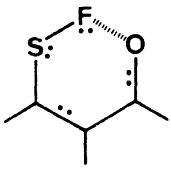

This destabilizing factor in the π-network is coupled with two other destabilizing factors in the σ-network namely lone pair - lone pair (F/O) repulsion and nuclear - nuclear (F/O) repulsion.

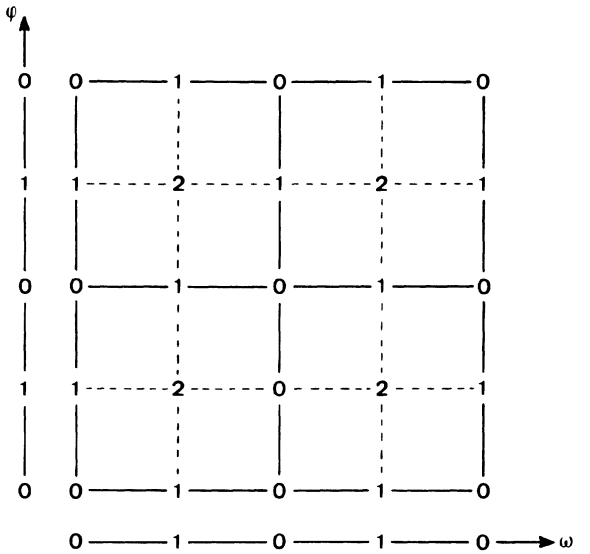

Figure 23. Topology of the potential energy surface, $E = E(\varphi.\omega)$ associated with the two independent torsions about the C-SH bond (φ) and about the C-CHO bond (ω) in (Z)-3-thio-2-propenal.

Consequently, the superimposition of these three destabilizing factors is manifested with a drastic modification of the potential energy surface. The (0, 0) conformation which used to be a minimum suddenly becomes a transition state almost as high in energy as the others. In addition, a pair of new degenerate minima appear on the surface that is a bit higher than the highest minimum. This pair of degenerate minima correspond to two equivalent non-planar structures when the F and O atoms are rotated out of the plane (φ = +31.6°, ω = +17.4° and φ = -31.6°; ω = - 17.4°). The topology of this modified potential energy surface is shown in Figure 24.

The one minimum at the centre changed to 1 transition state + 2 minima increasing the number of minima by 1 and the number of transition states also by 1. The alternating sum rule instead of

$$N_0 - N_1 + N_2 = 0$$

$$4 - 8 + 4 = 0$$

now becomes

$$5 - 9 + 4 = 0$$

therefore the rule is no longer valid

$$N_\lambda \neq \kappa\ \beta_\lambda$$

It is rewarding to see some general "pattern" to emerge from a theoretical study. However, the exceptions are more interesting than systems behaving in an ideal fashion since one might be able to learn more chemistry from the exceptions.

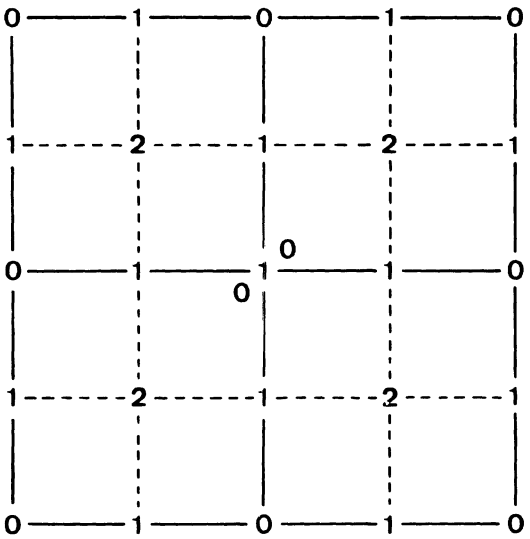

Figure 24. Topology of the potential energy surface, $E = E(\varphi, \omega)$ associated with the two independent torsions about the C-SF bond (φ) and about the C-CHO bond (ω) in (Z)-3-fluorothio-2-propenal.

A "selection rule" for the "creation" or "annihilation" of critical points on going from an "ideal" system (where the κ rule applies) to a "non-ideal" system (where the κ rule does not apply) has already been published elsewhere (25).

ACKNOWLEDGEMENTS

The research outlined in this article has been sponsored by the Natural Sciences and Engineering Research Council of Canada.

REFERENCES

1. Second Canadian Symposium on Theoretical Chemistry, Montreal, Canada, 1967.

2. R.E. Kari and I.G. Csizmadia, J.Chem.Phys. 46, 4585 (1967)

3. R.E. Kari and I.G. Csizmadia, J.Chem.Phys. 50, 1443 (1969)

4. S. Wolfe, L.M. Tel and I.G. Csizmadia, Can.J.Chem. 51, 2423 (1973)

5. P.G. Mezey, A.J. Kresge and I.G. Csizmadia, Can.J.Chem. 54, 2526 (1976)

6. R.E. Kari and I.G. Csizmadia, J.Chem.Phys. 56, 4337 (1972)
7. T.A. Modro, W.G. Lianw, M.R. Peterson and I.G. Csizmadia, J.Chem.Soc., Perkin Trans. 2, 1432 (1972)

8. International Symposium on Stereochemistry, Kingston, Canada, 1976.

9. M.R. Peterson and I.G. Csizmadia, J.Am.Chem.Soc. 100, 6911 (1978)

10. I. Ugi, J. Dugundji, R. Kopp and D. Marquarding, "Perspectives in Theoretical Stereochemistry" (Lecture Notes in Chemistry, Vol 36) Springer-Verlag, 1984.

11. K. Rasmussen, "Potential Energy Functions in Conformational Analysis" (Lecture Notes in Chemistry, Vol 37) Springer Verlag, 1985.

12. H.B. Schlegel, Ph. D. Thesis, Queen's University, Kingston, Ontario, Canada

13. M.J.D. Powell in P. Rabinowits (Ed), Numerical Methods for Nonlinear Algebraic Equations, Gordon and Breach, London, 1970, p 87.

14. W.C. Davidon, Mathematical Programming, 9, 1 (1975)

15. M.R. Peterson and I.G. Csizmadia. Progress in Theoretical Organic Chemistry, 3, 190 (1982) Elsevier

16. M. Greenberg, "Lectures on Algebraic Topology", W.A. Benjamin, New York, 1967, pp 99-103.

17. J. Milnor, "Morse Theory", Princeton University Press, Princeton, New Jersey, 1963, pp 28-33.

18. M.R. Peterson, I.G. Csizmadia and R.W. Sharpe, J.Mol.Struct. (THEOCHEM) 94, 127 (1983)

19. K. Ohno and K. Morokuma, Quantum Chemistry Database, Elsevier 1982. Additional summaries are published annually in the last issue of THEOCHEM.

20. L. Schafer, J.D. Ewbank, V.J. Klimkowski and K. Siam, J.Mol.Struct. (THEOCHEM) 135, 141 (1986)

21. I.G. Csizmadia and J.G. Angyan "Molecular Conformations and Potential Energy Topology" in "Applied Quantum Chemistry" (Edited by V.H. Smith, H.F. Schaefer and K. Morokuma) Reidel Publishing Co. 1986, pp 75-83.

22. P.G. Mezey, Chem.Phys Letters. 82, 100 (1981)

23. I.G. Csizmadia J.Mol.Struct. 138 (THEOCHEM 31) 1-11 (1986)

24. J.G. Angyan, A. Kucsman, R.A. Poirier and I.G. Csizmadia, J.Mol.Struct. (THEOCHEM) 123, 189 (1985)

25. J.G. Angyan, R. Daudel, A. Kucsman and I.G. Csizmadia, Chem.Phys. Letters 136, 1-8, (1987)

Some Practical Suggestions for Optimizing Geometries and Locating Transition States

H. Bernhard Schlegel
Department of Chemistry
Wayne State University
Detroit, Michigan, 48202
USA

ABSTRACT The optimization of equilibrium geometries and transition states by molecular orbital methods is discussed from a practical point of view. Most of the efficient geometry optimization methods rely on analytical energy gradients and quasi-Newton algorithms. For any optimization method, there are three areas of input that directly affect the behavior of the optimization: (a) the choice of internal coordinates, (b) the starting geometry and (c) the initial estimate of the Hessian. A number of topics related to these three areas are discussed with the aim of improving the performance of optimizations; these include symmetry, dummy atoms, avoiding coordinate redundancy, overcoming strong coupling among coordinates, conversion between coordinate systems, testing stationary points and what to do when optimizations fail.

1. Introduction

Equilibrium geometries can be calculated routinely, reliably and accurately by ab initio molecular orbital methods [1]. In principle, transition states can be calculated equally well; though, in practice, transition structures require a little more skill to optimize than equilibrium structures. The importance of geometry optimization is supported by the fact that most molecular orbital calculations appearing in the chemical literature in recent years involve geometry optimization to some degree [2,3]. In this Chapter, some of the practical aspects of geometry optimization are considered. The discussions are based on the GAUSSIAN series of programs [4] (the optimization tools available in the GAUSSIAN system are listed in the Appendix), but the concepts and suggestions can be applied directly to any semi-empirical or ab initio MO program that uses internal coordinates for geometry optimization. Most molecular mechanics or empirical force field programs carry out the optimization in Cartesian coordinates, and hence are outside the scope of this Chapter.

Geometry optimization has become routine primarily because of the availability of efficient programs to calculate analytical energy gradients (for recent reviews see [5-8]). Analytical gradient based geometry optimizations are almost an order of magnitude faster than optimization methods that use only the energy. Almost all user-friendly molecular orbital programs have analytical gradients at the Hartree-Fock (HF) level; many have analytical gradients for the second order Møller-Plesset perturbation theory (MP2). Some

J. Bertrán and I. G. Csizmadia (eds.),
New Theoretical Concepts for Understanding Organic Reactions, 33–53.
© 1989 by Kluwer Academic Publishers.

programs can also compute analytical gradients at the MP3 [9], MP4 [10], configuration interaction [11], coupled clusters [12] and MCSCF [13] levels. Many semi-empirical programs also have analytical gradients. In addition to first derivatives of the energy, some calculations also require second derivatives, e.g. vibrational frequencies. Second derivatives can be calculated by numerical differentiation of analytical first derivatives or, more efficiently, by analytical second differentiation of the energy [14]. A number of programs can calculate analytical second derivatives at the Hartree-Fock level; a few can calculate analytical second derivatives at the MP2 [15], CI [16] and MCSCF [17] levels. Third derivatives can also been calculated analytically at the Hartree-Fock [18] and two configuration SCF levels [19]. Additional details of the theory of analytical derivatives can be found in various articles and reviews [5-8, 20-22] and references cited therein..

Details of the various algorithms used for geometry optimization and transition structure searching can be found in recent reviews [23-25], and will not be covered in the present Chapter. From a numerical analysis point of view, geometry optimization is just a problem in unconstrained minimization [26-28]. The books by Scales [26], and Fletcher [27] are quite readable and discuss a wide variety of algorithms for unconstrained minimization, with special emphasis on methods employing gradients. Locating a transition structure is somewhat more difficult than finding a minimum. A transition structure is a maximum in one and only one direction on the potential energy, and is a minimum in all other directions (i.e. a first order saddle point or col). During the course of a transition structure search, the algorithm must choose the best direction along which the energy is maximized, as well as carrying out the maximization in that direction and the minimization in all other directions. Compared to unconstrained minimizations, the numerical analysis literature on saddle point optimizations is much less extensive ([26-28] and references cited). From a chemical point of view, a number of methods for finding transition states have been proposed; details of some of these algorithms can be found in recent reviews [23,24] and references therein.

Most programs provide a brief write-up of how to use their particular optimization code. A useful outline for geometry optimization can also be found in "A Handbook of Computational Chemistry" [29]. However, there does not seem to be a practical guide on the details of geometry optimizations and transitions structure searches. The purpose of this Chapter is to provide a few hints to help set up optimizations so that they will work better (Sections 4-12), and to provide some suggestions of what to try when optimizations go wrong (Section 13).

2. Symmetry and Stationary Points

Symmetry can be quite helpful in speeding up optimizations of minima and saddle points, but can also create difficulties by constraining the search to a subsection of the energy surface. If a molecule has any symmetry, it should be used to reduce the number of coordinates that must be optimized. This can be beneficial even if the molecule has only C_s or C_2 symmetry. Taking advantage of symmetry may also fix some flexible coordinates, such as internal rotations, that would otherwise slow down the optimization. In favorable circumstances, symmetry can even be used to turn a transition structure optimization into a minimization (see below).

Symmetry can also cause problems. By symmetry, the gradients must belong to the totally symmetric representation of the point group of the molecule. This means that a gradient based optimization method will not change the symmetry of the molecule during the course of an optimization (provided the internal coordinates properly reflect the symmetry of the molecule). Hence, a molecule will not distort to a lower symmetry during

an optimization, even if the lower symmetry structure is lower in energy. Therefore, once the structure has been optimized, it must be tested to ensure that displacements to lower symmetries do not lower the energy (see below - 12. Testing Stationary Points). By contrast, there are no restriction on optimizations going to higher symmetry; however such optimizations may be slow because of strong coupling between symmetry equivalent coordinates. Under such circumstances, it may be unclear if the optimization will converge to a slightly distorted structure or if the optimization is actually proceeding to a higher symmetry structure. If a higher symmetry structure is suspected, it is often more efficient to optimize the higher symmetry structure directly and test it for stability with respect to distortion to lower symmetry (Section 12).

Some transition structure optimizations can be turned into minimizations by symmetry. Stanton and McIver [30] have discussed a number of symmetry restrictions on transitions states; the ones directly relevant to transition structure optimization can be summarized as follows:

(a) a transition vector cannot belong to a degenerate representation (otherwise there would be at least 2 equivalent eigenvectors of the Hessian with negative eigenvalues, and the structure is at least a second order saddle rather than a first order saddle point),

(b) the transition vector must be symmetric for all symmetry operations of the transition state that also leave the reactants and products unchanged,

(c) the transition vector must be antisymmetric for any of the symmetry operations of the transition state that interconvert the reactants and products.

For most reactions, only (a) and (b) can be used to simplify the transition structure optimization. However, in some reactions, such as racemizations, degenerate isomerizations, identity exchanges, etc., reactants and products can be interchanged by a symmetry operation of the transition state (e.g. a C_2 axis for the 1,3 antara hydrogen shift $CH_3CH{=}CH_2 \rightleftharpoons CH_2{=}CHCH_3$; a σ plane for the identity S_N2 reaction $X^- + CH_3X \rightleftharpoons XCH_3 + X^-$). The effect of (c) for these types of reactions is to constrain the transition state to be at the midpoint of a symmetric reaction path connecting reactants and products. Since the reaction path is the direction along which a maximum must be found and the position of this maximum given by symmetry; what remains to be done in the transition structure optimization is to minimize with respect to all of the remaining (totally symmetric) displacements in the transition state. Thus, for these special cases, the transition structure optimization is reduced to a simple minimization. The final transition structure should still be tested to ensure that it is a valid transition state (i.e. with one and only one negative eigenvalue in the full Hessian, Section 12).

3. The Basic Optimization Step

Most of the algorithms for geometry optimization using gradients rely on a quadratic expansion of the energy surface [26-28]. In terms of the coordinates, $\vec{x}_o$, the calculated energy, E_o, the calculated gradient, $\vec{g}_o$, and an approximate second derivative matrix or Hessian, $\underline{H}$, the energy and gradient are written as:

$$E = E_o + \vec{g}^T (\vec{x} - \vec{x}_o) + {}^1/_2 (\vec{x} - \vec{x}_o)^T \underline{H} (\vec{x} - \vec{x}_o) \qquad (1)$$

$$\vec{g} = \vec{g}_o + \underline{H} (\vec{x} - \vec{x}_o) \qquad (2)$$

At the optimized geometry, the gradient is zero; therefore, the next estimate of the optimum geometry is found by solving eq (2) for $\vec{g} = 0$, i.e. a Newton-Raphson step:

$$\vec{x} = \vec{x}_0 - \underline{H}^{-1}\,\vec{g}_0 \qquad (3)$$

Almost all of the algorithms have these steps in common; thus, almost all optimization methods need a starting geometry and an initial estimate of the Hessian. Much of this Chapter will deal with the choice of internal coordinate system for an optimization, the starting geometry and the initial estimate of the Hessian.

The various optimization algorithms differ in the way the estimated Hessian is updated at each step (e.g. DFP, MS, BFGS, etc.), how the solution of eq (3) is constrained (e.g. reduction of steps that are larger than the trust radius) and how the one dimensional optimization is carried out along the direction predicted by eq (3) (e.g. accurate, approximate or not at all). The details can be found in a various books and review articles [23-28]. Given the same starting conditions, most of the recent gradient algorithms for minimizations perform similarly. The BFGS method with a very approximate line search seems to be quite efficient for geometry minimization [31]. Aside from GAUSSIAN (see Appendix), most molecular orbital programs have only a limited selection of optimization algorithms and one must work within the framework of the available code. Thus, success or failure in an optimization using a particular program will depend significantly on the starting conditions of the optimization. The 3 most important areas are (a) choice of the internal coordinates (Sections 4-7), (b) the starting geometry (Sections 8-10) and (c) the initial estimate of the Hessian (Section 11).

4. Choice of Internal Coordinates

Although a good geometry optimization program should converge regardless of the coordinate system, most practical optimization problems converge much faster when the coordinate system is constructed with some care. Strong coupling between coordinates invariably causes difficulties for optimizations. The coupling between stiff coordinates (stretch, bend etc.) and loose coordinates (e.g. internal rotations and inversions with low barriers) can be especially troublesome. Cyclic molecules have inherently strongly coupled internal coordinates, and suffer from additional difficulties because of redundant coordinates. Transition structures are sometimes quite flexible, and coupling between these flexible modes and the transition vector may lead to additional problems. Loosely bound clusters are a third category of potentially troublesome optimizations, because large changes in geometry may occur with small changes in the energy.

Internal coordinates for the GAUSSIAN system of programs are defined using the Z-matrix notation [4]; other programs use similar systems to define internal coordinates (see [29]) and the appropriate user manual should be consulted for details. To facilitate the discussion of internal coordinate systems, an example of a Z-matrix input for methanol is given below. For the first atom, C, only the name of the atom is required; for atom 2, the name of the atom (O), the number of the atom to which it is bonded (1) and the distance (1.48 Å) are required. The third line indicates that atom 3 is an H, bonded to atom 2 at a distance of 0.96 Å and makes an angle with atom 1 of 105.0° (i.e. <321). Atom 4 is an H, bonded to atom 1 at a distance of 1.08 Å, makes a valence angle with 2 of 109.5° (<412) and a dihedral angle with 3 of 180° (i.e. <4123, the angle of rotation between 4 and 3 about the axis formed by atoms 1 and 2). Subsequent atoms are defined in a similar way in terms of a distance, valence angle and a dihedral angle to previously defined atoms. In some programs (e.g. GAUSSIAN), a second valence angle can be used instead of the dihedral angle (see Example 7). The appropriate user manual should be consulted for the details of specifying internal coordinates for a particular MO program.

Example 1. Z-matrix for methanol

```
C
O  1  1.48
H  2  0.96  1  105.0
H  1  1.08  2  109.5  3  180.
H  1  1.08  2  109.5  4  120.
H  1  1.08  2  109.5  4  -120.
```

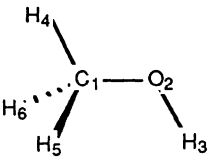

In addition to real atoms, most programs allow dummy atoms to be used in the description of the geometry. Dummy atoms have no charge and carry no basis functions; they are used solely to help define the geometry so that a more convenient set of distances and angles can be used. Dummy atoms are identified by a particular atomic symbol or atomic number (X, - or -1 in GAUSSIAN, see Example 3) and are specified in the same manner as regular atoms. Some examples that are discussed below include linear molecules (to avoid valence angles of 180°), molecules undergoing inversion (so that the entire path from reactants to products can be followed with the same Z-matrix), cyclic molecules (to uncouple coordinates that are too strongly coupled) and transition states (to help separate the transition vector from the remaining coordinates).

To permit geometry optimization in GAUSSIAN, the values for distances and angles to be optimized are replaced by variable names. Initial values are supplied for these parameters and the optimization code varies these parameters in the search for the stationary point. There are numerous other features in the GAUSSIAN Z-matrix input [4], but the limited set illustrated here is sufficient for the examples discussed below.

Example 2. Symbolic Z-matrix for methanol (HF/3-21G optimized values)

```
C
O  1  RCO
H  2  ROH    1  ACOH
H  1  RCH1   2  AOCH1  3   180.
H  1  RCH2   2  AOCH2  4   DHOCH2
H  1  RCH2   2  AOCH2  4  -DHOCH2
```

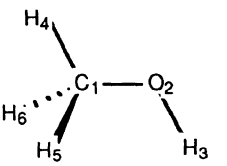

RCO=1.440, ROH=0.966, RCH1=1.079, RCH2=1.085, ACOH=110.4, AOCH1=106.3, AOCH2=112.3, DHOCH2=118.5

Most programs impose some restriction on the value of distances and angles used to construct the geometry. Distances are usually required to be positive, valence angle must be greater than 0° but less than 180° and dihedral angles typically have a range of -180° to +180° or -360° to +360°. Other restrictions may be imposed by the symmetry of the molecule (e.g. if an angle is tetrahedral by symmetry, 109.4712° ··· should be used and not 109.5°). Some care must be taken that the limits on the bond lengths and angles are not exceeded during the course of an optimization. For example, a molecule with 3 atoms nearly linear such as HOCN (or any molecule with a fragment that can approach linearity during an optimization) can be specified with a dummy atom and thus avoiding the restrictions on the valence angle.

Example 3. Symbolic Z-matrix for cyanic acid (HF/3-21G)

```
C
N  1  RCN
X  1  1.0    2  90.
O  1  RCO    3  AXCO  2  180.
H  4  ROH    1  ACOH  3  180.

RCN=1.140, RCO=1.308, ROH=0.970,
AXCO=88.7, ACOH=114.2
```

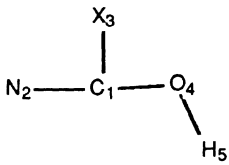

5. Internal Coordinates, Symmetry and Dummy Atoms

Some useful guidelines for constructing internal coordinate systems can be developed for molecules with some degree of symmetry [32a]. Specifically, symmetry can be quite helpful in setting up dummy atoms and in defining the connectivity for the internal coordinates. For example, cyclic molecules can lead to very strongly coupled coordinate systems, but if there is sufficient symmetry, a well behaved, relatively uncoupled coordinate system can be constructed. Even if a molecule possesses very little symmetry, a suitable set of internal coordinates may be obtained by taking a higher symmetry analogue of the molecule and systematically reducing the symmetry.

For molecules with more than 3 or 4 atoms and with some symmetry, it may be best to define the atoms on the highest symmetry elements first:

(a) If there is an atom at the center of inversion, the intersection of 2 or more rotational axes, or the intersection of an axis and a perpendicular plane, specify that atom first (e.g. S in SF_6). If there is no atom at the center of symmetry, put a dummy atom there (e.g. the middle of the ring in cyclopropane, C_3H_6).

(b) If there are axes of rotation, specify the atoms on the highest order axis first (e.g. C and F on the C_3 axis in CH_3F). If there is only 1 atom on the axis, add a dummy atom on the axis (e.g. in the direction of the lone pair NH_3, or on the bisector of <HCH and <FCF in CH_2F_2). Some cases, such as rings, may require 2 dummy atoms to define the axis (e.g. C_3H_6).

(c) If there is only a plane of symmetry and no other elements of symmetry, specify at least 2 and preferably 3 atoms in the plane first (e.g. N, O and H in H_2NOH). If there are less than 2 or 3 atoms in the plane, add enough dummy atoms to define the plane so that the remaining atoms can be specified relative to the plane.

In specifying the other atoms in the molecule, it is best to group them into symmetry equivalent sets (e.g. the 3 C's in cyclopropane form one set and the 6 H's form another set). For each atom in a symmetry equivalent set:

(d) Define the bond lengths and angles in symmetry equivalent ways (e.g. in CH_3F, each H is bonded to C and makes an angle with F).

(e) Use the same variable name for equivalent bond lengths, valence angles and dihedral angles (caution, while valence angles do not change under any symmetry operation, dihedral angles must change sign on reflection or improper rotation).

Example 4. Symbolic Z-matrix for cyclopropane illustrating the use of dummy atoms and symmetry

```
X
X 1 1.0
C 1 RXC 2 90.
C 1 RXC 2 90. 3 120.
C 1 RXC 2 90. 3 240.
H 3 RCH 1 AXCH 2 0.
H 3 RCH 1 AXCH 2 180.
H 4 RCH 1 AXCH 2 0.
H 4 RCH 1 AXCH 2 180.
H 5 RCH 1 AXCH 2 0.
H 5 RCH 1 AXCH 2 180.
```

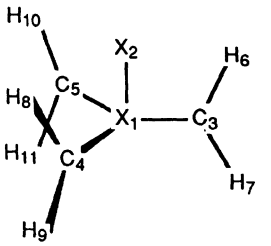

RXC=0.8735, RCH=1.072, AXCH=122.6

6. Full Optimizations and the Number of Internal Coordinates

Whenever possible, a full optimization should be carried out. With the current gradient based optimization methods, most full optimizations are not appreciably longer than partial optimizations and one has the assurance that subtle features of the energy surface are not masked by artificial geometric constraints. For a molecule without symmetry, there are 3n-6 internal coordinates, where n is the number of atoms and all 3n-6 degrees of freedom must be varied in a full optimization.

A frequent cause of difficulty in optimizations is the specification of too few or too many coordinates. Too few coordinates corresponds to a constraint on the geometry of the molecule and results in a less than complete optimization. Too many coordinates results in a redundancy among the internal coordinates, leading to zero eigenvalues in the Hessian and to very poor behavior during the optimization. If there are no dummy atoms and no symmetry, the Z-matrix input contains 3n-6 unique parameters, all of which must be varied in a full optimization. When dummy atoms are present, some of the Z-matrix parameters are redundant and must be held fixed.

In Example 5, a dummy atom is needed to specify a nearly linear NCO angle. Clearly, changing the distance to the dummy atom, RCX, does not alter the position of the real atoms. Hence RCX is redundant and must not be included in the optimization. A more subtle redundancy exists between the angles about the dummy atom, ANCX and AXCO. A change in either will bend the NCO angle. But if one angle is increased and the other is decreased by the same amount, the NCO angle remains the same. Hence, only one of the angles can be included in the optimization, and the other must remain fixed, as shown in Example 3 (the 2 dihedral angles are also fixed because the molecule is planar).

Example 5. Symbolic Z-matrix for HOCN with errors due to redundant coordinates.

```
C
N 1 RCN
X 1 RCX 2 ANCX
O 1 RCO 3 AXCO 2 180.
H 4 ROH 1 ACOH 3 180.
```

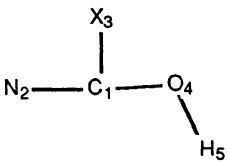

If the molecule has some symmetry, there are fewer than 3n-6 parameters to optimize (if symmetry is to be retained during the optimization). The number of parameters to be optimized can be determined from the symmetries of the normal modes of vibration of the molecule. Only displacements along totally symmetric vibrational modes will retain the symmetry of the molecule; displacement along any of the non-totally symmetric modes will distort the molecule to a lower symmetry. Thus, the number of degrees of freedom that must be included in a full optimization of a molecule within a given symmetry is equal to the number of totally symmetric vibrational modes.

If character tables are not available, an alternative scheme can be constructed to count the number of coordinates required in a full optimization. All the information needed is contained in the framework group notation for the molecule [33]. Each symmetry equivalent set of atoms (dummy atoms excluded) contributes the smallest of the following to the number of degrees of freedom:

(a) 0 if an atom in the set is at the center of inversion, the intersection of two axes of rotation or the intersection of a σ_h plane and an axis,

(b) 1 if an atom in the set is on a proper or improper rotation axis,

(c) 2 if an atom in the set is in a symmetry plane,

(d) 3 if not in any symmetry element.

To account for translational and rotational invariance, the smallest of the following is subtracted from the above sum to yield the number of internal coordinates that must be optimized in a full optimization:

(a) 0 if there is an intersection of two axes of rotation (D_n, D_{nh}, D_{nd} and the cubic groups),

(b) 1 if there is a rotational axis and a symmetry plane (C_{nv}, C_{nh}),

(c) 2 if there is only a rotational axis (C_n, S_n),

(d) 3 if there is only a center of inversion or one symmetry plane (C_i, C_s),

(e) 6 if there is no symmetry (C_1).

This procedure can be illustrated by examining pyramidal trimethylamine, $N(CH_3)_3$, which has C_{3v} symmetry. The N is on the C_3 axis (+1), 3 equivalent C's are in the σ_v planes (+2), 3 equivalent H's are in the σ_v planes (+2), 6 equivalent H's are not on any symmetry element (+3) and finally, subtract 1 for rotation and translation because of the σ_v planes and a C_3 axis. Thus, the total number of coordinates to be optimized is 1+2+2+3-1=7.

7. Strong Coupling between Internal Coordinates

Many of the problems encountered in optimizations (see Section 13) can be traced to a poor choice of coordinate system. In general, strong coupling between coordinates degrades the performance of any optimization algorithm. In particular, coupling between stiff modes (e.g. bond stretch, angle bend, etc.) and flexible modes (e.g. torsion about single bonds, inversions with low barriers, interfragment coordinates in loose clusters, etc.) should be kept to a minimum. Similarly in transition states, as few coordinates as possible should be combined to form the transition vector. It is difficult to make more specific statements about good coordinate systems versus bad, but often symmetry and the judicious choice of dummy atoms can be used to improve a coordinate system (Section 5).

As far as possible, natural valence coordinates (bond lengths and angles) should be used to define an internal coordinate system. For acyclic molecules, this is quite easy in the Z-matrix format. The use of symmetry is straight-forward and often dummy atoms are not needed. However, some care must be taken with torsional modes and with nearly planar trigonal centers. Example 6 illustrates the problem of methyl rotation in CH_3SHO. Each of the hydrogens in the methyl group could be defined with a dihedral angle to the SO bond; however, this would require all 3 angles to change by the same amount if the methyl group is rotated in the course of an optimization. Alternatively, a single dihedral angle can be used to specify the rotation of the entire methyl group, thereby decoupling the flexible mode (methyl rotation) from the stiff modes (HCH bend). The same idea can be applied to any group that can rotate.

Example 6. Symbolic Z-matrix for methyl sulphoxide

(a) Methyl rotation strongly coupled.

```
S
O 1 RSO
H 1 RSH 2 AOSH
C 1 RSC 2 AOSC 3 DHOSC
H 4 RCH1 1 ACH1 2 BCH1
H 4 RCH2 1 ACH2 2 BCH2
H 4 RCH3 1 ACH3 2 BCH3
```

(b) Methyl rotation decoupled from HCH bend.

```
S
O 1 RSO
H 1 RSH 2 AOSH
C 1 RSC 2 AOSC 3 DHOSC
H 4 RCH1 1 ACH1 2 BCH1
H 4 RCH2 1 ACH2 5 DCH2
H 4 RCH3 1 ACH3 5 DCH3
```

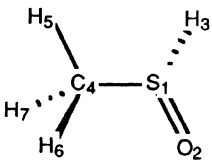

Example 7 shows pyramidal CH_3 that will become planar during the optimization. If 3 valence angles are used to define a nearly planar geometry, then a small change in the angles will cause a large out-of-plane displacement. However, if a dummy atom is placed on the C_3 axis, then the variable BXCH can define the entire inversion process smoothly.

Example 7. Symbolic Z-matrix for out-of-plane bending in CH_3

(a) potential problems

```
C
H 1 RCH
H 1 RCH 2 AHCH
H 1 RCH 2 AHCH 3 AHCH 1
```

(b) better coordinates

```
C
X 1 1.0
H 1 RCH 2 BXCH
H 1 RCH 2 BXCH 3 120.
H 1 RCH 2 BXCH 3 240.
```

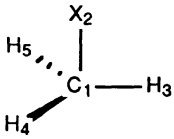

Cyclic molecules are considerably more difficult to specify than acyclic molecules, primarily because the natural valence coordinates have unavoidable redundancies. For example, a planar 5 membered ring has 5 bonds and 5 valence angles for a total of 10 in-plane coordinates; however, there are only 7 degrees of freedom to optimize (C_s symmetry). Thus each valence coordinate is necessarily strongly coupled to the others. Examples 8 and 9 illustrate 2 coordinate systems for each of three model planar rings C_5 (D_{5h}, e.g. the heavy atom skeleton for $C_5H_5^-$), C_4O (C_{2v}, the skeleton for furan) and C_3NO (C_s, the skeleton for isoxazole). If a ring is specified as a long chain of atoms, then a change in any one of the bonds or angles will change the length of the ring closure bond, thus resulting in a very strongly coupled coordinate system. The second coordinate system for each case is less strongly coupled (or for C_5 makes better use of symmetry).

Example 8. Strongly coupled coordinate systems for 5 membered rings

(a) C_5 (D_{5h} symmetry)

```
C
C 1 R
C 2 R 1 108.
C 3 R 2 108. 1 0.
C 4 R 3 108. 2 0.
```

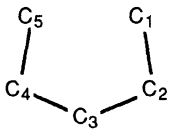

(b) C_4O (C_{2v} symmetry)

```
C
C 1 R1
O 2 R2 1 A2
C 3 R2 2 A3 1 0.
C 4 R1 3 A2 2 0.
```

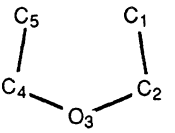

(c) C_3NO (C_s symmetry)

```
N
C 1 R1
O 2 R2 1 A2
C 3 R3 2 A3 1 0.
C 4 R4 3 A4 2 0.
```

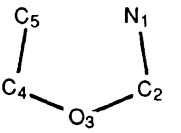

Example 9. Less coupled coordinate systems for 5 membered rings

(a) C_5 (D_{5h} symmetry)

```
X
X 1 1.0
C 1 R 2 90.
C 1 R 2 90. 3   72.
C 1 R 2 90. 3 144.
C 1 R 2 90. 3 216.
C 1 R 2 90. 3 288.
```

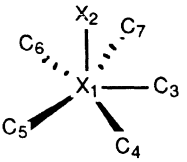

(b) C_4O (C_{2v} symmetry)

```
X
O 1 R1
C 1 R2 2 90.
C 1 R2 2 90. 3 180.
C 3 R3 1 A3  2 0.
C 4 R3 1 A3  2 0.
```

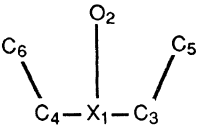

(c) C_3NO (C_s symmetry)

```
X
X 1 1.0
C 1 R1 2 90.
N 1 R1 2 90. 3 180.
C 3 R2 1 A2  2 180.
C 4 R3 1 A3  2 180.
O 1 R4 3 A4  2 180.
```

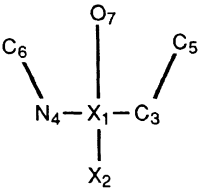

Loose complexes can also cause problems for optimization programs, in part because of the large changes in geometry that often occur during their optimization. It is important that the 2 (or more) molecules in the complex have the necessary rotational and translational freedom relative to each other (to the extent allowed by the symmetry of the complex), as shown in Example 10. Furthermore, the coordinates for the relative motion should not be coupled to any other coordinates. Even with these precautions, it may be necessary to freeze the internal degrees of freedom and optimize the interfragment modes first, before optimizing all coordinates of the complex at the same time.

Example 10. Symbolic Z-matrix for the SIHF - - HCl cluster

```
Si
H 1 RH
F 1 RF     2 AF
Cl 1 RCL   3 ACL   2 BCL
H 4 RHCL 1 AHCL 3 BHCL
```

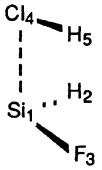

Strong coupling between coordinates can be particularly troublesome in transition structure optimizations. As far as possible, the transition vector should be dominated by only a few coordinates (preferably 1 or 2). The coupling between the coordinates of the transition vector and the remaining coordinates should also be as small as possible. Two coordinate systems for HCN isomerization are shown in Example 11. In the first case, the transition vector involves both the HCN bend and the CH stretch, but in the second case the transition vector is predominantly the XH displacement.

Example 11. Symbolic Z-matrices for the HCN → HNC transition state

(a) simple coordinates

```
C
N 1 RCN
H 1 RCH 2 AHCH
```

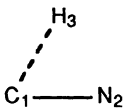

(b) better coordinates

```
C
N 1 RCN
X 1 RCX 2 90.
H 3 RXH 1 90. 2 0.
```

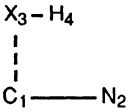

For some reactions, the coordinate system is easy to set up. For S_N2 reactions, abstractions and one center addition reactions, the transition vector is dominated by the bonds being made or broken. For other reactions, such as insertions, eliminations and cycloadditions, the choice of coordinates is less clear. These combine the difficulties of cyclic structures and loose complexes with the problems of transition states. In the elimination of H_2 from H_2CO, Example 12, the hydrogens could be specified by distances to the carbon and angles to CO; however, a small rotation of H_2 would require the concerted change of 2 distances and 2 angles. The alternate coordinate system avoids this problem and also reduces the coupling to the transition vector (primarily CX and XH stretch). Example 13 deals with the 1,2 cycloaddition of H_2 to N_2H_2. In this case symmetry is used to construct a less coupled coordinate system by locating the dummy atoms on the C_2 axis (as discussed in Section 5).

Example 12. Symbolic Z-matrices for the $H_2CO \rightarrow H_2 + CO$ transition state

(a) simple coordinates

```
C
O 1 RCO
H 1 RCH1 2 ACH1
H 1 RCH2 2 ACH2
```

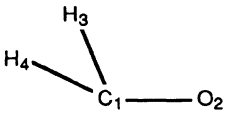

(b) better coordinates

```
C
O 1 RCO
X 1 RCX 2 AOCX
H 3 RXH 1 ACXH 2 0.
X 3 1.0   4 90.    1 180.
H 3 RXH   5 90.    4 180.
```

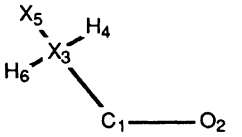

Example 13. Symbolic Z-matrix for the $H_2 + N_2H_2 \rightarrow N_2H_4$ transition state

```
X
X 1 RXX
H 2 RXH 1 90.
H 2 RXH 1 90. 3 180.
N 1 RXN 2 90. 3   0.
N 1 RXN 2 90. 3 180.
H 5 RNH 1 ANH 2 BNH
H 6 RNH 1 ANH 2 BNH
```

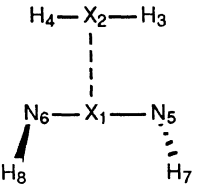

8. Initial Guess for Bond Lengths and Angles

One of the simplest ways to speed up an optimization is to make a good estimate of the geometry. Initial values for bond lengths and angles can be obtained from a number of sources:

(a) Standard geometries. There are various compilations of standard bond lengths and angles for a wide range of equilibrium structures [34, 35]. With a bit of chemical intuition and VSEPR theory, these standard values can be adjusted to give better estimates. It is not possible to construct a set of standard values of similar quality for the coordinates undergoing changes in transition states. However, concepts such as conservation of bond order, bond order-bond energy relations and the Pauling relation between bond length and bond order may be quite helpful.

(b) Empirical force field calculations. Although the range of molecules and the types of bonds can be somewhat limited, molecular mechanics calculations give good estimates of the optimized geometry for energy minima [36], especially of cyclic systems and cases where steric interactions are important. However, some care is needed with these methods in situations where electronic factors control the geometry.

(c) Semi-empirical MO calculations. Some semi-empirical MO programs predict optimized geometries as well as minimal basis set ab initio calculations. Known defects of various methods [29, 37, 38] should be taken into account when using semi-empirically optimized geometries for ab initio calculations.

(d) Lower level ab initio calculations. The various shortcomings of smaller basis sets [1] should be taken into account when scaling to calculations with larger basis sets and/or electron correlation.

(e) Quantum chemical data bases. Quite a wide variety of molecules have been optimized over the past decade or two. A large number of structures are available in machine readable and searchable form in the Carnegie-Mellon Quantum Chemistry Archive [3]. Many other calculations are referenced in Quantum Chemical Literature Data Base [2], also available on-line. The molecule may have already been optimized at the desired level of theory or at a lower level. Alternatively, these data bases are an excellent source for fragment geometries from which the molecule in question can be constructed.

(f) Experiment. X-ray, microwave and electron diffraction structures are highly desirable starting points for geometry optimizations, but frequently are not available for the structures studied theoretically.

9. Getting Close to the Transition Structure

Often a transition structure can be optimized directly without any problems, especially if the initial estimate of the Hessian has a suitable negative eigenvalue with an eigenvector that is a reasonable estimate to the transition vector (see Section 11). However, convergence to a transition state may sometimes require a better starting geometry than an optimization of a minimum. For difficult cases, standard geometries and chemical intuition may not yield estimates that are good enough for a direct transition structure optimization. Various techniques for getting close to a transition structure have been discussed in the literature (for leading references see [23]). A few of the methods are summarized below in order of increasing sophistication..

(a) Potential surface scan. If there is some doubt about the location of a saddle point along a reaction path, a series of energy only or energy + gradient calculations may be sufficient to locate the region of the transition state approximately. If more than one coordinate is important in the reaction path, a small grid of points may have to be calculated.

(b) Linear synchronous transit (LST) [39]. In this approach, the reaction path is approximated as a straight line in the space of interatomic distances (this may correspond to a curved path in Cartesian coordinates or internal coordinates). An estimate of the transition structure is obtained by finding the maximum along this one dimensional path. Since the true reaction path usually differs from the LST path, the LST estimate of the transition state is normally higher in energy than the true transition state, and may be outside the quadratic region of the true transition state. However, if a minimization is carried out perpendicular to the reaction path (akin to quadratic synchronous transit), a better estimate of the transition state can be obtained.

(c) Coordinate driving, walking up valleys and eigenvector following methods [40-42]. These methods attempt to follow the reaction path uphill toward the transition structure. In the coordinate driving approach, a coordinate dominating the reaction path is incremented at each step and the remaining coordinates are minimized. In the eigenvector following approach, steps are taken in the uphill direction along a selected eigenvector (usually the one with the lowest eigenvalue). This approach can be quite costly, if the method requires the Hessian to be recomputed frequently. The idea in both methods is to construct a path of shallowest ascent toward the transition structure.

However, both methods can miss the transition state, if it is not on the shallowest ascent path (see [23] for examples).

Once a reasonable initial estimate has been obtained for the transition structure, a suitable gradient optimization method [43-48] can be used to find the optimized geometry. If the initial estimate has been obtained by a potential surface scan or a linear synchronous transit calculation, it may be preferable to optimize the transition structure in 2 (or more) phases. First, the coordinates corresponding to the transition vector are frozen and the remaining coordinates are minimized. This brings the molecule closer to the reaction path. The second step is a full transition structure optimization with all coordinates varied. Some of the hill climbing and eigenvector following methods incorporate the equivalent of a direct gradient optimization as a final step.

10. Converting Between Different Z-Matrices

In setting up a calculation or during the course of an optimization, it is sometimes necessary to convert from one set of internal coordinates to another (e.g. the experimental geometry may be specified in an inconvenient coordinate system, or an attempt at optimization may reveal a strong coupling between coordinates). If the Cartesian coordinates are available, it is straight forward, but tedious, to determine the new internal coordinates manually. Alternatively, there are some programs that construct a new Z-matrix automatically [32b]. Most general purpose molecular modelling programs can also be used to calculate bond lengths and angles from the Cartesian coordinates. However, there may be some circumstances in which it is necessary or more convenient to interconvert a few valence and dihedral angles manually.

Schemes 1 and 2 show the construction of 2 of the more frequently used relations between valence and dihedral angles. In both cases, the Cartesian coordinates of appropriate fragments are constructed by rotating unit vectors by the required angles about particular axes. The desired angles are then obtained by simple dot products. Scheme 1 deals with the angles about a non-planar tricoordinate center or a tetracoordinate center: given valence angles α, β and γ, find dihedral angle δ, or given α, β and δ, find γ. Vector 1 is placed on the x axis (1, 0, 0); vector 2 is obtained by rotating vector 1 by α about the z axis (i.e. in the x,y plane) to give ($\cos\alpha$, $\sin\alpha$, 0). Vector 3 is obtained by rotating vector 1 by β about the z axis ($\cos\beta$, $\sin\beta$, 0), followed by δ about the x axis to give ($\cos\beta$, $\sin\beta\cos\delta$, $\sin\beta\sin\delta$). The dot product between vectors 2 and 3 is the cosine of the third valence angle, γ. If needed, the resulting expression for $\cos\gamma$ can be solved for any of the other angles.

Scheme 1

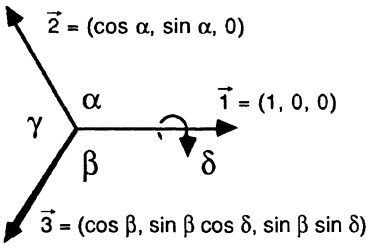

$$\vec{2} \cdot \vec{3} = \cos\gamma$$

$$\cos\gamma = \cos\alpha\cos\beta + \sin\alpha\sin\beta\cos\delta$$

$$\cos\delta = (\cos\gamma - \cos\alpha\cos\beta) / (\sin\alpha\sin\beta)$$

Scheme 2 deals with the more specialized case when a plane or axis bisects an angle. The analysis proceeds as before, but with the bisector placed on the axis. If the planes of the angles α and β are perpendicular, a particularly simple expression is obtained: $\cos\gamma = \cos\alpha/2 \cos\beta$. Many other relations can be derived in the same manner. The key is to place the right vector on the axis so that the remaining vectors can be generated by simple rotations about axes.

Scheme 2

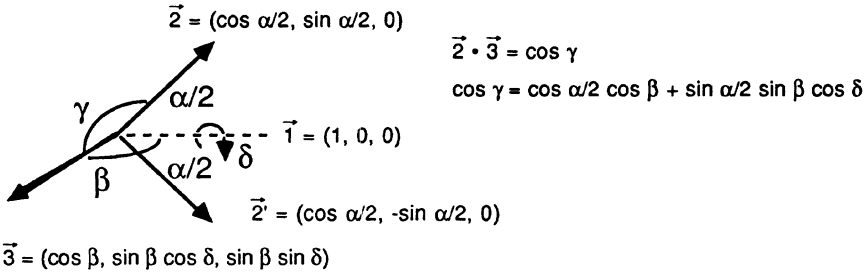

11. Estimating the Hessian

Like the choice of internal coordinate systems and the starting geometry, the initial estimate of the Hessian can strongly influence the rate of convergence of an optimization. As indicated in eq (3), the next estimate of the optimized geometry depends on the Hessian. The better the initial Hessian, the better the predicted geometry and fewer steps needed to converge to the optimized geometry (the final optimized geometry, of course, is independent of the Hessian). At each step in the optimization, the approximate Hessian is updated, so that it eventually approaches the correct Hessian. Thus, with a poor initial Hessian, many of the optimization steps are needed just to improve the Hessian.

For a minimization, the initial Hessian must at least be positive definite (i.e. no zero or negative eigenvalues). For a transition structure or first order saddle point, a Hessian must have one and only one negative eigenvalue, and the corresponding eigenvector must be a reasonable approximation to the transition vector. Several alternatives are available for estimating the initial Hessian (most are automated in the more flexible MO programs). In order of increasing cost, these include:

(a) Unit matrix (or a unit matrix scaled by a constant). This contains no useful structural data about the molecule. Information about the stiffness or flexibility of various modes and the coupling between coordinates must be accumulated via the Hessian updating scheme during the course of the optimization. This will increase the number of optimization steps substantially. A (scaled or unscaled) unit is unsuitable for a saddle point optimization because it does not provide an estimate of the transition vector.

(b) Empirical force field Hessian. Molecular mechanics force fields can be quite good for minima, but the types of molecules and bonding situations treated by these force fields can be somewhat limited. A less accurate but more general scheme for estimating the Hessian from a simple valence force field has been used successfully

for minimizations [49]. No empirical force field is sufficiently general and reliable for transition states.

(c) Semi-empirical Hessians. Hessians calculated by semi-empirical MO methods are generally quite reasonable. Usually the Hessian must be scaled if it is used for ab initio calculations, since semi-empirical methods over-estimate some terms and underestimate others. A bit of caution is necessary for transition structures, because the geometry (and hence also the Hessian) for some transition structures optimized by semi-empirical methods can be rather different from those computed by ab initio methods.

(d) Numerical calculation of key elements of the Hessian. Gradient calculations at small displacements from the initial geometry can be used to calculate the more important rows and columns of the Hessian. For transition structure optimizations, it is essential that these include the coordinates that dominate the transition vector.

(e) Calculation of the full Hessian. The full Hessian can be calculated analytically or by numerically differentiating the gradients. The Hessian can be calculated at the same level as the optimization or with a smaller basis set (or at the SCF level for an optimization with correlation). Alternatively (but less accurate), the approximate Hessian from a lower level optimization on the same structure can be used.

(f) Recalculation of the full Hessian at each step in the optimization. This is the most expensive option, but may be necessary in a few of the most difficult cases.

12. Testing Stationary Points

Any stationary point found in an optimization should be tested to be sure that it has the proper number of imaginary frequencies or negative eigenvalues of the Hessian: i.e. 0 for a minimum and 1 for a transition state or first order saddle point. This is done by computing the full Hessian, either analytically or numerically, and diagonalizing the matrix or computing the vibrational frequencies. Note that the approximate Hessian obtained by an updating procedure in an optimization is not sufficiently accurate to test a stationary point. Furthermore, it does not contain any information about displacements to lower symmetry structures. If the stationary point has the wrong number of negative eigenvalues [50], a lower energy stationary point with the right number of negative eigenvalues can be found by distorting the molecule along the offending eigenvector and re-optimizing. Often this leads to a structure with lower symmetry and requires the Z-matrix to be rewritten in a lower symmetry form.

If the potential energy surface is not too flat, it has been common practice to test a stationary point at one level of calculation and assume that the addition of more basis functions and/or electron correlation does not change the nature of the stationary point. Weakly bound complexes, very flexible transition states and structures with strong configurational mixing can provide exceptions to this practice. If there is any doubt, the stationary point should be tested at the highest level of calculation used for the optimization.

For transition structures, it is also important to check the nature of the eigenvector with the negative eigenvalue to be sure that the saddle point connects the correct reactants and products. For some reactions, especially those involving non-least motion pathways, it may not be immediately obvious from the transition vector that the appropriate saddle point for the reaction has been found. In such cases, it may be necessary to follow the reaction path part of the way from the saddle point toward the reactants and toward the products to verify that the transition state is on the correct reaction path. A number of

algorithms for reaction path following have been published [51-55]. The most efficient method for following paths by MO calculations appears to be a recent method by Gonzalez and Schlegel [55].

13. Things to Try When Optimizations Fail

Optimizations misbehave for a variety of reasons. Listed below are a number of conditions that can be encountered during a minimization or a search for a saddle point. Some optimizers check for these problems, reporting them when they occur and stopping if necessary. Other optimizers struggle to continue and may terminate without warnings or diagnostics when the situation becomes hopeless. For conditions listed below, some possible causes are given and some remedies are suggested (however, there are no guaranties that the remedies will work).

Forces too large While this is not normally a problem, it may signal an error in the input: (a) the starting geometry may be poor, or (b) the coordinate system may be badly chosen, causing the optimizer to predict a poor geometry. Either get a better starting guess for the geometry or reconstruct the Z-matrix to avoid the strong coupling that caused the optimization to take a bad step.

Negative eigenvalues of the Hessian during a minimization This indicates that (a) the structure is not a minimum, or (b) numerical problems occurred in updating the Hessian. For (a), displace along the offending eigenvector to get to a lower energy structure and continue the optimization. For (b), restart the optimization with a better estimate of the Hessian. If the problem persists, it may be necessary to freeze the coordinates that dominate the vector with the negative eigenvalue. When the remaining coordinates have converged, the frozen variables can be released so that all coordinates can be optimized simultaneously.

Too many negative eigenvalues of the Hessian during a transition structure optimization Either (a) the optimization is converging on a second order saddle point, or (b) there are numerical problems with the Hessian. In case (a), examine the eigenvectors with the negative eigenvalues and choose one that does not correspond to the transition vector for the desired reaction; displace along this eigenvector until a minimum is found and restart the transition structure optimization from the new geometry with a new estimate of the Hessian (e.g. re-compute the Hessian elements for the displaced coordinates). The remedy for case (b) is the same as above - restart with a better estimate of the Hessian. Like with minimizations, if the problems persist, it may be necessary to freeze a few of the more flexible coordinates until the optimization gets closer to the saddle point.

No negative eigenvalues of the Hessian during a transition structure optimization There are 2 possible causes: (a) the structure is not a saddle point or is not sufficiently close to the quadratic region of the saddle point, or (b) there are numerical problems with the Hessian. For (a), any of the methods for getting closer to the transition state can be tried (Section 9): (i) linear synchronous transit (starting from the current structure plus a corresponding structure on the other side of the transition state), (ii) coordinate driving (several steps of increment the coordinate dominating the reaction path and minimizing of the rest of the coordinates) or (iii) eigenvector following (choose the appropriate eigenvector and use one of the hill climbing algorithms to follow the path of shallowest ascent toward the transition structure). Once a more suitable starting structure has been found, one of the direct methods for transition structure optimization can be used. The remedy for case (b) is the same as above - restart with a better estimate of the Hessian.

Eigenvalue of the Hessian too large While this is not normally a problem, it may signal an error in the input. This may be due to (a) a bad initial Hessian (get a better estimate), (b) a bad update of the Hessian (restart with a new estimate of the Hessian) or (c) a strongly coupled coordinate system (reconstruct the Z-matrix to avoid the strong coupling).

Eigenvalue of the Hessian too small There are a number of possible causes for this problem: (a) the molecule is actually in a shallow minimum and should have small eigenvalues, (b) there is a redundancy in the choice of internal coordinates or (c) there are numerical problems with the Hessian. For (a) it may be necessary to tighten the convergence criteria (e.g. RMS gradient) as well as the optimization control parameters (like the test for small eigenvalues). Case (b) is the more likely problem and requires that the Z-matrix be reconstructed to remove the redundancy (see Section 6). The remedy for (c) is to restart with a better estimate of the Hessian.

Number of steps exceeded The possibilities are: (a) it really is a difficult optimization and needs more steps, (b) there is a redundancy in the internal coordinates (fix the Z-matrix and restart), (c) there are some very loose coordinates that are slowing the optimization (freeze the loose coordinates until the others have converged, then unfreeze the coordinates and optimize everything), (d) there is strong coupling in the coordinate system (restructure the Z-matrix and restart the optimization), or (e) the initial estimate of the Hessian was quite poor (recalculate a few of the elements of the Hessian and continue the optimization).

Maximum step size exceeded If the step size is larger than the trust radius, most optimizers scale the step to the appropriate length. If this occurs frequently, it may be indicative of a small eigenvalue in the Hessian; the causes and remedies for this have been discussed above.

Step size too small, optimization goes nowhere despite sizeable gradients This could be due to: (a) too small a trust radius, (b) tightly coupled coordinates and/or a very non-quadratic energy surface, or (c) a Hessian with some spuriously large matrix elements. Case (a) is probably caused by inappropriate updating of the trust radius; hence this feature should be temporarily disabled and the optimization continued. The remedy for (b) is to reconstruct the Z-matrix to avoid the strong coupling and to simplify the behavior of the energy surface. Case (c) can be overcome by continuing the optimization with an improved estimate of the Hessian.

Change in point group detected during an optimization Either (a) the Z-matrix does not reflect the full symmetry of the molecule and the optimization has inadvertently distorted the molecule (fix the Z-matrix and restart the optimization), or (b) the molecule has C_s or C_2 symmetry and the principle axes have changed order (continue the optimization, possibly with symmetry suppressed).

Conclusions

This Chapter has attempted to discuss some of the practical problems of geometry optimization. Though optimization algorithms vary from MO program to MO program, they share a number of features and shortcomings. The 3 areas of input that most affect the performance of a given geometry optimization algorithm are: (a) the choice of internal coordinates (redundancy and strong coupling must be avoided), (b) the starting geometry, and (c) the initial estimate of the Hessian. Symmetry, the use of dummy atoms, coordinate redundancy, strong coupling among coordinates, conversion between coordinate systems and testing of stationary points have been considered in some detail. Finally, some of the conditions that cause optimizations to misbehave have been discussed and some remedies have been suggested. Although much of the discussion draws on experience with the

GAUSSIAN series of programs, the concepts and suggestions should be applicable to most geometry optimizations and transition structure searches based on internal coordinates.

Appendix: Optimization, Searching and Numerical Differentiation Links in GAUSSIAN

L101 Symbolic Z matrix input.

L102 Fletcher-Powell minimization method using only the energy [56].

L103 Berny optimization method for equilibrium geometries and transition structures [43].

L105 Murtagh-Sargent minimization method using gradients [57].

L106 Calculation of the Hessian by numerical differentiation of the gradients.

L107 Linear synchronous transit (requires only the energy) [39].

L108 Potential surface scan.

L109 Fixed metric optimization for equilibrium geometries and transition structures using gradients obtained by numerical differentiation of the energy.

L110 Calculation of the Hessian by numerical second derivatives of the energy.

L111 Calculation of hyperpolarizabilities by numerical second derivatives of the dipole moment.

L113 Eigenvector following algorithm using numerical gradients [42].

L114 Eigenvector following algorithm using analytical gradients [42].

L115 Reaction path following using gradients [55].

References

1. Hehre, W. J., Radom, L., Schleyer, P. vR., and Pople, J. A., *Ab Initio Molecular Orbital Theory,* Wiley-Interscience,New York, 1986.
2. Ohno, K., and Morokuma, K., *Quantum Chemistry Literature Data Base,* Elsevier, Amsterdam, 1982; yearly supplements published in special issues of the journal *J. Mol. Struct./Theochem.*; on-line version available through Japan Assoc. for International Chemical Information.
3. Whiteside, R. A., Frisch, M. J., and Pople, J. A., *The Carnegie-Mellon Quantum Chemistry Archive,* 3rd Ed., Carnegie-Mellon University, Pittsburgh, 1983; current version available on-line from Gaussian, Inc.
4. Frisch, M. J., Binkley, J. S., DeFrees, D. J., Raghavachari, K., Schlegel, H. B., Whiteside, R. A., Fox, D. J., Martin, R. L., Fluder, E. M., Melius, C. F., Kahn, L. R., Stewart, J. J. P., Bobrowicz, F. W., and Pople, J. A., *GAUSSIAN 86,* Carnegie-Mellon Publishing Unit, Pittsburgh, 1984, and subsequent releases.
5. Pulay, P., *Adv. Chem. Phys.,* **69**, 241 (1987).
6. Jørgensen, P., and Simons, J. (Eds.), *Geometrical Derivatives of Energy Surfaces and Molecular Properties,* Reidel, Dordrecht, 1986.
7. Gaw, J. F., and Handy, N. C., *Annu. Rep. Prog. Chem. Sec. C,* **81**, 291 (1985).
8. Fogarasi, G., and Pulay, P., *Annu. Rev. Phys. Chem.,* **35**, 191 (1984).

9. Fitzgerald, G., Harrison, R., Laidig, W. D., and Bartlett, R. J., *J. Chem. Phys.*, **82**, 4379 (1985).
10. Gauss, J., and Cremer, D., *Chem. Phys. Lett.*, **138**, 131 (1987).
11. Krishnan, R., Schlegel, H. B., and Pople, J. A., *J. Chem. Phys.*, **72**, 4654 (1980); Brooks, B. R., Laidig, W. D., Saxe, P., Goddard, J. D., Yamaguchi, Y., and Schaefer, H. F., *J. Chem. Phys.*, **72**, 4652 (1980); Osamura, Y.; Yamaguchi, Y., and Schaefer, H. F.,*J. Chem. Phys.*, **77**, 383 (1982); Rice, J. E., Amos, R. D., Handy, N. C., Lee, T. J., and Schaefer, H. F., *J. Chem. Phys.*, **85**, 963 (1986); Shepard, R., *Int. J. Quantum Chem.*, **31**, 33 (1987).
12. Scheiner, A. C., Scuseria, G. E., Rice, J. E., Lee, T. J., and Schaefer, H. F., *J. Chem. Phys.*, **87**, 5361 (1987); Fitzgerald, G., Harrison, R., Laidig, W. D., and Bartlett, R. J., *Chem. Phys. Lett.*, **117**, 433 (1985); Adamowicz, L., Laidig, W. D., and Bartlett, R. J., *Int. J. Quantum Chem. Symp*, **18**, 245 (1984).
13. Kato, S., and Morokuma, K., *Chem. Phys. Lett.*, **65**, 19 (1979); Goddard, J. D., Handy, N. C., and Schaefer, H. F., *J. Chem. Phys.*, **71**, 1525 (1979); Schlegel, H. B., and Robb, M. A., *Chem. Phys. Lett.*, **92**, 43 (1982); Knowles, P. J., Sexton, G. J., and Handy, N. C., *Chem. Phys.*, **72**, 337 (1982); Taylor, P. R., *J. Comput. Chem.*, **5**, 589 (1984).
14. Pople, J. A., Krishnan, R., Schlegel, H. B., and Binkley, J. S., *Int. J. Quantum Chem. Symp*, **13**, 225 (1979).
15. Handy, N. C., Amos, R. D., Gaw, J. F., Rice, J. E., Simandiras, T. J., Lee, T. J., Harrison, R. J., Laidig, W. D., Fitzgerald, G., and Bartlett, R. J., in ref. [6]; Handy, N. C., Amos, R. D., Gaw, J. F., Rice, J. E., and Simandiras, T. J., *Chem. Phys. Lett.*, **120**, 151 (1985).
16. Lee, T. J., Handy, N. C., Rice, J. E., Scheiner, A. C., and Schaefer, H. F., *J. Chem. Phys.*, **85**, 3930 (1986).
17. Camp, R. N., King, H. F., McIver, J. W., and Mullally, D., *J. Chem. Phys.*, **79**, 1088 (1983); Hoffman, M. R., Fox, D. F., Gaw, J. F., Osamura, Y., Yamaguchi, Y., Grev, R. S., Fitzgerald, G., Schaefer, H. F., Knowles, P. J., and Handy, N. C., *J. Chem. Phys.*, **80**, 2660 (1984); Page, M., Saxe, P., Adams, G. F., and Lengsfield, *J. Chem. Phys.*, **81**, 434 (1984)
18. Gaw, J. F., Yamaguchi, Y., and Schaefer, H. F., *J. Chem. Phys.*, **81**, 6395 (1984); Gaw, J. F., Yamaguchi, Y., Schaefer, H. F., and Handy, N. C., *J. Chem. Phys.*, **85**, 5132 (1986); Gaw, J. F., Yamaguchi, Y., Remington, R. B., Osamura, Y., and Schaefer, H. F., *Chem. Phys.*, **109**, 237 (1986); Schaefer, H. F., and Yamaguchi, Y., *J. Mol. Struct.*,**135**, 369 (1986); Gaw, J. F., and Handy, N. C., in [6].
19. Duran, M., Yamaguchi, Y., Osamura, Y., and Schaefer, H. F., *J. Mol. Struct.*,**163**, 389 (1988).
20. Pulay, P., *J. Chem. Phys.*, **78**, 5043 (1983); Almlöf, J., and Taylor, P. R., *Int. J. Quantum Chem.*, **27**, 743 (1985).
21. Jørgensen, P., and Simons, J. *J. Chem. Phys.*, **79**, 334 (1983).
22. Schlegel, H. B., in *Computational Theoretical Organic Chemistry* (Eds. Csizmadia, I. G., and Daudel, R.), Reidel, Dordrecht, 1981.
23. Schlegel, H. B., *Adv. Chem. Phys.*, **67**, 249 (1987).
24. Bell, S., and Crighton, J. S., *J. Chem. Phys.*, **80**, 2464 (1984).
25. Head, J. D., Weiner, B., and Zerner, M. C., *Int. J. Quantum Chem.*, **33**, 177 (1988).
26. Scales, L. E., *Introduction to Non-linear Optimization*, MacMillan, Basingstoke, 1985.
27. Fletcher, R., *Practical Methods of Optimization*, Wiley, Chichester, 1981.

28. Gill, P. E., Murray, W., and Wright, M. H., *Practical Optimization,* .Academic Press, New York, 1982; Powell, R., *Non-linear Optimization,* Academic Press, New York, 1982.
29. Clark, T., *A Handbook of Computational Chemistry,* Wiley-Interscience, New York, 1985.
30. Stanton, R. E., and McIver, Jr, J. W., *J. Am. Chem. Soc.,* **97**, 3632 (1975).
31. Thiel, W., *J. Mol. Struct.,* **163**, 415 (1988).
32. (a) The author wishes to thank Dr. M. J. Frisch for the guidelines for using symmetry to place dummy atoms. These algorithms have been incorporated in the program NewZmat [33b]; (b) Frisch, M. J., *NewZmat,* 1986.
33. Pople, J. A., *J. Am. Chem. Soc.,* **102**, 4615 (1980); Pople, J. A., Sataty, Y. A., and Halevi, E. A., *Israel J. Chem.,* **19**, 290 (1980).
34. Pople, J. A., and Gordon, M. S., *J. Am. Chem. Soc.,* **89**, 4253 (1967); Radom, L., Hehre, W. J., and Pople, J. A, *J. Am. Chem. Soc.,* **93**, 289 (1971).
35. Peterson, M. R., and Csizmadia, I. G., *J. Mol. Struct.,* **125**, 399 (1985).
36. Burkert, U., and Allinger, N. L., *Molecular Mechanics,* American Chemical Society, 1981.
37. Sadlej, J., (Cooper, I. L., transl. ed.) *Semi-empirical Methods of Quantum Chemistry,* Ellis Horwood, Chichester, 1985.
38. Segal, G. A., *Semi-empirical Methods of Electronic Structure Calculation,* (Modern Theoretical Chemistry Vol. 7 and 8) Plenum, New York, 1977.
39. Halgren, T. A., and Lipscomb, W. N., *Chem. Phys. Lett.,* **49**, 225 (1977).
40. Cerjan, C. J., and Miller, W. H., *J. Chem. Phys.,* **75**, 2800 (1981); Simons, J. Jørgensen, P., Taylor, H., and Ozment, J., *J. Chem. Phys.,* **87**, 2745 (1983); Nguyen, D. T., and Case, D. A., *J. Phys. Chem.,* **89** 4020 (1985); Banerjee, A., Adams, N., Simons, J., and Shepard, *J. Phys. Chem.,* **89** 52 (1985).
41. Hoffman, D. K., Nord, R. S., Ruedenberg, K., *Theor. Chim. Acta.,* **69**, 265 (1986); Jørgensen, P., Jensen, H. J. A., and Helgaker, T., *Theor. Chim. Acta.,* **73**, 55 (1988)
42. Baker, J., *J. Comput. Chem.,* **7**, 385 (1986).
43. Schlegel, H. B., *J. Comput. Chem.,* **3**, 214 (1982).
44. Scharfenberger, P., *J. Comput. Chem.,* **3**, 277 (1982).
45. Tapia, O., and Andrés, J., *Chem. Phys. Lett.,* **109**, 471 (1984).
46. Bell, S., Crighton, J. S., and Fletcher, R., *Chem. Phys. Lett.,* **82**, 122 (1981).
47. Head, J. D., Weiner, B., and Zerner, M. C., *Int. J. Quantum Chem.,* **33**, 177 (1988).
48. Bálint, I., and Bán, M. I., *Theor. Chim. Acta.,* **63**, 255 (1983).
49. Schlegel, H. B., *Theor. Chim. Acta.,* **66**, 333 (1984).
50. Under some circumstances an imaginary frequency may also signal an instability in the wavefunction.
51. Ishida, K., Morokuma, K., and Komornicki, A., *J. Chem. Phys.,* **66**, 2153 (1977);Schmidt, M. W., Gordon, M. S., and Dupuis, M., *J. Am. Chem. Soc.,* **107**, 2585 (1985).
52. Müller, K., and Brown, L. D., *Theor. Chim. Acta.,* **53**, 75 (1979).
53. Garrett, B. C., Redmon, M. J., Steckler, R., Truhlar, D. G., Baldridge, K. K., Bartol, D., Schmidt, M.W., and Gordon, M.S., *J. Phys. Chem.,* **92** 1476 (1988).
54. Page, M., and McIver, Jr, J. W., *J. Chem. Phys.,* **88**, 922 (1988).
55. Gonzalez, C., Schlegel, H. B., submitted; also described in ref [23].
56. Fletcher, R., and Powell, M. J. D., *Comput. J.,* **6**, 163 (1963); Davidon, W., *Argonne Nat. Lab. Report,* ANL-5990; Binkley, J. S., *J. Chem. Phys.,* **64**, 5142 (1976).
57. Murtagh, B. A., and Sargent, R. W. H., *Comput. J.,* **13**, 185 (1972).

REACTION TOPOLOGY AND QUANTUM CHEMICAL MOLECULAR DESIGN ON POTENTIAL ENERGY SURFACES

Paul G. Mezey
Department of Chemistry and
Department of Mathematics,
University of Saskatchewan,
Saskatoon, Canada, S7N 0W0

ABSTRACT. The analysis of potential energy surfaces is of fundamental importance in placing the study of reaction mechanisms on a sound theoretical basis. The existence and stability of chemical species and the feasibility of various reaction mechanisms are determined by the differential geometrical and topological properties of energy hypersurfaces. Several rules have been determined for the interrelations among reaction mechanisms; collectively these rules define an energy-dependent algebraic group, the *fundamental group of reaction mechanisms* of a topological space obtained from the given potential energy hypersurface.

The actual, computational determination of the fundamental group of reaction mechanisms requires the calculation of a well selected set of points of the potential energy hypersurface by a quantum chemical method, followed by the application of a multidimensional contour following algorithm. A method has been proposed and a computer program has been written, based on a multidimensional osculation polynomial algorithm for a quasi-global optimization of potential energy surfaces. The algorithm is specially designed for exploiting the novel characteristics of information processing of computers with multiple processors.

J. Bertrán and I. G. Csizmadia (eds.),
New Theoretical Concepts for Understanding Organic Reactions, 55–76.
© 1989 by Kluwer Academic Publishers.

1. INTRODUCTION

Molecular conformational changes and chemical reactions can be represented by nuclear displacements, described in terms of a suitable set of internal coordinates (e.g. internuclear distances and angles). These coordinates define a multidimensional *nuclear configuration space.* Continuous functions of two variables can be represented as surfaces over a coordinate plane. By analogy, the molecular energy as a function of these internal coordinates may be regarded as a multidimensional *potential energy hypersurface* over the configuration space [see, for example, 1-14, and references therein]. Note that a hypersurface belongs to the family of all possible geometrical arrangements of a given set of atoms, more precisely, to a given set of nuclei and a number of electrons of some specified electronic state. That is, the hypersurface represents an entire family of molecules and molecular fragments with a fixed overall stoichiometry, and not just a single molecule.

The potential energy hypersurfaces contain the fundamental information about chemical reactions and conformational changes involving this family of atoms. The calculation and detailed analysis of such hypersurfaces is a very complicated task due to the large number of internal coordinates. Fortunately, most of the fundamental, chemically important properties of hypersurfaces are topological. For the study of the most essential aspects of reaction mechanisms, activation energy conditions, and conformational rearrangements, it is often sufficient to analyse these topological properties using the methods of differential and algebraic topology [14, and references therein]. The application of various topological methods for the analysis of chemical reactions and conformational changes, usually within the context of potential energy hypersurfaces, forms the basis of *reaction topology.*

In earlier chemical literature the word "topology" has often been used in a limited sense, with reference to graph theory of formal chemical bonds. It is important to realize that reaction topology of potential energy hypersurfaces has no direct connection with these graph theoretical approaches. Reaction topology is based on the techniques of point set topology, algebraic and diffferential topology, and manifold theory [15-25].

The purpose of this chapter is to provide a concise review of the background of reaction topology and to provide new suggestions for the representation and analysis of potential energy hypersurfaces, with some

emphasis on the problems of quantum chemical molecular design.

2. NUCLEAR CONFIGURATION SPACES

Each formal nuclear configuration of N nuclei can be characterized by 3N mass weighted cartesian coordinates, $x_1, y_1, z_1, \ldots x_i, y_i, z_i, \ldots x_N, y_N, z_N$, where the cartesian coordinates X_i, Y_i, Z_i of each nucleus i are multiplied by the square root of the nuclear mass m_i, for example $x_i = (m_i)^{1/2} X_i$. The resulting 3N numbers can be thought of as coordinates of a point **r** in a 3N-dimensional configuration space ${}^{3N}E$. The above mass weighting is advantageous for dynamical studies. For example, a small ΔX_i displacement of a heavy nucleus is more significant than the same displacement of a light nucleus; this is properly reflected in the kinetic energy expressions when using the weighted coordinates x_i.

Chemically distinct configurations are represented by distinct points **x** of this configuration space (formal elements of the space, $\mathbf{x} \in {}^{3N}E$). However, chemically equivalent configurations obtained from one another by rigid translations and rotations in three dimensions are also represented by different points **x** of ${}^{3N}E$, and from simple inspection, it is not immediately obvious whether two points $\mathbf{x}_1$ and $\mathbf{x}_2$ correspond to two chemically different or equivalent arrangements of the N nuclei. Whereas the concept of distance has a mathematically correct definition in space ${}^{3N}E$, this distance does not always reflect actual chemical differences in configurations, and two points $\mathbf{x}_1$ and $\mathbf{x}_2$ that are far apart in ${}^{3N}E$ may represent the very same relative arrangement of the nuclei. In fact, in ${}^{3N}E$ there are three translational and three rotational degrees of freedom for a general configuration **x** of any larger-than-diatomic system.

This difficulty can be avoided by using 3N-6 internal coordinates, such as bond angles, torsional angles, and bond distances, defined in terms of some reference configuration, usually a local energy minimum of a stable molecule. This is the usual approach followed in the normal coordinate analysis of molecular vibrations. However, a given choice of internal coordinates is not generally applicable for all possible configurations of the N nuclei, since their very definition may become meaningless in some configurations (for example, that of a torsional angle when the four nuclei involved in the definition of the

torsion angle become collinear). This is a serious disadvantage of bond angle / bond length internal coordinate systems, since they are not suitable for a global analysis of potential surfaces and nuclear configurations. In particular, no general measure can be defined in terms of them for the description of how different two configurations are.

It is possible to eliminate the translational and rotational degrees of freedom for all configurations in a consistent manner, and to obtain a nuclear configuration space with a distance defined so that it reflects the chemical differences for all pairs of configurations. Such a space is the metric space M, the reduced nuclear configuration space [26,14]. It is defined as follows. Within ^{3N}E an internal configuration is represented by a subset K of points, where K contains all those points **x** of ^{3N}E that are related to one another by a transformation that corresponds to a rigid translation and rigid rotation of the nuclear arrangement in the ordinary, three-dimensional space. Each *subset* K of ^{3N}E is a *point* K of space M, where for simplicity the same notation K is used in the two roles. (M is said to be the *quotient space* of ^{3N}E with respect to the equivalence of internal configurations of points **x** of ^{3N}E).

It can be shown that the distance d of the K subsets in space ^{3N}E is a proper metric within space M, providing a well-defined measure for the degree of similarity between any two nuclear configurations [27]. If K_1 and K_2 are two conformations of a molecule, then the M space distance $d(K_1, K_2)$ is a numerical measure for their similarity. One may answer questions of the following type: how much is the deviation of an actual configuration K_1 from point group symmetry G ? If M_G is the subset of the configuration space that contains all configurations of point group symmetry G , then the distance

$$d(K_1, M_G) = \min \{ d(K_1, K_2) : K_2 \in M_G \} \qquad (1)$$

defines a mathematically proper measure of the deviation of configuration K_1 from symmetry G .

3. LEVEL SETS OF POTENTIAL ENERGY HYPERSURFACES

An important tool for the simplification of the analysis of a complicated multidimensional energy hypersurface E(K) is the concept of *level set.* An

F(A) level set of a potential energy hypersurface E(K) is that part of the configuration space M where the energy is less than a given value A :

$$F(A) = \{ K : E(K) < A \} . \qquad (2)$$

By limiting our analysis to a level set F(A) of a suitably chosen energy bound A, one may focus the attention to the chemically most relevant low energy regions. Level sets allow one to use a physical criterion, energy, for separating the important configurations from the rest of the configuration space, and they serve as a basis for the introduction of an algebraic structure for the analysis of reaction mechanisms.

4. CATCHMENT REGIONS

For a specified energy hypersurface E(K), the *catchment regions* [28,14] of a level set F(A) are analogous with features of watersheds and basins of geographical terrains [29,30]. The catchment regions C(λ,i) are defined by the formal, vibrationless relaxations of various nuclear configurations: a catchment region is the collection of all formal nuclear configurations from where a steepest descent on the surface leads to a given critical point, that is, to a point where the surface is locally horizontal (the gradient vanishes there).

Note that it is advantageous to consider the decomposition of the configuration space in terms of steepest descent paths and local geometrical information along montain ridges is not sufficient. For example, in the two-dimensional case both slopes on the two sides of a mountain ridge may belong to the same catchment region that bends around one of the mountain tops. Also, a ridge may start at a saddle point, leading to another saddle point, hence on one side of the first ridge, infinitesimally close to the saddle point, there are points that may belong to two different catchment regions (one such example is given on p.433, ref.14). Hence, next to a saddle point of a single mountain ridge one may find just one, and possibly as many as four catchment regions of minima. Local differential geometrical conditions are insufficient to distinguish among the topologically distinct possible cases.

In the general, n-dimensional case if the critical point **c**(λ,i) of the catchment region is a minimum (having no negative canonical curvatures, λ=0)

then the catchment region $C(\lambda,i)$ represents a *stable chemical species.*

If $\mathbf{c}(\lambda,i)$ is a simple saddle point (one with a single negative canonical curvature, that is, if the local Hessian matrix has precisely one negative eigenvalue, $\lambda=1$), then the catchment region $C(\lambda,i)$ represents a *transition structure* ("transition state").

If the critical point has more than one negative canonical curvatures ($\lambda>1$) then the catchment region $C(\lambda,i)$ represents an unstable family of formal configurations (a formal "species") of little direct chemical importance.

In a two-dimensional (2D) example the ridges between two maxima, M_i and M_j are the 1D catchment regions $C(1,k)$ of saddle points s_k ; these line segments represent transition structures. The catchment regions $C(0,i)$ of minima m_i are 2D subsets enclosed by these lines; the $C(0,i)$ sets represent stable chemical species. The formal, 0D catchment regions $C(2,i)$ of the maxima M_i are of little direct chemical significance, however, they represent constraints on the existence and interrelations of the catchment regions of minima and simple saddle points. For sake of uniformity in the terminology, all catchment regions $C(\lambda,i)$ are referred to as formal (possibly unstable, or zero probability) chemical species. The catchment regions, as representatives of all the chemical species present within the level set $F(A)$, generate a decomposition of the level set. Various topological methods are applicable for the extraction of the most important information on the mutual interrelations of catchment regions. The resulting topological description can be given in a concise, algebraic form, by incidence matrices and various homology groups [14]. The incidence matrices correspond to reaction networks [31], involving all the chemical species occurring within the level set $F(A)$.

There are fundamental, quantum mechanical reasons for representing chemical species by subsets of the configuration space. Individual points of a nuclear configuration space represent precisely defined, "crisp" nuclear geometries. These points have no direct, physical interpretation, since they are in conflict with the Heisenberg relation. This conflict is only partially circumvented by taking infinite families of such points, the catchment regions $C(\lambda,i)$, to represent chemical species. In particular, the conflict is not fully resolved for the boundary points of catchment regions. One approach one may follow to resolve this conflict is the introduction of a well-defined fuzziness for catchment regions [32,14], using the methods of fuzzy set theory [33-35], that leads to a somewhat different description. However, it is important to realize

that the essential, *topological* structure of the model remains invariant even after the introduction of fuzzy sets for the representation of chemical species within the configuration space.

5. REACTION GLOBES AND REACTION POLYHEDRA

The important, topological properties of level sets F(A) are easier to recognize if they are transformed into hyperspheres, or into polyhedra, called *reaction spheres* and *reaction polyhedra,* respectively [36,37].

If the perimeter of the energy basin E{F(A)} is "pulled down" and contracted, in the extreme case, into a point, then one obtains an alternative representation of the energy function. On the resulting *reaction globe* H(F) the energy function is regarded as elevation over a sphere, a concept analogous to that of elevation over sea level on the planet Earth. Some of the original hilltops that lie above the energy bound A of the level set F(A), correspond to "holes" on H(F), and an additional hole corresponds to the original perimeter of F(A), at the boundary of the energy basin E{F(A)}.

An even simpler representation is possible by converting the reaction globe H(A) into a *reaction polyhedron* P(A). The basins of individual minima can be replaced by faces of a polyhedron, P(F), whereas mountain ridges and maxima correspond to edges and vertices, respectively. Note that in many cases this transformation leads to abstract polyhedra that fulfill the topological conditions but cannot be realized as actual, geometrical objects. For example, picture a two-dimensional reaction globe as a planet of a smooth surface. If there are precisely two minima, two maxima and two saddle points on the surface of this planet, an obvious possibility, then the resulting polyhedron P(F) has two faces, two edges and two vertices, that cannot be realized as an actual polyhedron. Nevertheless, all the chemically important topological constraints are satisfied and represented by such an abstract polyhedron. In all cases, the reaction polyhedron P(F) provides a concise representation of the most essential features of the original energy surface E{F(A)} over the level set F(A). Whereas the 2D examples are the easiest to visualize, nevertheless, the same technique is applicable for higher dimensional potential energy hypersurfaces. In particular, the reaction polyhedron model provides a clear representation of the relations among catchment regions, that can be given in a

concise form, by incidence matrices and various homology groups [14]. The reaction network model and the homology groups, based on the incidence relations of catchment regions, are applicable for the study of reactions and interrelations among all chemical species occurring in level set F(A).

6. THE FUNDAMENTAL GROUP OF REACTION MECHANISMS

The potential surface model is the basis for an alternative description of reaction mechanisms [38-40,14] using another family of groups of algebraic topology: homotopy groups. "Homotopy" means "continuous deformation", that in the present context is applied to formal reaction paths in a configuration space. Which continuous deformations are allowed and which are not is controlled by the topology of the potential energy surface. A reaction mechanism corresponds to a family of reaction paths that are deformable into one another. Similarly to an individual nuclear configuration, that is non-physical for a quantum mechanical molecule [41-43], an individual reaction path is also non-physical, being in conflict with the uncertainty relation. One may, however, represent a chemical reaction by a family of infinitely many reaction paths, where the very fact that infinitely many paths are used, circumvents the incompatibility of individual paths with the Heisenberg relation. All paths within a family show common topological features, and the methods of topology are the natural choice for the analysis of these features. Within a given level set F(A), a topological condition that may be used for identifying families of reaction paths is given in terms of homotopy. For an energy bound A all those formal reaction paths that are deformable into one another, that is, *homotopic* to one another, belong to one such family, to a *homotopy equivalence class.* A reaction mechanism corresponds to a homotopy class [38-40,14].

Each path p is regarded as a continuous assignment of parameter values u from the unit interval I to points of the set F(A). A formal product of two paths is defined as the continuation of one path by the other, if their endpoints coincide. The concept of product can be generalized for homotopy classes: the product of two classes is the class that contains the products of paths from the two classes. This leads to an algebraic structure of reaction mechanisms, called a *groupoid,* that has fewer useful properties than groups. However, it is

possible to introduce a much stronger algebraic structure. Each path may be regarded as a segment of a loop (self-returning, formal reaction path), and the same applies for their equivalence classes, representing reaction mechanisms. Hence, the topological model allows one to provide a representation of all possible reaction mechanisms within a level set F(A) in terms of "circular" (or loop) reaction mechanisms. These latter are called the *fundamental reaction mechanisms* of the level set F(A). They form an algebraic group, the one dimensional homotopy group of the level set F(A), called the *fundamental group of reaction mechanisms* of F(A) [38-40,14]. The group operation may be pictured as the continuation of one mechanism by another.

The actual existence (realization) of a reaction and the interrelations between reaction mechanisms are dependent on the available energy. Similarly, the fundamental group of reaction mechanisms is also dependent on the energy bound A of the level set F(A). At a low energy bound A there are few chemical species and few actual reaction mechanisms, at higher energy there are more. However, as the energy bound is further increased, some hilltops that were missing at lower energies will no longer rise above the current energy bound A. Consequently, at higher energies more formal reaction paths become interconvertible into one another (homotopically equivalent). Hence the distinction between some reaction mechanisms becomes meaningless: they merge into a single reaction mechanism. The fundamental group of rection mechanisms, as a function of the available energy A, reflects the most essential, topological properties of all possible chemical reactions associated with the potential energy hypersurface.

7. MOLECULAR ENGINEERING AND SYNTESIS DESIGN ON POTENTIAL ENERGY SURFACES

An important field of present and future chemical research activity involving novel mathematical methods is computer-based synthesis design [see, for example, 44,45]. The development of topological methods for the analysis of potential surfaces and reaction mechanisms are expected to provide new approaches and important tools for synthesis design and molecular engineering. A direct, quantum chemical "brute force" approach to most synthetic problems of larger molecules of real chemical interest appears much too complicated at

present, due to the high dimension and the size of the computational problem. However, the knowledge of variuos topological constraints potential energy hypersurfaces must satisfy can be exploited in the analysis. For example, if some of the critical points of E(K) are known, either from experimental data or from an earlier computational study, then their topological relations form a rational basis for any further analysis, since these critical points constrain the number and approximate location of other critical points. Reaction topology provides the tools for a systematic exploration of potential energy hypersurfaces. In the next two sections a possible approach will be described.

8. SIMULTANEOUS OPTIMIZATION OF CRITICAL POINTS WITH PARALLEL PROCESSORS

As it has been pointed out [14], the advances in computer hardware, in particular, parallel processing on a large scale, open up new possibilities for a combination of experimental and quantum chemical approaches into a consistent model. Local neigborhoods of potential minima and saddle points of transition structures can be studied experimantally, however, little experimental information is available for most other nuclear arrangements occurring during chemical reactions. In fact, theoretically calculated potential energy hypersurfaces may well serve as bridges covering the rather large gaps between experimental pieces of information. For the simultaneous calculation of several features of the potential surface parallel processing offers new strategies.

Data on several critical points, when taken collectively and tested for mutual consistency, represent a rather strong constraint on a potential energy hypersurface. Consequently, it is advantageous to devise methods for the simultaneous optimization of several critical points $\mathbf{c}_1, \ldots \mathbf{c}_i, \ldots \mathbf{c}_m$ within some chemically important domain D of a configuration space. Such algorithms are somewhat cumbersome to implement on single processor, scalar computers, however, parallel processing allows the simultaneous computation of several points of the hypersurface. It is advantageous to perform parallel iterations for these critical points, while *updating* mutual constraints and cross-references in each iterative step. These mutual constraints can be

represented by an approximate potential energy hypersurface $E^t(\mathbf{r})$. The very fact that the known points are connected by $E^t(\mathbf{r})$ guarantees the fulfillment of some topological criteria, and provides a rational strategy for choosing the new approximations to the critical points in the next step in the simultaneous optimizations. This is the simplest if $E^t(\mathbf{r})$ is generated in some analytic form. Here we shall outline the general method proposed in ref [14], and suggest an improved technique for the generation of analytic representations of potential energy hypersurfaces.

At each iteration t of the simultaneous optimization the points already calculated are sufficient to generate an approximate hypersurface $E^t(\mathbf{r})$ of some *closed, analytic form,* using a fitting procedure. The *actual* critical points $\mathbf{c}^t_1, \ldots \mathbf{c}^t_i, \ldots$ of the *approximate* analytic hypersurface $E^t(\mathbf{r})$ can be determined with much less computational effort than that needed for expensive optimizations on the quantum chemical hypersurface $E(\mathbf{r})$. These points serve as the new family of approximations to the critical points of $E(\mathbf{r})$, and are used in the next iteration $t + 1$. Their determination on the *analytic* hypersurface $E^t(\mathbf{r})$ is a much easier computational task than their direct optimization on the actual quantum chemical hypersurface $E(\mathbf{r})$. They automatically satisfy their mutual topological constraints, as this is guaranteed by the existence of an analytic form of the approximate function $E^t(\mathbf{r})$. In the following step $t + 1$, the expensive quantum chemical energy functional $E(\mathbf{r})$ is evaluated only at these points $\mathbf{c}^t_1, \ldots \mathbf{c}^t_i, \ldots \mathbf{c}^t_m$, and the corresponding quantum chemical function values f^t_1, f^t_i, ... f^t_m at these points are used to generate the next approximate, *analytic* potential surface $E^{t+1}(\mathbf{r})$. A new set of critical points $\mathbf{c}^{t+1}_1, \ldots \mathbf{c}^{t+1}_i, \ldots \mathbf{c}^{t+1}_m$ is determined on the improved analytic function $E^{t+1}(\mathbf{r})$, and the iterative steps are repeated until satisfactory convergence is reached.

This iterative process is a quasi-global optimization of the approximate function, restricted to the vicinity of a family of critical points. If the process converges then the critical points of the approximate function and those of the quantum chemical hypersurface must coincide. The types, the location, and the function values of various critical points represent some constraints on one another as well as on the type and location of all other critical points. This fact is utilized in *each* iteration, leading to an improved simultaneous convergence for all m critical points. Whereas m critical point determinations must be repeated in each iterative step, the actual optimizations requiring many

function evaluations are carried out on the "inexpensive" functions $E^t(\mathbf{r})$ of closed, analytic forms. Only m "expensive" function evaluations of the quantum chemical function $E(\mathbf{r})$ are needed in each iterative step t. This algorithm may require much less computational effort than m direct, "brute force" optimizations on the quantum chemical hypersurface $E(\mathbf{r})$.

When using most of the advanced *ab initio* computer programs, in most applications it is advantageous to determine the energy gradients of the quantum chemical hypersurface $E(\mathbf{r})$ in addition to the energy values at points $\mathbf{c}^t_1, \ldots \mathbf{c}^t_{m(t)}$ in each step t. In such cases the approximate hypersurfaces $E^t(\mathbf{r})$ may be chosen so as to reproduce both the quantum chemical function values $f^t_1, \ldots f^t_{m(t)}$ and all the quantum chemical partial derivatives collected in the gradient vectors $\mathbf{g}^t_1, \ldots \mathbf{g}^t_{m(t)}$ at the specified points $\mathbf{c}^t_1, \ldots \mathbf{c}^t_{m(t)}$. Unless the critical points $\mathbf{c}^t_1, \ldots \mathbf{c}^t_{m(t)}$ of the approximate hypersurface $E^{t-1}(\mathbf{r})$ happen to be the true critical points of the quantum chemical hypersurface $E(\mathbf{r})$, the quantum chemical gradient vectors calculated in iteration t will not in general be zero.

A rather general algorithm for the implementation of the above idea has been described in ref [14] :

(i) Choose a domain D of the nuclear configuration space and a set $\{\mathbf{c}^0_i\}^{m(0)}_{i=1}$ of "guessed" initial points, $\mathbf{c}^0_i \in D$. These initial guesses may be based on experimental as well as theoretical information.

(ii) Set iteration count $t = 0$.

(iii) Calculate the quantum chemical function values $\{f^t_i\}^{m(t)}_{i=1}$, and gradient vectors, $\{\mathbf{g}^t_i\}^{m(t)}_{i=1}$ for points $\{\mathbf{c}^t_i\}^{m(t)}_{i=1}$ using the quantum chemical potential energy hypersurface $E(\mathbf{r})$.

(iv) Generate an approximate hypersurface $E^t(\mathbf{r})$ of *closed analytic form* that fits all data accumulated in step (iii).

(v) Find all critical points $\{\mathbf{c}^{t+1}_i\}, \ldots \{\mathbf{c}^{t+1}_{m(t+1)}\}$ (or, possibly, only those with $\lambda = 0$ and $\lambda = 1$) of approximate function $E^t(\mathbf{r})$ within domain D. Since function evaluations for $E^t(\mathbf{r})$ are inexpensive, this step is only moderately time-consuming.

(vi) Compare the critical points $\{\mathbf{c}^{t+1}{}_i\}^{m(t+1)}{}_{i=1}$ obtained in step (v) to points $\{\mathbf{c}^t{}_i\}^{m(t)}{}_{i=1}$. If satisfactory convergence is reached, stop. Otherwise,

(vii) Set $t = t + 1$. If $t > t_{max}$, a threshold, then stop. Otherwise,

(viii) Repeat from step (iii).

The success of an algorithm of the above type is critically dependent on the choice of the analytic representation of the approximate function $E^t(\mathbf{r})$. In the following section we shall propose a damped osculation polynomial for this purpose.

9. ANALYTIC FIT TO ENERGY HYPERSURFACES: A DAMPED OSCULATION POLYNOMIAL

An approximate function $E^t(\mathbf{r})$ may be generated by least squares or other approximate fitting methods to a suitable combination of Gaussian, trigonometric, and polynomial functions. Using such a fitting procedure, it is generally very difficult to reproduce exactly the data on the various known points. By contrast, a general, n-dimensional osculation polynomial may be used to obtain an *exact* fit to the specified function values and to each partial derivative at each specified point. As has been described in ref. [14], it is possible to generate a polynomial that has the lowest overall degree necessary to accomodate all the constraints given by function values and partial derivatives, if these constraints are independent. This polynomial, however, has the disadvantage that it often shows large oscillations between the specified points, that may introduce non-physical, artificial topological features. In this section we shall describe a general damping scheme that is designed to reduce or avoid these oscillations.

We shall assume that all reference points $\mathbf{r}_i$ are unique. In order to generate the original osculation polynomial, we write the n-dimensional

Lagrange interpolation term as

$$L_j(\mathbf{r}) = \frac{\prod_{i\neq j}^{m} |\mathbf{r}_i - \mathbf{r}|}{\prod_{i\neq j}^{m} |\mathbf{r}_i - \mathbf{r}_j|} = \frac{\prod_{i\neq j}^{m} \{ \sum_{k=1}^{n} (r_{ik} - r_k)^2 \}^{1/2}}{\prod_{i\neq j}^{m} \{ \sum_{k=1}^{n} (r_{ik} - r_{jk})^2 \}^{1/2}} \cdot \tag{3}$$

Its square,

$$L_j^2(\mathbf{r}) = \frac{\prod_{i\neq j}^{m} \{ \sum_{k=1}^{n} (r_{ik} - r_k)^2 \}}{\prod_{i\neq j}^{m} \{ \sum_{k=1}^{n} (r_{ik} - r_{jk})^2 \}} \tag{4}$$

does not involve square roots, it is differentiable at every point $\mathbf{r}$, and it is also a proper polynomial of integer degrees in the vector components r_k. One may exploit the fact that at point $\mathbf{r} = \mathbf{r}_j$ the function $L_j(\mathbf{r})$ itself is differentiable, and one may take the following function

$$E^{\bullet}(\mathbf{r}) = \sum_{j=1}^{m} f_j \left\{ 1 - 2 \sum_{k=1}^{n} \frac{\partial L_j(\mathbf{r}_j)}{\partial r_k} (r_k - r_{jk}) \right\} L_j^2(\mathbf{r})$$

$$+ \sum_{j=1}^{m} L_j^2(\mathbf{r}) \sum_{k=1}^{n} (r_k - r_{jk})\, g_{jk}\,, \tag{5}$$

where g_{jk} is component k of the specified gradient vector at point $\mathbf{r}_j$. Note that the derivative of function $L_j(\mathbf{r})$ at point $\mathbf{r} = \mathbf{r}_j$ is a *number*, consequently, function $E^{\bullet}(\mathbf{r})$ is an everywhere differentiable *polynomial* of

integer degrees in the vector components r_k. As it is easily seen, the highest degree of the polynomial $E^{\blacktriangle}(\mathbf{r})$ is $2m - 1$, for any combination of products of the r_k components of the variable position vector of the formal nuclear geometry $\mathbf{r}$. It is simple to verify by substitution and differentiation that the polynomial $E^{\blacktriangle}(\mathbf{r})$ reproduces each specified function value f_j as well as each specified partial derivative in all n dimensions, at each of the m specified points $\mathbf{r}_j$ of the nuclear configuration space. Indeed, $E^{\blacktriangle}(\mathbf{r})$ is an n-dimensional osculation polynomial.

This polynomial has advantageous numerical behaviour. The denominators of the fractions appearing in the expressions are zero only if any one of the specified points $\mathbf{r}_j$ is repeated, for example if $\mathbf{r}_j = \mathbf{r}_{j'}$, that is, if one of these points is redundant.

Whereas the polynomial $E^{\blacktriangle}(\mathbf{r})$ reproduces exactly all the selected function values and partial derivatives, it may show strong oscillatory behaviour. These oscillations can be reduced greatly by the following technique. Take a positive number $\alpha < 1$, and assume that a function $W(\mathbf{r})$ is given with the following properties: $0 \leq W(\mathbf{r}) \leq 1$, $W(\mathbf{r}) = 0$ if and only if $\mathbf{r} = \mathbf{r}_j$ for any of the specified points $\mathbf{r}_j$, and for its partial derivatives $\partial W(\mathbf{r}_j)/\partial r_k = 0$ for any of the indices j and k.

Consider a correction term to $E^{\blacktriangle}(\mathbf{r})$ in the form of $-\alpha E^{\blacktriangle}(\mathbf{r}) W(\mathbf{r})$. At the specified points $\mathbf{r}_j$ this correction term will affect neither the function values nor the partial derivatives, hence the osculation properties of the original polynomial are preserved. At any other point $\mathbf{r}$, however, the correction term will counteract the oscillations of the original osculation polynomial $E^{\blacktriangle}(\mathbf{r})$.

For the *damped osculation polynomial*

$$E^{NT}(\mathbf{r}) = E^{\blacktriangle}(\mathbf{r})(1 - \alpha W(\mathbf{r})) \tag{6}$$

the choice

$$W(\mathbf{r}) = \frac{\prod_{i=1}^{m} \left\{ \sum_{k=1}^{n} (r_{ik} - r_k)^2 \right\}}{\prod_{i=1}^{m-1} \prod_{j=i+1}^{m} \left\{ \sum_{k=1}^{n} (r_{ik} - r_{jk})^2 \right\}^{2/(m-1)}} \tag{7}$$

provides a simple approximation. (This function is not necessarily bounded by 1, however, by choosing a small enough α value, the product $\alpha W(\mathbf{r})$ is bounded by 1 within the convex hull of point set $\{\mathbf{r}_i\}^m_{i=1}$). Other choices for $W(\mathbf{r})$, taking into account more of the detailed features of the original osculation polynomial $E^*(\mathbf{r})$, are described elsewhere [46].

10. THE REFERENCE CLUSTER APPROCH : VARIATIONS IN THE SYMMETRY AND SHAPE OF MOLECULES ALONG POTENTIAL ENERGY SURFACES

Molecular symmetry and molecular shape have a strong influence on molecular behavior. Understanding how the shape of molecular electron distribution affects other chemical properties is of importance beyond its theoretical significance, for example, it may also help in such applied fields as devising new synthetic strategies in drug design. The purpose of the development of quantum chemical molecular engineering is to explore the possibilities of designing "custom made" molecules of certain desired properties [14].

In order to analyse the interrelations among shape, symmetry and other properties, different molecules with similar symmetry and shape features may be compared to models of ideal, abstract shapes. One such approach is based on the model of "reference clusters" of homonuclear systems, isoelectronic with a family of molecules of interest. The highest degree of symmetry and most shape regularities are expected to be shown by such homonuclear systems, and by interrelating these systems with heteroatomic molecules, symmetry and shape studies can be carried out within a systematic framework. In the comparison of the potential energy hypersurfaces of the reference cluster and those of the actual molecules, various results on nuclear charge variations may be utilized [47-56,14]. By a formal variation of the nuclear charges and by the induced deformations of the potential energy surfaces, one may obtain any one of the actual potential surfaces for a given molecular family. By analyzing the topological constraints on these deformations, one can derive various rules and recognize certain common properties. In particular, the catchment region decompositions of potential surfaces of various N-nucleus sytems, containing

the same number of nuclei but of different nuclear charges, are not independent [52]. Knowledge of the catchment regions of the reference cluster provides constraints on the catchment regions of other N nucleus sytems obtained by formal nuclear charge variations. Strong global constraints are available for the special case of comparing potential energy hypersurfaces of isoelectronic and isoprotonic stoichiometric families [48], that is, isoelectronic systems where the sum of nuclear charges is the same. Note that the nuclear charges in the homonuclear reference cluster may be set equal to the average nuclear charge of a stoichiometric family, and this may be a noninteger number. In such cases the reference cluster is a fictitious, nonphysical model that, nonetheless, can provide a suitable mathematical framework for the analysis.

The basic idea of the proposed approach follows from an important theorem on catchment regions: it has been pointed out [ref. 14, p367] that the nuclear configuration represented by the critical point $\mathbf{c}(\lambda,i)$ in each catchment region $C(\lambda,i)$ must have the highest point symmetry within $C(\lambda,i)$. This *catchment region point symmetry theorem* follows from the point symmetry group distribution along steepest descent paths. It is known that along a steepest descent path the point symmetry (in fact, the framework group) of nuclear configurations may change only at a critical point, where it must have all the those point symmetry (framework group) elements that are present at non-critical points of the path [57]. Since the critical point $\mathbf{c}(\lambda,i)$ in each catchment region $C(\lambda,i)$ is the endpoint of all steepest descent paths that lie within $C(\lambda,i)$, it follows that $\mathbf{c}(\lambda,i)$ must have all the point symmetry elements of all nuclear configurations represented by points within the catchment region $C(\lambda,i)$. Hence the statement of the theorem follows. A somewhat stronger *catchment region framework group theorem* is also valid: the framework groups of nuclear configurations of all points $\mathbf{r}$ within a catchment region $C(\lambda,i)$ are subgroups of the framework group of the nuclear configuration represented by the critical point $\mathbf{c}(\lambda,i)$. Its proof is obtained by replacing the term "point symmetry" with "framework group" in the proof of the *catchment region point symmetry theorem* . Analogous theorems are valid for the catchment regions of the inverted potential energy hypersurface $-E(\mathbf{r})$, utilizing the analogous properties of steepest ascent paths, as well as for catchment regions of other physical properties defined as hypersurfaces over a nuclear configuration space [58].

Observe that the distribution of catchment regions and the location of critical points are the properties of the potential energy surface, that is, they depend on *energy relations,* whereas the point symmetries of various nuclear configurations are purely *geometrical properties,* independent from energetic relations. The symmetry of a fixed nuclear configuration is independent of the electronic state of the molecule; for example, a given nuclear configuration **r** has its particular point symmetry for all possible electronic states of various energy values.

The catchment region point symmetry theorem interrelates a purely geometric condition (symmetry), with an energy condition (the lowest point within a catchment region). The important fact is that this result is valid for the potential surfaces of all electronic states of the given set of nuclei. Hence point symmetries and framework groups of nuclear configurations provide a condition that interrelates the *catchment regions* of different electronic states.

In fact somewhat more is true. Among all N nucleus systems the most detailed point symmetry decomposition of the nuclear configuration space is obtained for the reference cluster, since the presence of N identical nuclei ensures the highest possible point symmetry for some configurations. The point symmetry (or framework group) decomposition of the nuclear configuration space of the reference cluster provides a common framework for the analysis of catchment region and symmetry relations for all chemical systems obtained by gradually replacing the nuclei of the reference cluster by heteronuclei. In particular, all boundaries of symmetry domains of the nuclear configuration space of a heteroatomic system must also be present as domain boundaries within the nuclear configuration space of the reference cluster. Further rules and detailes of the reference cluster approach are presented elsewhere [58]. These rules provide new tools for the analysis of regularities and symmetry properties of potential surfaces [59,60].

Acknowledgment

The research leading to the developments reviewed above have been supported by grants from the Natural Sciences and Engineering Research Council of Canada.

References

1 K. Fukui, J. Phys. Chem., **74**, 4161 (1970).

2 A. Tachibana and K. Fukui, Theor. Chim. Acta, **51**,189 (1979).

3 G. Leroy, M. Sana, L.A. Burke, and M.-T. Nguyen, in *Quantum Theory of Chemical Reactions,* R. Daudel, A. Pullman, L. Salem, and A. Veillard, Eds., Reidel, Dordrecht, 1979.

4 W.H. Miller, N.C. Henry, and J.E. Adams, J. Chem. Phys., **72**, 99 (1980).

5 K. Fukui, Acc. Chem. Res., **14**, 363 (1981).

6 D. Truhlar, Ed., *Potential Energy Surfaces and Dynamics Calculations,* Plenum, New York, 1981.

7 P. Pulay, in *The Force Concept in Chemistry* , B.M. Deb, Ed., Van Nostrand - Reinhold, Toronto, 1981.

8 T. Oie, G. M. Maggiora, R. E. Christoffersen, and D. J. Duchamp, Internat. J. Quantum Chem., Quant. Biol. Symp., **8**, 1 (1981).

9 J. Maruani and J. Serre, Eds., *Symmetries and Properties of Non-Rigid Molecules,* Elsevier, Amsterdam, 1983.

10 H.B. Schlegel, Theor. Chim. Acta, **66**, 333 (1984).

11 G.G. Hall, Theor. Chim. Acta, **67**, 439 (1985).

12 F. Bernardi, M. Olivucci, M.A. Robb, and G. Tonachini, J.Am.Chem.Soc., **108**, 1408 (1986).

13 J.N. Murrell, S. Carter, S.C. Farantos, P. Huxley, and A.J.C. Varandas, *Molecular Potential Energy Functions,* Wiley, New York, 1984.

14 P.G. Mezey, *Potential Energy Hypersurfaces,* Elsevier, Amsterdam, 1987.

15 T.W. Gamelin, and R.E. Greene, *Introduction to Topology,* Saunders College Publishing, New York, 1963.

16 G.F. Simmons, *Introduction to Topology and Modern Analysis,* McGraw-Hill, New York, 1963.

17 J. Munkres, *Elementary Differential Topology,* Annals of Math. Studies, **54**, Princeton Univ. Press, Princeton, 1963.

18 R.L. Bishop, and R.J. Crittenden, *Geometry of Manifolds,* Academic Press, New York, 1964.

19 M. Spivak, *Calculus on Manifolds,* Benjamin, Don Mills, Ont., 1965.

20 E.H. Spanier, *Algebraic Topology,* McGraw-Hill, New York, 1966.

21 M. Greenberg, *Lectures on Algebraic Topology,* Benjamin, New York, 1967.

22 S.-T. Hu, *Elements of General Topology,* Holden-Day, San Francisco, 1969.

23 J. Vick, *Homology Theory,* Academic Press, New York, 1973.

24 V. Guillemin, and A. Pollack, *Differential Topology,* Prentice Hall, Englewood Cliffs, 1974.

25 I.M. Singer, and J.A. Thorpe, *Lecture Notes on Elementary Topology and Geometry,* Springer-Verlag, New York, 1976.

26 P.G. Mezey, Theor. Chim. Acta, **63**, 9 (1983).

27 P.G. Mezey, Int. J. Quant. Chem., **26**, 983 (1984).

28 P.G. Mezey, Theor. Chim. Acta, **58**, 309 (1981).

29 C.A. Cayley, Philos. Mag., **18**, 264 (1859).

30 J.C. Maxwell, Philos. Mag., **40**, 233 (1870).

31 P.G. Mezey, Theor. Chim. Acta, **60**, 409 (1982).

32 P.G. Mezey, in *Mathematics and Computational Concepts in Chemistry,* N. Trinajstic, Ed., Ellis Horwood Publ. Co., Chichester, U.K., 1986.

33 L.A. Zadeh, Inform. Control, **8**, 338 (1965).

34 L.A. Zadeh, J. Math. Anal. Appl., **23**, 421 (1968).

35 P.P. Wang, and S.K. Chang, Eds., *Fuzzy Sets,* Plenum, New York, 1980.

36 P. G. Mezey, Internat. J. Quantum Chem., Quant. Chem. Symp., **19**, 93 (1985).

37 P.G. Mezey, Internat. J. Quantum Chem., **29**, 333 (1986).

38 P. G. Mezey, Internat. J. Quantum Chem. Symp., **18**, 77 (1984).

39 P. G. Mezey, Theor. Chim. Acta, **67**, 43, 91 (1985).

40 P.G. Mezey, Part 1, in *Structure and Dynamics of Molecular Systems,* R. Daudel, J.-P. Korb, J.-P. Lemaistre, and J. Maruani, Eds., Reidel, Dordrecht, 1985.

41 E. Prugovecki, J. Phys. A, **9**, 1851 (1976).

42 S.T. Ali and H.D. Doebner, J. Math. Phys., **17**, 1105 (1976).

43 S.T. Ali and E. Prugovecki, J. Math. Phys., **18**, 219 (1977).

44 W.T. Wipke and W.J. Howe, Eds., *Computer-Assisted Organic Synthesis,* ACS Symp. Ser. 61, American Chemical Society, Washington, 1977.

45 R.K. Lindsay, B.G. Buchanan, E.A. Feigenbaum, and J. Lederberg, *Applications of Artificial Intelligence for Organic Chemistry: The DENDRAL Project,* McGraw-Hill, New York, 1980.

46 P.G. Mezey, to be published.

47 P.G. Mezey, Theor. Chim. Acta, **59**, 321 (1981).

48 P.G. Mezey, Int. J. Quant. Chem. Symp., **15**, 279 (1981).

49 P.G. Mezey, Int. J. Quant. Chem., **22**, 101 (1982).

50 P.G. Mezey, J. Chem. Phys., **80**, 5055 (1984).

51 P.G. Mezey, J. Am. Chem. Soc., **107**, 3100 (1985).

52 P.G. Mezey, Int. J. Quant. Chem., **29**, 333 (1986).

53 G.A. Arteca and P.G. Mezey, Phys. Rev. A, **35**, 4044 (1987).

54 G.A. Arteca and P.G. Mezey, J. Chem. Phys., **87**, 5882 (1987).

55 G.A. Arteca and P.G. Mezey, Phys. Lett. A, **122**, 483 (1987).

56 G.A. Arteca and P.G. Mezey, J. Math. Phys., **29**, 119 (1988).

57 P. Pechukas, J. Chem. Phys., **64**, 1516 (1976).

58 P.G. Mezey, to be published.

59 F. Harary and P.G. Mezey, Discr. Appl. Math., **19**, 205 (1988).

60 P.G. Mezey, Theor. Chim. Acta, **73**, 221 (1988).

TOPOLOGY OF MOLECULAR SHAPE AND CHIRALITY

Paul G. Mezey
Department of Chemistry and
Department of Mathematics,
University of Saskatchewan,
Saskatoon, Canada, S7N 0W0

ABSTRACT. The three-dimensional shape of various functions, for example, of electron density contours describing the body of molecules, is an essential tool for the characterization of molecules in drug design. A detailed description of such shapes is possible by the symmetry-independent shape group method, developed recently. The shape group analysis of molecules is based on the initial generation of a molecular surface, such as a surface of a quantum chemical isodensity contour, a contour of the electrostatic potential, a van der Waals, or solvent accessibility, or a so-called union surface obtained for an enzyme cavity by the superposition of contour surfaces of several active drug molecules. The curvature properties and mutual interpenetrations of such contour surfaces define a family of topological objects, which are characterized by their homology groups of algebraic topology. These homology groups are the *shape groups* of the original contour surface, applicable for a precise shape characterization of arbitrary, asymmetric molecules. The shape group method (SGM) is combined with a novel representation of molecular chirality properties, using a simple algebraic test for chirality, based on a recent finding in a branch of topology, called knot theory.

A generalization of point symmetry groups, called symmorphy groups, is proposed for a precise algebraic characterization of the shapes of arbitrary objects, based on various shape function classes. The application of this approach to the molecular shape problem provides an alternative to the SGM.

The shape group and shape function techniques are suitable for a precise, computer-based, non-visual analysis of molecular similarity, that is an important concern in modern pharmaceutical, pesticide and herbicide research.

J. Bertrán and I. G. Csizmadia (eds.),
New Theoretical Concepts for Understanding Organic Reactions, 77–99.
© 1989 by Kluwer Academic Publishers.

1. INTRODUCTION

The traditional descriptions of molecular shape and stereochemistry have been formulated in terms of classical-mechanical, geometrical concepts, such as the three dimensional (3D) structural formulas, where formal chemical bonds, represented by lines of precise directions in 3D space have accounted for molecular structures. Such geometrical models have provided a simple chemical language for communicating some essential chemical information. It is also true, however, that the emphasis placed on geometrical lines as formal bond skeletons of a molecule has led to an unnecessarily oversimplified perception of chemical bonding. These perceptions have changed only slowly when subsequent developments, based on various diffraction experiments and the wider application of quantum chemistry have required a re-evaluation of some of the fundamental concepts of chemistry.

Although the relevance of the Heisenberg uncertainty relation to molecular problems, particularly to electron distributions has been universally accepted by chemists, the geometrical viewpoint has persisted, and the emphasis has been on the representation of *localized* electronic properties, such as electron pairs of formal bonds betwen atom pairs. An important component of research efforts has been devoted to the search for quantum chemical models that are suitable to interpret within quantum chemistry most of the traditional, classical and geometrical concepts of chemistry, e.g. those represented by the line drawing of a structural formula. These research efforts have been extensive, in spite of the fact that only a small fraction of the full 3D information can be represented by oriented, geometrical lines. The importance of 3D models, representing formal molecular bodies, has been recognized, but these models have been regarded little more than the dressing on a 3D structural skeleton of bonds. The mathematical tools used for their description, geometrical surfaces and bodies, have remained classical and geometrical. The usual 3D "space filling" molecular models are capable of formal single bond rotations, however, even the most versatile of these mechanical models can be modified and readjusted only in very restricted ways. For example, most of these models cannot preserve the continuity of a formal molecular surface in processes requiring bond stretching or bending.

The development in computer hardware and molecular graphics has led to a breakthrough in the modeling of molecules and chemical reactions. It is a routine task to create and manipulate the computer displays of 3D molecular models, and to visualize the wealth of detail of shapes of real, 3D molecules. Computer-based molecular modeling has revolutionized the treatment of 3D molecular information, leading to a new appreciation of the knowledge and concepts gained from quantum chemistry, and to new techniques of stereochemistry. This has led to a change in the conceptual framework: instead of thinking in terms of one-dimensional lines representing chemical bonds, modern approaches to interpret stereochemical properties are based on computer models of 2D molecular contour surfaces and 3D molecular bodies. This shift of emphasis from 1D bonds to 2D contour surfaces and 3D molecular bodies has led to a "dimension revolution" in chemical understanding.

The new computer approaches to 3D molecular modeling require a new set of mathematical tools. Differential geometry is the tool of choice if the molecular model used is defined in terms of smooth surfaces and bodies. This approach is based on classical mechanical analogies, for example, by assuming the existence of a molecular surface, or a molecular body with a well defined boundary. The familiar Van der Waals surfaces (VDWS') of molecules are models based on the above assumptions. By contrast, real molecules obey quantum mechanics and are subject to the Heisenberg uncertainty relation. As a consequence, there are no unique, precise, *physical* definitions for the instantaneous nuclear configuration of a molecule, for the surface, or for the body of a molecule. Instead of a single geometrical configuration, an infinite *family* of formal nuclear conformations (that is, a *family* of geometrical models) can be regarded to represent a molecule. Only some of the essential, common features of a whole family of possible geometrical models represents physical reality. Such common, invariant features within a family of geometrical models are usually topological properties, *topological invariants.* Consequently, it is natural to use topological techniques for their analysis. The above considerations provided the motivation for proposing new, non-conventional mathematical approaches for the study of the global, delocalised aspects of 3D *bodies* of actual, fuzzy electron distributions [1-7].

Topology is a powerful mathematical tool for doing qualitative analysis rigorously [8-14]. This is an important consideration if one is interested in the

underlying, essential features of a complicated entity, like a molecule, and some details of lesser importance are to be disregarded. Topology can provide a *discrete* description of some essential properties of *continuous* problems, that may be used for extracting the most relevant chemical information from complicated molecular models. In algebraic topology the essential properties of continuous functions are described by algebraic techniques, by groups and various topological invariants. The methods of algebraic topology are applicable to molecular surfaces, for example, to electronic isodensity contours, to contour surfaces of electrostatic potentials, or to Van der Waals surfaces. The topological analysis leads to a family of algebraic *shape groups.* In the process one obtains a discrete shape description, a *shape code,* that can be stored, processed, and compared easily by the computer. This offers a novel, non-visual, algorithmic approach to the analysis of 3D molecular shapes, molecular similarity of prospective drug molecules, as well as the shape-complementarity of reacting molecules of biochemical importance.

2. THE SHAPE GROUP METHOD (SGM) FOR MOLECULAR SHAPE AND SIMILARITY ANALYSIS

In drug design and molecular modeling of biomolecules [see, for example, 15-16] the comparison of molecular shapes is usually based on the analysis of electronic charge densities [for example, 17], electrostatic potentials [for example, 18,19], Van der Waals surfaces [e.g. 20-23], solvent accessibility surfaces [e.g. 24,25], and various other molecular functions. These comparisons are usually done by simple, visual inspection, using displays of these functions on a computer screen. This process can be rather time consuming and tedious if hundreds or thousands of molecules are involved. Clearly, computational methods for automatic, non-visual shape comparisons represent an attractive alternative in these cases. Recently a family of such computational methods, the *shape group methods* (SGM) has been developed for this purpose. The SGM is based on a topological analysis of a family of molecular contour surfaces.

In the following we shall illustrate the main ideas of the SGM using the electronic charge density to represent the shape of molecules, however, the

same shape group method is applicable to other molecular functions as possible shape descriptors. Among these functions the electrostatic potentials, various molecular orbitals, or in more special applications spin densities and charge deformation densities are of importance [1-7].

The electronic charge density of a general molecule is a 3D function that can be described in terms of a series of 2D isodensity contour surfaces G(a), where a is the density along the contour surface. Since there are infinitely many possible choices for parameter a, a complete description of the geometries of *all* of the associated density contours G(a) is impractical. Fortunately, such a complete description is not really needed, since the essential shape features, for example, the mutual arrangements of the locally convex, saddle, and concave domains of the isodensity contours G(a) remain invariant within certain ranges (a_1 , a_2) of density parameter a. Consequently, it is possible to characterize an entire *family* of the geometrical contours G(a) corresponding to a given *range* (a_1 , a_2) of parameter a by a *single* topological object describing these invariant features. In the topological object the existence and the interrelations of the various domains are preserved, although the information on distances, the sizes and precise locations of these domains as they are present in any given contour surface G(a) of the family is disregarded. This topological object contains the essential information on the shape properties, where what is essential is decided when choosing the domains of decomposition on the contour surfaces (e.g., convex, concave and saddle type domains, or domains where the absolute value of the density gradient falls between some prescribed limits, etc.). The important simplification of shape description is based on the fact that the topological object can be characterized by a *finite* number of topological invariants, leading to a *discrete* characterization of the given family of *continuous* isodensity contour surfaces. Note that one obtains only a *finite* number of ranges of density parameter a , each for a family of G(a) contours of distinct topological shape features, consequently, only a *finite* number of topological objects are required. The essential shape properties of the entire 3D charge density distribution can be characterized by a *finite* number of topological invariants.

Of course, there is a considerable freedom in the choice what are to be regarded as the essential shape features. This freedom is manifested in the choice of domains on the isodesity contours G(a). One of the most natural choices, convex, saddle, and concave domains [1,2], may be regarded as a

characterization of local curvatures with reference to a tangent plane, that is, to a reference curvature $b = 0$. The choice of domains, and the concept of local convexity, can be generalized by taking a reference curvature b different from zero, that is, by testing the local curvature of $G(a)$ against a tangent sphere, instead of a plane [2]. The shape domains D_0, D_1, and D_2 of the contour surface, defined in terms of tangent planes, correspond to the ordinary concave, saddle, and convex domains, respectively, according to the local curvatures. If the reference plane is replaced by a reference sphere T of some specified local curvature $b \neq 0$, then the shape domains D_0, D_1, and D_2 are the generalized concave, saddle, and convex domains, respectively, *relative to the test sphere* T. The appearence and distribution of shape domains depend on the choice of reference curvature b of the test sphere T, and in general, a different decomposition of $G(a)$ may result for a different b value. It is important to realize, however, that the essential, *topological* properties (for example, the neighbor relations of the domains and their boundaries, called incidence relations) remain invariant within certain ranges (b_i, b_j) of curvature values: these topological properties change only at specific values of reference curvature b. Hence, by listing these specific curvature values and the finite number of topological invariants associated with each range of the parameter b, one obtains a *discrete* characterization for the *continuous* contour surface $G(a)$. This list is a numerical *shape code*, that can be stored, analysed, and compared by the computer for a large series of molecules.

The simplest shape code is the *incidence matrix*, associated with the family of the D_μ domains [26]. Here the curvature index μ may take the following values: $\mu = 0, 1$, or 2. We recall that a non-empty 2D set is simply connected if every closed loop within the set can be contracted into a point. Otherwise the set is multiply connected. Note that a set D_μ may be multiply connected. By subdividing each multiply connected D_μ set into simply connected pieces, one obtains three families of sets: a family $\{C^2_i\}$ of 2D sets, a family $\{C^1_i\}$ of their 1D boundary line segments, and a family $\{C^0_i\}$ of 0D points where these line segments meet. (Note that the upper indices specify the dimensions and are not exponents). Each of these C^p_i sets is given a formal orientation, denoted by $+1$ or -1.

The *incidence matrix* $\mathbb{m}(1)$ is defined for the pair of 2D and 1D families $\{C^2_i\}$, $\{C^1_j\}$, and another incidence matrix $\mathbb{m}(0)$ for the pair of 1D and 0D families $\{C^1_i\}$, $\{C^0_j\}$, by

$$n_{ij}(p-1) = \begin{cases} 0 & \text{if } C^{p-1}_j \text{ is not on } \Delta C^p_i \\ +1 & \text{if } C^{p-1}_j \text{ is on } \Delta C^p_i \text{ and orientations match} \\ -1 & \text{if } C^{p-1}_j \text{ is on } \Delta C^p_i \text{ and orientations don't match,} \end{cases} \quad (1)$$

where ΔC^p_i is the *boundary* of C^p_i. The incidence matrix can be represented by an *incidence graph,* and can also be augmented with numerical information on the size, e.g., the area of each domain D_μ [26].

A concise topological representation of shape properties can be obtained by extracting the most essential information from the incidence relations. By formally "cutting out" domains of a specified type from the contour surface G(a), for example, by omitting all D_2 domains, a new topological object is obtained. The *homology groups* of algebraic topology for the truncated surface represent the essential properties of the shape domain decomposition of the contour surface G(a).

The generation of homology groups is based on the concept of p-chain c^p: a formal linear combination of domains of a common dimension p. For example, the 2-chain

$$c^2 = 4\,C^2_1 + 13C^2_2 - 5C^2_3 + \ldots . \quad (2)$$

is a formal linear combination of 2-dimensional D_μ sets and their subdivisions on the isodensity contour surface G(a), obtained by taking a given reference curvature b. The c^p chains can be added up and multiplied by numbers. The *bounding cycles* are special chains, which bound some other chains on G(a), but themselves have no boundaries. The algebraic properties of bounding cycles define a group, the p-dimensional homology group, for each of the dimensions p = 0, 1, and 2. These homology groups $H^p_\mu(a,b)$ of the truncated surfaces, for each truncation type μ, are called the *shape groups* of the original contour surface G(a) [1-3]. The shape groups are themselves topological invariants, and can be used to extract the most essential interrelations between the shape domains, their boundary lines, and boundary points. The most important topological invariants that are used as concise *shape codes* are the Betti numbers B^p, that are the ranks of the homology groups, and the Euler-Poincaré characteristics χ, where the following relation holds:

$$\chi = B^0 - B^1 + B^2 . \qquad (3)$$

An easily visualizable topological feature, the number of holes obtained by the truncation, has a simple relation to these invariants: it is equal to $B^1 + 1$.

The SGM can be further generalized by testing the local curvatures of contour surface G(a) against a *tangent ellipsoid* T [27]. If the orientation of the ellipsoid T with respect to G(a) is fixed, then the incidence matrix and shape group method is applicable for the shape characterization of *oriented* molecules, for example, in external electromagnetic fields, or within enzyme cavities.

It is possible to study the essential shape features of an isodensity contour G(a) in combination with those of another function, for example, the electrostatic potential. Specified ranges of the electrostatic potential can be mapped onto each isodensity surface G(a). One may take these ranges as a possible decomposition of G(a) into domains, for which the topological shape characterization by the SGM or incidence matrices is applicable. The SGM has been applied to various domain decompositions of Van der Waals surfaces, solvent accessibility surfaces, and the union surfaces of enzyme receptor sites, among others.

3. KNOT THEORETICAL CHIRALITY POLYNOMIALS FOR CHIRAL CENTERS AND FOR ARBITRARY MOLECULES

It is customary to define chirality in terms of mirror images. If an object and its mirror image are not superimposable on one another then the object is chiral. In a strict sense, chirality is dependent on the number of dimensions considered. For example, if the motions allowed when attempting to superimpose the objects are restricted to a single line, then one obtains the concept of one-dimensional chirality. An oriented interval on a line, thought of as an arrow, is chiral in one dimension, since no motion of the arrow, restricted to this line, can bring it into superposition with its mirror image, which is an arrow of opposite orientation, and where the mirror corresponds to a single point along the one-dimensional line. If the allowed motions are restricted to a plane, then an equilateral triangle of vertices labeled differently is chiral in two

dimensions, since no motion restricted to the plane can bring it into superposition with its mirror image, that is the triangle with two of the labels interchanged. The mirror in the plane corresponds to a straight line. Of course, neither the arrow nor the triangle is chiral in three dimensions, since there are three-dimensional motions which can bring them into superpositions with their mirror images, where the mirror is a plane.

Knots are among the simplest objects that may show three-dimensional chirality properties. A knot is a one-dimensional entity, embedded in three dimensions, and many of their special properties follow from this. In mathematical knot theory (a branch of topology), an important sequence of discoveries has been made recently [28,29], that allows one to assign a set of a new type of generalized polynomials to each knot. These polynomials have some remarkable properties, for example, by replacing the variable by its reciprocal, one obtains the polynomial assigned to the mirror image of the knot. For the single-variable polynomial $V_K(t)$ of knot K and for the polynomial $V_{K'}(t)$ of its mirror image K' one finds that

$$V_{K'}(t) = V_K(t^{-1}) . \qquad (4)$$

Hence, these polynomials are suitable for the study of chirality of knots: if these two polynomials, $V_K(t)$ and $V_{K'}(t)$ are different then the two knots K and K' are chiral: no rearrangement of the string of knot K can make it superimposable onto K', unless the string is cut and subsequently rejoined somewhere.

The above knot theoretical result has been applied to the chirality problem of molecules which themselves form knots, such as various DNA fragments [30].

Furthermore, it has also been shown that a knot may represent the chirality of the space around various molecules, even if the molecules themselves do not form knots [31]. Formally, a knot K may be tied around the molecule in a specified way, that in fact transfers the chirality information of the molecule to the knot. Consequently, the polynomial $V_K(t)$ of the knot may ultimately represent the chirality properties of the molecule. In fact, the actual generation of the knots is not required, and from the information of the location of substituents of various carbon centers it is possible to construct these polynomials directly. Only a subfamily of all possible knots may occur for

molecules, and knots in this subfamily have stronger mathematical properties than knots in general. In particular, it has been shown that for the molecular case the condition of achirality,

$$V_K(t) = V_{K'}(t) = V_K(t^{-1}), \qquad (5)$$

that is only a necessary condition for a general knot, becomes both a necessary and sufficient condition [31].

The above knot theoretical polynomial representation of molecular chirality, related to formal chiral centers, could be made free of contradictions only when the usual Cahn - Ingold -Prelog rules of R and S classification of chiral centers [32] were somewhat modified, by replacing the condition of "no two identical substituents on a carbon center" with "no two substituents are the mirror images of one another on a carbon center" [31]. If the above modified criterion is used, then the chirality properties of the polynomials can be treated using algebraic symbols and the construction of the polynomials is not required.

The same polynomial and algebraic method is applicable in a very general way, without specifying which atom groups are regarded to be linked by formal bonds. For any formal nuclear geometry of a molecular system of more than three nuclei one may consider all possible quadruplets of nuclei. Each quadruplet defines a tetrahedron, that may be degenerate, e.g. a planar quadrilateral, or a triangle, or just four points along a line, depending on the nuclear geometry. If any two of the tetrahedra are either superimposable on one another or are the mirror images of one another, then they are assigned the same variable; otherwise the tetrahedra are assigned different variables. For each tetrahedron a knot and a polynomial is generated according to the rules proposed for chiral centers [31], using the appropriate variable assigned to the tetrahedron. The overall polynomial of the molecular system is the product of the polynomials of the tetrahedra. The sufficient and necessary achirality condition (5) applies to this polynomial and to its symbolic, algebraic representation. The polynomial or the symbolic representation can be generated, stored and tested for chirality by a computer, that provides a nonvisual tool for the analysis of chirality properties of arbitrary nuclear configurations of molecules.

4. FROM SYMMETRY GROUPS TO SYMMORPHY GROUPS: GROUP THEORY OF SYMMORPHIC SHAPE FUNCTION CLASSES

Point symmetry groups are of great importance in many fields of chemistry and they certainly provide at least a partial characterization of molecular shapes. In this section we shall propose a particular extension of the point symmetry group concept from finite point sets, such as a collection of atomic nuclei, to a complete algebraic shape characterzation of continua, such as a three-dimensional electron distribution.

One may reformulate the definition of point symmetry groups in a special way that will lend itself for the generalization. Consider a labeled point set of fixed location in the three dimensional Euclidean space, where the points may fall into several classes and within each class the points are regarded equivalent according to some criterion:

$$\mathbf{A} = \{A_1, A_2, \ldots A_a, B_1, \ldots B_b, \ldots\ldots Z_1, \ldots Z_z\} \ . \qquad (6)$$

Here points with labels containing the same capital letter are regarded equivalent. For example, we may think of a nuclear configuration **A** involving certain nuclei among which some may be equivalent. Consider now all possible planes within the three-dimensional space and all the reflections of the space with respect to these planes. Most of these reflections will move the set of nuclei into new locations, with new orientations, that are distinguishable from the original placement. There may exist, however, some selected reflections by planes that are special with respect to the nuclear arrangement, and the resulting arrangements are indistinguishable from the original one. Similarly, among all possible straight lines in the space, taken as rotation axes by all possible degrees of rotations, there may exist only few, special choices that convert the nuclear arrangement **A** into one that is indistinguishable from the original one. The same applies to the set of all possible choices for rotation-reflection axes and points of inversion. The family of all these transformations is denoted by G'. We may consider a function f(**r**) in the three-dimensional space that assigns the nuclear symbol A (B, C, ..) to point

r of the space if a nucleus of type A (B,C,..) is located at **r**, otherwise it assigns 0 to **r**. Note that all point symmetry information of the nuclear arrangement is contained in f(**r**). Clearly, a general transformation t' from family G' may then have either one of the following two effects at a point **r** of the space:

$$f(t'\mathbf{r}) = f(\mathbf{r}), \tag{7}$$

or

$$f(t'\mathbf{r}) \neq f(\mathbf{r}). \tag{8}$$

Evidently, the infinite set of all possible reflection, rotation, rotation-reflection, and inversion operations in the space, with no reference to the nuclei, forms a group G', where the group operation is applying two transformations t' of the space, say t'_1 and t'_2, one after the other, $t'_2t'_1$, and where the neutral element is the identity transformation. The actual nuclear arrangement serves to identify a *subset* g'_f of these transformations of the space that brings the nuclei into an indistinguishable arrangement. For all transformations a sufficient and necessaray condition to belong to this subset g'_f is the fulfillment of condition (7) for every point **r** of the space. The transformations fulfilling this condition form the *point symmetry group* g'_f of the arrangement, a *subgroup* of the above infinite group G' :

$$g'_f \subset G'. \tag{9}$$

Note that G' contains, as subgroups, all point symmetry groups g'_f of all possible nuclear arrangements, with reference to all possible choices of origins. The important observation is that a special subset of the general set G' is the tool for the characterization of the specific symmetry properties of the given nuclear arrangement.

We shall generalize the above scheme by changing two of the conditions. First, instead of a finite point set, such as a nuclear arrangement **A** characterized by a function f(**r**), we shall consider a continuum, such as a three-dimensional electron distribution:

$$\rho = \rho(\mathbf{r}), \tag{10}$$

where $\mathbf{r}$ is a position vector in three-dimensional space. Second, we shall take a much larger family G of possible transformations of the three-dimensional space,

$$G' \subset G, \tag{11}$$

where G is the set of all one-to-one and continuous transformations of the space with a continuous and one-to-one inverse (all homeomorphisms of the three-dimensional space). This set G is evidently a group, with properties analogous to those of group G'. With reference to a given electronic charge distribution $\rho(\mathbf{r})$, a subset g_ρ of G can be identified that contains all transformations t from the family G that have the property

$$\rho(t\mathbf{r}) = \rho(\mathbf{r}) . \tag{12}$$

Note that $t\mathbf{r} = \mathbf{r}$ is only a sufficient condition for (12) to hold but not a necessary one; the transformation t may very well assign to some points $\mathbf{r}$ a point different from $\mathbf{r}$, yet the density values may agree. For example, the transformation may move points along an isodensity contour surface in a continuous deformation of the space that leaves the appearence of the contour surface unchanged.

Such transformations do not alter the appearence of the shape, the *morphology* of the continuous charge density $\rho(\mathbf{r})$, although the metric properties, such as the distance between two points may change. The subset g_ρ of all such transformations is a *subgroup* of group G; due to the special characteristics with reference to the continuum $\rho(\mathbf{r})$, it provides a complete characterization of the shape of $\rho(\mathbf{r})$.

However, the group g_ρ is unnecessarily complicated for the purposes of shape characterization, since the behaviour of transformations t of g_ρ far away from the object is of little importance. For the purposes of the following discussion let us assume that the function $\rho(\mathbf{r})$ becomes identically zero outside a sphere S of a sufficiently large radius. There are infinitely many transformations in group g_ρ that have precisely the same effect within this

sphere but have different effects in some domains outside the sphere. Evidently, differences in these transformations carry no information concerning the shape of $\rho(\mathbf{r})$. It is useful to collect such transformations t into equivalence classes and to consider these *classes* as the actual tools of shape characterization. All those transformations t_1 and t_2, of family g_ρ that agree at every point $\mathbf{r}$ where $\rho(\mathbf{r}) \neq 0$, that is,

$$t_1 \mathbf{r} = t_2 \mathbf{r} \tag{13}$$

for every point $\mathbf{r}$ such that

$$\rho(\mathbf{r}) \neq 0, \tag{14}$$

belong to the same equivalence class T. Since the transformations in these classes preserve the morphology of the continuum, e.g. the charge density $\rho(\mathbf{r})$, the terminology *symmorphy classes* T is proposed for them. The two transformations t_1 and t_2, fulfilling conditions (13) and (14), are said to be *symmorphic* to one another with respect to the given continuum $\rho(\mathbf{r})$; in notation

$$t_1 \; \boldsymbol{m}_\rho \; t_2 . \tag{15}$$

One may point out some analogies of this terminology with that of symmetry: in a symmetry operation some metric properties are preserved, whereas in a symmorphy operation some morphological properties are preserved, such as the actual appearence of the object, that may or may not involve preservation of metric properties. Evidently, symmorphy $\boldsymbol{m}_\rho$ is an equivalence relation, since it is reflexive, transitive, and symmetric. The symmorphy equivalence classes of a given continuum $\rho(\mathbf{r})$ form a group, the *symmorphy group* h_ρ, that is the quotient group of g_ρ with respect to the symmorphy equivalence $\boldsymbol{m}_\rho$. The product of two symmorphy classes T_1 and T_2 in the symmorphy group is the class T_3,

$$T_3 = T_1 T_2 \tag{16}$$

that contains the product $t_1 t_2$ of any two transformations t_1 and t_2 from

classes T_1 and T_2, respectively.

There are important relations among symmorphy classes that are useful for the characterization of shapes in general, and for shapes of molecular electron distributions, in particular. Some of these relations are discussed elsewhere[33]. Here we shall point out an important simplification that is a consequence of the Brouwer fixed point theorem of topology [see, e.g. 13]. Consider an isodensity contour G(a) of the electron density $\rho(\mathbf{r})$, where the density is equal to the value a. Any transformation t from set g_ρ maps this contour G(a) onto itself, that is,

$$tG(a) = G(a), \tag{17}$$

although one may have $t\mathbf{r} \neq \mathbf{r}$ for some points $\mathbf{r}$ of G(a). However, according to the Brouwer fixed point theorem there must exist at least one fixed point $\mathbf{r}_t$ of the isodensity contour G(a):

$$t\,\mathbf{r}_t = \mathbf{r}_t\,. \tag{18}$$

As it follows from the definition of symmorphy equivalence, for any two transformations t_1 and t_2 from the same symmorphy class T the fixed points must be the same,

$$\mathbf{r}_{t1} = \mathbf{r}_{t2}\,. \tag{19}$$

Hence, one may refer to these fixed points as those of an entire symmorphy class T. However, different symmorphy classes may also have common fixed points, since two transformations t_1 and t_2 from the two classes T_1 and T_2, respectively, may differ at other points of the contour surface while fulfill the common fixed point condition

$$t_1\,\mathbf{r}_t = t_2\mathbf{r}_t = \mathbf{r}_t \tag{20}$$

for some point $\mathbf{r}_t$ of the contour G(a). This allows one to introduce an equivalence relation f_ρ among the symmorphy classes, as follows:

$$T_1\, f_\rho\, T_2 \tag{21}$$

if and only if all fixed points $\mathbf{r}_t$ of T_1 and T_2, collected in a set φ, are common. Then the two symmorphy classes T_1 and T_2 belong to the same f_ρ equivalence class $\Phi_\rho(\varphi)$. Each equivalence class is a subgroup $\Phi_\rho(\varphi)$ of the symmorphy group g_ρ, its elements may be thought of as symmorphy classes that are "pinned down" at a specified set φ of fixed points $\mathbf{r}_t$ of the electron density $\rho(\mathbf{r})$, as required by their f_ρ equivalence. The subgroup $\Phi_\rho(\varphi)$ has an algebraic structure simpler than that of the symmorphy group h_ρ, and it provides an alternative shape characterization. Note that the continuity of each t transformation of the space implies that each set φ of fixed points is a continuum cutting across the $G(a)$ level sets.

The symmorphy groups are the generalizations of the point symmetry groups, from discrete point sets to continua of general shapes that may not show any symmetry properties at all. That point symmetry groups are special cases of symmorphy groups can be seen easily if one replaces the function $\rho(\mathbf{r})$ by $f(\mathbf{r})$ and a family of symmorphy classes by linear transformations as representative elements of the classes, that for a discrete point set $\mathbf{A}$ can be chosen as the symmetry operations. The symmorphy groups of any continuum $\rho(\mathbf{r})$ provide a complete shape characterization of $\rho(\mathbf{r})$.

One generalization is of some advantage if there are several physical properties of interest for the actual object that is to be characterized. Here we shall describe the case of two properties, the generalization to several properties is straightforward. Consider two functions, $\rho(\mathbf{r})$ and $\tau(\mathbf{r})$, of the same physical object (for example, the charge density and the highest occupied molecular orbital HOMO of a molecule). The subset $g_{\rho\tau}$ of G contains all transformations t from the family G that have both properties

$$\rho(t\mathbf{r}) = \rho(\mathbf{r}), \tag{22}$$

$$\tau(t\mathbf{r}) = \tau(\mathbf{r}), \tag{23}$$

for every point $\mathbf{r}$ of the space. That is, these transformations t of the space leave the *appearence* of both physical properies ρ and τ of the object unchanged, a strong restriction. Two transformations t_1 and t_2 of family $g_{\rho\tau}$ that agree at every point $\mathbf{r}$ where either $\rho(\mathbf{r}) \neq 0$ or $\tau(\mathbf{r}) \neq 0$, that is,

$$t_1 \mathbf{r} = t_2 \mathbf{r} \tag{24}$$

for every point $\mathbf{r}$ such that

$$|\rho(\mathbf{r})| + |\tau(\mathbf{r})| \neq 0, \tag{25}$$

are $m_{\rho\tau}$ symmorphic to one another,

$$t_1 \; m_{\rho\tau} \; t_2 , \tag{26}$$

and belong to the same $m_{\rho\tau}$ symmorphy equivalence class T. The quotient group of G according to the $m_{\rho\tau}$ symmorphy equivalence is the *symmorphy group* $h_{\rho\tau}$, that describes the combined shape properties of the two functions, $\rho(\mathbf{r})$ and $\tau(\mathbf{r})$ of the given physical object.

5. AN ALGORITHM FOR CONTINUOUS TRANSFORMATIONS BETWEEN ISODENSITY CONTOURS: FUSED SPHERES GUIDED HOMOTOPY (FSGH) METHOD

For appropriately chosen density values a the isodensity contour surfaces G(a) of formal, fixed configurations of most molecules often show only surprisingly small deviations from van der Waals surfaces obtained as the envelope surface of interpenetrating spheres

$$S_1, S_2, \ldots S_N, \tag{27}$$

of suitably chosen radii

$$r_1, r_2, \ldots r_N, \tag{28}$$

centered on the N atomic nuclei of position vectors

$$\mathbf{r}_1, \mathbf{r}_2, \ldots \mathbf{r}_N, \tag{29}$$

respectively.

This observation can be exploited in generating point sets for the computer representation of isodensity contours, and for representing transformations between such contour surfaces G(a) and G(a') when the density value of the contour changes from a to a'.

The starting point in developing this representation is the van der Waals surface, VDWS. While fixing the location of the center of each sphere from which the surface is generated, a suitable, common constant factor $k < 1$ is applied to the radii of each sphere, such that with the new radii

$$p^0_1 = kr_1,\ p^0_2 = kr_2, \ldots\ p^0_N = kr_N, \tag{30}$$

no two spheres have common points. On each new sphere S^0_i a set of m points,

$$P^0_i = \{\mathbf{r}^0_{i1}, \mathbf{r}^0_{i2}, \ldots\ \mathbf{r}^0_{im}\} \tag{31}$$

is chosen from a near uniform distribution along the spherical surface. By applying a series of increasing factors $k_1, k_2, \ldots\ k_t, \ldots\ k_n$,

$$1 < k_1 < k_2 < \ldots < k_t < \ldots < k_n \tag{32}$$

for the radii p^0_j of eqs. 30, the resulting envelope surfaces

$$F_1, F_2, \ldots\ F_t, \ldots F_n \tag{33}$$

of the spheres will approximate a sequence of isodensity contours of decreasing contour density values.

However, this sequence of gradually enlarged envelope surfaces will not in general approximate the isodensity contours sufficiently well for practical applications. For a better approximation an interpolation method is developed that uses points along the subsequent spherical surfaces to define lines along which one-dimensional interpolations are carried out. In each step t of the enlargement process a new set of surface points

$$P^t_i = \{\mathbf{r}^t_{i1}, \mathbf{r}^t_{i2}, \ldots\ \mathbf{r}^t_{im}\} \tag{34}$$

is generated for each new sphere,

$$S^t_1, S^t_2, \ldots S^t_i, \ldots S^t_N, \tag{35}$$

as the enlargement images of the surface points of sets $P^0_i = \{\mathbf{r}^0_{i1}, \mathbf{r}^0_{i2}, \ldots \mathbf{r}^0_{im}\}$ of the smallest spheres. Let us denote by

$$P^t_F = \{\mathbf{r}^t_1, \mathbf{r}^t_2, \ldots \mathbf{r}^t_u, \ldots \mathbf{r}^t_{v_t}\} \tag{36}$$

the set of all those surface points of all P^t_i sets in step t which fall on the surface F_t, that is the set of those selected points on all the current spheres that are not buried inside F_t. For the initial, disjoint spheres all points are on the surface of their envelope surface F_0, that envelope is in fact the collection of the spheres, hence P^0_F is the union of all P^0_i sets.

We shall say that the point pair $\mathbf{r}^t_{ij}$ and $\mathbf{r}^{t+1}_{ij}$ on two subsequent envelope surfaces F_t and F_{t+1}, respectively, are *pairs by enlargement,* if point $\mathbf{r}^{t+1}_{ij}$ is the image of point $\mathbf{r}^t_{ij}$ when the sphere S^t_i is scaled by the factor k_{t+1} / k_t.

The points occurring in subsequent sets P^t_F and P^{t+1}_F on subsequent envelope contours F_t and F_{t+1}, respectively, are interconnected according to the following criterion:

> Each point $\mathbf{r}^{t+1}_{u'}$ of set P^{t+1}_F of envelope F_{t+1} is connected by a straight line segment $s(\mathbf{r}^t_u, \mathbf{r}^{t+1}_{u'})$ to its unique pair by enlargement, $\mathbf{r}^t_u$, if the latter falls on the previous envelope surface F_t. Otherwise, each remaining point of set P^t_F or set P^{t+1}_F on either envelope surface, not yet assigned a pair by the above condition, is connected by a straight line segment $s(\mathbf{r}^t_u, \mathbf{r}^{t+1}_{u'})$ to the *nearest* point of the point set P^{t+1}_F or P^t_F, respectively, of the *other* envelope surface.
>
> (37)

The above rule, applied to the sequence of envelope surfaces, generates a collection of mN lines of approximately uniform distribution and approximately perpendicular to each local spherical domain of the envelope surfaces. Some of these lines may merge and possibly separate again as some of

the selected points get buried and possibly reappear in the enlargement process of the spheres.

Each line is composed from straight line segments $s(\mathbf{r}^t_u, \mathbf{r}^{t+1}_{u'})$, interconnecting subsequent envelope surfaces. We assume that function values of the electronic charge density $\rho(\mathbf{r})$ are available at each $\mathbf{r}^t_u$ point of each envelope surface F_t, hence the function values are known for the endpoints $\mathbf{r}^t_u$ and $\mathbf{r}^{t+1}_{u'}$ of each line segment $s(\mathbf{r}^t_u, \mathbf{r}^{t+1}_{u'})$. Using linear interpolation along these line segments one may generate a representation of the electronic isodensity contour surface $G(a)$ for any value a of the contour density, fulfilling the condition $a \leq a_0$, where a_0 is the minimum density value for points along F_0 in the union of all the P^0_i sets . The task is to locate all points $\mathbf{r}(a)$ on the line segments that fulfill the following conditions:

$$\mathbf{r}(a) \in s(\mathbf{r}^t_u, \mathbf{r}^{t+1}_{u'}), \tag{38}$$

$$\rho(\mathbf{r}(a)) = a. \tag{39}$$

This can be accomplished by linear interpolations along the line segments $s(\mathbf{r}^t_u, \mathbf{r}^{t+1}_{u'})$; in fact it is sufficient to carry out the interpolations for those line segments which fulfill either one of the following two conditions:

$$\rho(\mathbf{r}^t_u) \leq a \leq \rho(\mathbf{r}^{t+1}_{u'}), \tag{40}$$

or

$$\rho(\mathbf{r}^t_u) > a > \rho(\mathbf{r}^{t+1}_{u'}). \tag{41}$$

The set $P(a)$ of all $\mathbf{r}(a)$ points can be regarded as a dot representation of the isodensity contour surface $G(a)$, useful in computer graphics of molecular problems. However, the above representation has some further advantages: along each of the mN lines an analytic functional form is available for the electronic density. This allows one to construct explicitly a relatively simple function for an approximate representation of the *continuous deformations* of isodensity contours surfaces $G(a)$ as a function of the contour density value a. Such continuous deformations, *homotopies,* are advantageous in the analysis of the dependence of molecular shape properties as the functions of electronic

charge density. The suggested name of the method, Fused Spheres Guided Homotopy Method (FSGH), reflects the fact that the homotopy transformation is obtained by following the changes in envelope surfaces of families of fused spheres of gradually increasing sizes.

Note that the same technique is applicable to many other molecular functions that can be approximated by contour surfaces not drastically different from a fused sphere VDWS. This condition is not in general valid in the case of electrostatic potentials that may show even sign changes in various regions of the space, however, the method is applicable for local regions of the electrostatic potential, for example, one may apply it separately for positive and negative domains. The FSGH method provides a practical tool for the implementation of a variety of techniques suggested for molecular shape analysis [26,27,34-36].

Acknowledgment

The research leading to the developments reviewed above has been supported by grants from the Natural Sciences and Engineering Research Council of Canada.

References

1 P. G. Mezey, Internat. J. Quantum Chem., Quant. Biol. Symp., **12**, 113 (1986).

2 P.G. Mezey, J. Comput. Chem., **8**, 462 (1987).

3 P.G. Mezey, Int. J. Quantum Chem., Quant. Biol. Symp., **14**, 127 (1987).

4 G.A. Arteca and P.G. Mezey, Int. J. Quantum Chem., Quant. Biol. Symp., **14**,133 (1987).

5 G.A. Arteca, V.B. Jammal, P.G. Mezey, J.S. Yadav, M.A. Hermsmeier, and T.M. Gund, J. Molec. Graphics, **6**, 45 (1988).

6 G.A. Arteca, V.B. Jammal, and P.G. Mezey, J. Comput. Chem., **9**, 608 (1988).

7 G.A. Arteca and P.G. Mezey, J. Comput. Chem., **9**, 554 (1988).

8 T.W. Gamelin, and R.E. Greene, Introduction to Topology, Saunders College Publishing, New York, 1963.

9 I.M. Singer, and J.A. Thorpe, Lecture Notes on Elementary Topology and Geometry, Springer-Verlag, New York, 1976.

10 V. Guillemin, and A. Pollack, Differential Topology, Prentice Hall, Englewood Cliffs, 1974.

11 E.H. Spanier, Algebraic Topology, McGraw-Hill, New York, 1966.

12 M. Greenberg, Lectures on Algebraic Topology, Benjamin, New York, 1967.

13 S.-T. Hu, Elements of General Topology, Holden-Day, San Francisco, 1969.

14 J. Vick, Homology Theory, Academic Press, New York, 1973.

15 W.G. Richards, Quantum Pharmacology, Butterworths, London, 1977.

16 R. Franke, Theoretical Drug Design Methods, Elsevier, Amsterdam, 1984.

17 P. Coppens and M. B. Hall (Eds.), Electron Distribution and the Chemical Bond, Plenum, New York and London, 1982.

18 J. Tomasi, "On the Use of Electrostatic Molecular Potentials in Theoretical Investigations on Chemical Reactivity", in Quantum Theory of Chemical Reactions, R. Daudel, A. Pullman, L. Salem, and A. Veillard, (Eds.), Reidel, Dordrecht, 1979.

19 P. Politzer and D. G. Truhlar (Eds.), Chemical Applications of Atomic and Molecular Electrostatic Potentials", Plenum, New York, 1981.

20 A. Gavezotti, J. Am. Chem. Soc., **105**, 5220 (1983).

21 M. L. Connolly, Science, **221**,709 (1983).

22 K. D. Gibson and H. A. Scheraga, J. Phys. Chem., **91**, 4121 (1987);

23 K. D. Gibson and H. A. Scheraga, Mol. Phys., **62**, 1247 (1987).

24 F. M. Richard, Annu. Rev. Biophys. Bioeng., **6**, 151 (1977).

25 M. L. Connolly, J. Am. Chem. Soc., **107**, 1118 (1985).

26 P. G. Mezey, J. Math. Chem., in press.

27 P. G. Mezey, J. Math. Chem., in press.

28 V.F.R. Jones, Bull. Am. Math. Soc.(NS), **12**, 103 (1985).

29 P. Freyd, D.Yetter, J. Hoste, W.B.R. Lickorish, K.C. Millett, and A. Ocneanu, Bull. Am. Math. Soc.(NS), **12**, 239 (1985).

30 K.C. Millett, Croatica Chimica Acta, **59**, 669 (1986).

31 P.G. Mezey, J. Amer. Chem. Soc., **108**, 3976 (1986).

32 R.S. Cahn, C.K. Ingold, and V. Prelog, Angew. Chem., **78**, 413 (1966).

33 P.G. Mezey, to be published.

34 G.A. Arteca and P. G. Mezey, Folia Chim. Theor. Lat., **15**,115 (1988).

35 P.G. Mezey, Theor. Chim. Acta, **73**, 221 (1988).

36 F. Harary and P. G. Mezey, J. Math. Chem., in press.

Adiabatic and Diabatic Surfaces in the Treatment of Chemical Reactivity
I Theory

Michael A. Robb
Department of Chemistry
King's College London
Strand
London WC2R 2LS

Fernando Bernardi
Dipartimento Chimico 'G. Ciamician'
Universita di Bologna
40126 Bologna

Abstract

The diabatic surface model of Evans is discussed as a physically grounded model for chemical reactivity. The essential component of Evans' model (which was originally strictly empirical) is shown to be the Heisenberg hamiltonian and its projection onto reactant and product spin couplings. An implementation of this model is described within the formalism of effective hamiltonian theory. It is argued that this model can describe reactivity problems involving muti-bond reactions as well as ionic reactions.

I Introduction

These lecture notes are intended to provide an introduction to the theory and application of Diabatic Surfaces in the study of chemical reactivity of organic systems. They represent neither a review nor an original article and are intended to be pedagogical. Consequently the bibliography is restricted to those references that the authors feel are most helpful.

The study of organic reactivity has undergone a complete revolution in the past decade. The availability of standard quantum chemistry codes [1] with analytic gradients and frequency capabilities has enabled the investigation of molecular structures and transition states for real chemical reactivity problems. (For a survey of recent developments the reader is referred to two recent volumes of Adv. in Chem. Phys. ref [2,3]). The more recent availability of methods such as MC-SCF has extended these possibilities to bi-radicaloid systems and excited states.

However, chemistry is not just a science of measuring (either by experiment or theoretical computation) or synthesising new compounds. Rather, we also seek models or theories about why molecules react in the way that they do or have the physical properties that they have. In the past, theories of reactivity have been based on

J. Bertrán and I. G. Csizmadia (eds.),
New Theoretical Concepts for Understanding Organic Reactions, 101–146.
© 1989 by Kluwer Academic Publishers.

empirical correlations (viz. linear free energy relationships) or qualitative theoretical concepts (viz. Woodward-Hoffmann approach or the frontier orbital method). These notes are intended to describe the basis for a different approach, namely, the development of physically grounded models within the best state of the art methodology of quantum chemistry. These physically grounded models must be both quantitative and qualitative. On the one hand, any model used should reproduce the numerically computed quantities exactly, on the other, it should provide a basis for correlating experimental fact in a qualitative manner. We believe that the Diabatic Surface model, first proposed by Evans [4], provides a model that satisfies these criteria. It can be implemented to reproduce the results of MC-SCF, CI and perturbation theories exactly and the most difficult concept required of its qualitative application is the Valence Bond treatment of H_2.

These lecture notes are divided into 2 chapters. In the first we shall explain the Diabatic Surface model as it applies to organic reactivity in a simple non-mathematical way. In particular, we shall try to show why the Woodward-Hoffman approach has severe limitations. We shall then show how the Evans Diabatic Surface model can be implemented in a rigorous way. In the second chapter, we shall demonstrate that these ideas have wide applicability by giving some detailed applications. We must emphaise from the outset that we use the term "diabatic" in the way it was first used by Evans [4] and our use of this term should not be confused with its use in chemical dynamics (no derivative coupling). However, we shall give a brief discussion of this point at the end of these notes

II Motivation: A Valence Bond Approach to Pericyclic Reactivity

There can be no doubt as to the impact [5,6] of the Woodward-Hoffman /Fukui approach to chemical reactivity. This approach is now a part of the way every organic chemist thinks about chemical reactivity. Nevertheless, as we shall presently discuss this theory has some fundamental problems. However, there exists a complimentary theory due to Evans [4] which is now 50 years old which merits discussion because it does not suffer from some of the deficiencies of the Woodward-Hoffman /Fukui method. The Evans Diabatic Surface method is based upon Valence Bond (VB) Theory (see ref. [7] for review material) while Woodward-Hoffman/Fukui approach uses the MO method (Huckel theory). Of course, as every chemist has seen in his first studies in quantum chemistry on H_2, the VB and MO methods become identical when pushed to the limit; however, it is evident even in H_2, that certain ideas may be more easily formulated in one theory as opposed to the other. It is our intention in this section to provide the motivation for the more detailed theoretical exposition which follows. Taking the $2_s + 2_s$ cycloaddition of two ethylene molecules as an example, we will describe the both the Evans and Woodward-Hoffman approaches from a unified point of view.

To use Evans model one needs only the ideas that come from the VB method as applied to H_2 and the results of a two level secular equation. Thus we begin by reminding ourselves of the essential facts. The VB wavefunction for the ground state of H_2 is built from two H 1s orbitals

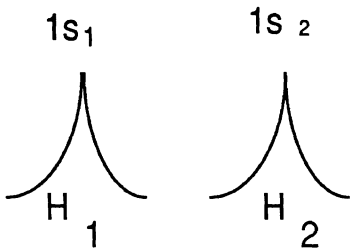

Fig. 1 H_2 Atomic Orbital Basis

and has the form

$$\Psi = 1s_1(1)\ 1s_2(2) + 1s_2(1)\ 1s_1(2) \qquad [1]$$

while that for the triplet (repulsive non-bonding) excited state has the form

$$\Psi = 1s_1(1)\ 1s_2(2) - 1s_2(1)\ 1s_1(2) \qquad [2]$$

For reasons that will become obvious we can denote these two states as

$$1 \longrightarrow 2 \qquad 2S+1 = 1$$

$$1 \bullet \qquad \bullet 2 \qquad 2S+1 = 3$$

The total energy is given as

$$E = \alpha + \beta / 1+S^2 \quad \text{or} \quad \alpha - \beta / 1-S^2 \qquad [3]$$

where

$$\alpha = 2\varepsilon_{1s} + J \text{ with } J = j-2j' \qquad [4]$$

$$\beta = (2\varepsilon_{1s} + 1/R)\ S^2 + K \text{ with } K = k - 2\ S\ k' \qquad [6]$$

The symbol S refers to the overlap of the orbitals and J and K are the coulomb and exchange:

$$j = \iint 1s_1(1)\ 1s_1(1)\ r_{12}^{-1}\ 1s_2(2)\ 1s_2(2)\ dr_1\ dr_2 \qquad [7]$$

$$j' = \int 1s_1(1)\ h\ 1s_1(1)\ dr_1 \qquad [8]$$

$$k = \iint 1s_1(1)\ 1s_2(1)\ r_{12}^{-1}\ 1s_1(2)\ 1s_2(2)\ dr_1\ dr_2 \qquad [9]$$

$$k' = \int 1s_1(1)\ h\ 1s_2(1)\ dr_1$$

We can write eq. 1 as

$$E = 2\varepsilon_{1s} + J \pm K / 1 \pm S^2 + 1/R \qquad [10]$$

If we neglect S^2 (since S is small and less than 1) and change the notation we have

$$E \cong Q \pm K \qquad [11]$$

with

$$Q = 2\varepsilon_{1s} + J + 1/R \qquad [12]$$

The term J (negative since J = j-2j' and -j' is negative electron attraction) balances the repulsive 1/R (nuclear repulsion). The term K = k - 2 S k' is negative due to the attraction of the overlap density. Thus for H_2 the various terms behave as shown in the figure below.

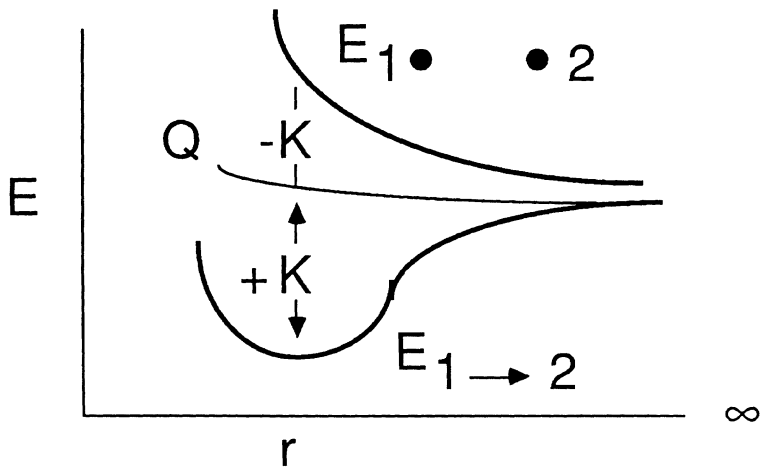

Fig. 2 Singlet and Triplet states of H_2

Thus the energetics of a single bond are very easy to understand in VB. The triplet 1. .2 with two unpaired electrons is repulsive due to the -K and the singlet 1-> 2 is attractive due to + K while Q is almost constant.

Now let us examine how these ideas are extended to more than two electrons. The ideas are much simpler than MO theory. Let us take the $2_s + 2_s$ cycloaddition as an example.

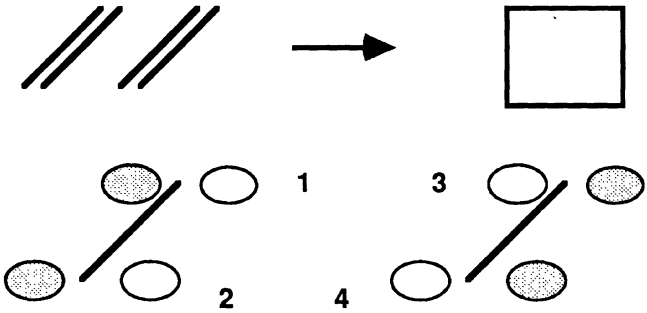

Fig. 3 Orbitals for a 2 + 2 cycloaddition

We take as our orbital basis the 4 p^{π} atomic orbitals (AO) of the ethylenic fragments. Using the notation introduced for H_2 we can write the wavefunctions for reactant and product symbolically as

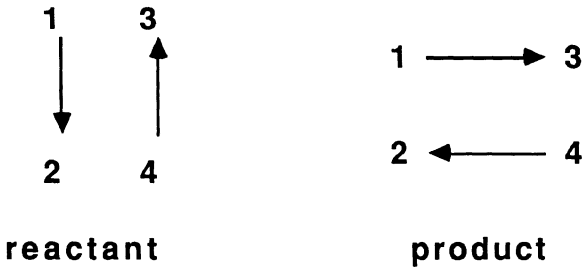

Using a two level secular equation, taking one reference wavefunction as the reactant and the other as the product we can find the wavefunction as a linear combination of these reactant and product wavefunctions through the solution of the usual secular equation

$$\begin{pmatrix} \alpha_R - E & \beta \\ \beta & \alpha_P - E \end{pmatrix} \begin{pmatrix} C_R \\ C_P \end{pmatrix} = 0 \qquad [13]$$

At this stage we will be content to write the matrix elements symbolically as

$\alpha =$ 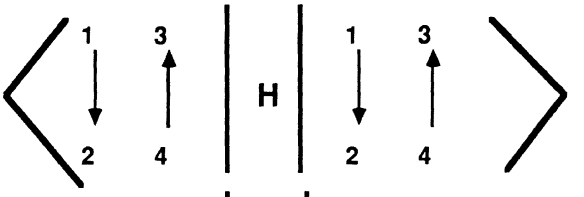

$\beta =$ 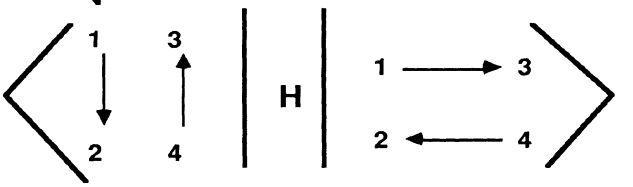

Similarly the wavefunction has the form

Ψ = C_R 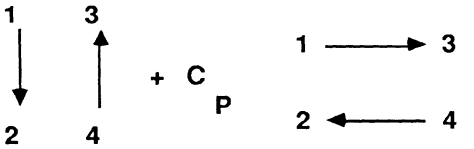

+ C_P

Remarkably, after some algebra which we will return to subsequently, one finds that

$$\alpha_R = Q^* - K^* \qquad [14]$$

and

$$\alpha_P = Q^* + K^* \qquad [15]$$

with

$$Q^* = Q_{12} + Q_{13} + Q_{14} + Q_{23} + Q_{24} + Q_{34} \qquad [16]$$

and

$$K^* = \sqrt{3}/2\,(K_P - K_R) \quad \text{with } K_P = K_{13} + K_{24} : K_R = K_{12} + K_{34} \qquad [17]$$

The exchange integral K_P is the exchange energy of the *product* electronic configuration, and K_R is the exchange energy of the *reactant* electronic configuration. Similarly β is given as

$$\beta = K_x - 1/2\,K_P - 1/2\,K_R : \quad K_X = K_{14} + K_{23} \qquad [18]$$

where K_X is the exchange energy of the *non-directly-bonded* interactions (like the 1. .2 triplet interaction in H_2). We now observe that

1)The Q_{ij} *and* K_{ij} *are defined in exactly the same way as in* H_2 *except of course that the integrals involve the ethylenic* p^{π} *orbitals. The* K_{ij} *are negative as in* H_2.
2)In K^*, K_P K_R *occur with the opposite sign (and will cancel approximately at the transition state).*
3)In β *(the resonance energy)* K_P K_R *occur with the same sign and this effect is reduced by* K_X.

From the solution of the secular equation [13] we have

$$E = Q^* \pm T \text{ with } T = \{ K^2 + \beta^2 \}^{1/2} \qquad [19]$$

and it is possible to show that

$$E = Q^* \pm \{ (K_P - K_X)(K_R - K_X) + (K_P - K_R)^2 \}^{1/2} \qquad [20]$$

We can represent the behaviour of these quantities as shown in the following figure:

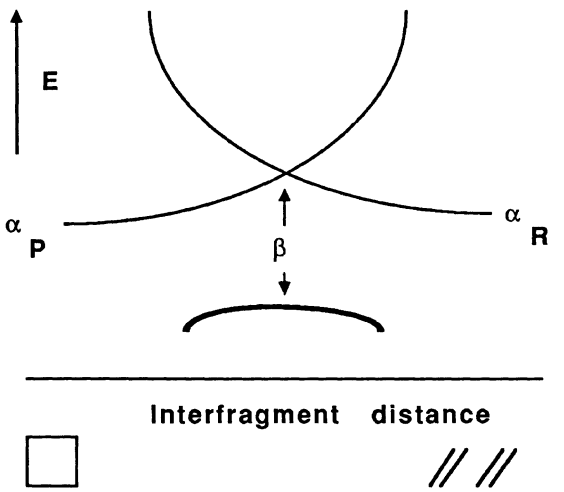

Fig. 4 Schematic representation of the interaction of two diabatic surfaces α_R and α_P under the effect of β (the resonance energy) to produce an adiabatic surface.

The behaviour of these curves can be rationalized qualitatively in the following way:

1)We can expect that Q^* is approximately constant (like H_2) since the terms in J (negative since J = j-2j' and -j' is negative electron attraction) balances the repulsive nuclear repulsion). Thus $\alpha_R = Q^* - K^*$, $\alpha_P = Q^* + K^*$ will behave like $\alpha_R = -K^*$ $\alpha_R = +K^*$. Further, each of the K_{ij} in K^* will behave as the K_{12} in H_2 as a function of distance between i and j (ie proportional to overlap). This as the interfragment distance in decreased the *magnitude of* a) K_p increases b) K_R decreases. Thus *the magnitude* of $K^* = \sqrt{3}/2\ (K_P - K_R)$ *decreases until the transition state (crossing in fig. 4) then increases again until the product is reached.*

2) The transition state occurs approximately where the curves $\alpha_R = Q^* - K^*$, $\alpha_P = Q^* + K^*$ cross . At this point the energy is just $Q^* \pm \beta$ **(where** β **is the resonance energy)**, and K^* is zero. As the interfragment distance in decreased the **magnitude of** K_X increases . The barrier height is controlled by β **the resonance energy.** Note that since K^* is zero, eq. 18 gives

$$\beta = K_x - 1/2\ K_P - 1/2\ K_R = K_x - K_P = K_x - K_R \qquad [21]$$

The barrier height for and 4 orbital 4 electron process depends only on

1) the change in coulomb energy (mainly steric effects). If the TS is stericly hindered then this term is important.

2) $|K_R^{react}|$ the magnitude of bonded effects in the reactant. If K_R^{react} is large then the bonding stabilization of the reactants is large and one expects a large contribution to the barrier as a result of breaking these bonds.

and

3)$|K_R^{TS} - K_X^{TS}|$ (the resonance interaction in the transition state) . The resonance interaction is a competition between the residual reactant bond stabilization in the transition state K_R^{TS} and the destabilizing effect of the non-bonded interactions K_X^{TS}.

All of the preceding discussion applies to any 4 orbital 4 electron problem. Thus there is no concept of forbidden and allowed. In general α_R and α_P are potential energy surfaces. The quantity α_R describes the energy of the reactant bonding situation at any geometry and the quantity α_p describes the energy of the product bonding situation at any geometry . The α_R and α_P are diabatic surfaces and $E = Q^* \pm \{ (K_P - K_X)(K_R - K_X) + (K_P - K_R)^2 \}^{1/2}$ describes the adiabatic surfaces on which the reaction takes place.

Now let us compare the preceding discussion with the Woodward-Hoffman approach. Although the Woodward-Hoffman approach was not explicitly formulated in terms of diabatic surfaces, it is convenient to approach the problem from this point of view. In contrast to the Evans model, the Woodward-Hoffman approach is formulated in terms of MO theory. The MO are allowed to interact (according to the rules of symmetry and the usual overlap principles). The interaction diagram is shown below in Fig. 5a (reactant orbital occupancy) and Fig. 5b (product orbital occupancy).

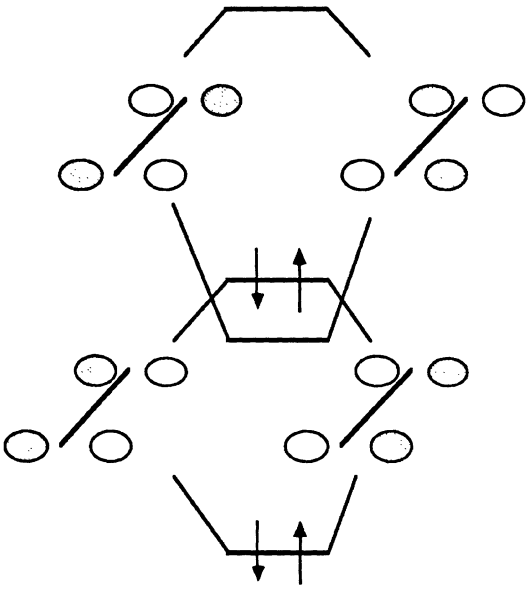

Fig. 5a Reactant interaction diagram (reactant diabatic surface)

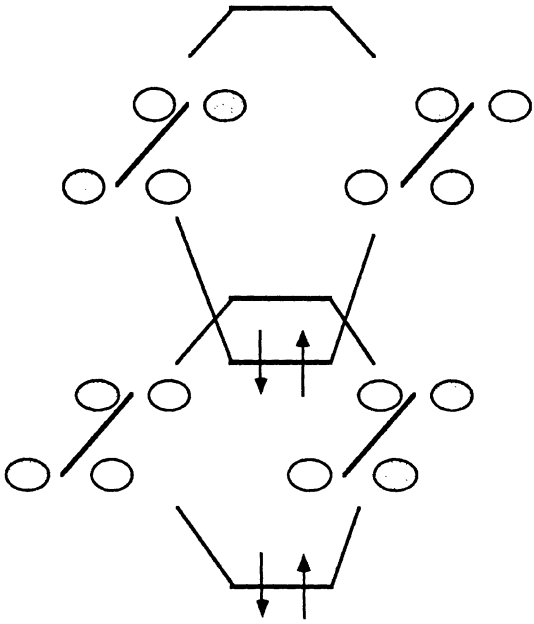

Fig. 5b Product Interaction Diagram (Product Diabatic Surface)

Each of these two "configurations" can be used in the same way as the reactant and product configurations in the Evans approach and the total energy is obtained from a similar 2 level secular equation. Obviously α_R and α_P have a different mathematical definition and in the Woodward-Hoffman approach they are merely sums of occupied orbital energies. As is well known one obtains the same avoided crossing as shown in Fig. 4.

The conceptual difficulty in the Woodward-Hoffman approach arises with "allowed" reactions. In this case the orbital interaction diagram has the form shown in Fig. 5c.

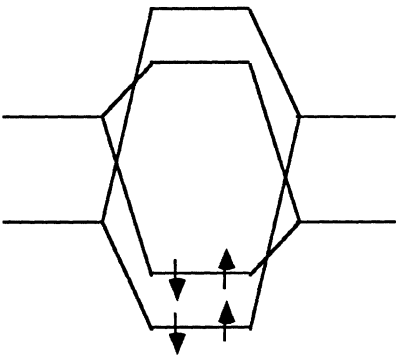

Fig. 5c Interaction diagram for an allowed reaction.

The electronic configuration is the *same* for reactant and product. Thus for a "forbidden" process the LUMO of one reactant cannot interact with the HOMO of the other so there are two different configurations one for the product the other for the reactant. For the "allowed" reaction the configuration of reactant and product is the same. *Thus we are left with no possibility of explaining the origin of the reaction barrier for an allowed process in terms of the intersection of two surfaces.* In contrast, in the Evans' approach, the origin of the barrier for forbidden and allowed processes is the same, and the differences in barrier heights can be explained in terms of $K_R^{TS} - K_X^{TS}$ and $Q^{\bullet}$. The essential difference in the two models arises from the fact that in the Evans VB approach the orbitals are fixed (AO centred on the C atoms) and it is the mixing of reactant and product VB structures that changes along the reaction coordinate while in the Woodward-Hoffmann MO model the orbitals are continually deformed along the reaction coordinate. As we shall presently discuss, the most important feature of the Evans' model is that it can be implemented in a rigorous way for MC-SCF and CI wavefunctions. Obviously, the Woodward-Hoffman approach is almost impossible to implement in a quantitative way for MCSCF and CI wavefunctions since it is formulated within Huckel theory.

Finally, we should briefly discuss a model, first suggested by Epiotis[8], that is similar to the Evans' model in that it is formulated within VB theory. However, it differs from the Evans' model in that the reactant and product configurations are built from the MO of the constituent fragments and thus it is usually referred to as MO-VB.

In this scheme, the reactant and product diabatic surfaces correspond to the configurations shown in Fig. 5d.

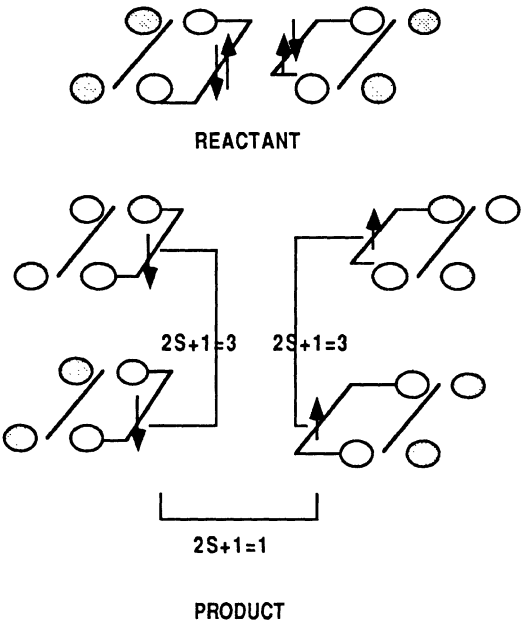

Fig. 5d Reactant and Product configurations in a MO-VB approach

The reactant configuration corresponds to the two doubly occupied ethylenic π orbitals. The product corresponds to two triplet $\pi\pi^*$ fragments which have been coupled to a singlet overall. At first sight it is not immediately obvious that this is the correct choice for the product diabatic. However, the triplet $\pi\pi^*$ fragments correspond to completely broken intrafragment π bonds and correlates correctly with the product bonding situation at infinite interfragment separation. We have used this definition in our early work [9] and the results were very useful. However, as we came to require very accurate results for quantitative analysis, the fact that the triplet $\pi\pi^*$ fragments did not completely dominate the wavefunction at the equilibrium geometry caused problems with this definition. Thus we now use a rigorous implementation of Evans model that we shall now describe in some detail.

The remainder of this chapter will be concerned with the rigorous implementation of Evans' model within the formalism of the standard methods of quantum chemistry. Since most of the standard methods of quantum chemistry use the MO method in one form or another, much of our discussion centres around the relationship between MO and CI theory and VB. On the one hand, one will almost certainly use MO based methods for molecular structure determination because of the availability of analytic gradient and hessian methods. On the other hand, the VB method provides the simple concepts that yield a simple rationalization of chemical reactivity via Evans' model. Thus the

relationship between MO CI (and MC-SCF) and VB is vital both from a practical and conceptual point of view.

III Orbitals for VB theory

While we are accustomed to the concept of orbital optimization in SCF theory, the use of optimized orbitals in VB theory (see the reviews [7a,b]), may be less familiar. It is convenient to illustrate the ideas using s simple VB treatment of H_2 in a minimal basis of 1s atomic orbitals. Later, having established the concepts, we return to a general development.

The most general minimum basis VB wavefunction for H_2 has the form

$$\Psi = \lambda_1 \{1s_1(1)\ 1s_2(2) + 1s_2(1)\ 1s_1(2)\} + \lambda_2\{1s_1(1)\ 1s_1(2) + 1s_2(1)\ 1s_2(2)\} \qquad [22a]$$

where $\{1s_1(1)\ 1s_2(2) + 1s_2(1)\ 1s_1(2)\}$ is a the covalent structure

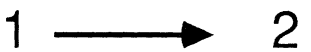

$1s_2(1)\ 1s_2(2)$ is an ionic structure

and λ_1 λ_2 are chosen to minimize the energy. However, the wavefunction of eq. 22 contains a full CI in the basis of the configurations that can be built from the 2 electrons and two orbitals (ie the simplest possible CAS CI wavefunction). Thus the energy in invariant to rotations of the $1s_1$ and $1s_2$ orbitals but of course the values of λ_1 λ_2 will change. (In particular if we replace the $1s_1$ and $1s_2$ orbitals by the $1s_1 + 1s_2$ and the $1s_1 - 1s_2$, a 45° rotation, then we have simply the MO CI wavefunction).

Within VB we have 4 choices for the the $1s_1$ and $1s_2$ orbitals:

1) "raw" non-orthogonal $1s_1$ and $1s_2$ atomic orbitals (see fig.1)

2) symmetrically orthogonal $1s_1$ and $1s_2$ atomic orbitals

3) non-orthogonal orbitals that optimize the energy of the covalent configuration $\{1s_1(1)\ 1s_2(2) + 1s_2(1)\ 1s_1(2)\}$

4)orthogonal orbitals that optimize the energy of the covalent configuration

This problem was considered many years ago by Coulson and Fischer[10]. The forms of the symmetrically orthogonal $1s_1$ and $1s_2$ atomic orbitals and the non-orthogonal orbitals that optimize the energy of the covalent configuration are crudely sketched in Fig. 6. Notice that they differ mainly in the signs of the "delocalization tails".

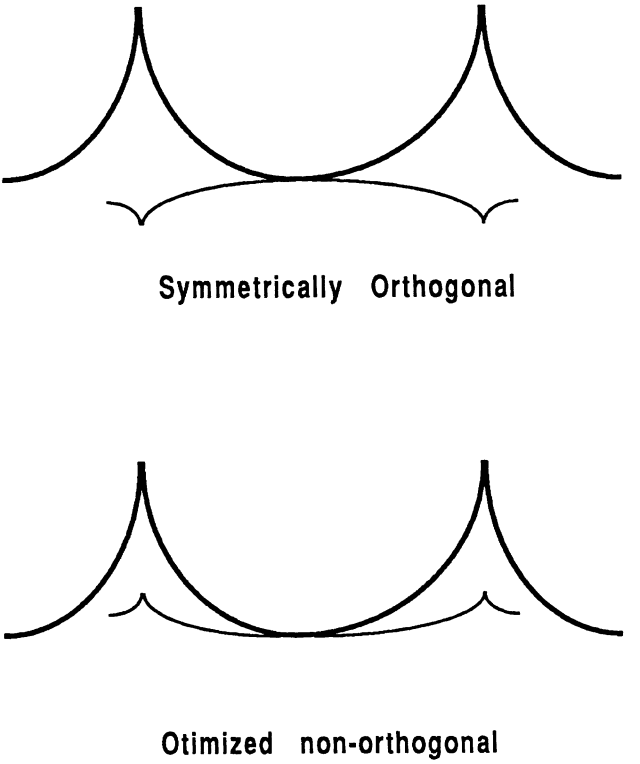

Fig. 6 Symmetrically orthogonalized and energy optimized non-orthogonal H_2 1s orbitals

With the non-orthogonal orbitals that optimize the energy of the covalent configuration, λ_2 goes to zero and the charge transfer structures $1s_2(1)\ 1s_2(2)$ are replaced by orbital delocalization. Conversely, with the symmetrically orthogonal $1s_1$ and $1s_2$ atomic orbitals λ_2 has a larger value than the case for "raw" non-orthogonal

$1s_1$ and $1s_2$ atomic orbitals. *Thus charge transfer and orbital delocalization /non-orthogonality are just different manifestations of the same physical effect.* In Evans' model, we wish to build wavefunctions from perfectly covalent structures. Thus we are implicitly dealing with non-orthogonal orbitals that optimize the energy of the covalent configurations and the charge transfer structures have been replaced by orbital delocalization.

The use of very general spin-coupled VB wavefunctions built from optimized distorted AO has been extensively developed by Gerratt and his co-workers in recent years [7a]. However, our interest is to construct such wavefunctions from the MO CI space that would have been used in a molecular structure determination. For H_2 VB the problem is easily described. If we write eq. 22 as combination of determinants we have

$$\begin{aligned}\Psi &= \lambda_1 \{1s_1(1)\ 1s_2(2) + 1s_2(1)\ 1s_1(2)\} \\ &\qquad + \lambda_2\{1s_1(1)\ 1s_1(2) + 1s_2(1)\ 1s_2(2)\} \\ &= \lambda_1\{\,|1_\alpha 2_\beta| + |2_\alpha 1_\beta|\} + \lambda_2\{\,|1_\alpha 1_\beta| + |2_\alpha 2_\beta|\}\end{aligned} \qquad [22b]$$

However, this equation can also be written as

$$\Psi = \exp(\mathbf{A})\{\,|1_\alpha 2_\beta| + |2_\alpha 1_\beta|\} \qquad [23]$$

where **A** has the form

$$\mathbf{A} = a_{12}\,\mathbf{E}_{12} + a_{21}\,\mathbf{E}_{21} \qquad [24]$$

The operator $\mathbf{E}_{12}$ annihilates orbital 1 and replaces it by orbital 2

$$\mathbf{E}_{12} = \mathbf{E}_{1\alpha 2\alpha} + \mathbf{E}_{1\beta 2\beta} \qquad [25]$$

so that

$$\mathbf{E}_{1\alpha 2\alpha} + \mathbf{E}_{1\beta 2\beta}\{\,|1_\alpha 2_\beta| + |2_\alpha 1_\beta|\} = 2\,|1_\alpha 1_\beta| \qquad [26a]$$

$$\mathbf{E}_{2\alpha 1\alpha} + \mathbf{E}_{2\beta 1\beta}\{\,|1_\alpha 2_\beta| + |2_\alpha 1_\beta|\} = 2\,|2_\alpha 2_\beta| \qquad [26b]$$

Clearly eq. 22 and eq. 23 are only the same if we choose $a_{12} = a_{21}$ then $|a_{12}|$ is merely proportional to λ_1/λ_2.

The parameters of **A** can also be thought of as the "rotational" angles between orbital 1 and orbital 2 and $a_{12} = a_{21}$ corresponds to a non orthogonal transformation while $a_{12} = -a_{21}$ is an orthogonal transformation. Thus if we rotate the orbitals using $a_{12} = a_{21}$ in **A** according to

$$\begin{matrix} 1s_1' \\ 1s_2' \end{matrix} = \exp(\mathbf{A}) \begin{matrix} 1s_1 \\ 1s_2 \end{matrix} \qquad [27]$$

then eq. 23 can be written in terms of the new non-orthogonal orbitals as

$$\Psi = \{ |1_\alpha{}'2_\beta{}'| + |2_\alpha{}'1_\beta{}'|\} \qquad [28]$$

Thus, in principle, since λ_1/λ_2 and a_{12} are linearly dependent ,given λ_1/λ_2 we can always rotate the orbitals so that the ionic terms vanish provided that the initial orbitals are chosen so that $a_{12} = a_{21}$. Note that the condition for optimum orbitals , the Brillouin condition,

$$< |1_\alpha{}'2_\beta{}'| + |2_\alpha{}'1_\beta{}'| \, H \, \mathbf{E}_{1'2'} \; |1_\alpha{}'2_\beta{}'| + |2_\alpha{}'1_\beta{}'| > \; = 0 \qquad [29]$$

is always satisfied since

$$H \lambda_1\{ |1_\alpha 2_\beta| + |2_\alpha 1_\beta|\} + \lambda_2 \{ |1_\alpha 1_\beta| + |2_\alpha 2_\beta|\}>$$
$$= \varepsilon \lambda_1\{ |1_\alpha 2_\beta| + |2_\alpha 1_\beta|\} + \lambda_2 \{ |1_\alpha 1_\beta| + |2_\alpha 2_\beta|\}> \qquad [30]$$

implies

$$H \, |1_\alpha{}'2_\beta{}'| + |2_\alpha{}'1_\beta{}'| > \; = \varepsilon \, |1_\alpha{}'2_\beta{}'| + |2_\alpha{}'1_\beta{}'| > \qquad [31]$$

as well. Thus one has merely used the linear dependence between the CI coefficients and the orbital rotations a_{12} coupled with the fact that λ_1/λ_2 are determine variationally to remove the ionic configurations. Later we shall generalize this argument.

Now let us consider another possibility, we choose $a_{12} = -a_{21}$ an orthogonal transformation and minimize the energy of $|1_\alpha 2_\beta| + |2_\alpha 1_\beta|$. The Brillouin condition is

$$< |1_\alpha 2_\beta| + |2_\alpha 1_\beta| \, H \, \mathbf{E}_{12} \; |1_\alpha 2_\beta| + |2_\alpha 1_\beta| >$$
$$- < |1_\alpha 2_\beta| + |2_\alpha 1_\beta| \, H \, \mathbf{E}_{21} \; |1_\alpha 2_\beta| + |2_\alpha 1_\beta| > = 0 \qquad [32]$$

which gives

$$< |1_\alpha 2_\beta| + |2_\alpha 1_\beta| \, H \, |1_\alpha 1_\beta|>$$
$$- < |1_\alpha 2_\beta| + |2_\alpha 1_\beta| \, H \; |2_\alpha 2_\beta|> = 0 \qquad [33]$$

It is easily verified that this reduces to

$$[11|12] - [22|21] = 0 \qquad [34]$$

However, this is exactly the same as the condition for localized or equivalent orbitals first used by Edmiston and Ruedenberg [11]. Thus if we minimize the energy of the covalent configuration of H_2 with respect to orthogonal rotations of the orbitals, one obtains localized orbitals. Of course these will be similar to the symmetric orthogonalized orbitals.

It is now clear that in VB wavefunctions, the orbitals must be optimized by some criterion. Only two possibilities remain i)non-orthogonal orbitals that optimize the energy of the covalent configuration ii)orthogonal orbitals that optimize the energy of the covalent configuration and are also localized. The first set can be obtained by obstructing the transformation of eq. 27 where the parameter a_{12} can be obtained from λ_1/λ_2 which has been variationally determined. The orbitals ii) represent the optimum VB expansion in an orthogonal set of orbitals. Since both sets of orbitals satisfy precise mathematical criteria, the definitions do not depend upon the use of a minimal basis. As one goes beyond a minimal basis, then the preceding concepts need to be applied within MC-SCF theory. The MC-SCF wavefunction will have the form

$$\Psi = C_1\sigma_g(1)\,\sigma_g(1) + C_2\,\sigma_u(2)\,\sigma_u(2) \qquad [35]$$

where σ_g/σ_u are expanded in the full extended basis. As an approximation, in this basis we could define a molecule adapted orthogonal minimum basis as

$$1s_1^* / 1s_2^* = \sigma_g + \sigma_u / \sigma_g - \sigma_u \qquad [36]$$

Since these orbitals are" equivalent", starting from this approximation, the best molecule adapted orthogonal minimum basis could be found by computing a_{12} which satisfies eq. 33 and 34. In this basis the MC-SCF wavefunction has the form given in eq. 22. Thus the optimum minimal basis of non-orthogonal orbitals can be determined from eq. 27. We thus have the ability to transform any 2 orbital CAS SCF wavefunction to VB space. In the molecule adapted non-orthogonal minimum basis , the roles of charge transfer and orbital delocalization/ non-orthogonality are interchangeable.

The preceeding ideas are generalizable to systems of more than two electrons. This fact has been exploited in the GVB-PP methods (see the review 7b). We shall return to a general discussion in section V.

IV The Heisenberg Hamiltonians and Spin Coupling in the Evans' Diabatic Surface model (VB theory)

In section II we formulated Evans' model of reactivity (using a 4 electron 4 orbital case as an illustrative example) in terms of the change in spin coupling between a reactant and product spin coupled function:

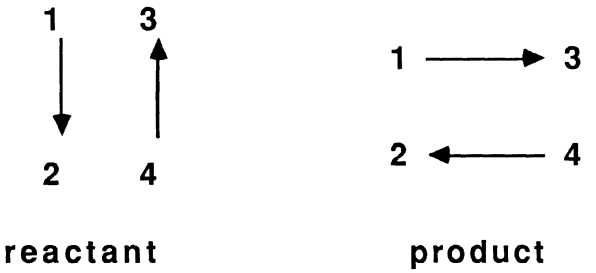

We assumed that each of the arrows corresponded to a factor that was similar to the singlet spin coupling in H_2. The energetics were formulated in terms of two centre coulomb and integrals over a minimum basis of atomic orbitals. In the preceding subsection, we have indicated how a molecule adapted minimum basis of AO might be obtained. In this section, we must consider the the way in which the energy expressions of section II are obtained in some detail. This involves a discussion of Heisenberg hamiltonians and the explicit form of the spin coupled functions for reactant and product. However, the subject of spin coupling is quite complicated and the general solutions are best formulated using group theoretical methods. Thus we will be content with making some general statements and then illustrating the basic ideas using a simple 4 orbital 4 electron example. For a detailed discussion the reader in referred to the book by Pauncz [13a] or the older but readible account in the book by Eyring et al [13b].

We have seen in section III, that with a suitable choice of orbitals, we can limit our discussion of VB theory to perfectly covalent structures in which each electron is singly occupied and there is one orbital per electron. The matrix representation of the hamiltonian in the space of all neutral-only VB determinants that can be built from n orbitals and n electrons is usually referred to as a Heisenberg hamiltonian [12,14]. (There are numerous examples of hamiltonians of this type in the text by Eyring et al [13b].) It has the property that it can be expressed exactly in terms of "formal" 1 and 2 centre coulomb and exchange integrals of the form introduced in section II and thus is the basic building block of the Evans' model. (We use the term "formal" to allow for the fact that the molecule adapted AO basis will be slightly delocalized). The Evans hamiltonian of eq. 13 is just the projection of this hamiltonian onto the space of the reactant and product spin couplings. Thus we now give some discussion of this simple hamiltonian.

It is instructive to use H_2 as an example to give some historical perspective. It is simple to verify that the energy expression for H_2 given in eq.11 can be written as the

expectation value

$$E = Q + K$$

$$= \langle 2^{-1/2} \{ |1_\alpha 2_\beta| + |2_\alpha 1_\beta| \} \, \mathbf{H_s} \, 2^{-1/2} \{ |1_\alpha 2_\beta| + |2_\alpha 1_\beta| \} \rangle \qquad [37]$$

of a *spin* hamiltonian $\mathbf{H_s}$ of the form

$$\mathbf{H_s} = (Q - 1/2\, K) - 2\, K\, \mathbf{S}(1) .\, \mathbf{S}(2) \qquad [38]$$

In eq. 38 the spin scalar product has the form

$$\mathbf{S}(1) .\, \mathbf{S}(2) = 1/2\, [\, \mathbf{S}_+(1) .\, \mathbf{S}_-(2) + \mathbf{S}_-(1) .\, \mathbf{S}_+(2)] + \mathbf{S}_z(1) .\, \mathbf{S}_z(2) \qquad [39]$$

and eq 37 can be verified using the usual rules of spin algebra

$$[\mathbf{S}(1) .\, \mathbf{S}(2)]\alpha(1)\alpha(2) = 1/4\ \alpha(1)\alpha(2) \qquad [40a]$$

$$[\mathbf{S}(1) .\, \mathbf{S}(2)]\alpha(1)\beta(2) = 1/2\ \beta(1)\alpha(2) - 1/4\ \alpha(1)\beta(2) \qquad [40b]$$

so that

$$\langle \{ |1_\alpha 2_\beta| + |2_\alpha 1_\beta| \} \, [\mathbf{S}(1) .\, \mathbf{S}(2)] \, \{ |1_\alpha 2_\beta| + |2_\alpha 1_\beta| \} \rangle = -3/4 \qquad [40c]$$

Thus the complexity of the energy expression is absorbed into Q and K and we have a simple "model" with a parameter K which could be taken as an empirical parameter.

This simple idea can be generalized to more than two electrons. However it is inconvenient to work in a spin operator formalism. For two electrons the complete set of neutral-only VB determinants is (S_z=0)

1) $|1_\alpha 2_\beta|$ 2) $|2_\alpha 1_\beta|$

and the matrix representation of H in this space is trivially

$$\mathbf{H_s} = \begin{pmatrix} Q & K \\ K & Q \end{pmatrix} \qquad [41]$$

Thus we shall limit our discussions always to the matrix representation of $\mathbf{H_s}$.

As a simple example for more than 2 electrons, we next consider the case of 4 orbitals and 4 electrons. In this case there are 6 determinants summarized in table 1 below. The corresponding Heisenberg hamiltonian is given in table 2.

Table 1 Determinants for 4 orbitals 4 electrons (S_z=0)

sequence no	determinant	
	α spin	β spin
1	3 4	1 2
2	2 4	1 3
3	2 3	1 4
4	1 4	2 3
5	1 3	2 4
6	1 2	3 4

Table 2 Symbolic (non-redundant §) form of Heisenberg hamiltonian H_s for 4 orbitals and 4 electrons.

	1	2	3	4	5	6
1	$Q_1-K_{12}-K_{34}$	K_{23}	$-K_{24}$	$-K_{13}$	$-K_{14}$	
2		$Q_2-K_{13}-K_{24}$	K_{34}	K_{12}		
3			$Q_3-K_{14}-K_{23}$			

§ The remaining matrix elements are equal to those given. Matrix elements between pairs of determinants that differ by two spin interchanges (eg. 1,6 or 2,5 or 3,4) are equal. Thus $H_{12} = H_{56}$, $H_{15} = H_{63}$ etc

It can be seen that the above hamiltonian is a function only of the "formal" 2 centre coulomb Q and exchange parameters K_{ij} which are assumed to have the functional form given in eq. 6.

Let us now raise a dilemma, that we will resolve subsequently. In the Heisenberg hamiltonian the parameter K is assumed to have the form

$$K_{ij} = [ij|ij] + 2\ S_{ij}\ \langle i|h|j\rangle \qquad [42]$$

(here [ij|ij] is the two electron repulsion integral k in eq. 6, $\langle i|h|j\rangle$ is the kinetic/nuclear attraction -k', and S_{ij} is the overlap. Thus in eq. 41 K is negative since

it is dominated by <i|h|j>. However, if we use the usual rules for the evaluation of matrix elements over determinants, the we obtain the hamiltonians given in eq. 41 or table 2. However, in this case, we must take K_{ij}= [ij|ij] which is positive. On the other hand, we know that if the orbitals are non-orthogonal, we ought to use the full expressions for matrix elements built from non-orthogonal orbitals. For H_2 this adds terms proportional to S_{ij} and S_{ij}^2 and in general we will have terms involving higher powers of S for systems with more than 2 electron. In the early days of quantum chemistry this dilemma was ignored and the K_{ij} were regarded as empirical parameters. As we shall subsequently show, in fact there is no dilemma. The Heisenberg hamiltonian can be rigorously derived from an effective hamiltonian that is easily computed from an MC-SCF or CI wavefunction.

In summary, the Heisenberg hamiltonian represents the matrix elements of the hamiltonian evaluated in the neutral-only VB determinants (covalent). These determinants are assumed to be built from an optimized set of non-orthogonal molecule adapted minimum basis set AO. The rule for construction of the Heisenberg hamiltonian is :

1) *evaluate the matrix elements using the rules for determinants built from orthogonal* AO

and

2) *replace (implicitly) the* K_{ij}= [ij|ij] *by* K_{ij}= [ij|ij] + 2 S_{ij} <i|h|j>.

The eigenvalues of the Heisenberg hamiltonian are assumed to reproduce those of a spin coupled VB [7a] or CAS SCF computation exactly.

Given the Heisenberg hamiltonian according to the above prescription, the computation of Evans' VB hamiltonian of eq. 13 requires only the computation of

$\alpha =$ 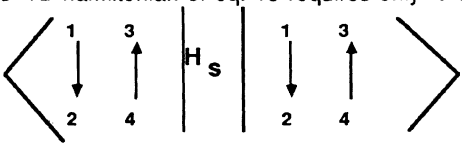

$\beta =$ 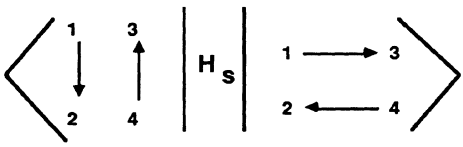

and its generalization to situations other than this 4 orbital 4 electron example. Since we have established the nature of $\mathbf{H_s}$, provided we can specify the reactant and product

spin coupled wavefunctions as linear combinations of determinants we can evaluate the parameters α and β. We shall proceed with a simple example of 4 electrons in for orbitals and then state the general result.

In valence bond theory we can represent the wavefunction ψ_R of the reactant in terms of a Rumer spin-eigenfunction as

$$\psi_R = \det [1_\alpha 2_\beta] [3_\alpha 4_\beta] \qquad [43a]$$

where [ab] = ab - ba and det means form the determinant of the linear combination. Thus ψ_R is a linear combination of 4 determinants. Similarly, the product wavefunction , ψ_P has the form.

$$\psi_P = \det [1_\alpha 4_\beta] [2_\alpha 3_\beta] \qquad [43b]$$

These spin functions are in simple one to one with the spin coupling diagrams given before. Thus det $[1_\alpha 2_\beta]$ is just the VB wavefunction for a 2 orbital 2 electron system. However, these spin coupled functions are not appropriate for use in the Evans model because they are not orthogonal. An examination of $< \psi_R | H_s | \psi_R >$ and $< \psi_R | H_s | \psi_P >$ shows why. Thus

$$\alpha_R = < \psi_R | H_s | \psi_R > = Q + K_{12} + K_{24} - K_{23} - K_{14} \qquad [44a]$$

$$\beta = < \psi_R | H_s | \psi_P > = S \{ Q + K_{12} + K_{24} + K_{23} + K_{14} - 2K_{23} - 2K_{14} \} \qquad [44b]$$

where S is the overlap $< \psi_R | \psi_P >$. Further the secular equation 13 must be modified to include overlap. Notice that in the Heisenberg hamiltonian Q occurs only along the diagonal. Thus Q serves as the energy zero. Any orthogonal projection of H_s also has Q along the diagonal. Thus the appearance of Q in the off-diagonal position in eq. 44b is undesirable since Q now occurs as part of the resonance interaction $\beta = < \psi_R | H_s | \psi_P >$.

For these reasons ,the simple Rumer functions must be replaced by orthogonal functions $\psi^\perp_R / \psi^\perp_P$. Any orthogonal combination of ψ_R / ψ_P is acceptable. The most common form of orthogonal spin coupling is the Yamanouchi-Kotani (or branching diagram, see ref. [13a])

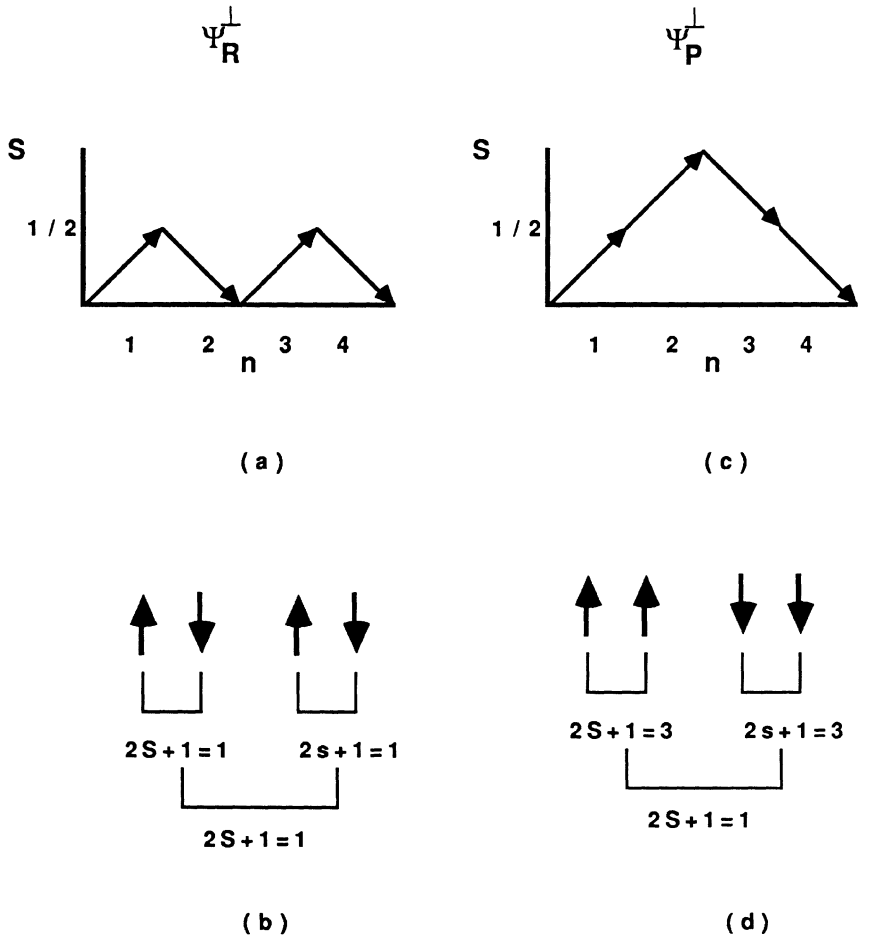

Fig. 7 Orthogonal Yamanouchi-Kotani spin coupling for 4 orbitals and 4 electrons.

There are two possibilities, either two pairs of electrons are first coupled to a singlet and the overall result coupled to a singlet as shown in figure 7 a and b, or two pairs of electrons are each coupled to a triplet and the resultant coupled to a singlet as shown in fig. 7c and d. Thus the first case is *identical* to the Rumer spin coupling so that

$\Psi_R^{\perp}$ =

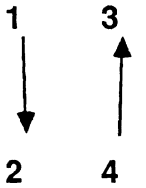

Thus the only possibility is the the second function is Schmidt orthogonalized to the first so that

$\Psi_P^{\perp}$ =

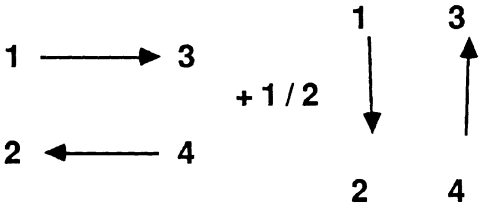

since $< \psi^{\perp}_R | \psi^{\perp}_P > = -1/2$. Of course, we could have started with ψ_P and forced $\psi^{\perp}_R$ to be orthogonal. Alternatively, we could have weighted each function equally and symmetrically orthogonalized.

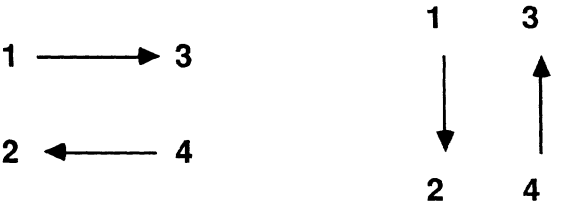

$\Psi_P^{\perp}$	1.0	$(\sqrt{6} - \sqrt{2})/(\sqrt{6} + \sqrt{2})$
$\Psi_R^{\perp}$	$(\sqrt{6} - \sqrt{2})/(\sqrt{6} + \sqrt{2})$	1.0

Clearly, the symmetric orthogonalization weights each Rumer function equally. (Note that both sets of orthogonal spin coupled functions are not normalized. The normalization factor for the second Yamanouchi-Kotani function is $2/\sqrt{3}$ while each of the symmetric orthogonalized functions must be normalized by $(\sqrt{6} + \sqrt{2})/2\sqrt{3}$). In the region of a diabatic surface crossing, the symmetric orthogonalization is the natural one to use. The different orthogonalization schemes can be represented

diagrammatically as in fig. 8 below.

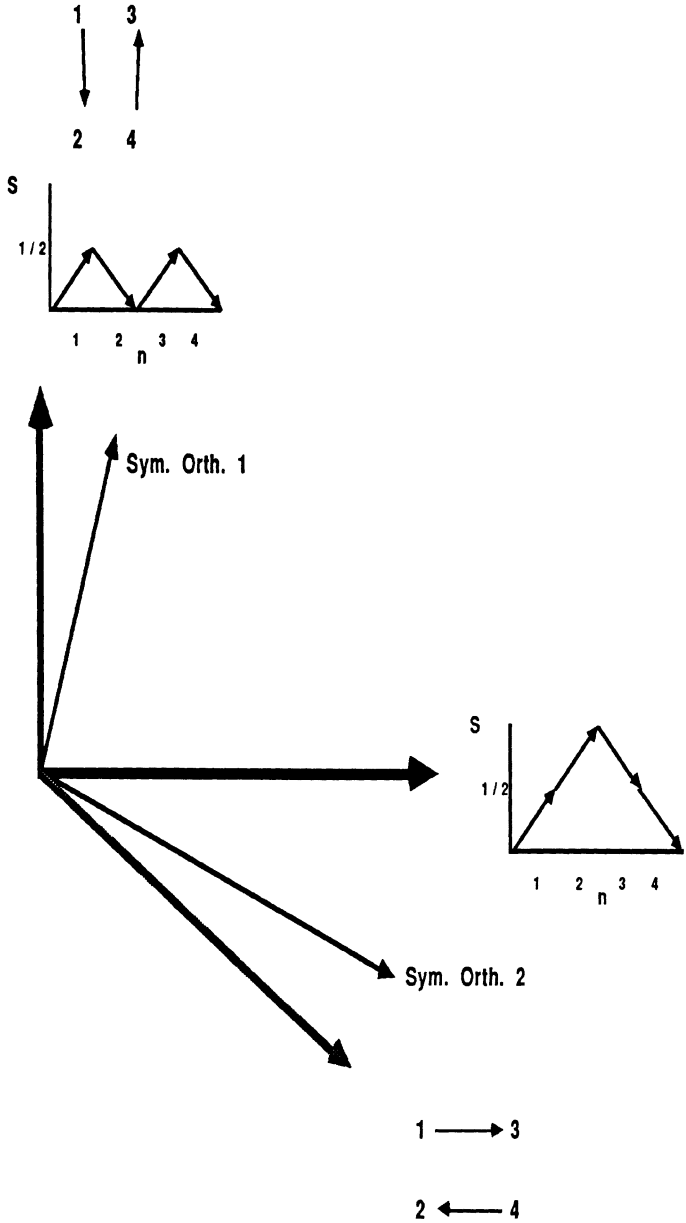

Fig. 8 Diagrammatic Representation of the possible orthogonal spin coupling schemes for 4 electrons in 4 orbitals.

Thus the expressions for α and β given in section II can now be easily derived from

$$\alpha_R = \langle \psi^{\perp}_R | H_s | \psi^{\perp}_R \rangle$$
$$\beta = \langle \psi^{\perp}_R | H_s | \psi^{\perp}_P \rangle$$

where $\psi^{\perp}_R$ / $\psi^{\perp}_P$ are symmetrically orthogonalized. The corresponding expressions for Schmidt orthogonalization are :

a) $\psi^{\perp}_R$ is Schmidt orthogonalized to ψ_P

$$K^* = K_P - 1/2\, K_X - 1/2\, K_R \qquad [45]$$

$$\beta = \sqrt{3}/2\, (K_X - K_R) \qquad [46]$$

b) $\psi^{\perp}_P$ is Schmidt orthogonalized to ψ_R

$$K^* = 1/2\, K_X + 1/2\, K_P - K_R \qquad [47]$$

$$\beta = \sqrt{3}/2\, (K_P - K_X) \qquad [48]$$

while the for symmetric orthogonalization one has

$$K^* = \sqrt{3}/2\, (K_P - K_R) \qquad [49]$$

$$\beta = K_X - 1/2\, K_p - 1/2\, K_R \qquad [50]$$

We have just seen that the construction of Evans' diabatic surface model involves the following steps

1) *Construction of a molecule adapted (energy optimized) non-orthogonal minimum basis of AO*

2) *Construction of a matrix representation of a Hamiltonian of the Heisenberg type,* H_s, *in a basis of neutral only VB determinants: (a)evaluate the matrix elements using the rules for determinants built from orthogonal AO and (b) replace the* $K_{ij} = [ij|ij]$ by $K_{ij} = [ij|ij] + 2\, S_{ij} \langle i|h|j \rangle$.

3) *Project this hamiltonian onto reactant /product spin couplings ,* $\psi^{\perp}_R / \psi^{\perp}_P$ *and compute* $\alpha = \langle \psi^{\perp}_R | H_s | \psi^{\perp}_R \rangle$, $\beta = \langle \psi^{\perp}_R | H_s | \psi^{\perp}_P \rangle$ *for the secular equation.*

$$\begin{pmatrix} \alpha_R - E & \beta \\ \beta & \alpha_P - E \end{pmatrix} \begin{pmatrix} C_R \\ C_P \end{pmatrix} = 0 \qquad [51]$$

The energy, α_R *is the diabatic energy of the "reactant bonding situation" ,* α_P *is the diabatic energy of the "product bonding situation" , and* β *is the resonance interaction.*

In the next subsection we shall discuss the purely technical problem of the computation of $\mathbf{H_s}$ from an MC-SCF, CI or MP wavefunction and the computation of a molecule adapted (energy optimized) non-orthogonal minimum basis of AO. However, at this stage we must consider 3) above in a general way.

We begin by reminding the reader of the chemical motivation for the Evans' model. Transition states in molecular reactions can be assumed to arise from two possible effects. Firstly, there are transition states that arise from steric /structural reasons where the electronic structure does not change between reactant and product. Rotation and inversion barriers associated with conformational change are examples. Secondly, there are barriers that involve a change in the bonding between reactants and products. In this case, at the transition structure, the wavefunction will be an almost equal admixture of $\psi^{\perp}_R$ and $\psi^{\perp}_P$ and we expect that $\alpha_R = \alpha_P$. However, at the reactant geometry the ground state wavefunction is described by $\psi_R = \psi^{\perp}_R$, while $\psi^{\perp}_P$ must represent an excited state and must be chosen so that $\psi^{\perp}_P$ must be Schmidt orthogonalized to ψ_R (ie the spin coupling must be Yamanouchi-Kotani). Similarly, at the product geometry the ground state wavefunction is described by $\psi_P = \psi^{\perp}_P$, while $\psi^{\perp}_R$ must again represent an excited state and must be chosen so that $\psi^{\perp}_R$ is Schmidt orthogonalized to ψ_P. Thus it is clear that the orthogonalization scheme used to define $\psi^{\perp}_R$ and $\psi^{\perp}_P$ at different regions of the surface must change. Clearly we must convince the reader that this is not an arbitrary element of the model. The spin coupling can be chosen by a *local criterion* or a *global criterion* . The *local criterion* can be stated as

i) $\psi^{\perp}_R$ is Schmidt orthogonalized to ψ_P (ie Yamanouchi-Kotani spin coupling) at the product geometry

ii) $\psi^{\perp}_P$ is Schmidt orthogonalized to ψ_R(ie Yamanouchi-Kotani spin coupling) at the reactant geometry

iii) ψ_R and ψ_P are orthogonalized so that $\alpha_R = \alpha_P$ at a transition structure. In this case the criterion $\alpha_R = \alpha_P$ determines the spin coupling at a transition structure. The most common situation that arises is that ψ_R and ψ_P are symmetrically orthogonalized

In contrast, the orthogonalization can be defined according to a *global criterion* so that the orthogonalization varies in a continuous fashion over the surface. The *global criterion* is defined so that

i) $\alpha_R = \alpha_P$ when ψ_R and ψ_P are symmetrically orthogonalized

ii) ψ_R and ψ_P are orthogonalized so that $C_R / C_P = r$ where r is chosen so that the ratios of the orthogonalized spin functions in the adiabatic wavefunction is the same as ratios of the non-orthogonal Rumer spin functions in the adiabatic wavefunction.

The *local criterion* and *global criterion* coincide in the common situation where $\alpha_R = \alpha_P$ implies that ψ_R and ψ_P are symmetrically orthogonalized . However, it does provide a prescription for a global diabatic representation of the surface and allows a smooth interpolation between reactants and products.

The Evans model is completely defined and can be extended to any number of electrons. However there are two apparent restrictions which we must consider.

1)Each possible Rumer spin-function defines a diabatic surface. The projection of H_S onto the two dimensional subspace spanned by $\psi^{\perp}_R / \psi^{\perp}_P$ to give Evans diabatic surface model appears at first sight to be limited to the case where one has at most two independent spin projections for a given number of "active" electrons and spin multiplicity.

2)By virtue of the need to construct a Heisenberg H_S , the model is limited to the situation where the number of active orbitals is equal to the number of active electrons.

Let us consider problem 1) where the number of independent spin projections is greater than 2. This problem is best illustrated using a 4+2 cycloaddition as an example (the reaction of 9a to give 9b in figure 9).

The important 6 electron spin couplings are illustrated in Fig. 9 c ,d and e. Clearly the reactant diabatic surface must be a linear combination of the spin coupling corresponding to fig. 9c and fig. 9d which becomes dominated by the spin coupling

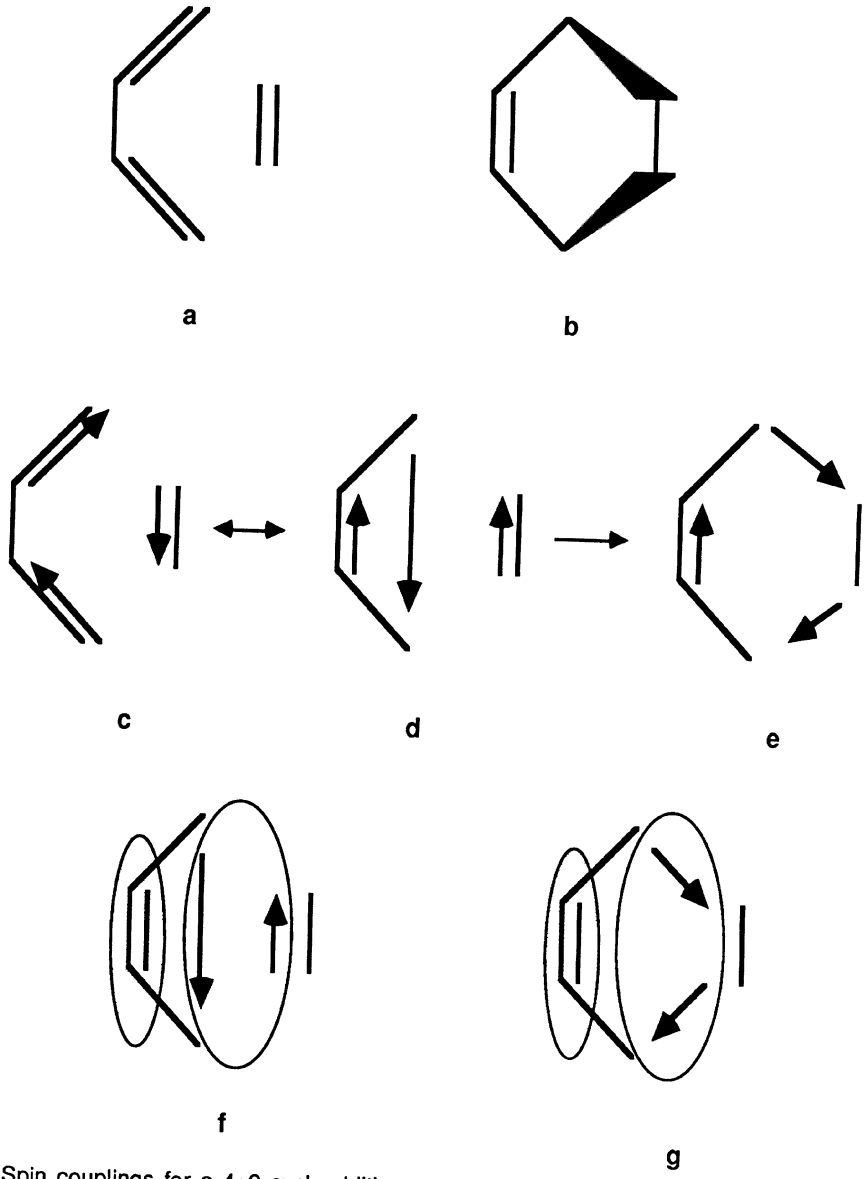

Fig. 9 Spin couplings for a 4+2 cycloaddition

corresponding to fig. 2d near the transition state. The product diabatic surface will correspond to the the spin coupling corresponding of fig. 9e. It is not immediately obvious how to choose $\psi^{\perp}_{R}/\psi^{\perp}_{P}$ in this case. Certainly, in the region of the transition structure 2 of the 6 electrons are inactive (the spin coupling corresponding fig. 9d) and a 4 orbital 4 electron representation becomes possible as shown in Fig. 9f and Fig. 9g. The shaded area corresponds to inactive doubly occupied orbitals. Thus there are two possible solutions to the problem which will be numerically very similar.

1)One could project H_s (for 6 active orbitals and 6 active electrons) onto the space of the orthogonalized Rumer functions corresponding fig. 9c, 9d, and 9e and deal with a 3 diabatic surface model.

2)Two of the 6 electrons can be regarded as inactive. In this case we construct H_s for 4 active orbitals and 4 active electrons and the contribution of the spin coupling corresponding to Fig. 9c will manifest itself in the delocalization of the orbitals.

Now let us turn to the second problem : *the Evans model is limited to the situation where the number of active orbitals is equal to the number of active electrons.* Thus while the Evans model could describe reactions in which covalent bonds are formed or broken (for example a 2+2 cycloaddition with two forming σ bonds and two π bonds that are broken), it is not so obvious that one could describe an ionic substitution reaction (for example the "addition" of a lone pair to a π bond which would involve 4 electrons and 3 orbitals). Fortunately, this in not the case. One need only represent a localized pair of electrons with two orbitals -one "tight" and one "diffuse". Thus, as been shown recently one can represent the 4 π electrons of nitrone (CH_2NO) using p_π orbitals centred on N C and O with an additional delocalized p_π on O [15,16].

We have recently published a study of an ionic substitution using such a representation of the lone pair [17].

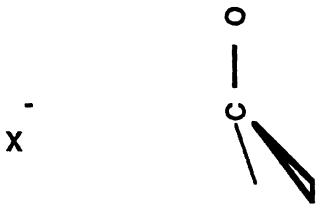

Firstly let us consider the conventional representation of such a reaction as illustrated in Fig. 10 below.

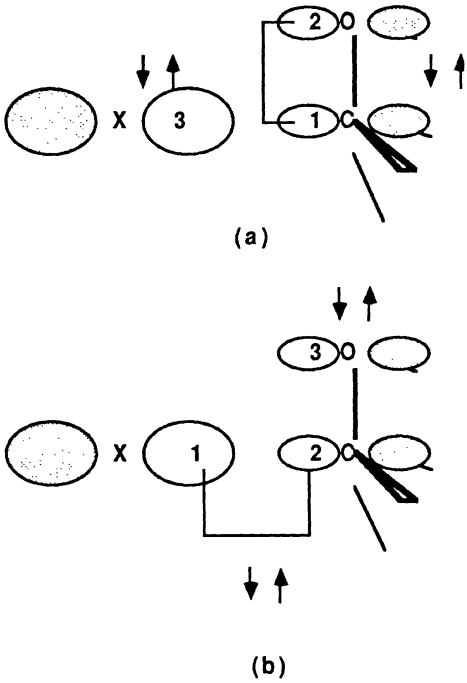

Fig. 10 An ionic reaction represented as a 4 electron 3 orbital model.

Normally one would represent the pair of electrons on X^- with a single orbital and the reaction would be viewed as a charge transfer reaction. However, we must remember that *charge transfer and orbital delocalization have been shown to be manifestations of the same phenomenon.* Thus, *there is only 1 spin coupling in the problem as formulated in this way.*

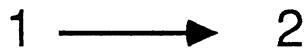

The charge transfer

just causes the orbitals to delocalize. The 3rd orbital is doubly occupied and thus "inactive". If we optimize the orbitals in VB for the single spin coupling we will proceed continuously from the situation of fig. 10a (reactant) to fig. 10b (product). The orbital optimization will deform the orbitals as appropriate. *There is only 1 diabatic.*

> Thus if we attempt to represent a 4 electron reaction with 3 orbitals we have the same dilemma that we have discussed in the case of the $2_s + 2_a$ cycloaddition reaction of two ethylene molecules. *Since there is only one configuration , we have no model for the barrier.*

Let us now consider the same ionic reaction using 4 orbitals and 4 electrons. Of course there are now 2 independent spin projections. However, the orbitals are assumed to be optimized and will distort as one moves from reactant to products. Some hypothetical possibilities in this case are illustrated in fig. 11 below.

In 11b we have the spin coupling of the reactants where the two orbital representation of the X^- lone pair is singlet spin coupled and the two CO p^{π} orbitals are spin coupled. At some stage the spin coupling must change to that of 11c where the C p^{π} orbital is coupled to one of the X^- lone pair orbitals. As one reaches the product 11c will continuously deform into 11d as a result of orbital optimization. Of course the details will depend upon a detailed study. However, the point to be emphasized at this stage is that charge transfer never needs to be considered in Evans model. It will always manifest itself via orbital distortion. With the use of n orbitals and n electrons all reactivity problems can be formulated in terms of spin coupling arguments.

In this section we have illustrated how reactivity problems can be formulated in the Evans model as a problem in spin coupling and that the quantitative expression of the model is straightforward given the spin coupling and the Heisenberg hamiltonian in a minimum basis of molecule adapted atomic orbitals. It remains to show how this model can be implemented in a rigorous way.

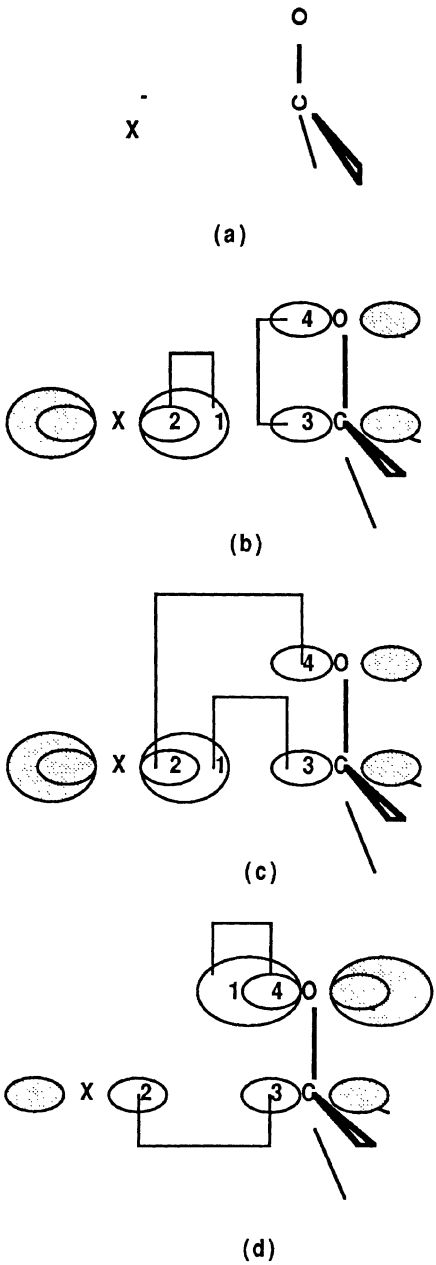

Fig. 11 Some hypothetical spin couplings for a 4 orbital ionic reaction where the "molecule adapted minimum basis" is allowed to be energy optimized.

V Rigorous Implementation of the Evans Diabatic Surface Model via effective hamiltonian theory

The rigorous implementation of Evans' model involves,the construction of a molecule adapted (energy optimized) non-orthogonal minimum basis of AO, the construction of a matrix representation of a Hamiltonian of the Heisenberg type, $\mathbf{H_s}$, in a basis of neutral only VB determinants, and the subsequent projection of this hamiltonian onto reactant /product spin couplings , $\psi^{\perp}_R / \psi^{\perp}_P$ with the computation of $\alpha = < \psi^{\perp}_R \mid \mathbf{H_s} \mid \psi^{\perp}_R >$, $\beta = < \psi^{\perp}_R \mid \mathbf{H_s} \mid \psi^{\perp}_P >$ for the secular equation [51]. The energy, α_R is the diabatic energy of the "reactant bonding situation" , α_P is the diabatic energy of the "product bonding situation" , and β is the resonance interaction.

Our central objective in this section is to indicate how the construction of a matrix representation of a Hamiltonian of the Heisenberg type, $\mathbf{H_s}$, in a basis of neutral only VB determinants is accomplished using an MC-SCF or CI wavefunction. The reader will recall that $\mathbf{H_s}$ was constructed by evaluating the CI matrix elements in a basis of neutral only VB determinants using the rules for determinants built from orthogonal AO and then replacing the $K_{ij}= [ij|ij]$ by $K_{ij}= [ij|ij] + 2\, S_{ij} <i|h|j>$. We now show that the apparent inconsistency in the definition of the K_{ij} be resolved through the construction of $\mathbf{H_s}$ via effective hamiltonian theory.

We begin with a brief summary of the equations of effective hamiltonian theory in a simple matrix formulation (for a full discussion the reader is referred to the recent comprehensive review of Durand and Malrieu[12]). We shall assume that we have an *orthogonal* basis of molecule adapted AO at our disposal (returning to the problem of its construction subsequently). We divide the full CI space (ie a VB space with all possible covalent and ionic configurations) into a reference space **P** spanned by the covalent configurations $\{ \Lambda_R \}$ and a secondary space **Q** containing the remainder of the (ionic or charge transfer) configurations $\{ \phi_t \}$. (We shall use subscripts R and S to denote the reference covalent configurations $\{ \Lambda_R \}$ and subscripts t and u to denote secondary charge transfer configurations $\{ \phi_t \}$) Our objective is to construct $\mathbf{H_s}$ as an effective hamiltonian ($\mathbf{H_{eff}}$) on the space of the covalent configurations **P** so that the subsequent diagonalization of $\mathbf{H_s}$ reproduces n eigenvalues (where n is the dimension of **P**) of the full CI hamiltonian *exactly.* The effective hamiltonian $\mathbf{H_{eff}}$ is defined via the solution of the Bloch equations (see reference[12,18] for a full discussion)

$$\begin{pmatrix} H_{pp} & H_{pq} \\ H_{qp} & H_{qq} \end{pmatrix} \begin{pmatrix} U_{pp} & U_{pq} \\ U_{qp} & U_{qq} \end{pmatrix} = \begin{pmatrix} U_{pp} & U_{pq} \\ U_{qp} & U_{qq} \end{pmatrix} \begin{pmatrix} H_{eff} & 0 \\ 0 & W^* \end{pmatrix} \qquad [52]$$

where H_{pp} means the projection of **H** onto the **P** subspace (H_{pp} =**P H P**) etc. The diagonalization of $\mathbf{H_{eff}}$ gives a subset of the eigenvalues of **H** exactly

$$\mathbf{H_{eff}}\ \mathbf{A}_\lambda = E_\lambda\ \mathbf{A}_\lambda \qquad [53]$$

By matrix multiplication it can be verified that the transformation **U** is given from the solution of

$$H_{qp}\, U_{pp} + H_{qq}\, U_{qp} - U_{qp}\, H_{eff} = 0 \qquad [54]$$

and

$$H_{pp}\, U_{pp} + H_{pq}\, U_{qp} = U_{pp}\, H_{eff} \qquad [56]$$

or

$$H_{eff} = [\, U^{-1}\, H\, U]_{pp} \qquad [57]$$

We can choose the normalization so that $U_{pp} = 1$ and **U** then has the form

$$U = (1 + X) \qquad [58a]$$

where

$$X = \begin{pmatrix} 0 & -C^t \\ C & 0 \end{pmatrix} \qquad [58b]$$

If we define

$$\begin{aligned} S &= (1+C)^t\ (1+C) \\ &= U^t\, U \end{aligned} \qquad [59]$$

then eq. 57 becomes

$$H_{eff} = S^{-1}\ (1-X)\ H\ (1+X) \qquad [60]$$

There are two methods for the solution of eq. 54. Each is instructive. Firstly, if we insert the definition of eq. 58 then obtain a set of coupled equations for each reference function of the form

$$\{\, H_{qp}\,\}_R + (\, H_{qq} - \{H_{eff}\}_{RR} 1\,)\, C_R - \Sigma_{S \neq R}\, \{H_{eff}\}_{RS}\ C_S = 0 \qquad [61]$$

where the subscripts R and S run over the reference configurations and $\{\, H_{qp}\,\}_R$ denotes the Rth column of the sub-block H_{qp} of **H** . However, the coupled eq. 61 are not easy to solve and a second method is possible. If the eigenvectors of the original CI problem are known

$$\begin{pmatrix} H_{pp} & H_{pq} \\ H_{qp} & H_{qq} \end{pmatrix} \begin{pmatrix} A_{pp} & M_{pq} \\ B_{qp} & N_{qq} \end{pmatrix} = \begin{pmatrix} \{E_\lambda\}_{pp} & 0 \\ 0 & \{E_\lambda\}_{qq} \end{pmatrix} \begin{pmatrix} A_{pp} & M_{pq} \\ B_{qp} & N_{qq} \end{pmatrix} \qquad [62]$$

then it is easily verified (see eq. 17 of ref. [12]) that

$$C = B_{qp} A_{pp}^{-1} \qquad [63]$$

The validity of eq. 63 can be checked from the fact that

$$\begin{pmatrix} A_{pp} & B_{pq} \\ M_{qp} & N_{qq} \end{pmatrix} \begin{pmatrix} H_{pp} & H_{pq} \\ H_{qp} & H_{qq} \end{pmatrix} \begin{pmatrix} A_{pp} & M_{pq} \\ B_{qp} & N_{qq} \end{pmatrix} = \begin{pmatrix} \{E_\lambda\}_{pp} & 0 \\ 0 & \{E_\lambda\}_{qq} \end{pmatrix}$$

(since the eigenvector matrix is unitary) and

$$H_{eff} = A_{pp} \{E_\lambda\}_{pp} A_{pp}^{-1}$$

The interpretation is easier if we make an approximation for illustrative purposes. We ignore the coupling in the 3rd term in eq. 61 we have

$$\{ H_{qp} \}_R + (H_{qq} - \{H_{eff}\}_{RR} 1) C_R = 0 \qquad [64]$$

which can be written as the "augmented" eigenvalue problem

$$\begin{pmatrix} \{H_{pp}\}_{RR} & \{ H_{qp} \}_R^{\,t} \\ \{ H_{qp} \}_R & H_{qq} \end{pmatrix} \begin{pmatrix} 1 \\ C_R \end{pmatrix} = \{H_{eff}\}_{RR} \begin{pmatrix} 1 \\ C_R \end{pmatrix} \qquad [65]$$

In this context we see that $\{H_{eff}\}_{RR}$ is obviously the energy of a CI expansion of the form

$$\Lambda_R' = \Lambda_R + \Sigma_t \{C_R\}_t \phi_t \qquad [66]$$

(We are using subscripts R and S to denote the reference covalent configurations $\{ \Lambda_R\}$ and subscripts t and u to denote secondary charge transfer configurations $\{ \phi_t\}$)
In other words we have

$$\{ (1-X) H (1+X)\}_{R\,S} = \langle \Lambda_R' \mid H \mid \Lambda_S' \rangle \qquad [67]$$

and

$$\{S\}_{RS} = \langle \Lambda_R' \mid \Lambda_S' \rangle \qquad [68]$$

Now eq. 66 has the same form as that considered in our example for H_2 (see eq. 22), namely, a covalent configuration Λ_R and a combination of charge transfer configurations ϕ_t. Thus it is obviously possible (by analogy with eq. 22, see ref. [15]) to replace the $\Sigma_t \{C_R\}_t \phi_t$ by an orbital transformation of the form

$$\Lambda_R' = \exp \mathbf{M} \ \Lambda_R \qquad [69]$$

where

$$\mathbf{M} = \Sigma_{ij} \ a_{ij} \ \mathbf{E}_{ij} \qquad [70]$$

(For a full discussion of this point with a numerical example see ref [15]).

Thus we have a rigorous identification of $\{ (1-X) \ H \ (1+X)\}_{RS} = \langle \Lambda_R' | H | \Lambda_S' \rangle$ *as the matrix elements of the CI hamiltonian* $\langle \Lambda_R \mid H \mid \Lambda_S \rangle$ *between determinants* Λ_R *and* Λ_S *built from non-orthogonal orbitals* and $\{S\}_{RS} = \langle \Lambda_R' | \Lambda_S' \rangle$ *as the overlap matrix between determinants* Λ_R' and Λ_S' *built from non-orthogonal orbitals .*

It remains now to make the final identification with the Heisenberg hamiltonian. In the Heisenberg hamiltonian there is no overlap matrix involved so that we cannot identify eq.60 with a Heisenberg hamiltonian. However, we can deal with this difficulty in the same way that we removed $(1 \pm S^2)$ in our discussion of H_2. We observe that $S^{-1} \ (1-X) \ H \ (1+X)$ and the symmetric form $S^{-1/2} \ (1-X) \ H \ (1+X) \ S^{-1/2}$ have the same eigenvalues. Thus we can make the identification

$$H_s = S^{-1/2} \ (1-X) \ H \ (1+X) \ S^{-1/2} \qquad [71]$$

which parallels the replacement

$$E = Q \pm K = (\alpha \pm \beta)/(1 \pm s^2) \qquad [72]$$

in the VB treatment of H_2. (Note that no approximation is involved here.) In fact one is making a very similar identification in the many electron case. Thus for a 4 orbital 4 electron problem a matrix element of the form

$$\langle \mid k_\alpha \, l_\alpha \ i_\beta \ j_\beta \mid \ \mathbf{H} \ \mid j_\alpha \, l_\alpha \ i_\beta \ k_\beta \mid \rangle$$

evaluated as if the orbitals were non-orthogonal yields a definition of K_{jk} as

$$
\begin{aligned}
K_{jk} = {} & [jk|jk] - [ii|ll]s_{jk}^2 + [ij|jl]s_{kl}s_{ik} + [kl|ik]s_{lj}s_{ij} \\
& - [kl|ij]s_{lj}s_{ik} - [lj|ik]s_{lj}s_{ij} \\
& + \{([jk|ll] + [jl|kl] - [jk|kl] - [jl|ll] - [jk|jl] - [kl|kk]) \quad (s_{jk} - s_{ij}s_{ik})\} \\
& + \{([jk|ii] + [ji|ki] - [jk|ki] - [ji|ii] - [ii|ij] - [ik|jk]) \quad (s_{jk} - s_{lj}s_{lk})\} \\
& + \langle j|h|k\rangle (2\, s_{jk} - s_{ij}s_{ij} - s_{lj}s_{kl})
\end{aligned}
\qquad [73]
$$

with second order terms in the overlap.

Thus we have completely resolved the dilemma whereby $\mathbf{H_s}$ is constructed by evaluating the CI matrix elements in a basis of neutral only VB determinants using the rules for determinants built from orthogonal AO and then replacing the $K_{ij} = [ij|ij]$ by $K_{ij} = [ij|ij] + 2\, S_{ij} \langle i|h|j\rangle$. The apparent inconsistency in the definition of the K_{ij} is resolved through the construction of $\mathbf{H_s}$ via effective hamiltonian theory. On the one hand, we have the identification

$$\mathbf{H_s} = \{ \mathbf{S}^{-1/2} \ (\mathbf{1-X})\ \mathbf{H}\ (\mathbf{1+X})\ \mathbf{S}^{-1/2} \}_{RS} = \langle \Lambda_R' | H | \Lambda_S' \rangle$$

as the matrix elements of the CI hamiltonian $\langle \Lambda_R \mid H \mid \Lambda_S \rangle$ between determinants Λ_R and Λ_S. On the other, if we neglect terms in S^2 in eq.73 we have $K_{ij} = [ij|ij] + 2\, S_{ij} \langle i|h|j\rangle$. The important point is that $\mathbf{H_s} = \{ \mathbf{S}^{-1/2} \ (\mathbf{1-X})\ \mathbf{H}\ (\mathbf{1+X})\ \mathbf{S}^{-1/2} \}$ reproduces the eigenvalues of the CI hamiltonian *exactly.* Thus the subsequent projection

$$\alpha_R = \langle \psi^{\perp}_R \mid \mathbf{H_s} \mid \psi^{\perp}_R \rangle, \ \beta = \langle \psi^{\perp}_R \mid \mathbf{H_s} \mid \psi^{\perp}_P \rangle$$

is *exact* as well.

There is only one minor difficulty which affects the interpretation. Consider the matrix element of two determinants that are related to each other by inverting the spin of each orbital. By the usual rules for matrix elements between determinants built from orthogonal orbitals, this matrix element is zero. However, in the same manner as for eq. 73, this matrix element has the form

$$\langle \ | j_\alpha l_\alpha \ i_\beta \ k_\beta | \ \ \mathbf{H} \ \ | i_\alpha k_\alpha \ j_\beta \ l_\beta | \ \rangle = n_{ijkl} \qquad [74]$$

where n_{ijkl} has the form

$$
\begin{aligned}
n_{ijkl} = {} & [il|jk]\, s_{il}s_{jk} + [ij|kl]s_{ij}s_{kl} \\
& + 2\{([ij|kl] + [il|jk] - [ij|jk] - [il|kl] - [ij|il] - [jk|kl]) \quad (s_{ij}s_{kl} - s_{jk}s_{il})\}
\end{aligned}
$$

$$+ \langle i|h|j\rangle s_{kl} (s_{ij}s_{kl} - s_{jk}s_{il}) + \text{etc}$$

which would be zero in a Heisenberg hamiltonian but arises in

$$\{ S^{-1/2} \quad (1-X)\ H\ (1+X) \quad S^{-1/2} \}$$

from many particle interactions. Thus to be *exactly* consistent, the Evans model must have more than 2 electron integrals in it. However, since the terms in s^2 are very small these effects are truly negligible.

There is only one step remaining in our implementation: the construction of the orthogonal molecule adapted minimum basis of AO. The role of this step may not be immediately obvious to the reader. If we take

$$H_{eff} = \{ S^{-1/2} \quad (1-X)\ H\ (1+X) \quad S^{-1/2} \}$$

then

$$H_{eff}\ A_\lambda = E_\lambda\ A_\lambda$$

will reproduce n eigenvalues of the full CI exactly. However, *which n eigenvalues* are to be reproduced? We implicitly answer this when we select the columns of B_{qp} and A_{pp} when we solve for $C = B_{qp}\ App^{-1}$ in eq. 63. Clearly, those vectors with the largest projection on the $\{ \Lambda_R \}$ should be chosen. But remember, that we assume that the $\{\Lambda_R'\}$ are the determinants built from the non-orthogonal molecule adapted minimum basis of AO. Thus we cannot select these vectors corresponding to the columns of B_{qp} and A_{pp} unless the $\{ \Lambda_R \}$ are quite good approximations to the $\{\Lambda_R'\}$. This in turn means that the CI problem needs to be expressed in an orthogonal molecule adapted minimum basis of AO which will be good approximations to the non-orthogonal molecule adapted minimum basis of AO. This situation is to be contrasted with the case where one uses a non-orthogonal AO basis explicitly in a spin coupled VB [7a] approach and constructs the VB hamiltonian directly. In the method described here the non-orthogonal basis is implicit (eq. 69 and 70) and never needs to be constructed explicitly (although this is possible [15])

We have already discussed this problem in some detail in section III so we shall be content with a simple generalization [19]. Since, the non-orthogonal molecule adapted minimum basis of AO is optimum in the space of the $\{\Lambda_R'\}$ the obvious choice of the orthogonal molecule adapted minimum basis of AO is the orbitals that optimize the energy in the space of the $\{ \Lambda_R \}$ (the covalent structures built from orthogonal AO). This is possible because the full CI energy is invariant to an orthogonal transformation of the "active" orbitals among themselves. Thus the optimization of the orbitals for the subspace $\{ \Lambda_R \}$ does not change the total energy. Thus we now consider the optimization of the orbitals for any covalent structure Λ_R.

The energy of a covalent structure

det[ij] [kl] ...

is given as

$$E = Q + \Sigma_{i>j} \text{ (coupled) } K_{ij} - 1/2\ \Sigma_{i>j} \text{ (uncoupled) } K_{ij} \qquad [75]$$

We seek to minimize the energy with respect to a_{ij} , the rotations between active orbitals i and j. The energy minimum occurs when the Brillouin condition is satisfied

$$\partial E/\partial a_{ij} = \langle \det[ij]\ [kl] \ldots |H\ E_{ij}| \det[ij]\ [kl] \ldots \rangle - \langle \det[ij]\ [kl] \ldots |\ E_{ij}\ H\ | \det[ij]\ [kl] \ldots \rangle = 0 \qquad [76]$$

It is trivial to verify that there is almost complete cancellation between the two terms in eq. 76 and as in our previous example

$$\partial E/\partial a_{ij} = 2\ \omega\ ([ii|ij] - [jj|ji] \qquad [77]$$

$\omega = 1$ if $i>j$ (coupled)

$\omega = 1/2$ if $i>j$ (uncoupled)

Again, the condition $\partial E/\partial a_{ij}$ for an orthogonal transformation yields the same condition as the original Edmiston Ruedenberg condition for *localized orbitals* . Thus minimization of the energy of a perfectly covalent structure yields a molecule adapted minimum basis of atomic orbitals.

We now have a complete program for the rigorous computation of the diabatic surface model of Evans as summarized on the following flow diagram.

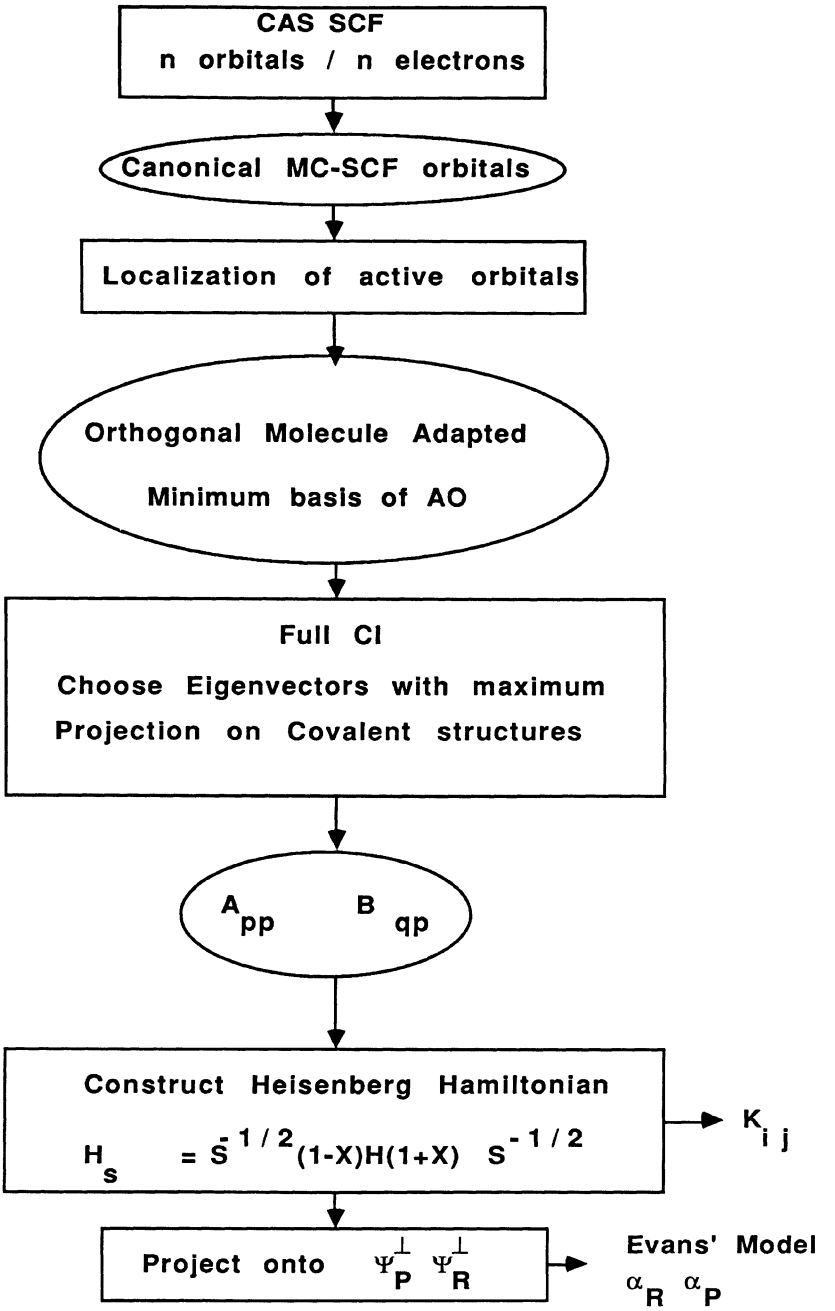

Fig. 12 Flow diagram for the Implementation of Evans' Diabatic Surface Model

As we will show in part II, the K_{ij} can be used to rationalize the energetics of bonding effects in reactivity problems in in a quantitative way. The diabatic surfaces α_R and α_P give a detailed understanding of the origin of barriers for reactions. Further, as we will show in part 2 the nature of critical points can be rationalized in terms of the derivatives of Q and the K_{ij}.

Finally, now that we have discussed effective hamiltcnian theory we can add a postscript to our discussion of the projection of $\mathbf{H_s}$ onto the reactant and product spin coupling for the case that there are more than 2 independent spin projections. In section IV we discussed a 6 orbital 6 electron problem. Referring to Fig. 9, we proposed two approaches

i) keep 2 electrons passive (in the inactive space) so that the reactant and product diabatic surfaces correspond to 9 f and 9 g. The effect of 9c manifests itself as a delocalization of the orbitals.
ii) use 3 diabatic surfaces (fig. 9c 9d and 9f)

However, there is a third approach which will yield a similar result to i yet yields information about the role of the structure 9c. For the 6 orbital 6 electron case there are 5 linearly independent spin projections. In Evans' model one requires 2 surfaces. However, it is immediately obvious that we can proceed in the following way:

1) project $\mathbf{H_s}$ onto a set of 5 symmetrically orthogonalized Rumer functions to give a hamiltonian $\mathbf{H_5}$
2)Solve the eigenvalue problem for $\mathbf{H_5}$
3)Identify the eigenvectors of $\mathbf{H_5}$ with maximum projection on the spin couplings of Fig. 9 d and 9 e
4)Construct an effective hamiltonian in the space of the spin couplings of Fig. 9 d and 9 e using eq. 58b 63 and 71.

Thus by a 2nd projection of $\mathbf{H_s}$ we can always reduce a problem with many independent spin projections to a 2 dimensional Evans model. It should be obvious that the electronic effect of substituents can be treated in exactly the same way. The advantage of a 2nd projection of $\mathbf{H_s}$ over keeping 2 electrons passive (in the inactive space) is that we obtain explicit information about the role of the passive electrons via the K_{ij} that occur in the 6 electron $\mathbf{H_s}$.

VI Applicability

In part II of these notes, the applications of the methodology presented in the

preceding sections will be discussed in some detail. In this section we confine ourselves to some very general remarks.

As we will discuss in detail in part II, the most useful quantities are those that come from the Evans' model are the Q and the K_{ij} from $\mathbf{H_s}$, and the nature of the spin coupling involved in the transition state diabatic surface crossing. We will show that in particular that the exchange energy for a 4 orbital 4 electron problem has the general form

$$K^* = a\,K_X + b\,K_R + c\,K_P \qquad [78]$$

where K_R and K_P are the total reactant and product exchange and K_X is the "non bonded" exchange where the coefficients a,b,and c depend upon the spin coupling. Thus the diabatic energies are given as

$$\alpha_R = Q^* + K \qquad [79]$$

$$\alpha_P = Q^* - K \qquad [80]$$

$$\beta = (c-b)/\sqrt{3}\ K_X + (a-c)/\sqrt{3}\ K_R + (b-a)/\sqrt{3}\ K_P \qquad [81]$$

In contrast to the above, it is easily verified that the adiabatic energy is always given as

$$E = Q^* \pm T \qquad [82]$$

with

$$T = \{K^2 + (\beta)^2\}^{1/2} \qquad [83]$$

Further, it can be shown that T, the interaction energy, can always be written (independent of any chosen spin coupling) as

$$T = \{(K_P - K_X)(K_R - K_X) + (K_P - K_R)^2\}^{1/2} \qquad [84]$$

Thus the adiabatic surface and diabatic surfaces for a 4 orbital 4 electron problem (viz. a 2 + 2 cycloaddition) have a very simple parametric forms in terms of the K_{ij}.

Similarly, the case of 3 electrons in 3 orbitals with 2S+1 = 2 gives a analogous result. All of the developments follow directly in the same fashion as the 4 electron 4 orbital problem. The reactant Rumer function is

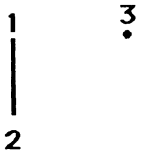

and the product is

1 ——— 3

2•

For this case

$$K_R = K_{12} \quad [85]$$

$$K_P = K_{13} \quad [86]$$

and

$$K_X = K_{23} \quad [87]$$

The total energy is again $E = Q^* \pm T$ where in this case

$$T = \{(K_R - K_X)^2 + (K_P - K_X)^2 + (K_R - K_P)^2\}^{1/2} \quad [88]$$

which is just the well known London formula. However, while the K_{ij} in eq. 88 are normally taken as empirical parameters in a LEPS [20] fit of a potential surface, in Evans' model the K_{ij} can be computed to reproduce MC-SCF energies exactly.

Finally, we should mention two tests that give one some additional confidence in the Evans' model as we have formulated it in this work. In section III and IV we argue that the Heisenberg hamiltonian, H_s and its projection onto the reactant and product spin couplings is consistent with the use of a non-orthogonal molecule adapted minimum basis. In fact, although this basis need never be generated explicitly, it could be computed explicitly using the methods described in eq. 23 to 27. The general theory has been derived in ref [15] and applied to Nitrone. The results reproduce the main features of a non-orthogonal VB calculation. As a second test, there is the possibility of finding diabatic surface intersection points. This is a well defined problem and consists of minimizing the energy of one diabatic surface (say α_R) subject to the constraint that $\alpha_P = \alpha_R$. This procedure has been implemented [21] and tested on a synchronous and asynchronous transition state for the addition of Fulminic acid to acetylene. The minimum energy diabatic surface crossing points lie very close to the transition structures.

We have seen that the central aspect of the Evans' diabatic surface model is the construction of the Heisenberg hamiltonian and its subsequent projection onto the reactant and product spin couplings. There may be more than one efficient method of implementing this model in practise. We have chosen an effective hamiltonian method because we use the CAS SCF method for molecular structure computations. We have shown that the use of the effective hamiltonian with a molecule adapted minimum basis of AO is essentially accomplishing the transformation to a VB space spanned by configurations built from a non-orthogonal molecule adapted minimum basis of AO. It is reasonable to ask whether or not it may be more efficient to work in a VB formalism

from the outset. The spin coupled VB method of Gerratt and co-workers [7a] is the most highly developed VB method. While the basic Evans 2X2 model could be obtained from Gerratt's spin coupled VB, it is not obvious that the parameters of H_s (the K_{ij}) could be obtained as easily in such an approach. This situation arises because by virtue of eq. 66 and eq. 70, one needs a *different* set of non-orthogonal molecule adapted minimum basis of AO for each determinant in H_s . Further, at this moment, one has analytic gradients and second derivatives available for CAS SCF but not for spin coupled VB. Thus the structure determination must be done using CAS SCF. However, while CAS SCF becomes tedious with more than 10 valence electrons, the VB method may prove to be much more efficient as the number of active orbitals gets large. The GVB method [7b] of Goddard (for a recent application see ref [22]) has also been extended to enable the direct computation of a 2X2 VB-like representation of the interaction of 2 spin functions. However, it is not that a new method of computation is being proposed in the Evans' model, rather, in these notes we have tried to indicate how a the results obtained using a standard method of quantum chemistry (eg. CASSCF) can be reproduced exactly using Evans' diabatic surface model.

Fianally we should briefly comment on the relationship of the diabatic surfaces as defined in this work with the use of the term "diabatic" in the context of non-adiabatic coupling that occurs in chemical dynamics. The definition of exact diabatic potentials in which there is no derivative coupling has been described by Mead and Truhlar [23]. However, Spiegelmann and Malrieu have demonstrated [24] that an approximately diabatic basis can be obtained from effective hamiltonian methods. Thus it appears that from a numerical point of view the two definitions of "diabatic" may be closely related in favourable circumstances.

VII Concluding remarks

The rationalization of computed reactivity data using simple physically grounded models is almost as important as the determination of transition structure and other chemical features themselves. "Why A reacts to give B and not C" is much more important than knowing simply that "A reacts to give B". However, most models of chemical reactivity are essentially *empirical or semi- empirical correlations* . Thus the fact that the Woodward-Hoffmann rules, for example, *correlate* forbidden reactions with an orbital crossing, does not really give any insight into why certain reactions occur since they offer no explanation of the barrier in the case of allowed reactions. Thus the objective of any model of chemical reactivity is that it should *reproduce the results of the best possible "state of the art" quantum chemistry computations* <u>*exactly*</u>. In other words, the model must be "faithful" to the theoretical method. The Evans diabatic surface model as we have described it in these notes fulfils this criteria in the sense that it will reproduce the results of a CAS SCF computation.

Acknowledgements

The implementation of the Evans' model that we have described in these notes has

evolved as a result of a collaborative effort between the authors' two research groups. This collaborative effort has been supported by NATO, the EEC, and the UK and Italian research councils. Two of the authors' research students Joe McDouall (London) and Massimo Olivucci (Bologna) have played a central role in this development and their contribution is gratefully acknowledged.

References

1)**GAUSSIAN 80:** J. S. Binkley, R.A. Whiteside, R. Krishnan, R. Seeger, D. J. Defrees, H.B. Schlegel, S. Topiol, L R. Kahn, and J. A. Pople, QCPE **13** (1980), **GAUSSIAN 82:** Carnegie-Mellon University, J. Binkley, M. Frisch, K. Raghavachari, D. DeFrees, H.B. Schlegel, R. Whiteside, E. Fluder, R. Seeger, and. J. A. Pople.

2) *Ab initio methods in Quantum Chemistry I* , Ed. K. P. Lawley Adv. Chem. Phys. **67** (1987)

3) *Ab initio methods in Quantum Chemistry II* Ed. K. P. Lawley Adv. Chem. Phys. **69** (1987)

4)M. G. Evans,and M. Polanyi, Trans. Far. Soc. **34,** 11 (1938);M. G. Evans and E. Warhurst, Trans. Far. Soc. **34,** 614(1938)

5)R.B. Woodward and R. Hoffman, *The Conservation of Orbital Symmetry* , Academic Press, 1970

6)*Orbital Symmetry Papers,* H.E.Simmons, and J.F. Bunnett Eds. American Chemical Society, 1974

7a)D.L. Cooper, J. Gerratt, and M. Raimondi, Adv. Chem. Phys. **67** 319 (1987)

b)F.W. Bobrowicz and W.A. Goddard III, in *Modern Theoretical Chemistry, Methods of Electronic Structure Theory,* H.F. Schaefer III (ed), Plenum, 1977

c)S.S. Shaik, this volume

d)R.D. Harcourt, *Qualitative Valence Bond Descriptions of Electron Rich Molecules,* (Lecture Notes in Chemistry) **30**, Springer-Verlag, 1982

8)N.D. Epiotis, *Theory of Organic Reactions*, Springer-Verlag, 1978

9) F. Bernardi and M. A. Robb, Adv. Chem. Phys. **67** 155 (1987)

10)C. A. Coulson and I. Fisher, Phil. Mag. **40**, 386 (1849)

11) C. E. Edmiston and K. Ruedenberg, Rev. Mod. Phys. **35**, 457 (1963)

12)P. Durand and J-P. Malrieu, Adv. Chem. Phys. **67** 321-412 (1987)

13a)R. Pauncz, *Spin Eigenfunctions , Construction and Use, Plenum, New York, 1979*

b)H. Eyring, J. Walter and G. Kimball, *Quantum Chemistry* , Wiley (1944)

14) C. Herring, Magnetism **2B**, 1 (1962)

15) J. J. W. McDouall and M. A. Robb, Chem. Phys. Lett. **142**, 131(1987)

16)D.L. Cooper, J. Gerratt, M. Raimondi, S.C. Wright, Chem. Phys. Lett. **138** 296 (1987)

17) F. Bernardi, M. Olivucci, G. Poggi, M. A. Robb and G. Tonachini, Chem. Phys. Lett. **144** 141 (1988)

18)B. H. Brandow, in *Effective Interactions and Operators in Nuclei* (Ed. B. R. Barrett) Lecture Notes in Physics **40** ,1 (1975)

19) J. J. W. McDouall and M. A. Robb, Chem. Phys. Lett. **132**, 319 (1987)

20)D.M. Hirst, *Potential Energy Surfaces, Molecular Structure and Reaction Dynamics,* Taylor and Francis, 1985

21)J.J.W. Mcdouall, M.A.Robb and F. Bernardi, Chem. Phys. Lett. **129**, 595 (1986)
22)A.F. Voter and W.A. Goddard, J. Chem. Phys. **57**, 253 (1981), J. Chem. Phys. **75**, 3638 (1981), J. Amer. Chem. Soc. **108**, 2830 (1986)
23)C. A. Mead and D.G. Truhlar, J. Chem. Phys. **77**, 6090 (1982)
24)F. Spiegelmann and J.-P. Malrieu, J. Phys. B, **17**,1235 (1984), **17**,1259 (1984),

Adiabatic and Diabatic Surfaces in the Treatment of Chemical Reactivity
II An Illustrative Application to the Diels Alder Reaction

Fernando Bernardi and Massimo Olivucci
Dipartimento Chimico 'G. Ciamician'
Universita di Bologna
40126 Bologna

Michael A. Robb
Department of Chemistry
King's College London
Strand
London WC2R 2LS

Abstract

The diabatic surface model as discussed in Part I is illustrated for a model problem of chemical reactivity - the Diels Alder reaction [1]. The transformation to a molecule adapted orthogonal minimum basis (localized orbitals), the explicit form of the Heisenberg hamiltonian, the geometrical properties of the K_{ij}, the nature of the diabatic intersection and the existence and nature of the critical point corresponding to the transition state are illustrated in detail.

I Introduction

It is our intention in this chapter to illustrate the theoretical discussion of the previous chapter (hereafter referred to as Part I) with the examination of a specific example in some considerable detail. It is our belief that one example explored in detail may provide the reader with a better indication of the salient features of the methodology than a survey of a number of applications.

The main features of the diabatic surface model that we shall illustrate are summarised in the diagram below.

J. Bertrán and I. G. Csizmadia (eds.),
New Theoretical Concepts for Understanding Organic Reactions, 147–163.
© 1989 by Kluwer Academic Publishers.

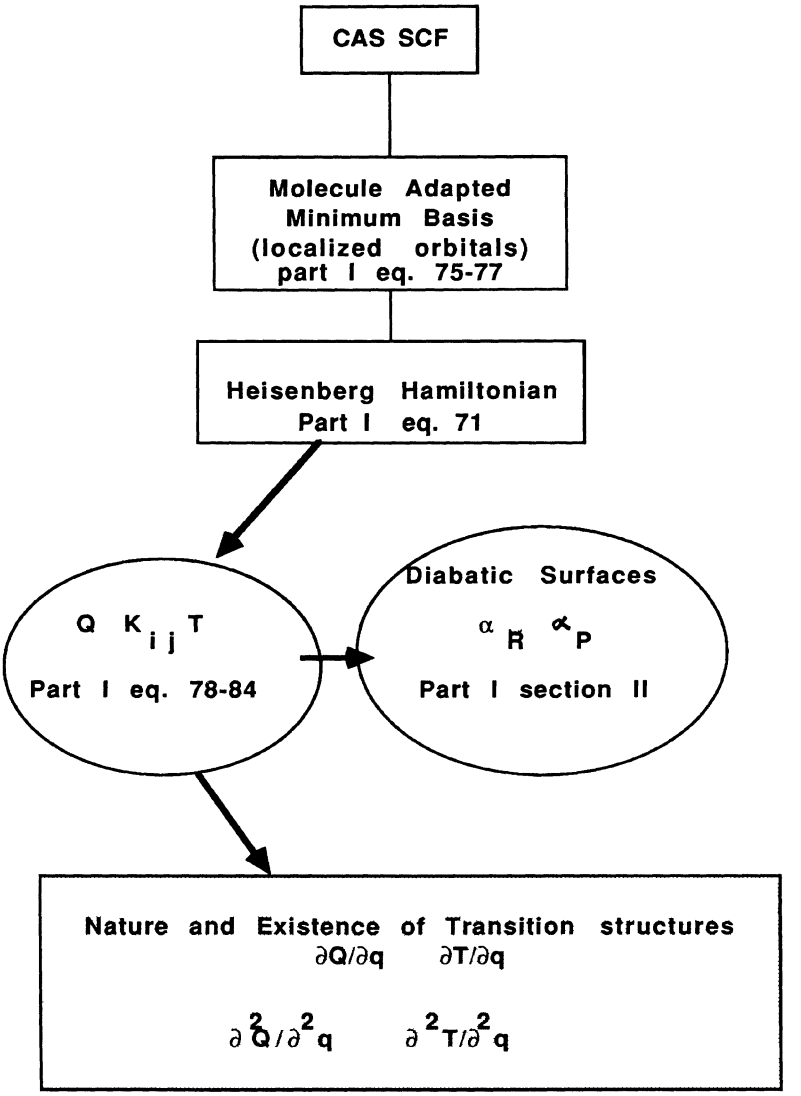

Fig.1 The main features of the Diabatic Surface Model in practical applications

From a computational point of view we assume that we have located (at the CAS MCSCF level) the various critical points (equilibrium structures ie. minima, and transition state ie. saddle points) on the potential energy surface that may be of interest in any reactivity problem. Our objectives are

1) to understand the electronic origin of reaction barriers in terms of diabatic

surface intersections

2) to understand the bonding at the transition state in terms of coulomb and exchange parameters obtained from the Heisenberg hamiltonian

3)to understand the conditions for the i)existence of a transition state ($\partial E/\partial q_i$ = 0) in terms of $\partial Q/\partial q_i$ and $\partial T/\partial q_i$ and ii)the nature (eigenvalues of the second derivative matrix $\partial^2 E/\partial^2 q_i$) in terms of $\partial^2 Q/\partial^2 q_i$ and $\partial^2 T/\partial^2 q_i$

Thus referring to fig.1, we can distinguish the various basic computational steps (square boxes in fig.1) which we have discussed in some detail in part I as opposed to the data derived from such computations (oval boxes in fig. 1) which will be used for chemical interpretation. In this section we shall concentrate on the latter. In part I we have attempted to demonstrate the wide applicability of the model while here we illustrate the details for one mechanistic pathway for a single non-trivial example.

II The 4_s+2_s cycloaddition of ethylene + cis butadiene (Diels Alder) reaction.

In recent work[1], we have made a detailed study of the various possible mechanistic pathways for this reaction. We begin with a brief discussion of the essential features of the mechanistically preferred synchronous concerted pathway.

The transition structure has the form shown in fig. 2. below.

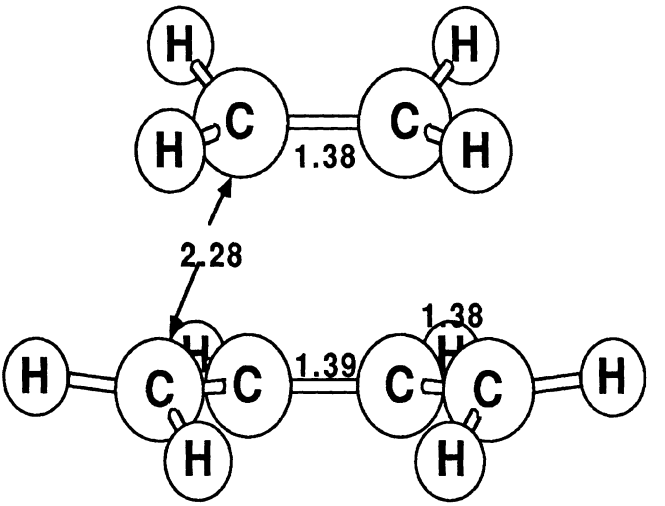

Fig.2 Transition structure geometry

In contrast, the geometry of the reactants is as shown in the figure 3 below.

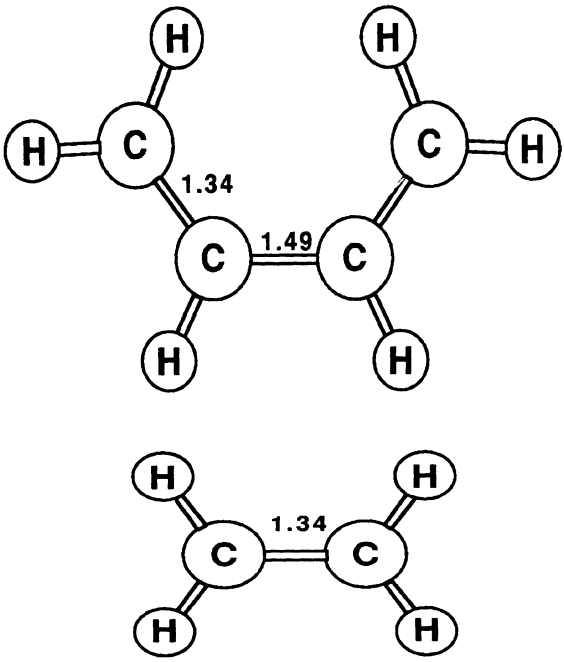

Fig. 3 Reactant Geometries.

For our purposes here we give data obtained at the STO-3G level (the extended basis set results can be found in ref. [1b]. The data were obtained using a 4 active orbital 4 active electron CAS SCF. In Part I, we have argued that two of the 6 electrons are localized in the middle double bond of cis-butadiene so that at the transition structure the two diabatic surfaces involved are

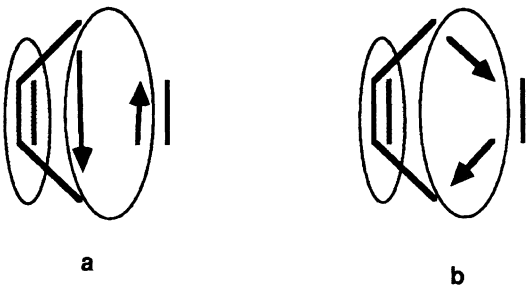

Fig. 4 Diabatic states a) reactants b) products

If one examines the geometric data in fig. 2 and 3, one sees that the middle C-C distance in butadiene is of the same order of magnitude as that of an isolated C=C. Further the

terminal methylene groups in the transition state are twisted by about 20 degrees.

There has been considerable discussion in the literature (see for example the work of Dewar [2] and references therein) as to whether the Diels Alder reaction is concerted (and synchronous) or asynchronous. Certainly, a synchronous pathway exists only if the transition structure has only one imaginary frequency. The normal co-ordinate for the single imaginary frequency is

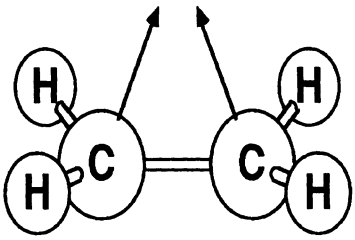

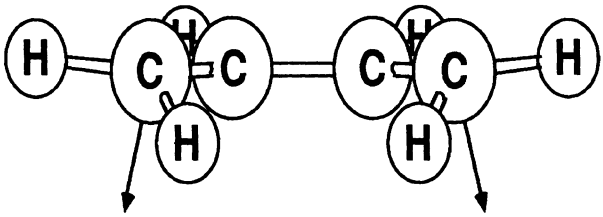

Fig. 5 a Transition vector -942 cm^{-1}

In contrast, the normal mode that would lead to an asynchronous transition state has the form

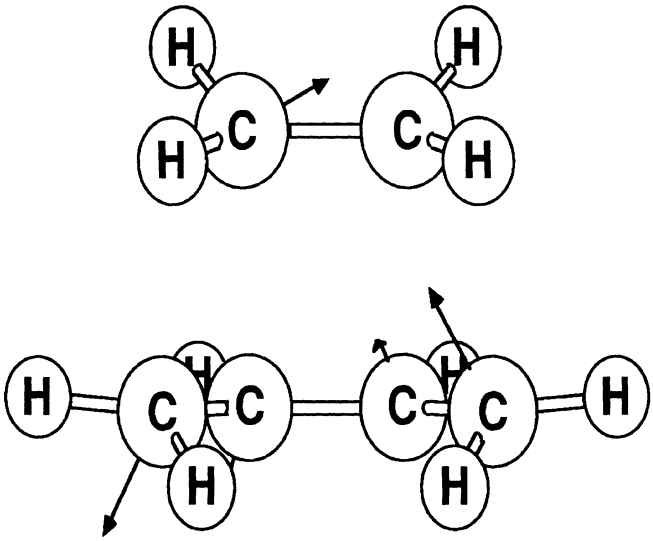

Fig. 5b Normal co-ordinate connecting synchronous transition structure with possible asynchronous transition structure 229 cm^{-1}

One of our objectives is to explain why the energy surface for motion along this co-ordinate (fig. 5b) is positively curved while for a forbidden reaction (see our results for the 2+2 cycloaddition of two ethylene molecules [3]) this direction is negatively curved. This information will be derived from the second derivatives of Q and T as mentioned in the introduction.

III Diabatic Surfaces: a detailed example

1) Molecule adapted Minimum AO Basis.

The active orbitals in the MC-SCF computation are built primarily from the π orbitals of ethylene and cis butadiene. The MC-SCF orbitals built from these π orbitals are shown schematically in fig. 6 below.

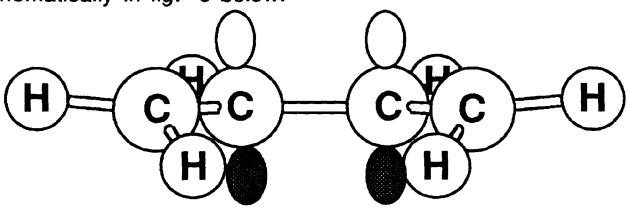

Fig. 6a MC-SCF CMO 1 (inactive core)

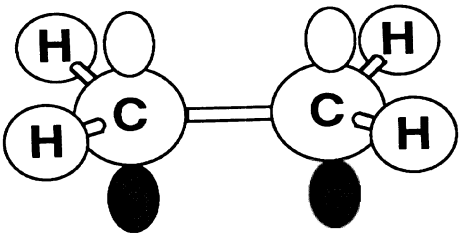

Fig. 6b MC-SCF CMO 2 (active valence)

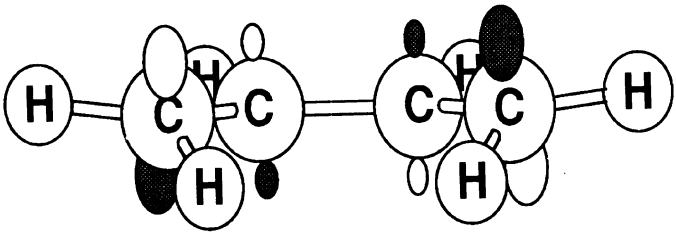

Fig. 6c MC-SCF CMO 3 (active valence)

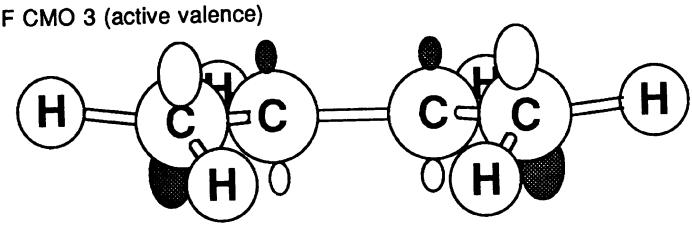

Fig. 6d MC-SCF CMO 4 (active valence)

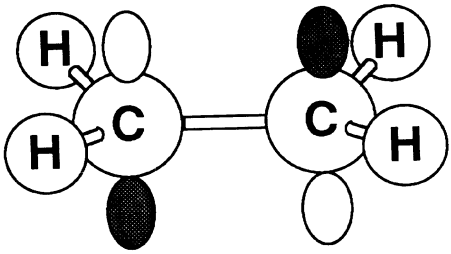

Fig. 6e MC-SCF CMO 5 (active Valence)

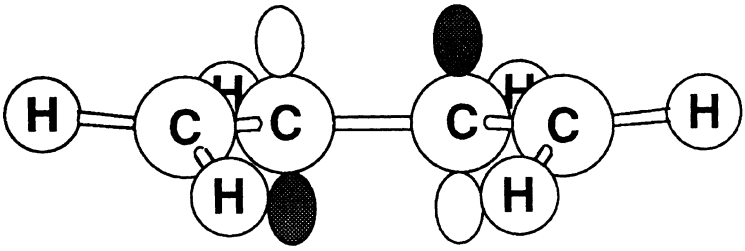

Fig. 6f MC-SCF CMO 6 (virtual)

The MC-SCF canonical MO (CMO) are quite localized onto either the ethylenic fragment or the cis butadiene fragment. Thus we have shown either one fragment or the other in Fig. 6. Two of the orbitals (CMO 1 fig.6a and CMO 6 fig. 6f) are localized on the middle C-C bond of cis butadiene and these orbitals are inactive (core) or virtual. This is consistent with fig. 9 of Part 1 where we argue that the diabatic surfaces involved in the region of the transition structure correspond to Fig. 4a and 4b where the middle C=C π bond is already formed at the transition structure. The active (valence) MC-SCF orbitals are CMO 2 3 4 5 (fig. 6b - 6e). They are localized mainly on the terminal methylene groups of the cis butadiene and ethylene. Note the "tails" on the middle C=C of cis butadiene. Theses tails represent the effect of the aditional "structure" shown below

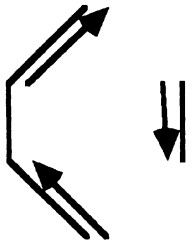

The corresponding molecule adapted minimum AO basis (localized orbitals) are illustrated in fig. 7 below.

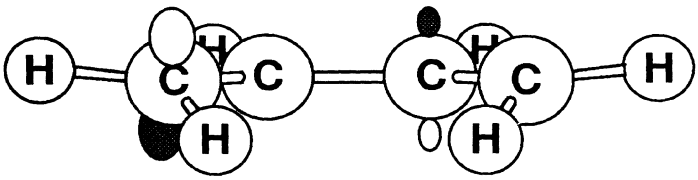

Fig. 7a MC-SCF LMO 1

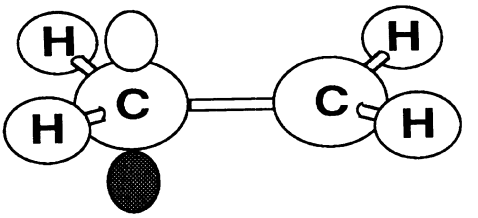

Fig. 7b MC-SCF LMO 2

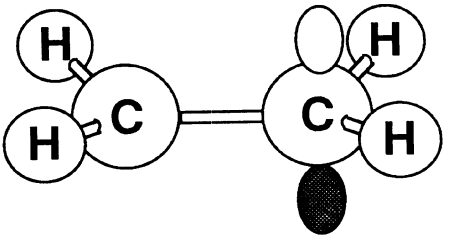

Fig. 7c MC-SCF LMO 3

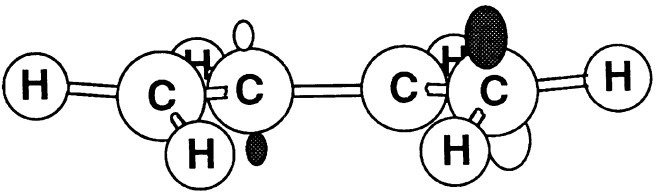

Fig. 7d MC-SCF LMO 4

The 4 active MC-SCF orbitals are again localized on the ethylene fragment or the terminal methylene groups of cis butadiene. Note the tails on the terminal methylene orbitals however. The overlap of the terminal methylene orbitals arises because of these tails which change phase in the non-orthogonal molecule adapted minimum basis (as discussed in Part I section III)

2)Parameters from Heisenberg Hamiltonian

Given the molecule adapted minimum basis, the Heisenberg hamiltonian can be constructed using the effective hamiltonian methods discussed in part I. The important result of the computation are the exchange integrals involving the active orbitals. These exchange integrals are assumed to have the same functional form as in H_2,

$$K_{ij} = [ij|ij] + 2 \langle i|h|j\rangle \; s_{ij}$$

Thus they are negative because of the dominance of the nuclear electron attraction in $\langle i|h|j\rangle$. The non-redundant K_{ij} for the concerted transition structure for the Diels

Alder reaction are shown in the following diagram.

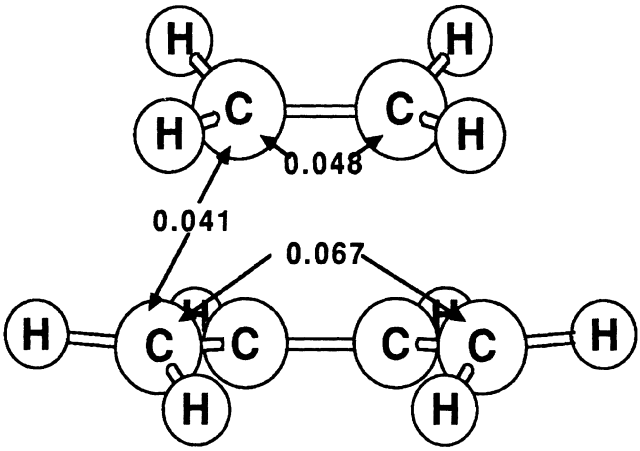

Fig. 8 Computed $-K_{ij}$ from Heisenberg hamiltonian for the transition state of the concerted Diels Alder reaction.

Note that there is a large $-K_{ij}$ between the terminal methylene groups. While this may seem strange at first, this situation arises because of the delocalization tails on the cis butadiene methylene orbitals. Of course this data is not interesting except by comparison with other molecules and with the reactants. The corresponding data for the transition state [3] for the 2_s+2_s cycloaddition of two ethylene molecules is illustrated for comparison in fig. 9 below.

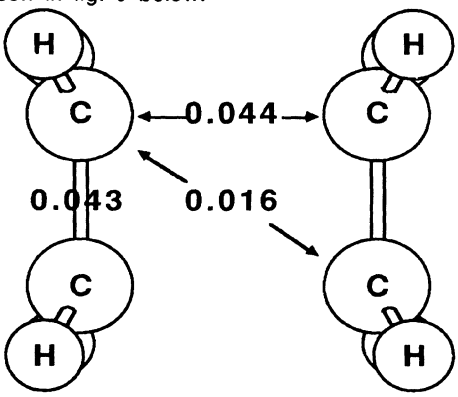

Fig. 9 Computed K_{ij} for " transition structure" (a second order saddle point [3]) for the 2_s+2_s cycloaddition reaction of two ethylene molecules.

One can observe the remarkable similarity of the $-K_{ij}$ in the forming C-C bonds and within the ethylenic fragment. The forming C-C bonds in the $2_s + 2_s$ cycloaddition reaction of two ethylene molecules are slightly shorter and this is the origin of the difference. Note that in ethylene there are contributions to K_x (see eq. 18 of Part I) but because of the larger distances these K_{ij} have dropped off to zero in the Diels Alder. The comparison with the same data at infinite interfragment separation is also instructive and the data is summarised in fig. 10 below.

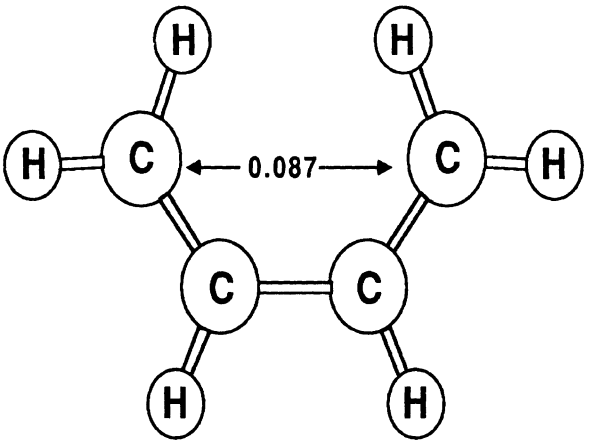

Fig. 10a

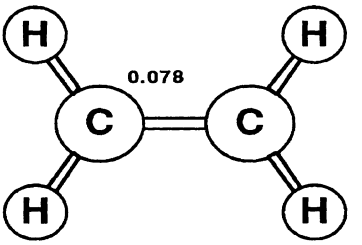

Fig. 10b $-K_{ij}$ for the reactants in the Diels Alder Reaction

Note again the $-K_{ij}$ between the terminal methylene groups that arise due to the

overlap of the delocalization tails. From this data we can obtain K_P , K_R etc to compare the reactants and transition state as discussed in section VI in Part I

Table 1 comparison of parameters of Heisenberg hamiltonian in the Diels Alder reaction for reactants and transition state

	K_R	K_P	K_X	T	Q
Transition Structure	-.1155	-.0824	.0005	.1035	-230.0029
Reactants	-.1659	.0000	.0000	.1659	-229.9846

Since the energy of the ground state is Q-T where T is the total exchange energy given by eq. 84 Part I, it can be seen that the barrier height is controlled mainly by T since Q is almost constant. The decrease in K_R on moving from reactants to transition state is only partly offset by the increase in K_P.

3)VB Wavefunction at the Transition Structure

As we have discussed in Sections IV and V of Part I, one can interpret the CAS MC-SCF wavefunction in the orthogonal molecule adapted minimum basis as an orthogonal VB expansion. On the other hand, the Evans hamiltonian (eq. 13 Part I) constructed from the effective Heisenberg hamiltonian corresponds to a VB expansion built from non-orthogonal molecule adapted AO. We have emphasized that orbital delocalization and charge transfer that connects these two expansions are just different manifestations of the same effect. Accordingly the two different wavefunctions are illustrated in fig. 11 and 12 below.

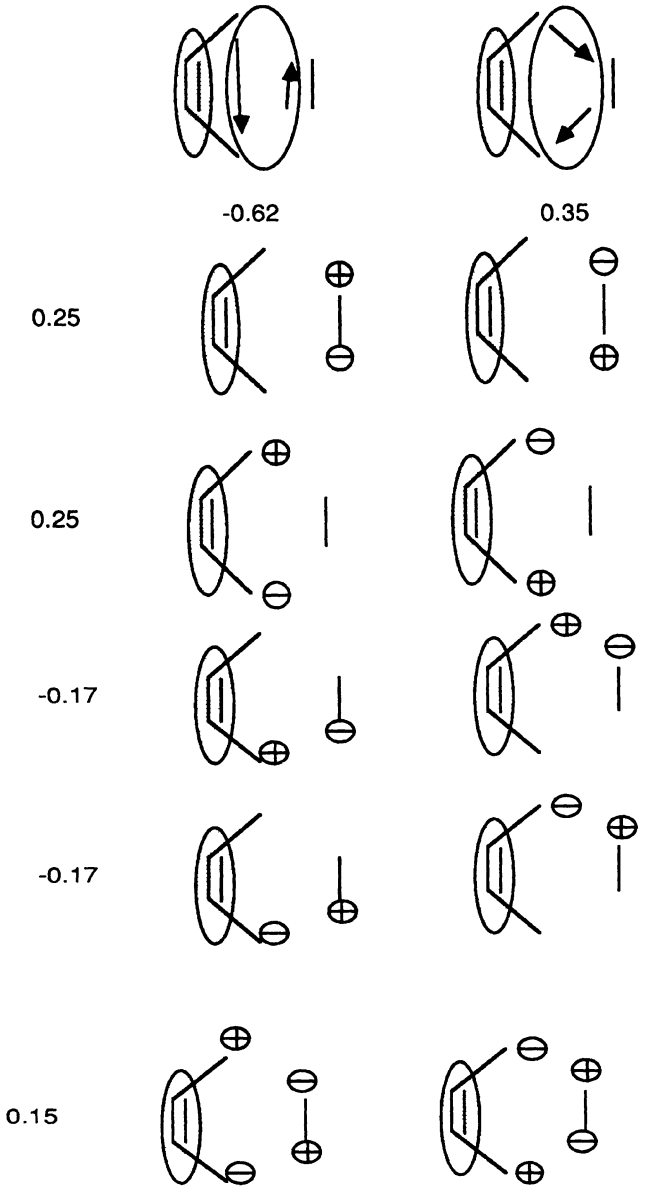

Fig. 11 VB wavefunction in the orthogonal Molecule Adapted Minimum basis

Fig. 12 VB wavefunction in the non-orthogonal Molecule Adapted Minimum basis

In these expansions we have used the symmetrically orthogonalized Rumer functions (see fig. 8 of Part I). In Fig. 12 we note that the spin coupling of the reactants dominates. The effect of orbital delocalization/ charge transfer is illustrated in fig. 11. One can see that the charge transfer is mainly intra-fragment. With reference to fig. 7a and 7c, for example, the charge transfer in the 3rd pair of configurations, will reverse the phase of the delocalization tails (see discussion in section III in Part I). The magnitude of interfragment charge transfer is smaller because of the early transition structure.

4) Analysis of the origin, existence, and nature of the transition structure.

As discussed in Part I, the projection of the Heisenberg hamiltonian onto the space of reactant and product spin couplings (see section V of Part I) yields reactant and product diabatic surfaces. Examination of the behaviour of these surfaces along the reaction co-ordinate gives the origin of the activation barrier for the reaction. In Fig. 13 below we show the behaviour of the reactant and product diabatic surfaces along the transition vector (fig. 5a)

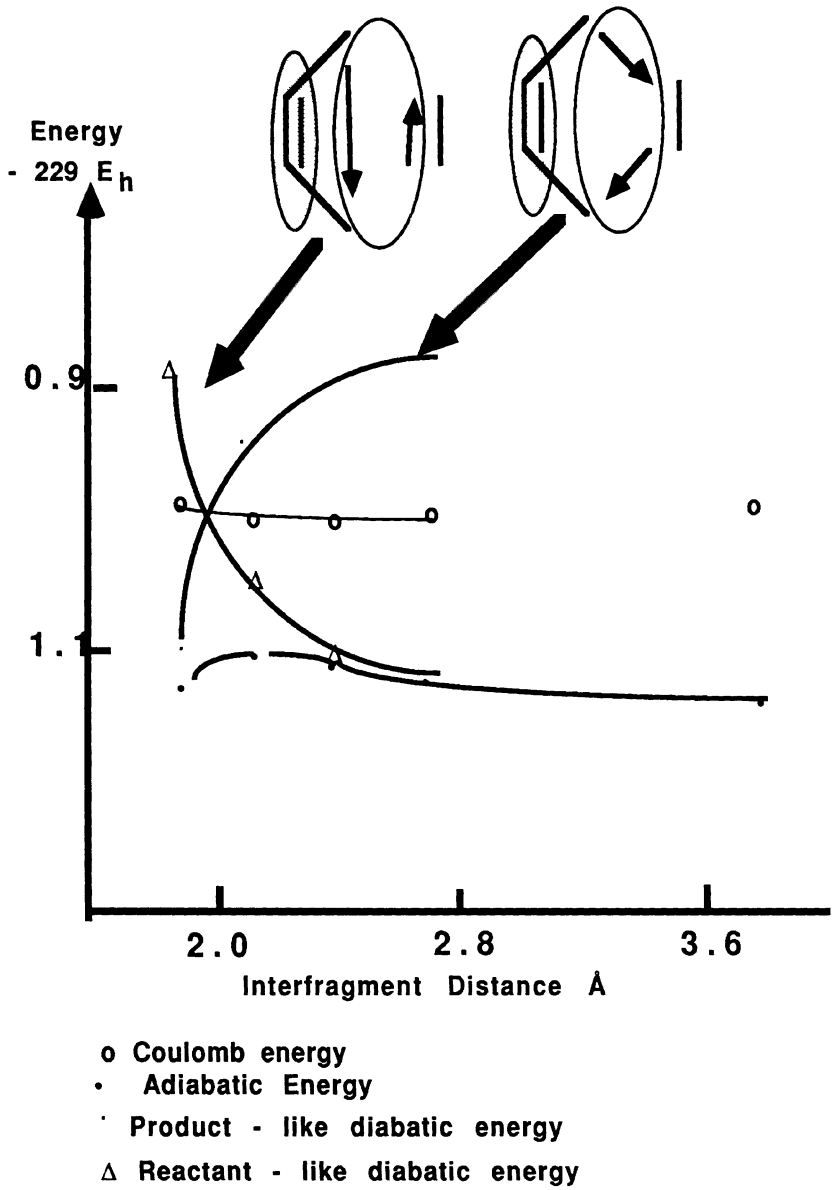

Fig. 13 Reactant and Product diabatic surfaces for the Diels Alder reaction

For this example the orthogonalization (the "global criterion" of section IV Part I) of the spin functions has been chosen so that the reactant and product diabatics will intersect when the energies of the two symmetrically orthogonalized Rumer spin functions have the same energy (Part I eq. 49 and 50). One can see that the curves intersect at an interfragment distance of approximately. 2.0 Å whereas the transition structure occurs at 2.28 Å because of the dominance of the reactant like spin coupling. Note that at the crossing $\alpha_R = \alpha_P = Q$. This figure confirms the origin of the barrier as change of spin coupling from that of fig. 4a to that of fig. 4b.

At the transition structure, $\partial E/\partial q_i = 0$ for all normal co-ordinates q_i. This expression can be decomposed into $\partial Q/\partial q_i$ and $\partial T/\partial q_i$ in order to understand the conditions for the existence of the critical point. Of course, by symmetry these values are automatically zero for non totally symmetric normal modes. Along the reaction co-ordinate (q_i corresponds to fig. 5a) at the transition structure

$\partial Q/\partial q_i = -.049 \quad - \partial T/\partial q_i = .049$

Thus as can be seen from figure 13 the slope of Q (and thus -T) is quite small. Thus, since Q is very flat, the transition structure arises essentially from a critical point in T. Obviously for species with large charge separations where Q is not flat, this will not be the case.

Similarly, $\partial^2 E/\partial^2 q_i$ can be decomposed into components from Q and T as illustrated in table 2 below

Table 2 Decomposition† of the $\partial^2 E/\partial^2 q_i$ into Q and T components

	$\partial^2 Q/\partial^2 q_i$	$-\partial^2 T/\partial^2 q_i$	$\partial^2 E/\partial^2 q_i$
Mode 5a transition vector	.060	- .272	-.212
Mode 5b to asynchronous	-.011	.012	.008

† the $\partial^2 E/\partial^2 q_i$ have been computed analytically, while $\partial^2 Q/\partial^2 q_i$ and $-\partial^2 T/\partial^2 q_i$ have been computed by finite difference. This is the origin of the discrepancy between the total and its Q and T components.

From this data, we see that the negative curvature of the reaction profile (fig. 5a) is dominated by the large positive curvature of T. In contrast, the curvature along the normal mode which would lead to an asynchronous transition state is positive (if this were not the case we would have a second order saddle point as in the 2_s+2_s addition of two ethylenes [3]). In this case the curvature of Q is negative arising from the

decrease in steric repulsions on moving to an symmetric geometry. On the other hand, the curvature of -T is positive and slightly larger in magnitude that Q. The behaviour of T arises from the fact that the bonding interactions are reduced in magnitude on going to the asymmetric geometry. In this manner we have a clear understanding of the nature of the transition state (first order saddle point, as opposed to second order saddle point as in the 2_s+2_s addition of two ethylenes [3])

IV Conclusions

In this short chapter we have illustrated the methodology discussed in Part I in application to the Diels Alder reaction which we have recently studied in some detail[1]. The results demonstrate the the reaction barrier can be viewed as a change in spin coupling of 4 electrons in 4 orbitals from the reactant spin coupling in fig. 4a to product spin coupling in fig. 4b (see fig. 13). The critical point is a true transition structure (ie $\partial^2E/\partial^2q_i$ is positive for q_i = mode 5b) because of the easily rationalized behaviour of $\partial^2Q/\partial^2q_i$ and $-\partial^2T/\partial^2q_i$.

Acknowledgements

Some of the drawings in this manuscript were done using the "Model" program kindly provided by Professor H.B. Schlegel. All computations were performed using the GAUSSIAN [4] suite of programs.

References

1)a. F.Bernardi, A. Bottoni, M.A. Robb, M.J. Field, I. H. Hillier, M.F. Guest, J. Chem. Soc., Chem. Commun. 1051-1052 (1985)

b.)a. F.Bernardi, A. Bottoni, M.A. Robb, M.J. Field, I. H. Hillier, M.F. Guest, J. Amer. Chem. Soc. **110**, 3050 (1988)

2) M.J.S. Dewar, S. Olivella, J.J.P. Stewart, J. Amer. Chem. Soc. **108**, 5771 (1988)

3) F. Bernardi, A.Bottoni, M.A.Robb, H.B.Schlegel, G. Tonachini ,J.Am.Chem.Soc. **107**,2260(1985) , F. Bernardi, A.Bottoni, M. Olivucci, M.A.Robb, H.B.Schlegel, ,J.Am.Chem.Soc. (in press)

4)**GAUSSIAN 80:** J. S. Binkley, R.A. Whiteside, R. Krishnan, R. Seeger, D. J. Defrees, H.B. Schlegel, S. Topiol, L R. Kahn, and J. A. Pople, QCPE **13** (1980), **GAUSSIAN 82:** Carnegie-Mellon University, J. Binkley, M. Frisch, K. Raghavachari, D. DeFrees, H.B. Schlegel, R. Whiteside, E. Fluder, R. Seeger, and. J. A. Pople.

A QUALITATIVE VALENCE BOND MODEL FOR ORGANIC REACTIONS

Sason S. Shaik
Department of Chemistry
Ben-Gurion University
Beer Sheva , 84105
Israel

ABSTRACT. This chapter develops a qualitative methodology for constructing states from their valence bond (VB) building blocks. The essence of the method is a mixing-diagram of the type used in qualitative molecular orbital (MO) theory. The method is used initially to describe states for representative species ; a covalent bond , species which possess an average of one electron per site (e.g., allyl radical , etc.,) and mixed-valence species (i.e., molecular ions). Then the method is applied to piece up potential energy profiles for two prototypical reactions (the exchange reactions of $H^{\cdot}$ and H^{-}). Finally , the conclusions are generalized to treat complex organic reactions , such as spin-transfer reactions (e.g., radical additions) electrophile-nucleophile combinations, cycloadditions and so on. The origins and variations of barriers and the importance of the quantum mechanical resonance energy of the transition state are discussed.

1. Introduction

To conceptualize reactivity patterns one must first understand the origins of the barrier in a chemical reaction. Since generally chemical reactions involve breaking and/or making of bonds, Valence Bond (VB) theory, rather than Molecular Orbital (MO) theory, provides a lucid insight into the mechanism of barrier formation [1]. However, some reactivity patterns, such as stereochemical selectivity, are more transparent by use of MO theory [2]. An optimal model of reactivity should combine therefore the insights of VB and MO theories [1]. The curve crossing diagrams which have been developed in recent years [1,3-6] possess this unified feature. Thus, by use of VB configurations which are based, either on fragment orbitals (the SCD model [1,3,4]), or on atomic orbitals (the VBCM model [3,5]) , it has been possible to describe the formation of the barrier in a variety of chemical reactions and to comprehend thereby complex reactivity patterns. Quantitative computations of curve crossing diagrams [7-9] have further shown that these models can be rigorously and meaningfully defined on quite sophisticated levels of theoretical calculations.

It appears therefore, that conceptualization of reactivity may eventually require a good qualitative command of VB theory. This seems especially timely because VB theory has been undergoing a serious revival [10] in the past decade and a half. This may be witnessed from the progress in the computational techniques [11] which begin to make the application of VB theory looking more and more competitive with MO-based calculations. Despite the surge of interest, there exist still -- in the chemical community by and large -- a chasm

J. Bertrán and I. G. Csizmadia (eds.),
New Theoretical Concepts for Understanding Organic Reactions, 165–217.
© 1989 by Kluwer Academic Publishers.

between the quantitative application of VB theory and its qualitative conceptualization. There has come the time then to build bridges and provide some qualitative tools with which to apply VB theory and relate it to the more familiar MO theory. A deeper insight into chemical reactivity in terms of curve crossing diagrams may thus follow.

This chapter is an attempt to outline qualitative principles of VB theory and to construct thereby states, in a methodical manner, much like the construction of delocalized molecular orbitals from atomic or fragment orbitals [12-14]. No doubt, the reader will recognize many of the principles underlying our qualitative approach. It constitutes a natural evolution and blending of the interest, our [1, 4, 15] and others [e.g, references 16-25], in the qualitative construction of states from VB building blocks.

The construction process is presented, in the following sections, in a hierarchy , from the fundamental problem of the states of a covalent bond all the way to potential energy surfaces of complex reactions. This is followed by analyses of barriers, their origins in chemical reactions, and some properties of the transition state such as its quantum mechanical resonance energy [26]. Since the main purpose of this chapter is to present the state construction process, we have avoided the detailed analyses of reactivity trends in specific reactions. The interested reader can find such analyses in the original literature [3-6,27,28].

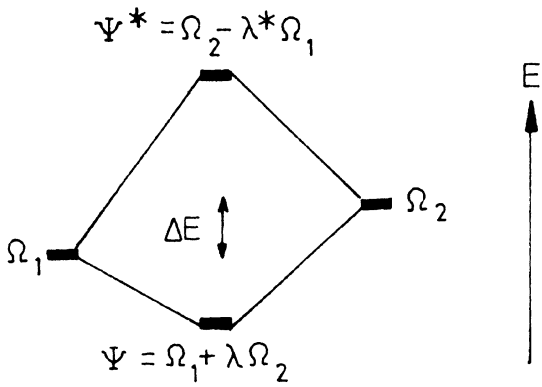

Figure 1. A mixing diagram which generates bonding and antibonding combinations (Ψ,Ψ^*) from two building block wave functions (Ω_1, Ω_2). The λ's are mixing coefficients that depend on the matrix element , $<\Omega_1| H |\Omega_2>$, and on the energy gap, ΔE.

2. A Qualitative VB Theory

Molecular orbital (MO) theory has become a daily conceptual frame in chemistry because it has become possible to convert mathematics into a pictorial language which retains the essence of the complex theory. This has been achieved by use of the interaction diagram and its quantitative mixing rules derived from perturbation MO theory [12-14, 29]. A general mixing diagram is illustrated in Figure 1 which shows it to be a device for construction of the "whole" from its building block constituents. This is in essence also an understanding of

the "whole".

Within qualitative MO theory , understanding means that the pictorial representation retrieves the ordering of the molecular orbitals and their correct "shapes" (i.e., nodes and coefficient sizes), as resulting from detailed computations. We may then begin by inquiring what are the best VB building blocks from which to form states ? and what are the matrix elements between the chosen VB wavefunctions ?

Anyone who has experience with VB theory [30] is aware of two major difficulties which are related to the above questions. Firstly, chemically "real" VB structures are often polydeterminental wave functions, which means that they are not the best building blocks in our construction process. Starting with single VB determinants appears to be a better choice. The second difficulty is with the matrix elements and energies of VB determinants. The corresponding expressions are extremely cumbersome and their qualitative enumeration is a very tedious task. This situation requires simplification but to a degree which still retains the essence of the mixing pattern. We think that such a simplification can be achieved by use of a monoelectronic Hamiltonian .

There is another feature of MO theory which is easily conceptualizable. This is the pictorial representation of the orbitals which allow an easy expression of a sometimes complex mathematical result. The corresponding difficulty in VB theory is that the final wavefunction is always polydeterminental, and while Lewis structures summarize the general bonding character of VB wavefunctions some salient features are still missing in the Lewis representation, for example the "long bond" characters of many 1,3-dipoles and "hypervalent" species[18; 21a,c]. What seems to be required is a representation which complements Lewis' by summarizing, in a compact and visualizable manner, the polydeterminental nature of a VB wavefunction. Such a pictorial representation can be achieved in our view by using both fragment orbitals (FOs) as well as atomic orbitals(AOs) in the VB wavefunction. Approaches of this nature have been discussed by Linnett [17] and Harcourt [18] , and more recently by us [1] and by Epiotis [19,31]. Epiotis especially, has developed this approach and showed the usefulness of the pictorial representation which he called "a bond-diagram" .

2.1 VB DETERMINANTS. ENERGIES, PICTORIAL PRESENTATIONS AND INTERACTION PATTERNS

A VB determinant is an antisymmetrized wavefunction which may or may not be also a proper spin eigenfunction [30, 32]. For example , $|a\underline{\mathbf{b}}|$ is a determinant which describes two spin-orbitals having each one electron . For typing-convenience we use regular and bold--underlined letters to denote the electron spin instead of the usual convention of barred and unbarred spin-orbitals. Thus,

$$a = a\alpha \; ; \; \underline{\mathbf{b}} = b\beta \longrightarrow \Omega = |a\underline{\mathbf{b}}| = 2^{-1/2}\{a(1)b(2)[\alpha(1)\beta(2)] - a(2)b(1)[\alpha(2)\beta(1)]\} \quad (1)$$

where the parenthetical numbers 1 and 2 are the electron indices . This determinant is not a proper spin eigenfunction , but by mixing with $|\underline{\mathbf{a}}b|$ there will result two spin eigenfunctions with a singlet and triplet spins (*vide infra*). On the other hand, the determinant $|a\underline{\mathbf{a}}b|$ is a proper spin eigenfunction which describes two spin-paired electrons in the orbital indicated by a and a single electron with spin α in the orbital indicated by b . This may sound confusing if one is not familiar with spin eigenfunctions. Knowledge of spin eigenfunctions is very useful in VB theory , and it is our hope that through the construction of the mixing diagram this knowledge can gradually be acquired.

Figure 2 shows some pictorial representations of VB determinants using $|a\underline{\mathbf{b}}|$ as an example . Thus we may use horizontal bars to indicate the energy level of the orbitals, and

arrows to indicate the electronic spin as in **1** . Alternatively , if we wish to convey that the electrons "belong" to atoms we may use **2** where the heavy dots indicate electrons and arrows indicate spins. This latter representation is more " chemical " and may be preferred when using a casual reference to a certain determinant. It should be remembered though that the determinant in Figure 2 does not represent a real chemical structure. The pictorial persentation projects this by showing that the determinant distinguishes between the electrons (via their spins) , something which is nonphysical.

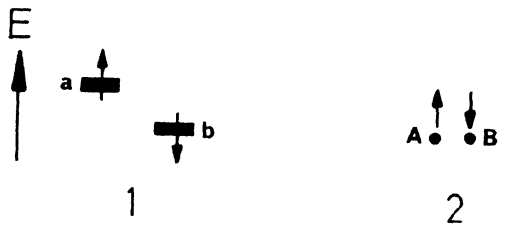

Figure 2. Pictorial representations of | a$\underline{b}$ |.

VB determinants may involve either atomic or fragment orbitals (AO and FO). The latter option is an economical way of representing a wave function which is a linear combination of several VB determinants based on AOs [1,4] , as much as MO determinants are linear combinations of VB determinants [1, 21b] . An example of a VB determinant based on FOs is |a$\underline{a}\sigma\underline{\sigma}$*|, which may be used to describe a certain spin-orbital occupancy of $(H\cdots H\cdots H)^-$, where the σ-type FOs can be, for example, the corresponding linear combinations of the AOs of the two terminal hydrogen atoms, while the a-orbital being the AO of the central hydrogen .

2.1.1 *Normalization Constants of VB Determinants.* Any determinantal wave function is represented by its diagonal element which is a specific product of spin orbitals. Consider for example the determinant in eq. 2a with its normalization constant, N. The diagonal spin-orbital product, ψ_d, is given in eq. 2b where the parenthetical indices are those of the electrons. The determinant itself is a sum of all the possible spin-orbital products which are obtained by allowing any electron to occupy any spin-orbital . These spin-orbital products are obtained by permuting the electron indices in the diagonal element of eq. 2b . Thus , the determinant can be expressed as a linear combination of all the possible permutations of the diagonal element, ψ_d , as shown in eq. 2c where P_i is a nonidentity permutation, and $(-1)^i$ is the sign of the permutation. An even permutation has a positive sign while an odd permutation has a negative sign.

$$\Omega = N\,|abcd...n| \qquad (a=a \text{ and/or } \underline{a}\text{ , etc.,}) \tag{2a}$$

$$\psi_d = a(1)b(2)c(3)d(4)...n(n) \tag{2b}$$

$$\Omega = N[\ \psi_d + \Sigma_i\ (-1)^i\ P_i\psi_d\ ] \tag{2c}$$

The normalization constant is determined from the condition in eq. 3

$$N^2[\,1 + \Sigma_i(-1)^i \langle\psi_d|P_i\psi_d\rangle] = 1 \qquad (3)$$

Each of the terms of the type $\langle\psi_d|P_i\psi_d\rangle$ is an overlap between the diagonal product and one of its permutations. For VB determinants this product overlap yields , in turn, an overlap term between AOs or FOs, which ever type is used to construct the determinant. These AO (FO) overlaps appear in certain powers which depend on the number of pairwise transpositions which are included in a permutation P_i . The final form of N^2 becomes then,

$$N^2 = 1 / [\,1 - F_N(s^m)\,] \qquad (4)$$

Here $F_N(s^m)$ is a function of the AO (FO) overlaps to a variable power (m). For example, if Ω is the determinant in eq. 5a its corresponding $F(s^m)$ is eq. 5b .

$$\Omega = N|a\underline{a}b\underline{c}| \qquad (5a)$$

$$F_N(s^m) = 1 / [\,1 - (\,s_{ab}^2 + s_{ac}^2 - s_{ab}^2 s_{ac}^2\,)\,] \quad ;\ (\text{e.g., } s_{ab} = \langle a|b\rangle\,) \qquad (5b)$$

The details of determining this function for a general case are given in the Appendix . What matters for the qualitative discussion is that $N^2 \geq 1$ for any VB determinant .

2.1.2. *Energies of VB Determinants.* We start with the assumption that the Hamiltonian is a sum of monoelectronic terms h(k) , so that for every electron there corresponds one term . This is a simplification which is meant to enable the conceptualization of the problem. This is in a way similar to the Heisenberg Hamiltonian formalism used for example, by the group of Malrieu [22a, 33], only that the present approach has a qualitative and pictorial goal . Using the monoelectronic Hamiltonian , the energy of a VB determinant , Ω, is given by eq. 6a and since Ω can be written as a sum of permutations (eq. 2c) , the energy expression becomes eq. 6b,

$$E(\Omega) = \langle\,\Omega\,|\,\Sigma_k h(k)\,|\,\Omega\,\rangle \qquad (6a)$$

$$E(\Omega) = N^2\,[\,\langle\,\psi_d\,|\,\Sigma_k h(k)\,|\,\psi_d\rangle + \Sigma_i\,(-1)^i \langle\,\psi_d\,|\,\Sigma_k h(k)\,|\,P_i\psi_d\,\rangle\,] \qquad (6b)$$

Equation 6b collects the energy terms from the diagonal spin-orbital product and from all the interaction terms between the diagonal product and its permutations. A systematic way to enumerate all the energy terms is described in the Appendix and here we give only some qualitative guides.

The energy of the diagonal term is simply the sum of the orbital (AO or FO) *monoelectronic* energies, ε_r, multiplied by the number of electrons in each orbital . The interaction terms in eq. 6b yield the same orbital energies, but these are multiplied now by orbital overlaps in different powers. The result is that for every orbital , r,which is occupied by n_r electrons in the VB determinant, we obtain the following energy contribution :

$$n_r\varepsilon_r\{[1 - F_r(\,s^m\,)\,]\,N^2\} \quad ;\ N^2 = 1/[\,1 - F_N(s^m\,)\,] \qquad (7)$$

The total orbital energy contribution is simply a sum of all the corresponding terms, that is ,

$$E(\text{orbital}) = \Sigma_r n_r \varepsilon_r \{[1 - F_r(s^m)] / [1 - F_N(s^m)]\} \quad (8)$$

Where $F_r(s^m)$ is a function of the orbital overlaps in analogy with $F_N(s^m)$ in eq. 4 and 5b above . The ratio of the two 1 - $F(s^m)$ terms in eq. 8 is only slightly larger than unity, unless all overlap terms are large ($s \geq 0.5$). Therefore, for qualitative purposes we may consider the orbital energy contribution to be simply a sum of the orbital energies multiplied by the number of electrons in each orbital , as follows:

$$E(\text{orbital}) \sim \Sigma_r n_r \varepsilon_r \quad (9)$$

The interaction terms in eq. 6b give rise also to overlap repulsion terms between every pair of electrons which have identical spins and which reside in overlaping spin-orbitals . This is shown pictorially in Figure 3 which illustrates three common possibilities. Thus for each such electron pair, in orbitals r and s, one obtains an overlap repulsion term whose expression is given by eq. 10,

$$\text{a pair-repulsion} = -2h_{rs}s_{rs}\{ [1 - F_{rs}(s^m)] / [1 - F_N(s^m)] \} \quad (10)$$

where the 1 - $F(s^m)$ terms have their usual meaning. Following the same reasoning as above, we may qualitatively consider the terms in brackets to exceed unity only slightly. Thereby, the total overlap repulsion can be simply summed over all the pairs of electrons that possess identical spins, as illustrated in Figure 3 and expressed in eq. 11.

$$E(\text{pair-repulsion}) \sim -\Sigma_r \Sigma_s 2h_{rs}s_{rs}; \quad (r \neq s \text{ , summation over identical spins}) \quad (11)$$

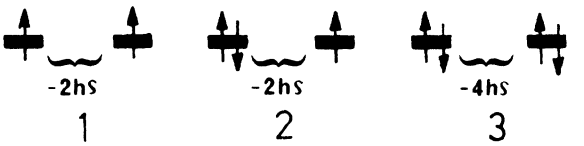

Figure 3. Electron occupancies and related overlap-repulsive interactions.

The total energy of a VB determinant becomes accordingly,

$$E(\Omega) = E(\text{orbital}) + E(\text{pair-repulsion}) \sim \Sigma_r n_r \varepsilon_r - \Sigma_r \Sigma_s 2h_{rs}s_{rs} \quad (12)$$

We note that the h_{rs} terms are the usual resonance integrals which are proportional to the corresponding orbital overlaps , as in MO theory . Thus ,

$$h_{rs} = \langle r | h | s \rangle \propto s_{rs} \quad (13)$$

From a physical point of view, the above monoelectronic treatment considers only one type of nonbonded interactions; the overlap repulsion. The more "classical' terms (electron-electron repulsion + electron-nuclear attraction + nuclear-nuclear repulsion) are not considered in this scheme. For atoms which possess strong bonds (e.g., first row elements) this kind of consideration is fairly good because the sum of the "classical" terms is small [30] and the energy of a VB determinant is dominated by the overlap-related terms . On the other hand , for metallic elements (e.g., Li) the sum of the "classical" terms is attractive and not negligible relative to the overlap term [19a, 22a, 33]. This limitation should be kept in mind when discussing metallic elements.

2.1.3. *Interaction Matrix Elements Between VB Determinants.* The interaction matrix element between two different VB determinants is the quantity which determines the composition of the final states and their energy ordering . This is given by eq. 14 for two determinants Ω_1 and Ω_2,

$$<\Omega_1 \mid H \mid \Omega_2> = N_1N_2 < \psi_{d,1} \mid \Sigma_k h(k) \mid (-1)^j \Sigma_j P_j \psi_{d,2} > \tag{14}$$

where now, Pj involves all the permutations (including now the identity permutation) on the diagonal spin-orbital product of Ω_2 . One of these permutations will be in maximum spin-orbital correspondence with $\psi_{d,1}$. For example, if Ω_1 = |a**a**b| and Ω_2 = |b**b**a| , then $\psi_{d,1}$ = a(1)**a**(2)b(3), while a(1)**b**(2)b(3) is the permutation of $\psi_{d,2}$ which has maximum spin-orbital correspondence with $\psi_{d,1}$. As may be seen, the two products have the same spin-orbitals in columns 1 and 3 and the same spin-type in column 2. This is the maximum correspondence that can be achieved between the above two VB determinants, while all other permutations of $\psi_{d,2}$ have less correspondence with $\psi_{d,1}$. The leading term of the matrix element is contributed from the interaction of the two maximally corresponding spin-orbital products . Thus the matrix element of eq. 14 can be rewritten as,

$$<\Omega_1 \mid H \mid \Omega_2> = N_1N_2\{< \psi_{d,1} \mid \Sigma_k h(k) \mid (-1)^t P_{max} \psi_{d,2} > + \\ + < \psi_{d,1} \mid \Sigma_k h(k) \mid (-1)^i \Sigma_i P_i \psi_{d,2} >\} \quad ; (P_i \neq P_{max}) \tag{15}$$

where P_{max} is the permutation which is required to create maximum correspondence with $\psi_{d,1}$,by acting on $\psi_{d,2}$. The other terms involve the interaction between $\psi_{d,1}$ and all the rest of the permutations of $\psi_{d,2}$. All the resulting terms are usually multiplied by overlap integrals taken to a certain power (s^m). The terms with the smallest overlap power are contributed by the leading (maximally correspondent) term in eq. 15.

A systematic way of enumerating all the terms is given in the Appendix. Since our purpose here is strictly qualitative, we must make concessions which simplify the matrix element while still conserving the essential features of the determinat-mixing. Our present experience shows that this can be achieved by considering only the leading term in eq. 15. With this simplification one can refer to two major calsses of determinant-mixing; determinants which differ by either one spin-orbital, or by two spin-orbitals with opposite spins.

CASE A. If the two VB determinants differ by one spin-orbital , for example , orbital a in

Ω_1 is replaced by orbital b in Ω_2 , then the corresponding leading term of the matrix element becomes,

$$< \Omega_1 \mid H \mid \Omega_2 > \sim (-1)^t h_{ab} \tag{16}$$

The term $(-1)^t$ in eq. 16 is the sign of the matrix element. This is determined by the number (t) of pairwise transpositions , in the order of the spin-orbitals, which are required to bring to maximum spin-orbital correspondence. An example of *CASE A* is the interaction matrix element between Ω_1 =|a**a**b| and Ω_2=|b**b**a| ,which differ by one spin-orbital (**a** in Ω_1 and **b** in Ω_2) and therefore , will interact via a $(-1)^t h_{ab}$ matrix element. Since, for bringing the two determinants into maximum correspondence, we have to interchange the order of the spin-orbitals a and b in Ω_2 , we get the matrix element with a negative sign as follows:

$$<|a\underline{a}b| \mid H \mid |b\underline{b}a|> = (-1)^1 <|a\underline{a}b| \mid H \mid |a\underline{b}b|> \sim -h_{ab} \tag{17}$$

CASE B. If the two VB determinants differ by two spin-orbitals which also possess different spins, for example , a and **b** in Ω_1 are replaced by c and **d** in Ω_2 , then the leading term of the matrix element becomes,

$$<\Omega_1 \mid H \mid \Omega_2> \sim (-1)^t \{ h_{bd}s_{ac} + h_{ac}s_{bd} \} \tag{18}$$

The simplest example of *CASE B* is the interaction between Ω_1 = |a**b**| and Ω_2 = |**a**b| which differ by two spin-orbitals . Since we need to transpose the order of **a** and b in Ω_2 , the sign of the matrix element is negative and the expression becomes,

$$<|a\underline{b}| \mid H \mid |\underline{a}b|> = (-1)^1 < | a\underline{b} | \mid H \mid b\underline{a} |> \sim - (2\, h_{ab}s_{ab}) \tag{19}$$

Clearly VB determinants which differ by any number of spin-orbitals may have a nonvanishing matrix element. But since the terms are multiplied by s^m ($s<1$) and m is related to the number of orbitals which are different in the two determinants, these matrix elements decrease rapidly with the number of spin-orbitals which are different in the two VB determinants. This is the reason why we have chosen to limit the qualitative discussion to the above two cases.

What happens if in a given problem the leading term , according to the above rules, vanishes ? Let us discuss this case by way of an example. Consider two VB determinants Ω_1 and Ω_2 in eq. 20,

$$\Omega_1 = N_1 \, |a\underline{a}b\underline{c}| \; ; \; \Omega_2 = N_2 |c\underline{c}\underline{a}b| \tag{20}$$

Two pairwise transpositions are required to bring Ω_2 to maximum spin-orbital correspondence with Ω_1, as shown in eq. 21 . The two determinants are seen here to differ by one spin-orbital (a in Ω_1 and c in Ω_2) and this situation corresponds to *CASE A* with a h_{ac} matrix element as shown further in eq. 21,

$$< \Omega_1 \mid H \mid \Omega_2> = < |a\underline{a}b\underline{c}| \mid H \mid |c\underline{a}b\underline{c}| > \sim h_{ac} \; ; \; (H = \Sigma_i h(i); \, i = 1 - 4) \tag{21}$$

Suppose now, that the two VB determinants refer to the electronic structure of the linear $H_A \cdots H_B \cdots H_C^-$ species. In this geometry of H_3^-, the A···C distance is so large that h_{ac} is

negligible. One then turns to the next leading term (in eq.15), by considering permutations with lesser spin-orbital correspondence. The next leading term, in our example, comes from a permutation which matches the spin-orbitals **a** and **c** in the two determinants and requires three pairwise transpositions. The resulting matrix element between the spin-orbital products is (consult the Appendix) ,

$$<a(1)\underline{a}(2)b(3)\underline{c}(4) \mid H \mid (-1)^3\, b(1)\underline{a}(2)c(3)\underline{c}(4)> \sim -\{h_{ab}s_{bc} + h_{bc}s_{ab}\} \qquad (22)$$

It would have been nicer of course, had *CASES A,B* been sufficient to cover all possible situations of determinant-mixings . However , albeit this is not the case , still the above example shows that one can work out in a logical fashion to uncover situations which require more detailed work than just a simple application of the interaction rules (see Appendix) .

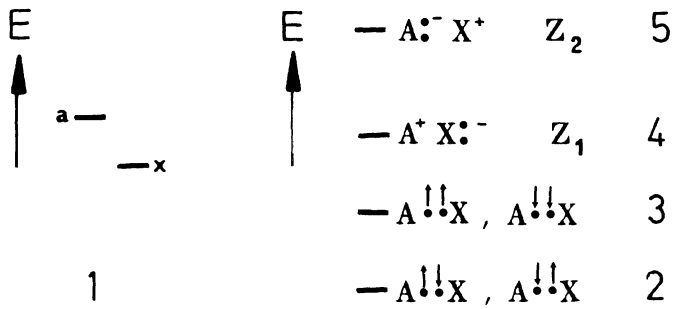

Figure 4. Orbitals (in **1**) and VB determinants (in **2-4**) for a covalent bond between A and X.

2.2. FORMING STATES BY VB DETERMINANT-MIXING DIAGRAMS.

This section shows how the above principles may be used to combine VB determinants into states.

2.2.1. *The States of a Covalent Bond.* The states of a single bond are probably well known [34] but nevertheless we feel that their construction from VB determinants is didactically useful. Consider two fragments A and X, each possessing a single orbital ; a and x respectively . These orbitals may be two AOs , two hybrids or a combination of the two orbital types. These orbitals are drawn in **1** in Figure 4 for a general heteronuclear case, though the discussion fits also a homonuclear case. The VB determinants which correspond to two electron occupancy are shown in **2-5** in Figure 4 in the pictorial manner discussed above. As may be seen there are two covalent determinants with no net spin in **2**, two covalent determinants with net spins in **3**, and two zwitterionic determinants in **4** and **5**. The determinants in **3** belong to the triplet state of the A-X bond, and according to eq.11 and 12 these two determinants are higher in energy than the other two covalent detrminants, in **2**, by the pair-overlap-repulsion, $\sim -2h_{ax}s_{ax}$.

Let us carry out the determinant-mixing in steps, and consider first the covalent

determinants of the lowest energy in Figure 4. These forms are expressed as determinants in eq. 23 and are seen to differ by two spin-orbitals. According to the interaction rule in *CASE B* the two determinants have a -2hs matrix element as written in eq. 24.

$$\Omega_1 = |a\underline{x}| \; ; \; \Omega_2 = |\underline{a}x| \tag{23}$$

$$< \Omega_1 \mid H \mid \Omega_2 > \sim -2h_{ax}s_{ax} \; ; \; (h_{ax} = <a \mid h \mid x>, \; s_{ax} = <a|x>) \tag{24}$$

Since the matrix element has a negtive sign ($h_{ax}s_{ax}$ itself is a negative quantity), then the negative combination of Ω_1 and Ω_2 is the bonding combination, while the antibonding combination is the positive combination. This is illustrated in **1** in Figure 5 and expressed in eq 25 and 26.

$$\Psi^- = \Psi_{HL} = N^- \{ |a\underline{x}| - |\underline{a}x| \} \; ; \; [N^- = N_{HL} = 1/(2+2s_{ax}^2)^{1/2}] \tag{25}$$

$$\Psi^+ = \Psi_T = N^+ \{ |a\underline{x}| + |\underline{a}x| \} \; ; \; [N^+ = N_T = 1/(2-2s_{ax}^2)^{1/2}] \tag{26}$$

The bonding combination in the Figure is the Heitler-London (HL) configuration, Ψ_{HL}, which is stabilized by roughly $2h_{ax}s_{ax}$ relative to the separate determinants . The two electrons in the HL configuration are paired up to a singlet state through the determinant-mixing. Thus, the stabilization energy of the HL configuration is a singlet-pairing energy whose magnitude is proportional to the orbital overlap, s_{ax}. This pairing energy becomes large at short internuclear separation, and is the major source of the covalent bond energy , while Ψ_{HL} itself makes the major contribution to the wavefunction of the bond [11c,30]. In further reference to HL configurations, we shall often drop the spins and draw a line between the two electrons to note their spin-pairing. This is indicated already in **2** in Figure 5.

The antibonding combination in **1** in Figure 5 and in eq. 26 is destabilized by roughly $2h_{ax}s_{ax}$ relative to the determinants. This state is actually the third component of the triplet state of the bond (the other two components being the two higher energy covalent determinants in Figure 4). The triplet nature of this Ψ_T component is not obvious, but can be assimilated if we remember that the three triplet components differ in the magnitude of their spin component in a given direction in space (*z* direction) but not in their total spin. The triplet component which is generated in Figure 5 by the determinant-mixing has the spin wave function in eq. 27a, which corresponds to a zero spin in the *z* direction, and to a total spin of unity. This value of *z*-spin-component is indicated by adding a superscript (o) to the wave function.The other two triplets have net *z*-spin components which equal the total spin ; their corresponding wave functions are written in eq. 27b and 27c. In further reference to the triplet state of a bond we shall simply draw two uncoupled dots, as shown in **2** in Figure 5 .

$$\Psi_T^o = N_T\{|a\underline{x}| + |\underline{a}x|\} = N_T\,[a(1)x(2) - a(2)x(1)]\{\alpha(1)\beta(2)+\beta(1)\alpha(2)\} \tag{27a}$$

$$\Psi_T^{+1} = N_T\{|ax|\} = N_T\,[a(1)x(2) - a(2)x(1)]\{\alpha(1)\alpha(2)\} \tag{27b}$$

$$\Psi_T^{-1} = N_T\,\{|\underline{a}\underline{x}|\} = N_T\,[a(1)x(2) - a(2)x(1)]\{\beta(1)\beta(2)\} \tag{27c}$$

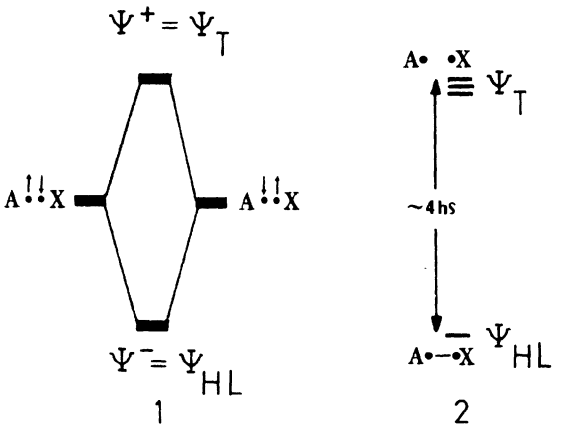

Figure 5. A determinant-mixing diagram of the covalent VB determinants (in **1**). The resulting HL configuration and the three components of the triplet state (in **2**).

This is a good place to display the HL wavefunction and indicate the difference between the singlet-pairing and the triplet spin of two electrons. The HL configuration is shown in eq. 28.

$$\Psi_{HL} = N_{HL}[a(1)x(2) + a(2)x(1)]\{\alpha(1)\beta(2) - \beta(1)\alpha(2)\} \tag{28}$$

As can be seen, by comparison with eq. 27a, the spin parts of Ψ_{HL} and Ψ_T^0 are similar in having $\alpha\beta$ spin combinations, but are different in sign of the combination. Thus, in both cases the z component of the spin is zero (owing to the $\alpha\beta$ combinations) but the minus sign in the singlet-pairing cancels the total spin in all other directions, while the plus sign in the triplet spin (eq. 27a) sums up the other spin components to a total spin of unity.

There are two additional VB determinants, the zwitterionic Z_1 and Z_2 in Figure 4, which can mix with the HL configuration but not with the triplet state. The two zwitterionic configurations are shown as determinants in eq. 29

$$\Psi_{Z,1} = |x\underline{x}|\,;\ \Psi_{Z,2} = |a\underline{a}| \tag{29}$$

Each of these configurations and each of the two determinants in the HL configurations differ by one spin-orbital. Therefore, according to the mixing rule in *CASE A* the interaction

matrix element between Ψ_{HL} and $\Psi_{Z,1}$ or $\Psi_{Z,2}$ will be proportional to h_{ax} as follows:

$$<\Psi_{HL}|H|\Psi_{Z,i}> \sim 2N_{HL}h_{ax} \sim 2^{1/2}h_{ax} \quad ; (i = 1,2) \tag{30}$$

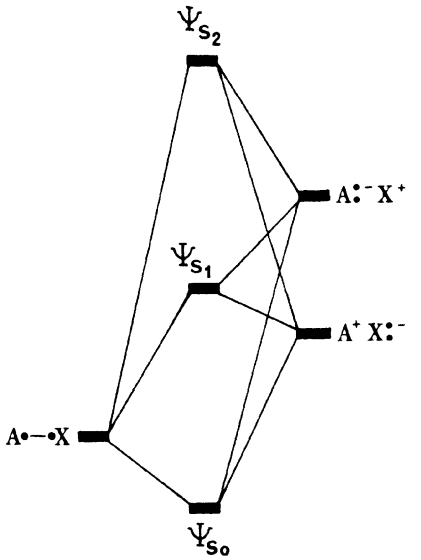

Figure 6. A VB-mixing diagram for the singlet states of a covalent two-electron bond

Figure 6 shows the complete VB-mixing diagram. The Z configurations usually lie higher than all the others. At infinite internuclear separation, the energy gap between the Z and HL configurations is given by the ionization potential of one fragment minus the electron affinity of the other fragment (i.e., the electron transfer energy). Normally, this is a very large quantity for what we consider to be typical covalent bonds . At shorter distances, the Z configurations are stabilized by the electrostatic interactions , while the HL configuration is stabilized by the spin-pairing energy. Therefore, in a qualitative sense, the gap between $Z_{1,2}$ and HL is roughly given by the corresponding electron transfer energy , at any internuclear separation. Also , in heteronuclear cases one of the Z configurations is lower than the other, as indicated in Figure 6 by the relative energies of the structures $A^+X:^-$ and $A:^-X^+$. All the configurations are indicated in the figure by their pictorial representations.

To understand the configuration mixing diagram in Figure 6, we may use guidelines which are known from the construction of the corresponding MO diagrams of three interacting orbitals [12 (pp.175)]. The combination of the lowest energy is all-bonding. The combination with the highest energy is all-antibonding. The combination in the middle is nonbonding-like. More precisely, it is a mixture which minimizes the strongest antibonding interaction.

Following these qualitative guidelines, the ground state of the bond is made of the HL configuration which mixes the two Z configurations in a bonding fashion. Since the corresponding matrix elements come with positive signs (eq. 30) , the all-bonding combination is also an all-positive combination. In addition, since the HL configuration is the lowest among the three, the resulting state will have a major HL character. Using a perturbation language and pictorial representations, the ground state of the bond will be given by,

$$\Psi_{So} = A\text{–}X = (A^{\bullet}\text{–}^{\bullet}X) + \lambda_1(A^+ X:^-) + \lambda_2(A:^- X^+) ; \lambda_1>\lambda_2 \qquad (31)$$

where A–X is the usual Lewis-type two-electron bond representation for a polar covalent bond.

The middle singlet state in the diagram is the first $\sigma\sigma^*$-type excited state of a two-electron σ bond or a $\pi\pi^*$ state of a π bond. This state is "initially" the antibonding combination of $A^{\bullet}\text{–}^{\bullet}X$ and $A^+ X:^-$, and in order to minimize this antibonding interaction , there is a mixing in of the $A:^- X^+$ structure with a negative sign. This is expressed in eq. 32,

$$\Psi_{S1} = (A\text{-}X)^* = (A^+ X:^-) - \lambda_1^* (A:^- X^+) - \lambda_2^* (A^{\bullet}\text{–}^{\bullet}X) \qquad (32)$$

Thus, for polar covalent bonds, this excited state is has a major zwitterionic character, $A^+X:^-$, while for a homonuclear case, it is a 50-50 mixture of the two zwitterionic structures with no HL character [34].

Finally, the second singlet excited state is the combination with the maximum antibonding interaction , and resembles mostly the highest of the two zwitterionic configurations . Since the largest matrix element is between the HL and the Z configurations , the state involves a positive combination of the two Z configurations which are mixed in a negative sign with the HL configuration, that is ,

$$\Psi_{S2} = (A\text{-}X)^{**} = (A:^- X^+) + \lambda_1^{**} (A^+ X:^-) - \lambda_2^{**} (A^{\bullet}\text{–}^{\bullet}X) \qquad (33)$$

Thus, this second singlet excited state has a major $A:^- X^+$ character for heteropolar cases , while for homopolar situations this state is composed of a 50-50 mixture of the two Z configurations mixed in an antibonding fashion with the HL configuration.

The interaction diagram in Figure 6 corresponds to a general internuclear distance. The configuration mixing is zero only at infinite distance , where the overlap, s_{ax}, and hence also the corresponding resonance integral are both zero. Thus, at infinite distance the states correspond to pure VB configurations ; the ground states are the covalent configurations (singlet and triplet), the first excited state is the structure $A^+ X:^-$ and the second excited state is the structure $A:^- X^+$.

2.2.2. *Singlet - Pairing. Bond-Diagrams and Bond-Pairs.* The preceding discussion projects the importance of the spin-paired configuration of the covalent bond. Figure 7 summarizes various representations of the spin-pairing information .

In **1** we show the determinant-mixing in the HL configuration in the language of "resonance" theory , namely, using a double headed arrow between the two spin exchanged forms of $A^{\bullet}\ {}^{\bullet}X$, and we also note the sign of the mixing between the two determinants . This representation mimics the wave function of the HL configuration in eq. 25. Another representation of Ψ_{HL} is **2** which, as noted already, indicates the spin-pairing by a line

connecting the two dots which represent electrons. In **3**, the information is conveyed by the *bond-diagram* [31]. The diagram shows the two orbitals in energy order, the electrons by vertical lines and the spin-pairing by the dashed line. The dashed line adds additional information about secondary configurations which mix with the HL configuration . These configurations are obtained by shifting single electrons between the two orbitals which are connected by the dashed line. The relative importance of the secondary configurations is apparent from the relative energy heighs of the two orbitals which participate in the electron shift . Thus the bond-diagram , in fact , mimics the complete wave function of the ground state of the bond , as given by eq. 31 and by the interaction lines in Figure 6 . Finally , in **4** we show the Lewis-type presentation of the two-electron bond by a line connecting the atoms. The line should mean both the HL spin-pairing of **2** as well as the secondary mixing of the zwitterionic configurations, as expressed in eq. 31.

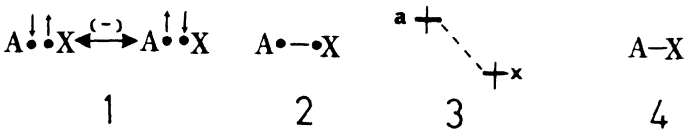

Figure 7. Various representations of singlet spin-pairing in a covalent bond.

The bond-diagram has one advantage over other presentations, in the sense that the "bond" it represents is not restricted to a two center interaction, and can be a generalized bond with multi center interactions. Thus, two spin-paired electrons in any two orbitals, be they AOs or delocalized FOs , constitute a "bond" or more generally , a *bond-pair* [1,4].

2.2.3. *Bonds and Effective VB Configurations in a Many Electron Treatment* . In discussing the states of an A-X bond, A and X were considered to possess one orbital each. In reality , fragments possess more than one orbital with a given symmetry . Consider for example the C-Cl bond of CH_3Cl . The orbitals which can overlap and contribute thereby to the C-Cl bond are shown in Figure 8 .

The orbitals in Figure 8 have six electrons available to them ; three from the σ and n orbitals of the methyl group and three from the s and p AOs of the Cl atom . These electrons can be distributed in various ways, to form determinants which represent the electronic distribution $CH_3^{\bullet}$ $^{\bullet}Cl$. We can, in turn, pair up the determinants into HL wave functions by a pairwise determinant-mixing as is done above for the simple two-electron case (Figure 5). The HL wave function with the lowest energy is going to be **2**, which is shown in Figure 8 by use of the bond-diagram formalism. There are as many such bond-diagrams as there are forms which obey the electronic distribution $CH_3^{\bullet}$ $^{\bullet}Cl$.

Each of the so generated HL configurations possesses two zwitterionic configurations (Z) which can be generated from it by shifting single electrons, between the two orbitals which are connected by the dashed line in the bond-diagram. These Z-types describe the general structures CH_3^+ $Cl:^-$ and $CH_3:^-$ Cl^+ . We can now take all the HL-types and their

corresponding Z-type configurations and interact them by use of a VB-mixing diagram as in Figure 6 above. Of course, the diagram for the many electron case will be considerably more complex than Figure 6, but the key principles will be retained to allow some generalizations.

The ground state of the bond will involve a linear combination of all the HL-type configurations in a bonding combination with their corresponding Z-type configurations. In this linear combination **2** (Figure 8) will have the highest weight among the HL configurations, while the zwitterionic configurations which are generated from **2** will have the highest weight among the Z-types. This has been shown recently by the Orsay group using ab initio VB computations [7, 11c].

Qualitatively, this polyconfigurational mixing can be thought of in terms of three *effective configurations* [1, 4, 7, 11c], one HL-type $H_3C^{\bullet}-{}^{\bullet}Cl$ and two zwitterionic-types, $H_3C^+\ Cl:^-$ and $H_3C:^-\ Cl^+$, as done in Figure 6 for the simple case of two electrons. In an approximate sense, the effective configurations of each type distribute the two electrons in two orbitals which are hybridized and optimized to yield the best bond energy. While some details are lost in this manner one can always unleash the procedure to analyze specific problems in more detail. In all the following sections we use effective configurations in the qualitative discussions.

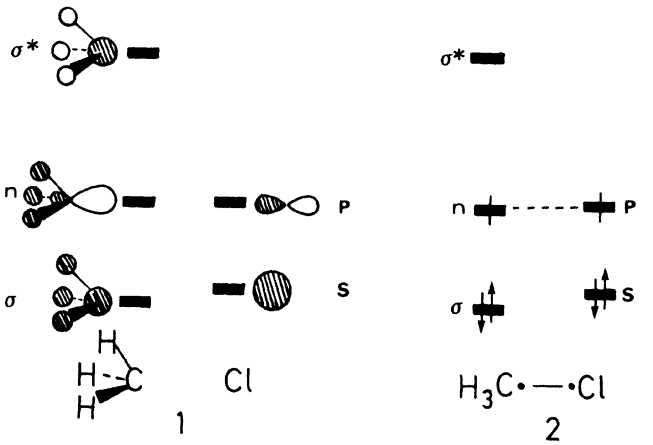

Figure 8. Fragment orbitals which participate in the C-Cl bond (in **1**). A bond-diagram corresponding to the lowest energy HL configuration (in **2**).

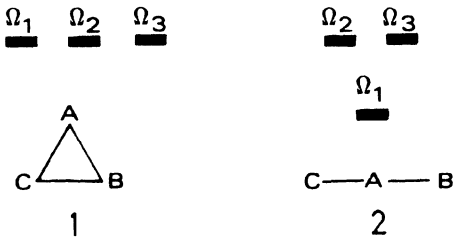

Figure 9. Energy ordering of the covalent determinants for a three-electron/three-center problem. A,B and C are atomic centers.

2.2.4. *Covalent States for Species with One Electron Per Site.* Species which possess an average of one electron per site have been treated by Malrieu and coworkers [22a, 33] by use of the Heisenberg Hamiltonian formalism. Our following qualitative treatment resembles theirs in the essential conclusions. The HL configuration and the triplet state (eq.25,26), for a two-electron/two-center case, are the simplest composite wave functions which describe species with an average of one electron per site. The underlying principles of the mixing, in the simple case, carry over to many electron cases such as conjugated π-systems, hydrogenic systems and so on ; all of which have an average of one electron per site.

The first step of the mixing procedure is to assemble all the VB determinants with a given net spin in the z direction, and to rank them in energy according to their number of pair-repulsive interactions (Figure 3, eq. 10 and 11). The determinants will either be degenerate or differ by multiples of 2hs units ; one such unit for each pair of electrons which have identical spins and therefore a pair-repulsion.

Let us exemplify the above argument with a case of three electrons and three centers, which may be the π-system of allyl , cyclopropenyl , or the σ system of the H_3 species, and so on. Suppose that we are interested in the covalent states which possess a single net spin in the z direction. The corresponding three covalent VB configurations which will be required for the mixing procedure are shown in eq. 34 .

$$\Omega_1 = |\underline{a}bc| \; ; \; \Omega_2 = |ab\underline{c}| \; ; \; \Omega_3 = |a\underline{b}c| \tag{34}$$

The energy ordering of these three determinants depends on the nuclear arrangement of the three centers, as shown in Figure 9. Thus, for an equilateral triangular arrangement each of the three configurations has a single pair-repulsion, and the configurations are therefore degenerate as shown in **1** . On the other hand, for a linear (or essentially so) arrangement, Ω_1 loses its repulsive interaction ($-2h_{bc}s_{bc}$) and becomes the most stable determinant, as shown in **2** .

In the second step of the mixing procedure we have to find the mixing matrix elements. Covalent determinants can in general be generated from each other by exchange of a pair of spins. Two such determinants are also necessarily different by two spin orbitals, and will therefore interact according to the mixing rule in *CASE B*. Only those spin-exchanges which involve electrons in orbitals of adjacent atoms will give rise to a nonvanishing matrix element of the type -2hs. If we think about a pair of interacting determinants as two

"connected vertices in a polygon", the determinant-mixing pattern will appear topologically identical to a corresponding Huckel or Mobius MO-problem with the same graphical connectivity. The problem can then be solved easily , in a pictorial manner, using the circle mnemonic for solving Huckel and Mobius systems [35]. Alternatively, once the matrix elements are known, one may then use determinant-mixing diagrams to generate the various states.

The resulting states from either approach will be all the possible covalent spin-states of the system . Since we are dealing with overlaping orbitals and with a single type of matrix element (2hs), *the state with the lowest energy will also have the lowest possible spin with the maximal spin-pairing , while the highest state will have the highest spin and the lowest possible spin-pairing*. Thus for example, the lowest spin state for cases with an even number of electrons will be the maximally-paired singlet state. Higher in energy there will be a triplet state , then a quintet state and so on . Similarly, for an odd number of electrons the lowest state will be a doublet, then a quadruplet and so on. This state ordering, for open chain and ring structures, will be retained unless the singlet-pairing energy becomes small . This is exactly the result which is obtained with the two electron case (Figure 5), and we now see that the same result carries over to many electron systems .

Let us go back , now in some detail, to our three electron example in Figure 9 and eq. 34. It may be seen that Ω_1 can generate both Ω_2 and Ω_3 , each by a pairwise spin exchange (e.g. , exchanging the spins of the orbitals a and b in Ω_1 in eq 34 generates Ω_2) . Likewise, Ω_2 and Ω_3 are related by a spin exchange over the orbitals b and c . For the equilateral arrangement all the matrix elements are identical and can be designated as follows:

$$-2h_{ab}s_{ab} = -2h_{bc}s_{bc} = -2h_{ac}s_{ac} = -h' \qquad (35)$$

The corresponding interaction pattern is shown graphically in **1** in Figure 10 where the determinants are denoted by asterisks and their -h' matrix elements by lines which connect the asterisks. This interaction-graph has a topology of a Mobius 3x3 problem. The resulting states can be obtained then by use of the corresponding circle mnemonic , as shown in **2** . As can be seen there are two degenerate low energy states , and one higher energy state. Referring to the generalization derived above , the lowest states should correspond to a doublet spin, while the highest state to a quadruplet spin .

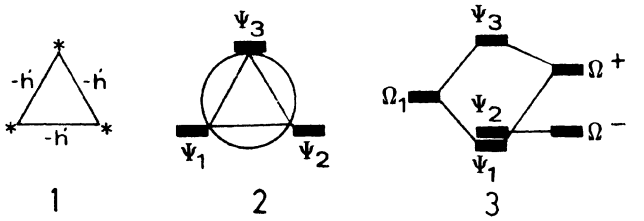

Figure 10. Determinants (* or Ω) and states (Ψ) for the equilateral triangular geometry of a three-electron/three-center system. The Mobius topology of the determinant interaction pattern (in **1**). The resulting states obtained by use of, the circle mnemonic (in **2**) and the determinant-mixing diagram (in **3**).

Alternatively , one can use the determinant-mixing diagram in **3** in the Figure to obtain the same information. Thus, we initially form a negative and positive combinations from Ω_2 and Ω_3 and interact the resulting combinations with the third determinant, Ω_1. The combinations are shown in the righthand side of the diagram as Ω^+ and Ω^- . The ngative combination is the lowest, because Ω_2 and Ω_3 have a matrix element with a negative sign . The determinant Ω_1 can interact only with the positive combination to form bonding and antibonding combinations Ψ_1 and Ψ_3 . At the same time, Ω^- which does not find an interaction partner becomes itself the state Ψ_2.

The explicit expressions for the states and their energies can be obtained as in the Mobius problem [35] . With neglect of overlap in the normalization constants we get,

$$\Psi_1 = 6^{-1/2} [\, 2\Omega_1 - \Omega_2 - \Omega_3 \,] \; ; \; E_1 = E(\Omega) + h' \quad (h' = 2h_{ac}s_{ac}) \tag{36a}$$

$$\Psi_2 = 2^{-1/2} [\, \Omega_2 - \Omega_3 \,] \; ; \; E_2 = E(\Omega) + h' \tag{36b}$$

$$\Psi_3 = 3^{-1/2} [\, \Omega_1 + \Omega_2 + \Omega_3 \,] \; ; \; E_3 = E(\Omega) - 2h' \tag{36c}$$

Let us turn to obtain some insight into the electronic character of these three states . This is done by appeal to Figure 11 which uses HL-type Kekule structures for a typical three-electron/three-center system , the cyclopropenyl radical in an equilateral triangular geometry . The Ψ_1 component of the ground state can be written as follows:

$$\Psi_1 = 6^{-1/2} [\, (\Omega_1 - \Omega_2) - (\Omega_3 - \Omega_1) \,] = 3^{-1/2} [\, \Psi_{HL}(A\text{-}C) - \Psi_{HL}(A\text{-}B) \,] \tag{37}$$

where it is apparent that the state is the negative combination of the two HL bond-wave functions of the bonds A-B and A-C , as shown in **1** in the Figure. Each one of the Kekule structures in **1** possesses a single net spin which accounts for the doublet spin of Ψ_1 .

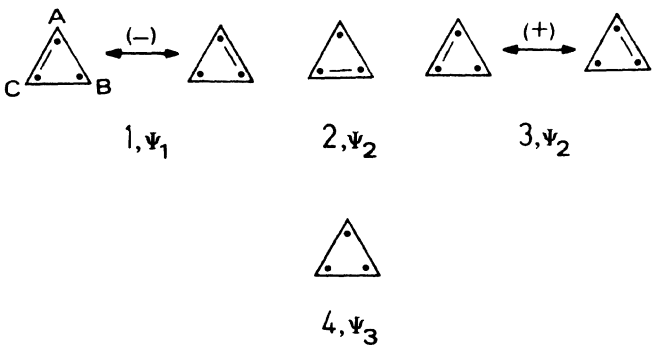

Figure 11. Pictorial descriptions of the covalent states of an equilateral triangular three-electron/three-center system.

The Ψ_2 component , in eq. 36b , has an uncoupled electron in orbital a (site A) , while the orbitals across b and c are coupled into a HL bond (B-C). This is shown in **2** in Figure

11 where the doublet spin character is apparent. However we, can rewrite Ψ_2 as follows:

$$\Psi_2 = 2^{-1/2}\{ - [(\Omega_1 - \Omega_2) + (\Omega_3 - \Omega_1)] \} = - [\Psi_{HL}(A\text{-}C) + \Psi_{HL}(A\text{-}B)] \qquad (38)$$

In this representation the wave function is simply the positive combination of the bond-wave functions of A-B and A-C , as shown in **3** in the Figure. Thus, the positive linear combination of two Kekule structures is identical here to a third structure. This happens because the two Kekule structures share a common determinant . Moreover , since there exist only three unique determinants for the three electron problem , the three Kekule structures are mutually dependent and constitute an over-complete basis set for VB-mixing. This is the common situation in cases with an average of one electron per center, and therefore care must be taken in applying the naive "resonance" theoretical ideas of mixing Kekule structures .

The highest lying state Ψ_3 has a positive combination of Ω_1 and Ω_2 which describe together a triplet pair of electrons across the A···C atoms and a third electron, also uncoupled , on atom B . The same exact situation is described by Ω_3. The total spin of this state is therefore quadruplet , as shown by the three unpaired electrons in **4** in Figure 11 .

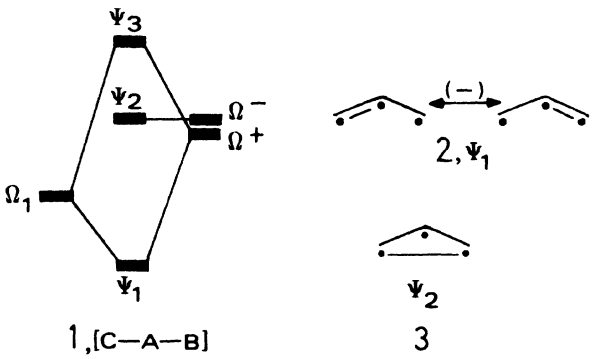

Figure 12. A determinant-mixing diagram for a three-electron/three-center system in a linear (or isosceles triangle) geometry (in **1**). Pictorial descriptions of the states, Ψ_1 and Ψ_2 (in 2,3).

Let us turn to the linear or isosceles triangular geometry. For this arrangement of the three atom , the matrix element between Ω_2 and Ω_3 which is $-2h_{bc}s_{bc}$, is almost zero due to the large B···C distance . The only matrix elements which are considerable are those between Ω_1 and either Ω_2 or Ω_3 . These matrix elements are identical and we can , as in the equilateral case , consider here too the determinant-mixing between Ω_1 and the Ω^+ and Ω^- combinations . The interaction-diagram is shown in **1** in Figure 12. The same three states as before are obtained but there is no state degeneracy as in the equilateral triangle . The lowest state Ψ_1 is as before the resonating mixture of the Kekule forms having A-B and A-C bonds , as shown in **2** using as an example the π-system of allyl radical . The intermediate state in Figure 12 is also, as before , the state with the B-C bond in **3**. But since this bond is now practically broken , the Ψ_2 state lies higher than the Ψ_1 state . The

third state , Ψ_3 , is the quadruplet state discussed above in Figures 10, 11.

The two diagrams in Figures 10 and 12 can be related through the energy level of the determinants in Figure 9, which shows that Ω_1 is lower in energy in the linear arrangement. This makes the corresponding Ψ_1(linear) lower in energy than Ψ_1(equilateral-triangular). Alternatively , one can relate the two Figures through the Jahn-Teller mechanism . Thus , the ground state in the equilateral triangle is degenerate , Ψ_1 and Ψ_2 in Figure 10, and is subject therefore to a Jahn-Teller distortion which stabilizes the ground state. One of the distortion modes is the elongation of the B-C bond which lifts the degeneracy and stabilizes Ψ_1 which becomes the only ground state of the linear system.

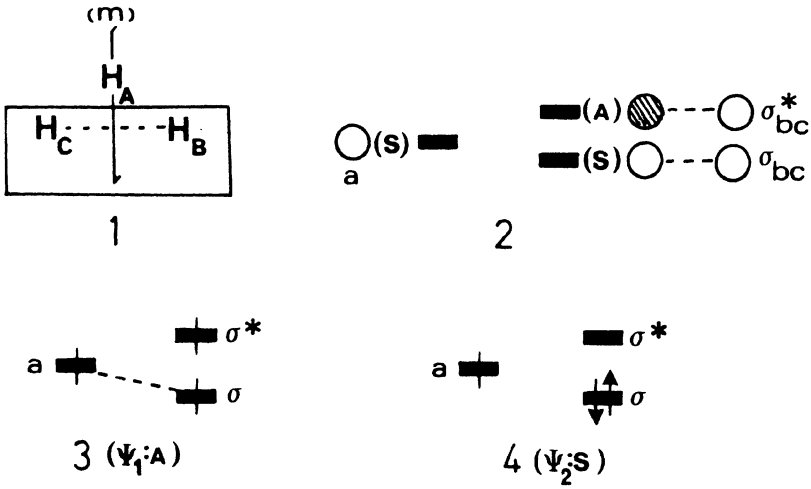

Figure 13. FO-VB diagrams for H_3, as an example of a three-electron/three-center system.

The three states can in turn be represented by use of VB wave functions which involve fragment orbitals (FOs) instead of AOs . This will economize the description and will clarify instantly the symmetry properties of the various states . The first step is to define the fragments in a way that takes advantage of the common elements of symmetry of the equilateral and linear arrangements. Exemplified with H_3, this fragmentation along with the appropriate mirror plan (m) are shown in **1** in Figure 13 . The orbitals in **2** are the terminal σ_{bc} and σ_{bc}* FOs and the central atomic orbital a. These orbitals can be classified according to their symmetry with respect to the mirror plan in **1** as symmetric (S) or antisymmetric (A) .

The bond-diagram **3** is antisymmetric (A) and shows the maximum bonding between the two fragment via a single bond-pair which binds the central atom to the two terminal atoms. The singlet-pairing energy is the usual 2hs term , taken over the σ_{bc} and a orbitals which form the bond-pair . The corresponding wave function is the negative combination of two

determinants, in analogy with the HL wavefunction in the atomic case . Thus,

$$\Psi(3) = N\,[\,|\sigma_{bc}{}^{*}\sigma_{bc}\mathbf{a}| - |\sigma_{bc}{}^{*}\underline{\sigma}_{bc}\mathbf{a}|\,] \tag{39}$$

A simple mapping of this wavefunction into atomic VB components shows that this state is Ψ_1 of Figure 11 and 12 (mixed with some of the zwitterionic configurations).

If the bond-pair in **3** is uncoupled, we will then obtain the quadruplet state Ψ_3 which has also a total symmetry **A**. In **4** in Figure 13, is shown another VB-FO diagram which has a symmetry **S** and lacks a bond-pair between the fragments. **4** has on the other hand , an electron-pair in the σ_{bc} FO. This electron-pair corresponds to a bond only at the equilateral triangular arrangement . Thus , **3** and **4** become degenerate at the equilateral triangular geometry , but **3** is below **4** at any other geomtry which deviates from this geometry toward a linear arrangement . By its properties, **4** must then be the state Ψ_2 of Figures 10-12 . It is apparent by now that the VB-FO approach is in a quick and easy way to construct a many electron VB wavefunction .

The principles exemplified above for constructing the states of three-electron/three-center case are quite general and may be applied to other systems with an average of one electron per center .

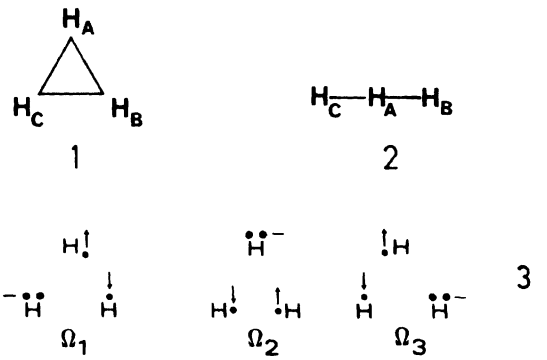

Figure 14. Geometries (in **1**,**2**) and three VB determinants for H_3^- (in **3**).

2.2.5. *State for Mixed-Valence Species* . These cases involve an average of a noninteger number of electrons per site, and in organic chemistry these constitute all the molecular ions. Qualitative and quantitative aspects of the state construction , for such species , have been discussed by Fischer and Murrell [24] , Soos [23] , Shaik [15a,b] , Malrieu [22b] and Epiotis [19,36] . The interaction and state ordering patterns are case dependent , and it is therefore, not reasonable to generalize in the way which we did for the preceding class of species. There is though a general aspect , and this is that the VB-mixing pattern resembles in each case a Mobius or a Huckel problem whose atomic connectivity is identical to the configuration-mixing-connectivity [15a, 36], in the same sense which is discussed above

for the three electron problem .This property of the VB mixing pattern allows also to construct VB-mixing diagrams quite easily . Let us demonstrate this general feature by way of an example .

The example we choose is the H_3^- species in the equilateral triangular and linear arrangements , as shown in **1** and **2** in Figure 14 . Let us restrict ourselves to the singlet and triplet states generated from determinants with no net spin in the *z* -direction . The corresponding determinants are shown as two sets in eq 40a and 40b,

$$\Omega_1 = |a\underline{b}c\underline{c}| \; ; \; \Omega_2 = |a\underline{a}b\underline{c}| \; ; \; \Omega_3 = |ab\underline{b}\underline{c}| \tag{40a}$$

$$\Omega_{1'} = |\underline{a}bc\underline{c}| \; ; \; \Omega_{2'} = |a\underline{a}\underline{b}c| \; ; \; \Omega_{3'} = |\underline{a}b\underline{b}c| \tag{40b}$$

The first set (Ω_1 - Ω_3) is shown in **3** in the Figure and the second set, which is not shown, involves simply exchange of the two spins. These determinants are all degenerate in the equilateral case. However, in the linear case, both $\Omega_{1,1'}$ and $\Omega_{3,3'}$, each lose a pair-overlap-repulsive interaction and descend below $\Omega_{2,2'}$.

Since there are six unique determinants, we can form from them three independent Kekule structures. The singlet Kekule structures corresponds to the negative combinations of the corresponding determinants from the two sets . For example , the combination which describes a structure with an A-B bond and an electron pair on site C is shown in eq. 41a . The corresponding triplet structure is the positive combination in eq. 41b (the normalization constants are written with neglect of overlap).

$$\Omega_{1-1'} = \Omega_{1S}(A\text{-}B) = N[\,\Omega_1 - \Omega_{1'}\,] \qquad ; N \sim 2^{-1/2} \tag{41a}$$

$$\Omega_{1+1'} = \Omega_{1T}(A^{\bullet}\,{}^{\bullet}B) = N[\,\Omega_1 + \Omega_{1'}\,] \; ; \; N \sim 2^{-1/2} \tag{41b}$$

There will be such a singlet-triplet pair for each one of the linkages in **1** and **2** in Figure 14. The singlets will be more stable than the triplets by the quantity 4hs (see Figure 5).

Let us begin with the equilateral case .Within each set (i.e., Ω_1 - Ω_3 and $\Omega_{1'}$ - $\Omega_{3'}$) the determinants differ by two spin-orbitals and their interaction matrix element are of the 2hs type. However, determinants which belong to the different sets, but not to the same Kekule structure, differ by one spin-orbital and interact via the matrix element h_{rs}. The matrix elements are detailed in eq. 42 and are all of equal magnitude.

$$< \Omega_1 \,|H|\, \Omega_{2'} > = h_{ac} \; ; < \Omega_1 \,|H|\, \Omega_{3'} > = h_{bc} \; ; < \Omega_2 |H|\, \Omega_{3'} > = h_{ab} \tag{42}$$

Since h > 2hs , unless s ≥ 0.5 , we may disregard the 2hs terms for qualitative purposes and focus only on the effect of the h terms (the conclusions are by the way *more clear cut* without the simplification of the matrix element). The matrix elements for the singlet and triplet Kekule structures follow then from eq. 42, and become,

$$<\Omega_{1S} \,|H|\, \Omega_{2S} > = < \Omega_{1S} \,|H|\, \Omega_{3S} > = < \Omega_{2S} \,|H|\, \Omega_{3S} > = -N^2 h \sim -h \tag{43}$$

$$< \Omega_{1T} \,|H|\, \Omega_{2T} > = < \Omega_{1T} \,|H|\, \Omega_{3T} > = < \Omega_{2T} \,|H|\, \Omega_{3T} > \sim +h \tag{44}$$

The interaction pattern of the singlet Kekule structures is shown in **1** in Figure 15 and is seen to correspond to a Mobius-connectivity . The resulting states after interaction have the expected ordering and ground state degeneracy of the Mobius pattern as shown in **2.** The

interaction pattern of the triplet Kekule structures is shown in **3** in the Figure and is seen to correspond to a Huckel connectivity with the typical state ordering in **4** [19b (pp. 432-437); 24]. Since the lowest triplet state results from a Huckel VB-mixing, then this state is stabilized by the VB-mixing more than does the lowest singlet state, which results from a Mobius VB mixing. Consequently, the ground state of the equilateral triangle becomes a triplet state .

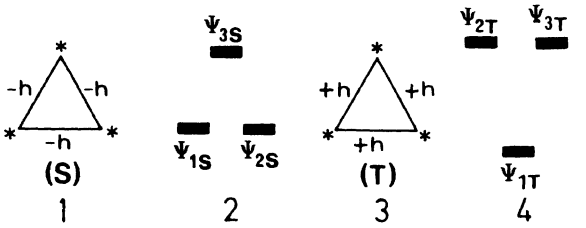

Figure 15. The interaction pattern of the singlet (in **1**) and triplet (in **3**) Kekule structures (symbolized by *), and the corresponding states (in **2,4**) of equilateral H_3^-.

This singlet-triplet state ordering will alternate with the number of electrons in the mixed valence polygon . Thus, for polygons with 4q electrons (e.g., H_3^- , H_5^+, etc.,) the ground state will be triplet , while for polygons with 4q+2 electrons (e.g., H_3^+, H_5^-, H_7^+, etc.,) the ground state will be singlet [24]. This is unlike the situation in polygons with an average of one electron per center, where the ground state is always a singlet state.

Before we can treat the linear H_3^-, it is worthwhile to generate the state manifold of the equilateral triangle by way of a VB-mixing-diagram. The three singlets of Figure 15 are the Mobius-like linear combinations of the singlet Kekule structures in the first column in eq. 45a-c:

$$\Psi_{1S} = 6^{-1/2}\,[2\Omega_{2S} - (\Omega_{1S} + \Omega_{3S})]\ ;\ \Psi_{1T} = 3^{-1/2}[\Omega_{2T} + \Omega_{1T} + \Omega_{3T}] \qquad (45a)$$

$$\Psi_{2S} = 2^{-1/2}\,[\,\Omega_{1S} - \Omega_{3S}]\ ;\ \Psi_{2T} = 2^{-1/2}\,[\Omega_{1T} - \Omega_{3T}] \qquad (45b)$$

$$\Psi_{3S} = 3^{-1/2}[\Omega_{2S} + \Omega_{1S} + \Omega_{3S}]\ ;\ \Psi_{3T} = 6^{-1/2}\,[2\Omega_{2T} - (\Omega_{1T} + \Omega_{3T})] \qquad (45c)$$

Here Ω_{2S} is taken as a pivot configuration , but as is common in degenerate states we can take any linear combination of Ψ_{2S} and Ψ_{1S} to represent the two degenerate states. The states of eq. 45 are generated in Figure 16 by use of interaction diagrams. In the first step in **1**, we form two linear combinations from Ω_{1S} and Ω_{3S} . Because of the negative sign of the matrix element (eq. 43), the negative combination Ω_S^- is the lower while the corresponding positive combination is the higher. In the next step in **2**, we interact the remaining configuration Ω_{2S}, with these two linear combinations . The negative linear combination does not find a match and becomes itself the state Ψ_{2S} . The only possible interaction is between Ω_{2S} and Ω^+ which generate Ψ_{1S} and Ψ_{3S}. Since the matrix element

has a negative sign , the lower state Ψ_{1S} is the negative combination of its constituents , while the upper state Ψ_{3S} , is their positive combination . This is in full accord with the states description in eq. 45.

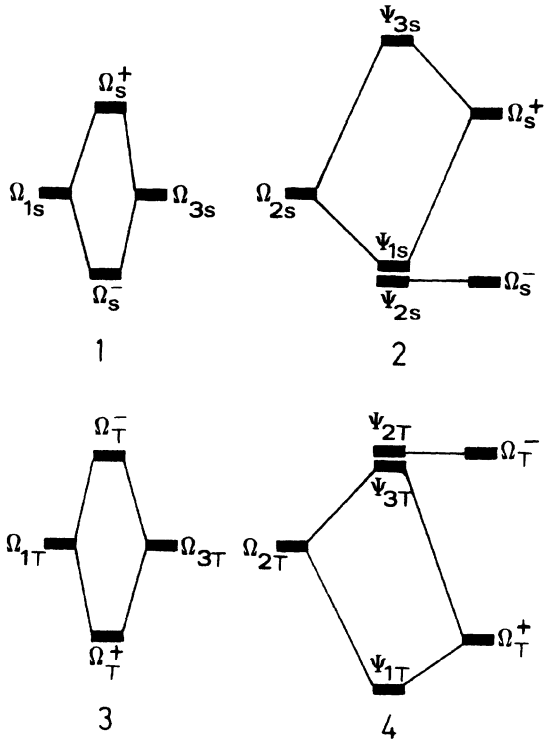

Figure 16. VB-mixing diagrams for the singlet (in **1,2**) and triplet (in **3,4**) states of equilateral H_3^-.

The triplet states have an inverse interaction pattern due to the positive matrix elements (eq. 43) . As shown in **3** in Figure 16 , the positive combination, of Ω_{1T} and Ω_{3T} , is now the lower . In **4** we see that the interaction between Ω_{2T} and the two combinations Ω^+ and Ω^-. As in the singlet case here too, Ω^- which has no match becomes the state Ψ_{2T}, while the interaction of Ω_{2T} with Ω^+ generates bonding and antibonding combinations. The bonding combination is the all-positive conbination , while the antibonding state is the corresponding negative combination . This is in full accord with the expression of the states in eq.45 .

Two features, in the linear arrangement, are different with respect to the equilateral arrangement. Firstly , in the linear geometry , the three Kekule structures are nondegenerate

because all h_{bc} and corresponding overlaps are practically zero, due to the large B···C distance. Accordingly Ω_{2S}, which possesses a "long-bond" B···C and two pairs of overlap-repulsion , is the singlet Kekule structure with the highest energy , as shown in **1** in Figure 17 . Secondly , because of the vanishing h_{bc} matrix element (see eq. 42) , we can not disregard anymore the 2hs elements we neglected in the case of the equilateral triangle. The resulting matrix element between Ω_{1S} and Ω_{3S} is now,

$$< \Omega_{1S} |H| \Omega_{3S} > \sim 2h_{ac}s_{ab} + 2h_{ab}s_{ac} = 4hs \tag{46}$$

The positive sign of the matrix element requires that the bonding combination of the two Kekule structures will now be the positive combination , as shown in the righthand side of

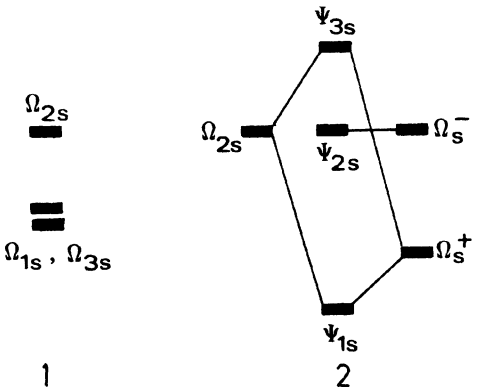

Figure 17. Kekule structures (in 1) and a VB-mixing diagram (in 2) for the singlet states of linear H_3^-.

the mixing-diagram in **2** in Figure 17. As before , Ω_S^- which has no match becomes a state, Ψ_{2S} . On the other hand, Ω_{2S} and Ω_S^+ interact to generate bonding and antibonding combinations, Ψ_{1S} and Ψ_{3S}. Since the interaction matrix element between Ω_{2S} and Ω_S^+ has a negative sign, that is,

$$< \Omega_{2S}|H|\Omega_S^+ > \sim 2^{-1/2}(-h_{ab} - h_{ac}) = -2^{1/2}h \tag{47}$$

the resulting bonding state Ψ_{1S} is the negative combination of Ω_{2S} and Ω_S^+, with a higher contribution from the latter constituent. The corresponding positive combination is the antibonding state, Ψ_{3S} which is made of a major contribution from Ω_{2S} . Thus , with

respect to the singlet manifold of the equilateral triangle , what change are the removal of the degeneracy between Ψ_{1S} and Ψ_{3S} , as well as the relative weights of their contributing Kekule structure.

The corresponding triplets are analyzed in Figure 18 . The three triplet Kekule structures are still degenerate , because all of them suffer now from the same number of pair-overlap repulsive interactions.The matrix element between Ω_{1T} and Ω_{3T} now vanish (counting up to hs terms) so that the Ω_T^+ and Ω_T^- combinations are approximately degenerate, as shown in the VB-mixing diagram **1**. The mixing pattern remains as in Figure16 (**4**), with the exception that the degeneracy of the equilateral arrangement is removed .

The global ground state of linear H_3^- is now the singlet state Ψ_{1S}, and a ground state inversion occurs as the geometry changes from an equilateral to a linear arrangement . This is illustrated schematically in **2** in Figure 18. The reason for the state ordering in the linear case is quite simple. To begin with, the triplet Kekule structures are higher than the corresponding singlets by twice the 2hs quantity , as shown in Figure 5 . The only chance for a triplet ground state occurs when the triplet configuration interaction is larger than the corresponding interaction in the singlet manifold ; a situation which is met in the equilateral triangular- but not in the linear-arrangement. An equivalent conclusion is reached by considering the Jahn-Teller argument on the doubly degenerate singlet state (**2**, Fig. 18).

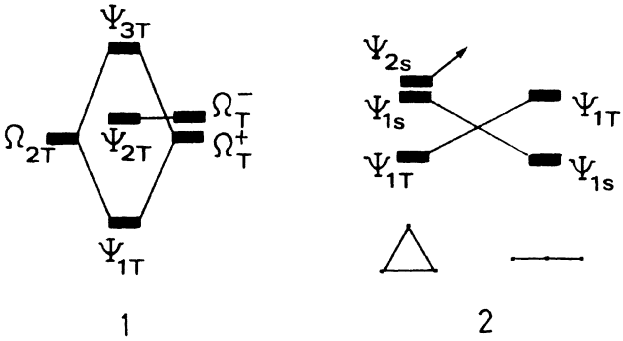

Figure 18. A VB-mixing diagram for the triplet states of linear H_3^- (in **1**). The interchange in the identity of the ground state, for H_3^-, as a function of geometry (in **2**).

Let us turn now to inspect the FO-VB representation of H_3^- and focus on the singlet states . Figure 19 illustrates in **1** the fragmentation and the orbitals of the fragments, with symmetry classification with respect to the mirror plan bisecting the molecule. The three lowest FO-VB diagrams are shown in **2**, **3** and **4**.

The diagram **2** has a bond-pair (dashed line) which links the two fragments. This bond-diagram corresponds to the positive combination Ω_S^+, of the Kekule structures Ω_{1S} and Ω_{3S} , as discussed above in Figure 17. The FO-VB diagram **3** has a bond between hydrogens B and C , due to the doubly occupied σ orbital . This diagram corresponds to the third Kekule structure Ω_{2S} . The two diagrams **2** and **3** possess the same symmetry (S) and can therefore mix to give two states , which are Ψ_{1S} and Ψ_{3S} , discussed above in Figure 17. In the equilateral arrangement the two diagrams contribute equally to the state

description . However , in the linear arrangement **3** is much less stable than **2** , so that the ground state will be composed of a higher contribution of **2** , while the upper state will have a higher contribution from **3** . Our approximate VB calculations (with neglect of overlap in the normalization constants) gives us a weight ratio of 72% of **2** vs 28% of **3** in the ground state while using Hiberty's method of mapping [21b] of an exact-CI wave function with an STO-3G basis gives a weight ratio of 85% vs 15% [37].

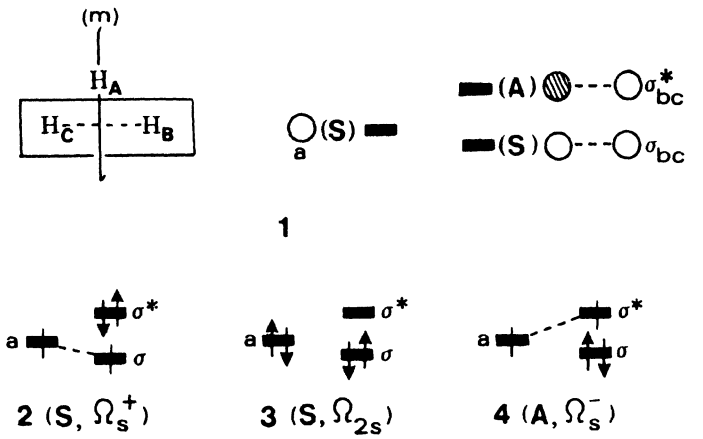

Figure 19. FO-VB diagrams for H_3^-, as an example of four-electron/three-center system. The Ω's are the singlet wave functions discussed in Fig. 17.

The diagram in **4** in Figure 19 has seemingly a bond-pair , in the orbitas σ* and a, which only pairs up the spins but does not contribute to bonding owing to a symmetry-mismatch between the orbitals. There is another electron pair though in **4**, in the σ orbital which is reponsible for the B-C bond . This diagram corresponds to the negative combination of the A-B and A-C Kekule structures, and therefore this is the state Ψ_{2S} discussed above in Figure 17. As may be seen from **4**, this state has a symmetry **A** unlike the preceding two states which have a symmetry **S** .

2.2.6.*VB States and Their MO Correspondences* . It is didactically useful to complete the correspondence all the way to the MO description of the various states [1]. Let us exemplify that with the two lower states of linear H_3^- and H_3. This is done in Figure 20 which shows in **1** the MOs , and in **2** the FOs which are used in the preceding discussions of the species. An approximate description of the ground state of H_3^- is the MO configuration $\varphi_1^2\varphi_2^2$ indicated in the Figure in **3**. This MO configuration corresponds to the

bond-diagram **4**, which itself is an approximate representation of the ground state Ψ_{1S}. In a similar manner, the MO configuration $\varphi_1^2\,\varphi_2^1\,\varphi_3^1$ in **5** is an approximate description of the second singlet state Ψ_{2S}. This MO configuration corresponds to the bond-diagram **6** which is a good representation of the VB state Ψ_{2S}.

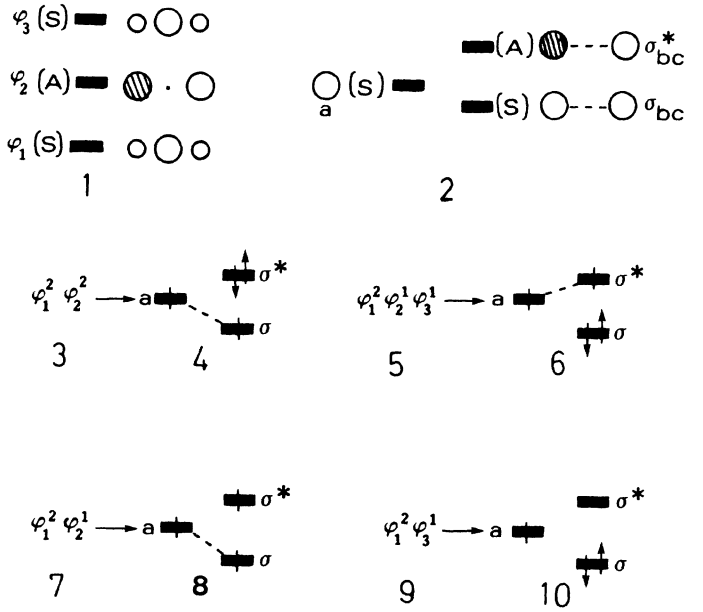

Figure 20. MO configurations and their corresponding FO-VB descriptions for linear H_3 and H_3^- species.

The correspondences for H_3 are also shown in Figure 20. Thus, the ground doublet state Ψ_1 is approximated by the MO configuration $\varphi_1^2\,\varphi_2^1$ in **7**, which is also an approximation of the bond-diagram **8**. The excited doublet state can in turn be approximated by the MO configuration **9** and the bond-diagram **10**.

Thus, in both H_3^- and H_3 *the energy gap between the two lowest states of the same multiplicity can be approximated by the energy gap between the MOs* φ_2 *and* φ_3. The same rule applies to all isoelectronic systems which delocalize three and four electrons over three centers. Some of these isoelectronic sytems are transition states in e.g., spin transfer and in S_N2 reactions, respectively. While the above correspondences may not seem all that exciting at first glance, they still have far reaching implications on transition state properties such as the quantum mechanical resonance-energy of the transition state, as we discuss in the following sections.

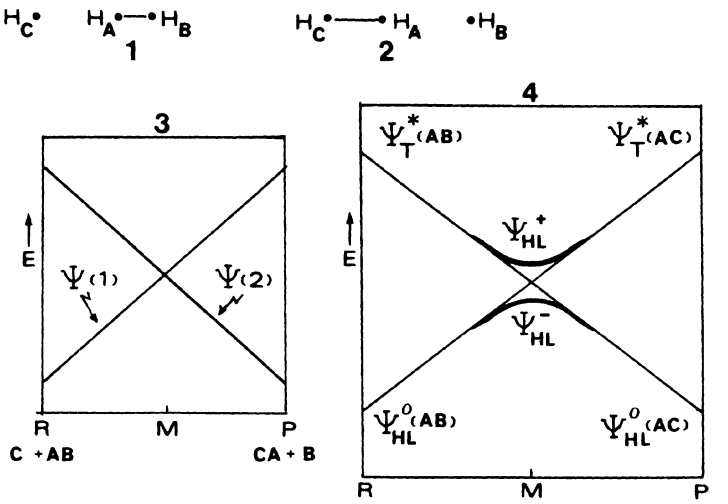

Figure 21. The HL configurations (in **1**,**2**), their energy variation along the reaction coordinate (in **3**) and their avoided crossing (in **4**) for the reaction $H_C^{\bullet} + H_A{-}H_B \rightarrow H_C{-}H_A + {}^{\bullet}H_B$.

3. Piecing up Potential Energy Curves for Prototypical Processes.

The preceding sections prepare the ground for the more complex construction process, of potential energy curves from VB-type building blocks. The principles of the approach have been developed in the reverse manner, by expanding MO-CI wave functions into VB components [1]. The expansion analysis has revealed a few principles which can be used to construct the potential energy curves of chemical reactions, and to understand the origins of their barriers and reactivity patterns [1, 3-6, 26-28]. Let us describe now the key principles by analyzing two prototypical reactions.

3.1. THE HYDROGEN ATOM EXCHANGE REACTION , $H^{\bullet} + H{-}H \rightarrow H{-}H + {}^{\bullet}H$.

This reaction belongs to a class of radical reactions which involve radical additions to unsaturated systems and atom abstractions by radicals. In all of these reactions, a net electron spin disappears on one atom and reappears on another . Therefore in keeping with the classification of reactions in term of electron- or group-transfers, these radical processes are referred to as spin-transfer reactions .

3.1.1. *The Covalent HL curves* . The key configurations which describe the H_3 complex along the reaction coordinate are the two HL forms which involve spin-pairing of the initial and final H-H bonds, and which are shown in **1** and **2** in Figure 21 . As shown in **3**, the two configurations interchange in energy along a reaction coordinate which stretches between *R*(reactants) and *P*(products). Let us consider first a reaction coordinate which involves a linear H_3 complex formed by a side-on attack of the radical on the molecule. Initially, at the *R* extreme of the reaction coordinate, where the A···B linkage is short

while the A···C linkage is infinitely long , the lowest configuration is $\Psi(1)$. Along the R-->P direction , $\Psi(1)$ rises in energy because the A-B bond is broken and replaced by C· · A repulsion. This repulsive interaction is evident in the form of the HL wave function in eq. 48, which shows that in the first determinant the A···C interaction is pure triplet , while in the second determinant this interaction is 50% triplet and 50% singlet . The two contributions together amount to 75% of a triplet A··C repulsion [26b, 38].

$$\Psi_{HL}(A\text{-}B) = N[\,|c\underline{a}\underline{b}| - |c\underline{a}b|\,]\,; \quad |c\underline{a}b| = 0.5[\,\Psi_{HL}(C\text{-}A) - \Psi_T(C{\cdot\cdot}A)\,] \qquad (48)$$

It is clear then that at the P extreme $\Psi(\mathbf{1})$ becomes an excited configuration of the HL wave function $\Psi(\mathbf{2})$ of the A-C bond, and this excited configuration is close in character to the triplet state of the A-C bond plus an uncoupled radical on H_B . Symmetric arguments apply to the second curve $\Psi(\mathbf{2})$, in the reverse direction P-->R .

The crossing between the two curves occurs at the uniform geometry where the C···A and A···B distances are equal . At this point (M), the two HL configurations are degenerate and will avoid the crossing by mixing. The mixing of these two HL configurations is described above in Section 2.2.4 and the corresponding configurations after mixing are Ψ_{HL}^{+} and Ψ_{HL}^{-} , the latter being lower in energy (consult e.g., Figure 12). This avoided crossing is shown in Figure 21 in **4**. Already at this stage we can see that the avoided crossing is a reorganization mechanism [39] whereby the reaction complex can change its electronic character from reactant-type to product-type, through a transition point which is approximately a resonance hybrid of the two. In the linear geometry, of the reaction complex, this transition point is also going to be the transition state of the reaction .

This avoided crossing of the HL curve merely reflects the chemical transformation , in which the respective bonds are interchanging. This feature will be common to all transformations which involve bond breaking and bond making , as recognized years ago by Evans and Polanyi [40] .

3.1.2. *Generation of a State Correlation Diagram Through Secondary Configuration Mixing.* Let us continue and convert the two curves into state curves [1, 3, 4] . For this purpose we need to specify a little better the nature of the two excited anchor points of the two HL curves in Figure 21. Consider curve $\Psi(\mathbf{1})$ at the P extreme of the reaction coordinate . As shown in eq. 48 , this wave function is 75% the triplet state of the C-A bond . This is so if we continue to regard the H_3 complex as a single entity, and use for it spin eigenfunctions of the total spin operator for three electrons. It is convenient to take this option, because we need not change the character of the curve and we can thereby quantitatively compute and define it rigorously [7, 26b (in the Appendix)]. For conceptual purposes however , we can regard the H_CH_A and $\cdot H_B$ fragments, at the P extreme, as two entities, each having a spin-eigenfunction of its own spin operator. Then at the P extreme, $\Psi(\mathbf{1})$ becomes the triplet state of the A-C bond plus the state of the radical $\cdot H_B$. Symmetric arguments can be used for the curve $\Psi(\mathbf{2})$ in the P--->R direction in **3** (Figure 21). There result then two intersecting curves which are anchored at the two HL ground configurations and the two triplet states of the interchanging bonds [15b]. This information is indicated on the anchor points of the curves in **4** in Figure 21, where Ψ_{HL}^{o} is the HL configuration at the equilibrium bond length of either the A-B or C-A bonds , while Ψ_T^* is the vertical triplet excited state of the bond at the same bond lengths .

To complete the conversion of the curves into states we need to consider the mixing of the secondary configurations into the covalent curves. The secondary configurations are zwitterionic structures which are expressed in eq. 49a-c , in their pictorial representations,

$$Z_1 = H_C\cdot\ H_A^+ :H_B^- \ ;\ Z_2 = H_C\cdot\ H_A:^-\ H_B^+ \tag{49a}$$
$$Z_3 = H_C:^-\ H_A^+ \cdot H_B \ ;\ Z_4 = H_C^+\ H_A:^-\ \cdot H_B \tag{49b}$$
$$Z_5 = H_C:^-\ H_A\cdot\ H_B^+ \ ;\ Z_6 = H_C^+\ H_A\cdot\ :H_B^- \tag{49c}$$

The behavior of these configurations along the reaction coordinate is shown in **1** in Figure 22 . Consider the crossing of Z_1 and Z_3 for example. Initially, at *R*, Z_1 is stabilized relative to Z_3 by the electrostatic attraction across the A···B linkage . Finally , at the *P* extreme, the situation is reversed and Z_3 is stabilized over Z_1 by exactly the same extent. Similar arguments apply to the pairs Z_2, Z_4 and Z_5, Z_6. Consequently , the Z configurations cross in pairs at the midpoint of the reaction coordinate (*M*) above the crossing point of the HL curves .

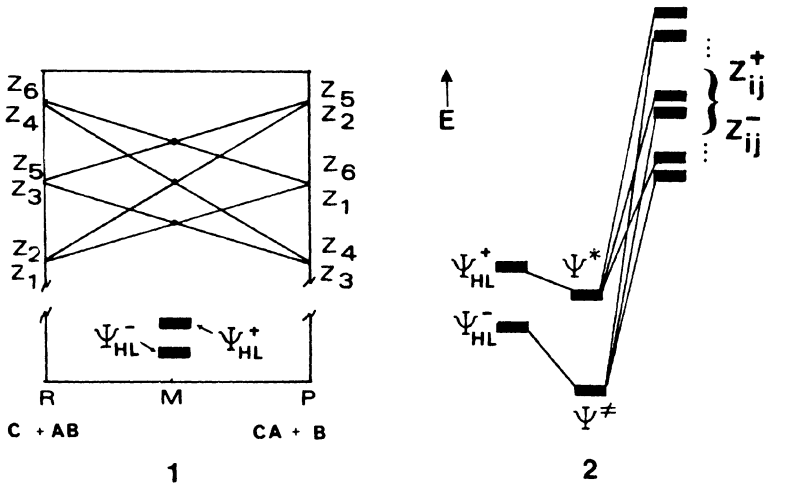

Figure 22. The behavior of the Z configurations, for the $H^\cdot + H_2$ reaction, along the reaction coordinate (in **1**). The VB-mixing diagram (in **2**) and the resulting twin states at the crossing point.

The mixing at the midpoint of the reaction coordinate will convert the two HL combinations into states. The HL and Z configurations are different by a single spin-orbital, in each case, because all the Z configurations can be generated from the HL configurations by shifts of single electrons. Therefore the mixing pattern can be deduced by appeal to the mixing rule in *CASE A* (Section 2.1.3). By taking positive and negative linear combinations between the $Z_{i,j}$ pairs, at the crossing point, we can facilitate their mixing patterns with Ψ_{HL}^+ and Ψ_{HL}^-.

The corresponding VB-mixing diagram is shown in **2** in Figure 22. Thus the lowest HL combination mixes with the negative combination of each $Z_{i,j}$ pair, while the positive HL combination mixes with the positive combination of the same $Z_{i,j}$ pair . The resulting states

are $\Psi^{\neq}$ and Ψ^{*} which correspond to the transition state and its vertical excited state; the twin states of the avoided crossing region. Written in a perturbational form, the two states are expressed as follows:

$$\Psi^{\neq} \sim [\,(\mathrm{H^{\cdot}\ H{-}H}) - (\mathrm{H{-}H\ {\cdot}H})\,] + \lambda\,[\,(\mathrm{H{:}^{-}\ H^{\cdot}\ H^{+}}) + (\mathrm{H^{+}\ H^{\cdot}\ H{:}^{-}})\,] \qquad (50a)$$

$$\Psi^{*} \sim [\,(\mathrm{H^{\cdot}\ H{-}H}) + (\mathrm{H{-}H\ {\cdot}H})\,] + \lambda\,[\,(\mathrm{H{:}^{-}\ H^{\cdot}\ H^{+}}) - (\mathrm{H^{+}\ H^{\cdot}\ H{:}^{-}})\,] \qquad (50b)$$

In accord with our convention, here too H–H stands for a mixture of the HL configuration and its two corresponding zwitterionic structures, $H^{+}:H^{-}$ and $H{:}^{-}\ H^{+}$. Thus, the transition state $\Psi^{\neq}$ is seen to involve configurations which are absent in the reactant's and product's bonds. These "foreign" characters are the Z_5 and Z_6 configurations which appear explicitely in eq. 50a.

Let us consider next the mixing of the Z configurations into the other points of the covalent curves, by appeal to **4** in Figure 21 . Thus, a positive combination of a pair of Z configurations mixes into each of the ground HL configurations to complete the corresponding bond wave functions at the two extremes of the reaction coordinate; Z_1+Z_2 mixes into the ground HL configuration at the *R* extreme , while Z_3+Z_4 mixes into the ground HL configuration at the *P* extreme . On the other hand, there is no mixing between the Z configurations and the upper anchor points of the curves, because these points correspond to the triplet states of the ground state bonds. In any other point along the reaction coordinate, all the Z configurations *mix into each of the covalent curves to form thereby state curves with a mixed VB character* [1, 4, 15b].

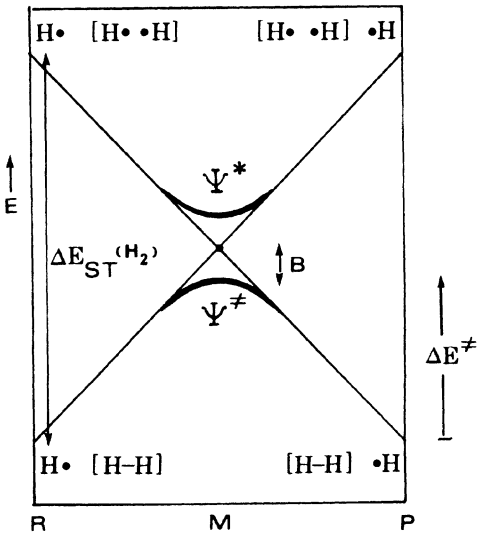

Figure 23. A state correlation diagram (SCD) for the process $H^{\cdot} + H_2 \rightarrow H_2 + {\cdot}H$. The diagram gap, $\Delta E_{ST}(H_2)$, is the singlet-to-triplet excitation of the short bond. The degree of avoided crossing is *B*. The barrier is $\Delta E^{\neq}$. The transition state is $\Psi^{\neq}$.

The situation is summarized in Figure 23. This is a state correlation diagram (SCD) which is composed from two curves that are anchored at the ground and triplet excited states of reactants and products [1, 15b, 38]. The two curves intersect along the reaction coordinate and by avoiding their crossing there result a barrier and a transition state for the spin transfer reaction , $H^{\cdot} + H_2 \text{-->} H_2 + {}^{\cdot}H$.

3.1.3. *Dependence of the State Correlation on the Reaction Coordinate* . How does the SCD depend on the choice of the reaction coordinate ? Consider the same spin-transfer reaction but now passing through an equilateral triangular H_3 transition structure. The reactant and product anchor states are, by definition, invariant to the choice of the reaction pathway . What remains therefore is to ascertain the nature of $\Psi^{\neq}$ and Ψ^* . From their expressions in eq. 50 , it is apparent that $\Psi^{\neq}$ and Ψ^* are the two degenerate doublet states of the equilateral triangular H_3, as discussed above in Section 2.2.5 and in Figures 10 and 11. Thus, the state correlation in Figure 23 does not change with the choice of the reaction coordinate . What changes is the degree of avoided crossing between the curves which goes to zero in the equilateral triangular structure.

The equilateral triangular structure is of course not a true transition state but a higher order critical point which is stabilized by distortion to a linear structure [e.g., pp. 97 in reference 12] . This stabilization is shown in Figure 24 which also illustrates the variation in the degree of avoided crossing in terms of the gap between the states $\Psi^{\neq}$ and Ψ^* .

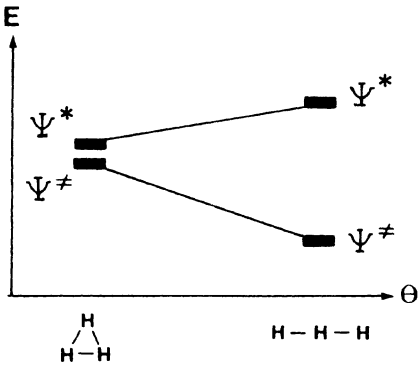

Figure 24. The energies of the $\Psi^{\neq}$ and Ψ^* states as a function of the H-H-H angle for $H_3^{\cdot}$. Note, the avoided-crossing is zero at the equilateral triangular geometry.

3.2. THE HYDROGEN ION EXCHANGE REACTION , $H^- + H\text{-}H \text{-->} H\text{-}H + H^-$.

This reaction is a prototype of ionic exchange and displacement reactions such as proton transfer , S_N2 (i.e., CH_3^+ transfer), and so on [1, 3-6].

3.2.1. *The Covalent HL Curves* . The two HL structures are shown in **1** and **2** in Figure 25, and their intersection along the reaction coordinate is shown in **3** in the same Figure . Let us consider only the linear approach. As in the H_3 reaction , here too the rise of the HL

configurations along the reaction coordinate is contributed by the loss of the spin-pairing energy as well as by a pair-overlap repulsion energy. For example, along the R-->P direction , the HL bond of $\Psi(\mathbf{1})$ is broken and a three electron repulsion develops across the C···A linkage . In the P extreme $\Psi(\mathbf{1})$ becomes **4**, with a repulsive interaction across the short A···C linkage and a completely broken bond across the A···B linkage . Similarly , $\Psi(\mathbf{2})$ becomes **5** along the reverse direction, P-->R .

The crossing of the covalent curves is avoided by configuration mixing of the two HL structures, as discussed in Section 2.2.5 (eq. 46 and Figures 16 and 17 there). The avoided crossing, which is shown in **3** in Figure 25, generates positive and negative linear combinations , the lowest of which being Ψ_{HL}^{+} .

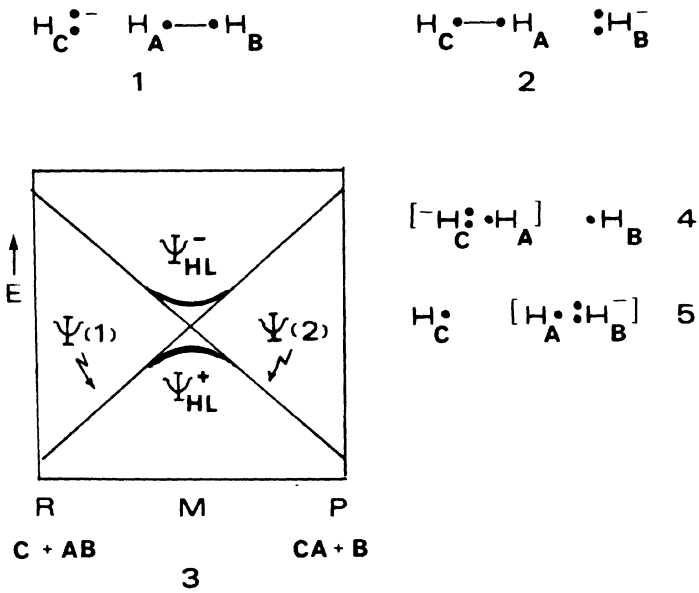

Figure 25. The HL configurations (in **1,2,4,5**), their crossing and avoided crossing (in **3**) along the reaction coordinate for $H_C{:}^- + H_A{-}H_B \text{ --> } H_C{-}H_A + {:}H_B^-$.

3.2.2. *Generation of a State Correlation Diagram by Secondary Configuration Mixing* . The secondary configurations, for the linear case, fall into two categories ; the long bond structure (LB) and the triionic structures (TI) . These are expressed in eq. 51a-c.

$$LB = H_C{\cdot}\, H_A{:}^-\ {\cdot}H_B \quad \text{(singlet-paired)} \tag{51a}$$

$$TI_1 = H_C{:}^-\ H_A^+\ H_B{:}^- \tag{51b}$$

$$TI_2 = H_C{:}^-\ H_A{:}^-\ H_B^+\ ; \quad TI_3 = H_C^+\ H_A{:}^-\ H_B{:}^- \tag{51c}$$

Figure 26 shows the energy variation of the secondary configurations along the reaction coordinate, $R \text{-->} P$, in **1** . Thus both LB and TI_1 replace, along the reaction coordinate, one interaction across the A···B linkage by the exact equal interaction across the C···A linkage . Qualitatively then, we may consider these curves to be fairly flat. On the other hand, TI_2 rises in energy because a favorable electrostatic interaction across A···B is replaced by overlap repulsion, due to the four electrons, across the C···A linkage. In TI_3, the behavior is the exact opposite, and therefore TI_2 and TI_3 cross one another at the midpoint of the reaction coordinate, above the crossing point of the two HL configurations.

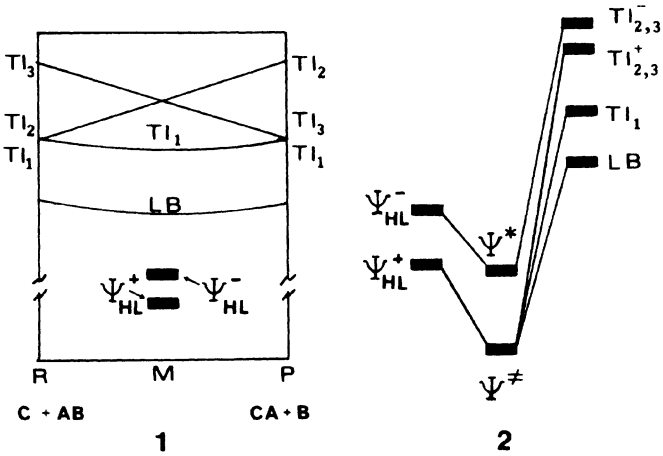

Figure 26. The behavior of the LB and TI configurations along the reaction coordinate (in **1**). The VB-mixing diagram and the resulting twin states at the crossing point (in **2**).

The mixing of the secondary configurations into the two HL combinations at the crossing geometry generates the twin states; the transition state and its vertical excited state, as shown in **2** in Figure 26 . The detailed expressions for the wave functions are as follows:

$$\Psi^{\neq} = [(H{:}^{-}\ H{\cdot}{-}{\cdot}H) + (H{\cdot}{-}{\cdot}H\ {:}H^{-})] - \lambda_1[LB] + \lambda_2[TI_1] + \lambda_3[TI_2 + TI_3] \quad (52a)$$

$$\Psi^{*} = [(H{:}^{-}\ H{\cdot}{-}{\cdot}H) - (H{\cdot}{-}{\cdot}H\ {:}H^{-})] + \lambda[TI_2 - TI_3] \quad (52b)$$

It is seen therefore, that the transition state involves mixing of the LB configuration , a character which is absent in both reactans and products.

Let us consider now the mixing of the secondary configurations into the two anchor points of the covalent curves, by appeal to Figures 25 and 26. At the R extreme, the ground HL configuration mixes with the positive combination $TI_2 + TI_1$ to generate the ground state of the reactants ($H_C{:}^{-} + H_A{-}H_B$) . A similar mixing with $TI_1 + TI_3$ at the P extreme,

generates the ground state of the products (H_C–H_A + :H_B^-). There is no mixing of LB into these ground states, because the connecting matrix elements are zero . For example , at the *R* extreme the LB and the ground HL configurations differ by a shift of one electron from H_C to H_A , and should therefore interact via the matrix element h_{ca} which is zero because of the infinite C···A distance , and so on [4, 15b].

None of the TI configurations can mix into the upper anchor points of the covalent curves, owing to the vanishment of the connecting matrix elements of the type h_{ca} (at the *R* extreme) and h_{ab} (at the *P* extreme) . On the other hand , LB differs from either of the two upper anchor points by single electron shifts across the short linkages. Thus LB mixes in, and generates the corresponding charge transfer (CT) states which consist of a radical and a radical-anion, as detailed in eq . 53a,b , where the entity with the short linkage is enclosed by parentheses :

$$\Psi_{CT}(R) = H_C\cdot\ (H_AH_B)^{\cdot -} = N\ \{[\ H_C\cdot\ (H_A\cdot\ :H_B^-)] - [\ H_C\cdot\ (H_A:^-\ \cdot H_B)]\} \qquad (53a)$$

$$\Psi_{CT}(P) = (H_C\,H_A)^{\cdot -}\ \cdot H_B = N\ \{[\ (H_C\cdot\ :H_A^-)\ \cdot H_B\ ] - [\ (H_C:^-\ \cdot H_A)\ \cdot H_B]\} \qquad (53b)$$

The corresponding mixing matrix elements have negative signs (see Section 2.2.5) , and therefore the CT states are the negative combinations of the corresponding configurations .

In all other points of the reaction coordinate, all the secondary configurations mix into each of the covalent curves which become thereby state curves. The resulting SCD is shown in Figure 27 which is composed of two intersecting curves, which are anchored at the ground and corresponding charge transfer states of reactants and products. By avoided crossing there result the transition state and barrier for the hydrogen ion exchange reaction .

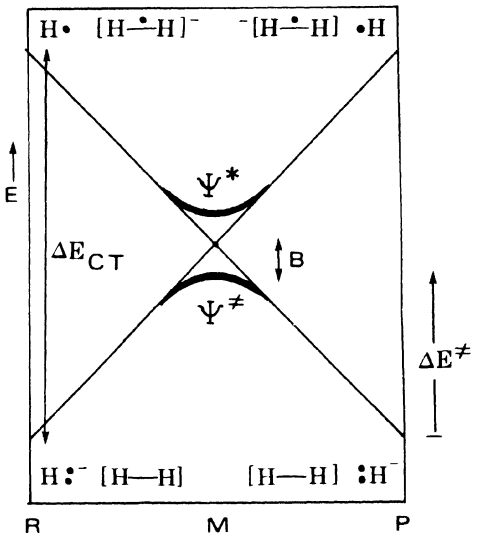

Figure 27. A state correlation diagram (SCD) for the process $H:^- + H_2 \rightarrow H_2 + :H^-$. The vertical charge transfer energy , that is, the diagram gap, is ΔE_{CT} . The degree of avoided crossing is *B* . The barrier is $\Delta E^{\neq}$. The transition state is $\Psi^{\neq}$.

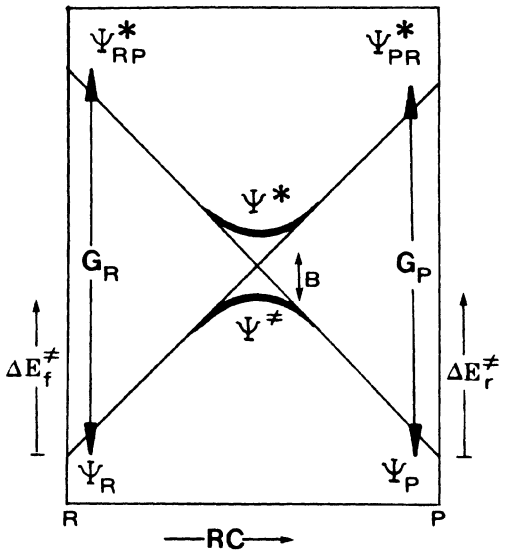

Figure 28. An SCD for a general chemical step. The *G*'s are energy gaps at the two extremes of the reaction coordinate (RC).

3.3. GENERALIZATIONS OF SCD's AND THEIR PHYSICAL INTERPRETATION.

The SCD's for other reactions can be generated in the same detailed manner as the above. By use of effective configurations (Section 2.2.3), one may also limit the discussion to a minimal number of configuratios which involve the bonds and electrons which are reorganized during the chemical transformation [1, 3, 4, 28a]. Instead of repeating this, by now, quite monotonous excercise we attempt hereafter to understand the underlying principles of the SCD and from there to generalize to other reactions [1,4]. A prerequisite for such a generalization is the understanding of the nature of the unique excited states of the SCD's .

3.3.1. *The Excited States of the SCD's , What Do They Signify ?* The SCD's of the two prototypical reactions can be represented by the general diagram in Figure 28 [4]. We saw that in each case, a direct correlation between the ground state wave functions of reactants and products was impossible because Ψ_R and Ψ_P constitute different spin-pairing schemes. The transformation of Ψ_R to Ψ_P requires therefore the involvement of two unique excited states, Ψ_{RP}^* and Ψ_{PR}^* . Thus , Ψ_{RP}^* is on the one hand , a vertical excited state of Ψ_R , and on the other hand, it possesess the same spin-pairing pattern of Ψ_P . Symmetrically, Ψ_{PR}^* is a vertical excited state of Ψ_P but has the spin-pairing pattern of Ψ_R . This spin-pairing similarity is the root cause for the correlations $\Psi_{RP}^* \rightarrow \Psi_P$ and $\Psi_{PR}^* \rightarrow \Psi_P$. For this reason , we have used the heuristic name , "electronic image" or "image state", to describe these unique excited states [1, 4]. Thus, all that needs to be established for a given reaction is the identity of the "image states" . The completion of the correlation lines will

then follow Figure 28 . The SCD in Figure 28 is appropriate for the description of any chemical step which involves an interchange of at least one bond, or of ionic by covalent bonds [3, 26a].

An easy way for identifying the "image states" is to use FO-VB representations of the anchor states [1, 4]. Figure 29 shows such representations of Ψ_R and $\Psi_{RP}*$ pairs , for the two prototypical reactions discussed above. Thus, in **1** we show the representation of Ψ_R for the spin-transfer reaction, and in **3** we show the corresponding representation for the hydride exchange reaction. In each Ψ_R case, the electrons are paired in the seperate reactants. On the other hand, in the $\Psi_{RP}*$ representations there exists, in each, a bond-pair which couples the electrons of the two reactants. This bond-pair will eventually become the new C-A bond at the *P* extreme of the reaction coordinate . Also, in each $\Psi_{RP}*$ there is an electron in a $\sigma*$ orbital of the molecule, and this electron occupancy is responsible for the eventual cleavage of the old A–B bond at the *P* extreme. These electronic features make each of the $\Psi_{RP}*$ states an "image state" of its corresponding product state , Ψ_P [1, 4].

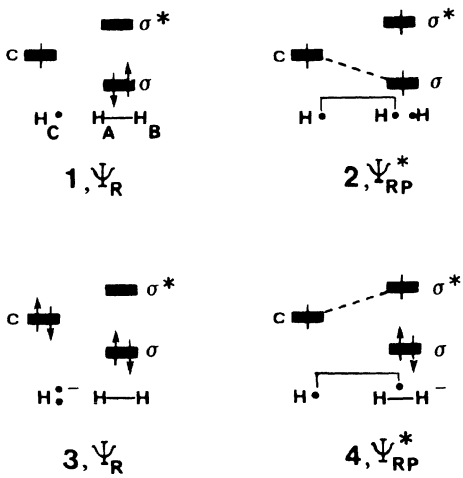

Figure 29. FO-VB representations of Ψ_R and $\Psi_{RP}*$ pairs for the exchange reactions of H· (in **1**,**2**) and of H^- (**3**,**4**).

3.3.2. *Generalization of SCD's.* Clearly then , to get the "image states" from their ground states all we need to do is to reorganize the electrons among the orbitals of the reactants and to generate intermolecular bond pairs; *one bond-pair for each new bond that is formed during the reaction* . This will automatically take care also of the bond breaking process. Thus a bond-paired "image state" enfolds the entire bond interchange event. Chemical processes can therefore be classified according to the excitations which are required to satisfy the correct number of bond-pairs in the "image states". The two prototypical reactions project the two elementary excitations. The triplet excitation is required when no change occurs in the oxidation state of the reaction centers, as in spin-transfer reactions . A

charge transfer excitation is required whenever the process involves changes in the oxidation state of the reaction centers, as typical in reactions between a nucleophile and an electrophile. Simple processes which involve exchange of only one bond will also involve one of these excitations, as summarized in the following statements :

STATEMENT 1 : The "image states" for spin transfer reactions are vertical triplet states, which involve a triplet excitation of the electron pair in the bond which has to be broken during the transformation .

STATEMENT 2 : The "image states" for reactions which involve electrophile and nucleophile combinations are vertical charge transfer states ,which involve a transfer of a single electron from the nucleophile to the empty orbital of the bond (in the electrophile) which has to be broken during the transformation .

More complex reactions involve exchanges of more than one bond, as is the case in elimination reactions or in cycloadditions, and so on. As a rule, each bond exchange requires a single excitation which may either be charge transfer or triplet excitation or a combination of the two [5, 28a] . This depends on the nature of the reaction, and the possibilities are summarized in the following statements :

STATEMENT 3 : For a reaction which is attended by bond exchanges without changes in the oxidation state of the reaction centers, the "image states" involve only triplet excitations, one for each bond which has to be broken in the reaction .

STATEMENT 4 : For a reaction which is attended by both bond exchange and changes in the oxidation states of reaction centers , the "image states" involve a charge transfer excitation for each pair of centers that udergo a formal redox. The rest of the excitations will be triplets. The total number of excitations must equal the number of bonds which are broken during the reaction.

3.3.3. *SCD's for Stereochemical and Regiochemical Pathways*. How does one construct the SCD's for the alternative regio- or stereochemical pathways which are possible for a given pair of reactants ? Consider for example, a radical abstracting an atom from a molecule . This reaction can occur in the two distinct ways described in eq. 54.

$$C^{\cdot} + A\text{–}B \longrightarrow C\text{–}A + B^{\cdot} \qquad (54a)$$
$$C^{\cdot} + A\text{–}B \longrightarrow C\text{–}B + A^{\cdot} \qquad (54b)$$

Figure 30 provides an analysis of these reactions in terms of the anchor states, at the reactant extreme *R* of the reaction coordinate. The reactant state in **1** is common to both pathways . Shown in **1** are only the orbitals and electrons of the bond which has to be broken during the reaction and the singly occupied orbital of the attacking radical [1, 4]. Since in each of the pathways one bond is broken and exchanged, this requires according to *STATEMENT 3* , a single triplet excitation which is the $\sigma \rightarrow \sigma^*$ promotion, shown in **1**-->**2** in the Figure . There are two ways to form a single bond-pair from the three unpaired electrons in **2** , and the two spin-pairing modes are the "image states" , **3** and **4** in the Figure.

The two "image states" in Figure 30 are initially degenerate at the *R* extreme of the reaction coordinate, where the bond-pair interaction is zero due to the infinite distance between the reactants. However as the reactants approach one another, maximization of the c-σ and c-σ^* bond-pair interactions will require different approaches of the radical to the

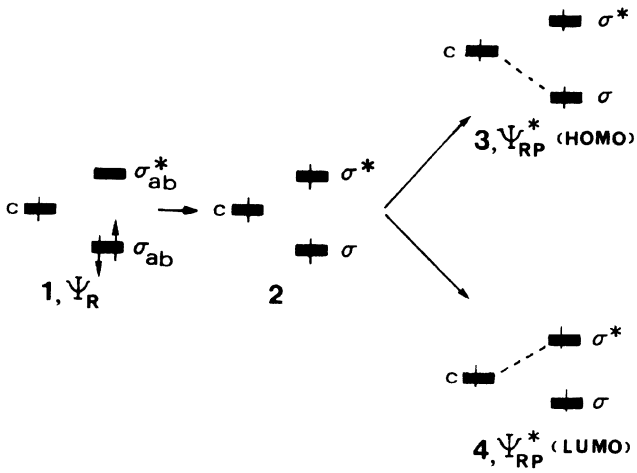

Figure 30. The Ψ_R and Ψ_{RP}* states in the SCD's which describe the regiochemical pathways of the reaction between C• and A-B (eq. 54).

molecule. Thus, **3** will correlate with the product state in a pathway which maximizes the bond-pair interaction of the radical with the σ orbital of the molecule. If the atom A is more electronegative than the atom B, then the σ orbital possesses usually a larger coefficient on atom A. Therefore maximization of the c-σ bond-pair interaction will involve a radical attack on the A site of the molecule, as in eq. 54a. On the other hand, **4** will correlate with the product state along the pathway which maximizes the bond-pair interaction with σ*, and this, in turn, requires attack on the less electronegative site B, as in eq. 54b.

The exact same analysis pertains to a radical attack on the two sites of a substituted olefin, only that in this case the orbitals of the molecule are π and π*. We may refer, in general, to the orbital pair of the molecule as the HOMO-LUMO pair of a given variety (e.g., σ–type or π-type). Using this terminology, it is apparent that the "image states" correspond to the regiochemical pathways, of radical attack, which are controlled by the HOMO (**3**) or LUMO (**4**) coefficients [41, 42].

Thus, to generate SCD's which describe two regiochemical pathways we use, at the *R* extreme of the reaction coordinate, Ψ_{RP}* states which involve the same electronic promotion but two distinct bond-pairing modes. By appeal to the quantities in Figure 28, these regiochemically related SCD's will have the same diagram gap, G_R, at the *R* extreme of the reaction coordinate, and will differ in their G_P gaps at the *P* extreme.

The above description is suitable also for stereochemically related SCD's. Consider for example, the cycloaddition reaction of two ethylenes which may in principle take place either in the two synchronous modes, supra-supra (*ss*) and supra-antara (*sa*) [2], or in an asynchronous fashion through a transoid-biradical intermediate, as shown in eq. 55.

$$2\,C_2H_4 \longrightarrow C_4H_8 \quad (ss \text{ or } sa) \tag{55a}$$

$$2\,C_2H_4 \longrightarrow {\cdot}CH_2CH\text{-}CHCH_2{\cdot} \longrightarrow C_4H_8 \tag{55b}$$

Figure 31 shows the anchor states corresponding to the *R* extreme of the reaction coordinate. Thus, in any pathway the ground state is described by **1**, where each molecule is represented by two electrons in its π orbital. Since two bonds are broken in all the pathways, this requires a double triplet excitation , which is shown in **1**--->**2** in the Figure [1,4] . The two distinct ways to couple these four electrons into two singlet spin-pairs are **3** and **4** . In **3** the spin-pairs involve π of one reactant with π* of another. Since π and π* have different nodal properties (different local symmetry), the only way to make the spin-pairs in **3** into bond-pairs is to couple the two ethylenes in an *sa* manner, which allows overlap between π and π*. On the other hand, to get two bond-pairs from the spin-pairs in **4** , the olefins must be coupled in the *ss* manner. Thus, **3** and **4** are the "image states" of the formally allowed ("A") and forbidden ("F") pathways .

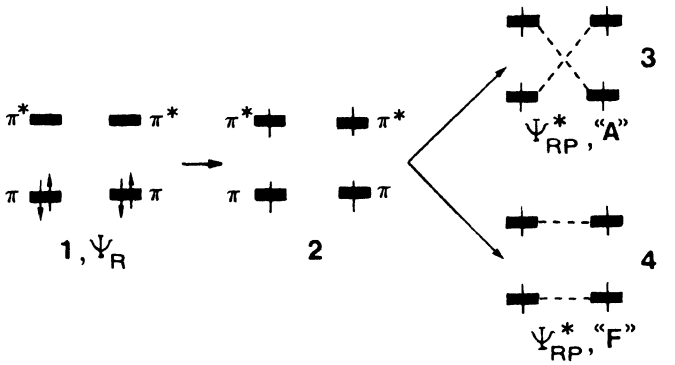

Figure 31. The Ψ_R and Ψ_{RP}^* states in the SCD's which describe the stereochemical pathways of a 2+ 2 cycloaddition (eq. 55). The Ψ_{RP}^* "image states" are appropriate also for a general cycloaddition where each reactant is represented by its HOMO and LUMO.

Figure 32 analyzes the situation for the biradical pathway which is illustrated in **1** . The corresponding "image state" is indicated in **3** as $\Psi_{RP}^*(BR)$. The main bond-diagram for the process is **3a** , while the minor diagram is **3b**. At the biradical geometry , this "image state" will correlate with the diradical state which possesses two electrons in the σ-type MO (**4**), and single electrons in each of the MO's shown in **5** and **6**. After rotation and ring closure to the final cyclobutane product , the contribution of the diagram **3b** will vanish for reasons of symmetry .

Thus, regardless of the stereochemical pathway which connects reactants and products, there is avoided crossing which involves the same anchor states which differ only in the mode of pairing up the spins in the four reactant orbitals. Since at the R extreme, all these spin-pairing modes are degenerate, then the SCD's involve the same energy gap, G_R (see Figure 28 for the various quantities) but may differ in the heights of the crossing point and

the degree of avoided crossing. These conclusions are in accord with detailed quantitative analyses of the avoided crossing [43] and with a related qualitative analysis [44].

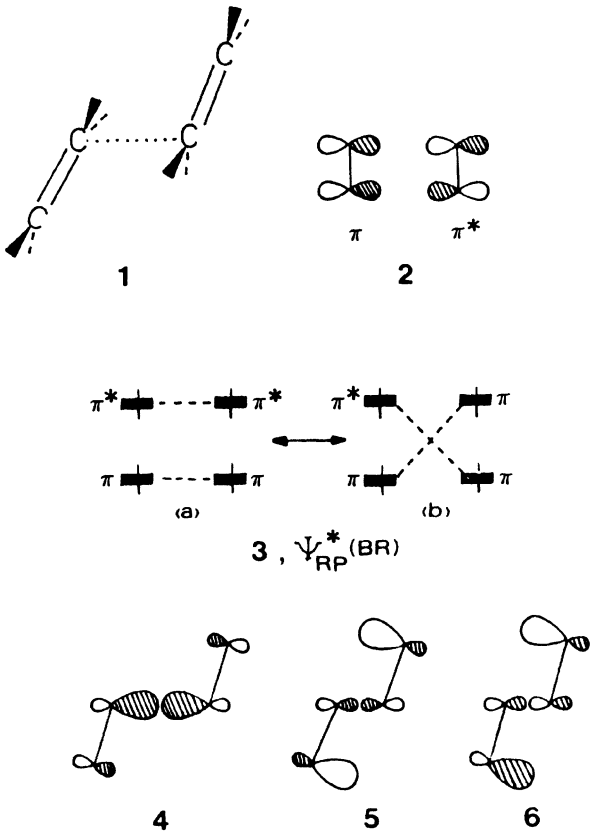

Figure 32. The biradical pathway (in **1**), the π and π^* orbitals which are possessed by each reactant (in **2**), and the "image state" for the process (in **3**). The σ bond-orbital (in **4**) and the singly occupied orbitals of the biradical intermediate (in **5**,**6**).

The above procedure can be repeated, for other cycloadditions (e.g., the Diels-Alder reaction) as well as for pericyclic reactions, without changes in the final description of the corresponding SCD's. The "image states" for the allowed ("A") and forbidden ("F") pathways will be identical to **3** and **4** in Figure 31, where now the orbitals are generally the HOMO and LUMO of the reacting molecules or fragments. The avoided crossing is thus a result of the nature of the electronic reorganization and not of orbital symmetry or of reaction pathway [1, 3-6, 15, 26b]. Figure 28 is accordingly applicable for the description

of any chemical step which involves bond exchange or changes in the oxidation states of reaction centers.

3.3.5. *The degree of Avoided Crossing - The Quantum Mechanical Resonance Energy of the Transition State. The Mechanism of Activation and the Form of the Reaction Barrier*. An important quantity in Figure 28 is B which is the energy stabilization due to the mixing of the two localized state curves in the crossing point. The term localized refers to the fact that each curve describes a single bond-pairing pattern. As such, the B parameter is the *Quantum Mechanical Resonance Energy (QMRE) of the transition state* [26].

Having a physical meaning for B, we turn to Figure 28 to show that the SCD describes the activation process as *a deformation which is required to cause electronic delocalization, so that new bonds may replace old ones* [1, 4, 26, 27f,g].

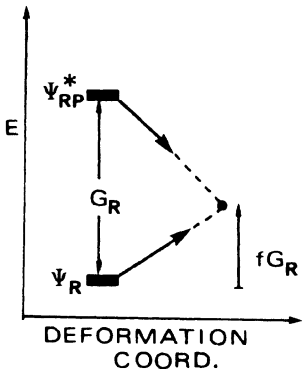

Figure 33. The crossing of Ψ_R and $\Psi_{RP}{}^*$ is achieved by deformations. The total deformation energy is fG_R.

According to Figure 28 the transition state is obtained at the crossing point of Ψ_R and $\Psi_{RP}{}^*$. But since initially these two states are separated by the vertical energy gap G_R, their energy equality will be acheived by bond distortions and nonbonded interactions. As schematized in Figure 33 these deformations (including bond distortions and nonbonded interactions) destabilize the ground state and stabilize the excited state until the gap is overcome and energy equality, that is crossing, is attained. It follows that the height of the crossing point is the total deformation energy which the ground state of the reactants has to experience in order to achieve resonance with the excited state. This is expressed in eq. 56

$$\Delta E_{def}(R) = fG_R \quad ; \quad f < 1 \tag{56}$$

which simply means that *the deformation energy is proportional to the gap that has to be overcome by the distortions in order to bring two different bonding schemes into resonance.* At the crossing point the two configurations mix and generate the transition state which is endowed with QMRE stabilization relative to its localized constituents.The barrier for the forward reaction, R --->P, is given then as a balance between the deformation required to

acheive resonance and the resulting stabilization due to delocalization , that is,

$$\Delta E_f^{\neq} = \Delta E_{def}(R) - B = fG_R - B \tag{57}$$

All the quantities in this equation have now a clear physical significance in terms of fundamental properties of the transition state and its constituent fragments [26].

Returning now to the activation scheme in Figure 33, it is important to recognize that while any distortion will raise the ground state, only specific distortions will stabilize the excited state in an efficient manner. Thus, *the geometry of the transition state will be determined by these distortions which cause simultaneously, the steepest decsent of* Ψ_{RP}* *and the shallowest ascent of* Ψ_R *. In this manner there will result the lowest crossing point and hence, the lowest barrier.* Clearly, the identity of the distortions and their extent may be deduced, for a given reaction, from the electronic structure of Ψ_{RP}* [4, 27f-h] .

The activation process of the products can be defined in a completely analogous manner by use of the gap G_P in Figure 28. The expression of the deformation is eq. 58a and the reverse barrier reads according to eq. 58b. Alternatively, the ΔE_{def} quantities of reactants and products can be related through the reaction energy , ΔE^o as shown in eq. 58c.

$$\Delta E_{def}(P) = f\,'G_P \tag{58a}$$

$$\Delta E_r^{\neq} = f\,'G_P - B \tag{58b}$$

$$\Delta E_{def}(P) = fG_R + |\Delta E^o| \tag{58c}$$

Equations 57 and 58b are compact expressions which describe a mechanism of activation by reliance on fundamental properties of the reactants or products; namely their vertical excitation energies G_R and G_P . These equations may be used to discuss reactivity trends in *reaction families* where the parameters f and B are family constants . Such families have been shown to exist in S_N2 reactions [4; 27a-g,i] and more recently we have used linear free energy relations based on eq. 57 to identify such families in; cation-anion recombinations [26a] , nucleophilic attacks on esters [26c] and in the Menschutkin reaction of substituted pyridines with alkyl iodides and fluorosulfonates [45].

There is another way to apply the model, by deriving an expression for the barrier with an explicit dependence on all the independent parameters of the two curves in Figure 28. Such an approximate expression is eq. 59 [4(Appendix A eq. A.15), 46].

$$\Delta E^{\neq} \sim \{[f_R + f_P + (0.5 - f_P)\,\Delta E^o / G_R]\, G_R\,(G_P + \Delta E^o) / (G_R + G_P)\} - B \tag{59}$$

Here, the f 's are parameters which describe, respectively, the curvatures of the two curves, Ψ_{RP}* --->Ψ_P and Ψ_R -->Ψ_{PR}*. The ΔE^o is the energy difference between products and reactants, and the G's are the energy gaps between the curves at the extremes of the reaction coordinate. While the energy quantities in eq. 59 have a clear physical significance, that of the f parameters is somewhat more complex. These parameters depend on ineractions between the reacting partners at both the ground and excited states of the SCD [4; 27c,f,h,i]. Thus, the f parameters are measures of the efficiency of the distortions, which are scematized in Figure 33, to cause shallowest ascents of the ground states and steepest descents of the excited states of the SCD. In the Marcus theory, for example, the two f parameters are 0.25 [47]. However our application of the model to nucleophilic substitution [4] and recent theoretical calculations give so far a range of f values, between 0.1 to

≥0.5[7, 48].

Equation 59 can be used to discuss the variation of the barrier as a function of substituent effects on all the above reactivity papameters. This has been achieved so far only for the S_N2 reaction , for which all the parameters of the curves are, in principle, understood and known [4, 49].

In summation , the model in Figure 28 and the resulting barrier equations, 57-59, offer a unified treatment of chemical steps.

4. Future Directions

In what ways can a theoretical model be useful ? We feel that one of these ways is to make the model interactive with the experimental observation, so that theoretical quantities can be derived from the empirical kinetic data. We have already shown that eq. 57 (or eq. 58b) can serve as a basis for linear free energy correlations [26a,c]. Thus, it is assumed that among the ensemble of reactions, which obey a single mechanism, there exist "families" in which both the f and B parameters are constants. If there exist indeed such series they will give linear plots of the type shown in Figure 34 where the $\Delta E^{\neq}$'s are the experimentally measured barriers, whereas the G_R's are the vertical gaps in the SCD of the reaction. As may be seen, the slope of the line and its intercept are the theoretical parameters f and B, respectively. Of course, the linearity of the plot may arise from compensating changes in all the parameters, and there is therefore a need to devise a check-up procedure to verify whether the line belongs to a real "family" or not. Such a procedure is in progress using the explicit barrier expression in eq. 59 [45].

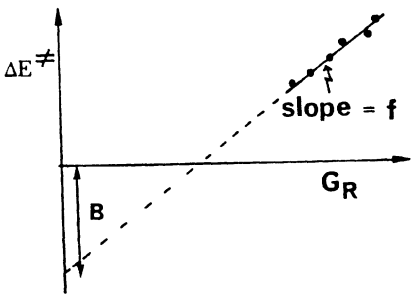

Figure 34. A linear free energy plot using eq. 57. The slope of the line and its intercept are f and B, respectively.

Let us assume for the sake of argument, that we have found such a "family" and that it has passed the check-up procedure. In such a case we have "measured" two properties of the transition state. The first propery is $\Delta E_{def}(R)$, namely the deformation energy of the reactants in their transition state geometry. This property is obtained from the f G_R quantity according to eq. 57. If we have also measurements of the reaction energy ΔE^o, we can then define, as well, the deformation energy of the products in their transition state geometry , by use of eq. 58c.

The second property is B . We thus have "measured", by the linear free energy plot , the quantum mechanical resonance energy of the transition state. This is in itself quite exciting, but there are further implications which appear equally appealing. By use of Figure 28 we can derive a general expression for B in terms of the energy gap between the twin-states of the avoided crossing, $\Psi^{\neq}$ and Ψ^{*}. This expression is eq. 60,

$$B = [(1 - S_{RP}) / 2] \Delta E(\Psi^{\neq}, \Psi^{*}) \qquad (60)$$

Here the S_{RP} is the overlap between the two state curves at the crossing point. Deriving an expression for this overlap would mean that a "measurement" of B is also a "measurement" of $\Delta E(\Psi^{\neq}, \Psi^{*})$. This last quantity is *a vertical electronic excitation of the transition state*, and at this point Figure 20 may be consulted for the MO interpretation of this electronic transition for our two prototypical reactions. It follows that the simple linear free energy plot of Figure 34 can potentially lead to *spectroscopic information on the transition state*, albeit with crude accuracy and in an incomplete manner.

Thus, by allowing the model to interact with the empirical kinetic data it is possible to extract significant information on the transition state. The next development must involve the translation of the so extracted properties of the transition state into its detailed geometric features. The whole process is schematized in Figure 35 which describes a classical dilemma in science. We have an unseen entity which is the transition state and which we nevertheless wish to observe. We carry out the observation by way of kinetic measurements which give, via the barrier of the reaction, the free energy of the transition state. We now bring a theory which pictures how transition states are formed, and we use the theory to cross-examine the experimental energy-data. This interplay provides us, in turn, with NEW properties of the transition state ; the deformation energy , the QMRE (i.e., B) and an electronic transition of the transition state. These new properties are related to the geometry of the transition state and to its orbital interactions, and therefore these "observables" may be used, in principle, to "solve" the structure of the transition state. For this process to take place we must derive rigorous expressions for the theoretical quantities, B and ΔE_{def}. This is where VB theory can help , and this is why we saw it essential to summarize in this chapter principles of qualitative VB theory [50].

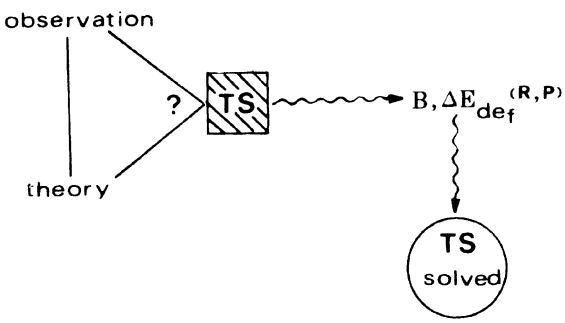

Figure 35. Description of the interaction of theory and experiment to "solve" the structure of the transition state (TS).

Appendix. Enumeration of Normalization Constants, Energies, and Matrix Elements of VB Determinants.

This Appendix describes a scheme, which can be easily taught , for enumerating VB terms. The scheme involves no approximations and can be use to obtain all the contributing terms, if one so wishes. The approximations are introduced later in order to minimize the number of terms. Let us exemplify the procedure with the following VB determinant,

$$\Omega = N\ |a\underline{a}b\underline{b}| \tag{A.1}$$

whose diagonal spin-orbital product is,

$$\psi_d = a(1)\underline{a}(2)b(3)\underline{b}(4) \qquad ;\ (1,2,\ldots \text{ are electron indices}) \tag{A.2}$$

To begin with there are a total of 24 permutations on this diagonal element , and this means a lot of work. This can be minimized by eliminating all the permutations which transpose spin-orbitals of a different spin variety (α and β), because these permutations have zero contributions to all the title quantities. We can therefore group the spin-orbitals of the determinant into two subsets and define elementary permutations which act exclusively within the subsets. From there we can build up more complex permutations, until we include all the contributing permutations.

The elementary permutations are the indentity , which leaves unchanged the ψ_d of any determinant, and the permutations which cause a single pairwise transposition in the order of the spin-orbitals. The sign of the elementary permutations is given by $(-1)^t$, where t is the number of pairwise transpositions. For the diagonal element in eq. A.2 the elementary permutations are,

$$(-1)^t P_{elem} = P_0\,,\ -P_{ab}\,,\ -P_{\underline{ab}} \qquad ;\ (P_0 = \text{identity}) \tag{A.3}$$

where the subscript of the permutation defines the transposition it applies.

Successive applications (mathematically this is a simple product of the operations) of the elementary permutations are used to construct more complex permutations. In this manner we generate composite permutations which perform two-, three-, and so on, pairwise transpositions within each spin-orbital subset, or composite permutations which perform the transpositions simultaneously on the two spin-orbital subsets. For our example, the only composite permutation is of the second kind, that is,

$$(-1)^t P_{comp} = (-P_{ab})\,(-P_{\underline{ab}}) = P_{ab}P_{\underline{ab}} \tag{A.4}$$

A further simplification can be acheived by realizing the equality of permutations which act on the different subsets but on the same space-orbitals. In our example this applies to,

$$P_{ab} = P_{\underline{ab}} \tag{A.5}$$

The total number of permutations which are selected by this process are then,

$$(-1)^t P_i = P_0\,,\ -2P_{ab}\,,\ P_{ab}P_{\underline{ab}} \tag{A.6}$$

where P_{ab} is seen to have a double weight. We have thus minimized the number of permutations in our example from 24 to 3. For a 6x6 determinant, this selection process leaves 15 of the 720 possible permutations.

Having the permutations, we now set a tableau which includes them , as shown below. The first column of the tableau lists all the permutations with their signs and weights. The title line in the second column of the tableau is the diagonal spin-orbital product , of eq. A.2, and lined up below it are all the permuted products which result after the permutations that are indicated in the first column, in each line. In the rest of the columns we list the contributions of each permutation to the overlap, ε_r and hs-energy terms.

$(-1)^t P_i$	a **a** b **b** 1 2 3 4	"s"	$\varepsilon_r[h(1) +...+ h(4)]$	$hs[h(1) +....+ h(4)]$
1)P_0	a **a** b **b**	1	$2\varepsilon_a + 2\varepsilon_b$	------
2)$-2P_{ab}$	b **a** a **b**	$-2s_{ab}^2$	$-2\varepsilon_a s_{ab}^2 - 2\varepsilon_b s_{ab}^2$	$-4h_{ab}s_{ab}$
3)$P_{ab}P_{\underline{ab}}$	b **b** a **a**	$+s_{ab}^4$	------	$+4h_{ab}s_{ab}^3$

The column entitled "s" corresponds to the overlaps between the product in the title line and any one of the permutations in the lines that are below it, that is,

$$"s" = \langle \psi_d | (-1)^t P_i \psi_d \rangle \tag{A.7}$$

The first line in the tableau is identical to the title line and the corresponding overlap is 1. The rest of the overlaps easily follow from the type of the permutation ; its subscript defines the orbital-overlap integral , while the sign and preceding multiplier of the permutation define the sign of the orbital overlap and its weight. Thus for example,

$$-2P_{ab} \text{ ---> } -2s_{ab}^2 \tag{A.8}$$

$$P_{ab}P_{\underline{ab}} \text{ ---> } +s_{ab}^4 \tag{A.9}$$

and in general (unless permutations share common indices),

$$(-1)^t m P_{ij} P_{kl} P_{no}... = (-1)^t m s_{ij}^2 s_{kl}^2 s_{no}^2... \tag{A.10}$$

This can be achieved also by a digit-to-digit comparison of the title product with each of the permuted products. Thus, by comparing the second line to the title line, in the second column, we observe that the first digit in the title is a, while the first digit of the second line is b. This accounts for an s_{ab} term. The same occurence in the third digit leads to another s_{ab} term . The corresponding total overlap is the product of the two s terms , and this is multiplied, in addition, by the weight and sign of the corresponding permutation. All taken

together we get the overlap term in the second line of the tableau , and so on .

The squared normalization constant of the determinant can be obtained by simply summing the "s" column , and by taking the inverse of this sum. For $|a\underline{a}b\underline{b}|$ this becomes,

$$N^2 = 1 / [\, 1 - 2s_{ab}^2 + s_{ab}^4 \,] \tag{A.11}$$

The third and fourth columns of the tableau include energy terms which are determined with respect to the monoelectronic Hamiltonian,

$$H = h(1) + h(2) + h(3) + h(4) \tag{A.12}$$

which has four terms, one for each electron. The energy terms correspond to the following integral,

$$\langle \psi_d \mid h(1) + h(2) + h(3) + h(4) \mid (-1)^t P_i \psi_d \rangle \tag{A.13}$$

Accordingly, the total energy contribution, in each of the tableau lines, must include a total of four terms (this number is of course multiplied also by the weight and sign of the corresponding permutation. The terms can be deduced again by a digit-to-digit inspection of any of the spin-orbital products against the title product of the tableau.

Consider for example the ε_r terms coming from the first line and the title line . Here all the digits are identical and the contribution is $2\varepsilon_a + 2\varepsilon_b$, which is a simple sum of the corresponding identical digits, and is nothing else but a sum of the spin-orbital monoelectronic energies . Moving on to the second line now we have , in comparison with the title line, two identical and two nonidentical digits . Two of the Hamiltonian terms, whose electron indexes correspond to the indexes of the identical digits, contribute each an ε_r term, which is multiplied by the overlaps of the orbitals in the nonidentical digits. This ε_r term is multiplied in addition by the weight and sign of the permutation. For the second line this gives, $-2\varepsilon_a s_{ab}^2 - 2\varepsilon_b s_{ab}^2$.

The hs-terms in the fourth column are determined in the same manner , but are contributed by the nonidentical digits. If we go back to the second line we see that the first digit is different than the corresponding digit of the title. This contributes a resonance integral term, $\langle a(1) \mid h(1) \mid b(1) \rangle$. This term is, in turn multiplied by an overlap of the orbitals in the third digit which is also nonidentical , leading thus to $h_{ab}s_{ab}$. The h(3) term of the Hamiltonian provides, via the third digit, the other hs energy-term. The two terms are multiplied in addition by the weight and sign of the corresponding permutation to give, $-4h_{ab}s_{ab}$ in the fourth column of the tableau.

The energy columns are then summed up, and the result is multiplied by the N^2 term in eq. A.11.

It must be emphasized that the energy terms due to the bielectronic part of the Hamiltonian can be enumerated by use of the same tableau. We think however, at present, that qualitative understanding of VB theory does not require the bielectronic terms, and that in any event their influence can be incorporated into the effective values of the monoelectronic terms.

Matrix elements between determinants follow from the equation,

$$\langle \Omega_1 \mid H \mid \Omega_2 \rangle = N_1 N_2 [\, \langle \psi_{d,1} \mid H \mid P_{max} \psi_{d,2} \rangle + \\ + \langle \psi_{d,1} \mid H \mid \Sigma_\iota P_\iota \psi_{d,2} \rangle] \tag{A.14}$$

Here P_{max} is the permutation which causes maximum spin and orbital correspondence with $\psi_{d,1}$ by acting on $\psi_{d,2}$. The P_i terms are the rest of the permutations . The enumeration of

the matrix element terms can be achieved by use of the same type of tableau shown above. Firstly we verify that the two diagonal elements have spin correspondence. If they do not, we must first rearrange $\psi_{d,2}$ to have spin correspondence with $\psi_{d,1}$. We then enumerate the permutations of this rearranged $\psi_{d,2}$ by the exact same methodology we used above, and we collect the terms also in exactly the same manner.

Consider as an example the determinants $\Omega_1 = N_1$ |a**a**b| and $\Omega_2 = N_2$ |b**b**a|. The two determinants are already in spin correspondence, and we can therefore set the tableau with no initial rearrangement. The title product is always $\psi_{d,1}$, while the products in each line of the tableau are $\psi_{d,2}$ and its permutations. The tableau is shown below:

$(-1)^t P_i$	a **a** b 1 2 3	"s"	$\varepsilon_r[h(1) + ... + h(3)]$	$hs[h(1) + ... + h(3)]$
1) P_0	b **b** a	s_{ab}^3	-----	$3h_{ab}s_{ab}^2$
2) $-P_{ab}$	a **b** b	$-s_{ab}$	$-\varepsilon_a s_{ab} - \varepsilon_b s_{ab}$	$-h_{ab}$

The matrix element is the sum of the energy terms in the tableau, multiplied in addition by the product of the normalization constants. The latter quantities are determined as described already above. The leading term is seen to be $-h_{ab}$. This term is contributed by the permutation in the second line, which is also the permutation that has maximum correspondence with the title product. This matrix element is the one we describe in *CASE A*, in the text, for determinants which differ by one spin orbital.

If we use the entire matrix element to solve the determinant-mixing for a case where, $\varepsilon_a = \varepsilon_b = \varepsilon$, we obtain that the bonding state is the negative combination while the antibonding state is the positive combination. The corresponding expressions for the energy stabilization and destabilization are given by,

$$\Delta E_1 = (h_{ab} - \varepsilon s_{ab}) / (1 + s_{ab}) \tag{A.15}$$

$$\Delta E_2 = -(h_{ab} - \varepsilon s_{ab}) / (1 - s_{ab}) \tag{A.16}$$

These expressions are equivalent to two states interacting via an effective matrix element which is given by the *leading term*, $-h_{ab}$. This, in a way, justifies the simplification of the matrix element as advocated in the text.

Consider now the determinants $\Omega_1 = N_1$|a**b**| and $\Omega_2 = N_2$|**a**b|. The corresponding tableau is shown below, where now there is only one permutation to consider, the one which brings $\psi_{d,2}$ to spin correspondence with $\psi_{d,1}$.

$(-1)^t P_i$	a **b** 1 2	"s"	$\varepsilon_r[h(1) + h(2)]$	$hs[h(1)+h(2)]$
1) $-P_{ab}$	b **a**	$-s_{ab}^2$	-----	$-2h_{ab}s_{ab}$

The two configurations differ by two spin-orbitals which possess also opposite spins. This type of matrix element is the one described by *CASE B* in the text. Solution of the determinant-mixing gives two states. The bonding state is the negative combination , while the antibonding state is the positive combination. The stabilization and destabilization energy expressions are given in the following equations:

$$\Delta E_1 = 2(h_{ab} - \varepsilon s_{ab})s_{ab} / (1 + s_{ab}^2) = 2h'_{ab}s_{ab} / (1 + s_{ab}^2) \quad (A.17)$$

$$\Delta E_2 = - 2(h_{ab} - \varepsilon s_{ab})s_{ab} / (1 - s_{ab}^2) = -2h'_{ab}s_{ab} / (1 - s_{ab}^2) \quad (A.18)$$

It is important to recognize that in each of the above examples, the *sign* of the leading term in the matrix element is identical to the *sign* of P_{max} ,the permutation with the maximum correspondence.

The enumeration of the bielectronic contributions to the matrix element can be carried out by use of the same tableau. The tableau offers then quite an easy and automatic recipe for enumerating VB related terms.

Acknoeledgements

I am thankful to the following students,colleagues and friends whose collaboration has contributed to and inspired this work on organic-chemical reactivity: R.Bar, E.Buncel, D.Cohen, P.C.Hiberty, J.M.Lefour, P.Maitre, G.Ohanessian, A.Pross, H.B.Schlegel, G.Sini, I.H.Um, and S.Wolfe.

References and Notes

1. S.S. Shaik, *J. Am. Chem. Soc.* **103**, 3692 (1981).
2. R.B. Woodward and R. Hoffmann, *The Conservation of Orbital Symmetry*, Academic Press, New York, 1970.
3. A. Pross and S.S. Shaik, *Acc. Chem. Res.* **16**, 363 (1983).
4. S.S. Shaik, *Prog. Phys. Org. Chem.* **15**, 197 (1985).
5. A. Pross, *Adv. Phys. Org. Chem.* **21**, 99 (1985).
6. For a recent review of the model see, T.H. Lowry and K.S. Richardson, *Mechanism and Theory in Organic Chemistry,* Harper and Row, New York, 1987, pp. 218-222; 354-360.
7. A. Sevin, P.C. Hiberty and J.M. Lefour, *J. Am. Chem. Soc.* **109**, 1845 (1987).
8. O.K. Kabbaj, F. Volatron and J.P. Malrieu, Chem. Phys. Lett. in press.
9. F. Bernardi and M.A. Robb, *J. Am. Chem. Soc.* **106**, 54 (1984).
10. See for example, R. McWeeny, *Nature* **323**, 666 (1986).
11. Four recent VB-based methodologies, which have been applied to various molecules and reactivity problems, are ; (a) F.W. Bobrowicz and W.A. Goddard, III in , *Modern Theoretical Chemistry. Methods of Electronic Structure Theory*, H.F Scaefer, III (Ed.), Plenum, New York,1977, **Vol 3**, Chapter 4. (b) D.L. Cooper, J. Gerratt and M. Raimondi, *Adv. Chem. Phys.* **59**, 319 (1987). (c) P. C. Hiberty and J.M. Lefour *J.Chim.Phys.* **84**, 607 (1987).(d) S.C. Leasure, T.P. Martin, and G.G. Balint-Kurti, *J. Chem. Phys.* **80**, 1186 (1984).
12. T.A. Albright, J.K. Burdett and M.H. Whangbo, *Orbital Interactions in Chemistry,* Wiley, New York, 1985.
13. L. Libit and R. Hoffmann, *J. Am. Chem. Soc.* **96**, 1370 (1974).

14. N.D. Epiotis, W.R. Cherry, S. Shaik, R.L. Yates and F. Bernardi, *Topics Curr. Chem.* **70**, 1-250 (1977).
15. (a) S. S. Shaik, *J. Am. Chem. Soc.* **104**, 5328 (1982). (b) S.S. Shaik and R. Bar, *Nouv. J. Chim.* **8**, 11(1984). (c) S. S. Shaik and P.C. Hiberty, *J. Am. Chem. Soc.* **107**, 3089 (1985).
16. (a) L. Pauling, *The Nature of the Chemical Bond* , Cornell University Press, Ithaca, New York, 1960. (b) G. Wheland, *Resonance in Organic Chemistry* , Wiley, New York, 1955.
17. D.M. Hirst And J.W. Linnett, *J. Chem. Soc.* 1035 (1962), 1068 (1963).
18. R.D. Harcourt, *Lecture Notes Chem.* **30**, 1-260 (1982), especially Chapter 23.
19. (a) N.D. Epiotis, *Lecture Notes Chem.* **29**, 1-305 (1982). (b) N.D. Epiotis, *Lecture Notes Chem..* **34**, 1-585 (1983).
20. (a) W.A. Goddard, T.H. Dunning, Jr., W.J. Hunt, P.J. Hay, *Acc. Chem. Res.* **6**, 368 (1973). (b) G. Levin and W.A. Goddard, *J. Am. Chem. Soc.* **97**, 1649 (1975). (c) A.F. Voter and W.A. Goddard, *J. Am. Chem. Soc.* **108**, 283 (1986).
21. (a) P.C. Hiberty, *Isr. J. Chem.* **23**, 10 (1983). (b) P.C. Hiberty and C. Leforestier , *J. Am. Chem. Soc.* **100**, 2012 (1978); P.C. Hiberty, Int. J. Quant. Chem. **Vol. XIX,** 259 (1981). (c) P.C.Hiberty and G.Ohanessian, *J. Am.Chem. Soc.* **104**, 66 (1982). (d) P.C. Hiberty and G.Ohanessian, *J. Am. Chem. Soc.* **106**, 6963 (1984). (e) A. Sevin and M. Fontecave, *J. Am. Chem. Soc.* **108**, 3266 (1986).
22. (a) J.P. Malrieu and D. Maynau, *J. Am. Chem. Soc.* **104**, 3021 (1982); **104**, 3029 (1982). (b) X. Gadea, D. Maynau and J.P. Malrieu, Int. *J. Quant. Chem.* **Vol. XXVI**, 1 (1984).
23. (a) Z.G. Soos, *Isr. J. Chem.* **23**, 37 (1983). (b) S. Mazumdar and Z.G. Soos, *Synth. Metals* **1**, 77 (1979/80). (c) I.R. ducasse, T.E. Miller and Z. G. Soos, *J. Phys. Chem.* **76**, 4094 (1982).
24. H. Fischer and J.N. Murrell, *Theor. Chim. Acta (berl)* **1**, 463 (1963).
25. M.A. Fox and F.A. Matsen, *J. Chem. Educ.* **62**, 477 (1985).
26. (a) S.S. Shaik, *J. Org. Chem.* **52**, 1563 (1987). (b) S.S. Shaik, P.C. Hiberty, J.M.Lefour and G. Ohanessian, *J. Am. Chem. Soc.* **109**, 363 (1987). (c) E. Buncel, S.S. Shaik, I.H. Um and S. Wolfe, *J. Am. Chem. Soc.* **110**, 1275 (1988).
27. (a) S.S. Shaik and A. Pross, *J. Am. Chem. Soc.* **104**, 2708 (1982). (b) S.S. Shaik, *Nouv. J. Chim.* **6**, 159 (1982). (c) S.S. Shaik, *J. Am. Chem. Soc.* **105**, 4359 (1983). (d) S.S. Shaik, *Nouv. J. Chim.* **7**, 201 (1983). (e) S.S. Shaik, *J. Am.Chem. Soc.* **106**, 1227 (1984). (f) D.J. Mitchell, H.B. Schlegel, S.S. Shaik and S. Wolfe,*can. J. Chem.* **63**, 1642 (1985). (g) S.S. Shaik *Isr. J. Chem.* **26**, 367 (1985).(h) D. Cohen, R. Bar and S.S. Shaik, *J. Am. Chem. Soc.* **108**, 231 (1986). (i) S.S. Shaik, *Can. J. Chim..* **64**, 96 (1986). (j) S.S. Shaik, *J. Am. Chem. Soc.* **110**, 1127 (1988).
28. (a) A. Pross and S.S. Shaik, *J. Am. Chem. Soc.* **104**, 187 (1982). (b) A. Pross and S.S. Shaik, *Tetrahedron Lett.* **23**, 5467 (1982). (c) A. Pross and S.S. Shaik, *J. Am. Chem. Soc.* **104**, 1129 (1982). (d) A.J. Shusterman, I. Tamir and A. Pross, *J. Organomet. Chem.* **340**, 203 (1988). (e) A. Pross, *J. Org. Chem.* **49**, 1811 (1984). (f) A. Pross and D.M. Chipman, *Free Radical Biol. and Medicine* **3**, 55 (1987). (g) A. Pross, *Acc. Chem. Res.* **18**, 212 (1985).
29. R. Hoffmann, *Angew. Chem. Int. Ed. Engl..* **21**, 711 (1982).
30. R. McWeeny and B.T. Sutcliffe, *Methods of Molecular Quantum Mechanics* Academic Press, London, 1969, Chapters 3 and 6 .
31. N.D. Epiotis and J. R. Larson, *Isr. J. Chem.* **23**, 53 (1983).
32. R. Pauncz, *Spin Eigenfunctions*, Plenum, New York, 1979.
33. J.P. Malrieu, D. Maynau and J.P. daudey, *Phys. Rev.* **B30**, 1817 (1984).

34. L. Salem and C. Rowland, *Angew. Chem. Int. Ed. Engl.* **11**, 92 (1972).
35. H.E. Zimmerman, *Quantum mechanics for Organic Chemists,* Academic Press, New York, 1975, pp. 24-26; 38-39.
36. N.D. Epiotis, *Nouv. J. Chim.* **8**, 421 (1984).
37. P.C. Hiberty and G. Sini, private communication.
38. S.S. Shaik, P.C. Hiberty, G. Ohanessian and J.M. Lefour, *Nouv. J. Chim.* **9**, 385 (1985).
39. For lucid discussions of avoided crossings see, (a) L. Salem, C. Leforestier, G. Segal and R. Wetmore, *J. Am. Chem. Soc.* **97**, 479 (1975). (b) L. Salem, *Science*, **191**, 822 (1976). (c) A. Devaquet, *Pure Appl. Chem.* **41**, 455 (1975).
40. M.G. Evans and M. Polanyi, *Tans. Faraday Soc.* **34**, 11 (1934); **33**, 448 (1937); **31**, 875 (1935); **32**, 1333 (1936).
41. V. Bonancic-Koutecky, V. Koutecky and L. Salem, *J. Am. Chem. Soc.* **99**, 842 (1977).
42. J.M. Poblet, E. Canadell and T. Sordo, *Can. J. Chem.* **61**, 2068 (1983).
43. F. Bernardi, M. Olivucci, M.A. Robb and G. Tonachini, *J. Am. Chem. Soc.* ***108***, 1408 (1986). (b) F. Bernardi, A. Bottoni, M.A. Robb, H.B. Schlegel and G. Tonachini, *J. Am. Chem. Soc.***107**, 2260 (1985). (c) F. Bernardi, M.Olivucci, J.J.W.McDouall and M.A. Robb, *J. Am. Chem.Soc.* **109**, 544 (1987).
44. Reference 19b pp. 151-155.
45. S.S. Shaik, unpublished results.
46. This explicit expression has been derived with the kind help of Professor H.B. Schlegel from Wayne State University.
47. R.A. Marcus, *Annu. Rev. Phys. Chem.* **15**, 155 (1964).
48. (a) P.C. Hiberty, G. Ohanessian, P. Maitre, G. Sini and S.S. Shaik, in preparation. (b) S.S. Shaik, P.C. Hiberty, G. Ohanessian and J.M. Lefour, *J. Phys. Chem.*, a Feature Article in press.
49. S.S. Shaik, D.J. Mitchell, H.B. Schlegel and S. Wolfe, *Theoretical Physical Organic Chemistry . Application to the S_N2 Transition State.* A Monograph in preparation, to be published by Wiley.
50. Expressions for *B* are available for the prototypical reactions and their isoelectronic analogues.

SOLVENT EFFECTS ON POTENTIAL ENERGY SURFACES AND CHEMICAL KINETICS

J.L. RIVAIL
Laboratoire de Chimie théorique
Université de Nancy I
B.P. 239
54506 Vandoeuvre
France

I. Intermolecular forces and the liquid state

A liquid is a condensed phase in which intermolecular forces compete with thermal molecular motion which tends to increase the disorder.

The interaction energy between molecules is the key to liquid properties. It can be analyzed by means of a quantum mechanical perturbation treatment of the supersystem constituted by two molecules ([1]).

As long as electron exchange between the two subsystems is negligible (i.e. long and medium distances) one distinguishes various contributions which the perturbation calculation evidences :

- one *first order* term corresponding to the interaction between the unperturbed molecular charge distributions giving rise to the *electrostatic* interaction energy. This quantity is often strongly dependant on the relative orientation of the partners and can be either positive or negative according to the nature of the interacting species (e.g. ions of like or opposite charge) and/or their orientation.
- two *second order* terms :

i) the *induction* energy which corresponds to the interaction between the permanent charge distribution of one molecule and the induced perturbation of the other. This term is always negative and is obtained by considering the mono-excitations of the system in which only one molecule is perturbed.

ii) the *dispersion* energy, which arises from the states in which all molecules are excited. It is a purely quantum mechanical term which can be analyzed approximately as a coupling between the induced perturbations of the charge distribution. This term is always negative and exists in all systems, even in the case of two rare gas atoms in which the previous terms vanish.

J. Bertrán and I. G. Csizmadia (eds.),
New Theoretical Concepts for Understanding Organic Reactions, 219–229.
© 1989 by Kluwer Academic Publishers.

In the case of small molecules, one usually expands the charge distribution in multipoles (net charge, dipole, quadrupole, ...) defined at a point considered as the center of the molecule. The induced moments are then governed by the corresponding polarizabilities which are tensorial quantities. The first contribution is the dipolar polarizability which expresses the proportionnality of the induced dipole moment with the electric field. The following terms deal with higher moments and to the various orders of the derivatives of the electric field required for a gradient expansion in the electric field strength.

The variation of the various components of the interaction energy with the intermolecular distance R is given in table 1.

TABLE 1

n	Electrostatic	Induction	Dispersion
-1	charge – charge		
-2	charge – dipole		
-3	dipole – dipole		
	charge – quadrupole		
-4	dipole – quadrupole	charge – induced	
	charge – octupole	dipole	
..	.....	.....	.....
-6	quadrupole – octupole	dipole – induced	induced dipole –
	dipole – hexadecapole	dipole	induced dipole

The R^n dependance of the first components of intermolecular energies

The long range behaviour of these intermolecular energies, especially the electrostatic ones, must be pointed out. A molecule in the bulk of the liquid is therefore influenced by a large number of other molecules.

In the case of large molecules, or even for small molecules at short distances, this multipole expansion does not converge well. Other techniques have been proposed, and among them, multicentre multipole expansions leading to a distribution of multipoles ([2],[3]) and of polarizabilities which can be located either on the atoms or on the bonds.

At short distances, the electronic exchange between the molecules cannot be neglected any more. It gives rise to a repulsive contribution in the intermolecular energy, which varies rapidly with the distance. This contribution is difficult to calculate accurately. It is often approximated by empirical formulae which assume that the repulsion part of the potential is a sum of atom-atom contributions which obey R^n ($n = -9$ to -12) or Ae^{-BR}.

II. Solute-solvent interactions

When a molecule disolves in a solvent, variation of the thermodynamic properties of the system becomes apparent. One then is able to define the energy, entropy, enthalpy, free energy and Gibb's free energy of solvation of a molecule. These quantities arise from the interaction of the solute with the solvent molecules and also from the subsequent variation of the structure and internal energy of the solvent. It is a many body problem which requires various approximations to render it tractable. At the present time, numerical simulations using a Monte-Carlo statistical treatment or molecular dynamics can be adopted. Most of the time, these simulated intermolecular interactions are limited to pairwise interactions thus the induction effects are not correctly accounted for.

The electric field far enough from the solute, created by this molecule, can be considered as uniform on a macroscopic scale. The behaviour of the liquid can then be represented by a macroscopic constant : the electric permittivity (or dielectric constant).

This description of solute-solvent interactions is essentially static. The response of the solvent to any modification occuring to the solute (even a change of orientation) is not instantaneous. The time dependance of this response can be illustrated by the macroscopic behaviour of the electric polarization of a dipolar polarizable liquid after a sudden application of an electric field (step function) at time $t = 0$, illustrated in figure 1.

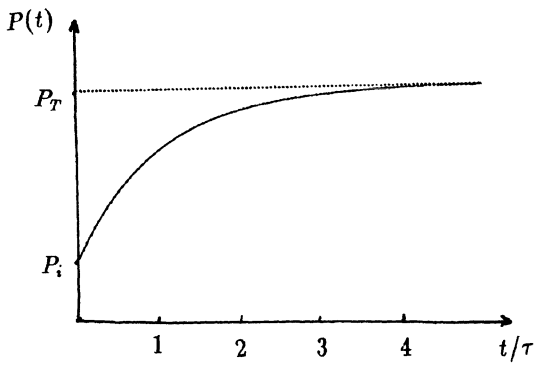

Figure 1

An instantaneous polarization P_i appears, followed by a time dependant contribution which asymptotically reaches a limit (P_t). These two contributions can be interpreted as follows : when the field is applied the molecules are polarized almost instantaneously and the resulting polarization is P_i although the re-orientation of the permanent dipoles takes some time and is hindered by the intermolecular forces. The time evolution of the polarization is often well approximated by an exponential law of the form :

$$P(t) = P_i + (P_T - P_i)\left(1 - e^{-t/\tau}\right) \quad (1)$$

where τ is a characteristic time called "*relaxation time*". In most of common polar solvents, at room temperature, the order of magnitude of τ is 10^{-11} to 10^{-12} s.

III. Reaction path in the liquid state.

A potential energy surface usually refers to free molecules, i.e. to the gas phase. In a solution, drastic modifications may occur due to differences in solvation energies from one characteristic point of the surface to another one.

Let us consider the simple case of the gauche $\rightleftharpoons$ trans isomerization of 1-2 dichloroethane ([4]). The reaction coordinate is the angle θ between the two C-C-Cl planes and the gas phase potential energy curve is represented on figure 2. On the same figure, we plotted the same curved obtained by a molecular dynamics statistical simulation for a molecule of 1-2 dichloroethane in solution in methyl chloride. From this curve one expects a modification of the equilibrium constant between the gauche and the trans conformations, corresponding to the increase of the gauche populations. This result is easy to understand, since the solvation energy of the gauche (polar) conformer is larger than that of the trans conformer. Experiment confirms this statement.

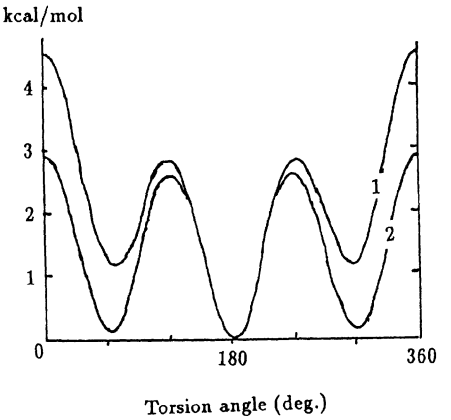

Figure 2 : Potential energy curve of 1,2-dichloroethane. 1 Gas. 2 Liquid.

If now one looks at the kinetic aspect of the reaction and if one wants to predict the rate constants with the help of Transition State Theory one may be tempted to use the potential energy curve as for a reaction in the gas phase and predict the same order of magnitude for the gauche-gauche and the gauche-trans rate contants. In reality the computed ratio of these two quantities is of the order of 10 because

one has to consider the Gibbs' free energy variation along the reaction path, which is only accessible through an appropriate representationof the solvent and of its interaction with the solute.

Let us now consider the solvation free energy. One notices that it consists mainly of two contributions : the interaction of the solute, occasionnally rigid, with the solvent and the modification of the solute (polarization) under the influence of the solvent. This last contribution may not be negligible and may modify the usual reactivity indices quite dramatically (charges, frontier orbitals, etc...). A proper tool to explore solvent effects on a chemical reaction should inform us on both aspects of the solvation phenomenon. In other words, the modification of the electronic structure of the reacting species should be described in some detail. This cannot be achieved without using quantum chemical computations.

IV. Principles of a liquid state quantum chemistry.

In this approach, we shall pay more attention to the detailed structure of the solute than to the solvent. Therefore we shall simplify the description of the solvent in a "true molecule in a model solvent" approach opposed to a "model molecule in a true solvent" picture which is possible by means of statistical simulations.

The simplest picture for the solvent is a macroscopic one : a *continuum* characterized by its macroscopic relative electric permittivity ϵ . It is well adapted to represent the long range interactions. In contrast, the influence of the immediate neighbourhood of the molecule, one is forced to introduce a discontinuity by creating a *cavity* in which the solute molecule is placed. By applying classical electrostatics to this interface, one is able to derive exact results within the framework of the model ([5]).

If one denotes by $V(\mathbf{r})$ the total electrostatic potential at point $\mathbf{r}$, $v(\mathbf{r})$ the contribution of the polarized continuum to this quantity and $\rho_o(\mathbf{r})$ the charge density of the solute at this point, the variation of the free energy of the system (the solution) when a molecule of solute is placed into the pre-defined empty cavity is simply :

$$\Delta F = \frac{1}{2}\int_{\text{space}} \rho_o(\mathbf{r})\, v(\mathbf{r})\, d\tau \tag{2}$$

i.e. just a half the energy of interaction of the molecule with the polarized continuum. This quite general result ([6]) can be understood if one bears in mind that energy has been spent to polarize the solvent and that this quantity is exactly $-\frac{1}{2}$ the energy of interaction.

If the charge density of the solute $\rho_o(\mathbf{r})$ is negligible outside the cavity (within the continuum), the integral (2) can be limited to the cavity itself, and one thus

shows that the electrostatic potential $v(\mathbf{r})$ can be conveniently computed by considering at the surface of the cavity a fictitious surface charge density $\sigma(P)$ defined as being proportional to the normal component of the electric field, $\mathbf{n}$ denoting the inner normal unit vector and ∇ the gradient operator :

$$\sigma(P) = -\frac{\epsilon - 1}{\epsilon} \nabla V(P).\mathbf{n} \tag{3}$$

This field comes from the potential $V_o(P)$ created by the molecule, and from the contribution of all the other surface elements so that :

$$V(P) = V_o(P) + \frac{1}{4\pi\epsilon_o} \int_{\text{surface}} \sigma(M) \frac{\cos\theta}{r} dS \tag{4}$$

with the notations defined by figure 3.

Equation (4) does not raise any convergence problem when the surface is regular, i.e. when it is possible to define everywhere a curvature radius R so that $\frac{\cos\theta}{r} \rightarrow \frac{1}{2R}$ as $r \rightarrow 0$. This is why we shall avoir any surface which should exhibit the intersection of two surfaces along which a curvature radius cannot be defined.

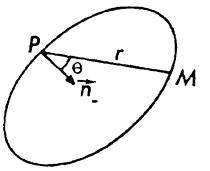

Figure 3

Therefore, for a given cavity, it is possible by using equations (2)(3) and (4), to compute the *electrostatic* contribution to the free energy of solvation of a molecule. Equation (2) shows that, in principle, the fact that the molecular electronic cloud is not limited to the cavity does not raise any problem since the contribution of the electric charges lying outside the cavity can be evaluated. But the physical meaning of this contribution is not clear at all in the case of a molecular liquid in which the continuum stands for an averaged ensemble of molecules.

Finally one notices that the free energy of solvation defined by this model depends on :

- the electrostatic properties of the solute through $V_o(\mathbf{r})$
- the electric permittivity of the solvent ϵ
- the geometry of the cavity

The first two factors are well known, the only degree of freedom regards the geometry of the cavity.

For the consistency of the model, the volume of the cavity is chosen to be equal to the partial molecular volume of the solute. In the end, one is left with only one

aspect to define : the shape of the cavity. Several surfaces can be envisaged. An electronic isodensity surface includes the largest fraction of the electronic population is a good candidate for the boundary of a cavity which, classically, would contain the whole of the molecule. A surface, on which the electrostatic potential due to electrons only is considered, would be another possibility : its area is minimum for nearly the same amount of electrons inside ([5]). The use of one or the other of these definitions makes a difference in the resulting electrostatic potential whithin the cavity, created by the polarization of the continuum by the solute. Nevertheless these differences are less than the error bars of the electrostatic potential obtained by a statistical simulation ([7]) so that at this stage one cannot decide which criterion is the best and the differences in the value of the solute-solvent interaction energy obtained by these two shapes should by considered as a measure of the intrinsic uncertainty of the model.

The cavity being chosen, there is no difficulty in computing the solute-solvent free energy of solvation, by means of an integration of the product of the electrostatic potential and the charge density (defined by the position of the nuclei and by the electronic wavefunctions). The electrostatic potential being defined, among other factors, by the shape of the cavity, it has to be computed numerically, so that this energy is obtained by a numerical integration which may be quite costly in time. The equilibrium properties of the solute corresponding to a minimum of the solute-solvent interaction free energy, the process appears as exceedingly long and a simplified version of the model is necessary.

The simplification which appeared to spoil the model the least is the replacement of the previous cavity by a constant coordinate surface (ellipsoid, spheroid or sphere) and to expand the solute's charge distribution in multipoles at the center of the cavity. Then the free energy of interaction takes an analytical form :

$$\Delta F = -\frac{1}{2}\sum_{l=0}^{\infty}\sum_{m=-l}^{l} R_l^m \langle M_l^m \rangle \tag{2}$$

where $\langle M_l^m \rangle$ is a component of a multipole moment in a spherical tensor formalism ([8]) and R_l^m the corresponding component of the reaction electric field, which is written :

$$R_l^m = \sum_{k=0}^{\infty}\sum_{n=-k}^{k} F_{lk}^{mn} \langle M_k^n \rangle \tag{3}$$

The elements F_{lk}^{mn} of the reaction field tensor only depend on the geometry of the ellipsoid and of the electric permittivity of the solvent. They are easily computed by using a method described earlier.

The equilibrium properties of the solute interacting with the solvent are reached when ΔF is minimum. This condition leads us, for the molecular orbitals of the solute, to a modified Hartree-Fock operator. Expressed in the basis of the atomic orbitals, the $\mu\nu$ element of the Hartree-Fock matrix is written :

$$F_{\mu\nu} = F^{o}_{\mu\nu} + \sum_{l=o}^{\infty} \sum_{m=-l}^{l} R^{m}_{l} \langle \mu | M^{m}_{l} | \nu \rangle \tag{4}$$

where the usual notation is used. $F^{o}_{\mu\nu}$ is the matrix element for the free molecule and M^{m}_{l} is the component of a multipole moment operator. The resulting Hartree-Fock-Roothaan equations can be solved iteratively and the computational time needed for such a calculation is not significantly longer than a SCF computation of a free molecule.

The energy obtained after such a calculation can be split into two parts :
1. the energy of the solute molecule, which is necessarily greater than the energy of this molecule when it does not interact with the solute, the difference being the energy needed to polarize the solute.
2. a contribution to the free energy of solvation. This contribution includes the electrostatic and the induction energy since the dielectric permittivity includes the induced polarization. It must be pointed out that two contributions to the total solvation free energy are lacking : the dispersion term, which can be included to the SCF scheme ([9]), or can be evaluated separately but is only slightly dependant on the structure of the solute, and a last contribution often called the cavitation term which represents the energy spent to create the cavity in the pure solvent before placing the solute in it. This quantity can be evaluated separately ([10],[11]). One must bear in mind that in some cases these terms may vary along a reaction path and modify the conclusion drawn by considering the electrostatic and induction contribution only.

Finally, one notices that, as in every SCF calculation, one obtains the eigenvalues of the modified Hartree-Fock operator. They give us information on the relative arrangement of the electronic levels, and in particular the HOMO and the LUMO position. These data are very important in chemical reactivity studies and we shall pay special attention to them in the last section of this review.

V. Nucleophilic and electrophilic substitution on aromatic compounds in solution.

In this section, we report results obtained by using the AM1 ([12]) semi empirical SCF method to compute the electronic wavefunction of solute species. The cavity is assumed to be ellipsoidal and its axes are set proportional to the cubic roots of the principal components of the polarizability tensor ([13]). The influence of the solvent is illustrated by the rather academic example of the electrophilic and nucleophilic

substitutions of benzonitrile ([14]). The reagents are the proton and the hydride ion respectively in order to get symmetric intermediate states obtained by addition of the reagent to the benzonitrile molecule in ortho, meta and para positions. The solvent is assumed to be water at room temperature ($\epsilon = 78$).

TABLE 2

	Charges		HOMO		LUMO	
	gas ph.	water sol.	gas ph.	water sol.	gas ph.	water sol.
ortho	0.058	0.091	0.27	0.51	-0.35	-0.38
meta	-0.004	0.009	-0.28	0.50	-0.22	-0.16
para	0.036	0.088	-0.54	0.00	0.54	0.50

Charges (a.u.) and frontier orbitals coefficients of benzonitrile

The electronic properties of the benzonitrile molecule in the gas phase and in solution which are relevant for the mechanisms of interest are given in table 2. One notices a change in the nature of the HOMO, which comes from a difference of the solvent effect on the two highest occupied orbitals ([15],[16]).

The differential energies of formation of the three possible intermediate complexes in the gas phase and in aqueous solution are given in table 3. One notices that the role of the solvent is limited to an increase of the differences between the energies of formation in the case of the electrophilic substitution. The nucleophilic substitution exhibits a more curious feature since the para isomer which was found, expectedly, to be the most stable in the gas phase becomes the least stable in solution. These modifications cannot be explained by the variations of the electronic structure under the influence of the solvent. Table 4 gives the free energy of solvation of the various intermediate complexes as obtained by the model. It evidences the crucial role of this quantity on the relative stability of the species. Obviously it is related to the electronic structure of the solute (through the charge distribution), but the geometry of the molecule plays a major role and it is not easy to do simple qualitative predictions of the overall effect.

TABLE 3

	H^+		H^-	
	1	2	1	2
ortho	1.3	35.9	8.3	0
meta	0	0	46.3	10.2
para	3.0	67.8	0	54.2

Differential stabilities of intermediate complexes ($kJ.mol^{-1}$).

TABLE 4

	BH^+	BH^-
ortho	281.6	344.2
meta	316.2	371.9
para	251.3	281.6

Free energies of solvation ($kJ.mol^{-1}$).

VI. Conclusion

The links between the electronic structure of a molecule and its reactivity are very familiar to the chemist, and quantum chemistry provides us with unique data to rationalize the phenomenon of chemical reactions, especially for molecules in the gas phase.

When dealing with liquid state reactions there is a need for the same kind of information, provided that the modifications of electronic structure under the influence of the molecular environment are duely accounted for, but a reaction path in a condensed phase requires the knowledge of the free energy surface. Such information usually needs long and difficult statistical simulations. In this paper, we develop a model which allows us, with little computation, to have an estimate of the electrostatic and induction contributions to the free energy of solvation which may give the answer to the free energy problem in the cases in which the other contributions to the computed quantities can be considered as constant.

This approach belongs to a class of models in which the liquid is represented by a continuum. Although such a representation of reality is rather crude and cannot pretend to a great accuracy, it proves rather usefull for semi quantitative investigations in a field of chemistry in which the lack of precise, tractable, quantitative theories is particularly important.

At the present stage of development, it seems that the contributions arising from electrostatic forces (i.e. the electrostatic and induction contributions) can be rather well represented. A careful assessment of the two other therms : the dispersion and the cavitation contributions, would allow us to investigate a whole potential energy surface in solution, in particular when several species enter the reaction scheme and require an absolute determination of their free energy of solvation. Nevertheless, it must be pointed out that, the use of the static dielectric permittivity to represent the solvent implies that the solvated species are in equilibrium with the solvent. This is another very crude assumption. The characteristic times of many reaction processes are of the same order of magnitude as the relaxation time of the solvent. Therefore a dynamic coupling between the solutes and the solvent has to be considered and the theoretical problems posed by such a treatment are far from being simple. The main advantage of the continuum model being its simplicity, it is probably more reasonable not to try to improve it too much and to look for another approach which would consider explicitly the discontinuous nature of the solvent.

References

(1) A.D. Buckingham, *Intermolecular Interactions : from Diatomics to Biopolymers*, B. Pullman ed. (J. Wiley, Chichester, 1978), p. 1.

(2) P. Claverie, *Intermolecular Interactions : from Diatomics to Biopolymers*, B. Pullman ed. (John Wiley, Chichester, 1978), p. 69

(3) A.J. Stone, *Chem. Phys. Letter*, **83** (1978) 233 ; *Mol. Phys.*, **56** (1985) 1065
(4) C. Millot and J.L. Rivail, to be published
(5) J.L. Rivail, B. Terryn, D. Rinaldi and M.F. Ruiz Lopez, *J. Mol. Struct. (THEOCHEM)*, **120** (1985) 387
(6) J. Barriol, *C.R. Acad. Sci. Paris*, **278 C** (1974) 637
P. Claverie, *Quantum Theory of Chemical Reactions*, Vol. III, R. Daudel *et al.* ed. (Reidel, Dordrecht, 1982), p. 151
(7) B.J. Costa Cabral, D. Rinaldi and J.L. Rivail, *Chem. Phys. Lett.*, **93** (1982) 157
(8) J.L. Rivail and B. Terryn, *J. Chim. Phys.*, **79** (1982) 1
(9) D. Rinaldi, B.J. Costa Cabral and J.L. Rivail, *Chem. Phys. Lett.*, **156** (1986) 125
(10) T. Haliciloglu and O. Sinanoglu, *Ann. N.Y. Acad. Sci.*, **158** (1969) 308
(11) R. Pierrotti, *Chem. Rev.*, **76** (1976) 717
(12) M.J.S. Dewar, E.G. Zoebish, E.F. Healy and J.J.P. Stewart, *J. Am. Chem. Soc.*, **107** (1985) 3902
(13) D. Rinaldi, M.F. Ruiz Lopez and J.L. Rivail, *J. Chem. Phys.*, **78** (1982) 834
(14) N. Rguini, J. Bertran and J.L. Rivail, unpublished results.
(15) J. Bertran, A. Oliva, D. Rinaldi and J.L. Rivail, *Nouv. J. Chim.*, **4** (1980) 209
(16) E. Sanchez Marcos, J. Maraver, M.F. Ruiz Lopez and J. Bertran, *Can. J. Chem.*, **64** (1986) 2353

MODIFICATIONS OF POTENTIAL ENERGY SURFACES BY SOLVATION AND CATALYSIS

J. BERTRAN
Departament de Química
Universitat Autònoma de Barcelona
08193 Bellaterra (Barcelona)
Spain

ABSTRACT. Non-specific effects of solvents, coming up from their physical properties, and specific effects, arising from chemical solvent behavior, are discussed. Static and dynamic non-specific solvent effects are studied by choosing an S_N2 reaction as an example. For specific effects, different cases of bifunctional catalysis are presented. Finally, other types of catalysis, such as the catalytic effect of an external uniform electric field, are analyzed.

1. Introduction

Almost all reactions in the Laboratory take place in solution, but normally theoretical calculations refer to isolated chemical systems. Different models have been proposed to take care of the solvent. Fundamentally there are two options: a discrete representation of the solvent, where its molecules are conferred an entity, and a continuum representation of the solvent, where it is characterized by its macroscopic magnitudes. For a long time, discrete models have been restricted to consider a very limited number of solvent molecules, but nowadays Monte Carlo and Molecular Dynamics techniques allow to consider a quite high number of molecules. In continuum models, the initial stage when solute polarization was not taken into account has already been overcome. At present, the reaction field feedback effect is often introduced, as shown in the preceding chapter.

To analyze solvent effects on chemical reactions, one can distinguish non-specific effects, coming up from physical solvent properties, and specific ones, arising from the chemical solvent behavior. This last type of solvent effect appears only for some chemical reactions with special solvents. As a matter of fact, it is a sort of homogeneous catalysis. In a general way, the homogeneous catalysis may be connected to a specific solvation. Within this point of view, this chapter will be divided into three main sections. In the first and second sections, non specific solvent effects on chemical reactions and specific effects, respectively, will be studied. The third section will deal with homogeneous catalysis.

2. Non specific solvent effect

From the very first beginning of transition state theory in 1935, Eyring, Evans and Polanyi [1,2] proposed its thermodynamic formulation in order to introduce the solvent effect on reaction rates. The different changes in free energy of reactants and transition state,

J. Bertrán and I. G. Csizmadia (eds.),
New Theoretical Concepts for Understanding Organic Reactions, 231–255.
© 1989 by Kluwer Academic Publishers.

going from gas phase to solution, leads to a change in the activation free energy, and hence in the reaction rate. In this static effect, the solvent plays a passive role. The fundamental hypothesis is that the solvent is in equilibrium with the transition state.

In a pioneering work, Kramers [3] pointed out that transition state theory is not valid in solution, because some reactive trajectories recross the barrier owing to solvent collisions. In the extreme case, the free flight across the barrier envisaged in transition state theory will turn into a diffusive passage over the barrier. Kramers' treatment idealizes both the reaction system and the solvent. The former is considered as an effective particle crossing a one dimensional potential barrier, whereas the latter is considered as a thermal bath. The solvent influence on the movement of the reactive particle is described by the stochastic Langevin equation. If the friction is small or the barrier is very sharp, transition state theory is valid. Otherwise, it is not. When the solvent response time is not small compared with the reaction time, the generalized Langevin equation must be used [4,5]. It must be emphasized that the one-dimensional generalilzed Langevin equation is equivalent to an intervention of the solvent in the reaction coordinate within a multidimensional perspective. In this dynamic effect, the solvent plays an active role.

To get a deeper insight on both aspects of solvent effect on chemical reactions, we have chosen the S_N2 reaction as an example.

2.1. STATIC EFFECT IN S_N2 REACTIONS

In these reactions there is a charge migration from the entering group to the leaving one. Given that there are strong interactions between charged species and polar solvents, important effects of the solvent on these reactions can be expected. As a matter of fact, it is well known experimentally that this process is very sensitive to the solvent, which is found to change both the reaction rate and the mechanism. In solution, the rate constant decreases up to 20 orders of magnitude, and the energetic profile, which exhibits a double well shape in the gas phase, becomes unimodal [6-13].

Given the dramatic effect of the solvent on their rate, S_N2 reactions have been likely the most studied processes with the different theoretical methods. In a pioneer work, Ingold [14,15] interpreted the increase in reaction barrier in solution starting from qualitative considerations by using a continuum model for the solvent. In an S_N2 reaction, where ionic species intervene, one of the reactants has a localized charge, whilst the transition state exhibits a diffuse charge distribution. A polar solvent causes a larger stabilization of the reactant, thus provoking a barrier increase. Later on, Parker [16] pointed out that specific interactions like hydrogen bonding and the solvent reorganization energy were of great importance when the reaction takes place in strongly structured solvents. Initial desolvation of the nucleophile has also been invoked by Ritchie [17] as one of the factors that account for the barrier. Dewar [18] has stressed two other points. On one hand, the intermediate is unfavoured from an entropic point of view, since there is a cancellation between ΔH and $-T\Delta S$ terms, so the double-well profile in gas phase dissapears if one takes into account the free energy profile. On the other hand, the ion-dipole stabilization of the reactant system in strong polar solvents is compensated by the energy loss associated to the ion-solvent complex cleavage. Shaik [19,20] has emphasized that the S_N2 reaction is a charge transfer process, and that the charge migration along the reaction must be accompanied by a large solvent reorganization.

By using the discrete model for the solvent, this reaction has been in the last years the subject of a variety of more quantitative studies. Several calculations where a reduced number of solvent water molecules are considered have been carried out [21-23]. However, they represent the experimental situation of a gas phase cluster reaction rather than the process in solution. Further, the contribution to the activation barrier of the bulk solvent reorganization is not taken into account. In a series of recent works [24-32] a high number of water molecules has been incorporated, so the effect of solvent reorganization has been evaluated. In particular, the work by Jorgensen [28-31] comes out as especially relevant.

In a first step, the gas phase energy profile of the chloride exchange reaction was determined by means of ab initio calculations. The data were then used to develop analytic functions for the calculated geometrical parameters and total energies in terms of a well-defined reaction coordinate. The next task was the development of intermolecular potential functions for use in simulations of the solution-phase reaction. Again, ab initio calculations were employed to obtain a large collection of energies and geometries of solute-water clusters at a variety of points on the potential surface. These results dictated the choice of the functional form as well as the parameters for the solute-water potential function as a function of the reaction coordinate. Finally, to model the reaction in aqueous solution Monte Carlo simulations with 250 water molecules along different points of the reaction coordinate were carried out. While it is straightforward to perform simulations of a few representative points along the reaction, the statistical errors in the calculated differential heats of solution can be of the same order of magnitude as the solvent effect on the activation barrier. A more reliable approach is to determine the solvent-averaged potential of mean force, $w(r_c)$, which represents the relative free energy of the system as a function of reaction coordinate (r_c). To carry out this evaluation, it is necesary to know the probability of ocurrence of each value of r_c. Its precise computation is not possible through a single long simulation, but requires the use of importance sampling.

A first main result of this work [28-30] is the unimodal nature of the free energy curve in solution in contrast to the double-well profile in the gas phase. In spite of the fact that the well depth in the gas phase diminishes when going from an internal energy profile to a free energy one, the double-well shape is preserved. The second significant result from the simulations is the large increase in activation energy caused by solvation. In fact, the entire activation process in solution is basically represented by the transformation of the ion-dipole complex to the symmetric transition state. Part of the barrier (ca. 14 kcal/mol) is due to the intrinsic barrier for the solute, but a meaningful contribution (ca. 12 kcal/mol) comes from the weak solvation of the transition state relative to the intermediate. The barrier increase when going from gas phase to solution is attributed to a larger solute-solvent interaction in reactants than in the transition state (37 kcal/mol) partially compensated by a larger breakage of the solvent structure (15 kcal/mol).

It is interesting to compare the aforementioned Monte Carlo simulations with the results that we have obtained for a very similar reaction by means of the continuum model [33]. We have chosen the model of Tomasi et al. [34,35], which represents the solvent by a continuous polarizable dielectric with permitivity ϵ. In this model, the solute is placed inside a cavity accurately defined by its own geometry [36]. In this way, the fluoride exchange reaction has been studied using the 3-21+G basis set [37]. The reaction coordinate q has been defined as the difference between the leaving group-carbon distance and the entering group-carbon distance. In Figure 1 we present the energetic profiles obtained upon introduction of the solvent effect by the continuum model on

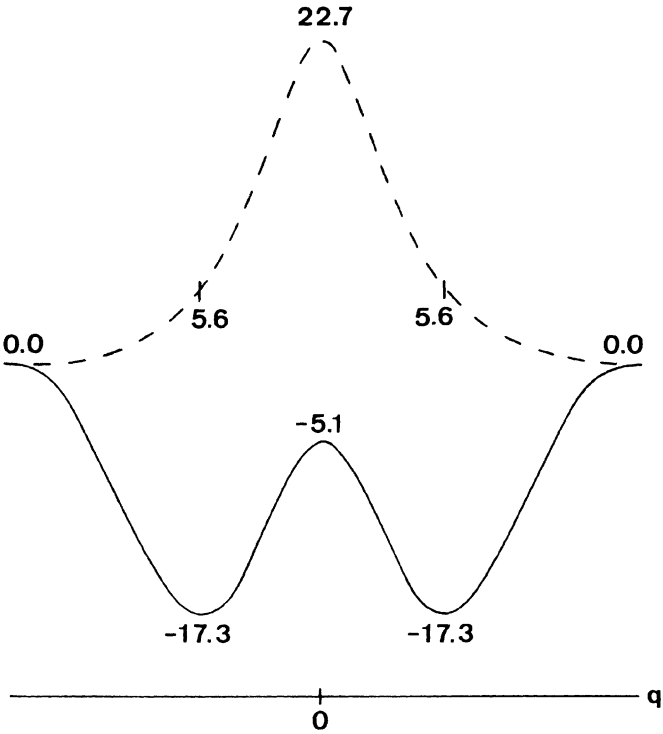

Figure 1: Energy profiles (in kcal/mol) vs. reaction coordinate q. Continuous line: gas phase reaction. Dashed line: continuum representation for the solvent.

the stationary points of the gas phase reaction. The decrease in solvation free energy when going from reactants to the intermediate and transition state produces a dramatic change in the energy profile of the reaction. The double-well shape in gas phase becomes unimodal in solution, in close agreement with experimental facts. These results can be compared to those obtained trough Monte Carlo calculations [28-30]. Both continuum model and Monte Carlo simulations suppose the solvent to be in equilibrium with the chemical system at each point along the reaction coordinate. The influence of the solvent turns out to be very similar in both studies in what regards to the destabilization of the transition state. The most important difference in the unimodal profiles in solution is that ours is broader, while the Monte Carlo one is sharper. We must stress that, as opposite to our calculations with the continuum model, Monte Carlo studies do not introduce the solute polarization owing to the solvent. For instance, in the transition state, the fluorine charges, which are 0.68 in gas phase, become 0.72 when the solvent is introduced through the continuum model. In a valence-bond language, the solvent increases the importance

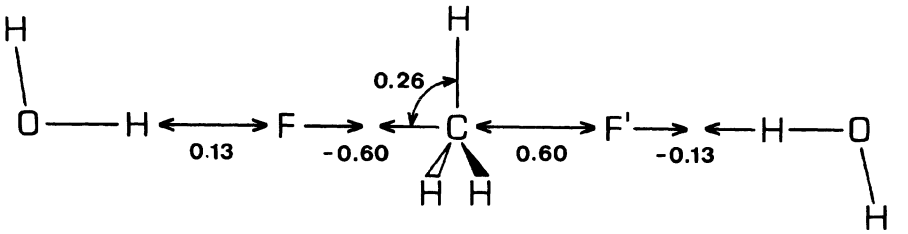

Figure 2: Main components of the transition vector for the solvated fluoride exchange reaction. Positive when the value of an internal coordinate increases (↔) and negative when it decreases (→←).

of ionic structures, as predicted already by Shaik [19,20]. Another effect worth noting is that the solvent slows down the charge transfer from the entering group. This feedback effect on the charge distribution in a similar chemical system has been recently considered by Karplus [32] using a semiempirical method through a different model. More recently, Warshel [38] has claimed that the coupling between the solvent charge distribution and the solute polarization is essential to describe correctly S_N2 reactions in solution.

2.2 LIMITATIONS OF THE STATIC SOLVENT TREATMENT OF S_N2 REACTIONS

All static treatments of solvent effect on S_N2 reactions suppose the solvent to be in equilibrium with the chemical system at each point along the reaction cooordinate. This fundamental hypothesis may be questioned in the first place from the different time scale of solvent relaxation and the chemical process. If the chemical reaction proceeds faster than solvent reorganization, the solvent is not likely to be in equilibrium with the chemical system. This point will be analyzed later, when we pay attention to the molecular dynamics results. In the second place, there is a more intrinsic reason arising from the participation of solvent parameters in the reaction coordinate.

A discrete model, where a reduced number of water molecules are considered, is especially well suited to investigate the participation of solvent parameters in the reaction coordinate. The gas phase fluoride exchange reaction and the same reaction with each fluorine atom solvated by one water molecule, have been studied at the Hartree-Fock level using the 3-21G basis set [23]. The solvation parameter (H-F distance) for the entering group oscillates from 1.25 Å in reactants to 1.87 Å in products. The situation of the leaving group is just opposite. Therefore, there is an expansion of the first solvation shell around the entering group, and a contraction around the leaving one, in parallel with the charge transfer process. The large variation of solvation parameters along the reaction path suggests that they are an important part of the reaction coordinate. In fig. 2 the main components of the transition vector, which defines the reaction coordinate at the transition state, are drawn. It can be observed that the larger components are associated with the geometrical parameters that are generally adopted to define the reaction coordinate for the Walden inversion reactions. However, it is worth noting that the solvation parameters

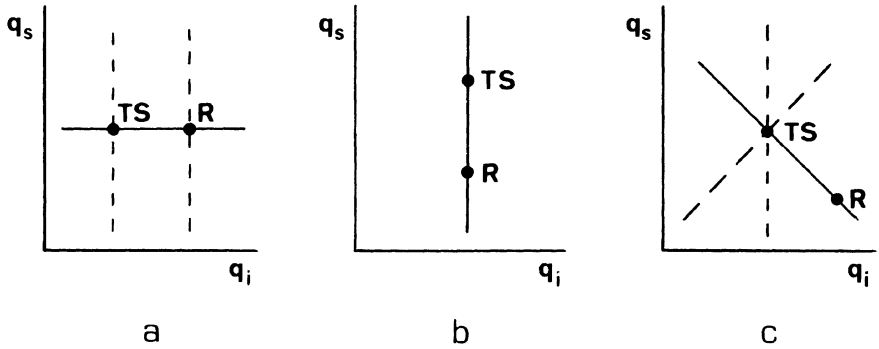

Figure 3: Three possible situations according to the participation of internal and solvation parameters in the reaction coordinate.

are also meaningful components of the transition vector. Therefore, the motion of the solvent molecules is an important part of the motion of the whole system along the reaction coordinate. A variation in the solvent parameters is enough to provoke the transfer of the methyl group. In fact, by solvating only the leaving fluorine atom of the intermediate with one water molecule, the methyl group transfer is provoked spontaneously when the solvation parameter is changed from 1.87 Å to 1.25 Å. Thus, the methyl group adjusts its position to the changes in solvation. Using the 3-21+G basis set, which describes anions much better, the results do not change qualitatively, although the quantitative values are slightly smaller than in the preceding 3-21G calculations.

The first consequence of the participation of solvation parameters in the reaction coordinate is that the hypothesis of an equilibrium between the solvent and the transition state is no longer valid. Let us represent the internal coordinates and solvation parameters by one generalized coordinate each. In fig. 3 the three possible situations are presented. In the first one, the reaction coordinate is defined solely by internal coordinates (fig. 3a). In the second one, solvent parameters define exclusively the reaction coordinate (fig. 3b). Finally, in the third situation, the internal and external parameters become part of the reaction coordinate (fig. 3c). It is well known that each point of the reaction path is an energy minimum with regards to a geometrical parameter orthogonal to the reaction coordinate. Therefore, in the first situation the hypothesis of solvent equilibrium with the chemical system at each point of the reaction coordinate is valid. When the reaction coordinate is defined solely by solvation parameters, the transition state is an energy maximum with respect to these parameters. Hence, solvent equilibrium describes the solvation of reactants, but not that of the transition state. Finally, in the mixed situation, as it happens in the S_N2 reaction, the transition state is not an energy minimum with respect to solvation parameters, and the hypothesis of solvent equilibrium with the transition state is no longer valid. In fact, it is not possible to separate internal parameters from external ones, since external parameters belong to the reaction coordinate.

Another consequence of the important participation of solvation parameters in the reaction coordinate is that the solvent plays an active role in chemical reactions. Solvent motion is correlated with the motion of the chemical system along the reaction coordinate.

Instead of the classic view that the solvent adjusts its position to the changing chemical system, an opposite view may also exist: solvent fluctuations originate the chemical process.

To make a deeper insight into this last aspect of solvent intervention in a chemical reaction, we shall analyze the outer sphere electron transfer reaction between two monoatomic ions, where the reaction coordinate is defined exclusively by solvation parameters. An insight into this process will help to understand the role of the solvent in a more complex process like the S_N2 reaction, which is also a charge transfer process.

2.3. SOLVENT FLUCTUATIONS IN ELECTRON TRANSFER PROCESSES

The fact that homogeneous outer sphere electron transfer reactions occur at a rate that is noticeably lower than the diffusion rate, has been explained through a three-step mechanism:

$$\begin{aligned} D + A &\rightarrow D....A \\ D....A &\rightarrow D^+...A^- \\ D^+...A^- &\rightarrow D^+ + A^- \end{aligned}$$

The reaction rate is controlled by the electron transfer step, which is governed by the Franck-Condon principle. According to this principle, internuclear distances and nuclear velocities do not change during an electron transfer. This principle is embodied in classical electron transfer theories using an activated-complex formalism in which the electron transfer occurs at the interseccion of two potential energy surfaces, one for the reactants and the other for the products [39]. For monoatomic ions, the internal coordinate does not change during the second step, and the reaction coordinate is defined exclusively by solvent reorganization. The intersection region is reached by a suitable solvent fluctuation. After the electron transfer is produced, a solvent relaxation occurs.

As Levich [40] mentioned in 1970, a consistent statistical theory of the liquid state did not exist at that time, this fact being particularly true in the case of such a complex liquid as a polar solvent. For this reason, very simple solvent models, with a drastic reduction in the dregrees of freedom, have been used to study electron transfer processes in solution. A two-mode harmonic vibrational model has been commonly employed: a high-frequency inner shell mode usually associated with the symmetrical stretching, and a low-frequency solvent mode to characterise bulk fluctuations. Nevertheless, in the last years statistical methods based on numerical simulations, such as the Monte Carlo technique, have proved to be a powerful tool to study chemical systems in solution.

To simulate theoretically an electron transfer process, we have chosen the outer-sphere self-exchange reaction:

$$Fe^+ + Fe^{2+} \rightarrow Fe^{2+} + Fe^+$$

in water. Monte Carlo simulations for clusters of 12 and 50 water molecules around both ions separated by a distance of 7 Å have been carried out [41]. The amount of 12 water molecules has been chosen in order to represent the first hydration shell of six water molecules around each metal ion. Further, the calculations with 50 water molecules permit to introduce the effect of the next solvation shells. For each solvent configuration,

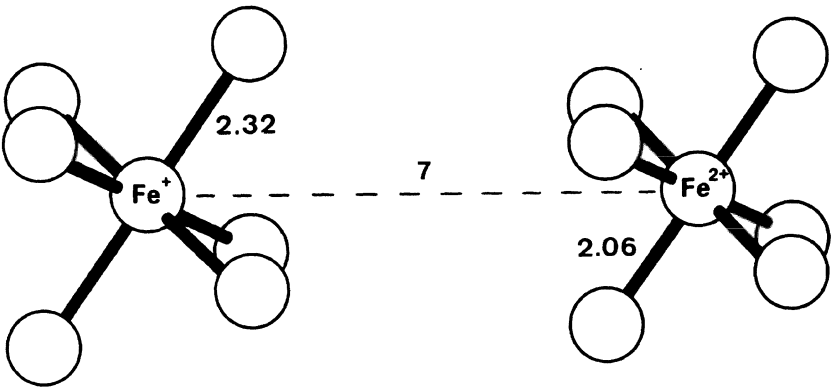

Figure 4: Configuration of the first solvation shell at 0 K.

we have calculated the difference ΔE_{sol} between solvation energies before and after the electron transfer.

For the clusters containing 12 and 50 water molecules, the configurations of the first solvation shell at 0 K that we have found are very similar. Six water molecules (fig. 4) are octahedrically disposed around each metal ion. ΔE_{sol} is 211.6 kJ/mol for 12 water molecules, and 536.5 kJ/mol for 50 water molecules. The larger value obtained for the cluster of 50 water molecules shows the influence of an increase in the number of solvent molecules in the reorganization energy. A large value of ΔE_{sol} indicates that the system is far away from the intersection region, where the electron transfer process may be performed according to Franck-Condon principle (fig. 5). It is obvious that only thermal agitation may cause the adequate solvent fluctuations that lead the precursor complex to the intersection region. Monte Carlo simulations at different temperatures for both clusters over 1,000,000 configurations, after previous equilibration, have been performed. Only those configurations with $\Delta E_{sol} = 0$ are rigorously isoenergetic and belong to the intersection region, although for practical purpose in this work the wider criterium $|\Delta E_{sol}| \leq 5$ kJ/mol has been adopted to classify a given configuration as isoenergetic. Nevertheless, no isoenergetic configurations are found in those runs. Isoenergetic configurations for these systems could be obtained by generating far longer runs, or using an umbrella sampling method. In order to analyze the reason why those fluctuations have such a low probability, we will present the results obtained when some constraints to solvent displacements in the cluster containing 12 water molecules are introduced. In these calculations with constraints, only radial movements have been allowed. In a first calculation, the six Fe^{+}-O distances are identical and the same happens to the six Fe^{2+}-O distances, the number of degrees of freedom being hence two. In a second calculation, the twelve iron-oxygen distances have been allowed to vary independently. In table 1 the percentage of isoenergetic configurations found in each case is presented. As expected, the

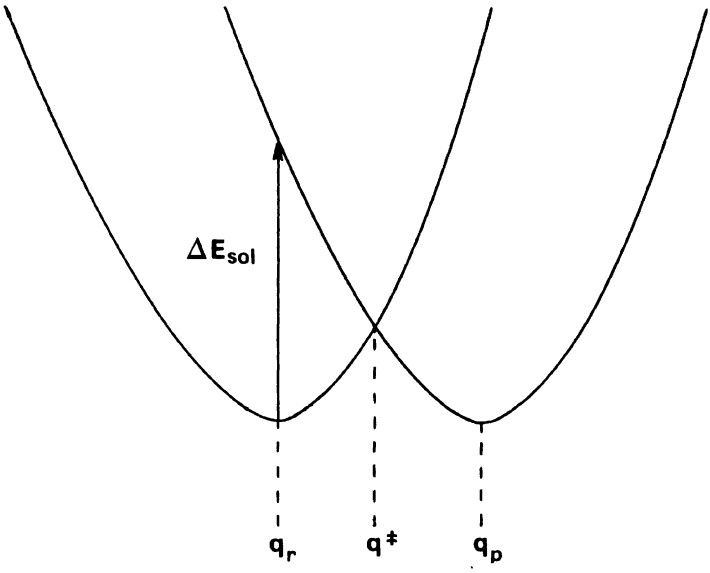

Figure 5: Schematic representation of the potential energy surfaces of the precursor and successor complexes.

Table 1: Percentage of isoenergetic configurations found at 500 K and 2000 K introducing constraints. f is the number of degrees of freedom.

T (K)	f=2	f=12
500	0.006	0.002
2000	1.14	0.214

percentage of isoenergetic configurations is drastically increased when the temperature is raised from 500 to 2000 K. Furthermore, it decreases when the number of degrees of freedom allowed to vary is increased, thus explaining why no isoenergetic configurations are found when no constraints are imposed.

In order to find isoenergetic configurations when no constraints to solvent displacements are imposed, we have used an averaged potential between the potentials of the situations before and after the electron transfer. This sampling method favours configurations belonging to the intersection region. In fact, many isoenergetic configurations for clusters of 12 or of 50 water molecules have been found. It is interesting to remark that they are in the same region of energy explored previously without the sampling method. The high number of degrees of freedom turns out to be the main reason for its low probability. The energy dispersion in the isoenergetic configurations increases with the number of degrees of freedom considered. The increase in the energy dispersion when the number of water molecules is increased shows that the outer hydration shells play a non negligible role for the system to reach an isoenergetic configuration. To set a more thoroughout understanding of the role played by the outer hydration shells in the electron transfer process, we have separated in ΔE_{sol} the effect of the first hydration shell from that of the remainder of hydration shells. The analysis of this decomposition clearly shows that the existence of isoenergetic configurations is usually due to a compensation between both contributions. For instance, in one of these isoenergetic configurations ΔE_{sol} (first shell)=46.06 kJ/mol and ΔE_{sol} (rest shells)=-45.93 kJ/mol. Therefore, any attempt to reduce the number of degrees of freedom of the system can be considered as an oversimplified model.

2.4 DYNAMICS OF S_N2 REACTIONS IN AQUEOUS SOLUTION

Let us go back to the S_N2 reaction and to the dynamic effect of the solvent. In two recent works [38,42-44] molecular dynamics simulations of an S_N2 reaction in aqueous solution have been carried out. In both works, the chloride exchange reaction has been studied. Hynes and Wilson [42-44] have used the S_N2 gas phase potential and solvent-solute potential established previously by Jorgensen [29] from ab initio calculations. Warshel [38] has studied the energetics and dynamics of the S_N2 class of reactions in aqueous solution by means of a combination of the empirical valence-bond method and a free-energy perturbation technique.

In the first work [42-44], the Authors emphasize that the atoms in the reacting system will feel a force from the solvent related to the switching charge which varies along the reaction coordinate in addition to the normal coulombic force for fixed charges. Near the transition barrier, the charge is shifting rapidly and the extra force which arises is proportional to the rate of change of this charge distribution with respect to the reaction coordinate.

The molecular dynamics of activated barrier crossing are computed using a technique in which trajectories are initialized from an equilibrium distribution at the top of the energy barrier, and dynamics are computed both forward and backward in time from the initial conditions. Thus, an ensemble of trajectories initially selected at the transition barrier but originating and ending with reactants or products are computed.

In the gas phase, very few trajectories recross the barrier, while in the simulations with 64 water molecules many trajectories recross it. The computed transmission coeficient

is 0.55, so transition state theory is not valid for that S_N2 reaction in solution. Another important result is that recrossing can be correlated with initial solvent configurations at the transition barrier. There is a greater attractive average electric potential at the left-hand side chloride atom for trajectories crossing the transition barrier twice from reactants to reactants, and a larger attractive potential at the right-hand side chloride atom for those trajectories which cross the transition barrier twice from products to products. Therefore, trajectories recross the potential barrier as a function of the electric potential created by the solvent. It may be assumed to be a nonadiabatic frozen solvent model, i.e., that the solvent does not move noticeably on the time scale 0.02 ps of the motion which decides the fate of the reaction process. The true potential, which contains the potential due to the solvent plus that of the gas phase reaction system, may be expanded in a Taylor series about the gas phase transition barrier site. For each instantaneous solvent configuration the gas phase transition barrier is shifted in location and in energy. The shift in energy is always positive. Thus, the particular trajectory must have an extra kinetic energy along the reaction coordinate in order to react.

In this fascinating study the Authors take as reaction coordinate the internal one, claiming that the reaction path does not consist exclusively of solvent motion, as was the case for outer sphere electron transfers, but rather is dominated by the intrinsic reaction system coordinate. This does not mean that the S_N2 reaction could not be induced by the appropriate solvent configuration in the nonadiabatic regime. Yet this is not the way the reaction proceeds.

In this work the longest time scale corresponds to the transfer of energy from the solvent to the reaction coordinate, the intermediate time scale corresponds to development of proper phasing of the reactants, and the shorterst time corresponds to the dying out of the recrossing. Given that calculations have been carried out starting from solvent distribution in equilibrium with the transition state, the time scale to reach suitable configurations of the solvent, which are solvent fluctuations starting from reactants, has not been analyzed.

Warshel [38] has emphasized the importance of the nature of the solute-solvent coupling. In the nature of the rare fluctuations that lead to a reactive event, it is important to determine whether the reactive fluctuations are driven by solvent fluctuations, by solute fluctuations, or by concerted solute-solvent fluctuations. A convenient way to explore the complicated nature of the reactive trajectories is provided by propagating trajectories downhill from the transition-state region. The time reversal of these trajectories generates the relevant set of reactive trajectories. In the chloride exchange reaction, the situation in Warshel's model is not simple. Some trajectories seem to be solvent driven, and some concerted or solute driven. A more complete examination would reqire computing many more downhill trajectories.

It seems to me that, in the present situation of dynamic studies on S_N2 reactions in aqueous solutions, the possibility that depopulation and replenishment of favorable fluctuations be not balanced cannot be neglected. In conclusion, although spectacular advances have been made on how the solvent influences the S_N2 reaction, we are far from being close to fully understand the solvent effect on it.

3. Specific solvent effect

This second aspect of solvent effect will lead us to homogeneous catalysis. A recent experimental study [45] on the excited-state proton transfer rate of 7-azaindole in alcohol solvents using picosecond time-resolved spectroscopy will allow us to introduce this topic. The time profile of the 7-azaindole tautomer emission in alcohol solvents consists of a superposition of two components with a different rise time. These observations are interpreted in terms of competitive hydrogen bonding leading to a ground-state equilibrium between different conformations of solute-solvent complexes. Cyclic hydrogen-bonded complexes give rise to instantaneous proton transfer, while other configurations can tautomerize only when a cyclic hydrogen bond is formed within the life time of the excited state. The slower process is determined by solvent-solute reorganization dynamics.

Many theoretical studies have shown that one or several solvent molecules may intervene in determined processes, acting as bifunctional catalysts [46-70]. It has been theoretically shown that the potential barrier of the 2-hydroxypiridine → piridone process decreases noticeably when one or two water molecules intervene in the hydrogen transfer process [46-49]. Analogous results have been obtained for the processes C-hydroxyimine → formamide [50-52], hydrogen interchange in formamide [53], hydrocyanic → isohydrocyanic acid [54], and ketoenolic tautomeries [55,56]. Intervention of one water molecule as a bifunctional catalyst also decreases noticeably the barrier to decarboxylation of a series of organic acids [57-62]. Finally, presence of a second solvent molecule, acting as a bifunctional catalyst, clearly favours numerous hydrolysis processes [62-70].

Let us analyze ketoenolic tautomerism, as an example for the specific solvent effect. The vinyl alcohol, the simplest member of the enol class of molecules, has been prepared only recently in the gas phase [71] and in solution [72]. The small barrier to ketonization of this species in aqueous solution contrasts with the high potential barrier in the gas phase. To understand this difference, we have studied the gas phase process and the same process through a chain of two water molecules [54,55].

In fig. 6 we present the STO-3G optimized structures of vinyl alcohol (fig. 6a) and acetaldehyde (fig. 6b) solvated by two water molecules, and the structure of the transition state (fig. 6c). Vinyl alcohol remains planar, whereas the atoms of the solvent chain gradually rise above the plane. The two-water chain connects the hydrogen atom to be transfered to the carbon atom. The mechanism of the process appears clearly in the structure of the transition state. The hydroxyl group has transfered the hydrogen atom to the first water molecule, while this molecule simultaneously starts to transfer one hydrogen atom to the second water molecule, and a strong hydrogen bond between this second water molecule and the carbon atom has been formed. The geometrical parameters of the solvent molecules take part in the reaction coordinate. The hydrogen transfer is being produced in a concerted way, but with a decreasing degree of advance through the chain. The potential barrier decreases dramatically from 91.7 kcal/mol to 21.8 kcal/mol. Therefore, the water chain behaves like a bifunctional catalyst, accepting a proton from the OH group and donating another proton to the CH_2 group.

To explain the water-catalyzed ketonization the following two step mechanism has been also sugested [72]:

$$CH_2CHOH + H_2O \rightarrow CH_2CHO^- + H_3O^+$$

$$H_3O^+ + CH_2CHO^- \rightarrow CH_3CHO + H_2O$$

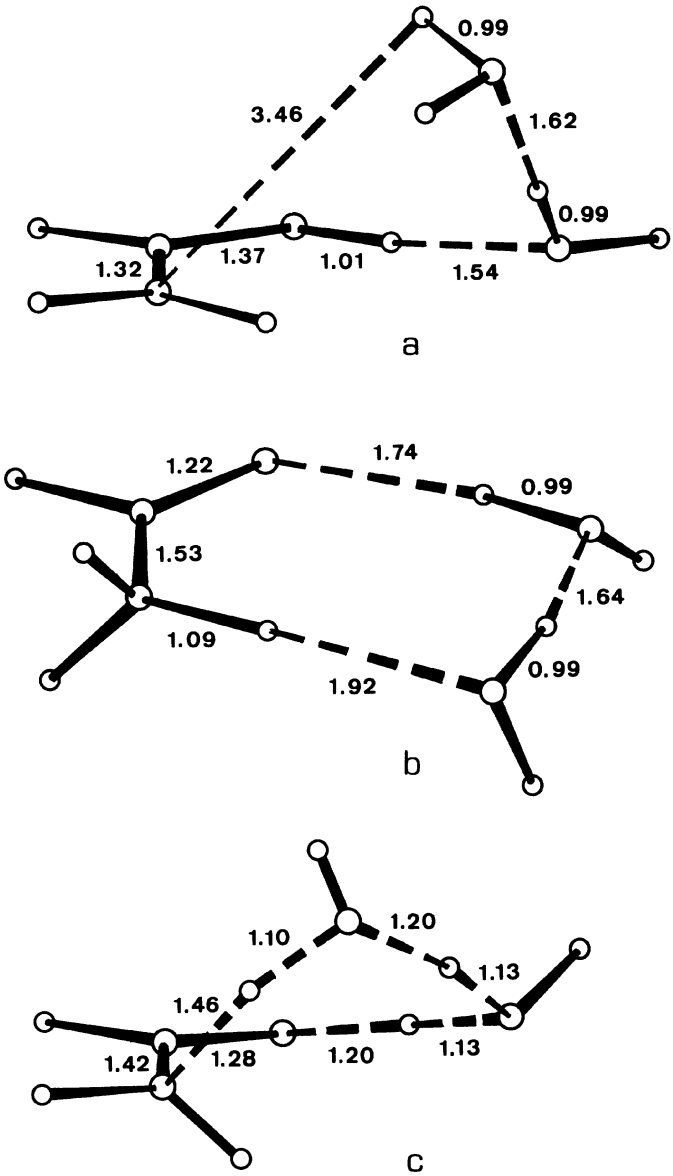

Figure 6: Optimized structures of vinyl alcohol (a) and acetaldehyde (b) solvated by two water molecules. Transition state structure (c).

Table 2: Potential barrier (kcal/mol) for the different processes considered.

	a	b	c	d	e
STO-3G	91.7	21.8	255.8	24.3	109.0
4-31G	82.9	35.8	198.5	38.5	56.

a Sigmatropic 1,3-hydrogen shift in the gas phase
b Molecular cluster reaction including two water molecules
c Two-step mechanism in gas phase
d Molecular cluster reaction in solution
e Two-step mechanism in solution

It is well known that an ionization process is very unfavourable if solvent effect is not taken into account. On the other hand, our calculations with a reduced number of water molecules represent the situation of a gas phase cluster reaction, rather than the process in solution. In both processes, concerted and two-step, the bulk solvent effect has been introduced by means of a continuum model [34-36]. The results obtained using STO-3G and 4-31G basis sets are sumarized in table 2.

As expected, ionic mechanisms are completely unfavourable in the gas phase. Using a continuum model for solvation, a large part of the solvation energy is recovered. In conclusion, given the evolution of the results with the basis set, one can expect that in solution mechanisms involving ionic intermediates should be as important as the concerted water-chain mechanism .

4. Homogeneous catalysis

Although in an industrial perspective heterogeneous catalysis is more important than homogeneous catalysis, the latter shows a faster development. One can expect hence a switching in the relative weight of both types of catalysis in the near future. Owing to its larger simplicity, homogeneous catalysis is especially suited to analyze the different factors which intervene in catalytic phenomena. However, since the catalyst modifies the reaction mechanisms, thus acting in a very specific way, it is difficult to propose general models for homogeneous catalysis. According to the larger or smaller intervention of the catalyst in the internal reaction coordinate, a first classification may be carried out. On one side, one may consider bifunctional catalysis, whereas acid catalysis may be placed at the other side. Non-intervention of the catalyst in the internal reaction coordinate is even clearer when an external electric field is the catalyst. In this section, we shall deal with the aforementioned three types of catalysis.

4.1 BIFUNCTIONAL CATALYSIS

In the preceding section, different examples have been presented where the solvent acts as a bifunctional catalyst. Recently, a new mechanism involving the intervention of a hydrogen halide dimer has been proposed to explain experimental data of hydrogen halide addition to olefins obtained in nonpolar solvents in abscence of radical initiators. From a

theoretical point of view, we have explored the possibility of this new mechanism [73,74]. For such purpose, we have compared the concerted bimolecular and trimolecular processes. The reaction with the dimer turns out to be favoured. The origin of the reaction barrier decrease for the trimolecular process is found in the presence of a second HX molecule, which acts as a bifunctional catalyst. If one compares the geometrical and electron density maps of the transition states for trimolecular processes of HF and HCl, one observes clear differences in the simultaneity of those two processes. For HF, the nucleophilic and electrophilic attacks and proton transfer in the HX dimer are highly concerted processes. On the contrary, for HCl the process is less concerted, and the electrophilic attack advances with respect to the other two processes, which are just initiated in the transition state. HBr and HI are not likely to differ very much from that HCl. HF turns out to be a special case, owing to its weak acid character.

In order to show the differences arising between a bifunctional catalysis and a very acid catalysis, we shall analyze the olefin hydrogenation reaction catalyzed by acids.

Ethylene hydrogenation is a prototype of a symmetry forbiden reaction. Moreover, recent theoretical calculations have shown that the barrier for a reduced symmetry path is also very high [75]. Heterogeneous catalysis of this reaction has been interpreted through a change in symmetry of the H_2 HOMO when it is adsorbed. In 1965, Wilkinson [76], using the $Rh(P\ Ph_3)_3Cl$ complex as a catalyst, found the first efficient way to catalyze homogeneously this reaction. A series of theoretical studies [77-79] have shown the process to proceed through a complex mechanism, where the first step is the oxydative addition of H_2 to the metal complex. Thus, in this transition metal catalysis the first step turns out to be the cleavage of H_2, which originated the large barrier in the uncatalyzed process. Acid catalysis of olefin hydrogenation is a third way. The main steps of this mechanism are the protonation of the olefin, and the cleavage of H_2 by the carbocation, in such a way that a hydrogenated olefin is formed, and the initial proton is recovered. In this catalysis, the first step is protonation [80].

To explore theoretically this last type of catalytic hydrogenation, we have compared three processes:

$$C_2H_4 + H_2 \rightarrow C_2H_6$$

$$C_2H_4 + H_2 + HF \rightarrow C_2H_6 + HF$$

$$C_2H_4 + H_2 + H_3O^+ \rightarrow C_2H_6 + H_3O^+$$

where HF and H_3O^+ have been chosen as examples for weak and strong acids respectively [81].

In table 3 we present the main energetic results for 3-21G calculations. The activation energy decreases noticeably when the process is catalyzed by a weak acid, and dramatically when it is by a strong acid, in such a way that the last mechanism appears as an efficient way of catalysis. The energy results can be strongly influenced when free energy is considered, since catalyzed trimolecular systems are highly structured, and thus unfavoured from an entropic point of view. In fact, for ΔG all intermediates disappears with the exception of $C_2H_4 \cdot H_3O^+ \cdot .H_2$ which is stabilized with respect to separated reactant by -7.9 kcal/mol. The entropic term is more unfavourable in the catalyzed than in the uncatalyzed reaction when free energy is taken into account.

When analyzing geometries and transition vectors of the three transition states (fig. 7), a concerted process arises where the acid acts as a bifunctional catalyst. The acid gives a proton to ethylene, and accepts a proton from H_2, so it collaborates in the

Table 3: Activation energies (kcal/mol) of ethylene hydrogenation.

	ΔE_1	ΔE_2	ΔG
Uncatalyzed reaction	113.4	113.9	120.6
Catalyzed by HF	62.2	69.9	82.1
Catalyzed by H_3O^+	-0.9	18.6	17.2

ΔE_1 is referred to separated reactants.
ΔE_2 is referred to initial complexes.
ΔG is referred to separated reactants.

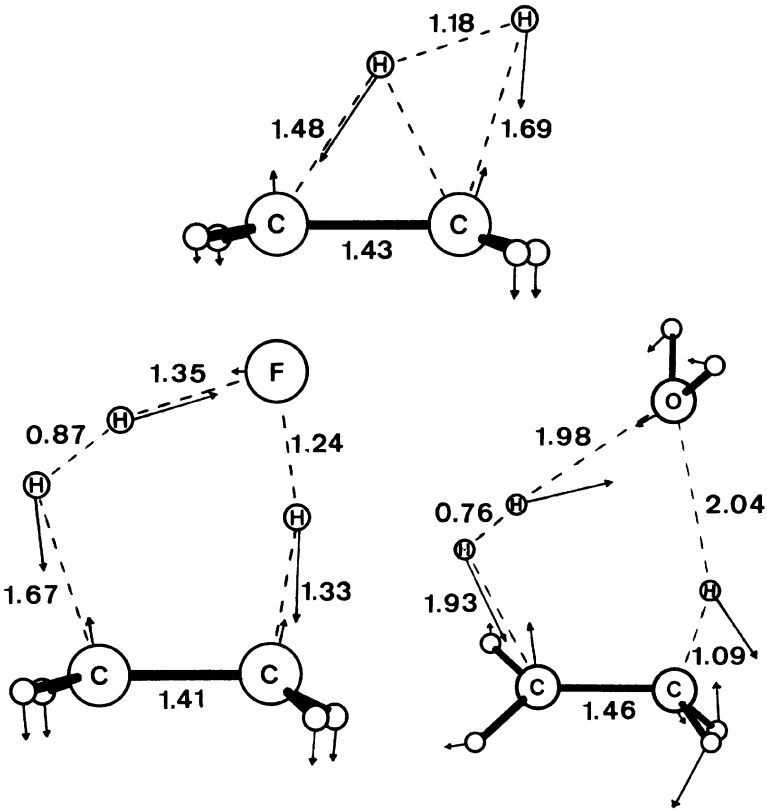

Figure 7: 3-21G optimized structures for the transition states of the three reactions. Arrows indicate the main components of the transition vector.

Table 4: Activation energies (kcal/mol) of the four mentioned processes

	a	b	c	d
ΔE	84.56	57.20	35.10	-7.93

nucleophile formation, hydride ion, which is neutralizing the emerging carbocation. The big difference in potential barrier in the catalyzed reaction comes from the smaller breakage of H_2 in the transition state, which translates into a smaller distortion energy, that is the main component of the barrier. The process is clearly concerted, with all steps being performed simultaneously in the HF case, whereas for H_3O^+ the proton is almost completely transferred to ethylene, and the remaining processes are just slightly initiated in the transition state. If we pay attention to the ordering between H_2 cleavage and proton transfer, one obtains with a weak acid an intermediate mechanism between the catalysis by transition metals and acid catalysis. With both weak and strong acids, it turn out to be a bifunctional catalysis, since geometrical parameters of the acid intervene in the internal reaction coordinate. A two-step process, as that which might be obtained perhaps in a polar medium, would not change the bifunctional character of the process.

4.2 ACID CATALYSIS

Opposite to the preceding example, we shall keep the term "acid catalysis" for processes where the catalyst does not intervene in the internal reaction coordinate. The Friedel-Crafts reaction will serve as an example of such catalysis, and will allow us in turn to differentiate the very acid catalysis from the bifunctional one.

In the Friedel-Crafts reaction, the electrophilic agent is an alkyl halide, and the most usual catalysts are Lewis acids. It has been shown that formation of complexes between alkyl halides and Lewis acids increases the electrophilic character of the alkyl groups [82,83]. We shall study [84] here the reaction path of the following processes:

a) CH_4 + HF
b) CH_4 + HF + BF_3 (acid catalysis)
c) CH_4 + HF + BF_3 (bifunctional catalysis)
d) CH_4 + HF + H^+ (acid catalysis)

Analysis of geometries and electron density plots at the transition states allows to understand the differences between the four processes studied, especially between the bifunctional [85] and the acid catalysis. The transition state of the uncatalyzed process exhibits a four-centered cyclyc structure with a symmetry plane. The C-H and F-H distances are 1.37 and 1.20 Å respectively. For process (d), the proton is tied to fluorine, and geometrically it still appears the four-centered cyclic transition state with the same plane of symmetry, but with a far more different C-H and F-H distances, 1.20 and 1.82 Å. Acid catalysis does not modify the internal reaction coordinate of the uncatalyzed process; however, electron density plots (fig. 8) of both processes show clearly some differences. Whereas in the uncatalyzed process a ring critical point appears, it does not in the catalyzed process, so the transition state is not a cyclic structure. It is an intimate ion-dipole pair, as can be shown from the positive charges of the CH_5 fragment and HF,

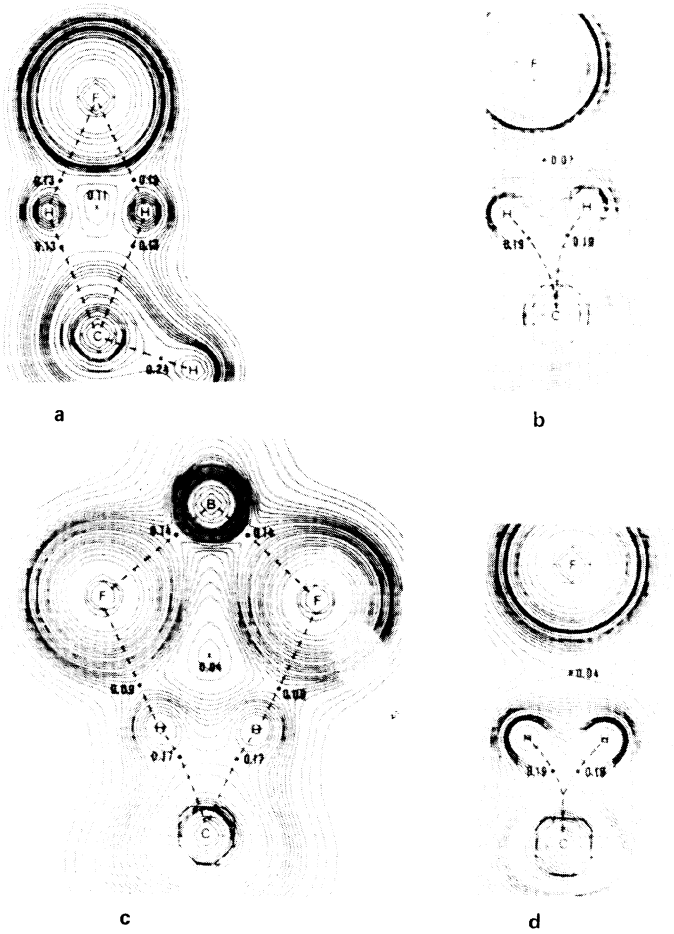

Figure 8: Contour plots of charge density in the plane of the cycle for the transition states of the reaction between CH_4 and HF uncatalyzed (a) and catalyzed by BF_3 (b and c) and H^+ (d). Numbers indicate electron density (in atomic units) in the bond critical points (.) and in the ring critical points (x).

0.91 and 0.09 au, respectively. When BF_3 is the catalytic acid, no ring critical point appears either in the density plot of the transition state. In this case, it is an intimate ionic pair, where the charge of the CH_5 and BF_4 fragments are 0.8 and -0.8 au. On the contrary, when BF_3 acts as a bifunctional catalyst, a ring critical point appears for a six-membered ring. Now both afore mentioned fragments are bound through two bonds that contain one H and one F atom each. Charge separation is 0.68 au. One can expect that a polar solvent will stabilize the transition state of the acid catalysis more than that of the bifunctional catalysis, so both types of catalysis may be competitive in solution. Recently, Heidrich [86] has discussed the intimate ion-pair character or this six-membered structures. In this case, opposite to acid catalysis, the catalyst, which accepts a fluorine from the entering hydrogen and releases a fluorine to the leaving hydrogen, intervenes in the internal reaction coordinate, so the difference between both types of catalysis becomes apparent.

4.3 CATALYTIC EFFECT BY AN EXTERNAL ELECTRIC FIELD

In the very acid catalysis there are several components in the acid-substrate interaction, but the leading component is electrostatic. There are other important terms in the interaction, but a certain compensation appears between them. This allows us to define a simplified model for this type of catalysis, so we stay limited to study the effect of an electric field generated by a point charge on chemical processes.

Again a Walden inversion process like the fluoride exchange reaction, will be taken as an example. In this process, a charge transfer is produced from the entering anion towards the leaving one. One can understand that the presence of a positive counterion in the surrounding of the FCH_3 fluorine will favour the process. In a previous work [87], we have placed a positive charge at different distances from the FCH_3 fluorine, along the FCF axis. For each localization the stationary points of the reaction profile are relocated. In fig. 9 it is shown that the reaction profile is noticeably affected, both with respect to the potential energy barrier and with respect to the position of the stationary points, owing to the presence of the charge. When the positive charge becomes closer, the barrier diminishes, the transition state is advanced towards reactants along the reaction coordinate, and both intermediates are found later in the reaction coordinate. The former field-free potential barrier of 12.2 kcal/mol becomes 3.4 kcal/mol for the charge placed at 4 Å and 0.6 kcal/mol at 3 Å. No potential barrier appears when the counterion is placed closer, at 2.5 Å. The external perturbation of the electric field does not intervene indeed in the internal reaction coordinate, and gives us a model of the acid catalysis that allows us to understand its action.

The reaction energy profile is dramatically altered as a function of the distance of the positive charge. For that reason, this parameter external to the chemical system must be included in the reaction coordinate, which cannot be defined exclusively in terms of internal parameters of the chemical system. Analysis of the electron density plot for the field-free first intermediate will allow us to get a deeper insight into the last observation. Along the FCF axis, two bond critical points appear with density values 0.032 and 0.182. If a positive charge is placed now at 1.07 Å, where the minimum of the molecular electrostatic potential is located, the density values at the bond critical points become 0.033 and 0.141. According to the relation between electron densities in bond critical points and bond strengths [88], it must be pointed out that the decrease in the distance of the

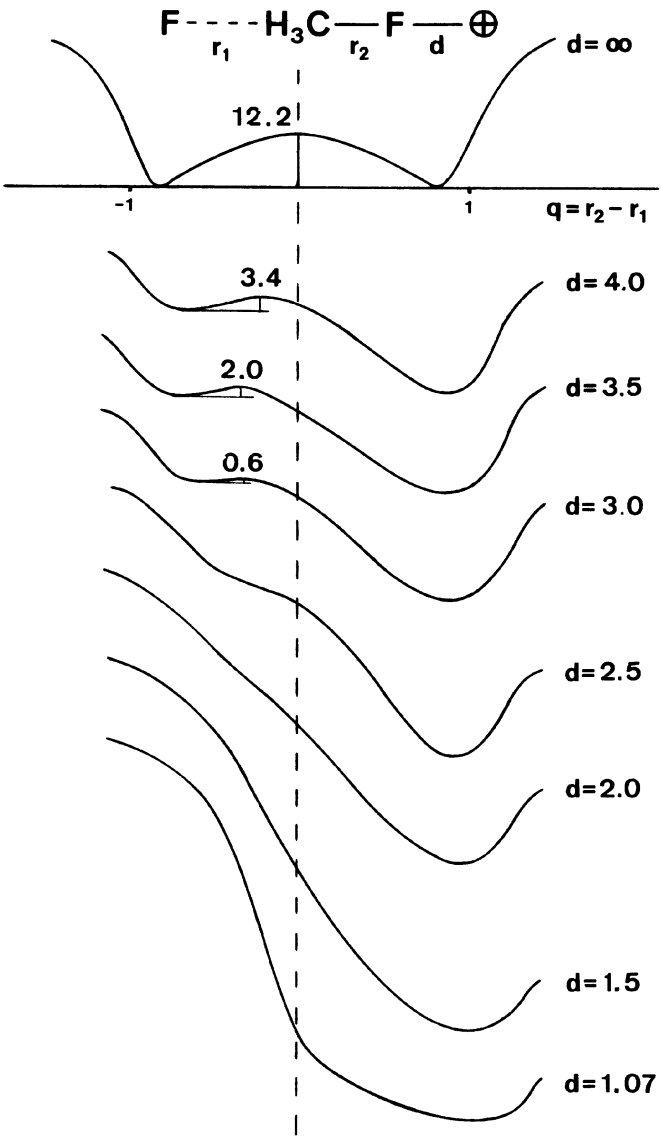

Figure 9: Energetic profiles for the $(FCH_3F^-)\cdot\oplus$ system for several values of the positive charge-fluorine distance. Energies are given in kcal/mol and distances in angstroms.

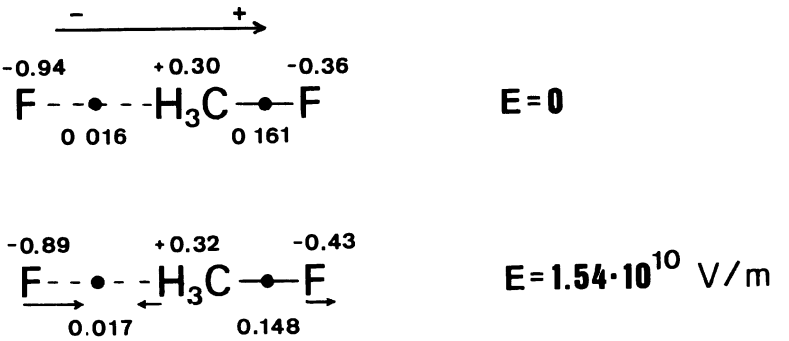

Figure 10: Charges on the fluorine atoms and the methyl group, along with electronic densities at the fluorine-carbon bond critical points, given as fractional electron units. Arrows show the net forces acting on the nuclei. Field intensities are given in V/m.

external positive charge has produced the same effect that would have been produced by of a shortening of the first F-C bond, and a lengthening of the second C-F bond. For instance, to get the same diminution in the electron density of the C-F bond, one should have lengthened such bond by 0.14 Å. It is clear that this internal parameter belongs to the reaction coordinate, so one must also include the external catalyst parameters in the definition of the reaction coordinate.

The preceding model opens the possibility of catalyzing a reaction without any catalyst. An external perturbation like an external field may speed up the chemical reaction in the same way a catalyst would do, so new perspectives in the control of chemical processes are opened. To illustrate this point of view, we shall deal with the same example of the preceding paragraph. We apply an variable-strength uniform electric field along the F-C-F axis, so as to favour the charge transfer process [89]. When the intensity of the applied field is increased, one can observe the same trends in the reaction profile as the preceding case. The field-free 12.2 kcal/mol barrier becomes 1.1 kcal/mol for $E=5.14\cdot 10^9$ V/m and dissapears for $E=1.54\cdot 10^{10}$ V/m. These fields are of the same order of those appearing in electrodic interfaces, in mass spectrophotometry, and in heterogeneous and enzimatic catalysis. Indeed, to cause such a catalytic effect, the electric field must be correctly oriented, which will be difficult in an isotropic medium, but easy in an anisotropic one. In other cases, like the foregoing studied reaction, electrophilic substitution by alkyl halides, the system would be spontaneously oriented owing to the very electric field.

Again, the external perturbation, the electric field, must be included in the reaction coordinate, within a less-strict definition of such a magnitude. For instance, when the first intermediate of the field-free reaction is perturbed by and $E=1.54\cdot 10^{10}$ V/m, 0.05 of charge are transferred from the entering towards the leaving fluoride (fig. 10). This represents an advance in the reaction analogous to that one would obtain by evolution of the internal reaction coordinate. With regards to changes in electron density at the bond critical points, they follow the same trends as in the preceding case: increase in

the forming bond and decrease in the breaking bond. A last consideration may help us to understand the spontaneous evolution of the system towards the final products owing to the electric field effect. When no electric field is present, the intermediate is in equilibrium, so forces acting on nuclei are zero. When an electric field is present, nuclei are subjected to a couple of forces of opposite sign. First of all, one opposite to the field owing to the direct effect of the electric field on positive charges, and another one indirect in the direction of the field, coming from the electronic cloud polarization. As a result, depending on the net charge on each atom, each nucleus will be subjected to a force in the direction of the field if the charge is negative, and opposite to the field if it is positive. Given that fluorine atoms are negative and the methyl group is positive, the intermediate will be no longer in equilibrium, and owing to the mentioned forces, will tend to the final product, so a new F-C bond is formed, and the initial C-F bond is broken.

The reaction field created on the solute by solvent polarization is also an electric field. Thus, non-specific solvent effects are also catalytic or inhibitor ones, depending on wether the reaction field does or does not favour the chemical process.

In conclusion, depending on whether geometrical parameters of the catalyst belong to the internal reaction coordinate, we have been able to study different types of catalysis i.e., bifunctional and acid. In the extremum case of an external perturbation, as that introduced by an electric field, the perturbation does not belong to the internal reaction coordinate, but the concept of reaction coordinate must be revisited by accounting also for the external parameters to the chemical system. This concept opens new perpectives in the control of chemical processes. One must not forget that the goal of the chemist is to do chemistry, and not to find it by chance.

5. Acknowledgments

The research presented in this chapter has been carried out in the Theoretical Chemistry Group of the Department of Chemistry of the Universitat Autònoma de Barcelona. I must thank all members of the Group for their collaborative effort. This work has been supported by the Spanish "Dirección General de Investigación Científica y Técnica" under Project No. PB86-0529.

6. References

[1] S. Glasstone, K. J. Laidler, and H. Eyring *The Theory of Rate Processes* , McGraw-Hill, New York, 1941

[2] M.G. Evans and M. Polanyi *Trans. Faraday Soc.* **31** , 875 (1935)

[3] H. A. Kramers *Physica* **7** , 284 (1940)

[4] R.F. Grote and J.T. Hynes *J. Chem. Phys.* **73** , 2715 (1980)

[5] R.F. Grote and J.T. Hynes *J. Chem. Phys.* **75** , 2191 (1981)

[6] K. Tanaka, G.I. MacKay, J.D. Payzant and D.K. Bohme *Can. J. Chem.* **54** , 1643 (1976)

[7] D.K. Bohme, and L.B. Young *J. Am. Chem. Soc.* **92** , 7354 (1970)

[8] D.K. Bohme, G.I MacKay and J.D. Payzant *J. Am. Chem. Soc.* 96, 4027 (1974)

[9] C.A. Lieder and J.I. Brauman *J. Am. Chem. Soc.* **96** , 4029 (1974)

[10] J.I. Brauman, W.N. Olmstead and C.A. Lieder *J. Am. Chem. Soc.* **96** , 4030 (1974)
[11] D.K. Bohme and G.I. MacKay *J. Am. Chem. Soc.* **103** , 978 (1981)
[12] W.N. Olmstead and J.I. Brauman *J. Am. Chem. Soc.* **99** , 4219 (1977)
[13] M.J. Pellerite and J.I. Brauman *J. Am. Chem. Soc.* **102** , 5993 (1980)
[14] E.D. Hughes and C.K. Ingold *J. Chem. Soc.* , 244 (1935)
[15] C.K. Ingold. *Structure and Mechanism in Organic Chemistry* , Cornwell University Press, Ithaca, New York, 1969.
[16] A.J. Parker *Chem. Rev.* **69** , 1 (1969)
[17] C.D. Ritchie, in *Solute-Solvent Interactions* , J.F. Coetzee and C.D. Ritchie, Eds., Marcel Dekker, New York, 1969, pag. 284.
[18] F. Carrion and M.J.S Dewar *J. Am. Chem. Soc.* **106** , 3531 (1984)
[19] S.S. Shaik *J. Am. Chem. Soc.* **106** , 1227 (1984)
[20] S.S. Shaik *Isr. J. Chem.* **26** , 367 (1985)
[21] K. Morokuma *J. Am. Chem. Soc.* **104** , 3732 (1982)
[22] K. Ohta and K. Morokuma *J. Phys. Chem.* **89** , 5845 (1985)
[23] J. Jaume, J.M. Lluch, A. Oliva and J. Bertrán *J. Chem. Phys. Lett.* **106** , 232 (1984)
[24] Y.S. Kong and M.S. Jhon *Theor. Chim. Acta* **70** , 123 (1986)
[25] I. Cernusák and M. Urban *Coll. Czech. Chem. Comm.* **49** , 1854 (1984)
[26] R.A. Chiles and P.J. Rossky *J. Am. Chem. Soc.* **109** , 6867 (1984)
[27] K.Y. Burshtein *J. Mol. Struct. Theochem* **153** , 209 (1987)
[28] J.Chandrasekhar, S.F. Smith and W.L. Jorgensen *J. Am. Chem. Soc.* **106** , 3049 (1984)
[29] J. Chandrasekhar, S.F. Smith and W.L. Jorgensen *J. Am. Chem. Soc.* **107** , 154 (1985)
[30] J. Chandrasekhar and W.L. Jorgensen *J. Am. Chem. Soc.* **107** , 2974 (1985)
[31] W.L. Jorgensen and J.K. Buckner *J. Phys. Chem.* **90** , 4651 (1986)
[32] P.A. Bash, M.J. Field and M.K. Karplus *J. Am. Chem. Soc.* **109** , 8092 (1987)
[33] C. Alemán, F. Maseras, A. Lledós, M. Duran and J. Bertrán, to be published.
[34] S. Miertus, E. Scrocco and J. Tomasi *J. Chem. Phys.* **55** , 177 (1981)
[35] R. Bonaccorsi, R. Cimiraglia, and J. Tomasi *J. Comput. Chem.* **4** , 567 (1983)
[36] R. Bonaccorsi, P. Palla and J. Tomasi *J. Am. Chem. Soc.* **106,** 1945 (1984)
[37] T. Clark, J. Chandrasekhar, G.W. Spitznagel and P.v.R. Schleyer *J. Comput. Chem.* **4** , 294 (1983)
[38] J. K. Hwang, G. King, S. Creighton and A. Warshel *J. Am. Chem. Soc.* **110** , 5297 (1988)
[39] R.A. Marcus *J. Chem. Phys.* **43** , 679 (1965)
[40] V.G. Levich, in *Physical Chemistry* , Vol 9B, H. Eyring, D. Henderson and W. Jost, Eds., Academic Press, New York, 1970 pag. 1004.
[41] A. González-Lafont, J.M. Lluch, A. Oliva and J. Bertrán, in *Chemical Reactivity in Liquids: Fundamental Apects* , M. Moreau and P. Turq, Plenum Press, New York, 1988, p. 197.
[42] J. P. Bergsma, B.J. Gertner, K.R. Wilson and J.T. Hynes *J. Chem. Phys.* **86** , 1356 (1987)
[43] B.J. Gertner, J.P. Bergsma, K.R. Wilson, S. Lee and J.T. Hynes *J. Chem. Phys.* **86** , 1377 (1987)

[44] K.R. Wilson, in *Chemical Reactivity in Liquids: Fundamental Aspects* , M. Moreau and P. Turq, Eds., Plenum Press, New York, 1988. p.231.
[45] D. McMorrow and T.J. Aartsma *Chem. Phys. Lett.* **125** , 581 (1986)
[46] A. Lledós and J. Bertrán *Tetrahedron Lett.* **22** , 75 (1981)
[47] H.J. Field, J.H. Hillier and M.F. Guest *J. Chem. Soc. Chem. Comm.* 1310 (1984)
[48] A. Lledós and J. Bertrán *J. Mol Struct. Theochem* **120** , 73 (1985)
[49] A. Lledós and J. Bertrán *An. Quim.* **82** , 194 (1986)
[50] J. Bertrán, A. Lledós and J. Revetllat *Int. J. Quantum Chem.* **23** , 587 (1983)
[51] T.J. Zielinski, R.A. Poirier, M.R. Peterson and I.G. Csizmadia *J. Comput. Chem.* **4** , 419 (1983)
[52] A. Lledós and J. Bertrán *J. Mol. Struct. Theochem* **107** , 233 (1984)
[53] T. Yamabe, K. Yamashita, M. Kaminoyama, M. Koizumi, A. Tachibana and K. Fukui *J. Phys. Chem.* **88** , 1459 (1984)
[54] J. Bertrán and A. Lledós *J. Mol. Struct. Theochem* **123** , 211 (1985)
[55] A. Lledós, J. Bertrán and O.N. Ventura *Int. J. Quantum Chem.* **30** , 587 (1986)
[56] O.N. Ventura, A. Lledós, R. Bonaccorsi, J. Bertrán and J. Tomasi *Theoret. Chim. Acta* **72** , 175 (1987)
[57] P. Ruelle, U.W. Kesselring and H. Nam-Tran *J. Mol. Struct. Theochem* **124** , 41 (1985)
[58] P. Ruelle, U.W. Kesselring and H. Nam-Tran *J. Am. Chem. Soc.* **108** , 371 (1986)
[59] P. Ruelle *Chem. Phys.* **110** , 263 (1986)
[60] P. Ruelle *J. Comput. Chem.* **8** , 158 (1987)
[61] P. Ruelle *J. Am. Chem. Soc.* **109** , 1722 (1987)
[62] M.T. Nguyen and P. Ruelle *Chem. Phys. Lett.* **138** , 486 (1987)
[63] I.H. Williams, D. Splanger, D.A. Femec, G.M. Maggiora and R.L. Schowen *J. Am. Chem. Soc.* **105** , 31 (1983)
[64] I.W. Williams *J. Am. Chem. Soc.* **109** , 6299 (1987)
[65] M.T. Nguyen and T.K. Ha *J. Am. Chem. Soc.* **106** , 599 (1984)
[66] M.T. Nguyen and A.I. Hegarty *J. Am. Chem. Soc.* **105** , 3811 (1983)
[67] M.T. Nguyen and A.I. Hegarty *J. Am. Chem. Soc.* **106** , 1552 (1984)
[68] A.D. Buckingham, N.C. Handy, J.E. Rice, K. Somasundram and C. Dijkgraaf *J. Comput. Chem.* **7** , 283 (1986)
[69] T. Oie, G.H. Loew, S.K. Burt, J.S. Binkley, and R.D. MacElroy *J. Am. Chem. Soc.* **104** , 6169 (1982)
[70] T. Oie, G.H. Loew, S.K. Burt and R.D. MacElroy *J. Am. Chem. Soc.* **105** 2221 (1983)
[71] S. Saito *Chem. Phys. Lett.* **42** , 399 (1976)
[72] B. Capon, D.S. Rycroft, T.W. Watson and C. Zucco *J. Am. Chem. Soc.* **103** , 1761 (1981)
[73] C. Clavero, M. Duran, A. Lledós, O.N. Ventura and J. Bertrán *J. Am. Chem. Soc.* **108** , 923 (1986)
[74] C. Clavero, M. Duran, A. Lledós, O.N. Ventura and J. Bertrán *J. Comput. Chem.* **8** , 481 (1987)
[75] M.S. Gordon, T.N. Truong and J.A. Pople *Chem. Phys. Lett.* **130** , 245 (1986)

[76] F.H. Jardine, J.A. Osborn, G. Wilkinson and J.F. Young *Chem. Ind. (London)* 560 (1965)

[77] A. Dedieu *Inorg. Chem.* **19** , 375 (1980); **20** , 2803 (1981)

[78] N. Koga, C. Daniel, J. Han, X.Y. Fu, and K. Morokuma *J. Am. Chem. Soc.* **109** , 3455 (1987)

[79] C. Daniel, N. Koga, J. Han, X.Y. Fu and K. Morokuma *J. Am. Chem. Soc.* **110** , 3773 (1988)

[80] J. Wristers *J. Am. Chem. Soc.* **97** , 4312 (1975); **99** , 5051 (1977)

[81] J.C. Siria, M. Duran, A. Lledós and J. Bertrán *J. Am. Chem. Soc.* **109** , 7623 (1987)

[82] E. Silla, E. Scrocco and J. Tomasi *Theoret. Chim. Acta* **40** , 343 (1975)

[83] J. Bertrán, F. Mora and E. Silla *J. Chem. Soc. Perkin Trans. 2* 647 (1982)

[84] V. Branchadell, A. Oliva and J. Bertrán *J. Molec. Catal.* **44** , 285 (1988)

[85] G. Alagona, E. Scrocco, E. Silla and J. Tomasi *J. Theoret. Chim. Acta* **40** , 343 (1975)

[86] D. Heidrich, M. Rückert and H.J. Köhler *Chem. Phys. Lett.* **136** , 13 (1987)

[87] E. Carbonell, J.L. Andrés, A. Lledós, M. Duran and J. Bertrán *J. Am. Chem. Soc.* **110** , 996 (1988)

[88] R.F.W. Bader, Y. Tal, S.G. Anderson and T. Nguyen-Dang *Isr. J. Chem.* **19** , 8 (1980)

[89] J.L. Andrés, A. Lledós, M. Duran and J. Bertrán, *Chem. Phys. Letters* , in press.

COMPUTATIONAL TESTS OF POTENTIAL ENERGY SURFACES FROM DYNAMICAL PROPERTIES

F.A. GIANTURCO
Department of Chemistry,
University of Rome,
Citta Universitaria, 00185 Rome
Italy

ABSTRACT. The quality of potential energy surfaces (PES) obtained from ab initio calculations is often tested in regions fairly close to the equilibrium geometries of the interacting systems, while very little is known about their reliability for configurations away from equilibrium. The present chapter intends to show that other possible ways have been developped over the last few years for directly evaluating either computed PES or empirical functional forms through the combined used of several different observables from dynamical experiments. The basic ingredients of the theory are briefly reviewed and examples are given for both ionic and neutral subreactive situations involving diatomics and simple atoms. They clearly show that dynamical properties indeed allow one to assess interaction potentials over a very wide range of possible configurations.

1. INTRODUCTION

The nature and structure of the field of forces which act between a set of gaseous molecules that, in a broad sense, are reacting with each other is of essential importance for putting together possible models or for unravelling the elementary mechanisms that are responsible for the chemical processes under study. On the other hand, such forces are very seldom obtainable from direct experiments but rather are gathered from ab initio calculations or from some type of parametrisation based on other properties of the relevant systems.

This therefore means that the quality assessment of such computed potential energy surfaces (PES) is most often carried out rather indirectly by seeing how they perform in reproducing the trend of behaviour, along a sequence of chosen partners, of simple features of the systems like force constants, equilibrium distances, dissociation energies and the like.

J. Bertrán and I. G. Csizmadia (eds.),
New Theoretical Concepts for Understanding Organic Reactions, 257–289.
© 1989 by Kluwer Academic Publishers.

The indirectness of the comparison of that feature with reaction observables, hence its being removed from the quantity that one would really like to obtain from that specific PES, is made even worse by the fact that the test properties discussed above are verifying the quality of the surface within a rather limited range of nuclear geometries, i.e. only around the equilibrium structures and in the bottom of the attractive well for each set of internal molecular coordinates, while during a chemical reaction the interacting partners are really sampling a broad range of impact parameters and relative orientations, thus require the knowledge of the PES over a much larger region of nuclear geometries. In sum, even within the approximate picture of the Born-Oppenheimer (BO) electronuclear decoupling, one needs to know the interaction forces for relative distances that are far away from equilibrium configurations and therefore one has often no way of assessing the quality of the calculations that are beeing used to produce those forces.

In the present chapter we will examine another possible way of evaluating and judging the quality of either an ab initio computed PES or of an empirically-determined functional form of it. We will consider in fact the combined use of several dynamical observables for the systems at hand so that we will be able to obtain, at the end, a fairly realistic assessment of the PES reliability over a rather wide range of internal coordinates. The latter will thus be very close to what is being sampled during a chemical reaction. The current comparisons have been limited mostly to atom-diatomics systems and to ion-diatomics situations, with only a few polyatomics having been considered in both the experimental and the theoretical analysis. For the cases considered, however, the comparison of several dynamical observables has been very successful in determining the shape of the surface around potential wells, the specific depths and positions of attractive wells, the onset of the repulsive wall and the higher energy repulsive forces at closer relative distances between partners. The theoretical approach relies heavily on its interplay with several experimental results and the great power of the present analysis is its direct connection with such detailed, microscopic data like partial differential cross sections, state-to-state inelastic transitions via collisions, angular distributions of all the products and the values of the average internal energy that is being transferred at each observed angle of scattering. Moreover, the more macroscopic data related to experiments in bulks, where velocity distribution can be treated as essentially maxwellian and state populations are largely thermalised, can also be used to further evaluate the quality of the interactions by computing diffusion and viscosity coefficients, thermal conductivity and line broadening coefficients.

The following section describes briefly the processes which can be related to dynamical information at the molecular level, i.e. the observables which stem from single collision situations in molecular beams experiments. Section 3 moves ahead to those quantities which are more closely related to the kinetic theory of gases and which require the computation of the so called collision integrals.

The general conclusions and the potentials of the present approach to deal with more complicated situations are reported in Section 4.

2. MICROSCOPIC DYNAMICS

In the present Section we will summarise the various types of information that originate from a testing of the interaction as closely as possible to the molecular level, i.e. the collision observables that arise in a single collision situation. As is well known, it is not possible to study a single molecular collision experimentally and therefore the simplest set up that can be devised involves the collision of two narrow beams of molecules having well-defined initial velocities (and possibly selected in well-defined internal states) and the measurement of the resultant scattering as a function of angle. So, although energy and angle may be both specified, it is not possible to confine the collisions to a single impact parameter. Experimental results are therefore reported in terms of collision cross sections, which are quantitative measures of the intensity of the observed scattering at the given angle and for the chosen relative energy. Cross sections can therefore be defined for three types of scattering: (i) Elastic, in which the internal states of the molecular partners do not change from before to after the collisional event; (ii) Inelastic, in which a change from one specified internal energy state to another occurs; (iii) Reactive, in which there is a change in the chemical nature of the molecules undergoing collisions.

The ultimate aim of the present study is, naturally, to understand the microscopic events occuring during the reactions, but the evaluation of the various features of potential energy surfaces has been most often carried out through (i) and (ii) processes.

The scattering at a particular angle θ is characterised by a differential cross section (DCS) at a given relative energy, $\sigma(\theta,E)$, which is defined by:

$$\sigma(\theta,E) = \frac{\text{Number of scattered particles/unit time/unit solid angle}}{\text{Number of incident particles/unit time/unit area}} \quad (1)$$

If one examines the elastic process through classical mechanics, then the above quantity is given as a sum over the impact parameters b which contribute to the collision [1]:

$$\sigma(\theta,E) = \sum \left|\frac{b}{\sin\theta\ (d\theta/db)}\right| \tag{2}$$

Its corresponding value integrated over all solid angles gives us a measure of all the scattering particles irrespective of the angle to which they go after collision:

$$Q(E) = \int \sigma(\theta,E)\ d\Omega =$$

$$= \int_0^{\pi} \sigma\ (\theta,E)\ 2\pi \sin\theta d\theta \tag{3}$$

In case one considers the inelastic processes of (ii), the definition of eq. (1) for the DCS remains obviously the same but we now have to take into account the internal degrees of freedom of the molecular partners. A collision for which the initial internal quantum states of all present molecules are characterized by a string of quantum numbers that are globally represented by the vector $\|i\rangle$, and the final states by the vector $\|f\rangle$, can then be characterized by the initial and final values of the wavevectors $\underset{\sim}{\kappa}_i$ and $\underset{\sim}{\kappa}_f$. The direction of these vectors is given by the centre of mass separation vector $\underset{\sim}{R}$ and the corresponding values of the wavenumber are given by:

$$\kappa_i^2 = (2\mu/h^2)(E-\varepsilon_i) \tag{4a}$$

$$\kappa_f^2 = (2\mu/h^2)(E-\varepsilon_f) \tag{4b}$$

where E is the total (conserved) positive energy of the system and ε_i, ε_f are the initial and final total internal energies of the colliding molecular partners. A particular differential cross section involving the internal degrees of freedom of the molecules can theorefore be identified either by the scattering angle and energy (θ,E) as before or, equivalently by $\underset{\sim}{\kappa}_f$. To distinguish inelastic DCS from those for which the collision is only elastic, $\sigma(\theta,E)$, we will use the symbol I.

Among the internal degrees of freedom we will include rotations and vibrations only for cases where one PES is considered of interest and we will examine electronic degrees of freedom when considering charge exchange processes.

Experiments have been able to obtain different levels of resolution when examining the first two degrees of freedom [2] and we will therefore define correspondingly different levels of discrimination for the cross sections. In them we will designate vibrational quantum numbers by ν, rotational quantum numbers by j and the corresponding azimuthal quantum numbers by m_j.

(i) At the highest level of possible resolution, one has the individual DCS (IDCS) which measures the scattering intensity due to a particular state-to-state transition for a specific set of (j, m_j, ν) values for each molecule:

$$ {}_{I}I_i^f = I(j'_1 m'_{j1} \nu'_1, j'_2 m'_{j2} \nu'_2 \leftarrow j_1 m_{j1} \nu_1,\ j_2 m_{j2} \nu_2 | \underline{k}_f) \qquad (5) $$

where the primed quantities correspond to the final state $\|f\rangle$. We are considering here a spherical rotor and a single vibrational degree of freedom. For more complex cases, one needs to specify a series of ν values for all the normal modes involved in the process considered.

(ii) In most experiments carried out in molecular beams, unless magnetic or electric state selection is being used, individual m_j states cannot be distinguished and therefore the experimental scattered intensity gives only a Degeneracy-averaged differential cross section (DADCS) that is defined as follows:

$$ {}_{DA}I_i^f = I(j'_1 \nu'_1,\ j'_2 \nu'_2 \leftarrow j_1 \nu_1 j_2 \nu_2 | \underline{k}_f) = \sum_{\substack{m_{j_1}, m_{j_2} \\ m_{j'_1}, m_{j'_2}}} {}_{I}I_i^f \qquad (6) $$

As a consequence of this reduced resolution, we will see below that the corresponding theoretical treatments can be simplified when computing the DADCS for the available experimental systems.

(iii) Many of the experimental set ups are able to measure scattered intensities which do not resolve the final states, even if a state-selected primary beam is available. Thus, they essentially yield a rotationally-summed, total differential cross section (TDCS) given by:

$$ {}_{T}I_i^f = I\ (\nu'_1 \nu'_2 \leftarrow j_1 \nu_1 j_2 \nu_2 |\ \underline{k}_f) = \sum_{j'_1, j'_2} {}_{DA}I_i^f \qquad (7) $$

and in some cases the initial state m_j values may also be selected. The corresponding integral cross sections can also be obtained from each of the obove DCS by integrating over all angles as done in the elastic case of eq. (3), viz.

$$Q_{i\to f} = \int I_i^f \, d\Omega \int_0^{\pi} I_i^f \, 2\pi \sin\theta d\theta = \int_{-1}^{1} I_i^f \, d(\cos\theta) \qquad (8)$$

In most cases, the only available experimental quantity is the total integral cross section (TICS) given by:

$$Q(\nu'_1\nu'_2 \leftarrow j_1\nu_1 j_2\nu_2) = \int_{-1}^{1} I_{T\,i}^f \, d(\cos\theta) \qquad (9)$$

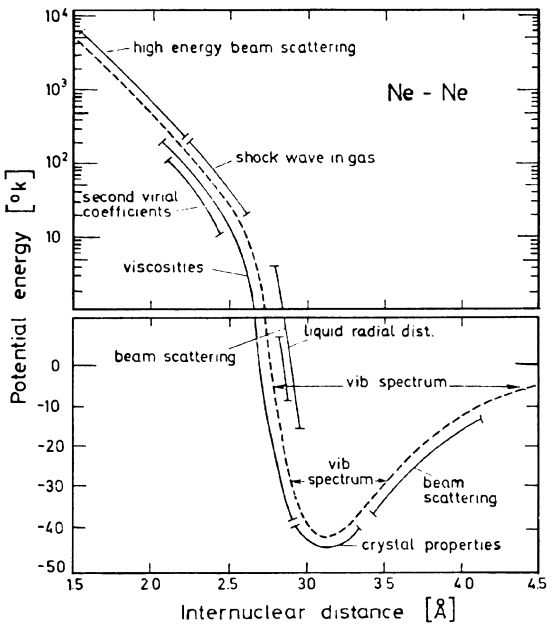

Fig. 1 Spherical interaction between Ne atoms and radial regions which are sensitive to different experimental data (from ref. [5]).

The above quantities are therefore providing quite an extensive array of data which obviously probe different features of the relevant PES as different final channels are involved. The experimental determina-

tion of them has been reviewed several times in recent years [3,4] and will not be discussed here. We will see below, however, how one can relate several of the outcomes of what we call microscopic dynamical events to the determination of different areas of the PES. As a general example, Figure 1 shows the spherical potential between Ne atoms and marks the various regions of it which are sampled by different experimental quantities: many of them are dynamical in origin and will be discussed in the following paragraphs. One clearly sees, however, that the types of tests that we are discussing here produce a reliable assessments of the full interaction only when combined together in a multiproperty analysis of as many quantities as possible.

2.1 INTEGRAL CROSS SECTIONS

As mentioned before, one the most effective ways of measuring integral cross sections - elastic, inelastic and reactive - is to use molecular beams. A molecular beam is a well-collimated stream of atoms or molecules which are at a sufficient low density and moving at sufficiently low velocities relative to each other as to eliminate collisions between them, hence minimizing both spatial and velocity broadening of the beam. The latter moves in a high vacuum to reduce the frequency of spurious collisions and impinges on a target gas (atomic or molecular) from which the scattering can be monitored by a suitable detector. The corresponding integral cross section can then be obtained by using the relation:

$$\ln \frac{I_0}{I} = n\, Q(E) l \qquad (10)$$

where I_0, I are the incident and scattered beam intensities, n is the number density of target molecules in the collision path of length l. The determination of Q(E) is then carried out at different velocities or energies, with enough E resolution and angular resolution as to be able to determine the absolute magnitude of Q(E) and its oscillatory behaviour as function of relative velocity [6].

The presence of oscillatory behaviour superimposed on the decreasing shape of the integral cross section as E increases is a very important tool for determination of various features of either a spherical potential or of the spherical average of an anisotropic PES. They are also important aspects of differential cross section behaviour, as will be discussed below, and originate from the quantum features of the scattering process [7].

The essential non-classical quantity is the scattering amplitude $f(\theta)$ and the corresponding phaseshift η contained in it. For a spherical interaction between systems in which internal structure is disregarded, the standard partial wave expansion can be used [8]:

$$f(\theta) = \frac{1}{2i\kappa} \sum_{l=0}^{\infty} (2l+1) \left(e^{2i\eta_l} - 1\right) P_l (\cos \theta) \tag{11}$$

where η_l (E) is the l-wave contribution to the phaseshift. It appears in the final expression for Q(E):

$$Q(E) = \frac{4\pi}{\kappa^2} \sum_l (2l+1) \sin^2 \eta_l \tag{12}$$

which, through the optical theorem, can be identified with the imaginary part of the forward-scattering amplitude:

$$Q(E) = \frac{4\pi}{\kappa} \operatorname{Im} \{f(o)\} \tag{13}$$

When considering scattering for non-monotonic interactions, the low-angle scattering classical result produces divergent cross sections as θ passes through zero (or through $N \cdot \pi$ if E is sufficiently low), a phenomenon that goes under the name of <u>forward glory</u>. One also knows that the quantum equation (11) produces interference between various contributing partial waves as the Q(E) is obtained from the corresponding phaseshifts. Semiclassically this means that some of the contributing trajectories correspond to coalescing branches of the deflection functions as $\theta \rightarrow 0$, while others have different path lengths that cause interference between contributions. Thus the correct Q(E) is a finite quantity, both semiclassically and quantally, and exhibits oscillatory behaviour as the maximum phase increases with a decrease in κ or in relative velocity. Provided that the potential well is deep enough, then the η_{glory} can pass successively through $N\pi/2$ [1] and the corresponding undulations observed in experiments can thus be used to obtain information on the long-range region of the PES [9,10] and on the high repulsive branch of the interaction. For instance, for a (12-6) spherical potential one can show [1] that the maxima occur when:

$$\eta_{glory} = (N - 3/8)\,\pi \qquad N = 1,2,3 \ldots \qquad (14)$$

and they oscillate about the low-velocity limiting shape corresponding to the r^{-6} attractive part of the potential. The number of maxima that can be observed have been shown to be equal to the number of bound states in the potential well [12]. At higher velocities, on the other hand, the repulsive branch of interaction dominates the scattering and, for the model (6-12) potential, the shape of log Q vs log g (with g being the relative velocity) approaches - 2/11 and the interference effects disappear since only one branch of the deflection function contributes to the scattering process [7]. Thus, whenever resolved information exists on integral cross section oscillatory structures, they can be used to obtain corresponding information on the two different regions on the non-monotonic interactions. For non spherical systems, however, no formal inversion procedures exist at present for determining the corresponding PES directly from cross section measurements involving polyatomic molecules [12], although some progress has been made in developing approximate methods [13]. Consequently, it is usually necessary to use the method of assuming a particular functional form for the anisotropy PES and of determining a limited number of variable parameters by fitting calculated cross sections to experimental measurements. Naturally, in the case of Q(E) fittings one can only control the PES parametric optimisation with regard to the region (s) of it to which the glory oscillations are sensitive. The most direct characterisation for the attractive well, or rather of its average value, can be provided by low-energy Q(E) measurements which show pronounced structures for collision velocities below ~ 0.5 km/sec, where orbiting resonances are also present, and where the oscillations are rather independent of absolute calibration [12]. This is, however, the most difficult region for measurements and with large calibration errors. On the other hand, the repulsive region of the PES is sensitive to Q(E) measurements above velocities of ~ 2 km/sec which are also difficult to reach but which allow for better calibration accuracy in the data. Finally, very often no oscillations are resolved for anisotropic systems where quenching effects are introduced by the orientational forces present in these systems and therefore only the velocity dependence of Q(E) becomes sensitive to the chosen PES form, thereby making absolute measurements and small calibration errors essential ingredients for sensitivity studies on 'well size' parameters like $\varepsilon \cdot R_m^6$, with ε being the well depth and R_m its position [14].

2.2 THE ANGULAR DISTRIBUTIONS

The centre-of-mass (CM) DCS is naturally related to the observed scattering intensity, in the LAB system, for two cross-beams of known fluxes and velocities [1]. The most important experimental factor in

reducing the resolution of $\sigma(\theta,E)$ is the spread of velocities that affects the angular resolution of the observed distributions and reduces the resolution in the LAB → CM transformation. The more experiments are able to overcome such difficulties the more structure will be present in the angular distributions for spherical systems or for molecular anisotropic systems -eqs. (2) and (7) - where inelasticity is either not present or not resolved [15].

Depending on the nature of the interactiong systems, viz. neutral species or ionic species, and on the relative strength of orientational forces, the main features that appear in the TDCS as superimposed on the classical prediction are the following:

(i) A finite rainbow maximum θ_r, where θ_r is the LAB frame angle corresponding to the CM rainbow angle X_r;
(ii) A series of supernumerary rainbow maxima on the 'bright' side of the main rainbow, i.e. for $\theta < \theta_r$;
(iii) High-frequency, lower-amplitude interference oscillations superimposed on the rainbow structure;
(iv) for strongly interacting, ion-molecule systems the additional presence of interference diffraction structures up to the small-angle region.

The semiclassical analysis of the phaseshift and scattering amplitudes via the classical deflection function and the uniform approximation [1,7], indicates that the above effects are related to dominant interference from the different turning points exhibited by a non-monotonic PES, at a given orientation, plus its centrifugal barrier. Physically this can be thought to arise from trajectories having a wide range of impact parameters all converging on the same scattering angle, θ_r, thus classically leading to an infinitely large rise in intensity over a small range of angles, while quantally producing positive interference of different groups of trajectories for the two features of (i) and (ii) reported above. A typical shape of the effective potential V^*_{eff} for various values of the centrifugal barrier (labelled in reduced units, b^*) is shown in Fig. 2 for a spherical (12-6) potential. Various possible collision energies are shown for the cases where: three turning points exist (E^*_1), an orbiting trajectory is possible (E^*_2) and a purely repulsive, monotonic potential controls the interaction (E^*_3). The reduced units of energy are given when dividing V(R) by ε and those of the distance when dividing R by R_m.

The high frequency quantum oscillations finally arise from further interference between the residual branches of the deflection function associated to the turning points shown in the above Figure. Such features are superimposed on the rising background due to the

attractive branch of the interaction that becomes increasingly dominant as one goes to lower angles [1]. The determination of θ_r for a given value of E therefore enables one to determine the well depth ε from E/E^* [7] within a few percent and also turns out to correlate with $R\cdot(\partial V_{eff}/dR)_{Ri}$, where R_i is the separation at the inflection point in the potential [12]. The R_m parameter can also be determined for a given spherical potential from the position of the rainbow maximum or, more accurately, from the positions of the supernumerary rainbows [7,12].

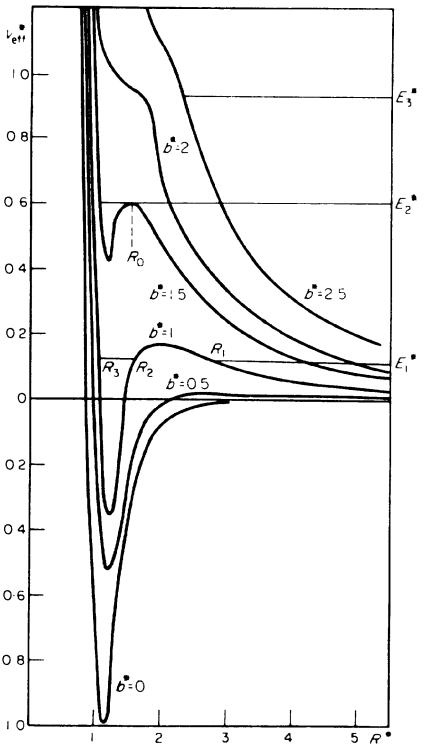

Fig. 2 - Effective, reduced model spherical potential, V^*_{eff}, as function of reduced distance R^* and for different values of the centrifugal barrier $b^* = l(l+1)/R^{*2}$.

An example of the sensitivity of observed quantities to features of the potential function is shown in Fig. 3, where the DCS for the ground-state interaction of Ar atoms and protons is shown for a specific value of collision energy. Both computed and measured values are given in the LAB frame of reference [16].

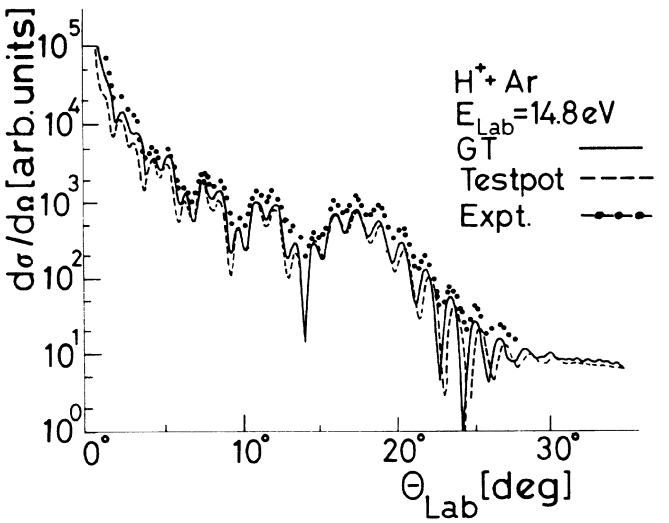

Fig. 3 - Computed and measured DCS for the Ar-H^+ system. The continuous line corresponds to the interaction optimized to scattering data at several energies (from ref. [16]).

The continous line corresponds to a parametric potential calculation in which the chosen parameters optimize all scattering data available over a wide range of collision energies [16]. As one can see, the calculated DCS perfectly reproduces the rainbow position, the supernumerary structures and the fast quantum oscillations. They also reproduce well the diffraction oscillations on the 'dark' side of the rainbow. The other potential shown, on the other hand, the TESTPOT function (dashed curve) of ref. [17], was obtained by optimizing the parameters to spectroscopic data only, viz. to the available observed transitions between the bound states supported by this ion-atom potential. One sees there that the accuracy with which the latter potential function determines the phase of all the oscillations observed with a lower accuracy than the previous potential. In fact, the R_m values only differ by less than 1 % and their ε values by about 2 % and yet the dynamical data are able to distinguish between the two functional forms.

For interacting molecular systems with small reduced masses, the anisotropy of the interaction appears as damping of the quantum mechanical diffractive oscillations of their TDCS [18]. This has been attributed primarily to anisotropy in the position of the potential minimum and in the onset of the repulsive wall of the PES [18]. For diatomic systems interacting with H or He atoms, the damping of the

diffraction oscillations is barely noticeable [19], while it appears much more markedly for systems with stronger interactions [20, 21]. When high-resolution, crossed molecular beam measurements are available on the TDCS at more than one energy, one can therefore use the damping features to obtain information on the orientational forces for simple atom-diatomics systems by comparing computed angular distributions for a spherical potential with those obtained via different estimates of anisotropic parameters and therefore selecting the ones which best reproduce the experimental measurements [22, 23].

In general, one finds that sensitivity to the repulsive wall of the interaction is limited to scattering angles beyond 30^0-35^0 for neutral systems at low collision energies (viz. $E_{coll} \leqq 1$ eV), a region usually wholly insensitive to the attractive well region and also affected the most by experimental errors [15]. Moreover, modifications in the long-range attractive part of the PES usually affect significantly the first diffraction oscillation and the classical rainbow region. Thus, TDCS tests from calculations turn out to be mostly sensitive to the attractive well and to the weakly repulsive regions of the PES. They are also sensitive to the anisotropic behaviour of the above regions through the amount of damping shown by theis DCS oscillatory features [24]. However, one should keep in mind that a selection of a shallower well can be offset by a displacement of the weakly repulsive wall, hence TDCS measurements alone may not be sufficient to characterize accurately the attractive well region. This point will be further analysed in the following paragraphs and sections.

2.3 INTERNAL ENERGYY TRANSFER

All the methods discussed so far involve some prior assumption about the functional form of the inter-molecular potential. Several prescriptions have been suggested for flexible functionals for atom-atom, atom-ion, atom-diatomics, atom-polyatomics and molecules interacting with simple ions. The relevant literature is too large to be reviewed here, but each of the examples that we are discussing in this chapter contains in the original reference an extensive analysis of this aspect of the general problem and we therefore refer the interested reader to those papers (e.g. refs. [14], [16], [19], [22-24]). As already indicated, the parametric form of the functional can sometimes give misleading results and generally much more confirmatory evidence is required to demonstrate that a particular assumed form for V(R) corresponds to the true potential [17,25]. Indeed when most of the quantum oscillations are resolved in the TDCS, application of the above procedures does not make maximum use of the scattering data and cannot extract all the information about V(R) that is contained in them. In principle, one should therefore try to invert

the scattering cross sections data and obtain V(R) without making any assumption about its possible shape. Such procedure is however frought with both theoretical and experimental difficulties. For spherical interactions two basic types of schemes exist for TDCS: Those requiring σ as a function of θ at fixed E, and those based on σ as a function of E at a fixed angular momentum. A detailed review of them is beyond the scope of this chapter and the interested reader is referred to existing, excellent reviews for atom-atom systems [12,26,27].

For molecular interactions, however, this procedure is neither rigorous nor unique [13,28] and therefore one needs to resort to the selection of a parametric functional form. A possible knowledge of inelastic processes like those defined in eqs. (5), (6) and (7) thus becomes an essential ingredient for adding a further set of experimental data for which the PES form could be tested via the computations of the relevant cross sections, integral and differential [29,30].

For the simple case of a diatomic molecule BC, intially in a set of quantum states designated by α, that collides with a structureless atom A and gets excited (or deexcited) into the new state β, the scattering process is:

$$A + BC_{\alpha} \longrightarrow A + BC_{\beta} \tag{15}$$

and the corresponding Schrödinger equation is:

$$(E - H)\ \Psi = 0 \tag{16}$$

where the Hamiltonian in the centre-of-mass coordinate system is:

$$H = -\frac{h^2}{2\mu R}\frac{\partial^2}{\partial R^2}R + \frac{\underset{\sim}{L}^2}{2\mu R^2} + H_{BC} + V(R,r,\gamma) \tag{17}$$

Here μ is the system reduced mass, $\underset{\sim}{L}$ the orbital angular momentum operator of the atom relative to the molecule and H_{BC} is the Hamiltonian for the isolated molecule BC:

$$H_{BC} = -\frac{h^2}{2mr}\frac{\partial^2}{\partial r^2}r + \frac{\underset{\sim}{j}^2}{2mr^2} + U\ (r) \tag{18}$$

where m is the molecular reduced mass and $\underset{\sim}{j}$ is the molecular angular momentum operator. The unperturbated states of BC having energy E_β and wavefunction Φ_β are given by:

$$(E_\beta - H_{BC})\ \Phi_\beta = 0 \tag{19}$$

and can constitute a convenient basis set for representing the total wavefunction Ψ under the additional presence of the anisotropic potential V of eq. (17), where arcos $\gamma = \hat{R}\cdot\hat{r}$, where the dependence on the collision coordinate R appears and where the r-dependence is also explicitely included. This potential is the quantity that we are seeking to determine, starting with some parametric model form and using it to solve eq. (16). The asymptotic expansion of the total wavefunction is therefore given by:

$$\Psi\ (R,r) = \sum_\beta \Phi_\beta\ (r)\ F_\beta(R) \tag{20}$$

where the unknown expansion coefficients represents the translational part of the w.f. in each exit channel β, both energetically accessible (open channel) and energetically forbidden (closed channel) [29]. For the elastic case the only coefficient has the asymptotic form:

$$F_\alpha(R) = e^{i\kappa_\alpha R} + f_\alpha\ (\alpha \leftarrow \alpha\ |k_\alpha)\ \frac{e^{i\kappa_\alpha R}}{R} \tag{21}$$

and for the inelastic case:

$$F_\beta(\underline{R}) = f_\beta(\beta \leftarrow \alpha\ |\kappa_\beta)\ \frac{e^{i\kappa_\beta R}}{R} \tag{22}$$

Substituting expansion (20) into eq. (16) gives:

$$\sum_\beta \Phi_\beta(\underline{r})\left(\frac{h^2}{2\mu R}\ \frac{\partial^2}{\partial R^2} + E - E_\beta - \frac{\underset{\sim}{L}^2}{2\mu R^2}\right)\ F_\beta(\underline{R}) = V(R,r,\gamma)\ \Psi\ (\underline{R},\underline{r}) \tag{23}$$

Multiplying on the left by $\Phi_\beta^*(\underline{r})$ and integrating over $\underline{r}$, gives the following equation:

$$\{\frac{h^2}{2\mu}\frac{\partial^2}{\partial R^2} + E - E_\beta - \frac{\underset{\sim}{L}^2}{2\mu R^2}\}F_\beta(\underline{R}) = \sum_\gamma F_\gamma(\underline{R})\ U_{\gamma\beta}(\underline{R}) \tag{24}$$

where:

$$U_{\gamma\beta}(R) = \int \Phi_\beta^*(\underline{r})\ U\ (r,R,\gamma)\ \Phi_\gamma(\underline{r})\ d\underline{r} \tag{25}$$

corresponds to a coupling matrix element between the PES and the rotovibrational, unperturbated, states of the target molecule. From eq. (24) one sees that such states are all coupled together by the potential and affect the specific form of each collisional exit channel $F_\beta(R)$.

Given that a certain number of states must be retained in the eq. (24) according to the energy range of the process considered and to the strength of the coupling elements of eq. (25), the first task is to reduce the number of coupled equations that need to be solved by a judicious choice of the functions used in eq. (20). In case of simple rotors, the angular parts of (20) are chosen to be eigenfunctions of the total angular momentum $\underset{\sim}{J} = \underset{\sim}{l} + \underset{\sim}{j}$, which leads to a block-diagonalisation of the matrix $\underline{U}$ of (25) and solutions are then seeked for only one of these blocks, for each value of $\underset{\sim}{J}$. The final coupled equations then become 1D coupled equations where the angular variables have been separated out through standard angular momentum coupling algebra [29]:

$$\frac{d^2}{dR^2}\ \underline{u}\ (R) + \{\ \underline{\underline{K}} - \underline{\underline{W}}\ (R) - \underline{\underline{L}}\ (\underline{\underline{L}}+\underline{\underline{I}})R^{-2}\}\ \underline{u}\ (R) = \underline{0} \tag{23}$$

where $\underline{u}$ is a column vector, $\underline{\underline{K}}$ and $\underline{\underline{L}}$ constant diagonal matrices and $\underline{\underline{W}}$ is the coupling matrix. The elements of $\underline{\underline{L}}$ are given by non-negative integers l_i which label the relative orbital angular momentum and $\underline{\underline{I}}$ is the unit matrix. The dimension of the vector space is N and controls the size of the numerical problem which we wish to solve.

One immediately sees that the range of action of the PES controls the size and strength of the matrix $\underline{\underline{W}}$ and therefore is affecting the form of the solution vectors. They are in turn producing the required phaseshifts which go into the scattering S-matrix that finally yields the cross sections of eqs. (5) to (7) [29]. Even when only vibrational and rotational states are considered, the vector space N is often very large.

For the test of the PES with experiments at relatively low energies, rather few vibrational functions may be needed, but the major problem remains the number of rotational levels. Because of the 2j+1 degeneracy associated with the energy levels of the molecular rotor, the number of coupled equation that need to be solved increases rapidly with the maximum value of j included in the basis set used in the expansion (20). As the computational time required to solve the coupled equations depends on the cube of the number in the set, the task becomes rapidly very difficult even at quite low J values. Consequently, a large number of approximate methods have been developed in the last few years, in an attempt to reduce solution time without significant less of accuracy [29, 31].

One of the most popular ways of markedly reducing the space of the $\underline{u}$ vectors is the so called Infinite-Order-Sudden-Approximation (IOSA) [29, 32], whereby two basic simplifications are introduced in the diagonal matrices $\underline{\underline{K}}$ and $\underline{\underline{L}}$. The first one is the centrifugal sudden approximation (CS) which replaces the angular momentum matrix by a prechosen l value, lo:

$$\underline{\underline{L}}\,(\underline{\underline{L}} + \underline{\underline{I}}) \tilde{-} h^2 l_0\,(l_0+1) \tag{24a}$$

and the second one is the energy sudden (ES) approximation which simplifies the wavevector matrix by selecting one reference energy level for all coupled channels:

$$\underline{\underline{K}} \tilde{-} \kappa_0 \tag{24b}$$

For a rigid rotor, i.e. disregarding for the moment the molecular vibrations, the above replacements result in an uncoupled set of ordinary differential equations for each value of the relative angle γ in the coupling potential of eq. (17):

$$\left\{\frac{d^2}{dR^2} + \kappa_0^2 - \frac{l_0(l_0+1)}{r^2} - \frac{2\mu}{h^2}\,V(R;\gamma)\right\} u_{l_0}(R,\gamma) = 0 \tag{25}$$

The angle dependent radial wavefunctions $u_{l_0}(R;\gamma)$ are obtained by solving eq. (25), for each of the contributing l_0 values and for each selected γ value, subject to the usual scattering boundary conditions:

$$g_{l_0}(R;\gamma) \underset{R\to\infty}{\sim} \kappa_0^{1/2} \left\{ e^{-i(\kappa R - l_0\pi/2)} - e^{-[(\kappa R - l_0\pi/2 + 2i\eta_{l_0}(\gamma)]} \right\} \quad (26a)$$

and:

$$g_{l_0}(0;\gamma) = 0 \quad (26b)$$

The phaseshift is obtained for each fixed orientation and produces in turn an angle dependent scattering amplitude:

$$f(\gamma|\theta) = \frac{i}{2\kappa_0} \sum_{l=0}^{\infty} (2l+1) \left[1 - e^{2i\eta_l(\gamma)}\right] P_l(\cos,\theta) \quad (27)$$

It can then be shown [29] that at the TDCS is simply the weighted orientation average:

$$_T I(\theta) = \frac{1}{2} \int_{-1}^{1} I(\gamma,\theta)\, d\cos\gamma \quad (28)$$

of the 'central field' DCS, at each γ, obtained from eq. (27):

$$I(\gamma,\theta) = \frac{1}{4\kappa^2} \left\{ \left[\sum_l (2l+1) \sin\left[2\eta_l(\gamma)\right] P_l(\cos\theta) \right]^2 + \left[\sum_l (2l+1) \cos\left[2\eta_l(\gamma)-1\right] P_l(\cos\theta) \right]^2 \right\} \quad (29)$$

Moreover, the degeneracy-averaged, state-to-state DCS can be determined [29] from the transition out of j=0:

$$_{DA} I(j' \leftarrow j|\theta) = \sum_{j''=|j-j'|}^{j+j'} C^2(j,j'',j',0,0,0)^2\, I(j'' \leftarrow o|\theta) \quad (30)$$

where:

$$I\ (j'' \leftarrow j|\theta) = |F_{j''}(\theta)|^2 \tag{31}$$

and:

$$f(\gamma|\theta) = \sum_L F_L(\theta) P_L\ (\cos\gamma) \tag{32}$$

The above IOSA decoupling is considered valid when two conditions are satisfied:

(i) The relative kinetic energy is large compared to the rotational energy spacing, i.e. the ES is acceptable;
(ii) Rotational transitions are dominated by relatively small values of the orbital angular momentum and the centrifugal barrier is therefore less important than the main potential in the regions of the relevant turning points (CS approximation).

In most collision experiments in molecular beams that involve Van der Waals (VdW) systems, the above conditions have been tested for many cases [14,20,24,33,34] and found to be satisfied at the energy considered. Thus, the state-to-state DCS of eq. (30) can be easily computed and used to test the anisotropic part of the PES. This method of testing is of course more reliable than the one based only on quenching effects in TDCS, as discussed in the previous section, since in the latter case the desired anisotropy is directly obtained from experimental cross sections.

An example of the sensitivity of such measured quantities on the details of the PES employed is shown in Figures 4 and 5 for the He-N_2 system [14,34].

The highly resolved experimental results for the TDCS and inelastic DCS for (0 → 2), (1 → 3) and (0 → 4) rotational excitation processes [35] reveal the presence of marked interference oscillations, in both types of angular distributions, which are very sensitive the position of the well depth, its depth and anisotropy, together with the anisotropies of the attractive well and of the lower part of the repulsive wall [34]. The results of Fig. 4 reveal a very good accord between the inelastic data computed via the IOS approximation (that are also identical with rigorous close-coupling calculations [34]) and the measured inelastic cross sections. The corresponding TDCS, however, show a slight shift of the phases of their oscillations with respect to the experiments. A change of collision energy of about 10 %, however, is able to reproduce perfectly the experimental data (Fig. 5) and still agrees with the state-to-state inelastic cross sections.

The theoretical results are therefore able to question and to test the accuracy of energy calibrations in beam experiments.

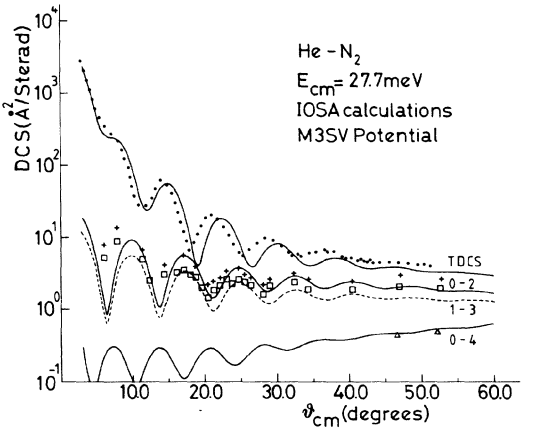

Fig. 4. Computed and measured TDCS and rotationally inelastic DCS for the He-N_2 system and for a specific parametric potential from ref. [14].

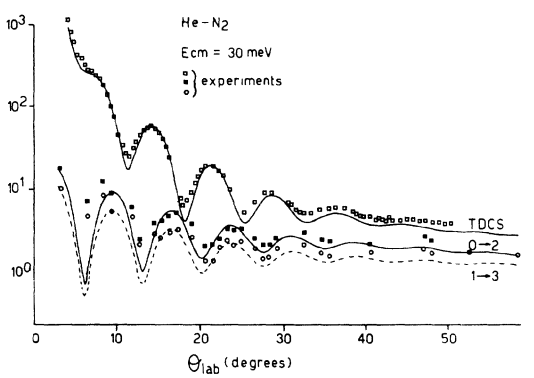

Fig. 5. Same as in Fig. 4 but for a collision energy of 30 meV. The same potential of ref. [14] is employed.

2.4 CHARGE TRANSFER PROCESSES

The test of potential functions from elementary dynamical processes has been discussed above via the use of one PES, viz. only for neutral systems colliding at relative energies which essentially exclude processes with changes in the electronic states of the molecules involved. One could, however, examine also collisional events where

the electronic degrees of freedom are coupled with the internal degrees of freedom and therefore obtain information on several PES that are possibly involved in the dynamical process.

One type of collision process, at near-thermal energies and at intermediate energies, that has recently offered several experimental data with which to test potential energy surfaces are the inelastic collisions of simple molecules with proton beams:

$$M(\nu_i, j_i) + H^+(\kappa_i) \rightarrow M(\nu_f, j_f) + H^+(\kappa_f) \qquad (33a)$$

$$M(\nu_i, j_i) + H^+(\kappa_i) \rightarrow M^+(\nu_f, j_f) + H(\kappa_f) \qquad (33b)$$

where the inelastic channel of (33a) only involves final rotovibrational state changes in the target molecule M, while the process of (33b) also indicates charge-transfer processes and therefore the involvement of several PES.

In recent years the vibrationally inelastic scattering part of the above processes involving light ions (H^+, Li^+) and simple polyatomics (CO_2, N_2O, CF_4, SF_6 etc.) has been the subject of extensive experimental and theoretical studies. Most of the work has been thoroughly reviewed recently [36] and the authors provide there a detailed presentation of the data available from beams as well as from bulk experiments. In the case of polyatomic targets several fundamental vibrational modes are available and their preferential, or selective, excitation has been found to be extremely sensitive to the dynamical conditions and to the particular mechanism involved in the coupling. Moreover, depending on whether the process of eq. (33b) is exothermic or endothermic, the charge-transfer is more likely to occur in either a Landau-Zener-type of curve crossing transition or via Demkov coupling between nearly parallel potential energy surfaces [37]. In either case, however, detailed knowledge of the surface is necessary and a test of its reliablity can be carried out by comparing its cross sections with those measured in the experiments.

The quantal nature of the collisions with ions can be seen when angular distributions are examined from calculations of DCS on a single PES and quantum and classical procedures are compared. This is shown by the results of Figure 6 for Li^+ colliding with H_2 at rather low energies, which present the state-to-state degeneracy averaged DCS, ${}_{DA}I_i^f$, for various rotationally inelastic and vibrationally elastic processes [38]. One clearly sees that the fast oscillations produced by quantum interference effects are not well reproduced by the classical results and the rainbow positions are also shifted to

higher energies. This suggests that the test of PES via classical mechanics for strongly interacting species can only provide qualitative comparisons with experiments [38].

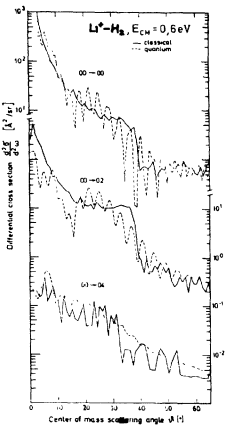

Fig. 6. Comparison of classical elastic and inelastic DCS with quantum calculations for Li^+-para H_2 at E = 0.6 eV (from ref. [38]).

The anisotropy of the interaction, i.e. the strength and the extension of the orientational forces is also much more marked in ionic PES than it is for neutral systems, unless chemical bonds are formed in the latter case. This therefore means that rotational energy transfer data can be used to obtain information on the quality of the employed PES [39], by comparing measured and computed average energy transfers from a given j_i level:

$$\langle \Delta E_{rot} \rangle_{j_i} = \sum_{j_f} \sigma\,(j_i \to j_f) \cdot \Delta E(j_i \to j_f) \cdot] \sum_{j_f} \sigma(j_i \to j_f)]^{-1} \qquad (34)$$

or, when resolved collisional data are not available by evaluating the total, rotational energy transfer:

$$\langle \Delta E_{rot} \rangle_{tot} = \sum \langle \Delta E_{rot} \rangle_{j_i} \times g_{j_i} \qquad (35)$$

where some distribution of rotational states in the molecular beam need to be used to provide the statistical weights g_j .

A common way of representing PES anisotropy is through the coefficients of an orthogonal expansion over angular functions. In the case of ion-diatomics, this can be written as:

$$V(R,\gamma) \cong \sum_{\lambda}^{\lambda_{max}} V_{\lambda}(R)\, P_{\lambda}(\cos\gamma) \qquad (36)$$

where the V_λ's are the multipolar coefficients and provide a measure of the potential anisotropy at the various ion-molecule relative distances R. An example of an ab initio computed PES, using highly correlated, MRD-CI wavefunctions [40], is shown in Figure 7 for the BF ($^1\Sigma$) interacting with H^+. One clearly sees there that attractive forces, with low-λ values in the coefficients, dominate the intermediate and long-range interaction while, as the ion approaches the molecule, more repulsive and highly anisotropic coefficients dominate in the description of the PES, as the higher coefficients plotted on the right of the Figure indicate.

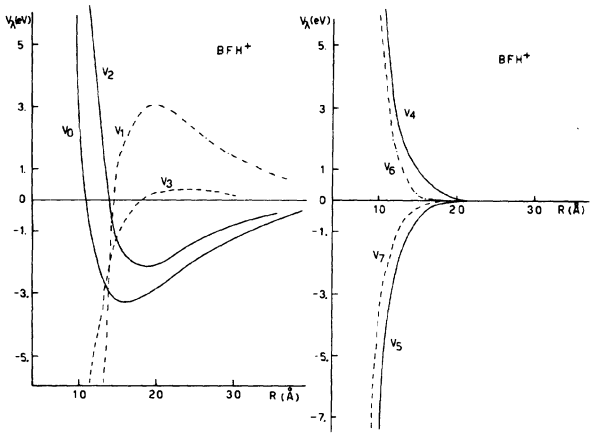

Fig. 7. Computed multipolar coefficients for H^+-BF ($^1\Sigma$) interaction, using MRD-CI wavefunction (from Ref. [40]).

As mentioned before, charge-transfer processes always involve different electronic PES being coupled during the collision and therefore these various potential surfaces can be tested against different data according to the mechanism which might dominate the dynamics [36]. In the case of $O_2(^3\Sigma_g^-)$ interacting with H^+, the experiments have clearly revealed the possible formation of O_2^+ ($^2\pi_g$) during the charge-transfer collision [41]. The suggested explanation, after computing the PES relevant for both processes [42], was of adiabatic, local charge-transfer through the change in the electronic structure within each surface. Dynamical calculations of TDCS and rotational energy transfer processes with the two adiabatic surfaces [43] surmise that the process leads to different rotational inelasti-

city by each PES but to an overall very low probability of exciting rotational modes, as also indicated by experiments [41]. The calculations also show that both processes should lead to essentially the same value of the rainbow angles in both channels, which is also confirmed by experiments. The TDCS, computed at the experimentally observed collision energy, are shown for both channels in Figure 8 and clearly exhibit the same value of rainbow maxima for the two adiabatic surfaces. This dynamical test therefore confirms that even for multisurface dynamics, the elementary collision processes can be used to evaluate the quality of the employed PES.

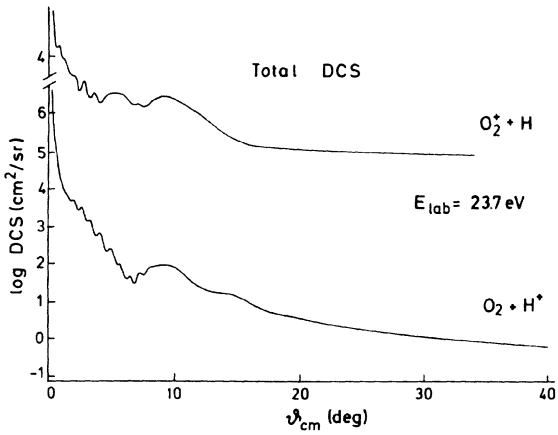

Fig. 8. Computed total differential cross sections for the two adiabatic surfaces of the charge transfer process (from ref. [43]).

3. MOLECULAR TRANSPORT PROPERTIES

The kinetic theory of dilute gases establishes that the transport coefficients are related to the forces between pairs of molecules and therefore provides observables which carry information on molecular interactions [9]. The molecular diffusion coefficient, the viscosity coefficient in pure gases and in gaseous mixtures, the thermal conductivity, the thermal diffusion and the virial coefficients, all quantify the difficulty for the transport of mass, momentum and energy in a molecular gas subjected to gradients of concentration, velocity or temperature [44]. Because, in a dilute gas, this transport is achieved by motion of the molecules the nature of the collision that the molecules undergo influences the difficulty of transport. Furthermore, since the outcome of the binary collisions is determined by the form of the intermolecular potential, the latter is going to influence the transport properties in a rather complicated but specific way.

The fundamental kinetic theory for transport coefficients can be formulated, however, in a way which involves only a set of well defined collision integrals [9,44] in addition to molecular masses, temperature and pressure in the gaesous mixture. These collision integrals represent variously weighted, energy-averaged cross sections for the binary encounters between molecules in the dilute gas.

The most significant feature of the above theory therefore is that each of the transport coefficients in the gas mixture can be expressed in terms of well defined integrals over the relevant PES for each of the possible binary encounters in the system. Thus, provided that the relevant PES is either known or estimated from other sources, it becomes possible to calculate the transport properties of a gas consisting of such molecules to any desired degree of accuracy at any temperature.

The great improvement, over the last ten years or so, that has occurred on the quality of the experimental determination of the various transport coefficients, and the corresponding increased efficiency of the computational tools used to generate collision integrals, is now making possible to test different potential surfaces against the outcome of experiments over rather wide ranges of temperature. In the following we briefly summarize the theoretical formulation and give some specific examples on how effective the various properties are in testing potential functions.

3.1 GENERALIZED COLLISION INTEGRALS

The necessary generalized collision integrals are defined by [9, 45]:

$$\Omega_{ij}^{(n,s)} = \frac{1}{2}\left(\frac{K_BT}{2\pi\mu}\right)^{1/2} \frac{1}{(K_BT)^{s+2}} \int d\zeta\, \zeta^{s+1}\, e^{-\zeta/K_BT}\, Q^{(n)}(\zeta) \quad (37)$$

where i and j refer to the collision partners and the $Q^{(n)}(\zeta)$ are the generalized integral cross sections:

$$Q^{(n)}(\zeta) = q_r^{-1} \sum_{j=0}^{\infty} (2j+1)\, e^{-\varepsilon_j/K_BT} \times$$

$$\times \sum_{j'=0}^{\infty} \int d(\cos\theta)\; I_{DA}(j' \leftarrow j|\theta)\; \Phi_n(\zeta, \theta) \quad (38)$$

where the degeneracy-averaged differential cross sections of eq. (30) are used and:

$$\Phi_1(\zeta,\theta) = 1 - (\zeta'/\zeta)^{1/2} \cos\theta \tag{38a}$$

$$\Phi_2(\zeta,\theta) = \left(\frac{\zeta'}{\zeta}\right) (1 - \cos^2\theta) + \frac{1}{3} \left(1 - \frac{\zeta'}{\zeta}\right)^2 \tag{38b}$$

In these expressions $\zeta = h^2\kappa^2/2\mu$ and $\zeta' = \zeta - (\varepsilon'_j - \varepsilon_j)$ are the incident and final relative kinetic energies, and q_r is the rotational partition function for the partner molecules in an atom (ion)-molecule mixture:

$$q_r = \sum_{j=0}^{\infty} (2j+1)\, e^{-\varepsilon_j/K_BT} \tag{39}$$

and ε_j is the rotational energy of the isolated molecule. If one assumes, consistently with the IOS approximation discussed before, that $\zeta = \zeta'$, then the Φ_n became independent of energy and are given by:

$$\Phi_n(\zeta,\theta) \simeq \Phi_n(\theta) = 1 - \cos^n\theta \tag{40}$$

If one uses the above prescription in eq. (38) than the generalized integral cross sections are considerably simplified as the final and initial rotational states can be summed over analytically to give:

$$Q^{(n)}(\zeta) = \frac{1}{2} \int_{-1}^{1} Q^{(n)}(\zeta;\gamma)\, d(\cos\gamma) \tag{41}$$

which in turn contains the following generalized IOS, angle-dependent cross section [46]:

$$Q^{(n)} = \frac{4\pi}{\kappa^2} \sum_l \sum_j C^{(n)}_{lj} \sin^2 [\eta_{l+j}(\gamma) - \eta_l(\gamma)] \tag{42}$$

where the phaseshifts have been defined before in Section 2 and the coefficients are given by:

$$C^{(n)}_{lj} = \sum_{k=j}^{n} \frac{2^{\kappa}(2\kappa+1)n![(n+k)/2]!(2l+1)(2l+2j+1)}{(n+k+1)![n-k)/2]!(2l+1)(2l+2j+1)} = \tag{43}$$

$$\times\ C^2\ (k,l,\ k+1;\ 0,0,0)$$

Thus, IOSA cross sections producing the $\eta(\gamma)$ can be directly, and rapidly, used to produce the relevant collision integrals. Only recently, however, has the IOS approximation been tested against rigorous calculations [47] and has been proved to ba accurate, at least for the He-N_2 case, within 1 %. The IOS scheme is therefore the one quantum approach that has been recently most frequently employed for the calculation of the above integrals.

3.2 DIFFUSION COEFFICIENTS

The first order diffusion coefficient, physically describing transport of mass in the gaseous mixture along a concentration gradient, is given by [9]:

$$D^{(i)}_{ij} = \frac{3K_BT}{16N\mu\Omega^{(1,1)}_{ij}} \tag{44}$$

where N is now the total number density (molecules/cm^3) of the gas. One can also go further [44] and define the second-order approximation which is given by:

$$D^{(2)}_{12} = D^{(1)}_{12}\ (1-\Delta_{12})^{-1} \tag{45}$$

where the Δ_{12} are defined in the literature as function of masses and of higher order Ω integrals [44]. In the cases currently tested, the corrections are often very small at the temperature examined [48] but obviously depend very markedly on the system at hand [49].

As an example of the selective power over chosen PES of this transport property, Fig. 9 shows the relative percentage error Δ% = (exp -calc.)/exp of computed diffusion coefficients for the He-N_2 system with various parametric potentials recently employed on an extensive study of transport coefficients [50]. Given the fact that different errors (ε) are stated by the experiments, one sees in that Figure that the multiproperty PES labelled M3SV and ESMSV are providing here the best accord with measurements, thus allowing us to treat the other choices as insufficiently accurate.

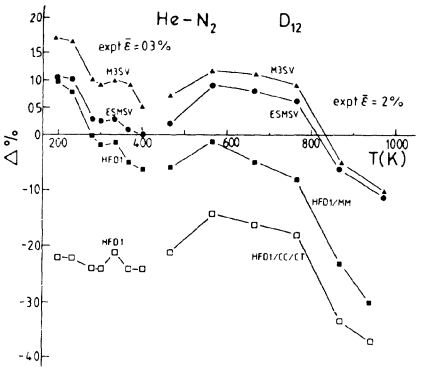

Fig. 9. Computed diffusion coefficients for the He-N_2 system using IOSA cross sections and different parametric potentials. From ref. 50. see there for the meaning of symbols.

3.3 VISCOSITY COEFFICIENTS

The first order interaction viscosity in a gaseous mixture corresponds to the transport of particle momentum along a velocity gradient. It can be considered as simplified viscosity of an hypothetical gas of molecules with a mass equal to twice the reduced mass of the two species in the mixture and whose intermolecular potential is the one acting between the two species.

It is given by:

$$\eta_{ij}^{(1)} = \frac{5\, K_B\, T}{8\, \Omega_{ij}^{(2,2)}} \tag{46}$$

and is related also to the diffusion coefficient of the same mixture by a simple relationship [9].

The first order mixture viscosity of the binary mixture depends more explicitely on the concentration [44]:

$$\eta^{(1)}_{mix} = \frac{H_{22}x_1^2 - 2H_{12}\, x_1x_2 + H_{11}x_2^2}{H_{11} \cdot H_{22} - H_{12}^2} \qquad (47)$$

where the x_i are the mole fractions of the two species and the H_{ij} are functions of mole fractions, interaction viscosity and viscosity coefficients of the pure systems [9].

Also in this case, higher order coefficients can be obtained and turn out to be within 1 % of the first-order values for many of the systems examined [49,50].

A comparison of computed values of interaction viscosity for the He-O_2 systems, using a recently proposed PES from scattering data [24,33] and employing different experimental data [50] is shown in Figure 10.

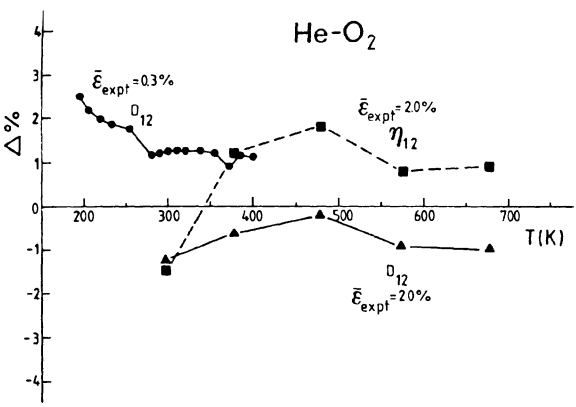

Fig. 10. relative percentage errors between computed and measured interaction viscosity coefficients for He-O_2. From ref. 50. see there for meaning of symbols.

One clearly sees there that the computed quantities are all within the stated error of the experiments and thus provide a further check on the quality of the PES produced from scattering data and supports the fact that inelastic processes examined via microscopic dynamics are very important for reliably testing PES.

This last point is explicitely underlined by the results shown in Figure 11 for the Ar-N_2 system. The various potential energy functions reported there were used to compute interaction viscosity coefficients and compared with the available experimental quantities [50]. The M3SV potential was obtained from integral cross sections only, without reference to inelastic processes, and is clearly ruled out by our calculations. The only one which is not excluded here is the BTT potential surface that is currently being tested in further dynamical calculations [51], thus proving the selecting power of transport property studies.

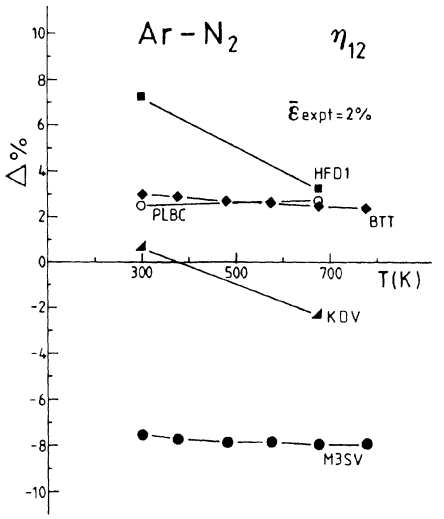

Fig. 11. Computed and measured interaction viscosity coefficients for Ar-N_2, using different forms of potential energy functionals. (From ref. 50).

4. CONCLUSIONS

In the present chapter we have looked into the use of several molecular properties for testing the reliability and the quality of simple potential energy surfaces (neutral and ionic). This is done by developing first the theoretical models which produce the relevant observables from first principles, and which employ the PES as an intermediate step for the calculation of such oberservables, and then by studying the sensitivity of the computed quantities on several different features of the surface employed.

The use of dynamical observables from elementary collision processes allows one to relate rather directly the employed PES with quantities that are measured without several convolutions that can distort the nature of the elementary event. Thus, we have shown that differential cross sections at various angles, inelastic processes as function of energy and orientation and charge-transfer cross sections in beam experiments can indeed tell us of various aspects of the intermolecular interaction for different regions of it. Moreover, the use of gas kinetic theory has been discussed for the formulation of other molecular properties, in a gas mixture, that can be related to generalized collision integrals viz. to the convoluted integral cross sections, elastic and inelastic, over velocity distributions of partners at the examined temperatures.

Even in this case, recent computational simplifications have allowed the rapid and efficient calculations of virial coefficients, diffusion and viscosity coefficients and thermal conductivity data for several potential functionals. The procedure indicates that the averaging over different velocities does reduce the possibility of testing finer details of the surfaces, for example their anisotropy in the short-range and in the attractive regions, but still produces results which are capable of selecting a possible PES functional form that can later be improved upon via the study of more direct dynamical observables.

The future of the present multiproperty tests looks therefore very promising, at least for simple molecular targets and interaction potentials. The computational tools have been made rather accurate and efficient and experiments are becoming both more precise and more capable of dealing with polyatomic species. The ultimate goal of analysing along similar lines truly reactive systems does not seem out of reach, although, several hurdles still need to be overcome, both theoretically and experimentally, before this can be reliably done.

5. ACKNOWLEDGEMENTS

I am grateful to Drs. M. Venanzi, A. Palma and F. Schneider for several useful discussions on various aspects of this work. I thank Dr. A.S. Dickinson, University of Newcastle, for providing illuminating comments on the calculations of transport properties. Finally I am grateful to Prof. J. Peter Toennies for his warm hospitality in Göttingen during the summer of 1988, when the present work was completed.

6. REFERENCES

[1] e.g. see: Child, M.S., Molecular Collision Theory, Academic Press, London (1974)

[2] e.g. see: Toennies, J.P., 'The calculation and measurement of cross sections for rotational and vibrational excitation', Ann. Rev. Phys. Chem. 27, 225 (1976).

[3] M. Faubel, 'Vibrational and rotational excitation in molecular collisions', Adv. At. Mol. Phys. 19, 345 (1983).

[4] A. Weber, Ed., Structure and Dynamics of Weakly Bound Molecular Complexes, Reidel, Dordrecht (1987).

[5] J.P. Toennies, Physical Chemistry, An Advanced Treatise, Vol. VIA, 227 (1974).

[6] H. Pauly and J.P. Toennies, Methods of Experimental Physics, 7A, 227, Academic Press, New York (1968).

[7] H. Pauly, 'The scattering by spherical potentials', in Atom-Molecular Collision Theory, pg. 111, R.B. Bernstein Ed., Plenum Press, New York (1979).

[8] C.J. Joachain, Scattering Theory, North Holland Publ. Co., Amsterdam (1978).

[9] G.C. Maitland, M. Rigby, E.B. Smith, W.A. Wakeham, Intermolecular forces, Clarendon Press, Oxford (1981).

[10] e.g. see: E.A. Mason and J.T. Vanderslice, Atomic and molecular processes, D.R. Bates Ed., Academic Press, New York (1962).

[11] R.B. Bernstein, J. Chem. Phys., 37, 1880 (1962)

[12] U. Buck, Rev. Mod. Phys., 46, 369 (1974)

[13] R.B. Gerber, V. Buck and U. Buck, J. Chem. Phys. 72, 3596 (1980)

[14] F.A. Gianturco, M. Venanzi, R. Candori, F. Pirani, F. Vecchiocattivi, A.S. Dickinson and M.S. Lee, Chem. Phys., 109, 417 (1986).

[15] M. Faubel and J.P. Toennies, Adv. At. Mol. Phys., 13, 229 (1978).

[16] F.A. Gianturco, G. Niedner, M. Noll, E. Semprini, F. Stefani and J.P. Toennies, Z. Phys. D, 7, 281 (1987)

[17] F.A. Gianturco and M. Patriarca, Nuovo Cim. D., XX (1988)

[18] R.T. Pack, Chem. Phys. Lett. 55, 197 (1978).

[19] M. Faubel, K.H. Kohl, J.P. Toennies and F.A. Gianturco, J. Chem. Phys. 78, 5629 (1983)

[20] F.A. Gianturco, A. Palma and M. Venanzi, Mol. Phys. 56, 399 (1985).

[21] L.J. Danielson, K.M. McLeod and M. Keil, J. Chem. Phys., 87, 239 (1987)

[22] L. Beneventi, P. Casavecchia and G.B. Volpi, J. Chem. Phys. 85, 7011 (1986)

[23] G.A. Parker, M. Keil and A. Kuppermann, J. Chem. Phys., 78, 1145 (1983)

[24] F.A. Gianturco and A. Palma, J. Phys. B, 18, L519 (1985).

[25] M. Keil and G.A. Parker, J. Chem. Phys., 82, 1947 (1985)

[26] U. Buck, J. Chem. Phys. 54, 1923 (1971)
[27] U. Buck, Comp. Phys. Rep. 5, 1 (1986)
[28] R.B. Gerber, M. Shapiro, U. Buck and J. Schleusener, Phys. Rev. Lett., 41, 236 (1978).
[29] for the general theory, see: F.A. Gianturco, The transfer of molecular energy by collisions, Springer Verlag, Berlin (1979).
[30] U. Buck, H. Meyer, M. Tolle and R. Schinke, Chem. Phys., 104, 345 (1986).
[31] For a composite presentation of various methods see the individual reviews in: R.B. Bernstein, ed., Atom-molecule Collision Theory, Plenum Press, New York (1979).
[32] G.A. Parker and R.T. Pack, J. Chem. Phys. 68, 1585 (1978) and references quoted therein.
[33] M. Faubel, K.H. Kohl, J.P. Toennies and F.A. Gianturco, J. Chem. Phys., 78, 5629 (1983).
[34] F.A. Gianturco, M. Venanzi and M. Faubel (to be published)
[35] M. Faubel, K.H. Kohl, J.P. Toennies, K.T. Tang and Y.Y. Young, Faraday Disc. Chem. Soc. 73, 205 (1982).
[36] D.J. Krajnovich, C.S. Parmenter and D.L. Catlett Jr., Chem. Rev. 87, 237 (1987)
[37] Y.N. Demkov, Sov. Phys. JETP 18, 138 (1964)
[38] G.D. Barg, G.M. Kendall and J.P. Toennies, Chem. Phys. 16, 243 (1976).
[39] B. Friedrich, F.A. Gianturco, G. Niedner, M. Noll and J.P. Toennies, J. Phys. B 20, 3725 (1987)
[40] F.A. Gianturco and F. Schneider, J. Phys. B (in press).
[41] M. Noll and J.P. Toennies, J. Chem. Phys., 85, 3313 (1986)
[42] F. Schneider, L. Zülicke, D. DiGiacomo, F.A. Gianturco, I. Paidarova and R. Polak, Chem. Phys. (to be published)
[43] F.A. Gianturco, A. Palma and F. Schneider (in preparation)
[44] S. Chapman and T.G. Cowling, The mathematical Theory of non-uniform gases, Cambridge U.P., England (1970)
[45] J.H. Ferziger and H.G. Kaper, Mathematical Theory of Transport Properties in Gases, North-Holland, Amsterdam (1972).
[46] R.J. Munn, F.J. Smith and E.A. Mason, J. Chem. Phys., 42, 537 (1965)
[47] G.C. Maitland, M. Mustafa, W.A. Wakeham, and F.R.W. McCourt, Mol. Phys., 61, 359 (1987)
[48] F.A. Gianturco and M. Venanzi, Mol. Phys. (in preparation)
[49] M. Keil and G.A. Parker, J. Chem. Phys. 82, 1947 (1985)
[50] F.A. Gianturco, M. Venanzi and A.S. Dickinson, Mol. Phys. (in press)
[51] F:A. Gianturco, M. Venanzi and A.S. Dickinson, (in preparation)

DYNAMICAL FORMULATION OF TRANSITION STATE THEORY: VARIATIONAL TRANSITION STATES AND SEMICLASSICAL TUNNELING

Susan C. Tucker and Donald G. Truhlar
Department of Chemistry and Supercomputer Institute
University of Minnesota
Minneapolis, MN 55455, U.S.A.

ABSTRACT. This paper is an introduction to recent research in generalized transition state theory. We derive the theory by considering the equilibrium flux through a surface dividing reactants from products, and we show its equivalence to the quasi–thermodynamic formulation of transition state theory. We show that conventional transition state theory is obtained from the generalized theory with a specific choice of dividing surface, but we stress that in many cases the variational identification of the transition state provides significant improvement. We discuss methods for including quantum effects, with special attention to the semiclassical treatment of tunneling. We briefly review tests of the theory and applications to gas–phase, condensed–phase, and interface reactions. Finally we discuss the importance of nonsubstantial contributions to quasi–thermodynamic quantities.

1. Introduction

Transition state theory (TST) has been the most widely used framework for the interpretation of reaction rate constants for many years [1,2]. Transition state theory is used in two quite different ways, which we will call the phenomenological approach and the absolute rate theory approach. In the former, experimental data are interpreted using transition state theory concepts, and — in favorable cases — parameters characterizing the transition state or the barrier to tunneling are extracted. In the latter, rate constants are calculated using semiempirical or *ab initio* information either about the electronic forces on the nuclei or about the Born–Oppenheimer potential energy hypersurface (which is usually just called the "energy surface"). Recent research on the latter approach, including both variational generalizations of the conventional theory and improved methods for calculating tunneling contributions, has led to much better estimates of the accuracy that can be achieved with this method than were previously available. It has also led to a better understanding of dynamical bottlenecks and tunneling paths, allowing us to interpret the phenomenological parameters obtained from experiment, even in cases where full force fields or energy surfaces are unavailable, and, consequently, full rate constant calculations cannot be performed. In the present review we summarize the principal concepts and equations which have emerged from this recent research and which provide us with a better framework for understanding many types of reactions, including gas–phase bimolecular and

J. Bertrán and I. G. Csizmadia (eds.),
New Theoretical Concepts for Understanding Organic Reactions, 291–346.
© 1989 by Kluwer Academic Publishers.

unimolecular reactions, reactions on surfaces, and reactions in solution.

As mentioned above, the absolute rate approach requires information about the potential energy as a function of nuclear coordinates; the amount of such information required is dependent upon which generalization of TST is used, and whether tunneling corrections are important. For a variational transition state theory calculation with a fully optimized multidimensional tunneling correction, the amount of information required is intermediate between a reaction–path Hamiltonian and a full energy surface.

Although derivations of TST may be found in many textbooks, these derivations are almost invariably based on a quasi–thermodynamic treatment of a postulated equilibrium between the reactant and transition state species [1,3]. One can obtain more insight into the validity of the theory, though, by deriving it from a dynamical approach [4–8], which makes the nature of the equilibrium assumption more transparent. This type of derivation, which we shall use here, allows for an explicit statement of the dynamical assumptions required by TST. It also provides a specific definition of the transition state "species", and — it will be seen — this definition naturally allows for variational improvements of TST. We will derive a result for generalized transition state theory (GTST), and we will obtain conventional and variational TST as special cases.

Section 2 contains a pedagogically oriented dynamical derivation of TST. We begin this section by defining a useful general coordinate system. Then we consider the continuity equation for an ensemble of reactive systems in phase space, and we present a simple derivation of an expression for the equilibrium flux through a phase–space hypersurface that divides reactants from products. We equate this hypersurface with the transition state species, and we make the TST approximation, which equates this flux to the rate constant. We end Section 2 by showing the equivalence of the dynamical result with the standard result derived by postulating the transition state to be in equilibrium with reactants. All considerations in Section 2 are entirely classical. In Section 3 we quantize all modes except the reaction coordinate, and in Section 4 we describe several methods for including quantum effects on the reaction coordinate.

Section 5 discusses tests and applications of the theory to various gas–phase processes, and Section 6 discusses extensions to reactions at crystalline surfaces and in condensed phases.

In Section 7 we discuss different ways to formulate GTST in terms of quasi–thermodynamic parameters of the transition state species. We show that nonconventional contributions to the enthalpy and entropy of the transition state species may be required in order to use these quantities to accurately estimate rate constants.

2. Classical Variational Transition State Theory

First we derive a classical generalized transition state theory rate constant expression, following Refs. 4–8. We consider, as a general example, a system of classical particles which interact according to a known energy surface V. Specifically, we consider systems in which reaction occurs electronically adiabatically in the ground electronic state with negligible vibronic coupling. The reaction may then be treated as the motion of N atoms governed by a single Born–Oppenheimer potential energy surface. We consider an N–atom system which can undergo chemical bond rearrangement. This system will be, at any

given time, in the reactant region of phase space, in the product region, or in some intermediate region. If the reaction is to be described unambiguously, the probability of being in the intermediate region should be small.

We shall consider both bimolecular and unimolecular reactions. In the former case we write

$$A + B \rightarrow AB^{\ddagger} \rightarrow P, \tag{1}$$

where A and B represent the reactant species, which may be atoms, radicals, molecules, or ions, $AB^{\ddagger}$ represents an activated complex, and P represents the products, which may be an associated product AB or two new subsystems, say C and D. In the case of unimolecular reactions, we write

$$A \rightarrow A^{\ddagger} \rightarrow P. \tag{2}$$

In both (1) and (2) we pay no explicit attention to inert collision partners or solvents, although these may play an essential role in promoting equilibrium among reactants, stabilizing nascent products, or both. If collision partners or solvents have interactions with the reactants or with the activated complex that alter the partition functions of these reacting species, they can be included by letting A, B, and $AB^{\ddagger}$ or A and $A^{\ddagger}$ represent solvated species rather than isolated ones.

Before deriving the classical transition state theory formalism for treating such reactions, we present the coordinate system we use to describe N–atom systems. For simplicity we formulate the description of such systems in terms of 3N isoinertial mass–scaled cartesian coordinates [9]. [These are essentially the same as the mass–weighted cartesians widely used in vibrational spectroscopy [10]. The difference is that the spectroscopists' coordinates have units $(\text{mass})^{\frac{1}{2}}$ length, but we introduce an extra factor $\mu^{-\frac{1}{2}}$ so that the coordinates have units of length.] Thus, if $R_{i\gamma}$, for $\gamma = x, y, z$, are the cartesian coordinates of atom i with respect to the center of mass of the system, then the mass–scaled coordinates are defined by

$$q_j = \left(\frac{m_i}{\mu}\right)^{\frac{1}{2}} R_{i\gamma}; \quad i=1,\ldots,N; \quad \gamma=x,y,z; \quad j=1,\ldots,3N, \tag{3}$$

where m_i is the mass of atom i, and μ is a parameter with units of mass. A convenient choice of μ is the one used by spectroscopists, i.e., 1 atomic mass unit (1 u = 1 universal amu based on ^{12}C). Another convenient choice, for gas–phase bimolecular reactions at least, is the reduced mass of reactant relative translational motion,

$$\mu_{rel} = m_A m_B/(m_A + m_B), \tag{4}$$

where m_A and m_B are the masses of reactant A and B, respectively. In the coordinate system of (3), the kinetic energy contains no cross terms, and the

reduced mass μ factors out, i.e.,

$$T = \frac{1}{2}\mu \sum_{i=1}^{3N} \left(\frac{dq_i}{dt}\right)^2, \tag{5}$$

which means that the same mass μ is associated with motion in any direction. (This is why the coordinates are called "isoinertial.") Therefore, motion of the N–atom system governed by the potential surface $V(\{R_{i\gamma}\})$ is equivalent to the motion of a single–particle of mass μ in 3N dimensions governed by the energy surface $V(\{q_i\})$. In other words, if we could construct the 3N–dimensional potential surface, $V(\{q_i\})$, and slide a frictionless point of mass μ along this surface, the position and momentum, $\{q_1(t)...q_{3N}(t), p_1(t)...p_{3N}(t)\}$, of this mass on the surface at any given time t would correlate to the actual configuration and momentum of the many–atom system at time t. Thus the use of mass–scaled coordinates reduces an N–body problem in three dimensions to a 1–body problem in 3N dimensions.

The classical statistical mechanics of the reaction will be treated using an ensemble of N–atom systems, each represented at a given time t by a point $(\vec{p},\vec{q})$ in 6N–dimensional phase space, where $\vec{p} = \mu\, d\vec{q}/dt$. The kinetic and potential energies of the system are functions of the 3N–dimensional vectors defining the phase points, i.e., $T = T(\vec{p})$ and $V = V(\vec{q})$. The Hamiltonian, which is needed below, is given by

$$H(\vec{p},\vec{q}) = T(\vec{p}) + V(\vec{q}). \tag{6}$$

We will derive the classical transition state theory rate constant in two steps. First we will derive an expression for the equilibrium flux of systems passing through a mathematical surface separating reactants from products. Then we will identify this surface with the transition state to reaction and make the fundamental assumption of transition state theory to relate the equilibrium value of the flux through the transition state to the overall reaction rate.

2.1. FLUX THROUGH A SURFACE

Consider an ensemble of systems like the one described in the previous section, each of which is described by a 6N–dimensional point in phase space. Defining the density of classical phase space points as $\rho(\vec{p},\vec{q})$ and the rate of change of this density with time as $(\partial\rho/\partial t)$, it is clear that conservation of the number of phase space points in the ensemble requires the satisfaction of the continuity equation [11,12]

$$\frac{\partial\rho}{\partial t} + \vec{\nabla} \cdot \rho\vec{v} = 0, \tag{7}$$

where $\vec{\nabla}$ is the 6N–dimensional divergence operator [11a] and $\vec{v}$ is the 6N–dimensional velocity of a point in phase space.

Different regions of phase space are governed by different parts of the potential surface $V(\vec{q})$, and, consequently, may correspond to different chemical species. Thus, by following the flow of points between specific regions of phase space, we can study the course of chemical reaction in our ensemble of chemical systems [4,5]. To this end we first consider a volume R in phase space corresponding to the reactants. Rearranging eq. (7) and integrating over the phase space volume R yields

$$-\frac{\partial}{\partial t}\int_R d^{6N}\tau\,\rho = \int_R d^{6N}\tau\,\vec{\nabla}\cdot\rho\vec{v}, \tag{8}$$

where we have introduced the 6N–dimensional volume element

$$d^{6N}\tau = \prod_{i=1}^{3N} dp_i dq_i \tag{9}$$

and we have used the fact that the volume R is not a function of time. Since the integral on the left–hand–side of eq. (8) is just the number N^R of systems in our ensemble that are in the region R, we define the quantity

$$N^R = \int_R d^{6N}\tau\,\rho, \tag{10}$$

and rewrite eq. (8) as

$$-\frac{dN^R}{dt} = \int_R d^{6N}\tau\,\vec{\nabla}\cdot\rho\vec{v}, \tag{11}$$

which clearly shows that the right–hand side counts the number of systems leaving the reactant region of phase space as a function of time.

Next we define S to be a (6N–1)–dimensional surface in phase space which bounds the volume R. We can use Gauss' theorem [11b] to rewrite eq. (11) as a surface integral, i.e.,

$$-\frac{dN^R}{dt} = \int_S da\,\rho\vec{v}\cdot\vec{n}, \tag{12}$$

where da is the differential element of area lying in the surface S, and $\vec{n}$ is a unit vector normal to the surface S and pointing out of the volume R.

Now we define S as a (6N–1)–dimensional hyperplane which divides the reactant region from the product region. We assume that the chemistry of the situation allows us to find a hyperplane dividing reactants from products such that all flux leaving R passes through it. There is then no error incurred in using this hyperplane instead of an enclosing surface to divide reactants from products. In this section, our goal is to calculate the local one–way flux F^+ through this

dividing surface, i.e. the local flux of systems going from reactants to products. Since eq. (12) gives the difference of the local forward flux and the local reverse flux through the dividing surface, i.e. the *net* local flux, we can define F^+ by analogy to eq. (12) as [5]

$$F^+ = \int_{S_+} da\, \rho \vec{v} \cdot \vec{n}, \tag{13}$$

where S_+ is the portion of the dividing surface S for which

$$(\vec{v} \cdot \vec{n}) > 0. \tag{14}$$

When we substitute the equilibrium density for ρ, eq. (12) will of course give zero, but eq. (13) will give the equilibrium one–way flux.

The most convenient way to evaluate F^+ for the specific case described above is to define our coordinates such that q_{3N} is a cartesian coordinate normal to S. This special coordinate is the local reaction coordinate, and it will be called z. The surface is then defined by setting z equal to a fixed value which we denote as z_*. With these definitions, the component of velocity orthogonal to the surface S, in the direction reactants–to–products, is

$$\vec{v} \cdot \vec{n} = \frac{dz}{dt} = \frac{p_z}{\mu} = \frac{p_{3N}}{\mu}. \tag{15}$$

The condition (14) then becomes $\frac{dz}{dt} > 0$ or $p_z > 0$, and the surface element da becomes

$$\begin{aligned} da &= dq_1 \ldots dq_{3N-1} dp_1 \ldots dp_{3N-1} dp_z, \\ &= d^{6N-2}\tau dp_z. \end{aligned} \tag{16}$$

Substitution of eq. (15) and eq. (16) into eq. (13) yields

$$F^+ = \int_{z=z_*} d^{6N-2}\tau \int_0^\infty dp_z\, \rho \frac{p_z}{\mu}. \tag{17}$$

Notice that the limits on dp_z are 0 to ∞, rather than $-\infty$ to ∞, because of eq. (14).

In this section, we shall confine our attention to systems for which it is a good assumption to consider the reactants to be in local equilibrium at a fixed temperature. The validity of this assumption for different types of reactions will be discussed in Section 2.4. In such systems, the density of states is given by a Boltzmann distribution [13],

$$\rho = \rho_0 \, e^{-H/\tilde{k}T}, \tag{18}$$

where H is the classical Hamiltonian of eq. (6), ρ_0 is a constant, $\tilde{k}$ is Boltzmann's constant, and T is the temperature. Substitution of this distribution into eq. (17) yields the one–way flux as a function of temperature,

$$F^+(T) = \rho_0 \int_{z=z_*} d^{6N-2}\tau \int_0^\infty dp_z \, e^{-H/\tilde{k}T} \frac{p_z}{\mu}, \tag{19}$$

while substitution into eq. (10) yields

$$N^R(T) = \rho_0 \int_R d^{6N}\tau \, e^{-H/\tilde{k}T}. \tag{20}$$

In order to perform the integration over dp_z in eq. (19), we separate the Hamiltonian as

$$H = \frac{p_z^2}{2\mu} + H^{GT}(\vec{u},\vec{p}_u;z) \tag{21}$$

where $(p_z^2/2\mu)$ is the kinetic energy associated with motion along z, orthogonal to the surface, and $H^{GT}(\vec{u},\vec{p}_u;z)$ is the remaining part of the Hamiltonian; $\vec{u}$ denotes the coordinates $q_1, q_2, \ldots, q_{3N-1}$, and $\vec{p}_u$ denotes the conjugate momenta $p_1, p_2, \ldots, p_{3N-1}$. (The superscript GT denotes the fact that the fixed–z hyperplane is a generalized transition–state.) Substitution of the separated Hamiltonian, eq. (21), into eq. (19) gives

$$F^+(T) = \rho_0 \int_0^\infty dp_z \frac{p_z}{\mu} e^{-p_z^2/2\mu\tilde{k}T} \int d^{6N-2}\tau \, e^{-H^{GT}(\vec{u},\vec{p}_u;z=z_*)/\tilde{k}T}. \tag{22}$$

Notice that we set $z=z_*$ in H^{GT} because the integral is only over the surface $S(z=z_*)$. Integration over dp_z yields the desired expression for the local one–way flux through a dividing surface,

$$F^+(T) = \rho_0 \tilde{k}T \int d^{6N-2}\tau \, e^{-H^{GT}(\vec{u},\vec{p}_u;z=z_*)/\tilde{k}T}. \tag{23}$$

Since eq. (23) can also be considered to be the one–way flux through a generalized transition state fixed at $z=z_*$, we shall refer to $F^+(T)$ as $F^{GT}(T,z_*)$ from here on.

2.2. FUNDAMENTAL ASSUMPTION OF TRANSITION STATE THEORY

Since the rate of a reaction depends on the concentration of the reactants, it is convenient to work not with the rate itself, as in eq. (12), but rather with the rate coefficient, k(T), which is defined as the reaction rate per unit volume divided by the product of the concentrations of the reactants. For simplicity we now consider the ideal case where back reaction is negligible. Then by "reaction rate" we mean net flux from reactants to products when the product concentration is negligible. Having calculated the rate coefficient for this ideal case, we will assume, as is standard in chemical kinetics, that it may also be used in more complicated circumstances, such as when back reaction or side reactions are not negligible.

We shall consider only gas–phase reactions in this section. The results for reactions in condensed phases, e.g., reactions in solution and reactions on surfaces, will be similar, but in these cases the overall translation of the reactant(s) and the overall translation of the transition state species are not free, i.e. they are hindered by interactions with the bath molecules, and, consequently these degrees of freedom cannot be separated from the rest of the problem, as they are in gas–phase systems.

For a unimolecular reaction [eq. (2)], the rate constant is given by

$$k(T) = \frac{F(T)}{V[A]} \tag{24}$$

where F(T) is the global net reactive flux through the surface bounding the reactant region of phase space, in molecules per unit time and in the absence of products; V is the volume; and [A] is the concentration of the reactant in molecules per unit volume. By the definition of concentration,

$$[A] = N_A/V, \tag{25}$$

where N_A is the number of molecules of the reactant A. For a unimolecular reaction, however, $N_A = N^R(T)$ as defined by eq. (20), and substitution of eq. (25) into eq. (24) will therefore yield

$$k(T) = \frac{F(T)}{N^R(T)}. \tag{26}$$

The local equilibrium one–way flux $F^+(T)$, as given by $F^{GT}(T,z_*)$ in eq. (23), is not, however, necessarily equal to the global net equilibrium flux in the absence of products, as required in eq. (26). In general, if reactants are at equilibrium, $F^{GT}(T,z_*)$ will be greater than F(T), since although all systems contributing to the flux out of the reactant region and into the product region must cross S at least once, there is no guarantee that they will cross S only once. Thus, a system which crosses S towards products and then recrosses S towards reactants will make a positive contribution to the local one–way flux, $F^{GT}(T,z_*)$,

but will not contribute to the net flux, F(T). It is easy to see [14,15] that any trajectory which crosses the dividing surface more than once will make a greater contribution to $F^{GT}(T,z_*)$ than to F(T); thus $F^{GT}(T,z_*)$ provides an upper bound to F(T) if reactant equilibrium is maintained. It is also clear that $F^{GT}(T,z_*)$ will only be a good approximation to F(T) if the dividing surface is defined in such a way that there is little or no recrossing of trajectories before they are thermalized in the reactant or product region, i.e., if the dividing surface is placed at a good bottleneck to reaction.

In order to further evaluate eq. (26), we employ the "last assumption" [4,16] of classical transition state theory, namely that we can find a dividing surface S(z) for which there is no recrossing and the local one–way flux $F^{GT}(T,z_*)$ equals the global net flux, F(T). (By "no recrossing" we mean that all paths crossing the surface toward products originate in R and cross S only once, ending in the product region of intrest [4].) If we then substitute eq. (23) into eq. (26), we obtain the classical generalized transition state theory rate constant $k_C^{GT}(T)$ as

$$k_C^{GT}(T) = \frac{\rho_0\ \tilde{k}T \int d^{6N-2}\tau\ e^{-H^{GT}(\vec{u},\vec{p}_u;z=z_*)/\tilde{k}T}}{N^R(T)}, \tag{27}$$

where the superscript GT again denotes the fact that the fixed–z hyperplane is a generalized transition state.

In order to further understand the expression for the GTST rate constant, eq. (27), it is useful to consider the general classical partition function for a system of N distinguishable particles which is given by [13]

$$Z_C(T) = \frac{1}{h^{3N}} \int d^{6N}\tau\ e^{-H(\vec{p},\vec{q})/\tilde{k}T}, \tag{28}$$

where $H(\vec{p},\vec{q})$ is defined by eq. (6), $d^{6N}\tau$ is defined by eq. (9), and h is Planck's constant. The classical partition function, eq. (28), is effectively a weighted sum of "single–quantum–state cells" in phase space; each cell is a box with volume h^{3N} in 6N–dimensional phase space and is weighted by its probability of being populated; the weighting factor is given by the Boltzmann factor $e^{-H(\vec{p},\vec{q})/\tilde{k}T}$. We also define here the classical partition function per unit volume, $\Phi_C(T)$, which is related simply to $Z_C(T)$ by

$$\Phi_C(T) = Z_C(T)/V, \tag{29}$$

where V is the volume of the system. By comparing eq. (20) to eq. (28), it is clear

that $N^R(T)$ is related to the reactant classical partition function $Z_C^A(T)$ [given by eq. (28), but with the integration restricted to the reactant region of phase space] by

$$N^R(T) = \rho_0\, h^{3N}\, Z_C^A(T). \tag{30}$$

Comparison of eq. (29) with eq. (30) yields the relation between $N^R(T)$ and the reactant partition function per unit volume, $\Phi_C^A(T)$, as

$$N^R(T) = \rho_0\, h^{3N}\, V\, \Phi_C^A(T). \tag{31}$$

The integral in the numerator in eq. (27) can also be related to a classical partition function. In particular, consider the partition function per unit volume, $\tilde{\Phi}_C^{GT}$ (where the tilde implies a specific zero of energy as discussed below), for systems which lie in the dividing surface, i.e., for systems which have a fixed value of $z=z_*$. Because $\tilde{\Phi}_C^{GT}$ encompasses only (3N–1) degrees of freedom, and is therefore not a partition function for any real species, it may be called a quasi–partition function [17,18]. Specifically, keeping 1 degree of freedom fixed in eqs. (28) and (29) leads to the defining relation for $\tilde{\Phi}_C^{GT}(T,z_*)$,

$$\tilde{\Phi}_C^{GT}(T,z_*) = \frac{1}{Vh^{(3N-1)}} \int d^{6N-2}\tau\, e^{-H^{GT}(\vec{u},\vec{p}_u;z=z_*)/\tilde{k}T}. \tag{32}$$

Computationally it is not convenient to define this quasi–partition function for the transition state "species" from the reactant zero of energy as in eq. (32). Instead we define a quasi–partition function $\Phi_C^{GT}(T,z_*)$ which has as its zero of energy the potential energy, $V_{RP}(z=z_*)$, of the reaction path at the point where the reaction path intersects the generalized transition state surface. (If no reaction path has been defined, we take the intersection point as the point of lowest energy in the hyperplane.) Thus $\Phi_C^{GT}(T,z_*)$ is related to $\tilde{\Phi}_C^{GT}(T,z_*)$ by

$$\Phi_C^{GT}(T,z_*) = e^{V_{RP}(z=z_*)/\tilde{k}T}\, \tilde{\Phi}_C^{GT}(T,z_*). \tag{33}$$

Combining eqs. (32) and (33) and rearranging gives

$$\int d^{6N-2}\tau\, e^{-H^{GT}(\vec{u},\vec{p}_u;z=z_*)/\tilde{k}T} = h^{(3n-1)} V \Phi_C^{GT}(T,z_*) e^{-V_{RP}(z=z_*)/\tilde{k}T} \tag{34}$$

Finally, substitution of eq. (31) and eq. (34) into eq. (27) gives the transition state theory rate constant in its quasi–equilibrium form,

$$k_C^{GT}(T,z_*) = \frac{\tilde{k}T}{h} \frac{\Phi_C^{GT}(T,z_*)}{\Phi_C^{A}(T)} e^{-V_{RP}(z=z_*)/\tilde{k}T} \tag{35}$$

Equation (35) may be simplified by canceling out the partition function for overall translation of the whole system in the numerator and denominator. To do this we note that

$$\Phi_C^X = \Phi_{trans}^X Q_C^X, \tag{36}$$

where Q_C^X is the internal partition function (including overall rotation) of X, and Φ_{trans}^X is the translational partition function per unit volume of X given by

$$\Phi_{trans}^X = (2\pi m_X \tilde{k}T/h^2)^{3/2}, \tag{37}$$

where m_X is the mass of X. Since the mass of the transition state species is the same as the mass of the reactant, Φ_{trans} will cancel in the numerator and denominator of eq. (35), yielding

$$k_C^{GT}(T,z_*) = \frac{\tilde{k}T}{h} \frac{Q_C^{GT}(T,z_*)}{Q_C^{A}(T)} e^{-V_{RP}(z=z_*)/\tilde{k}T} \tag{38}$$

We can derive a similar expression for bimolecular reactions by replacing eq. (24) with its bimolecular counterpart,

$$k(T) = \frac{F(T)}{V[A][B]}, \tag{39}$$

and noting that

$$[A][B] = \frac{N_A N_B}{V^2}, \tag{40}$$

which gives, with eq. (39),

$$k(T) = \frac{F(T)V}{N_A N_B}. \tag{41}$$

To continue, we note that in the reactant region, the reactants are independent of each other; consequently the reactant Hamiltonian may be written as

$$H = H_A + H_B, \tag{42}$$

i.e., as the sum of the Hamiltonians of the reactants. We also note that H_A is a function of $\{q_{1,A},\ldots,q_{3n_A,A};\ p_{1,A},\ldots,P_{3n_A,A}\}$ and that H_B is a function of $\{q_{1,B},\ldots,q_{3n_B,B};\ p_{1,B},\ldots,p_{3n_B,B}\}$, where $3n_X$ is the number of degrees of freedom for reactant X, and the union of these two sets of coordinates is equivalent to the set $\{q_1,\ldots,q_{3N};\ p_1,\ldots,p_{3N}\}$. We can then write the denominator of eq. (41) as

$$N_A N_B = \rho_o \int_R e^{-H_A/\tilde{k}T}\, dq_{1,A}\ldots dq_{3n_A,A}\, dp_{1,A}\ldots dp_{3n_A,A} \times$$
$$\times \int_R e^{-H_B/\tilde{k}T}\, dq_{1,B}\ldots dq_{3n_B,B}\, dp_{1,B}\ldots dp_{3n_B,B}, \tag{43}$$

which is related to the product of the reactants' classical partition functions per unit volume Φ_C^A and Φ_C^B by

$$N_A N_B = \rho_o h^{3n_A} V\Phi_C^A(T)\, h^{3n_B} V\Phi_C^B(T). \tag{44}$$

Making the TST assumption, we replace F(T) with $F^{GT}(T,z_*)$ in eq. (41). Using eq. (34) to write $F^{GT}(T,z_*)$ in terms of partition functions and eq. (44) for $N_A N_B$, eq. (41) yields

$$k_C^{GT}(T,z_*) = \frac{\tilde{k}T}{h}\, \frac{\Phi_C^{GT}(T,z_*)}{\Phi_C^A(T)\,\Phi_C^B(T)}\, e^{-V_{RP}(z=z_*)/\tilde{k}T}, \tag{45}$$

where we used the fact that $N = n_A + n_B$. In order to use eq. (36) to separate out

the overall translation from $\Phi_C^{GT}(T,z_*)$, $\Phi_C^A(T)$, and $\Phi_C^B(T)$, we note that the mass for the transition state species is $M = m_A + m_B$, where m_A and m_B are the masses of reactant A and B, respectively. Using eq. (37), we find the ratio of translational partition functions to be

$$\frac{\Phi_{trans}^{GT}(T)}{\Phi_{trans}^{A}(T)\Phi_{trans}^{B}(T)} = \frac{1}{\Phi^{rel}(T)} = \left[\frac{h^2}{2\pi\mu_{rel}\tilde{k}T}\right]^{3/2}, \tag{46}$$

where μ_{rel} is defined in eq. (4), and $\Phi^{rel}(T)$ denotes the reactants' relative translational partition function per unit volume. We define a reactant partition function per unit volume, $\Phi_C^R(T)$ as

$$\Phi_C^R(T) = \Phi^{rel}(T)Q_C^A(T)Q_C^B(T), \tag{47}$$

and eq. (45) the rate for a bimolecular reaction becomes

$$k_C^{GT}(T,z_*) = \frac{\tilde{k}T}{h}\,\frac{Q_C^{GT}(T,z_*)}{\Phi_C^R(T)}\,e^{-V_{RP}(z=z_*)/\tilde{k}T}. \tag{48}$$

To this point, we have considered only systems having a single reaction path. To account for reaction path multiplicity, we need only multiply eq. (48) [or eq. (38) for a unimolecular reaction]) by a symmetry factor, σ, which is determined by the number of equivalent reaction paths [19]. For example, the reaction OH + H_2 would have $\sigma = 2$, since either atom of the H_2 molecule could be abstracted. Thus, the rate is given by [17]

$$k_C^{GT}(T,z_*) = \sigma\frac{\tilde{k}T}{h}\,\frac{Q_C^{GT}(T,z_*)}{\Phi_C^R(T)}\,e^{-V_{RP}(z=z_*)/\tilde{k}T} \tag{49a}$$

for a bimolecular reaction, and by

$$k_C^{GT}(T,z_*) = \sigma\frac{\tilde{k}T}{h}\,\frac{Q_C^{GT}(T,z_*)}{Q_C^A(T)}\,e^{-V_{RP}(z=z_*)/\tilde{k}T} \tag{49b}$$

for a unimolecular reaction. When reaction path multiplicity is included in $k_C^{GT}(T,z_*)$ as in eq. (49), the rotational partition functions in $Q_C^{GT}(T,z_*)$, $\Phi_C^R(T)$, and $Q_C^A(T)$ should not include any symmetry factors [19].

2.3. CHOICE OF DIVIDING SURFACE

Because the degree to which the TST rate constant approximates the true rate constant is determined by the amount of recrossing of the dividing surface, and, therefore, by the precise choice of dividing surface, we discuss here a practical method [8,9] for choosing the dividing surface that has been used successfully in many applications. This method defines the (6N–1)-dimensional phase space dividing surface to be a (3N–1)–dimensional coordinate-space hyperplane orthogonal to the path of lowest potential energy connecting the reactant configuration to the product configuration. This path is loosely termed the reaction coordinate; more specifically it is known as the minimum energy path (MEP). The MEP is found from the potential energy surface by starting at the saddle point configuration, which is a maximum along the reaction coordinate but a minimum in the remaining 3N–1 dimensions, and following the path of steepest descents through the mass–scaled coordinate system [20–24]. (One would get a different path if one followed the same procedure in unscaled cartesians [22].) Computational details of the steepest descents procedure may be found elsewhere [17,25,26]. We now find it useful to characterize motion of the system along the MEP by the parameter s; s=0 defines the saddle point, s is negative on the reactant side of the saddle point, and it is positive on the product side. Now, at any given point s, we can rotate and translate our coordinate system such that one rotated coordinate, denoted z, is tangent to the MEP at s and is defined to have a value of zero at the point of tangency. The remaining rotated and translated coordinates $\{q_1(s),\ldots,q_{3N-1}(s)\}$ are orthogonal to the MEP (at s), and the set of all rotated and translated coordinates are called the local natural collision coordinates. We also define the momenta $\{p_1,\ldots,p_{3N-1},p_z\}$ conjugate to the coordinates $\{q_1,\ldots,q_{3N-1},z\}$ at each value of s. Thus, although the MEP may follow a curvilinear path in coordinate space, we have defined, at each value of s, a cartesian coordinate system that has one coordinate tangent to the MEP, i.e., lying along the MEP at s [8,9,17]. Using this coordinate system, any surface in the family of surfaces orthogonal to the MEP may be described by setting $z_* = 0$. The position of a particular surface along the MEP, however, will be determined by the value of the parameter s at which the dividing surface intersects the MEP. The classical TST rate constant of eq. (49) is thus a function of the parameter s, and, for a bimolecular reaction

$$k_C^{GT}(T,s) = \sigma \frac{\tilde{k}T}{h} \frac{Q_C^{GT}(T,s)}{\Phi_C^R(T)} e^{-V_{MEP}(s)/\tilde{k}T}, \tag{50a}$$

while for a unimolecular reaction

$$k_C^{GT}(T,s) = \sigma \frac{\tilde{k}T}{h} \frac{Q_C^{GT}(T,s)}{Q_C^A(T)} e^{-V_{MEP}(s)/\tilde{k}T}, \tag{50b}$$

where $V_{MEP}(s)$ is the value of the energy surface on the MEP at s.

The classical conventional transition state theory rate constant $k_C^{\ddagger}(T)$ is obtained from eq. (50) by setting s = 0, i.e., by placing the dividing surface at the saddle point. Note that $V_{MEP}(s=0)$ is just the barrier height for the reaction, and $Q_C^{\ddagger}(T) = Q_C^{GT}(T,s=0)$ is just the quasi–partition function for the saddle point species.

Because the TST rate constant provides an upper bound to the true equilibrium rate constant $[F^{GT}(T,s) \geq F(T)]$, a better approximation than $k_C^{\ddagger}(T)$ may be achieved by variationally minimizing $k_C^{GT}(T,s)$ with respect to the surface position, s. This method is called canonical variational transition state theory (CVTST) or, for short, canonical variational theory (CVT). The optimized surface position s_*^{CVT} is defined by the implicit equation

$$k_C^{CVT}(T) = k_C^{GT}(T,s_*^{CVT}) = \min_s k_C^{GT}(T,s), \tag{51a}$$

or, equivalently, by the condition

$$\frac{\partial}{\partial s}\left[k_C^{GT}(T,s)\right]\Big|_{s=s_*^{CVT}} = 0. \tag{51b}$$

The CVT rate constant is then [8,9,17]

$$k_C^{CVT}(T) = \sigma \frac{\tilde{k}T}{h} \frac{Q_C^{CVT}(T)}{\Phi_C^R(T)} e^{-V_{MEP}^{CVT}/\tilde{k}T} \tag{52a}$$

for a bimolecular reaction and

$$k_C^{CVT}(T) = \sigma \frac{\tilde{k}T}{h} \frac{Q_C^{CVT}(T)}{Q_C^A(T)} e^{-V_{MEP}^{CVT}/\tilde{k}T} \tag{52b}$$

for a unimolecular reaction, where $V_{MEP}^{CVT} = V_{MEP}(s = s_*^{CVT})$ and $Q_C^{CVT}(T) = Q_C^{GT}(T,s=s_*^{CVT})$.

By re–writing eq. (50) in a quasi–thermodynamic form, and applying the CVT minimization criteria, eq. (51), we can shed light on the physical meaning of the minimization process [8,17,18,27,28]. For this purpose, although eq. (50) has been derived entirely from dynamical considerations, we re–analyze it in terms of

quasi–thermodynamic parameters. Recalling the statistical expression

$$K = \sigma \frac{Q_B(T)}{Q_A(T)} e^{-\Delta E/\tilde{k}T}, \tag{53}$$

where σ is a symmetry factor, $Q_A(T)$ and $Q_B(T)$ are partition functions for systems A and B, respectively, ΔE is the difference between the zeros of energy for these two systems, and K is the equilibrium constant, allows us to equate the terms

$$K^{GT} = \sigma \frac{Q_C^{GT}(T,s)}{\Phi_C^R(T)} e^{-V_{MEP}(s)/\tilde{k}T} \tag{54a}$$

or

$$K^{GT} = \sigma \frac{Q_C^{GT}(T,s)}{Q_C^A(T)} e^{-V_{MEP}(s)/\tilde{k}T}, \tag{54b}$$

where K^{GT} is referred to as a quasi–equilibrium constant because $Q_C^{GT}(T,s)$ is not the partition function for a real species; rather, it is the partition function for a fictitious species which excludes one degree of freedom. Thermodynamics allows us to write

$$K^{GT} = K^0 e^{-\Delta G_T^{GT,0}(s)/RT} \tag{55}$$

where K^0 is the reaction quotient evaluated at the standard state concentration of each species, i.e., $[AB^{\ddagger}]^0/[A]^0[B]^0 = ([A]^0)^{-1}$ for (1) or $[A^{\ddagger}]^0/[A]^0 = 1$ for (2), and has the same units as K^{GT}, R is the ideal gas constant, and $\Delta G_T^{GT,0}$ is the standard–state molar free energy change between the reactant and transition state species. Like K^{GT}, the free energy, $\Delta G_T^{GT,0}$, is a quasi–thermodynamic quantity, since the transition state species excludes one degree of freedom; it will be called the standard–state generalized free energy of activation. Finally, equating the right–hand sides of eq. (54) and (55) allows us to re–write eq. (50) as [8]

$$k_C^{GT}(T,s) = \frac{\tilde{k}T}{h} K^0 e^{-\Delta G_T^{GT,0}(s)/RT}. \tag{56}$$

Applying the CVT criteria, eq. (51), to eq. (56) yields

$$0 = \left.\frac{\partial k_C^{GT}(T,s)}{\partial s}\right|_{s=s_*^{CVT}}$$

$$= \frac{\tilde{k}T}{h} K^0 \frac{\partial}{\partial s}\left[e^{-\Delta G_T^{GT,0}(s)/RT}\right]\Bigg|_{s=s_*^{CVT}}. \qquad (57)$$

It is clear from eq. (57) that, since the only surface–dependent quantity on the right–hand side is $\Delta G_T^{GT,0}(s)$, the position of the surface along the reaction coordinate which minimizes the canonical rate constant, defined by $s = s_*^{CVT}$, occurs at the position of the maximum of the free energy of activation curve $\Delta G_T^{GT,0}(s)$. Thus, a major difference between conventional TST and CVT is that in CVT a combination of entropic and energetic effects ($\Delta G_T^{GT,0}$) is considered when choosing which dividing surface will best act as a dynamical bottleneck, i.e., which surface will best satisfy the condition that every system which crosses the dividing surface does so only once; whereas, in conventional TST only energetic effects [$V_{MEP}(s=0)$] are considered in making this choice.

The discussion in this section has considered only a one–parameter sequence of hyperplanes perpendicular to s in mass–scaled coordinates. We close this section by considering two aspects of this restriction. First we note that such a hyperplane will not always divide reactants from products everywhere. Second we note that $Q_C^{GT}(T,s)$ is primarily sensitive to the shape of the potential near the reaction path, especially at low and moderate temperatures. We can then see how such a hyperplane could still provide a good estimate of the rate by imagining a true dividing surface that coincides with the orthogonal hyperplane in the vicinity of the reaction path but elsewhere, in regions that do not have a large effect on $Q_C^{GT}(T,s)$, curves into a high–energy region that divides reactants from products (unlike the hyperplane) [29]. This is the basis for the "Morse I" approximation [8,9] in which a vibrational potential orthogonal to the MEP is treated as increasing monotonically to a very high value on one side of the MEP and as increasing monotonically to the bond dissociation limit on the other, even though the true potential along the straight–line vibrational coordinate may not be so well behaved. Of course if vibrational partition functions are calculated harmonically one doesn't need to worry about these details.

Finally we consider the idea that more general dividing surfaces could be used to improve calculated rate constants. If one considers arbitrary variations of the dividing surface in phase space one should be able to obtain the exact classical equilibrium rate constant [4,5]. However this would be practical only for very simple systems, and even for systems with only three atoms it can be very complicated (and has never been carried out completely). Instead, we consider the simple one–parameter sequences of dividing surfaces discussed above, and we note, quite happily, that, even when quantum effects are incorporated by the

approximate methods discussed in Sections 3 and 4, one can obtain quite accurate results in many cases by using such simple prescriptions for the set of trial dividing surfaces over which minimization of the GTST rate coefficient is carried out [29–35].

2.4. VALIDITY OF REACTANT EQUILIBRIUM ASSUMPTION

The validity of the assumption of reactant equilibrium depends upon the ability of some energy transfer mechanism, such as collisions, to repopulate reactive elements of phase space at a rate at least as fast as the rate at which these states are depopulated by reaction. The conditions under which this assumption is valid for unimolecular gas–phase reactions have been widely studied; these conditions are usually called the high–pressure limit [36–38]. (This is a misnomer; actually it is a high–pressure plateau since new effects arise at ultrahigh pressures and in condensed media; see Section 6.) However, at typical pressures where gas–phase unimolecular reactions are studied, thermalization of the reactant states is usually incomplete and the rate is correspondingly lower than the value calculated under the equlibrium assumption. This is called the fall–off regime. In order to calculate accurate rate coefficients in this regime, one usually uses a mechanism including activating collisions, such as the Lindemann mechanism, for which, of course, the rate coefficients are no longer expressed in unimolecular form. For gas–phase bimolecular reactions it is usual to assume that activating collisions are efficient enough to maintain a thermal distribution of reactants, but the extent to which the breakdown of this assumption affects measured rate constants is not well understood. The most complete study available is that of Lim and one of the authors [39]. In condensed phases thermalizing collisions with the solvent are very frequent, but recent research shows that the thermalization of reactants is nevertheless not always assured, and, in addition, in condensed phases and very high–pressure gases one must consider frictional effects that may slow the rate constant by preventing a spatial equilibrium of reactants or interrupting the traversal of the transition state region [2,18,40]. If we refrain from treating low–pressure unimolecular reactions, and we assume reactant equilibration is perfect in other cases, then we may also assume without further error that equilibrium is maintained for species in the transition state dividing surface that originated in the reactant region of phase space. In classical mechanics, in the absence of trajectories trapped in the interaction region, i.e., trajectories that never emerge as reactants or products, this is a direct consequence [41] of Liouville's theorem [12a,42]. Further discussion of the equilibrium assumption of TST is given in Ref. 7. We note that once quantal effects are introduced it is not possible to justify TST so clearly, and eventually our confidence in the theory must be based on checking the computed rate constants against more accurate dynamical calculations and/or experiments. Such tests are discussed further in Refs. 2, 15, and 29–35 and in Section 5.

3. Semiclassical Canonical Rate Constants with Classical Reaction–Coordinate Motion.

Our treatment, up to this point, of both "exact" and transition state theory rate constants has been entirely classical. Yet for most systems quantum effects, especially vibrational zero–point effects and tunneling effects, are quite important.

Because the transition state theory formulation requires the simultaneous knowledge of the reaction coordinate position, z(s), and the corresponding momentum, p_z, and because this simultaneous knowledge is forbidden by the uncertainty principle of quantum mechanics, there is no unique way to rigorously quantize the classical TST result [43]. Instead it is common to use a semiclassical treatment which includes adiabatic quantization of all modes except the reaction coordinate [30,44,45]. In this context, "adiabatic" means that, at each value of s, energy levels are computed for degrees of freedom orthogonal to the reaction coordinate by deleting the kinetic energy in s and fixing s in the potential energy. In addition, in some cases one adds a separate correction for tunneling, which is the dominant nonclassical effect on the reaction coordinate, or at least the dominant one that is conveniently included in TST [15,29–31]. Thus, we separate the quantized generalized transition state rate constant into two factors as

$$k^{GT/G}(T,s) = \kappa^{GT/G}(T,s)k^{GT}(T,s), \tag{58a}$$

where $k^{GT}(T,s)$ is the semiclassical rate constant which includes quantization of all modes except the reaction coordinate, and $\kappa^{GT/G}(T,s)$ is a correction factor used to incorporate quantal effects on the reaction coordinate. The /G in the superscript denotes that a ground–state transmission coefficient method is used to evaluate this correction factor. In this section we will discuss $k^{GT}(T,s)$ and show how to use it to calculate the canonical variational theory rate coefficient $k^{CVT}(T)$. The evaluation of $\kappa^{GT/G}(T,s)$ will be discussed in Section 4 for the special case where CVT is used, and it becomes $\kappa^{CVT/G}(T)$.

Because we invoke a nonrigorous quantization in determining $k^{GT}(T,s)$, and because this quantization is applied only to selected modes, the semiclassical TST rate constant, $k^{GT}(T,s)$, does not provide a rigorous upper bound to the exact quantum rate constant the way the classical TST rate constant $k_C^{GT}(T,s)$ provides an upper bound to the exact classical rate constant. Nevertheless, we have found that variationally optimizing rate constants which have been quantized using this semiclassical scheme yields better numerical results than simply placing the dividing surface at s = 0 [2,15,29–35].

The modes which are quantized in the semiclassical treatment appear in eq. (50) only in the ratio $Q_C^{GT}(T,s)/\Phi_C^R(T)$ for a bimolecular reaction and $Q_C^{GT}(T,s)/Q_C^A(T)$ for a unimolecular one. Thus, eq. (50) can be converted to its semiclassical analog simply by replacing the classical canonical partition functions with their quantum mechanical analogs, i.e.,

$$k^{GT}(T,s) = \sigma \frac{\tilde{k}T}{h} \frac{Q^{GT}(T,s)}{\Phi^R(T)} e^{-\beta V_{MEP}(s)} \qquad \text{(bimolecular)}, \tag{59a}$$

$$k^{GT}(T,s) = \sigma \frac{\tilde{k}T}{h} \frac{Q^{GT}(T,s)}{Q^{A}(T)} e^{-\beta V_{MEP}(s)} \quad \text{(unimolecular)}, \tag{59b}$$

where $Q^{GT}(T,s)$ and $Q^{A}(T)$ are quantum partition functions, $\Phi^{R}(T)$ is a quantum partition function per unit volume and $\beta = 1/\tilde{k}T$. We make two major assumptions in this semiclassical treatment. First, our method of quantization assumes that the reaction coordinate is separable from the other degrees of freedom (i.e., that there is no coupling between the reaction coordinate and any of the other modes). Second, in evaluating the quantum partition functions, $Q^{GT}(T,s)$, $Q^{A}(T)$, and $\Phi^{R}(T)$, we ignore the coupling between the electronic, vibrational, and rotational degrees of freedom so that we can write

$$Q^{GT} = Q^{GT}_{el} Q^{GT}_{vib} Q^{GT}_{rot}, \tag{60}$$

$$Q^{A} = Q^{A}_{el} Q^{A}_{vib} Q^{A}_{rot}, \tag{61}$$

and

$$\Phi^{R} = Q^{A}_{el} Q^{A}_{vib} Q^{A}_{rot} Q^{B}_{el} Q^{B}_{vib} Q^{B}_{rot} \Phi^{rel}. \tag{62}$$

Note that, because translational partition functions are the same in quantum as in classical mechanics, the cancellations leading to eqs. (38) and (48) involving the separation of partition functions for overall translation remain valid in the semiclassical treatment. It has been shown numerically that quantization of the rotational degrees of freedom is generally unimportant, e.g., using classical rotational partition functions instead of quantum ones to evaluate CVT rate constants causes errors of less than 1% for most atom–diatom reactions [27]. For a nonlinear molecule, the classical rotational partition function is given by

$$Q_{rot} = \left[\left(\frac{2\tilde{k}T}{\hbar^2}\right)^3 \pi I_A(s) I_B(s) I_C(s) \right]^{\frac{1}{2}}, \tag{63}$$

where $\hbar$ is Planck's constant divided by 2π, and I_A, I_B, and I_C are the three principal moments of inertia. For Q^{GT}_{rot}, the moments of inertia depend on the position of the generalized transition state along the reaction coordinate s; numerical methods for calculating $I_A(s)I_B(s)I_C(s)$ have been described elsewhere [17]. For Q^{A}_{rot} or Q^{B}_{rot}, the moments of inertia are those for the specified reactant species, A or B, i.e., at $s = -\infty$. For linear molecules, the classical rotational partition function is given by

$$Q_{rot} = \frac{2I(s)\tilde{k}T}{\hbar^2}, \tag{64}$$

where again, for Q^{GT}_{rot}, the moment of intertia is a function of s, while for Q^{A}_{rot} and Q^{B}_{rot}, I is the moment of inertia for the specified linear reactant. Note that none of the rotational partition functions contain symmetry factors, as these are already accounted for in the inclusion of reaction path multiplicity [cf. eq. (49)].

When evaluating Q_{vib}, we make the independent–normal–mode approximation, which assumes no mode–mode coupling between vibrational modes. This approximation allows the vibrational partition function to be written as

$$Q_{vib} = \prod_{j=1}^{n_{vib}} Q_{vib,j} , \tag{65}$$

where $Q_{vib,j}$ is the vibrational partition function of mode (normal coordinate) j and n_{vib} is the total number of vibrational modes. Making the simplest vibrational approximation, assuming that the potential along each normal coordinate is harmonic, yields

$$Q_{vib,j} = \frac{e^{-\frac{1}{2}\hbar\omega_j\beta}}{(1 - e^{-\hbar\omega_j\beta})} \tag{66}$$

where ω_j is the frequency for mode j. For Q^{GT}_{vib}, the normal coordinates, and thus, ω_j and $Q^{GT}_{vib,j}$, depend upon the position of the dividing surface, s. Note that the zero of energy for each $Q^{GT}_{vib,j}$ must be $V_{MEP}(s)$ for eq. (66) to be correct. This definition is consistent with the exponential in eq. (59). Numerical methods for determining these quantities as a function of s are given elsewhere [17]. For Q^{A}_{vib} or Q^{B}_{vib}, a standard normal mode analysis of the specified reactant yields the quantities necessary to evaluate eqs. (65) and (66). Although we do not discuss them here, more complex treatments of the vibrations which allow for the anharmonicity of the potential along a given mode in the expression for $Q_{vib,j}$ have been used quite successfully [17]; however, the approximation inherent to eq. (65) is almost always retained.

An important case where anharmonicity effects are essential occurs when there are two low–energy reaction paths separated by a low–energy ridge. This may occur when two first–order saddle points are separated by a second–order saddle point slightly higher in energy [46] or when the minimum–energy path from a first–order saddle point encounters a valley–ridge inflection [47,48]. In such a case one may measure the reaction coordinate along a reference path riding the ridge rather than along the true MEP, and it is necessary to treat at least one vibration orthogonal to the reference path as an anharmonic double–minimum potential. If the valley–ridge inflection point occurs on the reactant side of the saddle point so that the MEP from the transition–state saddle point leads to a saddle point between two "reactant" minima, it may also be necessary to use the double–minimum treatment for reactants. When, however, the ridge separating the reaction paths is high enough and the paths are related by symmetry, one can treat only one of them explicitly and include the other in σ.

Finally, to calculate the reactant electronic partition function, we evaluate the sum over electronic states directly, i.e.

$$Q^{A}_{el} = \sum_{\alpha} d^{A}_{\alpha} e^{-\beta\epsilon^{A}_{el}(\alpha)}, \tag{67}$$

since it often converges after only 1 or 2 terms. In eq. (67) $\epsilon^{A}_{el}(\alpha)$ is the energy of electronic state α and d^{A}_{α} is the degeneracy factor of this electronic state. For many reactions of interest higher order electronic states tend to increase dramatically in energy with motion along the reaction coordinate, and we usually consider reactions for which this is so. For this type of reaction, we need only consider the lowest lying electronic state to calculate Q^{GT}_{el}. Because we define $V_{MEP}(s)$ as the zero of energy for all GT partition functions, the lowest lying electronic state has energy $\epsilon^{GT}_{el} = 0$ and Q^{GT}_{el} reduces to the ground electronic–state degeneracy factor, d^{GT}_{1}. Although this simplification is usually applicable [49], a few reactions have been treated for which it is not [50,51].

In the present section we contructed the hybrid rate constants [eq. (59)] by starting with an expression derived from the fundamental assumption of classical transition state theory and simply quantizing the partition functions. Another approach, which may be carried out without first neglecting quantization effects and then re–inserting them, is based on the adiabatic theory of reactions [8,17,30,52–56]. Although the adiabatic theory yields considerable insight, it is less general than TST because the flux–through–a–dividing–surface derivation of TST does not require for its validity that modes orthogonal to the reaction path be adiabatic, as required for the adiabatic derivation to be valid.

When there is more than one maximum in the free energy of activation curve, it is usually sufficient to base the calculated rate constant only on the highest one. However, if desired, one may attempt to include more than one maximum by a unified statistical model [17,57,58].

4. Quantum Effects on the Reaction–Coordinate Motion

In the previous section we introduced a semiclassical formalism for incorporating quantum effects into all modes except the reaction coordinate. This yielded a hybrid rate constant, eq. (59). Quantum effects on reaction coordinate motion are also quite important in many reactions [15,22,29–31]; here we introduce several methods for calculating a correction factor which accounts for these effects. The general form of the corrected rate constant will be written as

$$k^{CVT/G}(T) = \kappa^{CVT/G}(T) k^{CVT}(T), \tag{58b}$$

where $\kappa^{CVT/G}$, the correction factor, or transmission coefficient, depends on the

method (here CVT) used to calculate the hybrid rate constant, as well as on the method used to incorporate the reaction–coordinate quantum effects. The /G in the superscripts denotes that the correction factor is based on the reaction probability of the ground (G) state of reactants.

First consider the artificial case in which the reaction coordinate is separable; then reaction–coordinate motion is one–dimensional motion over a potential barrier. Classically, only those reactants with energy $E > V_B$, where V_B is the barrier height, will cross the barrier to products, thus the classical transmission probability P_C is given by

$$P_C = \Theta[E - V_B], \tag{68}$$

where the Heaviside step function Θ is defined as

$$\Theta(y) = \begin{cases} 0; & y < 0; \\ 1; & y \geq 0. \end{cases} \tag{69}$$

In quantum mechanics, however, there is a finite probability that reactants with energy less than V_B will proceed to products (tunneling) and also a finite probability that reactants with energy greater than V_B will not react (non–classical reflection [59]). If we could find the quantum transmission probability $P^G(E)$, we could calculate the correction factor as

$$\kappa^G(T) = \frac{\int_0^\infty P^G(E)e^{-\beta E}dE}{\int_0^\infty P_C(E)e^{-\beta E}dE}, \tag{70}$$

which is the ratio of the thermal averages of the quantum and classical transmission probabilities for the ground state of reactants (if the reaction–coordinate were separable these probabilities would be independent of the state of the reactants). If eq. (70) is to provide a reasonable model for the correction factor to CVT, the barrier height used to evaluate $P_C(E)$, eq. (68), must be consistent with the hybrid semiclassical scheme used in Section 3 [eq. (58)]; thus $P_C(E)$ is also dependent on the form of GTST being used, and, for clarity we re–write eq. (70) as

$$\kappa^{CVT/G}(T) = \frac{\int_0^\infty P^G(E)e^{-\beta E}dE}{\int_0^\infty P_C^{CVT/G}(E)e^{-\beta E}dE}. \tag{71}$$

When the reaction coordinate is not separable it is not strictly correct to

base the correction factor solely on ground–state transmission probabilities. Nevertheless we will still do so, based on the following arguments. Tunneling effects are primarily important at low temperatures. At these temperatures, the reactant system will be found almost entirely in its ground state or in a state energetically similar to the ground state. For thermoneutral or nearly thermoneutral reactions, this may be true along the entire reaction coordinate; however, for highly exothermic reactions, higher order product states may be energetically accessible even at the low temperatures where tunneling is important, and we should expect that they will often be populated significantly. Although we shall later discuss methods which will be applicable to exothermic reactions involving tunneling directly into an excited state, we shall for now consider only cases where it is reasonable to assume that the system is in the ground state both at the beginning and the end of the tunneling process. (This does not preclude high product vibrational excitation if tunneling occurs early along the MEP, and vibrational nonadiabaticity occurs later.) In this case we replace the quantum transmission probability $P^G(E)$ to be evaluated by our best approximation to the ground state–to–ground–state tunneling probability. For systems with small reaction–path curvature the simplest approximation uses, as the effective potential for the one–dimensional tunneling motion, the adiabatic ground–state one–dimensional potential, $V_a^G(s)$, i.e., we assume that the system remains adiabatically in its ground state along the entire tunneling path [17,22,29,31]. This potential curve is defined as

$$V_a^G(s) = V_{MEP}(s) + \epsilon^G_{int}(s) \tag{72}$$

where $V_{MEP}(s)$ is the value of the potential energy surface at point s on the MEP and $\epsilon^G_{int}(s)$ is the sum of zero point energies for the orthogonal modes at a given s, i.e.,

$$\epsilon^G_{int}(s) = \sum_{j=1}^{n_{vib}} \epsilon^0_{int,j}(s), \tag{73}$$

where $\epsilon^0_{int,j}(s)$ is the ground–state vibrational energy of the jth vibrational mode (rotational modes have no zero–point energy). We also note that to be consistent with CVT, the classical probability must be found using a barrier height of $V_a^G(s_*^{CVT})$, where s_*^{CVT} is the value of s at which the dividing surface is placed to calculate $k^{CVT}(T)$. Thus

$$P_C^{CVT/G} = \Theta[E - V_a^G(s = s_*^{CVT})]; \tag{74}$$

see Fig. 1. Note that the maximum, $\Delta G_T^{CVT,0}$, of the free energy of activation

curve $\Delta G_T^{GT,0}$ occurs at $s = s_*^{CVT}$ [see eq. (56)], which does not usually equal s_*^{AG}, the point where the maximum of $V_a^G(s)$ occurs, since states other than the ground state are included in determining the free energy of activation curve at a nonzero temperature.

Finally, we find that a good compromise between accuracy and efficiency is to use the WKB semiclassical approximation [60,61] to evaluate the approximate ground–state transmission probability, $P^G(E)$. The uniform WKB result for a general, smoothly varying potential barrier, if $E < V_B$, is given by [55,62–64]

$$P(E) = 1/[1 + \exp(2\theta)], \tag{75}$$

where θ, which governs the degree to which the wave function is damped, i.e., the degree to which the transmission probability is decreased by the presence of the barrier, is given by the following imaginary–action integral:

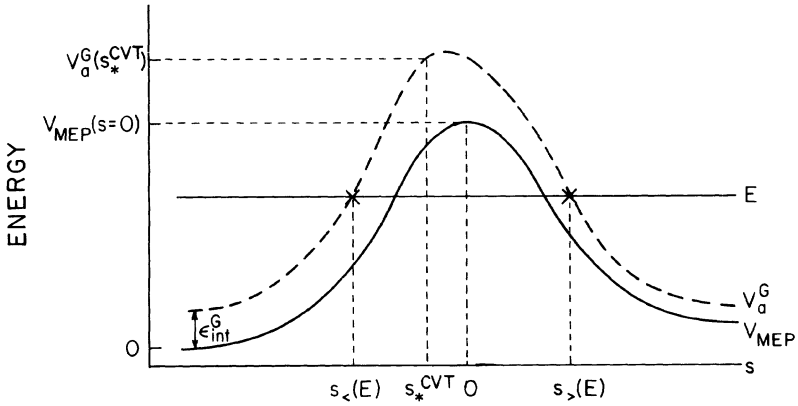

Fig. 1. Potential energy curves as a function of the reaction coordinate parameter s. The solid line represents the potential $V_{MEP}(s)$ along the minimum energy path, and the dashed line represents the adiabatic ground–state potential curve $V_a^G(s)$. The reactant region is at $s = -\infty$, the product region is at $s = +\infty$, the saddle point position is $s = 0$, and a typical generalized transition state position (which is only at the maximum of $V_a^G(s)$ for T = 0 K) is $s = s_*^{CVT}$. The x's denote the classical turning points, $s_<$ and $s_>$, for energy E.

$$\theta(E) = \frac{1}{\hbar}\int_{\xi_<}^{\xi_>} \sqrt{2\mu(V(\xi) - E)}\, d\xi, \tag{76}$$

where $\xi_<$, $\xi_>$ are the classical turning points along the tunneling path for energy E, and the integrand is the imaginary part of the tunneling momentum as a function of position. The tunneling momentum can be understood in terms of the following considerations. First, the total energy E is a sum of the local kinetic energy along the tunneling path, $T_{loc}(\xi)$, and the potential energy, $V(\xi)$. This gives

$$T_{loc}(\xi) = E - V(\xi), \tag{77}$$

where ξ denotes the position along the tunneling path. Since tunneling occurs when $E < V(\xi)$, a condition which is satisfied for all $\xi_< < \xi < \xi_>$, the right–hand side of eq. (77) is less than zero, yielding a negative kinetic energy. Converting to momentum, gives

$$\begin{aligned} p(E,\xi) &= \sqrt{2\mu(-|T_{loc}(E,\xi)|)} \\ &= i\sqrt{2\mu|T_{loc}(E,\xi)|} \\ &= i\sqrt{2\mu(V(\xi) - E)}, \end{aligned} \tag{78}$$

showing that the integrand in eq. (76) is indeed the imaginary part of the momentum. It should also be clear from eq. (76) that $\theta(E)$ is a measure of the effective height and width of the barrier. For energies appreciably below the barrier top, θ will be large and eq. (75) will be equivalent to the primitive form [60,61]

$$P(E) \approx \exp[-2\theta(E)], \tag{79}$$

which clearly demonstrates the exponential decay in tunneling probability as a function of barrier height and width.

Returning to the specific problem at hand, the simplest approximation we will consider is called the minimum–energy–path semiclassical adiabatic ground-state tunneling approximation. In this approximation the ground–state tunneling probability is [31,64]

$$P^{MEPSAG}(E) = \{1 + \exp[\frac{2}{\hbar}\int_{s_<}^{s_>}[2\mu(V_a^G(s) - E)]^{\frac{1}{2}}ds]\}^{-1}; \qquad E < V_a^G(s_*^{CVT}), \tag{80}$$

where we have combined eqs. (75) and (76) and substituted the appropriate values for V and ξ for tunneling through the adiabatic ground state curve, eq. (72). Note

that $s_<$ and $s_>$ are the reaction–coordinate turning points for energy E (see Fig. 1). The probability of equation (80) has the acronym MEPSAG because we have implicitly assumed [22] that the tunneling path passes through the same points in configuration space as does the MEP. Before considering this assumption further, we point out that nonclassical reflection can be treated sufficiently accurately by using a simple relation that is strictly valid only for a parabolic barrier. For a parabolic barrier the probability of reflection at an energy δE above the barrier top is equal to the probability of tunneling at an energy δE below it [62]. Using this to extend eq. (80) we get [17,31]

$$
\begin{aligned}
P^{MEPSAG}(E) &= \{1 + \exp[\tfrac{2}{\hbar}\int_{s_<}^{s_>} [2\mu(V_a^G(s) - E)]^{\frac{1}{2}} ds]\}^{-1}; \\
&\qquad V_a^G(s=-\infty) < E < V_a^G(s_*^{CVT}) \\
&= 1 - P^{MEPSAG}(2V_a^G(s_*^{CVT}) - E); \\
&\qquad V_a^G(s_*^{CVT}) \le E \le 2V_a^G(s_*^{CVT}) - V_a^G(s=-\infty) \\
&= 1; \\
&\qquad 2V_a^G(s_*^{CVT}) - V_a^G(s=-\infty) < E. \qquad (81)
\end{aligned}
$$

The replacement of eq. (79) by (81) is called "parabolic uniformization".

Returning to eq. (71), and making use of the Heaviside step function in eq. (74), we have, for the transmission coefficient,

$$
\kappa^{CVT/MEPSAG} = \frac{\int_0^\infty P^{MEPSAG}(E)e^{-\beta E}dE}{\int_{V_a^G(s_*^{CVT})}^\infty e^{-\beta E}dE}, \qquad (82)
$$

or

$$
\kappa^{CVT/MEPSAG} = \beta \exp[\beta V_a^G(s_*^{CVT})]\int_0^\infty P^{MEPSAG}(E)e^{-\beta E}dE, \qquad (83)
$$

where we have performed the integral in the dominator of eq. (82). To correct a CVT rate constant we would use

$$
k^{CVT/MEPSAG}(T) = \kappa^{CVT/MEPSAG}(T)k^{CVT}(T). \qquad (84)
$$

As mentioned previously, the MEPSAG transmission coefficient is calculated under the assumption that the tunneling path follows the MEP. This is a good approximation only for systems having little or no coupling between the

reaction coordinate motion and any of the other degrees of freedom — a situation that seldom occurs. One form of coupling is provided by the curvature of the MEP in mass–scaled coordinates; the vector $\vec{z}(s)$, which is tangent to the MEP at each value of s, will have a different orientation at each value of s. We can illustrate this pictorally for a system having two degrees of freedom — the reaction–coordinate motion plus an additional vibration. Figure 2 depicts such a curved reaction path for a metathesis reaction

$$A + BC \rightarrow AB + C, \tag{85}$$

where A, B, and C may be atoms or groups of atoms. If, for visual purposes, we

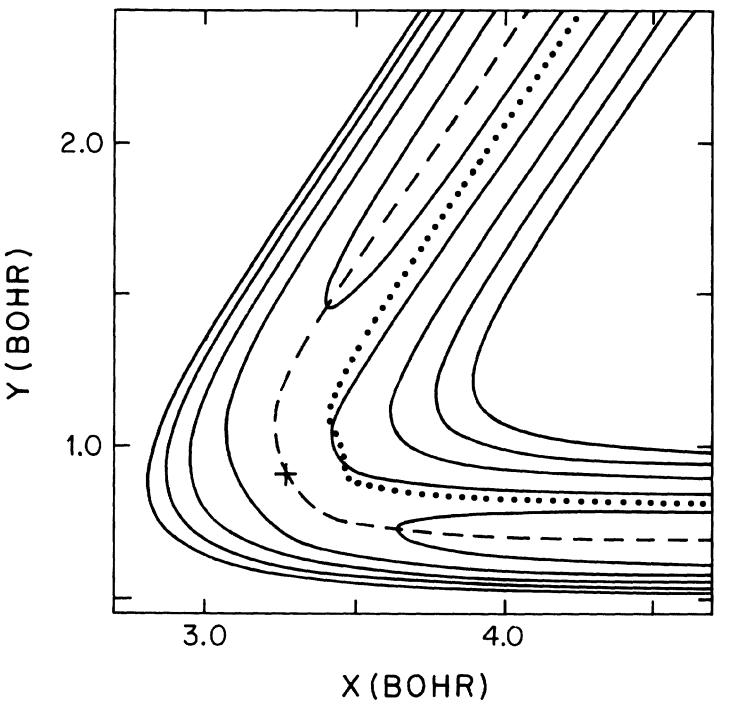

Fig. 2. The potential energy surface of Stern *et al.* [66] for the Cl + DH → ClD + H reaction. The abscissa is the distance from Cl to the center–of–mass of the DH diatom, and the ordinate is the mass–scaled H–D distance. The solid lines represent fixed–energy contours, the dashed line represents the minimum energy path (MEP), the + represents the saddle point, and the dotted line represents the path of classical vibrational turning points when the vibrational motion has zero point energy all along the reaction path.

force this reaction to occur at a fixed A–B–C angle and ignore any internal vibrations in the groups A, B, and/or C, we can plot the potential energy as a function of two coordinates in the mass–scaled system defined by eq. (3). If A, B, and C are all atoms, and we set μ in eq. (3) equal to μ_{rel} of eq. (4), this is equivalent to using two coordinates x and y, where x is the distance from A to the center–of–mass of the BC molecule, and y is a scaled distance from B to C [30] (similar pictures are obtained if one chooses $\mu = 1$ [65]).

Figure 2 is specifically for the medium–curvature system Cl + DH → ClD + H (and the potential energy surface is the GSW surface of Stern *et al.* [66]). The solid lines are potential energy contours, and the dashed line is the MEP. It is known both from analytical semiclassical mechanics [67] and analysis of multidimensional tunneling calculations [68,69] that most of the tunneling flux passes the saddle point on the concave side of the MEP. The dotted curve in Fig. 2 is the path of concave–side classical turning points for the zero point vibrational motion orthogonal to the MEP. For the collinear H + H_2 reaction, Marcus and Coltrin show that this path of turning points is an approximately optimal tunneling path [70]. In the adiabatic ground–state approximation, it is particularly easy to characterize tunneling along this type of shortened path. Because we assume the system is in the ground vibrational state all along the MEP, the classical turning points may be calculated for the vibrational energy $\epsilon^{G}_{int}(s)$ [eq. (73)]. From this assumption it also follows that the effective potential for tunneling along this path is given by the ground state adiabatic potential curve, $V^{G}_{a}(s)$. Thus, the transmission probability for tunneling along this path can be found from eq. (81), as was $P^{MEPSAG}(E)$, except that the coordinate of the tunneling path in the imaginary–action integral of eq. (80) is determined by this shorter path. This is called [31] the Marcus–Coltrin [70] approximation. A generalization of this approach, applicable for any number of atoms and for both collinear and noncollinear MEPs, is accomplished by evaluating the imaginary–action integral along the MEP but replacing the reduced mass μ with an effective reduced mass $\mu^{SC}_{eff}(s)$, which is determined [in the small–curvature (SC) approximation] by the local curvature of the MEP [17,71]. Using this reduced mass is mathematically equivalent to shortening the tunneling path. The transmission probability calculated with this effective reduced mass is called is called $P^{SCSAG}(E)$. This method has been found to give better results than using $P^{MEPSAG}(E)$ for systems with small (but not negligible) amounts of reaction path curvature [29,32]. The small–curvature semiclassical adiabatic ground–state transmission coefficient is given, by analogy to eq. (83), as

$$\kappa^{CVT/SCSAG} = \beta\exp[\beta V^{G}_{a}(s^{CVT}_{*})]\int_{0}^{\infty} P^{SCSAG}(E)e^{-\beta E}dE. \tag{86}$$

We note that for a nonlinear system with 3N degrees of freedom, the reaction-path curvature becomes a vector with as many as 3N–7 nonzero components [72]. These components may be used to define $\mu^{SC}_{eff}(s)$ in the general case [17,71].

For systems with a large amount of reaction path curvature (see Fig. 3), such as group– or atom–transfer reactions for which the exchanged group or atom is much lighter than both the donor and acceptor groups, the small–curvature approximation breaks down [28,46,73,74], and we need another approximation to treat this type of system. This problem has been treated using both hyperspherical [73] and mass–scaled cartesian [17,46,75] coordinates. Here we use the latter approach. In particular we will discuss a scheme which is called the large–curvature ground-state approximation, version 3 (LCG3); this approximation [17,76] is of special interest because it has been defined in such a way as to be particularly easy to apply to general systems with an arbitrary number of degrees of freedom.

Before discussing the LCG3 method, we first consider Fig. 3, which is a potential energy contour diagram in mass–scaled cartesian coordinates for the heavy–light–heavy system $^{37}Cl + D^{35}Cl \rightarrow {}^{37}ClD + {}^{35}Cl$ [46]. The solid lines are

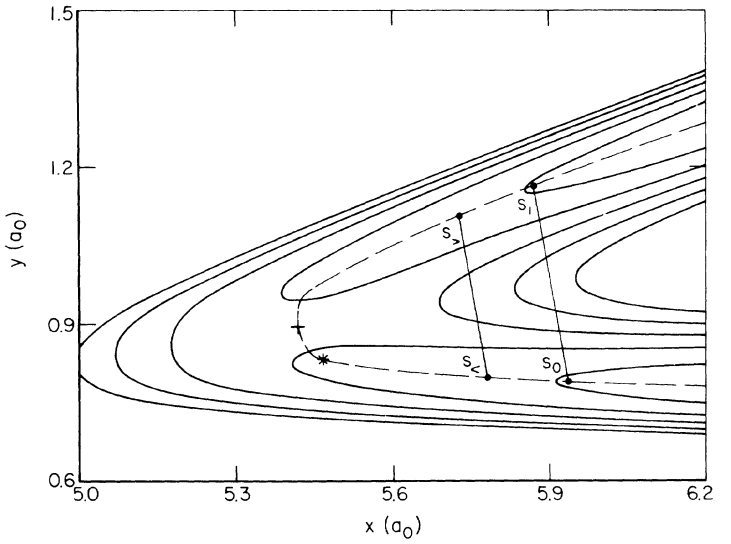

Fig. 3. Potential energy contour diagram for the large curvature system $^{37}Cl + D^{35}Cl$ [46]. The dashed line represents the minimum energy path, + marks the saddle point, and * marks a canonical variational transition state. The points marked $s_<$ and $s_>$ are the classical turning points for reaction–coordinate motion governed by the adiabatic ground–state potential curve $V_a^G(s)$ for energy E, and s_0 and s_1 represent classical turning points for a lower energy and also serve as additional tunneling path termini for energy E. The lines between $s_<$ and $s_>$ and between s_0 and s_1 are typical large–curvature tunneling paths.

the potential contours, the dashed line is the collinear MEP, + represents the saddle point, and * represents the maximum of the adiabatic ground state curve. The fact that the potential contours along a cut perpendicular to the MEP through the saddle point are extremely widely spaced indicates that the vibrational zero point energy is very low at the conventional transition state; this explains why the maximum of $V_a^G(s)$, positioned at a point of higher vibrational zero point energy, is so far removed from the conventional transition state. The saddle point vibrational frequency is low because a symmetric stretch in the heavy–light–heavy case involves only motion of the heavy donor and acceptor atoms. Now consider the reaction-coordinate turning points for some total energy below the maximum of $V_a^G(s)$; these are called $s_<$ for the reactant channel and $s_>$ for the product channel. Due to the curvature of the MEP, the shortest path connecting $s_<$ and $s_>$ has a large component in the direction representing the high–frequency motion of the central light atom, making tunneling from $s_<$ via such a path a highly probable event. We note that the positions of $s_<$ and $s_>$ along the MEP are determined by the total energy of the system and $V_a^G(s)$ (see Fig. 1). For systems with large reaction–path curvature, one finds [46,73–77] that there are also significant tunneling contributions along paths from s_0 to s_1 where $s_0 < s_<$ and $s_1 > s_>$, i.e., the system tunnels before it reaches the entrance–valley reaction-coordinate turning point $s_<$, and the final terminus of the tunneling path is at a point where the reaction–coordinate component of the kinetic energy is greater than zero. The LCG3 approximation includes contributions from all straight–line tunneling paths with equal pre– and post–tunneling reaction–coordinate components of the kinetic energy by using a quasiclassical distribution function to average over tunneling paths with various termini.

Since the degree of exponential damping of the tunneling wave function decreases for lower barriers and for shorter paths, the tunneling amplitude will be largest on the path which provides the best compromise between barrier height and path length. For large–curvature systems, the straight–line paths discussed above, each between a point s_0 in the reactant channel and a point s_1 in the product channel, are so much shorter than the MEP between these points that they yield the dominant tunneling contributions, even though the barriers along these paths are higher than the barrier along the MEP. These paths are shorter, in mass–scaled coordinates, because they involve mostly the motion of the very light central atom. Thus, in this type of system, we calculate the transmission probability by considering only the tunneling along this type of straight–line path. Calculation of the imaginary–action integral, θ [eq. (76)], is more difficult for this type of path, since the effective potential along this path is only given by $V_a^G(s)$ in the regions between the MEP and the classical turning points or between the MEP and the place where vibrational coordinates referenced to the MEP become multivalued. The potential along the rest of this type of path must be calculated from the actual value of the potential energy surface, and it also involves an interpolated value of the zero point energies of modes which are not

curvature–coupled to the reaction coordinate [17,46,75]. In this method, nonclassical reflection is treated by a parabolic uniformization of the MEPSAG action integral.

Since the LCG3 method does not assume adiabaticity throughout the tunneling region, it may be extended to high–barrier or exothermic reactions for which higher product vibrational states are directly populated by the tunneling event (endothermic reactions should be treated in reverse). The contribution to reaction due to tunneling into the various accessible vibrational product states (defined by the quantum number n') is calculated by separately evaluating the contribution for each product vibrational state, and then summing over all of these accessible states. The contributions to the ground vibrational product state are calculated as discussed above, using $V_a^G(s)$ to determine the reaction–coordinate component of the kinetic energy and the quasiclassical distribution function. For each additional available product state, $n' > 0$, we find the tunneling–path terminus $s_{1,n'}$, in the product region, by the relation

$$E_{s_0} = V_{MEP}(s_{1,n'}) + \epsilon_{int}(s_{1,n'},n'), \tag{87}$$

where E_{s_0} is the adiabatic ground–state energy of the system at s_0. We then calculate the tunneling along the straight–line path between s_0 and $s_{1,n'}$. The effective potential used for the calculation along this path is the same as in the general LCG3 method, except in the exit valley, where $V_a(s,n') = V_{MEP}(s) + \epsilon_{int}(s,n')$ is used instead of $V_a^G(s)$. Summation over the individual contributions of the final product states yields the total tunneling probability for this type of reaction [76,77].

Finally, another method has been developed for calculating quantum transmission probabilities which gives results which are similar to SCSAG in the small–curvature limit, similar to LCG3 in the large curvature limit, and of reasonable accuracy for intermediate–curvature systems [32,34,75]. This method, which is called the least–action ground–state approximation (LAG), considers for each pair of tunneling termini a series of tunneling paths ranging from the MEP at one extreme to the LCG3 path at the other. For each energy less than $V_a^G(s_*^{CVT})$, the contribution to the LAG transmission probability, $P^{LAG}(E)$, from each set of termini is given by the tunneling contribution from the path having the largest tunneling probability, i.e., the path giving the smallest imaginary–action integral, θ [eq. (76)]. The contributions from the various pairs of termini are averaged as in the LCG3 method. For the part of any path that is not between the MEP and the classical vibrational turning points or between the MEP and the location on the tunneling path where vibrational coordinates referenced to the MEP become multivalued, the ground–state potential along the path is determined as in the LCG3 method; for the part or parts of any path which are between the MEP and either the path of classical vibrational turning points or the point where local natural collision coordinates break down, $V_a^G(s)$ is used. Thus for each pair of tunneling–path termini the LAG method chooses the best

tunneling path, so that the integral over the quasiclassical distribution function of termini as well as the integral over energy in the expression for the transmission coefficient,

$$\kappa^{CVT/LAG} = \beta \exp[\beta V_a^G(s_*^{CVT})] \int_0^\infty P^{LAG}(E)\, e^{-\beta E}\, dE, \tag{88}$$

encompasses a series of different paths. Again, we incorporate nonclassical reflection into $P^{LAG}(E)$ by making a parabolic uniformization of the MEPSAG tunneling probabilities.

The ability to treat tunneling in high–barrier or exothermic reactions is incorporated into the LAG formalism in the same fashion as described above for the LCG3 formalism. In the LAG method, a best tunneling path is chosen for each pair of termini for each final vibrational product state, n', with the contributions to the various final states being summed at each energy. Again, the only difference in the calculation of the effective tunneling potential along the chosen path is that, in the region between $s_{1,n'}$ and the MEP, $V_a(s,n')$ is used instead of $V_a^G(s)$.

We note that both the LCG3 and the LAG approximations require more information about the potential energy surface than is required for VTST, MEPSAG, or SCSAG calculations. VTST, MEPSAG, and SCSAG calculations require knowledge of the MEP, the potential along the MEP, and the vibrational energies of modes orthogonal to the MEP, but LCG3 and LAG calculations require, in addition, the potential surface in wider swaths on the concave side of the MEP in tunneling regions.

5. Gas–Phase Applications

Sections 2–4 have presented the theoretical formulation of generalized transition state theory and semiclassical tunneling approximations. In order to illustrate the validity and usefulness of this theory for absolute rate calculations we now consider applications to reactions in the gas phase. Although conventional and generalized transition state theory have been applied to many gas–phase systems [33,35], we shall consider only a few examples. Except where stated otherwise, all GTST calculations include anharmonicity by methods discussed elsewhere [8,9,17,31,32,78].

Several studies on collinear atom–diatom reactions have been carried out in which accurate classical mechanical rate constants were calculated for a given energy surface, and these were used to test classical conventional and variational transition state theory. Table I gives some of these results [8,79] for two reactions. For the first reaction, Cl + HD, we see that at 300 K, both the conventional transition state (at $s = 0$) and the canonical variational transition state (at $s = s_*^{CVT}$) provide reasonable bottlenecks, and very little recrossing occurs at either transition state; both $k_C^{\ddagger}$ (300 K) and k_C^{CVT} (300 K) overestimate the accurate rate by only ~10%. At 2400 K, however, recrossing has increased much more

rapidly at the conventional transition state than at the variational one, and $k_C^{\ddagger}$ (2400 K) is nearly twice as large as k_C^{CVT} (2400 K). For the model of an organic hydrogen exchange reaction, R + HR′ → RH + R′, where the alkyl chains R and R′ are represented by carbon atoms having a mass equivalent to that of a butyl radical, the conventional transition state is a poor bottleneck even at as low a temperature as 300 K, while recrossing is so extreme at 2400 K that $k_C^{\ddagger}$ overestimates the accurate classical rate constant by over an order of magnitude. The canonical variational dividing surface, while not providing a perfect bottleneck, yields a rate constant which is high by only a factor of two or less over the whole temperature range. These examples clearly illustrate that the TST approximation — that the local net flux through the transition state, $F^{GT}(T,s)$ [eq. (23)], may be used instead of the global net flux F(T) [eqs. (24) and (39)], to calculate the rate — can be much improved by locating the transition state variationally ($s = s_*^{CVT}$) instead of defining it to be at the saddle point (s = 0).

TABLE I. Ratios of classical transition state theory rate constants to exact classical dynamical ones for two collinear reactions.

Reaction	Temperature, K	‡	CVT
(R1) Cl + HD → ClH + D[a]	300	1.1	1.1
	2400	5.0	2.8
(R2) ^{57}C+H^{57}C′ → ^{57}CH+^{57}C′[b]	300	4.3	2.0
	2400	11.4	2.0

[a]Ref. 8.
[b]Ref. 79; three–body model of C_4H_9+H–C_4H_9 → C_4H_9–H+C_4H_9.

In order to show that variational optimization of the transition state can also be important when calculating semiclassical TST rate constants, which no longer provide rigorous upper bounds to the accurate quantum mechanical rate constants, we consider two collinear reactions [29,80–82] for which tunneling effects are negligible; in particular, we consider I + H_2 → IH + H, and I + HI′ → IH + I′, which are called (R3) and (R4), respectively. For (R3) $k^{CVT}(T)$ agrees with $k^{CVT/SCSAG}(T)$ to three significant figures, and for (R4) $k^{CVT}(T)$ agrees with $k^{CVT/LAG}(T)$ to two figures. In these cases we consider the ratios of the semiclassical rate constants to accurate quantal ones for collinear reaction on the same energy surface. As discussed in Section 4, we expect variational effects to be especially important for the heavy–light–heavy mass combination of (R4) because

of the low value of the symmetric stretch frequency at the saddle point for a symmetric reaction with this mass combination. From Table II it is clear that the canonical variational transition state provides a good bottleneck at all temperatures considered for both reactions; $k^{CVT}(T)$ is within 10% of the accurate quantal results at 300–1500 K for the I + H_2 case and within 42% of the accurate results at 100–1000 K for the large–curvature case. The conventional TST results, however, are much worse — $k^{\ddagger}(T)$ overestimates the accurate quantal results for I + H_2 by a factor of 12 at 300 K, while for the more difficult heavy–light–heavy system, $k^{\ddagger}(T)$ overestimates the accurate results by over 4 orders of magnitude at 100 K and by a factor of 57 at 300 K. In general, variational effects (by which we mean the difference of VTST rates from conventional TST ones) may either increase or decrease in importance as the temperature is raised. Increasing importance with increasing temperature is the most common trend in classical calculations, because classical recrossing is more predominant at higher temperatures. This classical trend is typically retained in semiclassical calculations when variational effects are controlled by low–frequency modes. When high–frequency modes are important though, the effects are dominated by zero point energies, and zero point effects decrease with increasing temperature. The reactions in Table II are both examples where high–frequency stretches control the variational effect. The I + HI′ reaction is particularly interesting in this regard. Because the symmetric stretch frequency is so low at the saddle point, the value of the adiabatic ground state curve at the reactants,

TABLE II. Ratios of semiclassical generalized transition state theory rate constants to the accurate quantal ones for two collinear reactions.

Temperature, K	‡	CVT
	(R3) I + H_2 → IH + H[a]	
300	12.1	1.09
600	3.7	1.05
1500	2.1	1.03
	(R4) I + HI′ → IH + I′[b]	
100	1.75×10^4	0.77
300	57.0	1.07
600	21.3	1.22
1000	19.3	1.42

[a]GTST results, Refs. 29 and 30; accurate quantal results, Ref. 80.
[b]GTST results, Ref. 82; accurate quantal results calculated (see Ref. 82) from Ref. 81.

where this mode correlates to a high–frequency hydride vibration, is actually higher than the value of this curve at the saddle point, and the conventional TST rate constant increases with decreasing temperature at temperatures below about 600 K [82]. Consequently, variational effects are most important at low temperatures for this system.

Next we consider rate constants for which tunneling corrections are important. We compare semiclassical CVT rate constants with various transmission coefficients to accurate quantal rate constants, in each case calculated on the same potential energy surface, for 3–dimensional atom–diatom reactions. Table III shows results [34,83–85] for four reactions for which tunneling is quite

TABLE III. Ratios of semiclassical canonical variational transition state theory rate constants (with various transmission coefficients) to accurate quantal rate constants for 3–dimensional atom–diatom reactions.

T,K	CVT	CVT/ MEPSAG	CVT/ SCSAG	CVT/ LCG3	CVT/ LAG
	(R5) $H + BrH' \rightarrow HBr + H'$[a]				
200	0.042	0.59	2.4	1.1	1.5
250	0.14	0.70	1.8	0.98	1.1
300	0.26	0.79	1.6	0.95	0.99
	(R6) $H' + H_2 \rightarrow H'H + H$[b]				
200	0.0018	0.031	0.38	0.59	0.74
250	0.014	0.079	0.51	0.88	0.87
300	0.044	0.15	0.61	1.0	0.92
400	0.15	0.30	0.73	1.1	0.99
	(R7) $O + DH \rightarrow OD + H$[b]				
300	0.14	0.39	1.5	0.84	0.91
400	0.36	0.63	1.4	0.90	0.92
500	0.61	0.89	1.4	1.0	1.1
	(R8) $O + H_2 \rightarrow OH + H$[b]				
300	0.052	0.16	0.87	1.1	1.3
400	0.16	0.31	0.89	1.1	1.1
500	0.29	0.45	0.93	1.0	1.1

[a]GTST results, Ref. 83; accurate results, Ref. 84
[b]CVT, CVT/LAG, and accurate results, Refs. 34 and 85; CVT/MEPSAG, CVT/SCSAG, and CVT/LCG3 results, Ref. 85.

important, even at temperatures above room temperature. This point is illustrated by the fact that the CVT rate constant with no tunneling correction grossly underestimates the accurate rate constant values for all four reactions.

The reactions in Table III are arranged in order of increasing reaction–path curvature. Considering all four reactions as a group the LAG method provides the best overall agreement with the accurate quantal results. In three cases it provides a significant improvement over the SCSAG results at all temperatures considered, and in one case these methods are of comparable accuracy. Notice that the LAG results sometimes predict larger tunneling effects than the SCSAG results and sometimes predict smaller tunneling effects, because the approximations in the two methods are quite different. The LAG result for a given pair of tunneling path termini is always larger than the LCG3 one because the LCG3 tunneling path is a special (un–optimized) case of the LAG one. Thus when the methods differ appreciably the LAG result is always larger. When the results are similar, though, either one may be larger because of the semiclassical approach used in averaging over paths with various termini. In all cases shown, the $k^{CVT/LAG}(T)$ rate constants are in excellent agreement with the accurate quantal rate constants for 3–dimensional atom–diatom reactions.

TABLE IV. Ratios of 1–dimensional rate coefficients calculated with various tunneling approximations[a] to accurate quantal results.[b]

T,K	CVT	CVT/ MEPSAG	CVT/ SCSAG	CVT/ LCG	CVT/ LCG3	CVT/ LAG
	(R9) $^{37}Cl + H^{35}Cl \rightarrow {}^{37}ClH + {}^{35}Cl$					
200	0.13	0.15	0.15	0.61	0.61	0.55
300	0.33	0.35	0.35	0.81	0.82	0.76
600	0.82	0.83	0.83	1.2	1.2	1.2
1500	1.4	1.4	1.4	1.5	1.6	1.5
	(R10) $^{37}Cl + D^{35}Cl \rightarrow {}^{37}ClD + {}^{35}Cl$					
200	0.14	0.19	0.22	0.68	0.68	0.66
300	0.37	0.42	0.45	0.87	0.87	0.85
600	0.90	0.76	0.77	1.0	1.0	1.0
1500	1.4	1.3	1.3	1.4	1.4	1.4

[a]Previous GTST calculations on this system are reported in Refs. 32, 74, and 75. The present results (Ref. 86) all include anharmonicity by the WKB method.
[b]Calculated in Ref. 74 from data in Ref. 87.

There are no converged 3–D rate constants available for large–curvature systems, so we again return to the collinear world to compare to accurate quantal results; in particular, we consider the large curvature collinear reaction, $^{37}Cl + H^{35}Cl \rightarrow {}^{37}ClH + {}^{35}Cl$, and its isotopic analog, $^{37}Cl + D^{35}Cl \rightarrow {}^{37}ClD + {}^{35}Cl$ [46,74,85–90] The large ratios of the CVT/LAG rate coefficients to the CVT ones in Table IV indicate that tunneling is important; for example, LAG increases the rate for the H transfer case by about 30% for a temperature of 600 K and by a factor of ~4 at 200 K. The CVT/MEPSAG method provides little improvement over CVT, indicating that almost no tunneling occurs along the MEP path. The SCSAG method also fails badly in this case, but the LCG, LCG3, and LAG methods provide reasonable estimates of the tunneling contributions for both reactions, even though they do appear to consistently underestimate the tunneling effects at very low temperatures. (The LCG method is the original version of LCG3, and it gives very similar results.) Although accurate quantal results are not available for these reactions in the 3–dimensional case, it is interesting to compare to experiment, even though we are unable to separate the uncertainties in the potential surface from the uncertainties in the dynamical methods. From Table V, we see that tunneling is predicted to be important for both reactions in three dimensions; in reaction (R9) the calculated reaction rate increases by nearly an order of magnitude when tunneling is included at 368 K; in reaction (R10) this increase is smaller, at a factor of two and a half. In both cases the best calculated rate is in good agreement with experiment. The experimental results indicate that this system has only a moderate kinetic isotope effect, i.e., k(R9)/k(R10) = 5.0, yet from the theoretical results it is clear that tunneling contributions *are* important. In fact, the theoretical CVT kinetic isotope effect without tunneling contributions is less than 5%, indicating that there is almost no kinetic isotope effect at all in the absence of tunneling. Inclusion of tunneling in the theoretical calculations, however, brings the kinetic isotope effect much closer to the experimental value. Hence, moderate kinetic isotope effects do not necessarily mean that tunneling is unimportant for a reaction. This example provides a very significant caution about a common procedure for interpreting experimental data, by which tunneling effects are invoked only if the kinetic isotope effects are large. This example is particularly striking since the dominant tunneling paths are very

TABLE V. Comparison of 3–dimensional transition state theory rate constants (cm^3 $molecule^{-1}$ s^{-1}) and kinetic isotope effects with experiment at 368.2 K.[a]

	CVT	CVT/LCG	Expt.
k(R9)	3.8(–16)	3.3(–15)	5.1(–15)
k(R10)	3.7(–16)	9.8(–16)	1.0(–15)
k(R9)/k(R10)	1.0	3.3	5.0

[a]Theoretical results for the scaled surface of Garrett *et al.*, Ref. 46. Experimental results, Refs. 88–90.

far from the saddle point. Thus a conventional KIE interpretation based on saddle point force constants would be qualitatively misleading about what region of the energy surface is most critical in controlling the rate.

In some cases (e.g., [91]) neither the large–curvature nor the small–curvature limit is quantitatively reliable. In such cases the LAG method should be used for quantitative interpretation of kinetic isotope effects.

TABLE VI. Theoretical and experimental rate constants (cm^3 $molecule^{-1}$ s^{-1}) for the 3–dimensional reaction $OH + H_2 \rightarrow H_2O + H$.

	CVT/SCSAG[a]		
T,K	Harmonic	Anharmonic	Experiment[b]
298	2.37(−14)	1.04(−14)	6.1±0.4(−15)
400	7.26(−14)	4.03(−14)	3.7±1.1(−14)
600	3.35(−13)	2.23(−13)	2.9±0.9(−13)
1000	1.91(−12)	1.42(−12)	2.4±0.7(−12)

[a]Ref. 9; the potential surface is described in Ref. 92.
[b]Ref. 93.

Finally we discuss two gas–phase reactions involving larger molecules. Table VI shows 3–dimensional CVT/SCSAG and experimental rate constants for the reaction $OH + H_2 \rightarrow H_2O + H$ [9,92,93]. The second column gives the $k^{CVT/SCSAG}(T)$ rate constant calculated as described above, with the independent–normal–mode harmonic approximation used to evaluate the partition functions for vibrational modes orthogonal to the reaction coordinate. The third column gives the $k^{CVT/SCSAG}(T)$ rate constant calculated with principal anharmonicity included in the independent–normal–mode representation of these vibrations. The agreement with experiment is good for both calculations, though it is generally better with the inclusion of anharmonicity. This agreement with experiment is quite impressive, since the potential energy surface used for these calculations is entirely *ab initio* [92,94,95], i.e., it was not calibrated to reproduce any experimental results. In general one would often be satisfied if good agreement could be obtained over a range of temperatures by adjusting only the barrier height.

We also consider the gas–phase reaction $CH_3 + H_2 \rightarrow CH_4 + H$ [48,96,97] for which the CVT/SCSAG results (only the lowest–frequency vibrational mode includes anharmonicity, the rest are treated harmonically) are tabulated and compared with an exemplary set of experimental results (two other sets are tabulated in Ref. 48) in Table VII. These calculated results, which are for the best semiempirical surface of Joseph *et al.* [48], are quite good; they differ from the experimental results by less than 20% for all temperatures at which the experimental results are available. We also compare calculated kinetic isotope effects with experiment. These results are tabulated in Table VIII and are also

TABLE VII. Calculated and experimental rate constants (cm^3 $molecule^{-1}$ s^{-1}) for the 3–dimensional reaction $CH_3 + H_2 \rightarrow CH_4 + H$.

T,K	CVT/SCSAG[a]	Experiment[b]
372	3.2(−18)	2.7(−18)
400	7.4(−18)	6.5(−18)
424	1.4(−17)	1.3(−17)
500	7.6(−17)	7.3(−17)
600	3.9(−16)	3.8(−16)
667	9.1(−16)	9.0(−16)

[a]Ref. 48, surface J3.
[b]Computed from reverse rate constants of Ref. 97 and JANAF equilibrium constants. See Ref. 48.

TABLE VIII. Kinetic isotope effects for the reactions $CH_3 + H_2 \rightarrow CH_4 + H$ (R12) and $CH_3 + D_2 \rightarrow CH_3D + D$ (R13).

	k(R12)/k(R13)	
T,K	CVT/SCSAG[a]	Experiment[b]
400	4.5	4.8±0.4
500	3.5	3.5±0.2
600	3.0	2.8±0.2
667	2.7	2.5±0.1

[a]Ref. 48; surface J3.
[b]Ref. 96.

quite good. Because the potential energy surface used to calculate the $CH_3 + H_2$ results is semiempirical, and the CVT/SCSAG method has already been shown to be reasonably reliable, the comparisons with experiment in Tables VII and VIII are really tests of the shape and calibration of the potential energy surface used. This then provides an example of how CVT/SCSAG rate constants and kinetic isotope effects are used to elucidate information regarding potential energy surfaces [48]. We note that the variational transition state for the $CH_3 + H_2$ reaction occurs slightly (~0.1 a_0) earlier than the saddle point, a result which agrees well with an earlier 3–body model [27] of this reaction based on a rotated-Morse-bond-energy-bond-order approximation to the energy surface. In both the full surface

and the 3–body model the variational displacement of the transition state is determined primarily by the stretching frequency of the mode that correlates to H–H stretching in reactants and to the new C–H stretch in products.

VTST may also be applied to unimolecular reactions in the gas phase [2,17,98] and the semiclassical tunneling approximations discussed here may be applied to conformational rearrangements such as switches of hydrogen bonds [99]. Generalizations of the ideas and methods presented above may also be used to treat reaction rates of vibrationally excited molecules [51] and the state–specific decay of metastable states [100].

6. Condensed–Phase Reactions

The quasi–thermodynamic formulation of transition state theory, especially the expression of the rate constant in terms of the free energy of activation, has been extremely useful in understanding differences in reaction rates between the gas phase and solution [19a]. Thus it is very important to understand the validity of transition state theory assumptions for solution reactions, and this question has recently received considerable attention [2,18,40]. Unlike gas–phase TST, which has received extensive testing against accurate classical and quantal dynamics, as discussed in Section 5, condensed–phase TST is much harder to test than gas–phase TST. In this section we discuss some of the new considerations which should be incorporated into generalized TST for reactions in solution. Generalized TST has also been applied to reactions on solid surfaces, and we shall discuss this as well. We consider both static effects, which are easily incorporated into the quasi-thermodynamic formalism developed for TST in the gas phase, and dynamic effects, which require careful interpretation. We note that generalized TST has a great advantage over many molecular dynamics techniques which are currently used for condensed–phase reactions because quantization effects and tunneling can be included by consistent procedures that have already been well tested for gas–phase processes.

Before proceeding to discuss the effect of solvent we note a formal difference between gas–phase and condensed–phase reactions. In condensed phases we do not have free translations and thus we cannot factor out free translational partition functions for each species, even though the partition functions for each species are still proportional to the volume of the system. Thus, by analogy to eq. (45) and eq. (35), eqs. (59a) and (59b) are replaced by

$$k^{GT}(T,s) = \sigma \frac{\tilde{k}T}{h} \frac{\Phi^{GT}(T,s)}{\Phi^{A}(T)\Phi^{B}(T)} e^{-\beta V_{MEP}(s)} \qquad \text{(bimolecular)} \tag{89a}$$

and

$$k^{GT}(T,s) = \sigma \frac{\tilde{k}T}{h} \frac{\Phi^{GT}(T,s)}{\Phi^{A}(T)} e^{-\beta V_{MEP}(s)} \qquad \text{(unimolecular)}, \tag{89b}$$

respectively.

Because it is impossible to consider explicitly all of the solvent molecules in

a solution–phase reaction (or all of the atoms of the solid for a reaction on a crystalline surface) as part of the reacting system, all or most of the solvent molecules must be treated collectively as a "bath" — or ignored. A bath has both static and dynamical effects on a reacting system. Before considering these effects, we note that, if some solvent molecules (or solid–state atoms) play a significant role in the reaction coordinate, they *should* be treated explicitly as part of the primary reacting system rather than as part of the bath [18]. Thus, one should compromise between, on the one hand, minimizing computational effort by treating only a small number of solvent molecules (or solid–state atoms), if any, explicitly as part of the primary system and, on the other hand, accounting for important couplings between specific solvent molecules (or solid–state atoms) and the reaction coordinate. Once the primary system has been chosen, the effects of the bath on the rate constant for the primary system must be incorporated into the expression for this rate constant, eqs. (58) and (89). The simplest of these effects are static effects. In this first approximation, it is assumed that the bath solvent molecules (or solid–state atoms) adjust statistically to motions of the primary system, i.e., that the bath always remains in equilibrium with the primary system. The effect of the bath is then incorporated into the quasi–thermodynamic TST formalism [eq. (56) but without necessarily treating the left–hand side as classical] simply by considering its contribution to the free energy of the system (primary system plus bath) [1a,101]. Because the free energy of interaction of the bath and the system may vary greatly along the primary–system reaction coordinate, the free energy of activation, which directly determines the TST rate constant [see eq. (56)], may change drastically in the presence of the bath.

For many systems, however, it is questionable whether solvent (or surface) rearrangement is fast enough to allow solvent (or surface) equilibration at each step along the primary–system reaction coordinate. Such systems may exhibit dynamical, "nonequilibrium" solvation effects. As discussed in Section 2.4 equilibrium of phase space points originating in the reactants region is assured in classical mechanics if the reactants are in equilibrium and all molecules are treated explicitly; however, if we separate the system into a primary system and the rest, it may be a serious restriction to define the dividing surface entirely in terms of primary–system coordinates. In such a case the solvent is said to be "nonequilibrated" or to "participate in the reaction coordinate." The conceptually simplest way to include these effects is to include the solvent molecules or surface atoms showing the strongest interaction with the reacting solute (or adsorbate) in the primary system; this increases computational effort but avoids modifications to the TST formalism which, as described below, would otherwise be required to treat such nonequilibrium effects. This approach has been used successfully for treating the diffusion of hydrogen atoms on a metal surface [102–104]. Good convergence of reaction rates with respect to cluster size, i.e., with respect to the number of surface atoms included in the primary system, was achieved at and above room temperature, but convergence was harder to achieve below room temperature, because of the importance of tunneling. This indicates that tunneling is a more global, less localized phenomenon than classical barrier crossing. If dynamical solvent effects cannot be isolated to a treatably few solvent molecules or surface atoms, it is sometimes feasible to introduce a collective coordinate which can be included explicitly in the primary system. A good example of this technique is the introduction of a polarization vector when treating reactions in polar solvents [105–107].

In order to treat nonequilibrium solvation effects of bath molecules without

including them in the primary system, one may add a friction correction factor γ^{ζ} to the TST rate constant [18], e.g.,

$$k^{CVT/G,\zeta} = \gamma^{\zeta} k^{CVT/G}, \tag{90}$$

where the superscript on the correction factor indicates that it is determined by the degree of solvent friction on the primary system (ζ denotes a friction coefficient). In the case of solution reactions the friction correction factor may be approximated by a number of methods; among these are Kramers theory [108] and a generalized Langevin–equation approach [109,110]. Kramers theory is intended to account for a series of frequent, but weak, bath perturbations which interrupt motion along the reaction coordinate. In this theory the correction term is related to the ratio of the characteristic time scale for crossing the reaction coordinate barrier in the absence of friction to the characteristic time scale for relaxation of momentum along the reaction coordinate due to friction. The relaxation time due to friction may be estimated on the basis of the bulk viscosity of the solvent [18]. Work with the Langevin–equation approach, however, has indicated that the reaction rate is dependent upon the short–time solvent friction felt by the primary system [109,110], rather than on the bulk friction constant as used in Kramers theory; it is believed, therefore, that Kramers theory, with the relaxation time estimated from bulk viscosity usually overestimates the effect of friction on reaction rates [40]. An interesting perspective on the high–friction limit of Kramers theory is provided by a recent paper of Pollak [111]. Using a harmonic bath to model the generalized Langevin equation, Pollak showed that the frictional decrease of the rate calculated by TST for the primary system can also be calculated by doing TST (without friction) on the enlarged system consisting of the primary system plus the bath.

The dynamical friction effects that we have considered so far are based on the idea that the solvent molecules hinder the motion of the primary system along the reaction coordinate. This type of effect will predominate in the high–friction limit. There also may exist a regime where the time scale for barrier crossing is much faster than the time scale for solvent relaxation of reaction coordinate momentum, but still much slower than the time scale for energy redistribution in the reactant (see below). In this regime, the rate constant is expected to be independent of solvent friction. If there is very little coupling of the primary system to the solvent, however, the assumption that the reactants (or, for reversible reactions, the products, which are the reactants of the back reaction) are in local equilibrium may fail [108,112]. This failure results from the inability of collisions between primary system molecules and solvent molecules to exchange vibrational energy or to exchange vibrational with translational energy, and thus, the inability of these collisions to populate reactive regions of reactant phase space as rapidly as they are being depleted by reaction (or for reversible reactions, to depopulate highly excited nascent products before they react back), i.e., the time scale for energy redistribution in the reactants is slower than that for barrier crossing. This low–solvent–coupling regime is similar to the low–pressure limit for gas–phase reactions, as discussed in Section 2.4. Thus we expect three regimes for reactions in a bath. First, in the low–friction regime, the rate constant should increase with increasing friction as the reactant distribution of states approaches an equilibrium distribution. There may then be a regime where the reactant equilibrium assumption holds, but frictional effects on the reaction coordinate are

not yet important. In this regime the reaction rate constant will be independent of friction. Finally, as friction is increased still further, frictional slowing of reaction–coordinate motion becomes important, and the rate constant will decrease with increasing friction. This may be referred to as the "friction–controlled" regime. In both the first and third regimes, the uncorrected TST rate constant (even if this rate constant was calculated including static solvation effects) will overestimate the actual rate constant. In the middle, friction-independent regime, the uncorrected TST rate constant should be a good approximation to the true solution rate constant. Unfortunately, it is possible that, for many reactive systems, by the time the assumption of an equilibrium distribution of reactants is valid, frictional effects on the reaction coordinate will already be important, and the TST rate constant will overestimate the true rate constant in all cases if a correction term is not added [113,114].

Here we make two important notes. First, some studies of the importance of a friction correction term [113,114], as mentioned above, have been performed by including only the reacting solute in the primary system. It is possible that including just a few important solvent molecules in the primary system will yield a more realistic reaction coordinate, and, consequently, the TST or VTST dividing surface will be a better bottleneck, thus obviating the need for a friction correction term. Second, we note that recrossing of the transition state may cause errors in gas–phase TST rate constants, even when variational methods are used, of up to around a factor of two, especially for classical systems (see Section 5). One should be careful that these recrossing effects, which would be present even in the absence of solvent molecules, are not attributed to solvent friction when they occur for condensed–phase reactions. Detailed studies of a variety primary systems, both in the absence and in the presence of a solvent bath, could certainly help to clarify these issues. Both of these points raise uncertainties which cannot be resolved without further study.

Frictional effects occur in ultrahigh pressure gases as well as in solution [38]. In fact the binary–collision language of gas kinetics provides a simple way to think about the low–pressure and high–pressure fall–offs from the equilibrium plateau. At low pressures, when back reaction is neglected, the most energetic molecules, or the molecules with most energy in the most reactive modes, tend to react fastest, and energy–changing collisions are too infrequent to maintain thermal equilibrium concentrations of these states. For reversible reactions, collisions are also required to thermalize the products before they react back. At ultrahigh pressures, in contrast, collisions occur not only frequently enough to exchange energy on the kinetic time scale for reaction but also fast enough to interrupt the molecular motion along the reaction coordinate during a single reactive event.

Finally we mention a few recent applications of VTST and semiclassical tunneling concepts to organic reactions without invoking nonequilibrium, frictional, or solvation effects. In the language introduced at the beginning of this chapter these have all been based on the phenomenological approach rather than the absolute rate approach, and these concepts may be very useful for such reactions.

Houk and Rondan [115] and Doubleday *et al.* [116] have studied exothermic reactions with small or zero barriers. For such reactions the free energy of activation maximum may be controlled by the decrease in entropy of activation for generalized transition states located later along the reaction coordinate [117]. Since entropic effects become relatively more important compared to enthalpic

effects as the temperature is increased, this gives a handle for understanding temperture–dependent transition states and negative activation energies [115–117].

Kreevoy *et al.* [77] studied kinetic isotope effects for hydride transfer between carbons in nitrogen heterocycles, $R_1^+ + R_2H \rightarrow R_1H + R_2^+$. Quadratic free energy correlations indicated that the critical configurations for H^- transfer are geometrically more extended than those for D^-. This was interpreted in terms of large–curvature tunneling in which H^- tunnels at longer $R_1^+ - R_2^+$ distances than D^-.

7. Thermochemical Kinetics

In the quasi–thermodynamic formulation of transition state theory [eq.(56)], the transition state species is treated like a stable species, except that one degree of freedom, the unbound degree of freedom corresponding to the reaction coordinate, is removed. In conventional transition state theory, because the position of the dividing surface is determined entirely by the potential energy surface, i.e., the dividing surface is set at the saddle point, s = 0, the transition state species is independent of temperature. This is not true for the CVT transition state species, because the position of the dividing surface is re–optimized at each temperature. Thus, the conventional transition state can be related directly to a single molecular structure while the CVT transition state cannot. Using this relationship the quasi–thermodynamic quantities for the conventional transition state can be calculated directly from the temperature–independent structure and vibrational frequencies of the bound degrees of freedom of the conventional transition state. Furthermore, bond additivity and group additivity relationships can be used to approximate the enthalpy and the entropy [118]. In CVT, however, we must take account of the temperature dependence of the frequencies, bond strengths, and so forth.

The quasi–equilibrium constant, $K^{\ddagger}$, for the quasi–equilibrium between the reactants and the conventional transition state species is found from eq. (54) by setting s = 0, i.e.,

$$K^{\ddagger} = \sigma \frac{Q^{\ddagger}(T)}{\Phi^{R}(T)} e^{-V^{\ddagger}/\tilde{k}T} \quad \text{(bimolecular)}, \tag{91a}$$

$$K^{\ddagger} = \sigma \frac{Q^{\ddagger}(T)}{Q^{A}(T)} e^{-V^{\ddagger}/\tilde{k}T} \quad \text{(unimolecular)}, \tag{91b}$$

where we have replaced the classical partition functions with their quantum analogs, as discussed in Section 3, and we have defined $Q^{\ddagger}(T) = Q^{GT}(T,s=0)$ and $V^{\ddagger}(T) = V_{MEP}(s = 0)$. By analogy to eqs. (54)–(56), we can write the conventional TST rate constant in terms of a free–energy change between

reactants and the transition state species, $\Delta_{\ddagger} G_T^0$, as

$$k^{\ddagger}(T) = \frac{\tilde{k}T}{h} K^0 e^{-\Delta_{\ddagger} G_T^0/RT}, \tag{92}$$

where $\Delta_{\ddagger} G_T^0$ is defined by the relationship

$$K^{\ddagger} = K^0 e^{-\Delta_{\ddagger} G_T^0/RT}. \tag{93}$$

The free energy of activation may be further partitioned in terms of the enthalpy and entropy of activation at temperature T, $\Delta_{\ddagger} H_T^0$ and $\Delta_{\ddagger} S_T^0$, respectively, as

$$\Delta_{\ddagger} G_T^0 = \Delta_{\ddagger} H_T^0 - T\, \Delta_{\ddagger} S_T^0. \tag{94}$$

From eqs. (92) and (94), one could evaluate the conventional TST rate constant by evaluating $\Delta_{\ddagger} H_T^0$ and $\Delta_{\ddagger} S_T^0$, i.e., by evaluating the quasi–thermodynamic properties of the conventional transition state.

However, in systems where the conventional transition state does not provide a good bottleneck or where tunneling contributions are important, $k^{\ddagger}$ will not be a very good approximation to the actual rate [14–18]. A much better approximation for such systems would be $k^{CVT/G}$ defined in eq. (58b), which includes a ground–state transmission coefficient, $\kappa^{CVT/G}(T)$, as discussed in Section 4. For simplicity, we shall consider only the LAG approximation for the transmission coefficient in this section. Further, let us define the more concise notation, $\kappa_{tun}(T)$, where, for the methods suggested above,

$$\kappa_{tun}(T) \equiv \kappa^{CVT/LAG}(T). \tag{95}$$

If we define $\kappa_{var}(T)$, the contribution to the rate due to the optimization of the dividing surface position as a function of temperature, as

$$\kappa_{var}(T) = k^{CVT}(T)/k^{\ddagger}(T), \tag{96}$$

we can factor the rate constant, eq. (58b), as

$$k^{CVT/LAG}(T) = \kappa_{tun}(T)\kappa_{var}(T)k^{\ddagger}(T). \tag{97}$$

With this factorization, it is clear that one contribution, $k^{\ddagger}(T)$, to the rate constant, $k^{CVT/LAG}(T)$, is determined by a "substance" — the conventional transition state species — and its properties. This type of contribution is called a

substantial contribution [119]. The other two terms κ_{tun} and κ_{var}, do not depend only upon a single transition state species, but rather require characterization of the system along part or all of the reaction path as a function of temperature. Thus, this type of contribution is called a nonsubstantial contribution [119].

For the nonsubstantial contributions it is useful to introduce a factorization analogous to that used for the substantial contributions [eqs. (93) and (94)]. This factorization is [119]

$$\kappa_x(T) = \exp(\Delta_{n_x}S_T^0/R)\exp(-\Delta_{n_x}H_T^0/RT), \tag{98}$$

where $\Delta_{n_x}S_T^0$ and $\Delta_{n_x}H_T^0$ are nonsubstantial activation parameters which parameterize contributions for temperature–independent and temperture–dependent factors in $\kappa_x(T)$. These nonsubstantial parameters are obtained from the relations

$$\Delta_{n_x}S_T^0 = RT\,\frac{d\ \ell n\ \kappa_x}{dT} + R\,\ell n\,\kappa_x \tag{99}$$

$$\Delta_{n_x}H_T^0 = RT^2\,\frac{d\ \ell n\ \kappa_x}{dT}, \tag{100}$$

which are analogous to the Gibbs–Helmholtz relations between the entropy and enthalpy and the equilibrium constant for a given system. Both $\kappa_{tun}(T)$ and $\kappa_{var}(T)$ are factorized as in eq. (98) suggesting

$$\Delta_a H_T^0 = \Delta_{tun}H_T^0 + \Delta_{var}H_T^0 + \Delta_{\ddagger}H_T^0 \tag{101}$$

and

$$\Delta_a S_T^0 = \Delta_{tun}S_T^0 + \Delta_{var}S_T^0 + \Delta_{\ddagger}S_T^0, \tag{102}$$

such that eq. (97) is equivalent to

$$k^{CVT/LAG}(T) = \frac{\tilde{k}T}{h}\,K^0\,e^{\Delta_a S_T^0/R}\,e^{-\Delta_a H_T^0/RT}, \tag{103}$$

which is reminiscent of eq. (56) if we define

$$\Delta_a G_T^0 = \Delta_a H_T^0 - T\Delta_a S_T^0. \tag{104}$$

Equations (101)–(103) clearly illustrate that to provide a good estimate of the rate constant for systems where tunneling or variational effects are important, the nonsubstantial contributions must be included in the entropy and enthalpy of activation [119].

The specific factorization of the rate constant, as given by eq. (97), which yields the separation of enthalpic and entropic terms as given by eq. (101) and eq.

(102), is particularly useful if one has information about the potential energy surface, and thus about the properties of the saddle point species, since this information allows for the calculation of $\Delta_{\ddagger}S^0_T$ and $\Delta_{\ddagger}H^0_T$. Another possible factorization, which could be more useful for the interpretation of experimental data, is one which maximizes the substantial contributions to entropy and enthalpy, while minimizing the nonsubstantial contributions [119]. One such factorization is based on a single temperture-independent transition state which is set at the maximum, denoted by $s = s_*^{AG}$, of the adiabatic ground–state potential curve, $V_a^G(s)$ [eq. (72)], instead of at the saddle point. Alternatively it could be set at the location of the maximum free energy of activation for the center of the temperature interval of interest; the maximum of $V_a^G(s)$, in contrast, would be the variational, or CVT, transition state location for a temperature of 0 K. Thus, we can define a correction factor for the temperature dependence of the transition state location $\kappa_{therm}(T)$ as

$$\kappa_{therm}(T) = k^{CVT}(T)/k^{GT}(T,s_*^{AG}), \tag{105}$$

and the factorization, analogous to eq. (97), becomes

$$k^{CVT/LAG}(T) = \kappa_{tun}(T)\kappa_{therm}(T)k^{GT}(T,s_*^{AG}), \tag{106}$$

where $k^{GT}(T,s_*^{AG})$ gives rise to the substantial part of the enthalpy and entropy. With this factorization, we have for the nonsubstantial contributions to $\Delta_a H^0_T$ and $\Delta_a S^0_T$,

$$\Delta_n H^0_T = \Delta_{tun} H^0_T + \Delta_{therm} H^0_T \tag{107}$$

$$\Delta_n S^0_T = \Delta_{tun} S^0_T + \Delta_{therm} S^0_T. \tag{108}$$

For several hydrogen–atom transfer reactions with barriers of about 10 kcal/mol, it has been found [119] that $\Delta_{therm}H^0_T$ and $\Delta_{therm}S^0_T$ are small, especially at low temperatures where $\Delta_{tun}H^0_T$ and $\Delta_{tun}S^0_T$ are very significant. Table IX gives an example [119] for the $O + H_2$ reaction. We see, e.g., that the temperature dependences of the total enthalpy and entropy of activation are both opposite in direction to their substantial parts. As a result of the temperature dependences of both activation parameters the phenomenological Arrhenius activation energy decreases from 14 kcal/mol at T = 1400–1900 K to 8 kcal/mol at 318–471 K [120]. The latter value is considerably smaller than the saddle point height, which is $12\frac{1}{2}$ kcal/mol.

TABLE IX. Activation parameters for $O(^3P) + H_2 \rightarrow OH + H$.[a]

		T=200 K	T=1500K
ΔH (kcal/mol)	substantial	9.7	7.8
	therm	0.0	−0.1
	tun	−5.7	−0.3
total enthalpy of activation		4.0	7.4
ΔS (e.u.)	substantial	−19.6	−23.6
	therm	0.0	−0.1
	tun	−14.8	−0.1
total entropy of activation		−34.4	−23.8

[a]standard state = 1 atm.

8. Concluding Remarks

We have seen that transition state theory methods yield consistently good results when applied to gas–phase reactions. Variational methods and quantum corrections require more computational effort and more potential energy information than conventional transition state theory, but they yield much better results. We now have carried out and interpreted enough calculations to allow us to make informed decisions about which methods are required for various systems, based on a knowledge of barrier heights, vibrational frequencies, particle masses, and/or reaction–path curvature, as well as on which temperatures are of interest. Applications to larger and more complex systems are limited to a large degree by the availability of potential energy information, not by the state of the dynamical theories. The use of transition state theory to calculate reaction rates in condensed phases and at heterogeneous interfaces is just beginning, as is the understanding of extensions which may be required or useful for describing these systems, yet we are already witnessing some successful applications to these types of systems. Finally, we have tried to stress that more complicated aspects of reactions, which may be elucidated by examining variational and semiclassical tunneling corrections to conventional transition state theory, often play a large part in determining reaction rates, and must be considered when interpreting experimental results; otherwise their effects may be incorrectly attributed in the phenomenological analyses.

9. Acknowledgments

The authors are grateful to Bruce C. Garrett for long–standing and continuing collaboration on the subject of these review lectures and to the organizers of the NATO–ASI Workshop for making it possible for us to participate. This work was supported in part by the U.S. Department of Energy, Office of Basic Energy Sciences.

References

1. S. Glasstone, K. Laidler, and H. Eyring, *The Theory of Rate Processes* (McGraw–Hill, New York, 1941), pp. 10–16, (a) pp. 401–403.

2. D. G. Truhlar, W. L. Hase, and J. T. Hynes, *J. Phys. Chem.* **87**, 2664, 5523(E) (1983).

3. J. W. Moore and R. G. Pearson, *Kinetics and Mechanism*, 3rd ed. (John Wiley & Sons, New York, 1981), p. 163.

4. E. Wigner, *J. Chem. Phys.* **5**, 720 (1937).

5. J. C. Keck, *Adv. Chem. Phys.* **13**, 85 (1967).

6. B. H. Mahan, *J. Chem. Educ.* **51**, 709 (1974).

7. W. H. Miller, *J. Chem. Phys.* **61**, 1823 (1974).

8. B. C. Garrett and D. G. Truhlar, *J. Phys. Chem.* **83**, 1052 (1979), **87**, 4553(E) (1983).

9. A. D. Isaacson and D. G. Truhlar, *J. Chem. Phys.* **76**, 1380 (1982).

10. E. B. Wilson, Jr., J. C. Decius, and P. C. Cross, *Molecular Vibrations* (Dover, New York, 1980), p. 14.

11. G. Arfken, *Mathematical Methods for Physicists* (Academic Press, New York, 1970), p. 34, (a) p. 32, (b) p. 48.

12. H. Goldstein, *Classical Mechanics*, 2nd ed. (Addison–Wesley Publishing Company, Reading, MA, 1980), p. 556, (a) p. 426.

13. D. A. McQuarrie, *Statistical Mechanics* (Harper and Row, New York, 1976), §7–1.

14. J. B. Anderson, *J. Chem. Phys.* **58**, 4684 (1973).

15. D. G. Truhlar and B. C. Garrett, *Acc. Chem. Res.* **13**, 440 (1980).

16. E. Wigner, *Trans. Faraday Soc.* **34**, 29 (1938).

17. D. G. Truhlar, A. D. Isaacson, and B. C. Garrett, in *Theory of Chemical Reaction Dynamics*, edited by M. Baer (CRC Press, Boca Raton, FL, 1985), Vol. 4, p. 1.

18. M. M. Kreevoy and D. G. Truhlar, in *Investigation of Rates and Mechanisms of Reactions* (*Techniques of Chemistry*, edited by A. Weissberger, 4th ed., Vol. 6), edited by C. F. Bernasconi (John Wiley & Sons, New York, 1986), Part 1, p. 13.

19. R. E. Weston, Jr. and H. A. Schwarz, *Chemical Kinetics* (Prentice–Hall, Inc. Engelwood Cliffs, NJ, 1972), p. 100, (a) § 6.7–6.8.

20. I. Shavitt, University of Wisconsin Theoretical Chemistry Laboratory Technical Report No. WIS–AEC–23, Madison, WI, 1959.

21. R. A. Marcus, *J. Chem. Phys.* **49**, 2610 (1968).

22. D. G. Truhlar and A. Kuppermann, *J. Amer. Chem. Soc.* **93**, 1840 (1971).

23. K. Fukui, in *The World of Quantum Chemistry*, edited by R. Daudel and B. Pullman (D. Reidel, Dordrecht, Holland, 1974), p. 113.

24. H. F. Schaefer, III, *Chem. Brit.* **11**, 227 (1975).

25. D. G. Truhlar, F. B. Brown, R. Steckler, and A. D. Isaacson, in *The Theory of Chemical Reaction Dynamics*, edited by D. C. Clary (D. Reidel, Dordrecht, Holland, 1986), p. 285.

26. B. C. Garrett, M. J. Redmon, R. Steckler, D. G. Truhlar, K. K. Baldridge, D. Bartol, M. W. Schmidt, and M. S. Gordon, *J. Phys. Chem* **92**, 1476 (1988).

27. B. C. Garrett and D. G. Truhlar. *J. Amer. Chem. Soc.* **101**, 4534 (1979).

28. B. C. Garrett and D. G. Truhlar, *J. Amer. Chem. Soc.* **102**, 2559 (1980).

29. D. G. Truhlar, A. D. Isaacson, R. T. Skodje, and B. C. Garrett, *J. Phys. Chem.* **86**, 2252 (1982).

30. B. C. Garrett and D. G. Truhlar, *J. Phys. Chem.* **83**, 1079 (1979), **87**, 4553(E) (1983).

31. B. C. Garrett, D. G. Truhlar, R. S. Grev, and A. W. Magnuson, *J. Phys. Chem.* **84**, 1730 (1980), **87**, 4554(E) (1983).

32. B. C. Garrett and D. G. Truhlar, *J. Chem. Phys.* **81**, 309 (1984).

33. D. G. Truhlar and B. C. Garrett, *Annu. Rev. Phys. Chem.* **35**, 159 (1984).

34. B. C. Garrett, D. G. Truhlar, and G. C. Schatz, *J. Amer. Chem. Soc.* **108**, 2876 (1986).

35. D. G. Truhlar and B. C. Garrett, *J. Chim. Phys.* **84**, 365 (1987).

36. P. J. Robinson and K. A. Holbrook, *Unimolecular Reactions* (John Wiley & Sons, New York, 1972).

37. W. Forst, *Theory of Unimolecular Reactions* (Academic Press, New York, 1973).

38. J. Troe, in *Kinetics of Gas Reactions* (*Physical Chemistry: An Advanced Tretise*, edited by H. Eyring, D. Henderson, and W. Jost, Vol. VI B), edited by W. Jost (Academic Press, New York, 1975), p. 835.

39. C. Lim and D. G. Truhlar, *J. Phys. Chem.* **90**, 2616 (1986).

40. J. T. Hynes, in *Theory of Chemical Reaction Dynamics*, edited by M. Baer (CRC Press, Boca Raton, FL, 1985), Vol. 4, p. 171.

41. I. Mayer, *J. Chem. Phys.* **60**, 2564 (1974).

42. R. C. Tolman, *The Principles of Statistical Mechanics* (Oxford University Press, New York, 1938), §19.

43. P. Pechukas, in *Dynamics of Molecular Collisions, Part B*, edited by W. H. Miller (Plenum Press, New York, 1976), p. 239.

44. E. E. Nikitin, *Theory of Elementary Atomic and Molecular Processes in Gases* (Clarendon Press, Oxford, 1974), chap. 1.

45. I. W. M. Smith, *Kinetics and Dynamics of Elementary Gas Reactions* (Butterworths, London, 1980), §4.2.3.

46. B. C. Garrett, D. G. Truhlar, A. F. Wagner, and T. H. Dunning, Jr., *J. Chem. Phys.* **78**, 4400 (1983).

47. P. Valtzanos and K. Ruedenberg, *Theoret. Chim. Acta* **69**, 281 (1986).

48. T. Joseph, R. Steckler, and D. G. Truhlar, *J. Chem. Phys.* **87**, 7036 (1987).

49. D. G. Truhlar, *J. Chem. Phys.* **56**, 3189 (1972), **61**, 440(E) (1974).

50. A. F. Wagner, J. M. Bowman, and L. B. Harding, *J. Chem. Phys.* **82**, 1866 (1985).

51. B. C. Garrett and D. G. Truhlar, *Int. J. Quantum Chem.* **29**, 1463 (1986).

52. J. O. Hirschfelder and E. Wigner, *J. Chem. Phys.* **7**, 616 (1939).

53. M. A. Eliason and J. O. Hirschfelder, *J. Chem. Phys.* **30**, 1426 (1959).

54. L. Hofacker, *Z. Naturforsch.* **18a**, 607 (1963).

55. R. A. Marcus, *J. Chem. Phys.* **43**, 1598 (1965).

56. D. G. Truhlar, *J. Chem. Phys.* **53**, 2041 (1970).

57. W. H. Miller, *J. Chem. Phys.* **65**, 2216 (1975).

58. B. C. Garrett and D. G. Truhlar, *J. Chem. Phys.* **76**, 1853 (1982).

59. R. L. Liboff, *Introductory Quantum Mechanics* (Holden–Day, Inc. San Francisco, 1980), §7.7.

60. A. S. Davydov, *Quantum Mechanics*, translated and edited by D. ter Haar (Addison–Wesley Publishing Company, Inc., Reading, MA, 1968), §26.

61. E. Merzbacher, *Quantum Mechanics* (John Wiley & Sons, New York, 1970), chap. 7.

62. E. C. Kemble, *The Fundamental Principles of Quantum Mechanics with Elementary Applications* (Dover, New York, 1937).

63. W. H. Miller, *Faraday Discuss. Chem. Soc.* **62**, 40 (1977).

64. B. C. Garrett and D. G. Truhlar, *J. Phys. Chem.* **83**, 2921 (1979).

65. R. D. Levine and R. B. Bernstein, *Molecular Reaction Dynamics and Chemical Reactivity* (Oxford University Press, New York, 1987), p. 165.

66. M. J. Stern, A. Persky, and F. S. Klein, *J. Chem. Phys.* **58**, 5697 (1973).

67. R. A. Marcus, *J. Chem. Phys.* **45**, 4493 (1966).

68. A. Kuppermann, J. T. Adams, and D. G. Truhlar, Abstr. Pap. Int. Conf. Phys. Electron. At. Collisions, 8th, 149 (1973).

69. A. Kuppermann, in *Theory of Scattering: Papers in Honor of Henry Eyring* (*Theoretical Chemistry*, Vol. 6A, edited by D. Henderson, Academic, New York, 1981), p. 80.

70. R. A. Marcus and M. E. Coltrin, *J. Chem. Phys.* **67**, 2609 (1977).

71. R. T. Skodje, D. G. Truhlar, and B. C. Garrett, *J. Phys. Chem.* **85**, 3019 (1981).

72. W. H. Miller, N. C. Handy, and J. E. Adams, *J. Chem. Phys.* **72**, 99 (1980).

73. V. K. Babamov and R. A. Marcus, *J. Chem. Phys.* **74**, 1790 (1981).

74. D. K. Bondi, J. N. L. Connor, B. C. Garrett, and D. G. Truhlar, *J. Chem. Phys.* **78**, 5981 (1983).

75. B. C. Garrett and D. G. Truhlar, *J. Chem. Phys.* **79**, 4931 (1983).

76. B. C. Garrett, N. Abusalbi, D. J. Kouri, and D. G. Truhlar, *J. Chem. Phys.* **83**, 2252 (1985).

77. M. M. Kreevoy, D. Ostović, D. G. Truhlar, and B. C. Garrett, *J. Phys. Chem.* **90**, 3766 (1986).

78. R. Steckler, K. J. Dykema, F. B. Brown, G. C. Hancock, and D. G. Truhlar, *J. Chem. Phys.* **87**, 7024 (1987).

79. D. G. Truhlar and B. C. Garrett, *J. Phys. Chem.* **84**, 805 (1980).

80. J. C. Gray, D. G. Truhlar, L. Clemens, J. W. Duff, F. M. Chapman, Jr., G. O. Morrell, and E. F. Hayes, *J. Chem. Phys.* **69**, 240 (1978).

81. J. A. Kaye and A. Kuppermann, *Chem. Phys. Lett.* **77**, 573 (1981).

82. D. G. Truhlar, B. C. Garrett, P. G. Hipes, and A. Kuppermann, *J. Chem. Phys.* **81**, 3542 (1984).

83. G. C. Lynch, D. G. Truhlar, and B. C. Garrett, manuscript in preparation.

84. D. C. Clary, *J. Chem. Phys.* **83**, 1685 (1985).

85. B. C. Garrett and D. G. Truhlar, unpublished.

86. S. C. Tucker, G. C. Lynch, B. C. Garrett, and D. G. Truhlar, unpublished.

87. D. K. Bondi, J. N. L. Connor, J. Manz, and J. Römelt, *J. Mol. Phys.* **50**, 467 (1983).

88. F. S. Klein, A. Persky, and R. E. Weston, Jr., *J. Chem. Phys.* **41**, 1799 (1964).

89. A. Persky and F. S. Klein, *J. Chem. Phys.* **44**, 3617 (1966).

90. J. H. Lee, J. V. Michael, W. A. Payne, L. J. Stief, and D. A. Whytock, *J. Chem. Soc. Faraday Trans. I* **73**, 1530 (1977).

91. S. C. Tucker, D. G. Truhlar, B. C. Garrett, and A. D. Isaacson, *J. Chem. Phys.* **82**, 4102 (1985).

92. G. C. Schatz and H. Elgersma, *Chem. Phys. Lett.* **73**, 21 (1980).

93. A. R. Ravishankara, J. M. Nicovich, R. L. Thompson, and F. P. Tully, *J. Phys. Chem.* **85**, 2498 (1981).

94. S. P. Walch and T. H. Dunning, Jr., *J. Chem. Phys.* **72**, 1303 (1980).

95. T. H. Dunning, Jr., S. P. Walch, and A. F. Wagner, in *Potential Energy Surfaces and Dynamics Calculations*, edited by D. G. Truhlar (Plenum, New York, 1981), p. 329.

96. J. S. Shapiro and R. E. Weston, Jr., *J. Phys. Chem.* **76**, 1669 (1972).

97. R. Shaw, *J. Phys. Chem. Ref. Data* **7**, 1179 (1978).

98. W. L. Hase, *Acc. Chem. Res.* **16**, 258 (1983).

99. G. C. Hancock, P. Rejto, R. Steckler, F. B. Brown, D. W. Schwenke, and D. G. Truhlar, *J. Chem. Phys.* **85**, 4997 (1986).

100. R. T. Skodje, D. W. Schwenke, D. G. Truhlar, and B. C. Garrett, *J. Phys. Chem.* **88**, 628 (1984).

101. I. D. Clark and R. P. Wayne, in *The Theory of Kinetics* (*Comprehensive Chemical Kinetics*, Vol. 2), edited by C. H. Bamford and C. F. H. Tipper (Elsevier, Amsterdam, 1969), p. 302.

102. J. G. Lauderdale and D. G. Truhlar, *J. Chem. Phys.* **84**, 1843 (1986).

103. T. N. Truong and D. G. Truhlar, *J. Phys. Chem.* **91**, 6229 (1987).

104. T. N. Truong and D. G. Truhlar, *J. Chem Phys.* **88**, 6611 (1988).

105. G. van der Zwan and J. T. Hynes, *J. Chem. Phys.* **78**, 4714 (1983).

106. G. van der Zwan and J. T. Hynes, *Chem. Phys.* **90**, 21 (1984).

107. B. J. Gertner, J. P. Bergsma, K. R. Wilson, S. Lee, and J. T. Hynes, *J. Chem. Phys.* **86**, 1377 (1987).

108. H. A. Kramers, *Physica* (The Hague) **7**, 284 (1940).

109. R. F. Grote and J. T. Hynes, *J. Chem. Phys.* **73**, 2715 (1980).

110. S. A. Adelman and C. L. Brooks, *J. Phys. Chem.* **86**, 1511 (1982).

111. E. Pollak, *J. Chem. Phys.* **85**, 865 (1986).

112. J. M. Montgomery, Jr., D. Chandler, and B. J. Berne, *J. Chem. Phys.* **70**, 4056 (1979).

113. J. L. Skinner and P. G. Wolynes, *J. Chem. Phys.* **72**, 4913 (1980).

114. G. T. Evans, *J. Chem. Phys.* **78**, 4963 (1983).

115. K. N. Houk and N. G. Rondan, *J. Amer. Chem. Soc.* **106**, 4293 (1984).

116. C. Doubleday, J. McIver, M. Page, and T. Zielinski, *J. Amer. Chem. Soc.* **107**, 5800 (1985).

117. S. N. Rai and D. G. Truhlar, *J. Chem. Phys.* **79**, 6046 (1983).

118. S. W. Benson, *Thermochemical Kinetics*, 2nd ed. (John Wiley & Sons, New York, 1976).

119. D. G. Truhlar and B. C. Garrett, *J. Amer. Chem. Soc.*, in press.

120. B. C. Garrett, D. G. Truhlar, J. M. Bowman, A. F. Wagner, D. Robie, S. Arepalli, N. Presser, and R. J. Gordon, *J. Amer. Chem. Soc.* **108**, 3515 (1986).

Theoretical Models for Reaction Dynamics in Polyatomic Molecular Systems

William H. Miller
Department of Chemistry, University of California, and
Materials and Chemical Sciences Division, Lawrence Berkeley
Laboratory, Berkeley, California 94720 USA

ABSTRACT. The reaction path Hamiltonian based on the minimum energy reaction path is reviewed. Another reaction path Hamiltonian, this one based on a straight line path from reactants to products, is also introduced. It is argued that the latter model provides a better description of H-atom transfer reactions, a process for which the former one is poor. A variety of quantum and classical dynamical approaches based on these Hamiltonians are surveyed.

1. INTRODUCTION

One of the fundamental goals of theoretical chemistry is the quantitative description of chemical reactions from first principles ("ab initio"). One usually envisions accomplishing this in two steps, (1) determination of the (Born-Oppenheimer) potential energy surface by state-of-the-art ab initio quantum chemistry calculations, and (2) solution of the dynamical equations for nuclear motion on this potential surface. For the simplest chemical reactions A+BC → AB+C, where A, B, and C are all single atoms, this is rapidly becoming a reality: quantum chemistry calculations[1] continue to improve in accuracy, and there have recently been quite dramatic advances[2-4] in quantum mechanical reactive scattering theory that provides the rigorous solution to the nuclear dynamics. The goal of the work described in this paper, however, is to extend these capabilities to polyatomic molecular systems.

The first part of the task, i.e., determination of the potential energy surface, at first seems almost insurmountable for a polyatomic molecular system because of the high dimensionality of the problem: for an N atom system the potential (i.e., the Born-Oppenheimer electronic energy) depends on 3N-6 independent coordinates. If one were to try to map out the potential function in a straight-forward way on a grid of coordinate values, then $\sim 10^{3N-6}$ points - i.e., this many quantum chemistry calculations of the electronic energy - would be required, clearly an impossible task for N greater than 3 or 4.

To deal with this situation one introduces the idea of a

J. Bertrán and I. G. Csizmadia (eds.),
New Theoretical Concepts for Understanding Organic Reactions, 347–372.
© 1989 by Kluwer Academic Publishers.

reaction path.[5-7] Section 2 utilizes the minimum energy path (MEP), i.e., the steepest descent path (in mass-weighted cartesian coordinates) that descends from the saddle point (i.e., the transition state) of the potential energy surface forward to products and backward to reactants. It seems intuitively clear that this path, also called the "intrinsic" reaction path, passes through the most important part of the potential energy surface for the reaction through this transition state. A full-dimensional potential energy surface is obtained by computing the force constant matrix along the MEP, so that the model is that of a (multidimensional) harmonic valley about the reaction path in the many directions orthogonal to it. Section 2 describes this model more completely.

The practically important feature of this reaction path model is that the necessary quantum chemistry calculations are quite feasible by exploiting the analytic gradient methodology[8] that has been developed in recent years. One thus begins the reaction path calculation at the saddle point of the PES - whose location, in fact, is made efficient by using analytic gradient calculations - and then follows the (negative) gradient vector step-by-step down to reactants and to products. Along this steepest descent path one also computes the force constant matrix. The important point is that this is a one dimensional process; i.e., one is computing the potential energy along a one-dimensional curve that snakes its way through a 3N-6 dimensional space. The effort in doing this thus does not increase dramatically as the number of atoms in the system increases.

Section 2 describes how a complete Hamiltonian can be constructed in terms of a reaction coordinate, the distance along the MEP, and local normal coordinates for vibration perpendicular to the MEP (together with momentum variables conjugated to these coordinates). This is the reaction path Hamiltonian.[5a]

Although a reaction path Hamiltonian based on the minimum energy reaction path is often an appropriate description of the reaction of interest, there are cases for which this is not so. A most important example of this is an H-atom transfer reaction. For such reactions the minimum energy path has many sharp kinks as it passes from the transition state to the reactants and products minima; it is thus not a useful path on which to base the reaction path model. Section 3 shows how a straight line reaction path[9] is appropriate for these situations.

Finally, Section 4 considers some of the dynamical treatments that can be based on these reaction path Hamiltonians. Statistical approximations, i.e., transition state-like theories, are the simplest, and they are easily applied in terms of the reaction path Hamiltonian. Several more dynamically rigorous approaches are also described.

2. THE REACTION PATH HAMILTONIAN[5a]

If $\{x_{i\gamma}\} \equiv \underset{\sim}{x}$, $i = 1,\ldots,N$, $\gamma = x,y,z$, denote the 3N mass-weighted cartesian coordinates of the N atoms, then the steepest descent

path $\underset{\sim}{x}_0(s)$ is determined by starting at the transition state (s=0) and integrating the following equation

$$\frac{d}{ds}\,\underset{\sim}{x}(s) \equiv \underset{\sim}{x}'(s) = -\frac{\partial V(\underset{\sim}{x})}{\partial \underset{\sim}{x}} \Big/ \left|\frac{\partial V}{\partial \underset{\sim}{x}}\right|, \tag{2.1}$$

the solution of which is $\underset{\sim}{x}_0(s)$. The parameter s is the reaction coordinate, the distance along the path. (This is clear since it follows from Eq. (2.1) that

$$ds = |d\underset{\sim}{x}| = \sqrt{\sum_{i\gamma} (dx_{i\gamma})^2}, \tag{2.2}$$

which is the usual definition of arc length.)

There have recently been several papers[10] that have explored in detail the mechanics of determining minimum energy reactions paths. With the advent of analytic gradient methods[8] in <u>ab initio</u> quantum chemistry it is rapidly becoming practical to carry out these calculations for quite complex molecular systems.

For positions $\underset{\sim}{x}$ close to the reaction path one uses a standard Taylor's series expansion to approximate the potential energy

$$V(\underset{\sim}{x}) = V_0(s) + \underset{\sim}{D}(s)\cdot\left(\underset{\sim}{x}-\underset{\sim}{x}_0(s)\right) + \tfrac{1}{2}\left(\underset{\sim}{x}-\underset{\sim}{x}_0(s)\right)\cdot\underset{\approx}{K}(s)\cdot\left(\underset{\sim}{x}-\underset{\sim}{x}_0(s)\right) + \ldots \tag{2.3}$$

where

$$V_0(s) = V\left(\underset{\sim}{x}_0(s)\right) \tag{2.4a}$$

$$\underset{\sim}{D}(s) = \left(\frac{\partial V}{\partial \underset{\sim}{x}}\right)_{\underset{\sim}{x} = x_0(s)} \tag{2.4b}$$

$$\underset{\approx}{K}(s) = \left(\frac{\partial^2 V}{\partial \underset{\sim}{x}\partial \underset{\sim}{x}}\right)_{\underset{\sim}{x} = \underset{\sim}{x}_0(s)}. \tag{2.4c}$$

To define coordinates properly one must insure that the displacements $\underset{\sim}{x}-\underset{\sim}{x}_0(s)$ are perpendicular to the reaction path, and furthermore, conservation of total angular (and linear) momentum requires that they also be orthogonal to the directions which correspond to pure rotations (and translations). This is accomplished by introducing the projector $\underset{\approx}{P}(s)$ that, at position s on the reaction path, projects onto the 7 directions that corresponds to the 3 pure translations of the N atom system, the 3 pure rotations of the N atom system, and the direction along the reaction path,

$$P_{i\gamma,i'\gamma'}(s) = \sum_{k=3N-6}^{3N} L_{i\gamma,k}(s)\, L_{i'\gamma',k}(s), \qquad (2.5)$$

where $\{L_{i\gamma,k}(s)\}$ are the orthonormal vectors for these 7 directions. $k=3N-6$ is chosen to be the direction along the reaction path, so that

$$\underset{\sim}{L}_{3N-6}(s) \equiv \underset{\sim}{x}'(s); \qquad (2.6)$$

explicit formulae for the vectors $\underset{\sim}{L}_k(s)$, $k=3N-7,\ldots,3N$ for pure rotations and translations have been given.[5a]

One then diagonalizes the <u>projected force constant matrix</u>,

$$\left(\underset{\approx}{1}-\underset{\approx}{P}(s)\right)\cdot\underset{\approx}{K}(s)\cdot\left(\underset{\approx}{1}-\underset{\approx}{P}(s)\right); \qquad (2.7)$$

there are 7 zero eigenvalues, with the 7 eigenvectors given above, and 3N-7 non-zero eigenvalues, denoted $\{\omega_k(s)^2\}$, with eigenvectors $\{\underset{\sim}{L}_k(s)\}$, $k=1,\ldots,3N-7$. Displacements away from the reaction path, $\underset{\sim}{x}-\underset{\sim}{x}_0(s)$, are then expressed as

$$\underset{\sim}{x}-\underset{\sim}{x}_0(s) = \sum_{k=1}^{3N-7} \underset{\sim}{L}_k(s)Q_k, \qquad (2.8)$$

which guarantees that they are orthogonal to the reactive path and to the directions that are pure rotations and translations. The <u>normal coordinates</u> $\{Q_k\}$, $k=1,\ldots,3N-7$, are the amounts of displacement away from the reaction path in the 3N-7 independent directions that are perpendicular to it. The coordinates $(s,Q_1,\ldots,Q_{3N-7})$ are thus the 3N-6 coordinates that characterize the internal motion of the N atom system. In terms of them the potential energy of Eq. (2.3) takes the form

$$V(s,\{Q_k\}) = V_0(s) + \sum_{k=1}^{3N-7} \tfrac{1}{2}\omega_k(s)^2 Q_k^{\,2} + \ldots\,. \qquad (2.9)$$

The term $V_0(s)$ is often referred to as the <u>reaction profile</u>, i.e., the potential energy along the reaction path. The latter terms clearly have the form of a harmonic valley in displacements away from the reaction path, the frequencies of which vary with position along the path.

In terms of the original 3N mass-weighted cartesian coordinates the Hamiltonian of the N atom system is

$$H(\underset{\sim}{p},\underset{\sim}{x}) = \sum_{i\gamma} \tfrac{1}{2}p_{i\gamma}^{\;2} + V(\underset{\sim}{x}), \tag{2.10}$$

where $\{p_{i\gamma}\} = \underset{\sim}{p}$ are the momenta conjugated to $\underset{\sim}{x}$. One wishes to express H in terms of the 3N-6 reaction path coordinates $(s,\{Q_k\}, k=1,\ldots,3N-7)$ and momenta $(p_s,\{P_k\}\ k=1,\ldots,3N-7)$ conjugate to them, and also the 6 coordinates and momenta that describe pure rotations and translations. This is a tedious procedure, the details for which the reader is referred to the original paper.[5a] For the case of total angular momentum J=0 the result is

$$H(p_s,s,\underset{\sim}{P},\underset{\sim}{Q}) = \tfrac{1}{2}[p_s - \sum_{k,k'=1}^{F-1} Q_k P_{k'} B_{k,k'}(s)]^2/[1+\sum_{k=1}^{F-1} Q_k B_{k,F}(s)]^2$$

$$+ \sum_{k=1}^{F-1} \tfrac{1}{2}P_k^{\;2} + V_0(s) + \sum_{k=1}^{F-1} \tfrac{1}{2}\omega_k(s)^2 Q_k^{\;2}, \tag{2.11}$$

where $F \equiv 3N-6$ is the number of internal degrees of freedom, and the coupling functions are given in terms of the eigenvectors of the projected force constant matrix (and their derivative with respect to s)

$$B_{k,k'}(s) = \underset{\sim}{L}_k'(s)^T \cdot \underset{\sim}{L}_k(s) = \sum_{i\gamma} L_{i\gamma,k}'(s)\, L_{i\gamma,k'}(s), \tag{2.12}$$

where the prime denotes $\left(\frac{\partial}{\partial s}\right)$ and "T" transpose. $B_{k,k'}(s)$ is a skew-symmetric matrix

$$B_{k,k'}(s) = -B_{k',k}(s), \tag{2.13}$$

a consequence of which is that its diagonal elements are zero.

Eqs. (2.11)-(2.13) fully specify the reaction path Hamiltonian.[5a] If all the coupling functions were ignored, it would have the simple form of a one-dimensional Hamiltonian for motion along the reaction path,

$$\tfrac{1}{2}p_s^{\;2} + V_0(s), \tag{2.14}$$

plus a sum of harmonic oscillators for motion perpendicular to it. (The s-dependence of the frequencies $\{\omega_k(s)\}$, however, causes coupling between these motions.) The coupling functions $B_{k,k'}(s)$ are

the primary cause of coupling, i.e., energy transfer, between the various degrees of freedom. Most important among these are the curvature coupling's $B_{k,F}(s)$ that occur in the denomination of Eq. (2.11) and couple normal mode k directly to the reaction coordinate (labeled as mode F). Since

$$\underset{\sim}{L}_F(s) \equiv \underset{\sim}{L}_{3N-6}(s) = \underset{\sim}{x}'(s), \tag{2.15}$$

one can show that

$$\sum_{k=1}^{F} B_{k,F}(s)^2 = \sum_{k=1}^{F} \underset{\sim}{L}_F'(s)^T \cdot \underset{\sim}{L}_k(s)\ \underset{\sim}{L}_k(s)^T \cdot \underset{\sim}{L}_F'(s)$$

$$= \underset{\sim}{L}_F'(s)^T \cdot \underset{\sim}{L}_F'(s) = \underset{\sim}{x}''(s) \cdot \underset{\sim}{x}''(s)$$

$$\equiv \kappa(s)^2, \tag{2.16}$$

where $\kappa(s)$ is the curvature of the reaction path at position s along it. Thus $B_{k,F}(s)$ is essentially a measure of how the total curvature $\kappa(s)$ projects onto the various normal modes k, i.e., of which modes k the reaction path is "curving into" as one moves along it. The modes k for which $B_{k,F}(s)$ is large are strongly coupled to motion along the reaction path and exchange energy with it freely, and vice-versa if $B_{k,F}(s)$ is small. The values of s for which $B_{k,F}(s)$ is large also tell one where along the reaction path the energy transfer will take place.

The coupling functions $B_{k,k'}(s)$ for k and k' < F couple modes k and k' directly. As seen from the definition, Eq. (2.12), $B_{k,k'}(s)$ is the amount that the change in $\underset{\sim}{L}_k(s)$ with s projects onto $\underset{\sim}{L}_{k'}(s)$; i.e., it is a kind of coriolis-like interaction caused by the spiraling of the eigenvectors $\underset{\sim}{L}_k(s)$ about the reaction path.

The reaction path Hamiltonian of Eq. (2.11) can be generalized to deal with non-zero total angular momentum.[5a] The rotational Hamiltonian which is added to Eq. (2.11) is

$$H^J_{rot}(K,q_K) = A(s)\left[J^2-K^2\right]\cos^2 q_K + B(s)\left[J^2-K^2\right]\sin^2 q_K + C(s)K^2, \tag{2.17}$$

where A(s), B(s), and C(s) are the three rotation constants of the N-atom system at position s along the reaction path; K and q_K are the action-angle variables which characterize the internal rotation degree of freedom, and J is the (conserved) total angular momentum. There are also rotation-vibration coupling terms that are not given here.

Often it is adequate to make an "almost symmetric top" approximation to the rotational Hamiltonian. This corresponds to averaging Eq. (2.17) over the angle variable, giving

$$H^J_{rot} = \tfrac{1}{2}\big(A(s)+B(s)\big)\big(J^2-K^2\big) + C(s)K^2, \qquad (2.18)$$

so that K, as well as J, is now a conserved quantity (assuming that the rotation-vibration coupling terms are also neglected). Within this approximation Eq. (2.18) simply adds a centrifugal potential to Eq. (2.11); i.e., Eq. (2.11) is modified only by the replacement

$$V_0(s) \to V_{JK}(s) \equiv V_0(s) + \tfrac{1}{2}\big(A(s)+B(s)\big)\big(J^2-K^2\big) + C(s)K^2. \qquad (2.19)$$

This permits angular momentum effects to be accounted for (approximately) in a very simple way.

3. LINEAR REACTION PATH

For many purposes the minimum energy reaction path described in the previous Section is excellent. It has been successfully applied to a large number of reactions,[11-12] and will undoubtedly be the method of choice in the future in many situations.

There is one process, however, for which the minimum energy path is <u>not</u> a good description, namely an H-atom transfer process. This is the polyatomic version of a heavy + light-heavy mass combination,[13] e.g.,

$$C\ell + HC\ell \to C\ell H + C\ell, \qquad (3.1)$$

for which the minimum energy path is extremely sharply curved in the appropriately mass-weighted coordinates. A very curved reaction path means that the curvature coupling elements $\{B_{kF}(s)\}$ in Eq. (2.11) are very large for some modes k, and this causes singularities in the Hamiltonian because the denominator in the first term can vanish for small displacements Q_k away from the reaction path.

The situation is even more severe for a polyatomic system than it is for the simple atom-diatom system Eq. (3.1) This is because there will be <u>many</u> modes that are lower in frequency than H-atom motion, and one can prove in general that the <u>minimum energy path always approaches a potential minimum along the normal mode of lowest frequency</u> (of the appropriate symmetry).[9] For an H-atom transfer, therefore, the minimum energy path begins at the transition state being primarily H-atom motion, but abruptly switches to heavy atom motion further down the path. In general, many of these abrupt

switches (local Fermi resonances) occur, so that the minimum energy path will have many "kinks" on its journey from the transition state to the reactant (and product) potential minimum. This is clearly not a useful path on which to base the reaction dynamics.

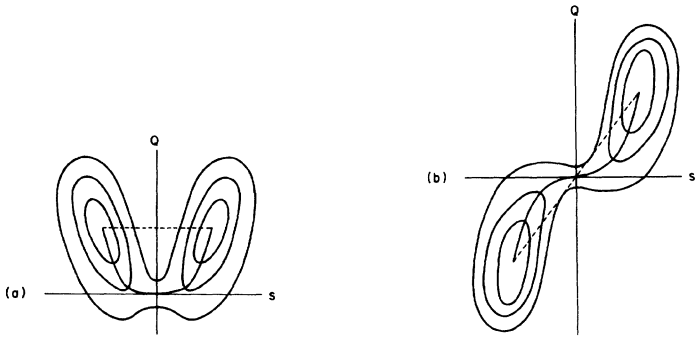

Figure 1. Sketch of contour plots for two characteristic potential energy surfaces. The solid lines indicate the minimum energy path from the transition state down to reactants and to products, and the broken line is the straight line path from reactants to products.

As an alternative a linear reference path between the reactant and product potential minima has been suggested.[9] Fig. 1 shows a sketch of two potential surfaces for a two-dimensional model of a symmetric H-atom transfer. Fig. 1a applies qualitatively to H-atom transfer in malonaldehyde

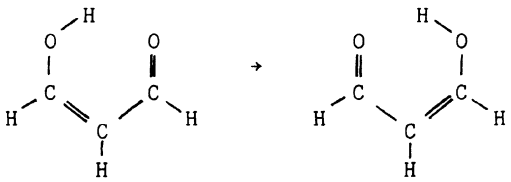

(3.2)

where the two modes are the H-atom motion (s) and the O-O stretch (Q), while Fig. 1b is illustrated by the double H-atom transfer in the formic acid dimer,

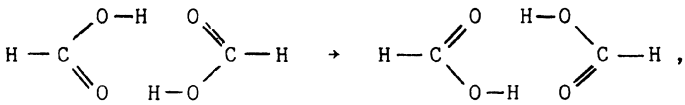

where the two relevant modes for the picture are the asymmetric H-atom motion (s) and the asymmetric O-C-O vibration (Q). In both cases the solid curves indicate the minimum energy path and the broken curve the straight line path. In the case of the Fig. 1a the straight line path misses the transition state by a large distance, but this is actually physically correct; i.e., the most important path for tunneling in this situation "cuts the corner"[14] of the potential surface. For the case in Fig. 1b the straight line path actually passes through the transition state.

The form of Hamiltonian based on this straight line reaction path is constructed in a similar way as that in Section II. The reaction, or reference path $\underset{\sim}{x}_0(s)$ is now, however, given by (again in mass-weighted cartesian coordinates)

$$\underset{\sim}{x}_0(s) = \tfrac{1}{2}(\underset{\sim}{x}_p+\underset{\sim}{x}_r) + s(\underset{\sim}{x}_p-\underset{\sim}{x}_r)/|\underset{\sim}{x}_p-\underset{\sim}{x}_r|, \tag{3.4}$$

rather than by following the minimum energy path, where $\underset{\sim}{x}_p$ and $\underset{\sim}{x}_r$ are the (mass-weighted) cartesian coordinates of the products and reactants, respectively (i.e., the geometries of these local minima on the potential energy surface). For Eq. (3.4) to apply it is necessary that the 3N cartesian coordinates $\underset{\sim}{x}_p$ and $\underset{\sim}{x}_r$ be defined in consistent coordinate systems. These conditions have been worked out and are easy to insure.[15]

The Hamiltonian for this linear reaction path is now constructed in precisely the same manner as Section II; the projected force constant matrix is diagonalized to obtain the 3N-7 non-zero frequencies $\{\omega_k(s)\}$ and corresponding eigenvectors $\{\underset{\sim}{L}_k(s)\}$, k=1,...,3N-7. The resulting Hamiltonian differs from Eq. (2.11) in only two ways. First, since the reaction path is <u>straight</u>, the curvature coupling element $B_{k,F}(s)$ are all zero. Second, since the linear path is not the minimum energy path, the linear term in the potential, Eq. (2.3), is not zero,

$$\underset{\sim}{D}(s)\cdot\left(\underset{\sim}{x}-x_0(s)\right) = -\underset{\sim}{f}(s)\cdot\underset{\sim}{Q}, \tag{3.5a}$$

$$f_k(s) = -\sum_{i\gamma} D_{i\gamma}(s)\, L_{i\gamma,k}(s). \tag{3.5b}$$

The Hamiltonian is thus given by

$$H(p_s,s,\underset{\sim}{P},\underset{\sim}{Q}) = \tfrac{1}{2}\left[p_s-\sum_{k,k'=1}^{F-1} Q_k P_{k'} B_{k,k'}(s)\right]^2 + \sum_{k=1}^{F-1} \tfrac{1}{2}P_k^{\,2} + V_0(s)$$

$$- \sum_{k=1}^{F-1} f_k(s)\, Q_k + \sum_{k=1}^{F-1} \tfrac{1}{2}\omega_k(s)^2\, Q_k^{\,2}. \qquad (3.6)$$

Finally, in this case it is also possible to eliminate the coriolis coupling elements $B_{k,k'}(s)$ in Eq. (3.6) by making a linear transformation of the coordinates $\{Q_k\}$ amongst themselves.[5b] The price paid for this is that the quadratic term in the potential involving the coordinate $\{Q_k\}$, the last term in Eq. (3.6), becomes non-diagonal. The details of this derivation are omitted here, but the final result for the Hamiltonian is[15]

$$H(p_s,s,\underset{\sim}{P},\underset{\sim}{Q}) = \tfrac{1}{2}p_s^{\,2} + \sum_{k=1}^{F-1} \tfrac{1}{2}P_k^{\,2} + V_0(s) - \sum_{k=1}^{F-1} f_k(s)\, Q_k$$

$$+ \sum_{k,k'=1}^{F-1} \tfrac{1}{2}\, Q_k Q_{k'}\, K_{k,k'}(s)\ . \qquad (3.7)$$

Here $\underset{\sim}{P}$ and $\underset{\sim}{Q}$ are actually not the same quantities as in Eq. (3.6), but related to them by a linear transformation; $\underset{\sim}{f}(s)$ and $\underset{\approx}{K}(s)$ in Eq. (3.7) are similarly related by a linear transformation to those in Eq. (3.6).

The advantage of Eq. (3.7) over (3.6) is that the coupling between modes k and k' is in the <u>potential</u> energy in Eq. (3.7) (via the $k \neq k'$ elements of $K_{k,k'}(s)$), while it occurs in the <u>kinetic</u> energy (via the $B_{k,k'}(s)$ elements) in Eq. (3.6). Eqs. (3.6) and (3.7) may thus be termed "adiabatic" and "diabatic" representations, respectively, of the vibrational modes, in analogy with the situation for vibronic Hamiltonians.[16]

4. DYNAMICAL MODELS

With a Hamiltonian one can begin to describe dynamics, and this section considers some of the dynamical models that have been based on the reaction path Hamiltonian, beginning with the simplest approaches and proceeding to more rigorous ones.

4.1. Transition State Theory and Related Models

The simplest dynamical models are statistical ones, and to define them in the most general way it is useful to introduce the microcanonical flux, i.e., the average flux for a given total energy (and, more generally, for a given total angular momentum). For the reaction path Hamiltonian of Section 2, the microcanonical flux

through a dividing surface that is perpendicular to the reaction path at distance s_0 along it is defined by

$$N(E,s_0) = \frac{2\pi\hbar}{(2\pi\hbar)^F} \int ds \int dp_s \int d\underline{P} \int d\underline{Q}\ \delta(E-H)\ \delta(s-s_0)\dot{s}h(\dot{s}) \quad (4.1)$$

where $\dot{s}$, the velocity along the reaction path, is given by Hamilton's equations

$$\dot{s} = \partial H/\partial p_s; \quad (4.2)$$

the step function $h(\dot{s})$

$$h(\dot{s}) = \begin{cases} 1 & \dot{s} > 0 \\ 0 & \dot{s} < 0 \end{cases}$$

ensures that Eq. (4.1) is the "one-way flux" through the dividing surface. With the reaction path Hamiltonian it is a straightforward calculation to show that Eq. (4.1) and (4.2) give

$$N(E,s) = [E-V_0(s)]^{F-1}/\{(F-1)! \prod_{k=1}^{F-1} \omega_k(s)\} \quad (4.3)$$

where s_0 has now been replaced simply by s. Remarkably, therefore, none of the coupling functions $B_{k,k'}(s)$ appear in the microcanonical flux; they have not been neglected in the calculation, they simply do not appear in the final result. (If the minimum energy path is not the reference path for the reaction path Hamiltonian, as for the linear reference path considered in the latter path of Section 3, then Eq. (4.3) is modified by the replacement

$$V_0(s) \to V_0(s) - \sum_{k=1}^{F-1} \frac{f_k(s)^2}{2\omega_k(s)^2}, \quad (4.4)$$

where $\{f_k(s)\}$ are the coefficients of the terms in the potential energy that are linear in the coordinates $\{Q_k\}$.)

Transition state theory corresponds to looking for the minimum (with respect to s) flux,[17] the main bottleneck to the reaction,

$$N_{TST}(E) = \min_{s} N(E,s) \tag{4.5}$$

The microcanonical rate constant, for example, is given in terms of N(E), the cumulative reaction probability - which is approximated in transition state theory by the minimum of the microcanonical flux - by

$$k(E) = N(E)/[2\pi\hbar\rho(E)], \tag{4.6a}$$

where $\rho(E)$ is the density of reactant states

$$\rho(E) = (2\pi\hbar)^{-F} \int ds \int dp_s \int d\underset{\sim}{P} \int d\underset{\sim}{Q}\ \delta(E-H). \tag{4.6b}$$

A calculation similar to that which leads to Eq. (4.3) gives $\rho(E)$ as

$$\rho(E) = (2\pi\hbar)^{-1}\left(\sqrt{2\pi}/\Gamma(F-\tfrac{1}{2})\right) \int ds\ [E-V_0(s)]^{F-3/2} / \prod_{k=1}^{F-1} \hbar\omega_k(s), \tag{4.7}$$

where the limits of the s integration are the classical turning points (the roots of $V_0(s) = E$).

The canonical, i.e., thermally averaged rate constant, is given by the ratio of the Boltzmann averages of N(E) and $\rho(E)$,

$$k(T) = \overline{N}(T)/2\pi\hbar Q_0(T), \tag{4.8}$$

where

$$\overline{N}(T) = \int^{\infty} dE\ \exp(-E/kT)N(E) \tag{4.9a}$$

$$Q_0(T) = \int^{\infty} dE\ \exp(-E/kT)\ \rho(E); \tag{4.9b}$$

$Q_0(T)$, of course, is the reactant partition function. From Eq. (4.7) one can obtain the following expressing for $Q_0(T)$,

$$Q_0(T) = \left(\frac{kT}{2\pi\hbar^2}\right)^{1/2} \int_{-\infty}^{\infty} ds \, \exp(-V_0(s)/kT) \prod_{k=1}^{F-1} \frac{kT}{\hbar\omega_k(s)}. \qquad (4.10)$$

A useful, though somewhat less rigorous result can be obtained by computing $\overline{N}(T,s)$, i.e., the Boltzmann average of $N(E,s)$, Eq. (4.1) - (4.3), before one minimizes this quantity with respect to s, and then minimizing $\overline{N}(T,s)$ with respect to s. The Boltzmann average of Eq. (4.3) can be evaluated explicitly, giving

$$\overline{N}(T,s) = kT \exp\left(-\beta V_0(s)\right) \prod_{k=1}^{F-1} \frac{kT}{\hbar\omega_k(s)}, \qquad (4.11)$$

where s is now chosen to be the value which minimizes $\overline{N}(T,s)$. This result, combined with Eq. (4.8), gives the well-known Eyring version of transition state theory

$$k(T) = \frac{kT}{h} \frac{Q^{\ddagger}(T)}{Q_0(T)} \exp(-V^{\ddagger}/kT), \qquad (4.12)$$

where

$$V^{\ddagger} = V_0(s)$$

$$Q^{\ddagger}(T) = \prod_{k=1}^{F-1} \frac{kT}{\hbar\omega(s)},$$

s being chosen as the value which minimizes the rate.

If there are several local minima of $N(E,s)$ as a function of s, then this corresponds to several "bottlenecks" of the reactive flux. If one assumes that microcanonical equilibrium is established locally in the regions between these bottlenecks - e.g., by the existence of long-lived intermediates - then one can derive a "unified" statistical model.[18,5b] This model approximates the cumulative reaction probability as

$$N(E) = \left[\sum_{k=1,3\ldots}^{2M+1} \frac{1}{N_k(E)} - \sum_{k=2,4\ldots}^{2M} \frac{1}{N_k(E)} \right]^{-1} \qquad (4.13)$$

where for k=1,3,5,..., 2M+1, $\{N_k(E)\}$ are the local minima of $N(E,s)$,

and for k=2,4,..., 2M they are the local maxima separating the local minima.

To apply these statistical theories one thus only needs the potential energy along the reaction path $V_0(s)$ and the frequencies $\{\omega_k(s)\}$ of the transverse modes. To locate the extrema of the flux $N(E,s)$ as a function of s one can show[5b] that the equation

$$\partial N(E,s)/\partial s = 0 \tag{4.14}$$

is equivalent to the following one

$$E = W(s) \tag{4.15a}$$

which involves the energy-independent function

$$W(s) = V_0(s) - V_0'(s)(F-1)/\sum_{k=1}^{F-1} \frac{\omega_k'(s)}{\omega_k(s)}. \tag{4.15b}$$

To find the various extrema of the microcanonical flux one thus needs only to plot the function W(s) and look to see where it is equal to the energy E. This is a simple way to see how the reaction "mechanism" changes with energy. Typically, for example, at low energy E there is only one bottleneck, i.e., one minimum in the flux, so that ordinary transition state theory is a good approximation, while at higher energies there may be several minima. This latter situation is a herald, even within this statistical description, of more complex dynamics, i.e., "recrossing trajectories", which cause the breakdown of simple transition state theory.[17]

4.2 Semiclassical Perturbation-Infinite Order Sudden Approximation

Going beyond statistical approximations to more dynamically based treatments opens the door to a wide variety of possibilities, from simple approximate models to more accurate treatments that are capable (with sufficient effort) of arbitrary accuracy. Here I note one particularly simple approximate model that has been developed and applied to a variety of different dynamical phenomena, namely the semiclassical perturbation-infinite order sudden (SCP-IOS) model.[19]

The SCP-IOS model is the semiclassical approximation of Miller and Smith[20] applied to the reaction-path Hamiltonian. It has the appealing feature that it behaves qualitatively correctly both in the adiabatic limit, which is the situation if the transverse vibrational motion is much faster than motion along the reaction coordinate, and also in the sudden limit, which is the case if reaction-coordinate

motion is much faster than transverse vibrational motion. For the case of a collinear atom-diatom reaction it becomes the Hofacker-Levine model.[21]

To illustrate how simple it is to apply, e.g., the probability of the vibrational transition $(n_1,\ldots,n_{F-1}) \to (n'_1,\ldots,n'_{F-1})$ in the transverse vibrational modes during motion from s_1 to s_2 along the reaction path is given by

$$P_{\underset{\sim}{n}_2 \leftarrow \underset{\sim}{n}_1}(E) = \sum_{k=1}^{F-1} |J_{\Delta n_k}(\gamma_k)|^2 \tag{4.16a}$$

where $J_{\Delta n_k}$ is the regular Bessel function of order Δn_k, and the "collision integrals" γ_k are given by

$$\gamma_k = \left| \int_{s_1}^{s_2} ds\, B_{k,F}(s)\, \{2[E-V_n(s)]\}^{1/2} [(2n_k+1)/\omega_k(s)]^{1/2}\, e^{i\delta_k(s)} \right|$$

with

$$V_{\underset{\sim}{n}}(s) = V_0(s) + \sum_{k=1}^{F-1} (n_k+\tfrac{1}{2})\, \omega_k(s)$$

$$\delta_k(s) = \int_{s_1}^{s} ds'\, \omega_k(s')/\{2[E-V_{\underset{\sim}{n}}(s')]\}^{1/2}$$

$$\underset{\sim}{n} = \tfrac{1}{2}(\underset{\sim}{n}_1+\underset{\sim}{n}_2). \tag{4.16b}$$

The collision integral γ_k is a measure of how much vibrational excitation is induced in mode k during motion from s_1 to s_2: the Bessel function $J_{\Delta n_k}(\gamma_k)^2$ has its maximum at $\Delta n_k = \gamma_k$, so that γ_k is the most probable vibrational quantum number change. A typical application of this expression would be to predict the product state distribution of an exothermic chemical reaction: with $\underset{\sim}{n}_1 = 0$, $s_1 = 0$, and $s_2 = \infty$, Eq. (4.16) gives the distribution of product internal degrees of freedom. Clearly the modes with the larger coupling element $B_{k,F}$ will be the ones excited most during motion from the transition state ($s_1 = 0$) to products ($s_2 = \infty$). Conversely, $s_1 = -\infty$ and $s_2 = 0$ and $\underset{\sim}{n}_2 = 0$ corresponds to the time-reversed situation. In this case the modes k for which γ_k is large are the most effective promoting modes for the reaction; i.e., vibrational energy initially in such a mode will be converted with high probability into energy along the reaction coordinate at the transition state.

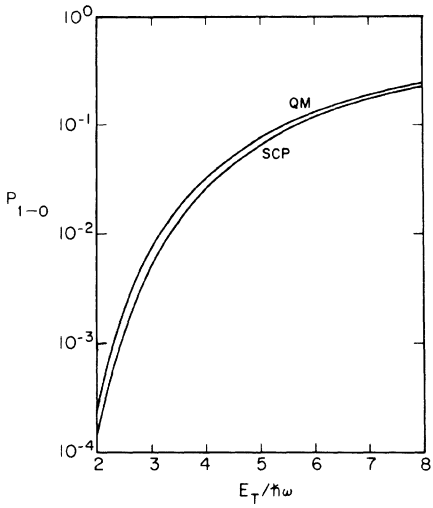

Figure 2. Transition probability for the 0 → 1 vibrational excitation of H_2 by collision with He, as a function of total energy. H_2 is modeled as a Morse oscillator. QM and SCP denote the essentially exact quantum mechanical results computed for this collinear system, and the present results of the SCP-IOS reaction path model.

Fig. 2 shows an example of the SCP-IOS model, i.e., Eq. (4.16), applied to vibrational excitation of H_2 by collision with He atoms.[19] One sees that this simple dynamical model based on the reaction path Hamiltonian does an extremely good job of describing vibrational inelasticity.

The SCP-IOS approximation has also been used to describe the effects of the curvature coupling elements on tunneling probabilities in chemical reactions. For example, the probability of tunneling through a simple barrier is given within the SCP-IOS model by

$$P = P_0 \prod_{k=1}^{F-1} I_0(\theta_k)^2 \tag{4.17a}$$

where

$$P_0 = e^{-2\theta_0} \tag{4.17b}$$

$$\theta_0 = \int ds \sqrt{2[V_{eff}(s)-E} \tag{4.17c}$$

$$\theta_k = \int ds \sqrt{2[V_{eff}(s)-E}\ \frac{B_{k,F}(s)}{\sqrt{\omega_k(s)}}\ \cosh\delta_k(s). \qquad (4.17d)$$

P_0 is the usual one-dimensional WKB tunneling probability, and the effect of curvature coupling is contained in the multiplicative factors $I_0(\theta_k)^2$, one for each mode k. I_0 is the Bessel function of imaginary argument which is an exponentially increasing function; i.e.,

$$I_0(0)^2 = 1$$

$$I_0(\theta_k)^2 \sim e^{2\theta_k}/(2\pi\theta_k) \qquad (4.18)$$

for $\theta_k >> 0$. Curvature coupling thus <u>increases</u> the tunneling probability.

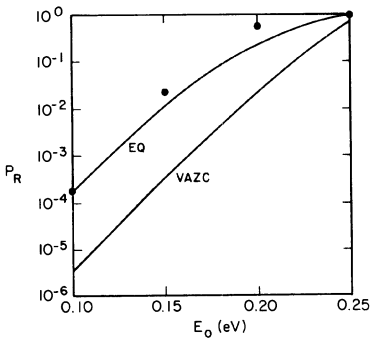

Figure 3. Reaction probability for collinear $H+H_2 \rightarrow H_2+H$ on the Porter-Karplus potential energy surface. EQ denotes the exact quantum mechanical values, VAZC the results of the vibrationally adiabatic zero curvature approximation, and the points the results of the present SCP-IOS reaction path model.

For the well-studied test case, the collinear $H+H_2$ reaction, for example, Fig. 3 shows the reaction probability as a function of initial translational energy.[5c] One sees that P_0 (i.e., VAZC) is a factor of ~50-100 too small, but the SCP-IOS model, i.e., Eq. (4.17), brings it to within a factor of 2 of the correct value.

The SCP-IOS model has also been used to determine the degree of mode specificity in state-selected unimolecular decomposition.[22,23]

If there were no coupling between the various modes of the polyatomic system, then the unimolecular decomposition would clearly be mode specific: i.e., different initial states with essentially the same total energy would decay at different rates because they would have various amount of energy in the reaction coordinate and there would be no energy transfer among the various degrees of freedom. Conversely, to the extent that coupling between the modes causes efficient energy transfer among them, one expects more statistical behavior, i.e., the rate of decomposition depending essentially only on the total energy of the initial state and not on the particular initial state that is prepared. The degree of mode specificity in the state-specific unimolecular decay rates is thus a sensitive measure of the intermode coupling and thus a direct test of the way that the SCP-IOS, or any other model, is able to describe this.

4.3 Dynamical Methods for 'System' Coupled to a Harmonic 'Bath'

The Hamiltonian that results with the linear reaction path described in Section 3, namely that given by Eq. (3.7), is sufficiently simple that it lends itself to special dynamical treatments. It has the generic form

$$H = H_{sys} + H_{bath} + H_{coupling}, \tag{4.19a}$$

where H_{sys} is the Hamiltonian for the "system" of interest, i.e., the reaction coordinate,

$$H_{sys} = \tfrac{1}{2}p_s^{\,2} + V_0(s), \tag{4.19b}$$

H_{bath} is the Hamiltonian of a harmonic "bath" that is of less interest,

$$H_{bath} = \sum_{k=1}^{F-1} \left(\tfrac{1}{2}P_k^{\,2}+\tfrac{1}{2}\omega_k^{\,2}Q_k^{\,2}\right), \tag{4.19c}$$

where the force constant matrix has here been assumed to be independent of the reaction coordinate, and $H_{coupling}$ is the term that couples the system and bath,

$$H_{coupling} = -\sum_{k=1}^{F-1} f_k(s)Q_k. \tag{4.19d}$$

All strategies for dealing with such Hamiltonians involve trying to eliminate the bath to as large an extent as possible and concentrate

attention on the system, while not altogether neglecting the effect of the bath on the system.

At the level of classical mechanics, for example, it is possible to solve the equations of motion for the bath exactly and obtain the following generalized Langevin equation[24] for the system,

$$\ddot{s}(t) = - V_0'(s(t))$$

$$+ \sum_{k=1}^{F-1} f_k'(s(t))[Q_k(0)\cos(\omega_k t)+P_k(0)\sin(\omega_k t)/\omega_k]$$

$$+ \sum_{k=1}^{F-1} f_k'(s(t)) \int_0^t dt' f_k(s(t'))\sin(\omega_k(t-t'))/\omega_k, \qquad (4.20)$$

where the first term is the force originating from the local potential $V_0(s)$, the second term is the so-called "random force" that involves the initial conditions of the bath degrees of freedom, and the third term is the non-local "friction" on the reaction coordinate. Eq. (4.20) is dynamically exact, i.e., one has "eliminated" the bath and obtained a one-dimensional equation of motion for the system alone (albeit a complicated equation because it includes the effect of the bath on the system).

To carry out an analogous procedure in quantum mechanics requires use of the Feynman path integral[25] version of quantum mechanics. I will mention here only schematically how this is done. The path integral is an expression for the kernel of the time evolution operator

$$\langle s_2 \underset{\sim}{Q}_2 | e^{-iH(t_2-t_1)/\hbar} | s_1 \underset{\sim}{Q}_1 \rangle = \int_{s_1}^{s_2} Ds(t)\, e^{i\phi[s(t),\underset{\sim}{Q}(t)]}. \qquad (4.21)$$

The integration symbols in Eq. (4.21) indicate a functional integral over all paths $s(t)$ and $\underset{\sim}{Q}(t)$ with the boundary conditions $s(t_1) = s_1$, $s(t_2) = s_2$, $\underset{\sim}{Q}(t_1) = \underset{\sim}{Q}_1$, and $\underset{\sim}{Q}(t_2) = \underset{\sim}{Q}_2$, respectively. $\phi[s,\underset{\sim}{Q}]$ is the classical action functional for a path $s(t),\underset{\sim}{Q}(t)$. Because the Hamiltonian has the simple form of Eq. (4.19), the action functional has the analogous form

$$\phi[s(t),\underset{\sim}{Q}(t)] = \phi_{sys}[s(t)]+\phi_{bath}[\underset{\sim}{Q}(t)]+\phi_{coupling}[s(t),\underset{\sim}{Q}(t)]. \qquad (4.22)$$

Furthermore, because the Schrödinger equation for the time-dependent forced harmonic oscillator is analytically solvable, one can evaluate

the $\int D\underset{\sim}{Q}$ path integral analytically, so that Eq. (4.21) takes the form

$$\langle s_2\underset{\sim}{Q}_2|e^{-iH(t_2-t_1)/\hbar}|s_1\underset{\sim}{Q}_1\rangle = \int_{s_1}^{s_2} Ds(t)e^{i\phi_{sys}[s(t)]} K_{s_2\underset{\sim}{Q}_2,s_1\underset{\sim}{Q}_1}[s(t)], \tag{4.23a}$$

where the influence functional K,

$$K_{s_2\underset{\sim}{Q}_2,s_1\underset{\sim}{Q}_1}[s(t)] \equiv \int_{\underset{\sim}{Q}_1}^{\underset{\sim}{Q}_2} D\underset{\sim}{Q}(t)e^{i\phi_{bath}[\underset{\sim}{Q}(t)]} e^{i\phi_{coupling}[s(t),\underset{\sim}{Q}(t)]}, \tag{4.23b}$$

is a known[25] exactly calculable functional of the path s(t). Eq. (4.23a) is thus a path integral for only one degree of freedom - analogous to Eq. (4.20), the classical equation of motion for only one degree of freedom - though it is a complicated one-dimensional quantum mechanical problem because it includes the effects of the bath on the system (through the influence functional K).

There is currently a great deal of effort being expended (and progress being made!) in learning how to carry out quantum calculations using path integral methods.[26-28] As has been indicated, this progress is all very relevant to the linear reaction path model described in Section 3. Using path integrals, for example, allows one to evaluate the flux-flux autocorrelation function[29a] $C_f(t)$,

$$C_f(t) = \mathrm{tr}\{F\ \exp[-(\beta/2-it/\hbar)H]F\ \exp[-(\beta/2+it/\hbar)H]\} \tag{4.24a}$$

where F is the "flux-through-a-surface" operator; the Boltzmann rate constant is given (<u>exactly!</u>) by the integral of this correlation function,

$$k(T) = Q_0(T)^{-1} \int_0^\infty dt\ C_f(t), \tag{4.24b}$$

$Q_0(T)$ being the reactant partition function. Several applications using this methodology to compute thermal rate constants have been reported, some for simple A+BC gas phase reactions and some for diffusion of H atoms on solid surfaces.[29b,c,d,e]

Other, less rigorous theoretical treatments can also be usefully applied to the system-bath Hamiltonian of Eq. (4.19). One of the most useful of these is the time-dependent self consistent field

(TDSCF) approximation.[30-34] Here the time dependent wave function is written as a product of factors ("orbitals"), one for each degree of freedom,

$$\psi(s,\underset{\sim}{Q},t) = \chi(s,t) \prod_{k=1}^{F-1} \phi_k(Q_k,t). \tag{4.25}$$

Substituting this ansatz for the wavefunction into the time-dependent Schrödinger equation leads to equations for the bath orbitals $\phi_k(Q_k,t)$ that can be solved exactly, and to the following one-dimensional Schrödinger equation for the system orbital,[34]

$$i\hbar \frac{\partial\chi(s,t)}{\partial t} = \{H_{sys} - \sum_{k=1}^{F-1} f_k(s)[\bar{Q}_k\cos(\omega_k t) + \bar{P}_k\sin(\omega_k t)/\omega_k]$$

$$- \sum_{k=1}^{F-1} f_k(s) \int_0^t dt'\bar{f}_k(t')\sin\big(\omega_k(t-t')\big)/\omega_k\}\chi(s,t), \tag{4.26}$$

where

$$\bar{Q}_k = \langle\phi_k(0)|Q_k|\phi_k(0)\rangle \tag{4.27a}$$

$$\bar{P}_k = \langle\phi_k(0)|P_k|\phi_k(0)\rangle \tag{4.27b}$$

$$\bar{f}(t) = \langle\chi(t)|f_k|\chi(t)\rangle. \tag{4.27c}$$

One recognizes Eq. (4.26), the one-dimensional Schrödinger equation for the system orbital $\chi(s,t)$, to be directly analogous to the classical equation of motion, Eq. (4.20); in Eq. (4.27) $\bar{Q}_k$ and $\bar{P}_k$ are the expectation values of the coordinate and momentum operators with the initial orbital for mode k, $\phi_k(Q_k,0)$, and $\bar{f}(t)$ is the expectation value of the operator $f_k(s)$ with the system orbital $\chi(s,t)$. Note that Eq. (4.26) is a <u>non-linear</u> Schrödinger equation because the function $\chi(s,t)$ appears in the definition of $\bar{f}(t')$; Eq. (4.26) would thus have to be solved iteratively.

An even better approximation is the <u>multiconfiguration</u> TDSCF approach[34] which expands the wavefunction as <u>sums</u> of products of the type in Eq. (4.25). This is particularly necessary if the wavefunction is composed of physically distinct parts as, for example, for the case a (multidimensional) double well potential function characteristic of an <u>isomerization</u> reaction.

Another very useful way of treating the system-bath Hamiltonian of Eq. (4.19) is via a basis set of shifted oscillator wave-functions.[35] This has been seen to give an excellent description of coupling effects on double well isomerization reactions. The reader is referred to the original papers for the specifics of this approach.

5. CONCLUDING REMARKS

Use of a reaction path, either the minimum energy path or the linear path, with a local harmonic approximation to the potential energy about it allows one to overcome the intimidating problem of dealing with a potential energy surface in 3N-6 dimensional space. The minimum energy path will be useful for describing many, but not all reactions. It is not useful, for example, for H-atom transfer reactions, but the linear reaction path described in Section 3 should treat these processes quite well.

With either of these model Hamiltonians there may be cases when the local harmonic approximation to modes away from the reaction path may fail. If this happens for only a few of the modes then one can readily correct the situation simply by including higher order terms (i.e., cubic, quartic, etc.) in the potential in these few coordinates.

A variety of dynamical approaches are available for determining the reaction dynamics that result from these Hamiltonians. Section 4 has surveyed some of these, concentrating primarily on quantum mechanical methods. Classical trajectory methods are also always possible, and for other than H-atom transfer reactions should be adequate for most phenomena. The trajectories may be determined by "integrating out" the harmonic bath, i.e., Eq. (4.20), or probably simpler by integrating the trajectories in the full $F \equiv 3N-6$ dimensional space.

These two types of reaction path Hamiltonians, and a large array of dynamical tools should allow one to carry out realistic calculations to model a variety of dynamical processes in polyatomic systems.

ACKNOWLEDGMENT

This research was supported by the Director, Office of Energy Research, Office of Basic Energy Sciences, Chemical Sciences Division of the U.S. Department of Energy, under Contract Number DE-AC03-76SF00098. The calculations were performed on the Berkeley Theoretical Chemistry computing facility, supported by National Science Foundation grant CHE84-16345.

REFERENCES

1. See, for example,
   (a) W. J. Hehre, L. Radom, P. v.R. Schleyer, and J. A. Pople, Ab Initio Molecular Orbital Theory, Wiley, N.Y., 1986.
   (b) H. F. Schaefer, The Electronic Structure of Atoms and Molecules, Addison-Wesley, Reading, MA, 1972.
2. (a) J. Z. H. Zhang and W. H. Miller, Chem. Phys. Lett. **140**, 329 (1987).
   (b) J. Chem. Phys. **88**, 4549 (1988).
   (c) J. Z. H. Zhang, S. I. Chu, and W. H. Miller, J. Chem. Phys. **88**, 6233 (1988).
3. (a) K. Haug, D. W. Schwenke, Y. Shima, D. G. Truhlar, J. Z. H. Zhang, and D. J. Kouri, J. Phys. Chem. **90**, 6757 (1986).
   (b) D. W. Schwenke, K. Haug, D. G. Truhlar, Y. Sun, J. Z. H. Zhang, and D. J. Kouri, J. Phys. Chem. **91**, 6080 (1987).
4. For a review, see G. C. Schatz, Ann. Rev. Phys. Chem. **39**, 0000 (1988).
5. (a) W. H. Miller, N. C. Handy, and J. E. Adams, J. Chem. Phys. **72**, 99 (1980).
   (b) W. H. Miller, in Potential Energy Surfaces and Dynamics Calculations, edited by D. G. Truhlar, Plenum, New York, 1981, p. 265.
   (c) C. J. Cerjan, S.-h. Shi, and W. H. Miller, J. Phys. Chem. **86**, 2244 (1982).
   (d) W. H. Miller, J. Phys. Chem. **87**, 3811 (1983).
6. For early work on reaction paths and reaction coordinates, see
   (a) S. Glasstone, K. J. Laidler, and H. Eyring, The Theory of Rate Processes, McGraw-Hill, New York, 1941.
   (b) R. A. Marcus, J. Chem. Phys. **45**, 4493, 4500 (1966); **49**, 2610 (1968).
   (c) G. L. Hofacker, Z. Naturforsch. Teil A **18**, 607 (1963); J. Chem. Phys. **43**, 208 (1965).
   (d) S. F. Fischer, G. L. Hofacker, and R. Seiler, J. Chem. Phys. **51**, 3941 (1969).
7. Some of the recent papers by other workers on reaction path models are
   (a) S. F. Fischer and M. A. Ratner, J. Chem. Phys. **57**, 2769 (1972).
   (b) P. Russegger and J. Brickman, ibid. **62**, 1086 (1975); **60**, 1 (1977).
   (c) M. V. Basilevsky, Chem. Phys. **24**, 81 (1977); **67**, 337 (1982); M. V. Bailevsky and A. G. Shamov, ibid. **60**, 349 (1981).
   (d) K. Fukui, S. Kato, and H. Fujimoto, J. Am. Chem. Soc. **97**, 1 (1975); K. Yamashita, T. Yamabe, and K. Fukui, Chem. Phys. Lett. **84**, 123 (1981); A. K. Fukui, Acc. Chem. Res. **14**, 363 (1981).
   (e) K. Ishida, K. Morokuma, and A. Komornicki, J. Chem. Phys. **66**, 2153 (1977).

(f) A. Nauts and X. Chapuisat, Chem. Phys. Lett. **85**, 212 (1982); X. Chapuisat, A. Nauts, and G. Durrand, Chem. Phys. **56**, 91 (1981).
(g) J. Pancir, Collect. Czech. Commun. **40**, 1112 (1975); **42**, 16 (1977).
(h) G. A. Natanson, Mol. Phys. **46**, 481 (1982).

8. (a) P. Pulay, in Applications of Electronic Structure, edited by H. F. Schaefer, Plenum, New York, 1977, p. 153.
(b) J. W. McIver, Jr. and A. Komornicki, J. Am. Chem. Soc. **94**, 2625 (1972).
(c) B. R. Brooks, W. E. Laidig, P. Saxe, J. D. Goddard, Y. Yamaguchi, and H. F. Schaefer, J. Chem. Phys. **72**, 4652 (1980).
(d) J. A. Pople, R. Krishnan, H. B. Schlegel, J. S. Binkley, Int. J. Quant. Chem. Symp. **13**, 225 (1970)
(e) Y. Osamura, Y. Yamaguchi, P. Saxe, M. A. Vincent, J. F. Gaw, and H. F. Schaefer, Chem. Phys. **72**, 131, (1982); Y. Yamaguchi, Y. Osamura, G. Fitzgerald, H. F. Schaefer, J. Chem. Phys. **78**, 1607 (1983).
(f) P. Pulay, ibid. **78**, 5043 (1983).

9. B. A. Ruf and W. H. Miller, Faraday Disc. Chem. Soc., in press (1988).

10. (a) M. Page and J. W. McIver, Jr., J. Chem. Phys. **88**, 922 (1988).
(b) T. H. Dunning, Jr., and L. Harding, Faraday Disc. Chem. Soc., in press (1988).
(c) B. C. Garrett, M. J. Redmon, R. Steckler, D. G. Truhlar, K. K. Baldridge, D. Bartol, M. W. Schmidt, and M. S. Gordon, J. Phys. Chem. **92**, 1476 (1988).

11. (a) S. K. Gray, W. H. Miller, Y. Yamaguchi, and H. F. Schaefer, J. Chem. Phys. **73**, 2733 (1980).
(b) S. K. Gray, W. H. Miller, Y. Yamaguchi, and H. F. Schaefer, J. Am. Chem. Soc. **103**, 1900 (1981).
(c) Y. Osamura, H. F. Schaefer, S. K. Gray, and W. H. Miller, J. Am. Chem. Soc. **103**, 1904 (1981).
(d) B. A. Waite, S. K. Gray, and W. H. Miller, J. Chem. Phys. **78**, 259 (1983).

12. See also,
(a) R. T. Skodje, D. G. Truhlar, and B. C. Garrett, J. Phys. Chem. **85**, 3019 (1981).
(b) R. T. Skodje, D. G. Truhlar, and B. C. Garrett, J. Chem. Phys. **77**, 5955 (1982).
(c) A. D. Isaacson and D. G. Truhlar, ibid. **76**, 1380 (1982).
(d) D. G. Truhlar, N. J. Kilpatrick, and B. C. Garrett, ibid. **78**, 2438 (1983).
(e) R. T. Skodje and D. G. Truhlar, ibid. **79**, 4882 (1983).
(f) R. T. Skodje, D. W. Schwenke, D. G. Truhlar, and B. C. Garrett, J. Phys. Chem. **88**, 628 (1984).
(g) B. C. Garrett and D. G. Truhlar, J. Chem. Phys. **81**, 309 (1984).

13. See, for example
(a) J. Manz and J. Römelt, Chem. Phys. Lett. **81**, 179 (1981).
(b) J. A. Kaye and A. Kuppermann, ibid. **77**, 573 (1981); **78**, 546 (1981).
(c) V. K. Babamov and R. A. Marcus, J. Chem. Phys. **74**, 1790 (1981).
(d) C. Hiller, J. Manz, W. H. Miller, and J. Römelt, ibid. **78**, 3850 (1983).
(e) B. C. Garrett, D. G. Truhlar, A. F. Wagner, and T. H. Dunning, Jr., ibid. **45**, 120 (1973).
14. See, for example, T. F. George and W. H. Miller, J. Chem. Phys. **56**, 5722 (1972); **57**, 2458 (1972).
15. Y. T. Chang, B. A. Ruf, and W. H. Miller, J. Chem. Phys., to be published.
16. See, for example, F. T. Smith, Phys. Rev. **179**, 111 (1969).
17. For an excellent review and recent developments see
(a) P. Pechukas, in 'Dynamics of Molecular Collisions' Part B, Vol. 2 of Modern Theoretical Chemistry, edited by W. H. Miller, Plenum, New York, 1976, p. 285 et seq.; Annu. Rev. Phys. Chem. **32**, 159 (1981).
(b) D. G. Truhlar, W. L. Hase, and J. T. Hynes, J. Phys. Chem. **87**, 2664 (1983).
18. W. H. Miller, J. Chem. Phys. **65**, 2216 (1976).
19. W. H. Miller and S.-h. Shi, J. Chem. Phys. **75**, 2258 (1981).
20. (a) W. H. Miller and F. T. Smith, Phys. Rev. A **17** 939 (1978).
See also related works by:
(b) R. J. Cross, Jr., J. Chem. Phys. **49**, 1753 (1968); **58**, 5178 (1973).
(c) I. L. Beigman, L. A. Vainshtein, I. I. Sobel'man, Zh. Eksp. Teor. Fiz. **57**, 1465 (1969) (Sov. Phys.--JETP (Engl. Transl.) **30**, 920 (1973).
(d) R. D. Levine and B. R. Johnson, Chem. Phys. Lett. **7**, 404 (1970).
(e) I. C. Percival and D. Richards, J. Phys. B **3**, 1035 (1970).
(f) A. P. Clark, A. S. Dickinson, and D. Richards, Adv. Chem. Phys. **36**, 63 (1977).
21. G. L. Hofacker and R. D. Levine, Chem. Phys. Lett. **9**, 617 (1971).
22. B. A. Waite and W. H. Miller, J. Chem. Phys. **76**, 2412 (1982).
23. W. H. Miller, Chem. Rev. **87**, 19 (1987).
24. See, for example, S. A. Adelman and J. D. Doll, J. Chem. Phys. **61**, 4242 (1974).
25. R. P. Feynman and A. R. Hibbs, Quantum Mechanics and Path Integrals, McGraw-Hill, New York, 1965.
26. For a review, see B. J. Berne and D. Thirumalai, Ann. Rev. Phys. Chem. **37**, 401 (1986).
27. (a) J. D. Doll, J. Chem. Phys. **81**, 3536 (1984).
(b) R. D. Coalson, D. L. Freeman, and J. D. Doll, ibid. **85**, 4567 (1986).
(c) J. D. Doll and D. L. Freeman, Science **234**, 1356 (1986).
28. (a) J. Chang and W. H. Miller, J. Chem. Phys. **87**, 1648 (1987).

(b) N. Makri and W. H. Miller, Chem. Phys. Lett. **139**, 10 (1987).
29. (a) W. H. Miller, S. D. Schwartz, and J. W. Tromp, J. Chem. Phys. **79**, 4889 (1983).
(b) R. Jaquet and W. H. Miller, J. Phys. Chem. **89**, 2139 (1985).
(c) Y. Yamashita and W. H. Miller, J. Chem. Phys. **82**, 5475 (1985).
(d) J. W. Tromp and W. H. Miller, J. Phys. Chem., **90**, 3482 (1986).
(e) J. W. Tromp and W. H. Miller, Faraday Disc. Chem. Soc., to be published.
30. (a) R. B. Gerber, V. Buch, and M. A. Ratner, J. Chem. Phys. **77**, 3022 (1982).
(b) V. Buch, R. B. Gerber, and M. A. Ratner, Chem. Phys. Lett. **101**, 44 (1983).
(c) R. B. Gerber, V. Buch, and M. A. Ratner, ibid. **91**, 173 (1982).
(d) G. C. Schatz, V. Buch, M. A. Ratner, and R. B. Gerber, J. Chem. Phys. **79**, 1808 (1983).
31. R. B. Gerber, V. Buch, and M. A. Ratner, in Proceedings of the 15th Jerusalem Symposium on Quantum Chemistry and Biochemistry, edited by J. Jortner and B. Pullman, Reidel, Dordrecht, 1982.
32. (a) R. Harris, J. Chem. Phys. **72**, 1776 (1980).
(b) D. L. Yeager and P. Jørgensen, and D. L. Yeager, Mol. Phys. **41**, 409 (1980).
33. E. J. Heller, J. Chem. Phys. **62**, 1544 (1975).
34. N. Makri and W. H. Miller, J. Chem. Phys. **87**, 5781 (1987).
35. N. Makri and W. H. Miller, J. Chem. Phys. **86**, 1451 (1987).

PRACTICAL APPLICATIONS OF NEW THEORETICAL CONCEPTS IN ORGANIC CHEMISTRY

A. BOTTONI, *Dipartimento di Chimica "G. Ciamician", Università di Bologna, Via Selmi 2, 40126 Bologna, Italy*

M. DURAN and J.M. LLUCH, *Departament de Química, Universitat Autònoma de Barcelona, 08193 Bellaterra (Barcelona), Spain*

M.R. PETERSON, *Department of Chemistry, University of Toronto, Toronto, Ontario M5S 1A1, Canada*

ABSTRACT. The computational problems related to the theoretical lectures are outlined. The problems cover conformational energy surfaces, optimization of transition structures, the MCSCF method applied to chemical reactivity, solvent effect and variational transition state theory.

1. Introduction

Theoretical interpretation of chemical problems proceeds through different stages. First of all, general formulation of the theory must be done. Second, once the theory has been well established, realistic algorithms must be designed and codified into efficient computer programs. In a third step, the programs must be run by computers, thus applying them to chemical problems, and producing numbers which can give an insight into these chemical problems.

The lectures given in this A.S.I., which are compiled in the preceding chapters, correspond to the first stage. The computer codes, i.e., the second stage, were taken generally from the public domain, although some of them were provided by the Lecturers. In order to satisfy the third stage, the codes were run on a properly configured on-site computer installation, which will be outlined below, and several applications were proposed to chemical problems related to the theoretical lectures. The description of these computational problems is the purpose of the present chapter.

The computer facility was composed of a network of two Digital Equipment Corporation microVAX-II computers, with eleven interactive terminals permanently connected. Furthermore, a remote access connection to a VAX-8800 at the Universitat Autònoma de Barcelona was available for special time-consuming jobs. A 240 cps printer was used for printouts. Terminals were actually personal computers, which allowed students to bring in and take away their own files easily. A suitable isolated room was provided twenty-four hours a day.

J. Bertrán and I. G. Csizmadia (eds.),
New Theoretical Concepts for Understanding Organic Reactions, 373–385.
© 1989 by Kluwer Academic Publishers.

2. Applications

In this section the applications of the theoretical methods related to conformational energy surfaces, optimization of transition structures, the MCSCF method and chemical reactivity, solvent effect and variational transition state theory will be presented.

2.1 PROBLEMS INVOLVING CONFORMATIONAL ENERGY SURFACES

Most configurational changes are those that originate by rotation about a bond. For rotation studies, analytic functions containing sine and cosine terms are sometimes fitted to a set of computed points. These functions of one, two or several angles are especially well suited to study the topology of potential energy surfaces. The number of stationary points is well defined by a series of mathematical rules, so a global knowledge of the surface can be obtained before the actual calculations are carried out.

There were three problems concerning conformational energy surfaces and hypersurfaces. The first involved refitting equations to previously computed (and fitted) data points [1-6], which illustrated the mechanics of formulating proper equation terms and using the stepwise regression program to obtain a sufficiently accurate fit to the pre-existing data. The resulting equation could then be plotted and searched for its critical points. The other two problems involved the generation of the data points, followed by fitting and critical point analysis: the second involved a series of surfaces that were expected to be "ideal", while the third proposed a surface expected to be highly "non-ideal".

In the first practise problem, the conformational potential surfaces

$$E = E(x_1, x_2) \tag{1}$$

and hypersurfaces,

$$E = E(x_1, x_2, x_3) \tag{2}$$

were fitted by analytic functions of the form

$$E = E_0 + \sum c_i \cdot f_{1i}(x_1) \cdot f_{2i}(x_2) \tag{3}$$

and

$$E = E_0 + \sum c_i \cdot f_{1i}(x_1) \cdot f_{2i}(x_2) \cdot f_{3i}(x_3) \tag{4}$$

The computed points were provided online for each case, but the students prepared the remainder of the input files containing the candidate equation terms, although sample input jobs for each step of the process were also available online. The results obtained by the students were compared with published results.

The second problem involved a complete solution to a conformational energy surface as the student was required to generate the data points for the chosen system. This required other considerations, including the choice of geometry (rigid rotation versus relaxed rotation where some or all non-rotating geometrical parameters were optimized), choice of grid point spacing, and the choice of basis set and computational level. Practical limitations based on the available computing resources and the duration of the A.S.I. led to the selection of rigid rotation at the STO-3G level, but this problem emphasized that the data to be fitted could be computed in any manner.

The systems proposed for this problem were the double rotors with 2 torsional angles: x_1 and x_2, associated with the systems of fully hydrogenated molecules of the type X-Z-Y. The least amount of unusual behaviour is expected when the central atom is carbon (Z=C), with X and Y chosen from C, N or O:

C-C-C	C-C-N	C-C-O
	N-C-N	N-C-O
		O-C-O

The simplest of these species is $CH_3 - CH_2 - CH_3$, located at the upper left hand corner of the above matrix. The other two hemi-matrices with Z=N and Z=O have a similar set of fully hydrogenated compounds that may not yield reasonable results at low levels of theory.

Once the grid of points had been generated (preferably taking into account the symmetry of the selected system), the surface equation was fitted and analyzed as in the first problem. Although many of these cases have been examined in the literature, none has been the subject of a detailed conformational surface.

The final problem in this section was a proposal for a system that would probably not possess an "ideal" surface. Conformational surfaces obey the following alternating sum rule [7] for the number of critical points (N_l), where l runs from 0 to n, and n is the dimensionality of the problem (for surfaces n=2 and for hypersurfaces n=3)

$$\sum(-1)^l N_l = 0 \tag{5}$$

For an ideal surface

$$N_l = m_1 \cdot m_2 \cdot B_l \tag{6}$$

and for an ideal hypersurface

$$N_l = m_1 \cdot m_2 \cdot m_3 \cdot B_l \tag{7}$$

where the m_i's represent the topological periodicity along each of the one dimensional rotors, and B_l are the Betti numbers (which are the binomial coefficients (n!/l!) for conformational problems).

Certain chemical systems with too much repulsive or too much attractive interaction will not obey equations (6) or (7). This unusual conformational situation might arise in the 1-fluorine-3-lithiumpropane, where there is an interaction between the fluorine and the lithium atoms, and with two torsional angles (x_1 and x_2) along the pair of C-C bonds. This disubstituted propane is expected to show a markedly different potential energy surface topology in comparison to that of unsubstituted propane. Another example [8,9] of such a system, including the effect of rigid versus relaxed rotation, is available as a model for this problem.

This problem again requires the generation of the data points, and subsequent fitting and analysis of the surface equation, as in the second problem.

2.2 OPTIMIZATION OF TRANSITION STRUCTURES

A first step to deal with chemical reactivity is the location of transition structures in the full potential energy surface. Location of transition structures is far more difficult than findig minima. Transition structures are maxima in one and only one direction of the potential energy surface, whereas they are minima in all other directions. A number of methods for finding transition states have been used.

Three problems involving the location of transition structures using GAUSSIAN 86 [10] were proposed: the "classic" case of the HCN $\leftrightarrow$ HNC rearrangement, the SiH_2 + $H_2 \rightarrow SiH_4$ insertion reaction, and the inversion of CH_4 through a planar tetracoordinated carbon.

The HCN $\rightarrow$ HNC reaction [11] has been used frequently to illustrate transition structure optimization methods. At the HF/STO-3G level, the reactant geometry is: R(CN)=1.153 Å, R(CH)=1.070 Å(linear); the product geometry is: R(CN)=1.170 Å, R(NH)=1.011 Å(linear). In this project with GAUSSIAN 86, the linear synchronous transit (LST) method [12] was used to get near the transition state, followed by gradient optimization methods to locate it exactly [13].

The suggested plan of attack was the following: (1) Starting from the reactants and products, make use of the linear synchronous transit method to locate the transition structure approximately. (2) Calculate the gradient and frequencies at the LST optimized structure. Test whether it is a stationary point and a saddle point. (3) Optimize the transition structure using OPT=TS. Do not forget to have the program calculate a few critical force constants. (4) Test the optimized transition state by calculating the frequencies.

The ground state of SiH_2 is a singlet with an sp^2 lone pair. Like singlet carbene, SiH_2 inserts readily into covalent bonds. The least motion pathway would proceed through a C_{2v} symmetry transition state (sp^2 lone pair pointing at the H_2 sigma bond). However, this path is forbidden by orbital symmetry, and the reaction goes via a non-least motion pathway [14]. The allowed transition state has C_s symmetry with the sp^2 lone pair of SiH_2 nearly parallel to H_2. The geometry of the reactants is R(SiH)=1.531 Å, /HSiH=93.8, R(H_2)=0.735 Å; for the product R(SiH)=1.487 Å (all data at HF/3-21G). The transition state has a 50 percent elongation of the H_2 bond. In this project, GAUSSIAN 86 was used to determine the transition state at the HF/3-21G level [15].

The suggested plan of attack was the following: (1) Construct several different Z-matrix coordinate systems for the transition state. Choose the best coordinate system for the rest of the calculations. (2) Calculate the energy and gradients at several points along an approximate reaction path to get a rough location of the transition state. (3) Optimize the transition structure using gradients. Start with an analytically calculated Hessian (the CALCFC option). (4) Test the transition state by calculating the vibrational frequencies. Sketch the transition vector and the transition structure. (5) Draw an orbital interaction diagram for the transition state and discuss why the non-least motion pathway is allowed but the least motion pathway is forbidden.

The possibility of planar tetracoordinated carbon has long fascinated theoretical and experimental chemists. The simplest hydrocarbon, CH_4 (T_d symmetry), can be distorted planar (D_{4h} symmetry). Planar methane is a potential transition state for the inversion of configuration of tetrahedral methane to give its mirror image.

In this project, GAUSSIAN 86 was used to explore the potential energy surface of methane at the HF/4-31G level. The aim of the exercise was to illustrate higher order saddle points and how to get to lower order saddle points, and eventually to the transition state (first order saddle point) [16].

The suggested plan of attack consisted of the following steps: (1) Optimize tetrahedral methane. (2) Optimize planar methane (D_4h) and calculate the frequencies. Check whether it is a transition state (first order saddle point). (3) Displace the structure along any one of the normal modes with an imaginary frequency (except for the mode that leads to the T_d minimum). (4) Optimize the distorted structure and calculate the frequencies. If it is not a first order saddle point, go back to (3). (5) Make a sketch of the methane potential energy surface indicating the energetics and connectivity of the minima and the various first and higher order saddle points.

As an interesting illustration of basis set effects, the problem could be redone at the HF/3-21G level, which would also serve as a simple example of a transition structure optimization.

2.3 THE MCSCF METHOD AND ITS APPLICATION TO CHEMICAL REACTIVITY

The study of chemical reactions involves the description of the rupture and the formation of chemical bonds. These types of problems cannot be correctly treated using a single configuration wavefunction method like the HF-SCF method. To deal with this type of problems a multi-configuration wavefunction like that provided, for example, by the CI (Configuration Interaction) method, is necessary. In the CI method, which is a straightforward application of the variational principle, the wavefunction is written as a linear combination of Slater determinants representing different electronic configurations. Even if this method is, in principle, capable of providing accurate solutions of the Schrödinger equation for any stationary point of a reaction surface (like transition states and intermediates), its application to molecular systems of chemical interest can involve a very large number of configurations, which leads to serious computational problems.

Another possible approach to obtaining reliable wavefunctions for the description of bond breaking and bond forming is the MCSCF (Multi-Configuration Self Consistent Field) method [17] which represents a natural expansion of the HF-SCF procedure and consists of optimizing both the mixing of several configurations as well as the coefficients of the molecular orbitals from which these configurations are obtained.

At this school a certain number of computational exercises on this quantum mechanical approach have been proposed to the students. One of the major aims of these problems was to make people more familiar with the MCSCF approach and with the strategy which is convenient to follow in order to investigate a reaction surface, locate the critical points of chemical interest (intermediates, transition states) and find their optimum geometries using MCSCF gradient techniques [18]. To solve the various exercises an MCSCF code [17] was made available to the students: this code was running as a part of the GAUSSIAN 82 series of programs [19].

The first problem the students had to solve was the choice of an appropriate 'active space'. In the use of the MCSCF method, applied here in its CAS (Complete Active Space) form, it is in fact convenient to define a partition of the orbitals into three different subsets: (i) core orbitals which are doubly occupied in all configurations, (ii) valence orbitals which define the 'active space' and which are characterized by all possible occupancies, (iii)

virtual orbitals which are unoccupied in all configurations. The choice of the 'active space' is done in such a way to include all the orbitals which are involved in bond making and bond breaking. To illustrate this point we have proposed three simple examples of organic chemical reactions for which detailed MCSCF studies have already been published [20]. They are:

(a) (2+2) cycloaddition reaction between two ethylene molecules to give cyclobutane [20a].

(b) 1,3 dipolar cycloaddition reaction of fulminic acid with acetylene which gives isoxazole [20b].

(c) (4+2) cycloaddition reaction between 1,3 butadiene and ethylene (Diels-Alder reaction) [20c,d].

A good method, proposed to the students, for choosing a correct valence space is to perform, at the minimal STO-3G level [21], an MCSCF computation on reactant molecules at infinite separation using the MO's obtained from one of the semi-empirical codes (Extended Hückel, CNDO, INDO) implemented in GAUSSIAN 82, as starting orbitals for the MCSCF procedure. At infinite separation the orbitals are clearly localized on the fragment molecules which makes easier to recognize the correct valence space.

All the three above examples can be described as four electron-four orbital problems. Thus, for example, to describe correctly the breaking of two π bonds and the formation of two new σ bonds in the case of the ethylene-ethylene reaction, we must choose as valence space the two π (HOMO) and the two π^* (LUMO) orbitals of the isolated fragments.

After these introductory exercises we have focused the student's attention only on the ethylene-ethylene reaction. For this reaction the students had to compute, using the MCSCF gradient method [18] implemented in GAUSSIAN 82, the optimum geometries of the possible transition structures associated with a supra-supra approach and a trans approach [20a].

For this purpose we suggested the MCSCF MO's obtained at infinite separation be used as initial MO's for the MCSCF calculations and a starting geometry obtained from standard values for the two ethylene molecules with a value for the C-C forming bond in the range of 2.0-1.9 Å.

Once a transition structure (or a transient minimum like a short lived intermediate) has been obtained, it is necessary to investigate the real nature of the optimized structure. To this purpose, as a final step, the student had to compute, by finite differences, the matrix of the second derivatives of the energy with respect to the various geometrical parameters (Hessian matrix) and find the corresponding eigenvalues and eigenvectors. An intermediate (a minimum on the reaction surface) is characterized by all positive eigenvalues of the Hessian matrix, while a transition state (first-order saddle point) must have only one negative eigenvalue corresponding to the direction of negative curvature.

Another objective of these computational exercises was to show how it is possible to extract a simple VB representation from the results of an MCSCF computation and to use such a representation for building a diabatic decomposition scheme like that suggested by Bernardi and Robb [22].

To illustrate this point we have suggested to consider again the ethylene-ethylene reaction as a model example. Focusing our attention only on the valence orbital space, this reaction can be treated in VB theory as a four electron problem [23]. If we consider only covalent structures the reactant bonding situation (the reactant diabatic), and the

product bonding situation (the product diabatic) can be associated with the following Rumer diagrams [23]:

```
                d-----c                          d     c
                                                 :     :
R(ab,cd)=>                        P(ad,bc)=>     :     :
                                                 :     :
                a-----b                          a     b

     Reactants                         Products
```

where a,b and c,d denote the atomic orbitals of π symmetry on the ethylene Carbon atoms.

The two diabatic functions R(ab,cd) and P(ad,bc) can be computed as linear combinations of the following six determinants:

```
det{a'bcd'}  det{a'b'cd}   det{a'bc'd}

det{ab'cd'}  det{abc'd'}   det{ab'c'd}
```

where a represents an atomic orbital with α spin and a' an atomic orbital with β spin.

To obtain all the information necessary for this VB representation the student had to perform the following computations:

i) an MCSCF computation on the trans or the supra-supra transition structure followed by a transformation of the valence MO's to a set of localized MO's (atomic orbitals localized on the carbon atoms) using Boys' method (implemented in the MCSCF code) [24].

ii) a CI computation, using the localized MO's of the previous step, associated with the evaluation of an effective hamiltonian matrix (using the Van Vleck method implemented in the MCSCF code [25]) in the basis of the six determinants used for describing the diabatic functions R and P.

iii) evaluation of the diabatic energies from the following matrix expressions, using the effective hamitonian matrix obtained in the previous step:

$$E(R) = \langle R \mid H \mid R \rangle \qquad E(P) = \langle P \mid H \mid P \rangle$$

where H denotes the hamiltonian operator.

2.4 SOLVENT EFFECT

In the Laboratory, chemical reactions involving several atoms are mostly carried out in solution, using a wide variety of solvents with different polarity. However, practical restrictions have limited theoretical calculations using quantum chemical methods to isolated systems. Several models have been developed to account for the solvent effect in quantum chemical calculations. These models may be roughly classified into discrete ones, where the solvent molecules are conferred an entity, and continuum ones, where the solvent is represented by its macroscopic magnitudes. The main limitation of discrete models is the

reduced number of solvent molecules that can be included in the calculations. Continuum models have the drawback that solute polarization by the solvent has not usually been taken into account. Monte Carlo and molecular dynamics methods [26] can be used to partially overcome those problems, but they turn out to be quite expensive. In these practise sessions of the A.S.I., only quantum chemical methods were employed.

One of the most widely used continuum models is that of the cavity [27-29]. The solute is supposed to be imbedded into a cavity generated inside the solvent. The latter is characterized by its dielectric constant ϵ. The cavity may be chosen in several ways, e.g., according to the Van der Waals radii [29] of the constituent atoms. Other cavities are chosen to be ellipsoidal or spherical [28,29], the volume being determined for instance by the Claussius-Mossoti equation that relates the volume of the solute to its polarizability. In the program of Rivail et al. [30,31], which was that used for continuum-model calculations, the SCF equations for a system of electrons and nuclei surrounded by a dielectric continuum are derived by using a multipolar expansion of the interaction energy.

It is well known that the larger the ionic character (or charge separation) of a chemical system, the larger the solvent effect will be. A first example can be found in the electronic and nuclear relaxation effects in formamide, owing to the electric reaction field. Amides are especially well suited for this purpose, because ionic structures (in a valence bond language) are likely to have a meaningful weight, which will be modified upon introduction of a reaction field. This will translate into important electronic and nuclear relaxation effects. A first problem therefore was carried out on the structure of formamide, by means of the MNDO semiempirical method [32], using the GEOMO program [31]. The charge distribution of the optimized gas phase molecule had to be compared to the distribution in solution with the same geometry. The spherical cavity model was used to characterize the solvent, which was taken to be water, i.e., ϵ=78. Finally, the geometry of the formamide molecule had to be reoptimized inside the cavity to study the nuclear relaxation owing to the presence of the solvent.

Although structural studies are quite important and constitute a leading part of modern quantum chemical studies, kinetic studies, i.e., calculations on chemical reactions, are also a major part of them. Two examples were proposed as subject of study: the attack on benzene derivatives by nucleophiles or electrophiles, and the S_N2 Walden inversion reaction. The site attack of benzene derivatives by nucleophiles or electrophiles has been interpreted through two static indexes, namely, the charge index if the reaction is charge-controlled, and the frontier orbitals if the reaction is orbital-controlled [33]. The change from the gas phase to solution will modify charges and frontier orbitals, and the relative distribution of the different adducts may be altered. In particular, an example was given on the benzonytrile molecule, using the MNDO semiempirical method [32]. Static indexes had to be found in the gas phase and in solution, using the ellipsoidal cavity model and water as solvent. Dipole moments, charge distributions and frontier orbitals had to be analyzed. Further, the entrance of H^+ and H^- at the three ortho, meta and para positions had to be analyzed by studying the respective intermediates, and compared to the predictions given by static indexes, both for the gas phase and in solution.

A third example was provided by means of the S_N2 Walden inversion process

$$F^- + CH_3F \rightarrow FCH_3 + F^-$$

Theoretical calculations in the gas-phase show a double-well energy profile [34]. The purpose of this problem was thus to determine the reaction profile in solution. The solvent was characterized either by a discrete model or by a continuum one. The AM1 semiempirical method [35] was used, given the poor description by other methods of the hydrogen bonding. Reactants, intermediates and transition state were located and characterized in the gas phase. The solvent effect was included by the discrete model, where each fluorine atom was attached to one water molecule. The changes in the energetic profile, well depth of the intermediate with respect to reactants, barrier height to the methyl transfer with respect to intermediates, and overall activation barrier, were discussed. Finally, the same analysis had to be performed through a continuum representation of the solvent by means of the cavity model at the stationary points of the gas-phase energetic profile.

2.5 VARIATIONAL TRANSITION STATE THEORY

A satisfactory theory of chemical kinetics should be capable of predicting reactions rate constants from properties of the reactive molecules. Since the 1930s Transition State Theory (TST) has been the principal approach used in theoretical discussions of chemical reactions rates. The fundamental assumption in conventional TST is that the net equilibrium rate of the forward reaction is given by the one-way flux of trajectories in the product direction across a configuration space dividing surface that passes through the highest potential energy point (saddle point) on the minimum energy path (MEP) from reactants to products. However, there is the possibility that some trajectories may cross the dividing surface more than once, with many of these being reflected back to the reactant side. Because this recrossing usually occurs, conventional TST provides only an upper bound to the equilibrium rate constant. To improve TST, in Canonical Variational Transition State Theory (CVT) [36], location of the configuration space dividing surface or Generalized Transition State (GTS) is optimized variationally as a function of the site where it intersects the MEP, in order to obtain the minimum rate constant at a given temperature T. Therefore, CVT locates Canonical Variational Transition States at the highest free energy of activation point on the MEP. In this way, entropic and zero-point effects are incorporated in finding the dividing surface. Generalized Normal Modes orthogonal to the MEP have to be computed at regular intervals along the MEP, by using the projector given by Miller et al. [37]. A threshold-corrected version of CVT is called Improved Canonical Variational Theory (ICVT).

Several problems based in the bimolecular reaction

$$OH + H_2 \rightarrow H_2O + H$$

were proposed to students to apply and discuss these theories. This process is a very imporant chain-branching reaction in the H_2/O_2 explosion and one of the main sources of water in typical hydrocarbon-air flames at atmospheric pressure. The calculations were performed by using the POLYRATE program [38] which can compute unimolecular and bimolecular gas-phase chemical reaction rates of polyatomic species from potential energy hypersurfaces. The analytic potential energy surface obtained by Schatz and Elgersma [39] by a fit to the ab initio calculations of Walch and Dunning [40] was supplied as a subprogram, along with the geometries of reactants, products and saddle points in the input data file.

Initially, vibrational modes of the reactants, products and GTS were assumed to be harmonic. To obtain all the required information about the reaction, we suggested the students the following steps [41-43]:

a) Normal mode analysis of reactants, products and saddle points.

b) Construction of the MEP. A scaled coordinate system was employed, in such a way that the MEP corresponds to the Intrinsic Reaction Coordinate (IRC). A mapping of the supermolecule's geometry (e.g., a draw) along the MEP allows to follow the motion of the atoms during the reaction.

c) Representation of the classical potential energy (V_{MEP}), the zero-point energy and the vibrationally adiabatic ground-state potential energy (V_a^G) as a function of the distance s along the MEP from the saddle point. It can be seen that the maximum value of V_a^G (GTS at 0 K) does not coincide with the maximum value of the MEP (saddle point).

d) Vibrational-mode adiabatic and diabatic correlation analysis along s: the frequencies versus s for the various normal modes orthogonal to the MEP can be plotted and the character of each mode can be identified.

e) Representation of the generalized free energy versus s at several temperatures by using both CVT and ICVT. An interpolation of the free energy of activation to its maximum determines the variational transition state location and the forward and reverse rate constants (CVT or ICVT) corresponding to the given temperature.

f) Calculation of the transmission coefficients in order to model the quantum effects on reaction-coordinate motion. Tunneling can be taken into account by using several formalisms, such as Minimum-Energy-Path Semiclassical Adiabatic Ground-State (MEP-SAG) and Small-Curvature Semiclassical Adiabatic Ground-State (SCSAG) methods.

g) Calculation of the equilibrium constants.

In a second step, we remarked that, in general, the vibrational degrees of freedom of the reactants, products and GTS are bound by an anharmonic potential which contains terms in normal coordinates of order higher than two. Substantial differences can be obtained between rate constants computed from harmonic and anharmonic vibrations. The students were required to repeat the preceding calculations including now the anharmonicity, by using several models, such as the Morse-I-quadratic-quartic approximation. An interesting point is the discussion about which results are expected to be invariant upon introduction of anharmonicity.

Finally, we focused the attention of the students in the field of state-to-state chemistry, in which non-Boltzmann distributions over internal energy states are induced in reactant molecules and detected in product molecules. Investigations of the influence of internal energy on the rate of reactions have been concentrated mainly on vibrational excitation. Usually it is found that the reaction rate is enhanced, sometimes by several orders of magnitude. This fact can be demonstrated for the reaction

$$OH\,(n_{OH}) + H_2(n_{HH}) \rightarrow H_2O + H$$

where n_{OH} and n_{HH} are vibrational quantum numbers. Because of its importance in combustion systems, this reaction has been the subject of numerous experimental studies. A large effect of vibrational excitation of H_2 to give a factor of 120 to 150 increase in the rate coefficient for $n_{HH}=1$ compared to $n_{HH}=0$ at room temperature was found. Moreover, the general idea that vibrational excitation of a bond that is broken (H_2) in a reaction is

more effective than other excitations (H_2O) in promoting the reaction was confirmed. In this A.S.I., a vibrationally diabatic version [42] of Variational Transition State Theory was applied to calculate the rate constants $K(n_{OH}, n_{HH}, T)$ for the vibrational-state-selected reaction above mentioned, where the rotational and translational degrees of freedom are at temperature T and the rate constant is summed over all final states. Three cases were considered at different temperatures:

a) $n_{OH}=0$, $n_{HH}=0$
b) $n_{OH}=1$, $n_{HH}=0$
c) $n_{OH}=0$, $n_{HH}=1$

The results obtained in each case were compared with the completely thermally averaged and the experimental ones.

3. Acknowledgments

We thank the Murlà Park Hotel for providing the computer room. We also thank the Universitat Autònoma de Barcelona Computer Center for providing one of the microVAXes and other computing equipment. We must acknowledge Digital Equipment Corporation for supplying a microVAX-II for the duration of the A.S.I., as well as Ofimatic Sabadell, S.A., for generously providing the Olivetti personal computers. Finally, we must thank the Lecturers for supplying some of the problems and programs, and for useful discussions about them.

4. References

[1] M.R. Peterson and I.G. Csizmadia, *J. Amer. Chem. Soc.*, **100**, 6911 (1978).

[2] M.R. Peterson and I.G. Csizmadia, *J. Amer. Chem. Soc.*, **101**, 1076 (1979).

[3] T.A. Modro, W.G. Liauw, M.R. Peterson and I.G. Csizmadia, *J. Chem. Soc., Perkin Trans. 2*, 1432 (1979).

[4] G.R. De Mare, M.R. Peterson, I.G. Csizmadia and O.P. Strausz, *J. Comp. Chem.* **1**, 141 (1980).

[5] M.R. Peterson, G.R. De Mare, I.G. Csizmadia and O.P. Strausz, *J. Molec. Struct. (Theochem)* **86**, 131 (1981).

[6] M.R. Peterson and I.G. Csizmadia, in *Molecular Structure and Conformation: Recent Advances, Progress in Theoretical Organic Chemistry*, Vol. 3, I.G. Csizmadia (Ed.), Elsevier, Amsterdam, 1982, p. 190.

[7] M.R. Peterson, I.G. Csizmadia and R.W. Sharpe, *J. Molec. Struct. (Theochem)* **94**, 127 (1983).

[8] J.G. Angyan, R.A. Poirier, A. Kucsman and I.G. Csizmadia, *J. Amer. Chem. Soc.* **109**, 2237 (1987).

[9] J.G. Angyan, R. Daudel, A. Kucsman and I.G. Csizmadia, *Chem. Phys. Letts.* **136**, 1 (1987)

[10] *Gaussian 86*, M.J. Frisch, J.S. Binkley, H.B. Schlegel, K. Raghavachari, C.F. Melius, R.L. Martin, J.J.P. Stewart, F.W. Bobrowicz, C.M. Rohlfing. L.R. Kahn, D.J. Defrees, R. Seeger, R.A. Whiteside, D.J. Fox, E.M. Fleuder and J.A. Pople, Carnegie-Mellon Quantum Chemistry Publishing Unit, Pittsburgh PA, 1984.

[11] K. Ishida, K. Morokuma and A. Kormornicki, *J. Chem. Phys.* **66**, 2153 (1977).

[12] T.A. Halgren and W.N. Lipscomb, *Chem. Phys. Letters* **49**, 225 (1977).

[13] (a) H.B. Schlegel, *Adv. Chem. Phys.* **67**, 249 (1987); (b) *J. Comp. Chem.* **3**, 214 (1982).

[14] I. Fleming, *Frontier Orbitals and Organic Chemical Reactions*, John Wiley & Sons, London, 1976.

[15] (a) M.E. Colvin, S. Grev, H.F. Schaefer and J. Bicerano, *Chem. Phys. Letters* **99**, 399 (1983). (b) C. Sosa and H.B. Schlegel, *J. Amer. Chem. Soc.* **106**, 5847 (1984).

[16] J.B. Collins, J.D. Dill, E.D. Jemmis, Y. Apeloig, P.v.R. Schleyer, R. Seeger and J.A. Pople, *J. Amer. Chem. Soc.* **98**, 5419 (1976).

[17] D. Hegarty ad M. A. Robb, *Mol. Phys.* **38**, 1795 (1979)

[18] H.B. Schlegel and M.A. Robb *Chem. Phys. Letters* **93**, 43 (1982).

[19] *GAUSSIAN 82*: Carnegie Mellon University, J.S. Binkley, M. Frisch, R. Raghavachari, D.J. De Frees, H.B. Schlegel, R.A. Whiteside, E. Fluder, R. Seeger, and J.A. Pople, Carnegie-Mellon University, Pittsburgh, PA.

[20] (a) F. Bernardi, A. Bottoni, M.A. Robb, H.B. Schlegel, G. Tonachini, *J. Amer. Chem. Soc.* **107** 2260 (1985). (b) F. Bernardi, A. Bottoni, J.J.W. McDouall, M.A. Robb, H.B. Schlegel, *Faraday Symp. Chem. Soc.* **19**, 137 (1984) (c) F. Bernardi, A. Bottoni, M.A. Robb, M.J. Field, I.H. Hillier and M.F. Guest, *J. Chem. Soc., Chem. Commun.* 1052 (1985) (d) F. Bernardi, A. Bottoni, A. Venturini, M.A. Robb, M.J. Field, I.J. Hillier and M.F. Guest, *J. Amer. Chem. Soc.* **110**, 3050 (1988).

[21] W.J. Hehre, R.F. Stewart and J.A. Pople, *J. Chem. Phys.* **51**, 2657 (1969).

[22] (a) F. Bernardi, M. Olivucci, M.A. Robb and G. Tonachini, *J. Amer. Chem. Soc.* **108**, 1408 (1986). (b) F. Bernardi and M.A. Robb, *Adv. Chem. Phys.* **67**, 155 (1987)

[23] (a) H. Eyring, J. Walter and G.E. Kimball, *Quantum Chemistry*, John Wiley & Sons Inc., New York., 1944 (b) R. McWeeny and B.T. Sutcliffe, *Methods of Molecular Quantum Mechanics*, Academic Press Inc., London, 1969.

[24] S.F. Boys *Rev. Mod. Phys.* **32**, 296 (1960).

[25] (a) I. Shavitt and L.T. Redmon *J. Chem. Phys.* **73**, 5711 (1980) (b) F. Bernardi, S.A.H.D. Paleolog, J.J.W. McDouall and M.A. Robb, *J. Mol. Struct. (Theochem)* **138**, 23 (1986).

[26] *Chemical Reactivity in Liquids: Fundamental Aspects*, M. Moreau and P. Turq, Eds. Plenum, New York, 1988.

[27] J. Bertrán, A. Oliva, D. Rinaldi and J.L. Rivail, *Nouv. J. Chimie* **4**, 209 (1980).

[28] J.L. Rivail and D. Rinaldi, *Chem. Phys.* **18**, 233 (1976)

[29] S. Miertus, E. Scrocco and J. Tomasi, *Chem. Phys* **55**, 117 (1981)

[30] D. Rinaldi, *Computers and Chemistry* **1**, 108 (1976).

[31] Program *GEOMO, Q.C.P.E.* No. 290.

[32] M.J.S. Dewar and W. Thiel, *J. Amer. Chem. Soc.* **99**, 4899 (1977)

[33] E. Sánchez Marcos, J. Maraver, M.F. Ruiz López and J. Bertrán, *Can. J. Chem.* **64**, 2353 (1986)

[34] M. Urban, I. Cernusak and V. Kello, *Chem. Phys. Letters* **105**, 625 (1984)

[35] M.J.S. Dewar, E.G. Zoebisch, E.F. Healy and J.J.P. Stewart, *J. Amer. Chem. Soc.* **107**, 3902 (1985)

[36] D.G. Truhlar, A.D. Isaacson and B.C. Garrett, *Theory of Chemical Reaction Dynamics* Vol. IV, M. Baer, Ed., CRC Press, Boca Raton, FL, 1985.

[37] W.H. Miller, N.C. Handy and J.E. Adams, *J. Chem. Phys.* **72**, 99 (1980).

[38] A.D. Isaacson, D.G. Truhlar, S.N. Rai, R. Steckler, G.C. Hancock, B.C. Garrett and M.J. Redmon, *Comp. Phys. Comm.* **47**, 91 (1987)
[39] G.C. Schatz and H. Elgersma, *Chem. Phys. Letters* **73**, 21 (1980).
[40] S.P. Walch and T.H. Dunning, *J. Chem. Phys.* **72**, 1303 (1980).
[41] A.D. Isaacson and D.G. Truhlar, *J. Chem. Phys.* **76**, 1380 (1982).
[42] D.G. Truhlar and A.D. Isaacson, *J. Chem. Phys.* **77**, 3516 (1982).
[43] A.D. Isaacson, M.T. Sund, S.N. Rai and D.G. Truhlar, *J. Chem. Phys.* **82**, 1338 (1985).

Subject Index

Acid catalysis 244, 245, 247, 249, 252
Activation 207, 208
Activation barrier 160, 233, 242, 249
Activation energy 233, 246, 247, 306, 307, 312, 314, 331, 332-339
Adiabatic potential, vibrational-rotational 309, 314-317, 319-323, 325, 338
Adiabatic states, electronic 312
Adiabatic states, vibrational 312, 314, 322
Adiabatic surface 147, 279
Allowed and forbidden pathways 205, 206
Allowed reactions 110
Allyl 180, 183
AM1 381
Analytic expansion 8, 10
Analytic gradient 33-35, 45, 49, 348, 349
Anchor state 202, 203
Angular momentum 349, 352, 353
Antibonding 166, 174, 176, 177, 182, 188, 189
Asymptotic expansion 271
Asynchronous 151, 204
Atom abstractions 193
Avoided crossing 193, 194, 196-198, 200, 205-207, 210, 279
Barrier 165, 166, 193, 196
Betti numbers 13-15, 17, 18, 28
Bifunctional catalysis 231, 242, 244-247, 249, 252
Binomial coefficients 13, 17
Biradical intermediate 204, 206
Bond distortions 207, 208
Bond-diagram 167, 177, 178, 184, 190, 205
Bonds-pairs 177, 178, 184, 185, 190, 191, 202-204
Bottleneck 291, 299, 307, 323-325, 336, 357, 359, 360
Butane 5, 14, 17-24
CASMCSCF 148, 158
CASSCF 150
Catalysis 231, 242, 244, 245, 249, 251
Catchment regions 59-61, 70-72
Cation-anion recombinations 208
Cavity 223, 380
CH_3^+ transfer 197
Charge exchange 261
Charge transfer 114, 130, 133-136, 158, 160, 200, 203, 232, 235, 237, 240, 249, 251, 276, 277, 279
Chemical reactivity 147
Clausius-Mossoti equation 380
Collision integrals 281
Concerted 151
Concerted transition structure 156, 245, 247
Configuration interaction 190, 198, 207
Conformational rearrangements 340, 374
Continuum 223, 231, 232-234, 244, 379
Contour surfaces 77, 79, 80, 81, 83, 84, 89, 91, 93, 96, 325, 318-321
Coriolis coupling 352, 356
Correlation 194, 201
Coulomb parameters 149
Counting 295
Coupling functions 351, 352, 357
Covalent bond 166, 173, 177, 202
Covalent curves 196, 198-200
Covalent determinants 173, 177, 180
Critical point relations 64-66

Critical points 33-35, 48-49, 311
Crossing point 199, 205, 207, 208
Cumulative reaction probability 358, 359
Curvature coupling 319, 322, 352, 353, 355, 362, 363
Curvature of reaction path 304, 318-323, 327-329, 335, 339, 352
Curvature properties 77, 82
Curve crossing diagrams 165, 166
Cycloaddition 102, 131, 149, 152, 156, 203-206, 244, 378
Cyclobutane 205
Cyclopropenyl 180, 182
Deflection function 264, 265, 266
Deformation energy 207-210
Density of states 294-299, 358
Determinant-mixing 171, 174, 177, 183
Diabatic surface 101, 102, 117, 125, 127, 129, 133, 140-144, 147-148, 150, 160-161
Diels Alder Reaction 147, 158, 206, 378
Differential cross section 257-261, 263, 270, 274, 282
Diffusion coefficients 283
Discrete 231, 233, 235, 379
Dispersion energy 219
Displacement reactions 197
Dividing surface 304
Dummy atoms 38-44
Dynamic shape properties 93
Effective Hamiltonian 155
Electric field 231, 244, 249-252
Electric permittivity 221
Electron transfer 176, 203, 237-241
Electrophile 203
Electrophilic substitution 226, 247, 251
Electrostatic interaction energy 219
Elimination reaction 203
Energy first derivatives 33-35, 45, 49
Energy second derivatives 34, 45, 57, 49-50
Energy third derivatives 34
Entropic effects 232, 245, 292, 307, 325, 326, 334-339
Enumeration of internal coordinates 39-40
Ethane 11, 14, 15
Ethylene hydrogenation 245-247
Exchange integral 106, 117, 155
Exchange parameters 149
Exchange reaction 202
Excited state 177, 196, 199, 201, 207, 208
Feynman path integral 365, 366
Flux 356-359, 366
FO-VB diagrams 184, 185, 190, 202
Forbidden reaction 152
Force constant 5, 6, 8, 329
Force constant matrix 34, 45, 47, 49-50, 348, 350, 351, 364
Free energy of activation 232, 245, 306, 307, 312, 313, 331, 334-339
Friction 308, 333, 334, 365
Friedel-Crafts reaction 247-249
Gaussian 86, 33, 36-37, 51, 376
Generalized Langevin equation 232, 333, 365
Generalized transition state 299, 381
GEOMO 380
Global analysis of PES 56-58, 63
Gradient 5, 6, 8-10, 33-35, 45, 49, 376
Gradient length 7

H-atom transfer 318-321, 323-331, 334, 335, 338, 339, 348, 353, 354, 368
Heisenberg Hamiltonian 101, 117-121, 125, 131, 133, 136, 140, 143, 147, 149, 155, 158, 160, 169, 180
Heitler-London 174, 177-180, 182, 183, 185, 193-195, 198-200
Hessian 34, 45, 47, 49-50, 376, 378
HOMO 226, 378
HOMO-LUMO 204-206
Homology groups 83
Homotopy group 62-63
Hückel 181, 185
Hydrocarbons 17, 329-331
Ideal surface 1, 29
Image state 201-206
Index of critical point 5-12, 14-20, 27, 311
Induction energy 219
Internal coordinates 36-45, 49-50
Intersection curves 194
Ionic exchange 197
Jahn-Teller mechanism 184, 190
Kekule structures 182, 183, 186-191
Ketoenolic tautomerism 242-244
Kinetic measurements 210
Knots and chirality polynomials 84, 85
Lewis structures 167, 178
Linear free energy relations 208-210
Linear reaction path 348, 353, 357, 364, 368
Long bond 167, 189, 198
LUMO 226, 378
Marcus theory 208
Matrix elements 167, 171, 172, 176, 180, 186-190, 200, 213-215
Maxima 5-9, 11, 13-18, 20, 23, 24, 312
MCSCF 110, 112, 116, 120, 126, 140, 143, 152, 154, 377
Menschutkin reaction 208
Minima 2, 5-11, 13-18, 20, 22, 24, 26, 28, 33-35, 48-49
Minimum energy path 48, 49, 51, 304, 305, 309-311, 315-323, 326-328, 331, 335, 348, 349, 353, 355, 357, 368, 382
Mixed-valence species 185
MNDO 380
Mobius 182, 185, 186
Molecular beams 263, 269
Molecular body vs. molecular skeleton 78, 79
Molecular Dynamics 231, 240, 380
Monte Carlo 231, 233, 234, 237, 238, 380
Multiconfiguration TDSCF 367
Multipoles 220, 225
Newton-Raphson optimization step 35-36
Nodal properties 205
Non-ideal surface 1, 29
Non-linear Schrodinger equation 367
Nonbonded interactions 207
Normal coordinates 311, 314, 330, 350, 353, 356, 357
Normal mode 162
Nucleophile 203
Nucleophilic substitution 208, 226
Optimization 33-51, 304-308
Orbital interactions 210
Orbital symmetry 206
Oriented relative convexity 82
Overlap repulsion 170, 171, 186, 189
Parallel algorithm for quasi global optimization 55, 64-65

Partition functions 293, 299-306, 309-312, 331, 335
Pericyclic reaction 206
Permutations 211-213
Perturbation language 177, 196
Phase space 292-303, 307, 308, 332
Polarizability 220
Polyrate 381
Potential Energy Surfaces 34, 193, 231, 249, 250, 291, 292, 294, 304-323, 347, 348, 354, 355, 368, 374
Propane 14-16, 20
QMRE 207, 210
Quadratic expansion 5, 8, 35-36, 317
Quasi-Newton methods for optimization 34-36
Radical anion 200
Radical attacks 293, 323-331, 335, 338, 339
Radical reactions 193, 204-206
Reaction barriers 148
Reaction coordinate 160, 197, 201, 233, 235, 236, 241, 244, 247, 249, 251, 252, 292, 296-307, 309-323, 331-335, 352, 360, 361, 364, 365
Reaction Field 225, 231, 252
Reaction mechanism 55-56, 59, 62-63
Reaction path 48-51, 300-304, 307, 311, 314-323, 327-329, 335, 337
Reaction path Hamiltonian 292, 297, 300, 348, 351, 352, 355, 360, 362, 364, 368
Reaction profile 162, 232, 233, 249, 250, 300-307, 309-312, 314-323, 331, 350
Reactive flux 291-303, 312, 319, 324
Reactivity patterns 165, 193
Recrossing 232, 240, 241, 298, 299, 323, 325, 333
Reference cluster approach 70-72
Regiochemical pathways 204
Relative convexity 82
Relaxation times 222, 235, 308, 332-334
Resonance 170, 177, 183, 192, 207, 208
Rotation-inversion 4
Rotational excitation 261, 275, 308
Rumer functions 160
Rumer spin functions 162
Saddle point 2, 5, 7-10, 13, 15-18, 20, 22-24, 26, 33-35, 45-46, 48-49, 304, 305, 318-321, 324, 326, 329
Saddle point optimization 33-51
SCD 165, 194, 196-198, 200-202, 204-209
SCF 226
Second derivative 5, 7, 8
Semiclassical approximation 264, 266 , 308-331, 334-339, 360, 362-364
Shape groups 77, 80, 81, 83, 84
Singlet-pairing 174, 175, 177, 181
S_N2 reaction 35, 192, 197, 208, 209, 231-237, 240, 241, 249-252, 380
Solute-solvent interactions 221
Solvation 221, 231
Solvation free energy 332
Solvation parameter 235-237
Solvent 221
Solvent dynamic effect 231, 240, 331-334, 339
Solvent effects 231, 232, 241, 379, 293, 308, 331-335
Solvent fluctuations 237, 238, 241

Solvent reorganization 232, 233, 237, 238, 242
Solvent static effect 231, 232, 235, 331, 332
Space-orbitals 211
Spin correspondence 214
Spin transfer 192, 193, 197, 202, 203
Spin-eigenfunction 167, 194
Spin-orbital 167-173, 175, 195, 211-213, 215
Spin-pairing 174, 177, 178, 181, 193, 198, 201, 203, 205
Stationary points 33-35, 48-49, 234, 249
Statistical approximations 294, 306, 308, 312, 333, 356, 360
Stereochemistry 1, 5, 14, 17
Strong coupling of internal coordinates 40-44
Substituent effects 209
Supra-antara 204, 205
Supra-supra 204, 205
Symmetry 245, 247, 376, 303, 311, 325
Symmetry and dummy atoms 38-39
Symmetry and optimization 34-35
Symmetry and transition vectors 3
Symmetry constraints on PES 70, 72
Synchronous 151
Synthesis design on PES 54, 57, 63
TDSCF 366
Testing stationary points 48-49
Thermal conductivity 280
Thermal diffusion 280
Topological periodicity 11, 13, 14, 26
Topology 1, 5, 10, 11, 13-20, 24-29
Total cross section 261, 274
Torus 11-13
Transition state 33-35, 45-46, 48-49, 108, 126, 129, 142, 147-150, 158, 162, 192, 196, 197, 199, 200, 205-210, 242-248, 291-312, 324-326, 331, 332, 336-339, 348, 349, 353, 355, 361, 376
Transition state optimization 33-51
Transition state theory 222, 232, 241, 291, 298, 356-360, 381
Translation 301-303
Transmission coefficient 240, 241, 309, 313, 317, 323, 335, 347-339
Triionic structures 198
Triplet state 173, 174, 177, 180, 186-188, 190, 194, 196, 205, 207
Tunneling 291, 292, 308, 309, 313-324, 326-332, 336-337, 355, 362, 363, 382
Valence Bond 102, 111, 112, 116-118, 120, 121, 125, 133, 136-138, 143, 144 165-167, 179, 191, 193, 194, 196, 197, 200, 203, 207-210, 213
Van Vleck method 379
Variational transition state theory 292, 381
VB determinants 165, 167-175, 178, 180, 185, 211, 215
VB-mixing diagram 173, 176, 179, 181-183, 185-190, 195, 199
VBCM 165
Vertical excitations energies 208-210
Yamanouchi-Kotani 121-123, 126
Z-matrix 36-44, 46-47, 376
Zwitterionic determinants 173, 175, 177-179, 194-196